

ATMOSPHERIC PLUME MODELING WITH APPLICATIONS TO COOLING TOWERS

by

Shuo Li

A thesis submitted in partial fulfillment of the requirements for the degree of

Doctor of Philosophy

Department of Mechanical Engineering

University of Alberta

© Shuo Li, 2020

Abstract

Visible plumes discharged by cooling towers have gained much attention due to their negative aesthetic and environmental impact. To achieve plume abatement, many previous designs mix warm, dry air with the hot, humid air rising from the cooling tower fill in the plenum chamber and thereby generate an air mixture that is unsaturated upon discharge. Here, we allow only partial mixing within the plenum chamber and the mixing continues above the cooling tower in the form of a wet plume core shielded by a dry plume envelope, i.e. a so-called coaxial plume. This coaxial plume structure is modeled via a three-way entrainment formulation between the inner and outer plumes and the ambient. Theoretical results predict that the inner plume rises quickly but shrinks until it disappears at some height. As the dry air mixing fraction (DAMF) increases, there is less likelihood of fog formation and/or recirculation. To further validate our theory and to inform the quantification of entrainment coefficients whose values cannot be obtained analytically, planar laser-induced fluorescence experiments have been performed. A pixel-by-pixel comparison of the scalar concentration images generated respectively by theory and experiment is conducted in order to determine the optimal entrainment coefficients. Experiments consider a still ambient, but a wind may be included in a similar fashion to the theoretical model, assuming, somewhat optimistically, that the axial symmetry is not broken. To this end, and in a windy environment, the inner plume is more rapidly cut off by the outer plume with increasing wind speed. For fixed DAMFs, the visible plume length varies nonmonotonically with the wind speed. Moreover, nontrivial differences in the visible plume length are predicted using two different entrainment formulations.

In contrast to a single plume, multiple plumes tend to merge and thereby the dilution

characteristics are modified. Another major objective of this thesis is to explore the effect of plume merger under different cooling tower configurations. Previous theoretical descriptions of plume merger often consider nearly idealized plume sources, which are probably inappropriate in the case of the large area source plumes discharged by e.g. cooling towers. For two adjacent area source plumes, a theoretical model is proposed whereby (i) the boundaries of the merging plumes are prescribed and (ii) the entrainment coefficient varies exclusively with the plume boundary curvature. Theoretical results (full merger height, the total volume flux, etc.) are in good agreement with previous theoretical and experimental data.

Finally, we investigate the merging of long rows of plumes, which include (i) dual rows of plumes in a quiescent environment and (ii) a single row of plumes in a crosswind. With a moderate to large vertical to horizontal spacing ratio, the theory of the dual row case predicts an intermediate line plume scaling before approaching the far-field line plume limit. The theory describing a single row of plumes in a crosswind predicts the correct near- and far-field similarity limits. Model results of plume trajectories agree satisfactorily with previous theoretical and experimental data.

Preface

This thesis is an original work by Shuo Li. All the novel theoretical formulations in the thesis are derived by Shuo Li with the assistance of Dr. Morris Flynn. Moreover, the experimental set-up presented in Chapter 4 was designed by Shuo Li with some assistance from Univ. of Alberta MECE Machine shop and Cameron Science & Technology Library.

Chapter 2 of this thesis has been submitted for publication as **Li, S.** & Flynn, M.R. Cooling tower plume abatement and plume modeling: A review. (submitted to *Journal of Wind Engineering and Industrial Aerodynamics*). Chapter 3 has been published as **Li, S.**, Moradi, A., Vickers, B. & Flynn, M.R. (2018). Cooling tower plume abatement using a coaxial plume structure. *International Journal of Heat and Mass Transfer*, 120, 178-193. Chapter 4 has been submitted for publication as **Li, S.** & Flynn, M.R. Coaxial plumes: theory and experiment. (submitted to *International Journal of Heat and Mass Transfer*). Chapter 5 has been published as **Li, S.** & Flynn, M.R. (2020) Coaxial plumes in a windy ambient with applications to cooling towers. *Journal of Wind Engineering and Industrial Aerodynamics*, 196, 104054. Chapter 6 has been published as **Li, S.** & Flynn, M.R. (2020) Merging of two plumes from area sources with applications to cooling towers. *Physical Review Fluids*, 5, 054502. Chapter 7 has been submitted for publication as **Li, S.** & Flynn, M.R. Merging of long rows of plumes: Crosswinds, multiple rows and applications to cooling towers. (submitted to *Physical Review Fluids*). Shuo Li (name in bold) was both the leading author and the corresponding author for all the submitted or published manuscripts. Dr. Morris Flynn was the supervisory author and was involved with concept formulations and manuscript revisions.

The Master said, in the morning, hear the Way; in the evening, die content.

– CONFUCIUS

Acknowledgements

First and foremost, I wish to thank my PhD supervisor, Dr. Morris Flynn, for his guidance and support during the past five years. Morris is definitely a great teacher, a responsible graduate student supervisor and a trustworthy collaborator to work with. I am deeply grateful to him for teaching me the fundamental knowledge of fluid dynamics and giving me freedom to work on topics of my own interest. I also wish to thank Drs. Bruce Sutherland and Marc Secanell for their constructive suggestions in the supervisory committee meetings. As far as I know, Bruce and Marc are very passionate researchers in their own fields, and Bruce is one of the fluid dynamicists who I admire most. In particular, I have worked in Bruce's laboratory for about two years, which is both challenging and enthusiastic. In retrospect, there are several times that I was quite rude to the above senior researchers in either weekly research meetings or supervisory committee meetings. Even so, they are always tolerant, generous and supportive to this uncultured student. I also wish to thank Drs. Scott Socolofsky and Jaime Wong for reviewing my thesis and raising some good questions during my defense.

Many senior group members have helped in training me as a serious researcher. These include: Ali Moradi, a former MSc student, who generously delivered his Matlab code to me on which basis I later developed my own code; Chunendra Sahu, a former PhD student, who kindly transferred his research and teaching experience to me; Yongxing Ma, a former PhD student, from whom I learned a lot about plume theories and experiments. I also quite enjoy working with the other researchers and our industrial partners in the cooling tower project. These mainly include: Lisa Clare, Aditya Kodkani, Harshil Pisavadia, Brad Vickers and Mitch Nicholson.

Regarding the specific plume study, I am deeply indebted to many great authors of plume theories. Precisely speaking, the plume theories developed in my thesis are essentially on the basis of the original work of Drs. Gary Hunt, Gabriel Rooney and Nigel Kaye. A short

conversation with Dr. Colm Caulfield on coaxial plumes is also greatly acknowledged, with thanks. Mentioning these plume experts keeps reminding me that I know very little about plumes and I have not written a paper of such originality.

My gratitude also goes to some friends that I have made in Edmonton. These include my office mates, Bharath Kattamalalawadi, Mitch Baker and Imran Khan, and a number of Chinese friends. Of the most importance to me is the continuous support from my girlfriend, Xuehui Lei, who has accompanied me in the most difficult times. Looking back on the past few years, I wish that I had devoted less time to my research but more time to her. No matter what happens to us in the future, I will always remember those days when we were poor graduate students and we were very happy together.

Finally, I wish to thank my family members in China, including my grandfather, mother, father, sister and nephew. This thesis cannot be accomplished without their long-lasting support and love.

Financial support was generously provided by Natural Sciences and Engineering Research of Canada (NSERC), International Cooling Tower Inc. and the China Scholarship Council (CSC).

Contents

1	Introduction and overview	1
1.1	Background	1
1.1.1	Turbulent plume models	1
1.1.2	Laboratory experimental modeling	8
1.2	Atmospheric plumes and their relation to cooling towers	11
1.3	Knowledge gaps	14
1.4	Thesis scope and outline	15
1.5	Appendix A: Entrainment coefficient for plume in a stationary ambient	16
1.5.1	Connection between PB and MTT models	17
1.5.2	Further discussion	21
2	Cooling tower plume abatement and plume modeling: A review	22
2.1	Abstract	22
2.2	Introduction	22
2.3	Plume visibility	26
2.4	Visible plume abatement	27
2.4.1	Superheating the exhaust air	28
2.4.2	Enhanced mixing by static devices	29
2.4.3	Enhanced mixing by stirring devices	31
2.4.4	Coaxial plume mixing	32
2.4.5	Water conservation and recovery	34
2.5	Plume modeling	37
2.5.1	Analytical models	37
2.5.2	CFD models (single and multiple sources)	42
2.5.3	Similitude laboratory experiments (single and multiple sources)	46
2.5.4	Plume in a turbulent environment	48
2.5.5	Plume bifurcation	51
2.5.6	Cooling tower drift	53
2.6	Conclusions	55
3	Cooling tower plume abatement using a coaxial plume structure	57
3.1	Abstract	57
3.2	Introduction	57
3.3	Theory for uniform plumes and its application to counterflow cooling towers	59
3.3.1	Formulation	61
3.3.2	Representative solutions	64
3.3.3	Discussion	66
3.4	Theory for coaxial plumes and its application to crossflow cooling towers	68
3.4.1	Formulation	68
3.4.2	Representative solutions	71
3.5	How much mixing should occur in the plenum of a crossflow cooling tower?	78
3.5.1	Hybrid cooling tower calculations – the effectiveness-NTU method	78
3.5.2	Visible plume resistance and recirculation	78
3.6	Conclusion and future work	83

3.7	Appendix A: Plume merger	84
3.7.1	Uniform plumes	84
3.7.2	Coaxial plumes	86
3.8	Appendix B: Hybrid wet/dry cooling tower calculation	87
3.8.1	Effectiveness-NTU method for a crossflow dry section	87
3.8.2	Effectiveness-NTU method for a crossflow wet section	89
3.8.3	The PPWD crossflow cooling tower calculation	90
4	Coaxial plumes: theory and experiment	92
4.1	Abstract	92
4.2	Introduction	92
4.3	Theory of coaxial plumes in a homogeneous ambient	94
4.3.1	Coaxial plumes	95
4.3.2	Body force formulation	97
4.3.3	The merged single plume	97
4.3.4	Nondimensionalization and reformulation to solve for \hat{r}_1 , \hat{r}_2 , \hat{U}_1 , \hat{U}_2 and Γ_1	98
4.3.5	Representative solutions	100
4.3.6	Entrainment coefficients	101
4.4	Laboratory experiments	103
4.4.1	Experimental set-up	103
4.4.2	Experimental results (qualitative)	106
4.4.3	Experimental results (quantitative)	107
4.5	Theory vs. experiment	110
4.5.1	Pixel-by-pixel comparison	110
4.5.2	Centerline and radial concentration profiles	113
4.6	Applications to cooling tower plume abatement	116
4.7	Conclusions	118
4.8	Appendix A: BFI and BFII formulations	119
4.9	Appendix B: Post-processing of PLIF images	120
4.10	Appendix C: Complimentary data to table 4.1	122
4.11	Appendix D: Pixel-by-pixel comparison for uniform plumes	124
5	Coaxial plumes in a windy ambient with applications to cooling towers	127
5.1	Abstract	127
5.2	Introduction	127
5.3	Theory for uniform plumes in a windy ambient	129
5.3.1	Formulation	129
5.3.2	Representative solutions	135
5.4	Theory for coaxial plumes in a windy ambient	137
5.4.1	Formulation	137
5.4.2	Entrainment coefficient and body force formulation	141
5.4.3	Representative solutions	141
5.4.4	Sensitivity of theoretical results to entrainment coefficients	147
5.4.5	Coaxial plumes under various ambient and source conditions	147
5.5	Conclusions	152
5.6	Appendix A: Plume merger in a crosswind	154
6	Merging of two plumes from area sources with applications to cooling towers	157
6.1	Abstract	157
6.2	Introduction	157
6.3	Rooney's theory	160
6.3.1	Complex potential	160
6.3.2	Flow speed, flux and area integrals	162
6.3.3	Plume theory	162

6.4	Alternate form for f_m	165
6.4.1	Plume-boundary curvature	165
6.4.2	Height of full merger	167
6.4.3	Comparison with previous theoretical and experimental results	167
6.5	Finite source effect	168
6.5.1	Modified contours approximating plume boundaries	168
6.5.2	Flow speed and cross-sectional area	170
6.5.3	Entrainment flux	170
6.5.4	Representative results	171
6.5.5	Effects of varying ρ_0 and Γ_0	173
6.5.6	Comparison with the saline plume experiment of Davis <i>et al.</i> (1977)	174
6.5.7	Extreme case of $\rho_0 = 1$	175
6.6	Applications to cooling towers	176
6.6.1	Governing equations	176
6.6.2	Representative results	177
6.7	Conclusions	179
6.8	Appendix A: A note on the derivation of (6.34)	182
6.9	Appendix B: Note on $n \geq 3$ area source plumes	183
6.10	Appendix C: Entrainment flux for sources with $\rho_0 > 0$	183
7	Merging of long rows of plumes: Crosswinds, multiple rows and applications to cooling towers	186
7.1	Abstract	186
7.2	Introduction	186
7.3	Single row of infinite line sinks (Rooney's theory)	188
7.3.1	Irrotational flow theory for entrainment flow	188
7.3.2	Plume equations and entrainment closure	189
7.3.3	Merging plumes in an unstratified ambient	190
7.3.4	Representative solution	191
7.4	Two rows of infinite line sinks	192
7.4.1	Non-offset parallel line sinks	192
7.4.2	Offset parallel line sinks	196
7.4.3	Effective entrainment perimeter	202
7.5	Plume merger in a neutral crosswind	204
7.5.1	Formulation	204
7.5.2	Near- and far-field similarity scalings	205
7.5.3	Representative results	207
7.5.4	Comparison with the towing tank experiments of Kannberg & Davis (1976)	207
7.6	Applications to cooling towers	209
7.7	Conclusions	211
7.8	Appendix A: Entrainment flux calculation using the stream function	213
7.9	Appendix B: Comparison between the present theory and Wu & Koh (1978)	214
8	Conclusions and future work	217
8.1	Conclusions	217
8.1.1	Coaxial plumes	217
8.1.2	Plume merger	218
8.1.3	Limitations	219
8.2	Future work	220
8.2.1	Plume abatement	220
8.2.2	Plume studies	222
	References	225

Appendix A Derivation of the integral form of governing equations for a uniform plume in stationary ambient	242
A.1 Conservation of mass	242
A.2 Conservation of momentum	244
A.3 Conservation of any scalar component	246
A.4 Governing equations for a uniform cooling tower plume	249
Appendix B Derivation of the integral form of governing equations for a coaxial plume in stationary ambient	251
B.1 Conservation of volume, thermal energy and moisture	251
B.2 Momentum conservation - BFI	254
B.3 Momentum conservation - BFII	254
Appendix C Derivation of the integral form of governing equations for a uniform plume in windy ambient	257
C.1 Control volume analysis for uniform plume in a windy ambient	257
C.2 Entrainment in a windy ambient	261
C.3 Dry uniform plume theory vs. experiment	262
Appendix D Point source vs. line source plumes	267
D.1 Stationary ambient	267
D.2 Windy ambient	268
Appendix E Effect of condensation on plume dynamics	270
Appendix F Merging of two area source plumes in a linearly stratified ambient	273
F.1 Theory of He & Lou (2019)	273
F.2 Finite source effect	274
F.3 Maximum rise height	275

List of Tables

1.1	Publications arising from the thesis.	16
2.1	The evolution of plume abatement designs as summarized in Lindahl & Mortensen (2010).	28
2.2	Three hybrid cooling technologies compared to a typical counterflow wet cooling tower.	36
3.1	Representative operating and environmental conditions for a single cooling tower cell and a line array of $n = 9$ cells.	64
3.2	Sensitivity of $Z_{c,5\%}$ to variations in the values of the entrainment coefficients α , β and γ	73
3.3	Input parameters for a hybrid cooling tower calculation.	78
3.4	Output parameters for a hybrid cooling tower calculation.	79
4.1	Summary of the source conditions for the inner and outer plumes. The experiments consider an outer plume that is dyed with Rhodamine 6G. Densities are considered accurate to within $\pm 0.00005 \text{ g/cm}^3$, volume flow rates to within $\pm 0.083 \text{ cm}^3/\text{s}$ and velocities to within $\pm 0.14 \text{ cm/s}$. The background fresh water density is $\rho_a = 0.9982 \text{ g/cm}^3$. The source velocities U_{10} and U_{20} are fixed whereas the source densities ρ_{10} and ρ_{20} are variable. The combination of Q_{10} and Q_{20} are chosen to ensure that the total source volume flux and momentum flux are approximately the same for all experimental categories.	106
4.2	Environmental and operating conditions for the cooling tower example considered in section 4.6.	117
4.3	Source Reynolds number, flux-balance parameter, inner potential core height, cut-off height of the inner plume and optimal entrainment coefficients (β and γ) for experimental categories A, B, C and D.	123
4.4	Source conditions for the uniform plume experiments. The nozzle diameter was $D_0 = 0.4 \text{ cm}$. The ambient fresh water density was measured as $\rho_a = 0.9983 \text{ g/cm}^3$	125
5.1	Representative operating and environmental conditions for a single cooling tower cell and a single row of $n = 9$ cells.	135
6.1	Height of full merger predicted by R15, R16, the present analysis and measured/predicted in Kaye & Linden (2004).	167
6.2	Heights of first contact and full merger and the far-field virtual origin correction for the source conditions considered in figure 6.9. Values correspond, in sequence, to the original model (6.19), the revised model (6.24) with $S = 0.1$ and with $S = 1$, and the curvature method (6.31).	172
6.3	Representative operating and environmental conditions for cooling towers (Kröger, 2004).	178
7.1	Representative operating and environmental conditions for the back-to-back and single row cooling towers illustrated in figure 7.20 (Kröger, 2004).	211

C.1	“Top-hat” entrainment coefficients (γ_1 and γ_2) for plume in a crosswind. . .	262
C.2	Experimental conditions for turbulent plumes in neutral crossflows (Contini & Robins, 2001).	264
F.1	Cases with nonnegligible ρ_0 in table I of He & Lou (2019). The numbers in brackets correspond to the case numbers in table I of He & Lou (2019). . . .	276

List of Figures

1.1	Schematic of an axisymmetric plume in a linearly stratified ambient.	4
1.2	For a point source plume in a linearly stratified ambient, panel a shows the solutions of fluxes of volume, momentum and buoyancy and panel b shows solutions of plume radius, vertical velocity and reduced gravity. Results are obtained with $F_0 = 1 \text{ m}^4/\text{s}^3$, $N = 1 \text{ s}^{-1}$ and $\alpha = 0.13$ (from MTT).	5
1.3	Schematics of plume behaviors in unstratified environments with different Γ_0 . The arrows denote the flow directions. Panel (b) illustrates that a contraction occurs near the source for a lazy plume with $\Gamma_0 > 5/2$. Panel (c) illustrates the upflow and downflow in a turbulent fountain.	6
1.4	Schematic of a plume element under Lagrangian frame of reference.	8
1.5	[Color] Two instantaneous images of a turbulent plume. The dark regions denote the dense plume fluid and the surrounding small dark spots denote the small particles in the PIV experiments. The red arrows denote the two-dimensional velocities measured on the centerplane of the plume. The green circles indicate the small velocities just outside and inside the plume edge at the locations where eddies are locally present. By contrast, the red circles indicate the relatively large velocities at the locations where eddies are locally absent. (Copied from figure 1 of BurrIDGE <i>et al.</i> 2017 with permission)	10
1.6	[Color] Instantaneous PLIF images (labels denote the sequence of images with a constant time interval) of the cross section of a turbulent plume in a cross-flow. (Copied from figure 8 of Diez <i>et al.</i> 2005 with permission)	11
1.7	Schematic of plume rise in a stably stratified and windy environment. The three stages of plume rise, i.e. quasi-vertical, quasi-horizontal and final rise stages, are labeled.	12
1.8	Visible plumes above a single row of cooling tower cells. (Photo used with permission of International Cooling Tower Inc.)	13
2.1	Schematic of a counterflow wet cooling tower. The thick white and black arrows denote the incoming ambient air into the cooling tower and the hot, humid air coming out of the wet section, respectively. The thin arrows denote the water stream.	23
2.2	Schematic of a crossflow wet cooling tower. Arrow types are as in figure 2.1. Note that the fill is installed at an angle to the vertical to account for the inward motion of water droplets due to the drag associate with the incoming air (Kröger, 2004).	24
2.3	(a): A fogging frequency curve from Winter (1997). Similar curves can be found in figure 15 of Lindahl & Jameson (1993) or figure 2 of Lindahl & Mortensen (2010). (b): Method of generating the fogging frequency curve.	26
2.4	Visible plume potential defined in Tyagi <i>et al.</i> (2007).	27
2.5	A water/air cooled flat plate solar collector to heat the exhaust from wet cooling towers.	29
2.6	The tapered V-shaped deflecting surface proposed by Carbonaro (1983).	30
2.7	Schematic of air ducts in a forced draft cooling tower (Ruscheweyh, 1985).	31

2.8	The model scaled experiment of plenum chamber without (left) and with (right) the delta-shaped mixer (Ruscheweyh, 1985). The dashed curves denote the boundary between the wet and dry air streams in the absence of any internal mixing device.	32
2.9	The stirring vortex mixing device proposed by Moon (2017).	32
2.10	The plume abatement cooling tower illustrated in Koo (2016 <i>a,b</i>). (Figure taken from Li <i>et al.</i> 2018)	33
2.11	[Color] (a): Schematic of an Air2Air TM heat exchanger (Mortensen, 2009). (b): Psychrometric processes of Air2Air TM technology for plume abatement.	34
2.12	Schematic of the passive vapor recovery technology consisting of a thermosyphon and porous media in a crossflow cooling tower (Mantelli, 2016).	35
2.13	Plumes under neutral (left) and stably stratified (right) crosswinds.	39
2.14	(a): Plume merger occurs when the area of the central trapezoid bounded by dashed lines is the sum of the areas of the two half round plumes on both sides. (b): The induced flows into the two adjacent plumes are represented by link sinks $\Omega = -\frac{m}{2\pi} \ln Z$ and $\Omega = -\frac{m}{2\pi} \ln (Z - \chi)$, where m is the line sink strength and $Z = x + iy$	41
2.15	[Gray scale] Initial and boundary conditions used in the CFD simulation of Takata <i>et al.</i> (2016). The fan exit velocity distributions (U , V and W) measured in Takata <i>et al.</i> (1996) are used as the velocity boundary conditions. Measured ambient dry- and wet-bulb temperatures and the wind speed are also used as the boundary conditions. The exiting air velocity, temperature and moisture of the wet and dry sections are determined from design calculations. (Figure taken from Takata <i>et al.</i> 2016)	44
2.16	[Gray scale] Effect of wind speed on the scale of the visible plume produced above a hybrid wet/dry cooling tower; wind speeds of (a) 0, (b) 1 m/s, (c) 3 m/s and (d) 5 m/s are considered. (Figure taken from Takata <i>et al.</i> 2016)	44
2.17	Plume velocity vector map near the tower exit in a crosswind. (Figure taken from Klimanek <i>et al.</i> 2015)	45
2.18	Wind tunnel experimental set-up of Liu & Bao (2014). Dry ice is put inside each cooling tower cell for flow visualization. Carbon monoxide is used as a tracer whose concentrations at the inlet and outlet of the tower are measured to determine the recirculation ratio.	47
2.19	A water channel experimental image of a plume in a stably stratified crossflow (Contini <i>et al.</i> , 2011). The plume starts to oscillate after reaching its maximum rise height. (Figure taken from Contini <i>et al.</i> 2011)	48
2.20	Schematics of mechanical and convective turbulence.	48
2.21	Division of plume modeling suggested by Hamza & Golay (1981). The effective stack height, $h_{\text{eff}} = h_{\text{stack}} + l_{\text{b}}$, where h_{stack} is the stack height measured from the ground and l_{b} is a so-called buoyancy length defined as the radius of curvature of a pure plume at the stack exit.	50
2.22	Vortex motion at different elevations of a plume in a crosswind. At cross section A, the plume behaves like a jet that has a circular cross section. At this stage, the plume's self-generated turbulence is dominant in the dilution process. At cross section B, the edge of the plume is sheared off by the wind thus resulting in a kidney-shaped cross section. Thereafter at cross section C where the plume is fully bent-over, the dilution process is dominated by the interaction between the two counter-rotating line vortices and the ambient crossflow. (Fanaki, 1975)	51

2.23	Image effect of the free surface on the vortex pairs A–B. The free surface acts as an image plane in which the vortex pairs A–B are mirrored, thus creating the image vortex pairs C–D. The velocity induced at vortex A (or B) by the other vortices B, C and D (or A, C and D) is vectorially represented using the corresponding lower-case letters. Note that the resultant horizontal velocity vectors at vortex A are opposite to those of vortex B, which leads to the separation of the vortex pairs. (Ernst <i>et al.</i> , 1994)	52
2.24	(a): Plume trajectories from Lucas <i>et al.</i> (2010), Meroney (2006), the 1977 Chalk Point Dye Tracer Experiment and Briggs’ plume rise formulae. (b): Drift deposition rates (mass/area/time) from Lucas <i>et al.</i> (2010), Meroney (2006), the 1977 Chalk Point Dye Tracer Experiment and the Industrial Source Complex (ISC3) Dispersion Models. The definition of drift deposition rate in CFD simulations is given in Meroney (2006). (Figure taken from Lucas <i>et al.</i> 2010)	54
3.1	Schematic of a PPWD counterflow cooling tower. The white arrows denote the ambient air. The black and light gray arrows denote, respectively, the hot, saturated air from the wet section and the warm, dry air from the dry section. The dark gray arrows at the top of fan shroud denote the resulting well-mixed air stream (We assume complete mixing within the plenum chamber.). In the dry section, t_a is the ambient dry-bulb temperature, t_{wb} is the ambient wet-bulb temperature, t_d is the temperature of the sensibly heated air from the dry section (also called the dry cooling temperature), T_{D1} is the dry section inlet water temperature, T_{D2} is the dry section outlet water temperature, $R_D = T_{D1} - T_{D2}$ is the range temperature in the dry section and $A_D = T_{D2} - t_a$ is the approach temperature in the dry section. For the wet section, t_w is the temperature of the saturated moist air discharged from the drift eliminator, T_{W1} is the wet section inlet water temperature where, ideally, $T_{W1} = T_{D2}$. Moreover, T_{W2} is the wet section outlet water temperature, $R_W = T_{W1} - T_{W2}$ is the range temperature in the wet section and $A_W = T_{W2} - t_{wb}$ is the approach in the dry section. Finally, t_0 is the temperature of the well-mixed air at the top of the fan shroud/base of the (uniform) plume.	60
3.2	The coordinate system associated with a (four cell) cooling tower in a still ambient. The z axis points upwards, i.e. out of the page.	61
3.3	[Color] Non-dimensional plume excess temperature (panel a) and relative humidity (panel b) as functions of height where $Z \equiv z/D_0 = 0$ corresponds to the top of the fan diffuser. Panel c shows the plume temperature, specific humidity and the corresponding non-dimensional elevations on the psychrometric chart. Ambient and operating conditions are specified in table 3.1. . .	65
3.4	The hybrid cooling tower design of Koo (2016a, 2016b). Visible plume abatement is achieved by enveloping the wet air stream within a sheath of drier air.	67
3.5	As in Figure 3.1 but with a different fill configuration and internal structure inside the plenum chamber. A limited amount of dry air is mixed into the wet air inside the plenum. The remaining fraction is assumed to leave the tower without mixing so that it envelopes the core of wetter air upon discharge to the atmosphere.	67
3.6	Coaxial plume structure. Entrainment from the outer plume to the inner plume, from the inner to the outer plume and from the ambient to the outer plume are parameterized by entrainment velocities ω_α , ω_β and ω_γ , respectively. Meanwhile, r_1 and r_2 are the respective characteristic radii for the inner and outer plumes. ω_α , ω_β and ω_γ are defined by equation (3.24).	69

3.7	[Color] Non-dimensional plume radii (panel a), vertical velocities (panel b) and reduced gravities (panel c) as functions of height. The solid black curves in panel c denote the non-dimensional body force $(g'_1 - g'_2 + U_2 \frac{dU_2}{dz})/g$ in the inner plume. Labels of 5% and 95% denote the dry air mixing fraction (DAMF).	72
3.8	[Color] Non-dimensional plume temperature (panel a) and relative humidity (panel b) as functions of height. Solid curves show the results of a single cooling tower cell, with blue for the inner plume and red for the outer plume. Labels of 5%, 50% and 95% denote the dry air mixing fraction (DAMF).	75
3.9	[Color] As in figure 3.7 but with $\frac{\dot{m}_d}{\dot{m}_w} = 0.3$ and 5% DAMF.	76
3.10	[Color] As in figure 3.8 but with $\frac{\dot{m}_d}{\dot{m}_w} = 0.3$.	77
3.11	[Color] (a) plume velocity vs. relative humidity. (b) resistance factor vs. height. (c) resistance factor, averaged over height, vs. DAMF. For the single cell case, 5%, 50% and 95% DAMFs are presented, while for multiple cells only 5% DAMF is shown in panels (a) and (b). In panel (c), the maximum relative humidities are specified for select DAMF.	80
3.12	[Color] As with figure 3.11 but with ambient temperature $t_a = -10^\circ\text{C}$, and other input parameters remain the same in table 3.3.	82
3.13	Regime diagram indicating the combinations of ambient temperature and relative humidity for which a coaxial plume structure is (to the right of the curves) and is not (to the left of the curves) advantageous. Only single cell results are presented; results for multiple cells are qualitatively similar.	83
3.14	A cross-sectional view of the merged plume shape. The dashed circles represent the individual plumes at the moment that the merging criterion is satisfied and the solid curve shows the geometry of the merged plume.	85
3.15	A cross-sectional view of the modified shape of the merged plume. The calculated plume cross-section shape (dashed line), defined by a and b , shows discontinuities at the junctions of the slot and round plumes. A modified smooth plume cross-section (solid line), defined by A and B , is proposed according to equations (3.54) and (3.55).	86
3.16	A cross-sectional view of four coaxial plumes upon merging. The solid curves or circles represent the merged coaxial structure.	87
3.17	The dry section calculation diagram.	88
3.18	The wet section calculation diagram.	89
3.19	The PPWD crossflow tower calculation diagram. Figures B.1 and B.2 corresponds to figures 3.17 and 3.18, respectively.	91
4.1	(a): Schematic of a coaxial plume in a stationary ambient. The cone-shaped region bounded by the dashed black line is the inner plume. $D_{10} = 2r_{10}$ and $D_{20} = 2r_{20}$ are the respective source diameters for the inner and outer plumes. ρ_a , ρ_1 and ρ_2 are the densities of the ambient fluid, the inner and outer plumes, respectively. The entrainment velocities (ω_α , ω_β and ω_γ) are labeled and the corresponding directions are indicated by the solid arrows. (b): The cone-shaped regions bounded by the dotted lines are the inner and outer potential cores, respectively. z_p and z_c are, respectively, the inner potential core height and the cut-off height of the inner plume; these are defined in section 4.4.3.	94
4.2	[Color] Effects of varying Γ_{20} (a, c and e) and \hat{U}_{10} (b, d and f) on plume radii, vertical velocities and flux-balance parameters. The letters I, O and U represent the inner and outer plumes and the merged uniform plume, respectively.	102
4.3	Schematic of a turbulent fountain. The flow is initiated by a negatively buoyant jet, which grows in size and slows down due to its negative buoyancy (left sketch). After reaching the initial (or maximum) fountain height, the flow reverses its direction and a plume-like downflow surrounds the jet-like upflow (right sketch).	103

4.4	Schematic of the PLIF experimental set-up including the laser optics. The coaxial plumes consist of an inner circular plume (shaded gray) and an outer annular plume (shaded black).	104
4.5	A cross-cut view of the coaxial nozzle. The inner nozzle and outer shell were connected by a threaded connection and were 3D printed using PLA and ABS plastics, respectively. The locations labeled with crosses show where the wire crosshairs were inserted. Note that the inner diameter of the inner nozzle is 8 mm and the inner slot has a thickness of 0.1 cm. As a first approximation, the source diameter for the inner fluid is $D_{10} = 0.9$ cm.	105
4.6	[Gray scale] Instantaneous images showing vortex roll-up for the coaxial plumes of experiments A3, B3, C3 and D3.	107
4.7	[Gray scale] As in figure 4.6 but showing time-averaged rather than instantaneous images. In each case, images are generated by averaging together 500 snapshot images, collected over a time interval of 255 s.	108
4.8	Log-log mean centerline concentration with corresponding “-5/3” dashed line (panels a and b) and log-log centerline standard deviation with corresponding “-5/3” dashed line (panels c and d) of coaxial plumes in experiments A3 (left) and D3 (right), respectively. The “-5/3” relationship is anticipated from the work of Papanicolaou & List (1987, 1988).	109
4.9	Radial concentration profiles at successive downstream distances for experiment A3.	110
4.10	Radial concentration profiles (panels a and b) and radial standard deviation profiles (panels c and d) for experiments A3 (left) and D3 (right) at successive downstream distances, i.e. $z/D_0 = 2, 4, 6, 8$ and 10. The radial mean concentration and standard deviation are non-dimensionalized by the corresponding maximum radial mean concentration, c_m	111
4.11	Φ -minimizing values of β_{lb} (panel a), γ_{lb} (panel b), β_{ub} (panel c) and γ_{ub} (panel d) for experiments A, B, C and D. The legend indicates the number within each experimental category, e.g. A1, A2, A3, A4 and A5. The different symbols thereby show the effect of changing the source velocities of the inner vs. the outer plume. The horizontal lines denote the mean entrainment coefficients in each panel. A representative error bar is shown in panel d.	112
4.12	[Color] Comparison of the centerline concentration profiles in experiments A1, A5, B1, B5, C1, C5, D1 and D5.	114
4.13	[Color] Comparison of the radial concentration profiles in experiments A1, A5, B1, B5, C1, C5, D1 and D5 with the same sequence as in figure 4.12.	115
4.14	Uniform and coaxial plumes in the cooling tower context. The black arrows (above the drift eliminator) and white arrows (close to the heat exchangers) denote the hot, humid air from the wet section and the warm, dry air from the dry section, respectively. The light gray arrows at the fan exit denote the air mixture formed by complete or partial mixing within the plenum chamber. The variables t_w and t_d denote the respective temperatures of the wet and dry airstreams. We consider $z = 0$ as coinciding with the top of the fan diffuser.	116
4.15	Theoretical prediction of the relative humidity, excess temperature, radius and vertical velocity of the inner and outer plumes for the example considered in section 4.6. Note that the inner plume disappears when $z/D_0 = 4.8$	118
4.16	Variation of the mean pixel intensity within a mask from 1000 calibration images taken in a duration of approximately 8.5 mins. The dashed white line denotes the time-averaged intensity over the time interval in question.	121
4.17	Schematic of the calibration tank that contains a homogeneous concentration of Rhodamine 6G. The dimensions of the tank were 6 cm \times 6 cm \times 20 cm (length \times width \times height). The incremental dye concentrations were 0, 0.01, 0.02, 0.03, 0.04, 0.05, 0.06, 0.07, 0.08, 0.09, 0.10, 0.12, 0.14, 0.16, 0.18, 0.20, 0.22, 0.24, 0.26, 0.28 and 0.30 mg/L.	122
4.18	Laser light attenuation in the calibration tank of figure 4.17.	124

4.19	Φ -minimizing entrainment coefficient as a function of Γ_0 . The horizontal line denotes the average entrainment coefficient of 0.106. Error bars are of a size comparable to the marker symbols and are therefore omitted.	125
4.20	Φ -minimizing entrainment coefficient as a function of varying Z_{\max}	126
5.1	Definition sketch. s and n are the streamwise and normal coordinates, respectively. x and z are the horizontal and vertical coordinate axes, respectively. λb ($\lambda \geq 1$) and b are the respective major and conjugate radii of the elliptical cross section.	129
5.2	Non-dimensional plume excess temperature (panel a) and relative humidity (panel b) as functions of plume rise height. Panel (c) illustrates the plume temperature, specific humidity and the corresponding non-dimensional vertical elevations on the psychrometric chart for the case of single cell with $U_a/U_0 = 0.5$. The environmental and operating conditions are specified in table 5.1.	133
5.3	Non-dimensional plume centerline trajectories (panel a), vertical velocities (panel b) and streamwise velocities (panel c) as functions of plume rise height. The source conditions are the same as in figure 5.2.	134
5.4	Surface plots of visible plume length for different ambient temperatures, relative humidities and wind speeds.	138
5.5	Variations of entrainment velocity (left panel) and entrainment flux per unit height (right panel) with streamwise distance for different wind speeds. The ambient temperature and relative humidity are $t_a = 2^\circ\text{C}$ and $\text{RH}_a = 60\%$, respectively.	139
5.6	Schematic of a coaxial plume in a windy ambient. b_1 and b_2 are the conjugate radii of the inner and outer plumes, respectively. The respective streamwise velocities for the inner and outer plumes are U_1 and U_2	139
5.7	[Color] Non-dimensional plume centerline trajectories (panels a and b), conjugate radii (panels c and d) and streamwise velocities (panels e and f) as functions of plume rise height. Panels a, c and e correspond to an EI entrainment formulation whereas panels b, d and f correspond to an EII entrainment formulation.	142
5.8	[Color] Non-dimensional plume excess temperature (panels a and b) and relative humidity (panels c and d) as functions of plume rise height. Panels e and f illustrate the dilution curves for the inner (blue) and outer (red) plumes on the psychrometric charts.	143
5.9	[Color] Non-dimensional plume centerline trajectories (panels a and b), conjugate radii (panels c and d) and streamwise velocities (panels e and f) as functions of plume rise height. The thick dashed curves denote the results for multiple cooling tower cells.	145
5.10	[Color] Non-dimensional plume excess temperature (panels a and b) and relative humidity (panels c and d) as functions of plume rise height. Panels e and f illustrate the dilution curves for the inner (blue) and outer (red) plumes on the psychrometric charts. The thick dashed curves denote the results for multiple cooling tower cells.	146
5.11	[Color] Contour plots of the inner visible plume length (ΔS_1) as a function of α and β assuming an EI formulation. The reference entrainment coefficients are $\alpha_{\text{ref}} = 0.039$ and $\beta_{\text{ref}} = 0.065$	148
5.12	[Color] Contour plots of visible plume length (ΔS_1) under various dry air mixing fractions (DAMFs) and for different wind speeds assuming an EI entrainment formulation. Panels a, c and e correspond to the same t_a but different RH_a , whereas panels a, b, d and f correspond to the same RH_a but different t_a	149

5.13	The velocity differences between the inner and outer plumes as functions of streamwise distance for different wind speeds. The solid curves are labeled with values of U_a/U_0 with the dashed curve corresponding to the special case $U_a/U_0 = 1.4$. The other parameters are $t_a = 7^\circ\text{C}$, $\text{RH}_a = 70\%$ and $\text{DAMF} = 30\%$	150
5.14	[Color] As in figure 5.12 but assuming an EII entrainment formulation.	151
5.15	Surface plots of visible plume length under varying ambient temperature and relative humidity with $\frac{m_a}{m_w} = 0.3$ and $\text{DAMF} = 30\%$. The regions above the upper sawteeth in panels b, c and d correspond to conditions where fog forms in the outer plume. Note the difference of vertical axis limits between the top and bottom panels.	152
5.16	(a): Schematic of a line array of four tower cells that is perpendicular to the wind direction. (b): Top view of the cooling tower configuration with ϕ denoting the angle between the wind direction and the cooling tower axis.	154
5.17	A cross-sectional view of the merged plume in a crosswind. The dashed ellipses show the cross sections of individual plumes. The solid curve shows the geometry of the merged uniform plume.	155
5.18	A cross-sectional view of four coaxial plumes upon merging in a crosswind. The solid curves and ellipses show the geometry of the merged plume.	155
6.1	[Color online] Surface plots illustrating plume merger from small (panel a, $\rho_0 = 0.1$) and large (panel b, $\rho_0 = 0.6$) sources with $\Gamma_0 = 1$. The parameters, ρ_0 , Γ_0 , x/R , y/R and \hat{z} , are defined in section 6.3 below. The plume boundaries are shaded according to the height between 0 and 1, and these contours are also projected onto the bottom plane. Note that these results are produced using a so-called curvature method, which is outlined in section 6.4.	158
6.2	[Color online] Evolution of the plume cross section as described by Wu & Koh (1978). Panel (a) denotes the initial stage of two individual plumes. Panel (b) denotes the stage of first contact, however, no plume interaction occurs until full merger, which is depicted in panel (c) and which is defined as the elevation where the area of the central rectangle (shaded red) equals the sum of the areas of the two half round plumes (shaded blue). Panel (d) denotes a stage of the combined plume post merger. Panel (e) shows an axisymmetric plume in the very far field.	160
6.3	Sketch of two plumes from an area source of radius r_0 . As $r_0 \rightarrow 0$, the flow becomes identical to the $n = 2$ case exhibited in figure 1 of R16.	160
6.4	Contours of velocity potential in Z' -space. The numerical values of k are labeled. For closed contours with $k \leq 1$, the dashed (solid) curves represent the negative (positive) square root in (6.3).	161
6.5	Evolution of \hat{w} (panel a) and Γ_m (panel b) as predicted by the original model (dashed curve), revised model with $S = 0.1$ (solid curve) and with $S = 1$ (dash-dotted curve). The dotted lines in (a) denote the near- and far-field self-similarity solutions.	165
6.6	The evolution of f_m and Γ_m in the original model (dashed line or curve), revised model with $S = 0.1$ (dash-dotted curve) and with $S = 1$ (dotted curve) and the curvature method using (6.31) (solid curve). In contrast to figure 6.5 b, a virtual origin correction is not included because the small offset by \hat{z}_{vm} does not significantly alter the positions of the curves.	166
6.7	As in figure 6.4, but with $\rho_0 > 0$. (a) $\rho_0 = 1/3$, (b) $\rho_0 = 2/3$. The closed black circles in both panels denote the plume source.	169
6.8	Plume cross-sectional area as a function of k for different source radii, i.e. $\rho_0 = 0.1, 0.4, 0.8$ and 0.99 . The stars indicate where $k = 1 - \rho_0^2$	171

6.9	Non-dimensional vertical velocity (panels a and b) and volume flux (panels c and d) as functions of height for the original model (dashed curve), the revised model with $S = 0.1$ (solid curve) and with $S = 1$ (dotted curve) and the curvature method (solid curve). The thin dotted lines denote the far-field similarity solutions for \hat{w} and \hat{Q} , respectively.	172
6.10	Evolution of Γ_m for $\rho_0 = 0.1$ and $\rho_0 = 0.6$ with $\Gamma_0 = 1$	173
6.11	Evolution of Γ_m for $\rho_0 = 0.1$ and $\rho_0 = 0.6$ with $\Gamma_0 = 0.2, 0.4, 0.6, 0.8$ and 1	173
6.12	Effective entrainment with $\Gamma_0 = 1$ and $\rho_0 = 0.1, 0.3, 0.5, 0.7$ and 0.9 . The thin dashed vertical line denotes the far-field limit, $2^{-1/2}$	174
6.13	Comparison of the curvature method with the experimental data of Davis <i>et al.</i> (1977). The solid curve denotes the curvature method with $\alpha = 0.14$. The open diamonds correspond to volume flux measurements made at $z/D_0 = 10, 20$ and 30 . The dashed curve is a curve fit to all the experimental data of Davis <i>et al.</i> (1977).	175
6.14	[Color online] Plume volume flux for the limiting case of $\rho_0 = 1$ and $\Gamma_0 = 1$	176
6.15	[Color online] Height of full merger, \hat{z}_{fm} , as a function of the source flux-balance parameter, Γ_0 , with $\frac{\dot{m}_d}{\dot{m}_w} = 0.3$. Note that the variation in Γ_0 corresponds to the variation in the cooling tower exit velocity, w_0 . Meanwhile all other parameters correspond to the values given in table 6.3.	178
6.16	[Color online] Non-dimensional plume reduced gravity (panels a and b), vertical velocity (panels c and d) and relative humidity (panels e and f) as functions of height above the stack exit. The stack exit velocity is $w_0 = 6$ m/s.	180
6.17	[Color online] As in figure 6.16 but with a stack exit velocity of $w_0 = 10$ m/s.	181
6.18	Schematic illustrating the geometric details associated with (6.34). The left and right circles are centered at $C_1 (-1, 0)$ and $C_2 (1, 0)$, respectively and both have radius ρ_0 . From the point N , the straight lines NN_1 and NN_2 are tangent to the circles centered at C_1 and C_2 , respectively; N_1 and N_2 are the respective tangent points.	182
6.19	Flux integral as a function of k for various ρ_0 . Dashed curves follow (6.68) whereas the solid line follows (6.73).	185
7.1	Velocity potential contours for a range of p , i.e. $p = 0.1, 0.4, 0.7, 1, 1.2, 1.5, 2$ and 5 . The thick curve, which corresponds to $p = 1$, represents the height of first contact.	189
7.2	Evolution of \hat{w} and \hat{Q} as a function of \hat{z} . The horizontal dashed lines denote the height of first contact, $\hat{z}_{fc} = 0.340$. The solid straight lines denote the near-field ($p < 1$) and far-field ($p > 1$) similarity scalings.	191
7.3	[Color] Surface plot illustrating plume merger in a long row of plumes. The plume boundaries are shaded according to the height between 0 and 1 , and these contours are also projected onto the bottom plane.	192
7.4	Schematic of two non-offset parallel rows of an infinite number of line sinks.	192
7.5	Velocity potential contours for $b' = \pi/2$. The contours start from $(0, \pi/2)$ and expand outward with p selected from the set $\{1, 2, 4, 8, 10, \cosh 2b' - 1, 11, \sinh 2b', 12, \cosh 2b' + 1, 15, 20, 30, 40, 50\}$. The thick half solid and half dashed contour corresponds to $p = \cosh 2b' - 1$, the thick dash-dotted contour corresponds to $p = \sinh 2b'$ and the thick solid contour that extends into the corners corresponds to $p = \cosh 2b' + 1$. Within the dash-dotted contour ($p < \sinh 2b'$), the solid and dashed parts of the contours correspond, respectively, to the positive and negative roots in (7.29).	194
7.6	l' and A' as a function of p for $b/a = 0.5$. The horizontal line denotes a constant value of π	195
7.7	Evolution of \hat{w} and \hat{Q} as a function of \hat{z} for $b/a = 0.25, 0.5$ and 1 . In all cases, $\Gamma_0 = 1$	197

7.8	[Color] Surface plot illustrating plume merger in case of two parallel rows of non-offset plumes with $b/a = 0.5$. The plume boundaries are shaded according to the height between 0 and 2, and these contours are also projected onto the bottom plane.	198
7.9	The contact heights $\hat{z}_{c,1}$ and $\hat{z}_{c,2}$ plotted as a function of b/a . In all cases, $\Gamma_0 = 1$	198
7.10	Schematic of two parallel rows of an infinite number of line sinks with an offset.	198
7.11	Velocity potential contours for $b' = \pi/4$. The contours start from $(0, \pi/4)$ and expand outward with p selected from the set $\{0.5, 1.5, \sinh 2b', \cosh 2b', 3, 4, 5, 8, 10\}$. The thick half solid and half dashed contour corresponds to $p = \sinh 2b'$ and the dash-dotted contour corresponds to $p = \cosh 2b'$. The solid and dashed curves correspond, respectively, to the positive and negative roots in (7.54).	199
7.12	l' and A' as a function of p for $b/a = 0.5$. The horizontal line denotes a constant value of π	200
7.13	Evolution of \hat{w} and \hat{Q} as a function of \hat{z} . In all cases, $\Gamma_0 = 1$	201
7.14	[Color] Surface plot illustrating plume merger in case of two offset parallel rows of plumes with $b/a = 0.5$. The plume boundaries are shaded according to the height between 0 and 2, and these contours are also projected onto the bottom plane.	202
7.15	As in figure 7.9 but in case of offset plumes with an offset distance of $a/2$. In all cases, $\Gamma_0 = 1$	203
7.16	Effective entrainment perimeter as a function of p . For two rows of plumes, the vertical to horizontal spacing ratio is fixed as $b/a = 0.2$	203
7.17	Evolution of plume trajectory (a), volume flux (b), horizontal (c) and vertical (d) velocities. The horizontal dashed (solid) line denotes the height of first contact for $\bar{a} = 0.2$ ($\bar{a} = 1$). In both cases, $\Gamma_0 = 1$	208
7.18	Contact height as a function of \bar{a} . In all cases, $\Gamma_0 = 1$	209
7.19	Effects of varying Fr_0 (a), R (b) and a/D (c and d) on the plume trajectory. The experimental data are taken from Appendix A of Kannberg & Davis (1976).	210
7.20	Top view of single and dual rows of cooling tower cells. The black circles denote cells at the center and the gray half circles denote the half cells at the two ends.	210
7.21	Relative humidity profiles for single (a and b) and dual (c and d) rows of plumes. The model input parameters are specified in table 7.1.	212
7.22	Comparison between the present irrotational flow theory and the theory of Wu & Koh (1978). The horizontal solid and dashed lines denote the respective heights of first contact for the above theories. In all cases, $\Gamma_0 = 1$	215
8.1	Solar collector assisted plume abatement in a PPWD cooling tower. The fan directly drives air through the solar collector (a) or induces air through the solar collector (b). The filled rectangles on the two sides of the fan shroud denote solar collectors.	220
8.2	Thermosyphon system for plume abatement in a PPWD. The portion of the thermosyphon that is bounded by dashed rectangles denote the porous media structure.	221
8.3	Coaxial plumes in a stratified ambient. For small values of N , coaxial plumes behave like a uniform plume and the merged uniform plume spreads out horizontally at a height above the cut-off height. By contrast, and for large values of N , the peeling height of the outer plume may be below the cut-off height thus the inner plume rises continuously to its own maximum height then falls to the neutral buoyancy height.	222
8.4	Cross-cut view of the nozzles needed to produce the closed core and open core annular plumes. Solid and dashed lines denote forced and induced flows, respectively.	223

A.1	Schematic of an axisymmetric plume in a homogeneous ambient. $b = b(z)$ is the plume radius and $\bar{w} = \bar{w}(r, z)$ is the time-averaged vertical velocity. $\bar{w}_m = \bar{w}_m(z)$ is the mean vertical velocity assuming a “ top-hat ” profile (the plume properties e.g. velocity and buoyancy are taken to be constant within the plume and zero outside).	243
B.1	Schematic of a coaxial plume in a homogeneous ambient. w_1 and w_2 are the respective vertical velocities of the inner and outer plumes, corresponding to plume radii b_1 and b_2 (denoted by solid arrows). ω_α , ω_β and ω_γ (denoted by dashed arrows) are the respective entrainment velocities from the outer to the inner plume, from the inner to the outer plume and from the ambient to the outer plume. Hereafter subscripts 1 and 2 are used to denote the inner and outer plumes, respectively.	251
C.1	Schematic of a cooling tower plume in a windy ambient. s and n are the streamwise and normal coordinates, respectively. λb ($\lambda \geq 1$) and b are the respective major and conjugate radii. x and z are the horizontal and vertical axes, and y is the axis into the page.	258
C.2	Mass conservation (or volume conservation for incompressible flow) for the control volume.	259
C.3	Momentum conservation for the control volume.	260
C.4	Theory vs. experiment for cases 1 to 4.	264
C.5	Theory vs. experiment for cases 5 to 8.	265
C.6	Theory vs. experiment for cases 9 to 12.	266
E.1	Mixing process on a psychrometric chart.	271
E.2	Specific liquid moisture as a function of mixing ratio.	271
E.3	Latent to sensible heat ratio as a function of mixing ratio.	271
F.1	[Color] Amplification coefficient, ζ , as a function of the dimensionless separation distance, \hat{R}	276
F.2	Schematics of single (left) and two merging (right) turbulent fountains. Dashed and solid lines represent the boundaries of the inner (upflow) and outer (downflow) plumes, respectively. The arrows denote the flow directions.	277

Chapter 1

Introduction and overview

1.1 Background

Turbulent buoyant plumes are ubiquitous in either the natural or man-made environment. A comprehensive summary for the applications of buoyant jets or forced plumes is given by Jirka (2004). Moreover, studies of turbulent plumes have been reviewed by a number of different authors, such as Linden (2000), Lee & Chu (2003), Kaye (2008), Woods (2010), Hunt & Van den Bremer (2011) and Hunt & Burridge (2015). On the basis of these reviews, this section gives a basic introduction on several theoretical models of turbulent plumes and (laser-based) laboratory modeling of plumes. We restrict our focus on Boussinesq plumes for which density difference is only important in the buoyancy force.

Turbulent plumes are usually characterized by the following nondimensional numbers:

$$\text{Reynolds number : } \text{Re} = \frac{Ud}{\nu}, \quad (1.1)$$

$$\text{Rayleigh number : } \text{Ra} = \frac{g\Delta\rho d^3}{\kappa\nu}, \quad (1.2)$$

$$\text{Richardson number : } \text{Ri} = \frac{g'd}{U^2}, \quad (1.3)$$

where U is a characteristic velocity scale, d is a characteristic length scale, g is the gravitational acceleration, ν is the kinematic viscosity, $\Delta\rho$ is the density difference across distance d , κ is the thermal diffusivity and g' is the reduced gravity that is defined in section 1.1.1.1. Physically, the Reynolds number, defined as the ratio of inertial forces to viscous forces, is large thus the flow is turbulent; the Rayleigh number, defined as the ratio of the destabilizing effect of buoyancy to the stabilizing effects of viscosity and of thermal or mass diffusion, is large thus the convection is turbulent; the Richardson number represents the relative importance of natural convection resulting from density differences and forced convection resulting from the source momentum flux (Hunt & Van den Bremer, 2011).

1.1.1 Turbulent plume models

For turbulent plumes in a homogeneous ambient, it was generally accepted in the past that the primary mechanism of entrainment is turbulent “engulfment” by large-scale eddies (cf. Turner 1986). Some more recent literature, e.g. Westerweel *et al.* (2009), argued

that another process, i.e. small-scale “nibbling”, plays an important role in the overall rate of entrainment into turbulent jets. To be precise, we follow the respective definitions for engulfment and nibbling by Burrige *et al.* (2017).

“Engulfment is defined as the transport of ambient fluid to within the envelope of the turbulent flow at scales larger than the Taylor micro-scale¹. Nibbling is the process wherein vorticity is imparted to the entrained fluid from the ambient due to viscous stresses at the interface between turbulent and nonturbulent flow at a length scale close to Taylor micro-scale.”

By simultaneous measurements of the velocity field and the scalar edge of a high Péclet number turbulent plume, Burrige *et al.* (2017) concluded that the turbulent engulfment of ambient fluid by large-scale eddies at the plume edge comprises a significant portion of the turbulent entrainment process. Building on the aforementioned conclusion, we review several theoretical models of turbulent plumes as follows.

1.1.1.1 Morton *et al.* (1956)

On a timescale much greater than the eddy (of the largest size) turnover time², G.I. Taylor’s entrainment hypothesis states that the mean horizontal inflow velocity, u_e , is proportional to the mean vertical velocity, \bar{w} , at the same height. In mathematical terms, we write

$$u_e = \alpha \bar{w}, \quad (1.4)$$

where $\alpha \simeq 0.1$ is an empirical entrainment coefficient. Note that (1.4) is consistent with the similarity theory which implies that u_e and w have the same height dependence, i.e. $\propto z^{-1/3}$ (Batchelor, 1954; Rooney & Linden, 1996). As pointed out by Batchelor (1954), (1.4) is a fundamental consequence of the similarity arguments. The volume flux (Q), momentum flux (M) and buoyancy flux (F) for a vertical axisymmetric plume are defined as follows:

$$Q = 2\pi \int_0^\infty r w dr = \pi b^2 \bar{w}, \quad (1.5)$$

$$M = 2\pi \int_0^\infty r w^2 dr = \pi b^2 \bar{w}^2, \quad (1.6)$$

$$F = 2\pi \int_0^\infty r g \frac{\rho_a - \rho}{\rho_{\text{ref}}} w dr = \pi b^2 \bar{w} g', \quad (1.7)$$

where $w = w(r, z)$ and $\rho = \rho(r, z)$ are the vertical velocity and density, respectively; $\rho_a = \rho_a(z)$ is the ambient density and ρ_{ref} is a reference density; b is the plume radius, \bar{w} is the “top-hat” vertical velocity and $g' = g \frac{\rho_a - \bar{\rho}}{\rho_{\text{ref}}}$ is the top-hat reduced gravity with $\bar{\rho}$ denoting the

¹In isotropic turbulence, the dissipation rate can be estimated as $\epsilon = 15\nu u'^2/\lambda^2$ where ν is the kinematic viscosity, u' is the r.m.s. velocity and λ is Taylor micro-scale (Taylor, 1935). At high Reynolds number, the Taylor micro-scale, λ , is intermediate in size between the Kolmogorov micro-scale, $\eta = (\nu^3/\epsilon)^{1/4}$, and the integral scale, l , which represents the size of the largest eddies or the width of the flow (Tennekes & Lumley, 1972; Pope, 2001).

²The eddy turnover time is defined as $\tau(l) = l/u(l)$ where l is the eddy size and $u(l)$ is the corresponding characteristic velocity of size l . (Pope, 2001)

top-hat density. On this basis, Morton *et al.* (1956) (hereafter denoted MTT) formulated the conservation equations of volume, momentum and buoyancy, which are given, respectively, by

$$\frac{dQ}{dz} = 2\alpha\pi^{1/2}M^{1/2}, \quad (1.8)$$

$$\frac{dM}{dz} = \frac{QF}{M}, \quad (1.9)$$

$$\frac{dF}{dz} = -N^2Q, \quad (1.10)$$

where $N = \left(-\frac{g}{\rho_{\text{ref}}}\frac{d\rho_a}{dz}\right)^{1/2}$ is the buoyancy frequency. A full derivation of (1.8)-(1.10) is given in Linden (2000). For a point source plume i.e. source conditions $Q(z=0) = M(z=0) = 0$ and $F(z=0) = F_0 > 0$, in a neutral ambient with $N = 0$, (1.8)-(1.10) yield the following analytical solution

$$b = \frac{6}{5}\alpha z, \quad \bar{w} = \frac{5}{6\alpha} \left(\frac{9\alpha F_0}{10\pi}\right)^{1/3} z^{-1/3}, \quad g' = \frac{5F_0}{6\pi\alpha} \left(\frac{9\alpha F_0}{10\pi}\right)^{-1/3} z^{-5/3}. \quad (1.11)$$

Assuming Gaussian profiles of vertical velocity and reduced gravity that read, respectively, as follows:

$$w(r, z) = w_G \exp\left[-\left(\frac{r}{b_G}\right)^2\right], \quad (1.12)$$

$$g'(r, z) = g'_G \exp\left[-\left(\frac{r}{\Lambda b_G}\right)^2\right], \quad (1.13)$$

where b_G is the Gaussian characteristic plume radius, $w_G = w_G(z)$ and $g'_G = g'_G(z)$ are the Gaussian characteristic vertical velocity and reduced gravity, respectively, and Λ is the ratio of the half-width of the buoyancy profile to the half-width of the velocity profile (i.e. b_G). Hence, the flux parameters are given by

$$Q = \pi b_G^2 w_G, \quad M = \frac{\pi}{2} b_G^2 w_G^2, \quad F = \frac{\pi \Lambda^2}{\Lambda^2 + 1} b_G^2 w_G g'_G. \quad (1.14)$$

From (1.5)-(1.7) and (1.14), the relation between top-hat plume radius, vertical velocity and reduced gravity and their Gaussian counterparts is given by

$$b = \sqrt{2}b_G, \quad \bar{w} = w_G/2, \quad g' = \frac{\Lambda^2}{\Lambda^2 + 1} g'_G. \quad (1.15)$$

Analogous to (1.4), the Gaussian entrainment assumption reads

$$u_e = \alpha_G w_G, \quad (1.16)$$

where α_G is the Gaussian entrainment coefficient. By equating the rate of entrainment per unit height (denoted by E) using, respectively, the top-hat and Gaussian properties that reads

$$E = 2\pi b \alpha \bar{w} = 2\pi b_G \alpha_G w_G, \quad (1.17)$$

we obtain the following relation between the top-hat and Gaussian entrainment coefficients

$$\alpha = \sqrt{2}\alpha_G. \quad (1.18)$$

In a linearly stratified ambient, i.e. $N = \text{Constant}$, the plume behavior is shown schematically in figure 1.1. The plume in question overshoots its neutral buoyancy level (z_{nb}) at which the plume density is equal to the ambient density, then reaches its maximum rise (z_{max}) with zero velocity. Thereafter, the plume fluid falls back and spreads horizontally around its neutral height. Referring back to the governing equations, (1.10) implies a decrease in F , which in turn decreases the rate of increase in M as implied by (1.9). The evolution above the neutral buoyancy level is essentially a turbulent fountain type behavior, for which MTT cannot apply. Nonetheless, MTT gives good estimate for z_{max} – see equation (6.4.6) and figure 6.18 of (Turner, 1973). The numerical solution to (1.8)-(1.10), upon integrating up to z_{max} , is illustrated in figure 1.2.

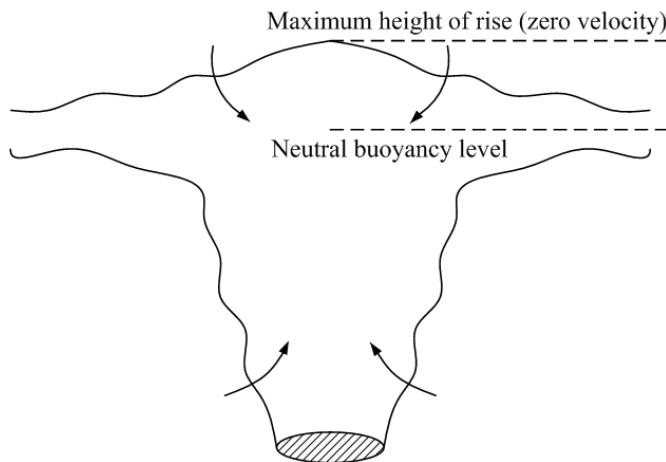


Figure 1.1: Schematic of an axisymmetric plume in a linearly stratified ambient.

1.1.1.2 Priestley & Ball (1955)

Compared to the numerous attention received by MTT, the slightly earlier model of Priestley & Ball (1955) (hereafter denoted PB) has gained much less recognition. However, recent and not-so-recent literature, such as Fox (1970), Kaminski *et al.* (2005) and van Reeuwijk & Craske (2015), have indicated that PB may reveal more insights into the physics about the entrainment coefficient for jets or plumes in unstratified environments.

In contrast to MTT, PB formulates the integrated conservation equations of momentum, kinetic energy of vertical mean motion and buoyancy. Derivation of the governing equations in the PB model is given in section 1.5, which follows the procedure in Kaminski *et al.* (2005) but uses the standard top-hat definitions for the plume properties. The closure condition is a Reynolds stress assumption in the kinetic energy equation. Morton (1971) compared PB and MTT models and pointed out the difference in parameterizing turbulent entrainment, mathematically by

$$-(ru)_{\infty} = \begin{cases} \alpha \bar{R} \bar{W}, & \text{(MTT)} \\ 2I \bar{R} \bar{W} + \bar{R}^2 \frac{d\bar{W}}{dz}, & \text{(PB)} \end{cases} \quad (1.19)$$

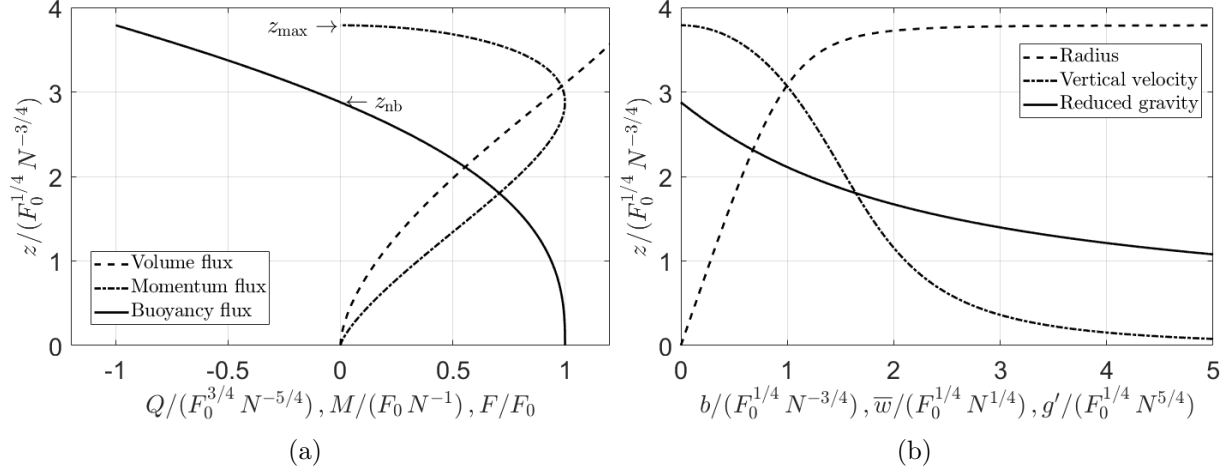


Figure 1.2: For a point source plume in a linearly stratified ambient, panel a shows the solutions of fluxes of volume, momentum and buoyancy and panel b shows solutions of plume radius, vertical velocity and reduced gravity. Results are obtained with $F_0 = 1 \text{ m}^4/\text{s}^3$, $N = 1 \text{ s}^{-1}$ and $\alpha = 0.13$ (from MTT).

where \bar{R} and \bar{W} denote the local radial and vertical velocity scales, respectively; $I = \frac{d\bar{R}}{dz}$ is a constant related to the shape functions of vertical velocity, reduced gravity and the Reynolds stress term $\overline{u'w'}$. The upper expression in (1.19) (i.e. MTT) relates turbulent entrainment to the local mean flow and a constant of proportionality. By contrast, the lower expression in (1.19) (i.e. PB) relates turbulent entrainment to both the mean vertical velocity and the vertical acceleration (Baines, 2014). Furthermore, MTT predicts that $\bar{R} \rightarrow \infty$ when $z \rightarrow z_{\max}$ (cf. figure 1.2b) whereas PB predicts a conical plume with linear spreading. Morton (1971) concluded that MTT and PB yield similar results in the flow below the neutral buoyancy level, but remarkable differences in the flow of negative buoyancy (i.e. above the neutral buoyancy level).

van Reeuwijk & Craske (2015) generalized the PB model to include the contributions due to pressure and turbulence³ in the governing equations. They predicted that

$$\alpha_p = \frac{5}{3}\alpha_j, \quad (1.20)$$

where the subscripts p and j denote a pure plume and a pure jet (see the discussion in section 1.1.1.3), respectively. This relation, which has been validated by the experimental results of Wang & Law (2002), is consistent with the PB model (cf. section 1.5).

1.1.1.3 Γ -approach

The flux-balance parameter (also called the Morton number in Mingotti & Cardoso 2019), Γ , is defined as

$$\Gamma = \frac{5Q^2F}{8\alpha\pi^{1/2}M^{5/2}}, \quad (1.21)$$

³Compared to the original PB model, the pressure term and the vertical transport of momentum and buoyancy due to turbulent fluctuation are included in van Reeuwijk & Craske (2015).

where Γ is proportional to the local Richardson number defined as $Ri = bg'/w^2$. Specifically, $\Gamma = 1$ represents a pure plume balance, $\Gamma > 1$ ($\Gamma < 1$) represents a lazy (forced) plume with a deficit (excess) of momentum flux compared to a pure plume. $\Gamma = 0$ represents a pure jet with zero buoyancy flux. $\Gamma < 0$ represents a negatively buoyant jet for which the buoyancy acts against momentum. With different $\Gamma_0 \equiv \Gamma(z = 0)$, the corresponding plume behaviors are sketched in figure 1.3. Important to note is that, a pure plume represents a state of local equilibrium with height, which allows spatially invariant parameterizations of turbulent entrainment, i.e. a constant entrainment coefficient (Ciriello & Hunt, 2020).

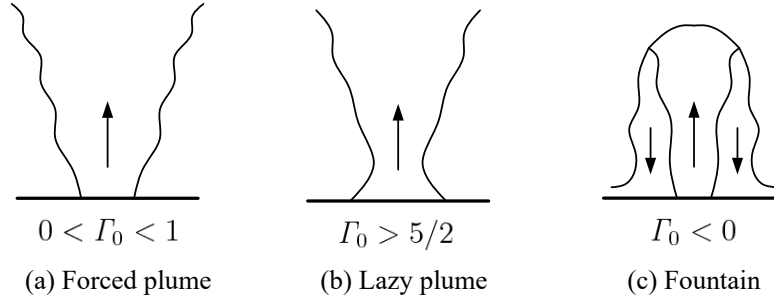


Figure 1.3: Schematics of plume behaviors in unstratified environments with different Γ_0 . The arrows denote the flow directions. Panel (b) illustrates that a contraction occurs near the source for a lazy plume with $\Gamma_0 > 5/2$. Panel (c) illustrates the upflow and downflow in a turbulent fountain.

Hunt & Van den Bremer (2011) argued that the advantage of introducing Γ is that, a solution of $\Gamma(z)$ indicates the departure of the plume from a pure plume balance at all heights. To this end, (1.8)-(1.10) can be reorganized as follows:

$$\frac{d\Gamma}{d\zeta} = \frac{\Gamma(1-\Gamma)}{\hat{b}}, \quad (1.22)$$

$$\frac{d\hat{b}}{d\zeta} = \frac{1}{5} \left(\frac{5}{2} - \Gamma \right), \quad (1.23)$$

$$\frac{d\hat{w}}{d\zeta} = \frac{2\hat{w}}{5\hat{b}} \left(\Gamma - \frac{5}{4} \right), \quad (1.24)$$

where $\zeta = 4\alpha z/b_0$, $\hat{b} = b/b_0$ and $\hat{w} = w/w_0$. The analytical solutions to (1.22)-(1.24) with source conditions $\Gamma = \Gamma_0$ and $\hat{b}_0 = \hat{w}_0 = 1$ are referred to section 3 of Hunt & Van den Bremer (2011). For a lazy plume with $\Gamma_0 > 5/2$, (1.22) indicates that the far-field solution is $\Gamma = 1$; (1.23) indicates that the minimum plume radius occurs when $\Gamma = 5/2$; (1.24) indicates that the maximum vertical velocity occurs when $\Gamma = 5/4$.

Consistent with (1.20), the entrainment coefficient for a forced plume is given as (List & Imberger, 1973)

$$\phi = \phi_j + (1 - \phi_j)\Gamma, \quad (1.25)$$

where $\phi = \alpha/\alpha_j$, $\phi_j = \alpha_j/\alpha_p = 3/5$ and α_j and α_p are the entrainment coefficients for pure jets and pure plumes, respectively. Kaye (2008) gave a physical explanation for why plumes

have greater entrainment over jets. This is accomplished by looking at the variable-density vorticity equation as follows:

$$\frac{\partial \boldsymbol{\omega}}{\partial t} + \mathbf{u} \cdot \nabla \boldsymbol{\omega} = \boldsymbol{\omega} \cdot \nabla \mathbf{u} + \frac{1}{\rho^2} \nabla \rho \times \nabla p + \nu \nabla^2 \boldsymbol{\omega}, \quad (1.26)$$

where the symbols in bold denote vectors. \mathbf{u} and $\boldsymbol{\omega} = \nabla \times \mathbf{u}$ are the velocity and vorticity vectors. According to Kundu *et al.* (2015), the first term on the right-hand side denotes vortex stretching and tilting; the second term on the right-hand side denotes the rate of generation of vorticity due to baroclinicity (baroclinic torque); the last term on the right-hand side denotes the rate of change of $\boldsymbol{\omega}$ due to viscous diffusion. For steady and large Reynolds number flows, the time dependent term on the left-hand side and the diffusion term on the right-hand side can be neglected. Adopting index notation, and assuming $u_i \sim w$, $\omega_i \sim w/b$ and $\frac{\partial p}{\partial x_i} \sim \rho g'$, scaling analysis yields

$$\frac{w^2}{bz} \sim \frac{w^2}{bz} + \frac{g'}{z} \quad (1.27)$$

and because $u_e \sim w$,

$$u_e \sim w + \frac{g'b}{w}, \quad (1.28)$$

where the first term on the right-hand side represents the effect of shear and the second term represents the effect of baroclinic torque. Correspondingly, the second term on the right-hand side of (1.25), i.e. $(1 - \phi_j)\Gamma$, is due to baroclinic torque.

1.1.1.4 Lagrangian approach

In this context, we only discuss the Lagrangian approach proposed in Lee & Chu (2003). Two key underlying assumptions are listed as follows:

- (i) Spreading hypothesis: the change in the width of the shear layer, in a frame of reference moving with the eddies, is assumed to be proportional to the relative velocity between the plume element and its surroundings. Mathematically, this is expressed as

$$\frac{db}{dt} = \beta w, \quad (1.29)$$

where β is a spreading coefficient with $\beta = 0.17$ for both jets and plumes (Chu, 1994).

- (ii) Concept of dominant eddy: the irrotational ambient fluid and the smaller eddies are drawn into and remain within the dominant eddies, i.e. the largest eddies.

As shown in figure 1.4, we follow the motion of the shaded material volume. At time instant t , the plume element has mass of $\rho A(w\Delta t)$ where $A = \pi b^2$ is the cross-sectional area, momentum of $\rho A(w\Delta t)w$ and buoyancy force of $(\rho_a - \rho)gA(w\Delta t)$. Applying Newton's second law on this plume element yields

$$\frac{d}{dt}(\rho A(w\Delta t)w) = (\rho_a - \rho)gA(w\Delta t), \quad (1.30)$$

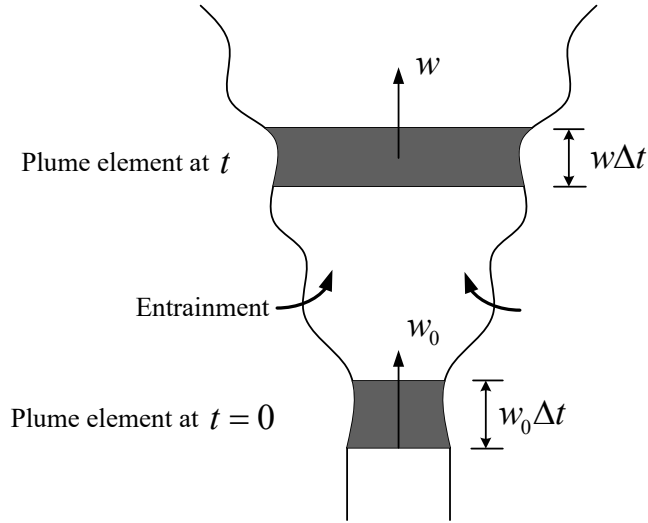


Figure 1.4: Schematic of a plume element under Lagrangian frame of reference.

thus

$$\frac{dM}{dt} = F, \quad (1.31)$$

where $M = Aw^2$ is the kinematic momentum flux and $F = Awg \frac{\rho_a - \rho}{\rho_a}$ is the buoyancy flux. For an unstratified environment, $F = F_0 = F(t = 0)$. Integration on both sides of (1.31) yields

$$M(t) = F_0 t + M_0, \quad (1.32)$$

where $M_0 = 0$ for an ideal source plume. Solving (1.29) and (1.32) produces the following results:

$$b = \left(\frac{4\beta}{3}\right)^{1/2} \left(\frac{F_0}{\pi}\right)^{1/4} t^{3/4}, \quad (1.33)$$

$$w = \left(\frac{4\beta}{3}\right)^{-1/2} \left(\frac{F_0}{\pi}\right)^{1/4} t^{-1/4}, \quad (1.34)$$

$$g' = \left(\frac{4\beta}{3}\right)^{-1/2} \left(\frac{F_0}{\pi}\right)^{1/4} t^{-5/4}, \quad (1.35)$$

$$z = \left(\frac{3\beta}{4}\right)^{-1/2} \left(\frac{F_0}{\pi}\right)^{1/4} t^{3/4}, \quad (1.36)$$

where $\frac{db}{dt} = \frac{db}{dz} \frac{dz}{dt} = w \frac{db}{dz} = \beta w$ thus $z = \frac{b}{\beta}$. Equations (1.33)-(1.36) are identical to (1.11) provided that

$$\beta = \frac{6}{5}\alpha. \quad (1.37)$$

1.1.2 Laboratory experimental modeling

A review of laboratory experiments on atmospheric plumes is given in Chapter 2. Here we restrict our attention to laser-based experiments, particularly particle image velocimetry

(PIV) and laser-induced fluorescence (LIF), the latter of which is adopted in Chapter 4. Both PIV and LIF are non-intrusive techniques that are used to measure velocity and scalar concentration fields, respectively. Specifically, PIV involves seeding small tracer particles to the flow of interest, and subsequently, the region of interest in the flow field is illuminated twice within a short time interval by a laser light sheet. Therefore, the velocity field is determined by the tracer particle displacement between two successive images. Detailed calibration, evaluation and post-processing processes are referred to a well-written book on PIV by Raffel *et al.* (2018). LIF, on the other hand, makes use of a fluorescent dye as a scalar proxy, which is also illuminated by a laser light sheet. The fluorescence light emitted by the dye is related to the dye concentration through some calibration processes. Details of LIF calibration and post-processing are referred to the review article of Crimaldi (2008) and Chapter 4 of the present thesis.

For turbulent plumes in which density variation plays a significant role, the variation in density is associated with variation in the refractive index. This affects the determination of particle positions in PIV and results in attenuation of light intensity in PLIF (i.e. planar LIF). The error associated with the change in refractive index can be enlarged by the distance over which the laser light travels in the dyed flow (Mishra & Philip, 2018). For PLIF, in particular, the concentration of fluorescent dye also increases the light attenuation. In the following, we will discuss PIV and PLIF experiments of turbulent plumes separately.

1.1.2.1 PIV

In the saline plume experiment of BurrIDGE *et al.* (2017), the seeding particles were approximately neutrally buoyant so that the Stokes settling velocity was small and sedimentation of particles was avoided. The refractive index difference between the plume fluid and the ambient fluid was estimated as

$$g' \sim z^{-5/3} \implies \Delta n \sim z^{-5/3} \quad (1.38)$$

where Δn denotes the refractive index difference. Because the measurement region of the plume was $64 \leq z/r_0 \leq 130$ where r_0 is plume source radius, the corresponding $\Delta n \sim 10^{-4}$ thus the effect of refractive index mismatch was negligible. Although refractive index matching (hereafter denoted RIM) was not performed, their PIV measurements were validated by checking the self-similar velocity profiles and the entrainment coefficient. One of the approaches to estimating the entrainment coefficient is to measure the plume radial growth rate, as expressed by the first equality in (1.11). A best fit to the data in their figure 3 yielded that $\alpha = 0.11 \pm 0.01$, which lies within the range of α reported in previous studies. One of the novel contribution in the PIV measurements of BurrIDGE *et al.* (2017) is that the flow within the plume and in the surrounding ambient fluid is significantly influenced by the absence or presence of large-scale eddies – see figure 1.5. When eddies are present, the vertical velocities near the plume are small and essentially all the vertical transport is within the plume. However, and when eddies are absent, large vertical velocities are observed outside the plume which indicates that ambient fluid is engulfed into the plume by eddies.

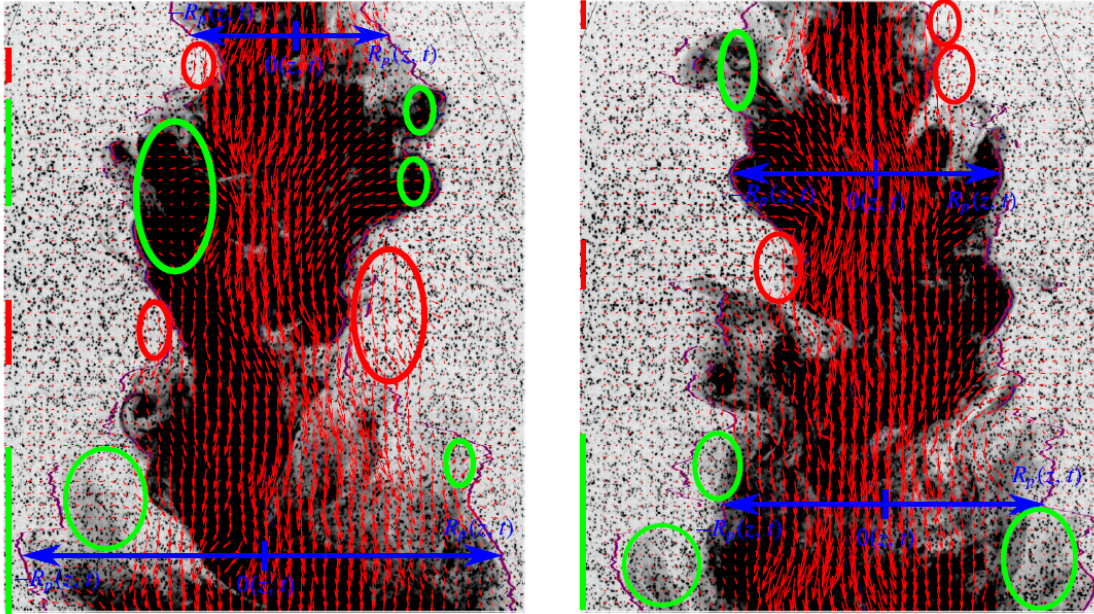


Figure 1.5: [Color] Two instantaneous images of a turbulent plume. The dark regions denote the dense plume fluid and the surrounding small dark spots denote the small particles in the PIV experiments. The red arrows denote the two-dimensional velocities measured on the centerplane of the plume. The green circles indicate the small velocities just outside and inside the plume edge at the locations where eddies are locally present. By contrast, the red circles indicate the relatively large velocities at the locations where eddies are locally absent. (Copied from figure 1 of Burrige *et al.* 2017 with permission)

1.1.2.2 PLIF

Vanderwel & Tavoularis (2014) carefully examined the possible errors associated with PLIF experiments of slender plumes. These include the non-negligible laser sheet thickness, laser light attenuation and re-emission of the primary fluorescence of the dye. Their approach to estimating the attenuation coefficient using Beer-Lambert law is adopted in Chapter 4. For buoyant jets or plumes in crossflowing environments (Tian & Roberts, 2003; Diez *et al.*, 2005), RIM is required to avoid image distortion and laser intensity nonuniformities. In the experiment of Diez *et al.* (2005), potassium phosphate was added to the source saline fluid with an increase in plume density; ethyl alcohol was added to the crossflowing water with a decrease in ambient fluid density. Thus the refractive indices of the source fluid and the ambient fluid were matched. The instantaneous PLIF images are shown, in sequence, in figure 1.6. It is evident that the cross section of the plume in a crossflow consists of two counter-rotating vortices at the two sides of the plane of symmetry. Moreover, these vortices are largely distorted due to the entrainment of ambient fluid.

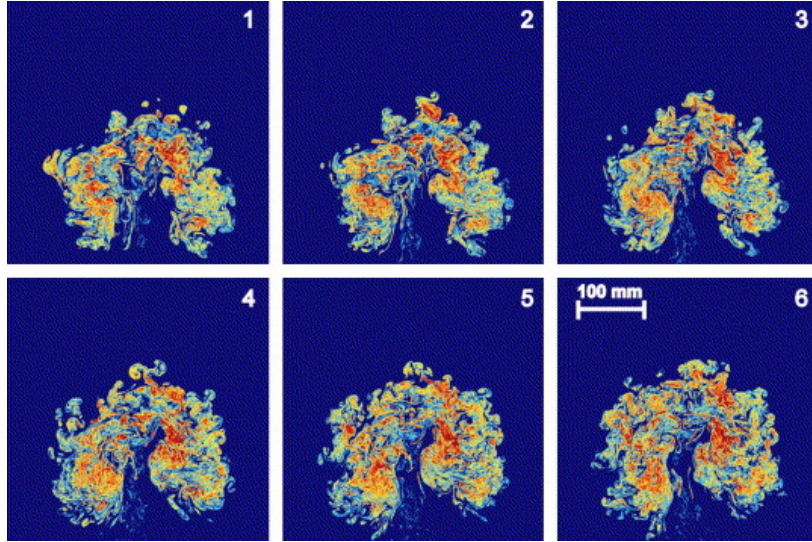


Figure 1.6: [Color] Instantaneous PLIF images (labels denote the sequence of images with a constant time interval) of the cross section of a turbulent plume in a crossflow. (Copied from figure 8 of Diez *et al.* 2005 with permission)

1.2 Atmospheric plumes and their relation to cooling towers

Atmospheric plumes exhibit complex behaviors due to the changeable ambient conditions, such as wind, ambient stratification (e.g. a temperature inversion layer) and turbulence in the atmospheric boundary layer. A sketch of an atmospheric plume, e.g. from a smoke stack, is given in figure 1.7. The vertical plume scenario described in section 1.1.1 is a special case assuming no wind in the atmosphere.

Briggs (1975, 1984) gave a comprehensive review of plume behaviors in the atmosphere. Some arguments made by Briggs are presented as follows:

- (i) Plume rise can be considered as an adiabatic process assuming no significant heat transfer other than that via turbulent mixing. Considering the compressibility, the entrainment equation, i.e. (1.8), can be rewritten as

$$\frac{dQ}{dz} = 2\pi b u_e + \frac{Q}{z_s}, \quad (1.39)$$

where $z_s = T_a/(g/R - g/c_p) \simeq 10$ km is the scale height of the atmosphere where T_a is the ambient absolute temperature, R is the gas constant for air and c_p is the heat capacity at constant pressure. The second term on the right-hand side of (1.39) is only important when the plume rise height is a nontrivial fraction of z_s , say, 1 km or beyond.

- (ii) The buoyancy frequency, N , in a compressible atmosphere, is expressed as

$$N = \left(\frac{g}{\theta_a} \frac{d\theta_a}{dz} \right)^{1/2}, \quad (1.40)$$

where $\theta = T(p_s/p)^{R/c_p}$ is the potential temperature where p_s is a standard pressure; the subscript a denotes the ambient. θ remains constant as air is adiabatically lifted.

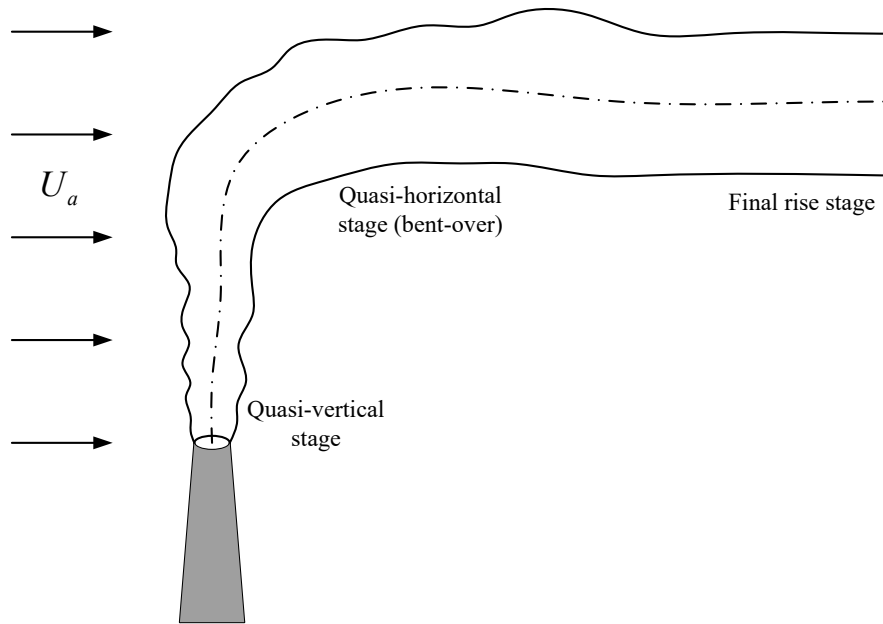


Figure 1.7: Schematic of plume rise in a stably stratified and windy environment. The three stages of plume rise, i.e. quasi-vertical, quasi-horizontal and final rise stages, are labeled.

- (iii) For bent-over plumes, approximately half of the theoretical models reported in literature include a drag term in the momentum conservation equation, whereas the other half do not. This drag force assumption, or alternatively, an added mass concept, is discussed in Chapter 2.
- (iv) The most commonly used set of conservation equations is continuity-momentum-buoyancy i.e. the MTT type model (cf. table 1 of Briggs 1975).
- (v) For moist plumes, e.g. cooling tower plumes (see figure 1.8), the effect of latent heat release on plume rise is modest. This argument is justified in Appendix E.

The aforementioned arguments summarized by Briggs provide a good theoretical basis for atmospheric plume modeling. The effect of ambient turbulence on plume rise is reviewed in Chapter 2.

In the context of evaporative cooling towers that achieve cooling mainly via latent heat transfer from water to air, the exhaust air is assumed to be saturated with respect to water vapor (Lindahl & Jameson, 1993). This hot, humid air mixes with the cold ambient air by turbulent entrainment and a visible plume ensues if the plume temperature drops below the dew-point temperature. Whereas Briggs discussed the calculation of cooling tower plumes in Appendix B of Briggs (1975), the prediction of plume visibility was only briefly mentioned. More sophisticated models, which carefully integrate the thermodynamics of moist air, have been formulated by Schatzmann & Policastro (1984) and Janicke & Janicke (2001).

In the past, visible plumes above cooling towers were regarded as an unavoidable consequence of industrial activities and a sign of thriving manufacturing industry (Fisher, 1997). More recently, the release of visible plumes is of great concern to the public. Though essentially comprised of water, visible plumes are often confused with air pollution by laypeople.



Figure 1.8: Visible plumes above a single row of cooling tower cells. (Photo used with permission of International Cooling Tower Inc.)

Moreover, and under adverse weather conditions, these plumes may persist for long distances and reduce visibility on nearby roadways. Since 1960's, various cooling tower designs have been proposed to achieve plume abatement (cf. Chapter 2). The most commonly used approach is to add a dry cooling section by which the ambient incoming air is sensibly heated, and thus the relative humidity is greatly reduced. This dry air is mixed with the more humid air from the wet section, and as a result, the air mixture is at least unsaturated. Strategies of this type have been proved to effectively abate visible plumes, however, their efficiency depends on the quality of the air mixture at the tower exit. In order to achieve a homogeneous mixture upon discharge, mixing devices are usually added within the plenum chamber to enhance mixing, however, at the cost of increased pressure drop.

On the other hand, Houx Jr *et al.* (1978) proposed a tower design that consists of a central wet section and four surrounding dry sections. Though designed primarily for water conservation and prevention of recirculation, this design partially or completely eliminates fog in that the central hot, moist air is enveloped by the surrounding dry air, i.e. a coaxial wet/dry plume structure is formed. Several advantages of this coaxial plume structure are summarized as follows:

- (i) The hot, humid air at the core is prevented from low level deflection and spreading which may cause corrosion on nearby structures.
- (ii) Due to the indirect contact between the hot, humid air and the ambient fluid, the former is expected to be more buoyant and thus rise more rapidly.
- (iii) Under windy environments, the inner, wet and the outer, dry plumes are mixed more effectively thus reducing the possibility of condensation.
- (iv) Even without premixing, the coaxial plume structure serves to adequately prevent fog formation.

Note that the arguments (i)-(iii) made by Houx Jr *et al.* (1978) are only qualitative. Argument (iv) is most likely due to the large dry sections and the relatively small wet section,

which produces a coaxial plume structure dominated by the dry plume. Similar coaxial plume structure has been observed above a crossflow wet/dry cooling tower (Lindahl & Jameson, 1993). They found a converging cone-shaped visible plume that persisted for two or three stack diameters above the tower.

1.3 Knowledge gaps

Further to the description of coaxial plumes in section 1.2, we are aware of the fact that this nontrivial flow phenomenon has not been completely understood. As compared to the numerous studies of uniform plumes, plumes issued from unevenly distributed sources of buoyancy, e.g. coaxial plumes, are rarely investigated. Whereas Hunt & Van den Bremer (2011) suggested that computational fluid dynamics is apt to incorporate complex source conditions as such, the high computational costs associated with the so-called “numerical experiments” restrict their wide applicability. Therefore, we aim to explore the possibility of the MTT-type theoretical models to describe the bulk properties of coaxial plumes. In the context of cooling towers, on the other hand, plume merger is expected to occur and modify the dilution rate compared to an isolated plume. All of these topics merit better insights and improved understanding. To be clear, we propose the following knowledge gaps:

- (i) The fluid dynamics and thermodynamics associated with the evolution of coaxial moist plumes in the atmosphere are incompletely understood. Double plume models have been formulated for coaxial jets (Morton, 1962) and turbulent fountains (Bloomfield & Kerr, 2000), however, a similar theory for co-flowing coaxial plumes has not been formulated.
- (ii) The coaxial plume model, on the basis of a three way entrainment assumption, incorporates three undetermined entrainment coefficients. Similitude laboratory experiments are expected to give some insight into how to determine the entrainment coefficients in theoretical models. For uniform plumes, the entrainment coefficient, i.e. α in (1.4), is generally determined by measuring the growth rate in plume radius or the volume flux at different vertical locations (Kaye, 2008). For coaxial plumes, however, it is not at all obvious how to define the boundary between the inner and outer plumes. A proper method to determine the entrainment coefficients in the case of coaxial plumes is yet to be proposed and validated.
- (iii) In a windy environment, it is unknown whether arguments (ii) and (iii) made by Houx Jr *et al.* (1978) are quantitatively correct. Whereas the theoretical formulation of uniform plumes in windy environments has been well established (Briggs, 1984), the counterpart “windy” theory for coaxial plumes has not been formulated.
- (iv) Most of previous irrotational flow models consider merger of ideal plumes (Kaye & Linden, 2004; Rooney, 2016), which cannot be directly applicable for cooling tower plumes characterized by large sources. The recent work of Rooney (2016) proposed that velocity potential contours can be approximated as boundaries of two or more merging plumes at different elevations. An extension of Rooney (2016) to the merger of two nonpoint source plumes remains to be explored.

- (v) Plume merger has not been studied thoroughly in the context of a back-to-back tower configuration. This configuration consists of two parallel rows of cooling tower cells connected by a common central wall (cf. Chapter 7). Of parallel importance are the dynamics of a single row of plumes in a crosswind. Rooney (2015) studied the merging of a single row of plumes in a quiescent environment using his irrotational flow theory. Analogous to (iv), possible extensions of Rooney (2015) to dual rows of plumes and a single row of plumes in a crosswind have not been explored.

1.4 Thesis scope and outline

The present document is written to fill those knowledge gaps described in section 1.3. All of the studies are closely tied together in the context of atmospheric plume modeling. Notwithstanding the fact that cooling towers are of particular interest, we have explored several novel and fundamental aspects of generic Boussinesq plume dynamics. In this spirit, the thesis is divided into two parts with Chapters 3, 4 and 5 examining the dynamics of coaxial plumes in stationary and windy ambient environments and Chapters 6 and 7 examining plume merger with applications to cooling towers.

Prior to those chapters describing novel research outputs, Chapter 2 gives a comprehensive overview of plume abatement approaches and atmospheric plume modeling. The history of cooling tower plume abatement is elaborated in detail and the approaches from different principles are summarized. On the other hand, the review of atmospheric plumes covers almost all aspects of modeling approaches, which can be analytical, or computational or laboratory experimental. Some specific topics are also included, such as plumes in turbulent environments, bifurcation instability and cooling tower drift deposition.

Chapter 3 explores the dynamics of coaxial plumes above hybrid crossflow wet/dry cooling towers with particular reference to a stationary and unstratified ambient. This purely theoretical study reveals that, compared to uniform plumes, coaxial plumes allow a higher rise velocity of the inner plume accompanied by a possible delay in the onset of condensation. However, some empirical entrainment coefficients in the theoretical model are left undetermined. To resolve this ambiguity, in Chapter 4 we conduct similitude laboratory experiments and perform a pixel-by-pixel comparison of theory vs. experiment, this in the interests of estimating the value of these entrainment coefficients. Further in Chapter 5, we investigate theoretically the dynamics of coaxial plumes in a windy environment.

Chapter 6 extends the irrotational flow analysis of Rooney (2016) to describe the merging of two plumes arising from area sources. We define the height at which two plumes fully merge and compare the irrotational flow prediction with the merging criteria of Wu & Koh (1978). Moreover, we propose a correction factor to the constant-entrainment-coefficient model that is purely dependent on the plume boundary curvature. Further to the analyses in Chapter 6, which focuses on the merging of two plumes, Chapter 7 examines the merging of plumes situated within one or two long rows. Specifically, Chapter 7 extends the theory of Rooney (2015) to describe (i) the merging of dual rows of plumes in a quiescent environment and (ii) merging of a single row of plumes in a crosswind.

Key conclusions (future topics) obtained from (related to) the present analyses are summarized and discussed in Chapter 8. Moreover, detailed derivations of uniform and coaxial

plume theories, experimental procedures and other related discussions are included in the appendices. In particular, Appendix A presents a derivation of uniform plume theory following the studies of Wu & Koh (1978) and Linden (2000). Appendix B presents a derivation of coaxial plumes following the studies of McDougall (1978) and Bloomfield & Kerr (2000). Unlike Appendices A and B, which focus on a stationary ambient, Appendix C considers a uniform plume in a windy ambient and the derivation of governing equations in question follows a control volume approach. Also presented in Appendix C is a comparison of theories using different entrainment formulations with the experimental results of Contini & Robins (2001). Appendix D derives the scaling of plume rise height and vertical velocity for point vs. line source plumes on dimensional grounds. Appendix E gives a rigorous justification for the fact that moisture effect on the plume dynamics is modest. Appendix F incorporates the finite source effect in the case of two area source plumes in a linearly stratified ambient.

Several parts of the thesis have been accepted or submitted for publication as journal papers, which are summarized in table 1.1. Note that the theoretical formulation for a uniform cooling tower plume in Chapter 3, originally adopted from the model of Wu & Koh (1978), was first implemented using MATLAB by Ali Moradi.

Table 1.1: Publications arising from the thesis.

Chapter	Journal	Status	Authors
2	<i>J. Wind Eng. Ind. Aerod.</i>	Submitted	S. Li & M.R. Flynn
3	<i>Int. J. Heat Mass Transf.</i>	Published	S. Li, A. Moradi, B. Vickers & M.R. Flynn
4	<i>Int. J. Heat Mass Transf.</i>	Submitted	S. Li & M.R. Flynn
5	<i>J. Wind Eng. Ind. Aerod.</i>	Published	S. Li & M.R. Flynn
6	<i>Phys. Rev. Fluids.</i>	Published	S. Li & M.R. Flynn
7	<i>Phys. Rev. Fluids.</i>	Submitted	S. Li & M.R. Flynn

1.5 Appendix A: Entrainment coefficient for plume in a stationary ambient

Reviews on entrainment coefficients can be found in Kaminski *et al.* (2005), Carazzo *et al.* (2006) and Kaye (2008). The conclusion made by Kaye (2008) is quoted here: “In conclusion, entrainment coefficient models are appropriate for fully developed self-similar flows and can also be used (with care) in some flow development regions such as the forced plume to pure plume transition. However, entrainment coefficient models are unlikely to be valid whenever the vertical length scale of a change is not significantly larger than the plume radius.”

The entrainment coefficient model discussed by Kaye (2008) is originally credited to the seminal work of Morton *et al.* (1956) (MTT hereafter), which is based on the conservation equations of mass, momentum and buoyancy and G.I. Taylor’s entrainment hypothesis as the closure condition. Recent publications on entrainment coefficients, e.g. van Reeuwijk & Craske (2015), seem to justify that the model of Priestley & Ball (1955) (PB hereafter) provides better physics underlying the entrainment assumption than the MTT model. The PB model imposes energetic restrictions on the entrainment coefficient introduced in MTT.

The derivation of PB model is given below following part of the notations in Kaminski *et al.* (2005).

1.5.1 Connection between PB and MTT models

The assumptions made in the PB model are as follows:

- (i) The flow is steady, axisymmetric and fully turbulent.
- (ii) The Boussinesq approximation is valid.
- (iii) Pressure is hydrostatic everywhere.
- (iv) The vertical transport due to turbulent fluctuations are small compared to the horizontal transport due to turbulent fluctuations.
- (v) The covariance in (1.55) is a quadratic function of vertical velocity, which serves as the closure condition for the kinetic energy conservation equation.

With the above assumptions, the volume, momentum and buoyancy conservation equations are as follows:

$$\frac{\partial}{\partial z} (r\bar{w}) + \frac{\partial}{\partial r} (r\bar{u}) = 0, \quad (1.41)$$

$$\frac{\partial}{\partial z} (r\bar{w}^2) + \frac{\partial}{\partial r} (r\bar{u}\bar{w}) = r\bar{g}' - \frac{\partial}{\partial r} (r\overline{u'w'}), \quad (1.42)$$

$$\frac{\partial}{\partial z} (r\bar{w}\bar{g}') + \frac{\partial}{\partial r} (r\bar{u}\bar{g}') = 0. \quad (1.43)$$

The conservation equation of kinetic energy of the axial mean motion can be derived from (1.41) and (1.42), which is expressed mathematically by

$$\frac{\partial}{\partial z} \left(\frac{1}{2} r\bar{w}^3 \right) + \frac{\partial}{\partial r} \left(\frac{1}{2} r\bar{u}\bar{w}^2 \right) = r\bar{w}\bar{g}' - \bar{w} \frac{\partial}{\partial r} (r\overline{u'w'}), \quad (1.44)$$

$$\begin{aligned} \text{LHS} &= \frac{1}{2} \left[\bar{w} \left(\frac{\partial}{\partial z} (r\bar{w}^2) + \frac{\partial}{\partial r} (r\bar{u}\bar{w}) \right) \right] + \frac{1}{2} \bar{w} \left(r\bar{w} \frac{\partial \bar{w}}{\partial z} + r\bar{u} \frac{\partial \bar{w}}{\partial r} \right) \\ &= \frac{1}{2} \left[r\bar{w}\bar{g}' - \bar{w} \frac{\partial}{\partial r} (r\overline{u'w'}) \right] + \frac{1}{2} \bar{w} \left[r\bar{w} \frac{\partial \bar{w}}{\partial z} + r\bar{u} \frac{\partial \bar{w}}{\partial r} + \bar{w} \left(\frac{\partial}{\partial z} (r\bar{w}) + \frac{\partial}{\partial r} (r\bar{u}) \right) \right] \\ &= \frac{1}{2} \left[r\bar{w}\bar{g}' - \bar{w} \frac{\partial}{\partial r} (r\overline{u'w'}) \right] + \frac{1}{2} \bar{w} \left[\frac{\partial}{\partial z} (r\bar{w}^2) + \frac{\partial}{\partial r} (r\bar{u}\bar{w}) \right] \\ &= r\bar{w}\bar{g}' - \bar{w} \frac{\partial}{\partial r} (r\overline{u'w'}) = \text{RHS}. \end{aligned}$$

Multiplying (1.42) by \bar{w}^n and integrating (from $r = 0$ to ∞) to get

$$\int_0^\infty w^n \left(\frac{\partial}{\partial z} (r\bar{w}^2) + \frac{\partial}{\partial r} (r\bar{u}\bar{w}) \right) dr = \int_0^\infty \bar{w}^n \left(r\bar{g}' - \frac{\partial}{\partial r} (r\overline{u'w'}) \right) dr,$$

$$\begin{aligned}
\text{LHS} &= \int_0^\infty \bar{w}^n \left(\frac{\partial}{\partial z} (r \bar{w}^2) + \bar{w} \frac{\partial}{\partial r} (r \bar{u}) + r \bar{u} \frac{\partial \bar{w}}{\partial r} \right) dr \\
&= \int_0^\infty \bar{w}^n \left(\frac{\partial}{\partial z} (r \bar{w}^2) - \bar{w} \frac{\partial}{\partial z} (r \bar{w}) + r \bar{u} \frac{\partial \bar{w}}{\partial r} \right) dr \quad \leftarrow \text{using (1.41)} \\
&= \int_0^\infty \bar{w}^n \left(r \bar{w} \frac{\partial \bar{w}}{\partial z} + r \bar{u} \frac{\partial \bar{w}}{\partial r} \right) dr \\
&= \int_0^\infty r \bar{w}^{n+1} \frac{\partial \bar{w}}{\partial z} dr + \frac{1}{n+1} \int_0^\infty r \bar{u} \frac{\partial \bar{w}^{n+1}}{\partial r} dr \\
&= \int_0^\infty r \bar{w}^{n+1} \frac{\partial \bar{w}}{\partial z} dr + \frac{1}{n+1} \left\{ [r \bar{u} \bar{w}^{n+1}]_0^\infty - \int_0^\infty \bar{w}^{n+1} \frac{\partial}{\partial r} (r \bar{u}) dr \right\} \quad \leftarrow \text{integration by parts} \\
&= \int_0^\infty r \bar{w}^{n+1} \frac{\partial \bar{w}}{\partial z} dr + \frac{1}{n+1} \int_0^\infty r \bar{w}^{n+1} \frac{\partial \bar{w}}{\partial z} dr \quad \leftarrow \text{using (1.41)} \\
&= \frac{n+2}{n+1} \int_0^\infty \frac{1}{n+2} r \frac{\partial \bar{w}^{n+2}}{\partial z} dr \\
&= \frac{1}{n+1} \int_0^\infty \frac{\partial}{\partial z} (r \bar{w}^{n+2}) dr \\
&= \frac{1}{n+1} \frac{d}{dz} \int_0^\infty r \bar{w}^{n+2} dr \\
\text{RHS} &= \int_0^\infty r \bar{w}^n \bar{g}' dr - \int_0^\infty \bar{w}^n \frac{\partial}{\partial r} (r \bar{u}' \bar{w}') dr \\
&= \int_0^\infty r \bar{w}^n \bar{g}' dr - \left\{ [r \bar{u}' \bar{w}' \bar{w}^n]_0^\infty - \int_0^\infty r \bar{u}' \bar{w}' \frac{\partial \bar{w}^n}{\partial r} dr \right\} \quad \leftarrow \text{integration by parts} \\
&= \int_0^\infty r \bar{w}^n \bar{g}' dr + \int_0^\infty r \bar{u}' \bar{w}' \frac{\partial \bar{w}^n}{\partial r} dr \\
&\quad \therefore \frac{d}{dz} \int_0^\infty \frac{1}{n+1} r \bar{w}^{n+2} dr = \int_0^\infty r \bar{w}^n \bar{g}' dr + \int_0^\infty r \bar{u}' \bar{w}' \frac{\partial \bar{w}^n}{\partial r} dr. \tag{1.45}
\end{aligned}$$

Substituting n with 0 and 1, we respectively obtain the momentum and mean kinetic energy conservation equations, which are written as follows:

$$\frac{d}{dz} \int_0^\infty r \bar{w}^2 dr = \int_0^\infty r \bar{g}' dr, \tag{1.46}$$

$$\frac{d}{dz} \int_0^\infty \frac{1}{2} r \bar{w}^3 dr = \int_0^\infty r \bar{w} \bar{g}' dr + \int_0^\infty r \bar{u}' \bar{w}' \frac{\partial \bar{w}}{\partial r} dr. \tag{1.47}$$

Integration of (1.43) yields the buoyancy conservation equation as follows:

$$\frac{d}{dz} \int_0^\infty r \bar{w} \bar{g}' dr = -N^2 \int_0^\infty r \bar{w} dr, \tag{1.48}$$

where the buoyancy frequency is $N = \sqrt{-\frac{g}{\rho_a} \frac{d\rho_a}{dz}} = 0$ for an unstratified ambient. We further define the volume, momentum, buoyancy and mean kinetic energy fluxes of the plume as follows:

$$Q = 2\pi \int_0^\infty r \bar{w} dr, \tag{1.49}$$

$$M = 2\pi \int_0^\infty r \bar{w}^2 dr, \quad (1.50)$$

$$F = 2\pi \int_0^\infty r \bar{w} \bar{g}' dr, \quad (1.51)$$

$$K = 2\pi \int_0^\infty \frac{1}{2} r \bar{w}^3 dr. \quad (1.52)$$

Meanwhile, we introduce three shape functions, $f(r, z)$, $h(r, z)$ and $j(r, z)$, which are defined as follows:

$$\bar{w}(r, z) = w_m(z) f(r, z), \quad (1.53)$$

$$\bar{g}'(r, z) = g'_m(z) h(r, z), \quad (1.54)$$

$$\overline{u'w'}(r, z) = -\frac{1}{2} w_m(z)^2 j(r, z), \quad (1.55)$$

where $w_m(z)$ and $g'_m(z)$ are the characteristic vertical velocity and reduced gravity, respectively. Substituting the above shape functions into (1.46)-(1.48) yields

$$\frac{dM}{dz} = 2\pi I_2 b_m^2(z) g'_m(z), \quad (1.56)$$

$$\frac{dK}{dz} = 2\pi \left(I_1 b_m^2(z) w_m(z) g'_m(z) - \frac{1}{2} I_5 b_m(z) w_m^3(z) \right), \quad (1.57)$$

$$\frac{dF}{dz} = -N^2 Q = 0, \quad (1.58)$$

where $M = 2\pi I_3 b_m^2(z) w_m^2(z)$, $K = \pi I_4 b_m^2(z) w_m^3(z)$, $F = 2\pi I_1 b_m^2(z) w_m(z) g'_m(z)$ and $b_m(z)$ is a characteristic radial length scale. The integral parameters, i.e. I_1 to I_5 , are defined as

$$I_1 = \int_0^\infty r^* f(r^*, z) h(r^*, z) dr^*, \quad (1.59)$$

$$I_2 = \int_0^\infty r^* h(r^*, z) dr^*, \quad (1.60)$$

$$I_3 = \int_0^\infty r^* f(r^*, z)^2 dr^*, \quad (1.61)$$

$$I_4 = \int_0^\infty r^* f(r^*, z)^3 dr^*, \quad (1.62)$$

$$I_5 = \int_0^\infty r^* j(r^*, z) \frac{\partial f}{\partial r^*} dr^*, \quad (1.63)$$

where $r^* = r/b_m(z)$. The volume flux, Q , can also be expressed using the above integral parameters

$$Q = 2\pi b_m^2(z) w_m(z) \int_0^\infty r^* f(r^*, z) dr^* = 2\pi \frac{I_2 I_3}{I_1} b_m^2(z) w_m(z), \quad (1.64)$$

where

$$\int_0^\infty r^* f(r^*, z) dr^* = \frac{\int_0^\infty r^* h(r^*, z) dr^* \int_0^\infty r^* f(r^*, z)^2 dr^*}{\int_0^\infty r^* f(r^*, z) h(r^*, z) dr^*}. \quad (1.65)$$

Equation (1.65) is similar to the relation, i.e. equation (3.37), proposed in Linden (2000). $b_m(z)$, $w_m(z)$ and $g'_m(z)$ can be expressed in terms of Q , M and F

$$b_m(z) = \sqrt{\frac{I_1^2 Q^2}{2\pi I_2^2 I_3 M}}, \quad (1.66)$$

$$w_m(z) = \frac{I_2 M}{I_1 Q}, \quad (1.67)$$

$$g'_m(z) = \frac{I_2 I_3 F}{I_1^2 Q}. \quad (1.68)$$

Thus (1.56) can be rewritten as

$$\frac{dM}{dz} = \frac{FQ}{M}. \quad (1.69)$$

To connect the PB model with the MTT model, the kinetic energy conservation equation, (1.57), is used to derive a volume conservation equation. The LHS of (1.57) is rewritten as

$$\begin{aligned} \frac{dK}{dz} &= \frac{d}{dz} (\pi I_4 b_m^2(z) w_m^3(z)) \\ &= \frac{d}{dz} \left(\frac{I_2 I_4}{2 I_1 I_3} \frac{M^2}{Q} \right) \\ &= \frac{I_2 I_4}{2 I_1 I_3} \left(2F - \frac{M^2}{Q^2} \frac{dQ}{dz} \right) + \frac{M^2}{2Q} \frac{d}{dz} \left(\frac{I_2 I_4}{I_1 I_3} \right). \end{aligned} \quad (1.70)$$

Replacing $A = \frac{I_2 I_4}{I_1 I_3}$ on the RHS of (1.57), $\frac{dQ}{dz}$ is obtained as

$$\begin{aligned} \frac{dQ}{dz} &= \frac{2Q^2 F}{M^2} + \frac{Q}{A} \frac{dA}{dz} - \frac{2Q^2}{AM^2} \frac{dK}{dz} \\ &= \frac{2Q^2 F}{M^2} \left(1 - \frac{1}{A} \right) + \frac{Q}{A} \frac{dA}{dz} + C\sqrt{\pi M} \\ &= 2\sqrt{\pi M} \left[\frac{Q^2 F}{\pi^{1/2} M^{5/2}} \left(1 - \frac{1}{A} \right) + \frac{Q}{2\pi^{1/2} M^{1/2}} \frac{d \ln A}{dz} + \frac{1}{2} C \right], \end{aligned} \quad (1.71)$$

where $C = \frac{I_2 I_3^{1/2} I_5}{I_1 I_4}$. The counterpart volume conservation equation in MTT is mathematically as

$$\frac{dQ}{dz} = 2\sqrt{\pi M} \alpha_e. \quad (1.72)$$

Therefore, the entrainment coefficient is explicitly given in the PB model as follows:

$$\alpha_e = \text{Ri} \left(1 - \frac{1}{A} \right) + \frac{R}{2} \frac{d \ln A}{dz} + \frac{1}{2} C, \quad (1.73)$$

where $\text{Ri} = \frac{Q^2 F}{\pi^{1/2} M^{5/2}}$ is the local Richardson number and $R = \frac{Q}{\pi^{1/2} M^{1/2}}$ is defined as the top-hat plume radius. Equation (1.73) indicates a linear dependence of α_e on Ri . The integral parameters, A and C , can be rewritten as

$$A = \frac{2QK}{M^2} = \frac{\int_0^\infty \frac{1}{2} r \bar{w}^3 dr}{\frac{1}{4} R^2 W^3}, \quad (1.74)$$

$$C = \frac{R}{\sqrt{2}b_m} \frac{\int_0^\infty r^* j \frac{\partial f}{\partial r^*} dr^*}{\int_0^\infty r^* f^3 dr^*}, \quad (1.75)$$

where $W = \frac{M}{Q}$ is defined as the top-hat plume vertical velocity. C is interpreted as the ratio of the energy transferred from the mean motion to the turbulent fluctuations, over the total flux of the mean kinetic energy, which also indicates the fraction of the mean kinetic energy responsible for turbulent entrainment. A indicates the influence of the shape of the velocity profile on entrainment. For top-hat profiles, the shape functions are equal to unity, thus $A = 1$. For Gaussian profiles, the velocity and reduced gravity are respectively as follows:

$$\bar{w}(r, z) = w_m(z) \exp \left[- \left(\frac{r}{b_m} \right)^2 \right] = w_m(z) \exp(-r^{*2}), \quad (1.76)$$

$$\bar{g}'(r, z) = g'_m(z) \exp \left[- \left(\frac{r}{\Lambda b_m} \right)^2 \right] = g'_m(z) \exp \left[- \left(\frac{r^*}{\Lambda} \right)^2 \right], \quad (1.77)$$

where Λ is the ratio of the half-width of the buoyancy profile to the half-width of the velocity profile. Thus A is simplified as

$$A = \frac{I_2 I_4}{I_1 I_3} = \frac{\int_0^\infty r^* \exp \left[- \left(\frac{r^*}{\lambda} \right)^2 \right] dr^* \int_0^\infty r^* [\exp(-r^{*2})]^3 dr^*}{\int_0^\infty r^* \exp(-r^{*2}) \exp \left[- \left(\frac{r^*}{\lambda} \right)^2 \right] dr^* \int_0^\infty r^* [\exp(-r^{*2})]^2 dr^*} = \frac{\frac{\lambda^2}{2} \frac{1}{6}}{\frac{\lambda^2}{2(\lambda^2+1)} \frac{1}{4}} = \frac{2}{3} (\lambda^2 + 1). \quad (1.78)$$

1.5.2 Further discussion

On the basis of laboratory experimental results in related literature, Kaminski *et al.* (2005) obtained different values of A and C . Their table 3 showed that there are modest variations in C but large variations in A . Moreover, they found a systematic increase in the value of A as a function of downstream distance, which was referred to as a so-called similarity-drift. This similarity-drift may help reconcile the various results on entrainment coefficient measured by different groups.

van Reeuwijk & Craske (2015) extended the work of Kaminski *et al.* (2005) and proposed the general entrainment relation, i.e. their equation 3.1. The effects of mean flow quantities, turbulence and pressure on entrainment are included. Specifically, the universal entrainment coefficient is composed of contributions from the ratio of turbulence production to energy flux, the net effect of buoyancy and the similarity drift, respectively. One of their findings is that the enhanced mixing in plumes compared to jets is primarily associated with the mean flow of the plume and not buoyancy-enhanced turbulence. The more recent work of Ciriello & Hunt (2020) has referred to the linear dependence of the entrainment coefficient on Richardson number as a universal entrainment function, which is given as

$$\alpha_e = \gamma_1 + \gamma_2 \text{Ri}, \quad (1.79)$$

where γ_1 and γ_2 are constant coefficients that are summarized in table 1 of Ciriello & Hunt (2020).

Chapter 2

Cooling tower plume abatement and plume modeling: A review

2.1 Abstract

Visible plumes above wet cooling towers are of great concern due to the associated aesthetic and environmental impacts. The parallel path wet/dry cooling tower is one of the most commonly used approaches for plume abatement, however, the associated capital cost is usually high due to the addition of the dry coils. Recently, passive technologies, which make use of free solar energy or the latent heat of the hot, moist air rising through the cooling tower fill, have been proposed to minimize or abate the visible plume and/or conserve water. In this review, we contrast established vs. novel technologies and give a perspective on the relative merits and demerits of each.

Of course, no assessment of the severity of a visible plume can be made without first understanding its atmospheric trajectory. To this end, numerous attempts, being either theoretical or numerical or experimental, have been proposed to predict plume behavior in atmospheres that are either uniform vs. density-stratified or still vs. windy (whether highly-turbulent or not). Problems of particular interests are plume rise/deflection, condensation and drift deposition, the latter consideration being a concern of public health due to the possible transport and spread of *Legionella* bacteria.

2.2 Introduction

Cooling towers are heat dissipation devices commonly found in industrial plants and HVAC systems. In general, two types of cooling towers, i.e. wet and dry, are used; these exploit evaporative and non-evaporative heat transfer mechanisms, respectively. As shown in figures 2.1 and 2.2, wet cooling towers are classified as counterflow and crossflow according to the respective directions of the air and water streams. As defined by Holiday & Alsayed (2015), sustainability in a cooling system encompasses efficient operation, impact on the environment, depletion of natural resources and ecology. For instance, a reduction in the fan power consumption or pump head facilitates a more efficient operation. On the other hand, visible plumes, water conservation and drift deposition are closely related to the environmental

impact, as is plume rise, which dictates the maximum ground concentration of air pollutants.

Modeling the heat and mass transfer in a wet cooling tower, particularly within the fill zone, has been performed since the seminal work of Merkel (1925), followed by the ϵ -NTU method (Jaber & Webb, 1989), Poppe method (Poppe & Rögener, 1991) and Klimanek method (Klimanek & Bialecki, 2009). A comprehensive comparison between the Merkel, ϵ -NTU and Poppe methods is presented in Kloppers & Kröger (2005a,b), which concluded that the Poppe method, being the most algebraically-involved, is also the most accurate for the design of hybrid wet/dry cooling towers. Meanwhile, the Klimanek method is largely equivalent to the Poppe method (cf. table 1 of Klimanek & Bialecki 2009) except that its governing equations consider as the independent variable elevation within the tower rather than the water temperature. In the Merkel method, the cooling tower exit air is always assumed to be exactly saturated, which is inaccurate in case of extreme (hot dry or cold humid) conditions. The Poppe and Klimanek methods, on the other hand, avoid this deficiency and thus improve the prediction of the water evaporation rate.

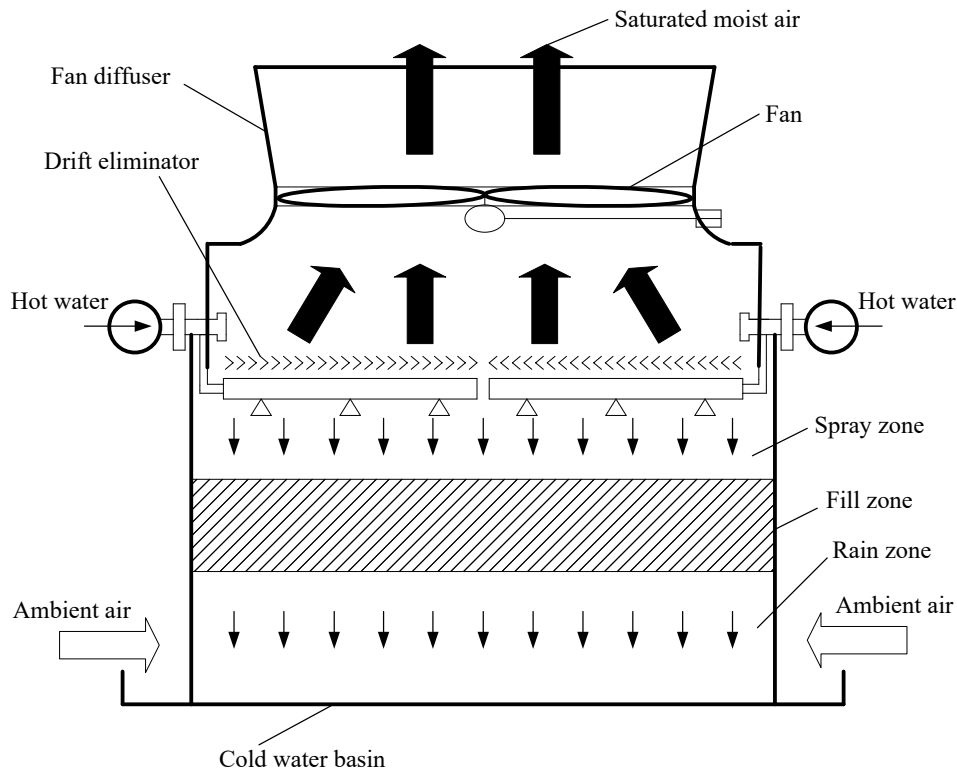


Figure 2.1: Schematic of a counterflow wet cooling tower. The thick white and black arrows denote the incoming ambient air into the cooling tower and the hot, humid air coming out of the wet section, respectively. The thin arrows denote the water stream.

The water lost due to evaporation, drift and blowdown¹ in a typical wet cooling tower is 3% to 5% of the circulating water (Hensley, 2009). To compensate this loss, make-up water, where available, is required, this to avoid an accumulation of impurities and contaminants. The source and chemistry of this make-up water have an obvious impact on the difficulty

¹Blowdown is the water discharged from the system to control the concentrations of salts and other impurities in the circulating water.

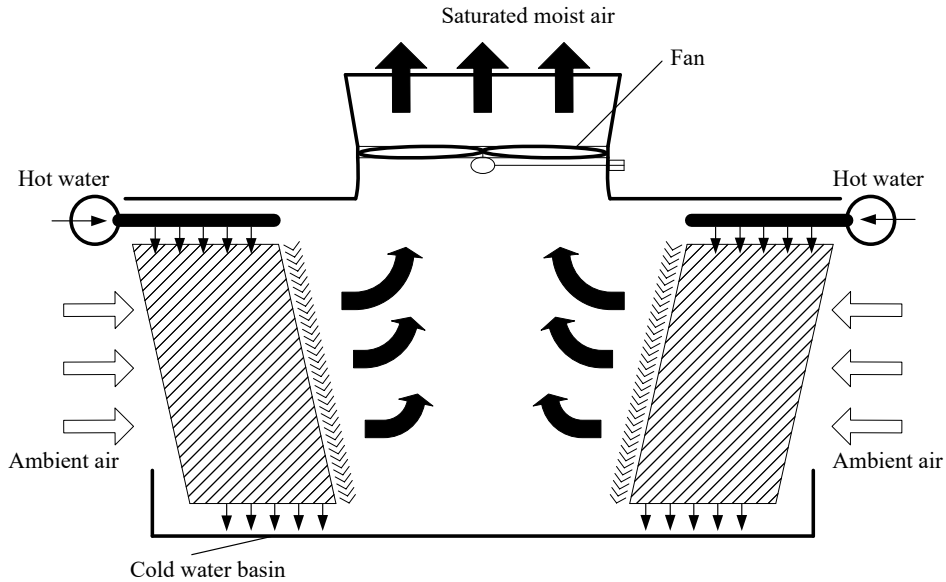


Figure 2.2: Schematic of a crossflow wet cooling tower. Arrow types are as in figure 2.1. Note that the fill is installed at an angle to the vertical to account for the inward motion of water droplets due to the drag associated with the incoming air (Kröger, 2004).

of maintaining water quality. Also, although blowdown ensures that a portion of the recirculating water is discharged and replenished with pure make-up water, the challenges associated with contaminant concentration increases is not restricted to engineering equipment/process: water quality adversely affects the discharged air quality due to e.g. drift contained in the moist air exiting the tower. The situation is especially significant when considering *Legionella* bacteria, which may be carried by the drift. Talbot (1979) revealed the acute effects of salt drift on vegetation from a closed-cycle salt water cooling tower, but the damage was limited to the close proximity of the tower. A review by Walser *et al.* (2014) summarized the severe health problems of legionellosis outbreaks due to the operation of cooling towers. Even when *Legionella* bacteria are eradicated by appropriate chemical treatments, a visible plume may be considered as a nuisance for the fact that it is perceived as aesthetically-unpleasant and it has the potential to cause reduced visibility and/or icing on neighboring surfaces (e.g. roadways) when the ambient temperature is sufficiently low. Latimer & Samuelsen (1978) conducted a theoretical examination of the visual impact of a cooling tower plume focusing on the effects of plume coloration and reduced visual range. This work was followed up many years later by Lee (2018) who performed an environmental impact assessment of cooling towers in a nuclear power plant. Notably, Lee (2018) quantified the effects of visible plumes in terms of plume length and shadowing (and the commensurate loss of solar energy), fogging and icing, and salt and water depositing. Moreover, these effects were tested by Lee (2018) under different cooling tower configurations, heat load per tower and air flow rate per tower.

In the context of plume abatement, reference is often made to the standard plume performance testing code – CTI ACT 150 (ATC, 2011). The 150 code proposes two levels of plume guarantee for hybrid wet/dry cooling towers, Level 1 and Level 2. Level 1 specifies that the measured exhaust relative humidity should be lower than the guarantee relative humidity,

determination of which comes from the plume characteristic performance curves provided by the cooling tower manufacturer. However, Level 1 does not require complete mixing of the wet and dry airstreams within the plenum chamber (defined as the enclosed space above the drift eliminator and below the fan in an induced draft tower). Level 2, on the other hand, is more stringent than Level 1, i.e. it requires satisfaction of a mixing criteria. The principle of this mixing criteria is to check whether all measured exhaust air properties are within an acceptable variation compared to the average properties. The measured parameters of key interest are the relative humidity and air velocity. To achieve complete mixing, mixing devices are commonly added to the plenum chamber as a result of which fan power consumption increases. Notwithstanding the distinction between Level 1 and Level 2, recent studies, e.g. Li *et al.* (2018), indicate that visible plumes can be partially or completely eliminated even with partial mixing within the plenum chamber. Using the approach of Li *et al.* (2018), fewer internal mixing devices are required and the moist air discharged to the environment is “shielded” by a sheath of buoyant but much drier air in the manner of Houx Jr *et al.* (1978).

In addition to fan power, strategies for plume abatement also impact electrical energy consumption by recirculating pumps. Traditional hybrid cooling tower designs tend to locate the dry cooling coils above the wet section, thus increasing the total pump head. Some recent designs abandon the dry cooling coils and instead use an air-to-air heat exchanger or a thermosyphon system – see Lindahl & Mortensen (2010) and Mantelli (2016). Alternatively, the dry section may be arranged in parallel with the wet section (Libert *et al.*, 2015). Moreover, the dry coils, in the context of plume abating cooling towers, can be replaced with solar collectors similar to the one shown in figure 2.5 below.

The previous discussion focuses principally on heat and mass transfer processes internal to a cooling tower. Having set the stage, we turn for the remainder of this section to exterior processes, i.e. plumes in the atmosphere. Cooling tower plumes are similar to, but different than, chimney stack plumes. One obvious distinction is the presence of large amounts of water vapor in the cooling tower case. Nonetheless, only a moderate amount of water vapor will condense contributing, in the process, to an increase of plume buoyancy. Thus simple analytical formulas like Briggs’s “two thirds” law, gives reasonable estimates for cooling tower plume rise (Briggs, 1984). To improve model performance, more sophisticated theoretical models have been proposed to predict the plume trajectory and dilution simultaneously. These integral-type theoretical models are efficient and useful tools, but are limited to boundary layer type flows in unbounded environments. Some phenomena are beyond the reach of these models, e.g. recirculation, which occurs when a strong wind blows over a line of cooling tower cells, leading to a one-sided increase in the wet-bulb temperature for the incoming air. To resolve these more complex flow interactions, guidance is sought from CFD simulation and/or similitude laboratory experiment. A similar appeal must be made when examining the details of plume bifurcation or the complicated manifestations of plume rise through a turbulent environment.

The main goals of this review are two-fold: (i) to summarize the strategies for plume abatement and to describe some of the physics that underlie these strategies, (ii) to give a selective description of plume modeling approaches that are necessary to better understand plume abatement strategies. These two goals serve to improve efforts to design and construct cooling towers that are more sustainable and less energy intensive.

The rest of the review is organized as follows. Section 2.3 discusses the frequency and

severity of plume visibility. Section 2.4 describes various plume abatement approaches. Section 2.5 focuses on plume modeling with emphasis on theoretical, CFD and laboratory experimental approaches. Special topics such as plume rise in a turbulent environment, plume bifurcation and drift deposition are discussed in sections 2.5.4, 2.5.5 and 2.5.6, respectively. Finally in section 2.6 we draw conclusions and outline knowledge gaps/areas for future research.

2.3 Plume visibility

Winter (1997) reviewed the influence of increasing public awareness of visible plumes on cooling tower selection for combined cycle gas turbine power stations in the UK. He suggested that the fogging frequency be used to evaluate plume abated towers; this can be calculated by making reference to a fogging frequency curve on a psychrometric chart as shown in figure 2.3 a. According to the 150 code (ATC, 2011), and for a given operating condition, the fogging frequency curve is defined as a curve that divides the psychrometric chart according to whether a visible vs. invisible plume is expected. Illustrated in figure 2.3 b is the method for generating such a curve; this method references the collection of ambient conditions (for a given operating condition) that allow the fan to ambient mix-lines to be exactly tangent to the saturation curve. Given site-specific weather statistics, it is possible to determine the fogging frequency at a given location, which can be expressed as the proportion of operating hours wherein visible plumes may occur. The 150 code argues that a typical plume abatement design point should allow 15% to 20% visible plume occurrence based on full year day-night weather statistics. Although theoretically any point on the fogging frequency curve can be chosen as the design point, a design point above the freezing point is recommended in order to test the cooling tower. For example, and in figure 2.3 a, the plume abatement design point corresponds to an ambient temperature of 5°C and relative humidity (RH) of 90%.

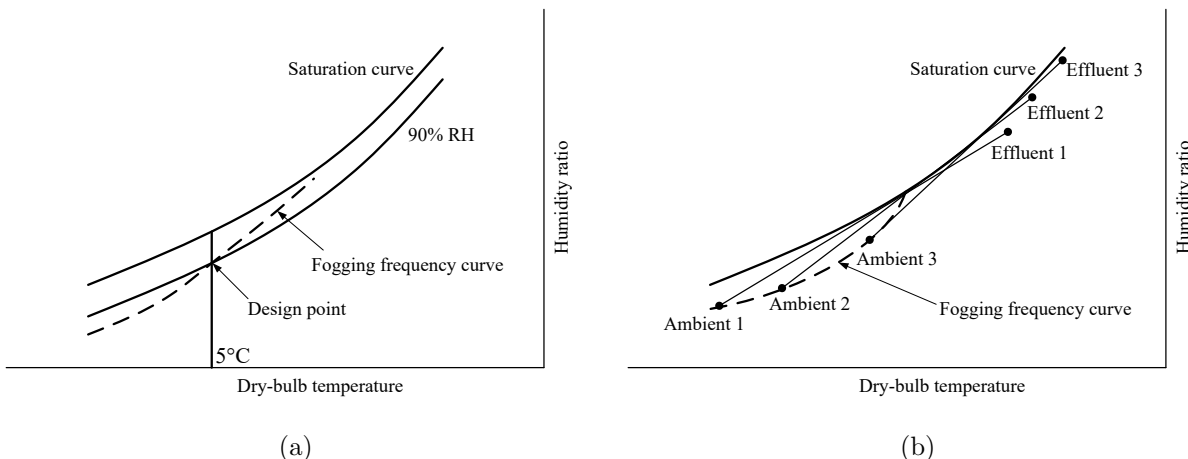


Figure 2.3: (a): A fogging frequency curve from Winter (1997). Similar curves can be found in figure 15 of Lindahl & Jameson (1993) or figure 2 of Lindahl & Mortensen (2010). (b): Method of generating the fogging frequency curve.

Tyagi *et al.* (2007) proposed the so-called plume potential to quantify the visible plume

intensity, which is defined as the area between the fan to ambient mix-line and the saturation curve on a psychrometric chart – see figure 2.4. The greater this area, which is given mathematically by (2.1), where w is the humidity ratio in g/kg dry air, the more intense will be the fog.

$$A = 2 \int_{w_2}^{w_1} \sqrt{w} \, ds. \quad (2.1)$$

More recently, and rather than examining intersected areas in a psychrometric chart, Cizek & Nozicka (2016) considered the overall volume of the visible plume, which is expressed as an empirical coefficient times the third power of the cooling tower diameter. Cizek & Nozicka (2016) revealed that the overall visible plume volume depends sensitively on the cooling tower diameter, the temperature and humidity of the exhaust and ambient air, but does not depend on the plume source velocity.

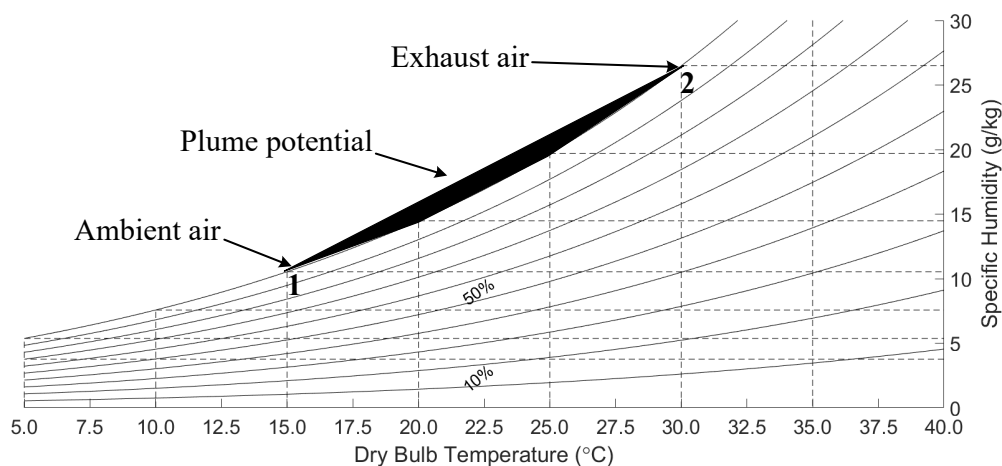


Figure 2.4: Visible plume potential defined in Tyagi *et al.* (2007).

2.4 Visible plume abatement

Veldhuizen & Ledbetter (1971) presented a summary of approaches to fog control: (i) preventing fog formation by superheating the plume and altering the cooling method, (ii) removing the fog by sedimentation after particle growth by impaction of water droplets on cold surfaces, by chemical desiccation or by electrostatic sweeping (or related air-cleaning methods) of droplet-nucleating particles, and, (iii) restricting the fog from reaching ground level by elevating the plume through mechanical jetting or heating. Veldhuizen & Ledbetter (1971) pointed out that the difficulty in fog control is the large flow rate of air containing small water droplets.

A more comprehensive review of plume abatement technologies was conducted by Lindahl & Mortensen (2010) – see table 2.1. The main comparisons are made between PPWD towers and more novel approaches such as condensing module technology. Lindahl & Mortensen (2010) argued that condensing module technology offers a means to reduce capital and oper-

ating costs, and is especially suitable for large back-to-back towers². The physical principles underlining condensing module technology are detailed in section 2.4.5.

Table 2.1: The evolution of plume abatement designs as summarized in Lindahl & Mortensen (2010).

Timeline	Tower design	Advantages	Disadvantages
1960's	Series path wet/dry (SPWD) towers	Well-mixed exhaust air	Full-time pressure drop, widely spaced fins and high pump head for hot water coils
1970's	Parallel path wet/dry (PPWD) towers	Face dampers added to the dry and wet sections, water conserving compared to wet cooling towers	Additional pressure drop due to mixing devices typically used in PPWD counterflow towers
2000's	Condensing module technology	No dry section, high water conservation capability, no mixing devices, low drift rate, less blowdown and make-up through recovery of the near condensate quality water, no pumping head above the wet section, suitable for back-to-back tower configurations	Full-time pressure drop due to its series air path, increased pressure drop due to the air ducts and air-to-air heat exchangers in the plenum chamber

Following the framework outlined in table 2.1, the rest of this section is structured as follows. Section 2.4.1 discusses the method of superheating the exhaust air, which generally occurs in series path wet/dry (SPWD) towers. Sections 2.4.2, 2.4.3 and 2.4.4 focus on different mixing techniques in the context of PPWD towers. Section 2.4.5 reviews various water conservation approaches and some novel tower designs.

2.4.1 Superheating the exhaust air

In a SPWD cooling tower, sensibly heating the exhaust air can not only decrease its relative humidity, but also increase its temperature and therefore buoyancy. Research in this category mainly focuses on the heat sources and the associated control strategies for plume abatement. For instance, Wang & Tyagi (2006) and Tyagi *et al.* (2007) used heat pumps to heat the exhaust air from wet cooling towers. The advantage is that the coefficient of performance for a heat pump is much greater than unity. However, the inclusion of heat pumps obviously adds

²The back-to-back tower configuration combines two lines of cooling tower cells into one line, which has a common wall located at the centerplane of the “dual row” towers. The advantage of the back-to-back tower configuration is its reduced footprint compared to an equal number of cooling tower cells arranged in two parallel lines.

to the capital, operational and maintenance costs associated with the cooling tower proper. Later Wang *et al.* (2009) compared three arrangements of heat pump system for plume abatement in a large chiller plant in a subtropical region. Specifically, the evaporative side of the heat pump can be located at the inlet or outlet side of the cooling towers to decrease the cooling water temperature, or alternatively at the evaporative side of the chillers to reduce the return chilled water temperature – see their figures 1 and 3. Meanwhile, the hot water in the dry coils of the hybrid wet/dry cooling tower are provided by heat pumps. Their study indicated that the aforementioned three arrangements have almost identical plume control performance. Regarding the overall energy efficiency, the latter arrangement had much better performance than the former two arrangements. More generally, heat pumps have the thermodynamic advantage of offering combined heating and cooling.

As exhibited schematically in figure 2.5, Wang *et al.* (2007) investigated the application of a solar collector to mitigate the visible plume from wet cooling towers as a case study in Hong Kong. Their discussion revealed that water cooled collectors were more cost-effective than air cooled collectors. They also argued that there should be some alternate heat sources to assist due to the intermittency of solar energy during the day and its complete absence at night.

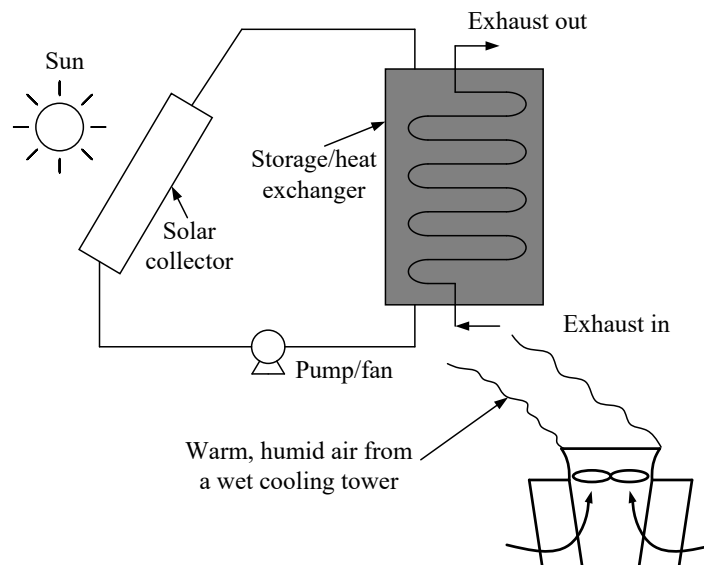


Figure 2.5: A water/air cooled flat plate solar collector to heat the exhaust from wet cooling towers.

2.4.2 Enhanced mixing by static devices

Whereas the discussion of section 2.4.1 focused primarily on small-scale cooling towers e.g. those that form part of air-conditioning systems for commercial buildings, here we return to the larger models more typically found in industry. In a PPWD counterflow cooling tower, the warm, dry air from the dry section and the hot, humid air from the wet section are mixed in the plenum chamber thus reducing the possibility of condensation upon discharge. As expected, a visible plume may occur if the mixing is inadequate. Because the mixing length is relatively short (no more than the height of the plenum plus the fan diffuser), mixing devices

are commonly added to promote the mixing between those two (initially) perpendicular air streams. Streng (1998) noted that “the optimal shape and arrangement of static mixers as a function of the specific cooling tower geometry is of particular significance”.

Generally, deflecting surfaces are used to channelize the flow of dry air and to thereby promote the penetration of at least some fraction of this dry air into the central region of the plenum chamber. Thus the area of contact between the wet and dry air streams greatly increases. Meanwhile, the deflecting structure, if not streamlined in the direction of the wet airstream, tends to generate flow separation and turbulent mixing ensues downstream. Unavoidably, the structural expense can be heavy as can the increased pressure drop. Nonetheless, deflecting surfaces are particularly effective for back-to-back cooling towers where it is difficult to convey adequate dry air to the central wall.

Kinney Jr *et al.* (1999) argued that the geometric orientations of the dry and wet sections impose restrictions on the air flow patterns such that the warm, dry air from the dry section tends to follow a path directly to the nearest lower edges of the fan diffuser. The hot, humid air from the wet section, on the other hand, occupies the central part of the plenum chamber. For enhanced mixing, they proposed that simple flat plates, extending from the lower part of the dry section to the central core of the plenum chamber, are adequate for mixing the two air streams in certain instances.

Carbonaro (1983) introduced a type of rectilinear deflecting surface (referred to as an air channeling device) with a decreasing V-shaped cross section – see figure 2.6. As compared to e.g. a flat plate, this V-shaped structure along which the dry air travels is expected to impose less obstruction to the upward moving wet air. Moreover, the tapered V-shape cross section can cause some fraction of the dry air flow to overflow and thereby mix into the wet air all along the length of the channel.

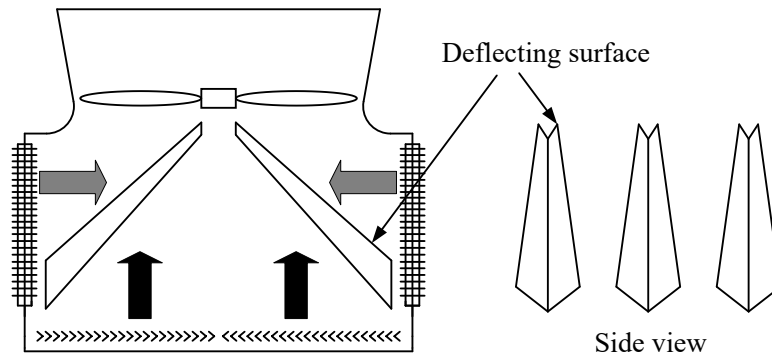


Figure 2.6: The tapered V-shaped deflecting surface proposed by Carbonaro (1983).

Schulze (2010) proposed the use of truncated pyramid-like mixing baffles inside the plenum chamber. These baffles project transversely into the ascending wet air and direct the dry air into the central region of the plenum chamber. The roof surface of the baffles can be open or closed automatically according to the varying operation modes of the hybrid cooling tower. In winter mode of high plume abatement demand, the roof should be closed to allow more mixing between the wet and dry air. In summer mode when the demand for plume abatement is less, the roof should be fully open to minimize the pressure drop. Similar air ducts to convey dry air into the central region of the plenum chamber are applied in forced

draft cooling towers, where the fans are located at the air inlet – see e.g. figure 2.7. Vortex mixing occurs as the wet air flows over the air ducts.

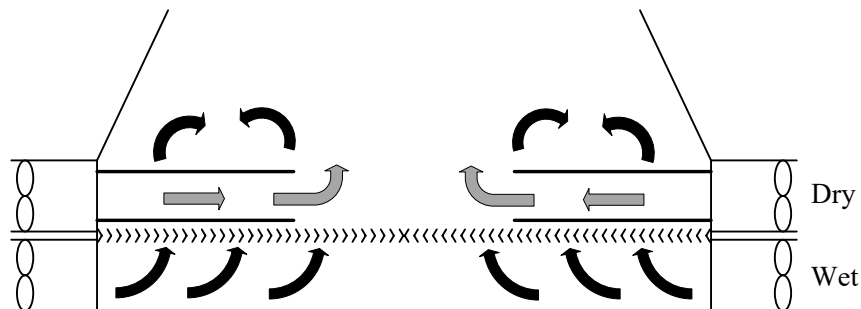


Figure 2.7: Schematic of air ducts in a forced draft cooling tower (Ruscheweyh, 1985).

Lee (2017) proposed an air distributor to promote mixing between wet and dry airstreams. According to this scheme, the plan area of the plenum chamber can be divided into regions for the wet and dry airstreams, which are separated by partition walls. Analogous to the deflecting device in Schulze (2010), enough dry air ought to be directed to the central region and/or, in a back-to-back configuration, the common central wall. Although this design suffers from a significant flow obstruction experienced by the wet air, the mixture quality can be superior to the simple baffle case.

Ruscheweyh (1984, 1985) introduced a delta-shaped vortex generator, which facilitates enhanced mixing at the cost of moderate pressure drop. The performance of this type of vortex generator was tested using reduced-scale laboratory experiments. In these experiments, and as shown in figure 2.8, the air introduced into the plenum chamber through the dry section is clean air and the counterpart stream from the wet section is a mixture of smoke and clean air. The addition of smoke facilitates flow visualization and, more importantly, the quality of the mixture at the fan exit can be determined by measuring the smoke concentration in the radial direction. Figure 2.8 a indicates that, without the benefit of the vortex generator, the “wet air” accumulates in the central core upon discharge due to the poor mixing. By contrast, figure 2.8 b shows a relatively uniform smoke plume as a result of enhanced mixing caused by addition of the vortex generators.

2.4.3 Enhanced mixing by stirring devices

Moon (2017) put a number of circularly spaced guide vanes below the cooling tower fan to induce vortex mixing. In Moon’s design, the guide vanes surround a central cylinder that is attached to the axis of rotation of the fan, thus forming a stirring device to blend the dry and wet air – see figure 2.9. The guide vanes are similar to the devices proposed in a much earlier patent by Fernandes (1979), who invented a so-called vortex cooling tower. This vortex cooling tower creates a tornado-like motion within the tower and results in low pressure in order to induce flow through the air inlet. The fan illustrated in figure 2.9 may be put to other secondary uses, e.g. a rotary dehumidifier in the absence of the dry section (Golubovic *et al.*, 2007).

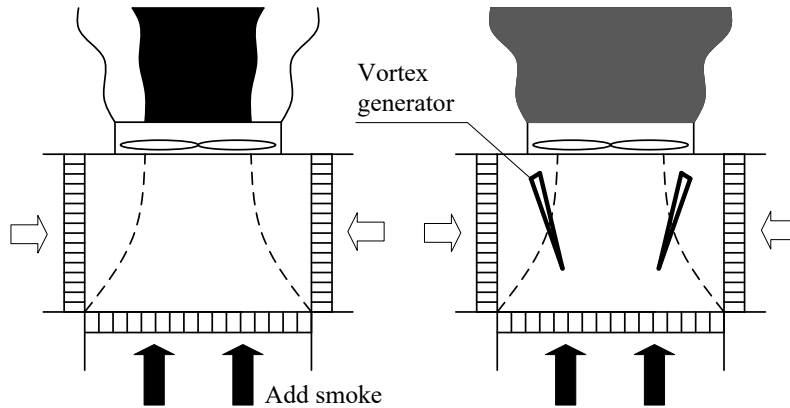


Figure 2.8: The model scaled experiment of plenum chamber without (left) and with (right) the delta-shaped mixer (Ruscheweyh, 1985). The dashed curves denote the boundary between the wet and dry air streams in the absence of any internal mixing device.

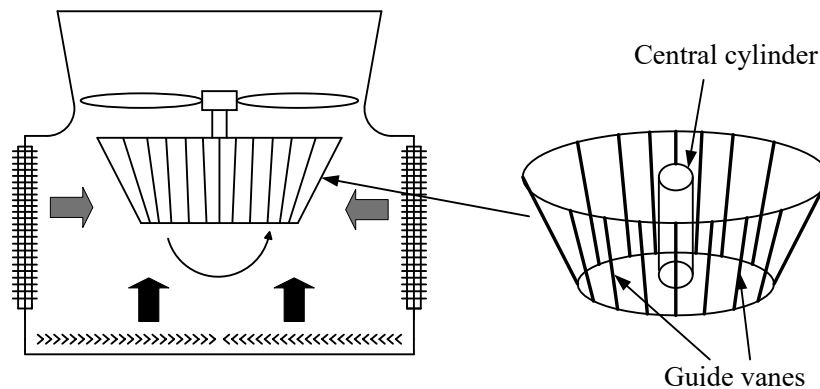


Figure 2.9: The stirring vortex mixing device proposed by Moon (2017).

2.4.4 Coaxial plume mixing

Houx Jr *et al.* (1978) designed a type of hybrid wet/dry cooling tower with good resistance to recirculation and almost complete elimination of visible plumes. In their design, the dry and wet airstreams are in a coaxial configuration with the former enveloping an inner core of the latter. It should be emphasized that their tower has a large dry cooling section and a small backup wet section. Therefore, this type of tower is categorized as water conserving (see section 2.4.5) as compared to a more traditional plume abatement cooling tower in which the cooling load is mainly undertaken by the wet section.

Lindahl & Jameson (1993) argued that in crossflow PPWD cooling towers, the saturated wet air leaves the wet section at a velocity twice that of the dry air leaving the dry section. Thus the slower moving dry air tends to surround the faster moving wet air, which naturally results in a coaxial wet/dry plume structure above the cooling tower – see e.g. figure 2.8 a. They argued that at conditions where a uniform plume would, in theory, be exactly invisible³,

³The fan to ambient mix-line is exactly tangent to the saturation curve on a psychrometric chart, see figure 2.3 b.

the aforementioned coaxial plumes continue to mix to become invisible within two to three fan stack diameters. Unfortunately, the coaxial plume structure does not occur naturally in counterflow PPWD cooling towers where the wet and dry airstreams have approximately the same velocity.

Koo (2016*a*, 2016*b*) proposed a hybrid cooling tower which facilitates mixing resulting in a coaxial structure. Figure 3.4 shows that the external dry air is sucked into the space between the fan stack and the outer shroud. Thereafter, the dry air is mixed with the wet air discharged by the fan. To increase the mixing efficiency, the inner shroud is made corrugated to induce streamwise vorticity that enhances the mixing between the two airstreams (cf. Waitz *et al.* 1997). This type of lobed mixer can also be put below the fan or at other strategic locations within the plenum chamber to augment mixing. One possible extension associated with a coaxial plume structure is the replacement of the dry coils with solar collectors, which are similar to those used in a solar chimney system (cf. Zandian & Ashjaee 2013).

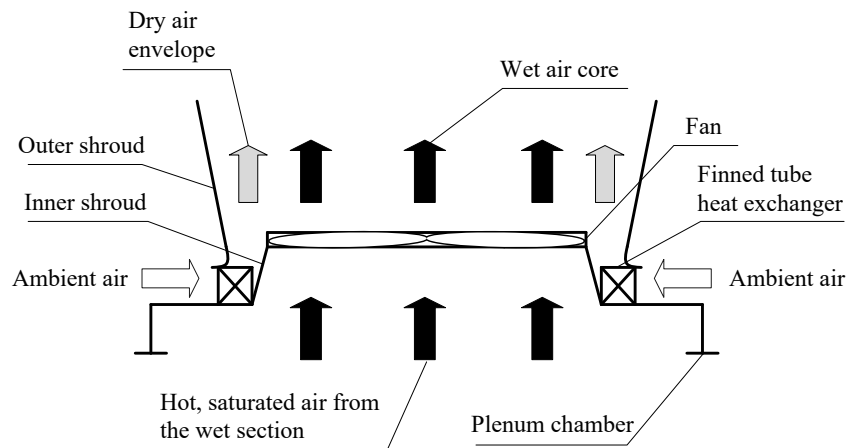


Figure 2.10: The plume abatement cooling tower illustrated in Koo (2016*a,b*). (Figure taken from Li *et al.* 2018)

Another possible advantage of the coaxial plume structure is that the onset of condensation may be delayed compared to the conventional uniform plume structure (Li *et al.*, 2018). For a uniform plume (unsaturated at the source) under adverse ambient conditions, the fan to ambient mix-line starts in the unsaturated region then crosses the saturation curve and reaches the supersaturation region – see e.g. figure 2.4. In fact, and according to Monjoie & Libert (1994), the visible plume occurs immediately at the fan exit, not some elevation above the stack exit. This is because mixing first occurs at the plume boundary upon discharge. Considering a coaxial plume structure, the mixing initially occurs at the ambient/dry air and dry/wet air boundaries, thus both mix-lines are below the saturation curves. As a result, a visible plume is at least abated near the fan stack exit. On the other hand, forcing the dry air envelope with a much higher velocity yields a jet-like air curtain. Such a curtain has been proposed to effectively enhance plume rise in the presence of wind (Veldhuizen & Ledbetter, 1971), albeit at the cost of increased fan power.

2.4.5 Water conservation and recovery

Even though plume abatement does not necessarily guarantee water conservation, water conservation achieves plume abatement as a side effect. In addition to the previously-discussed model due to Houx Jr *et al.* (1978) from section 2.4.4, water-conserving towers may be designed in a variety of ways. For instance, Palmer (2006) used a cover above the cooling tower to trap the water vapor then channel it back to the cold water basin. During the process of traveling downwards, the water vapor is cooled by the ambient and condensed by which means the water is recycled. Generally, these towers need special internal designs such as air channels and extra fans to drive the air.

A relatively new and commercially-successful technology is the condensing module technology, which incorporates the patented air-to-air (Air2AirTM hereafter) heat exchanger designed by Hubbard *et al.* (2003). The condensing module is located above the drift eliminator in a counterflow tower, transferring heat from the hot, humid air to the inflowing ambient air through which process water vapor is condensed – see figure 2.11 a. The corresponding psychrometric process is illustrated in figure 2.11 b. The condensed water can be replaced back into the cold water basin or can be used as a source of purified water thus saving the cost associated with maintaining and improving the water quality. Compared to a conventional PPWD cooling tower, the Air2AirTM technology significantly reduces the amount of blowdown, and avoids the piping and pumping of hot water to the dry section. Although additional fan power is required to increase the static pressure to pull the air streams through the compact Air2AirTM, the increased power consumption is approximately equal to the counterpart power consumed by a PPWD tower that uses two pass (dry) coils with a siphon loop to reduce pump head (Hubbard *et al.*, 2003). Mortensen (2009) reported the capability of the first Air2AirTM water conservation cooling tower at a power plant located in New Mexico. Tests showed that the evaporated water recovery rate was typically 10% to 25% depending on the local climate. Moreover, the Air2AirTM technology achieved effective plume abatement without mixing baffles. In a later report, Mortensen (2011) explains how the performance of first generation Air2AirTM heat exchangers was improved in terms of manufacturability, constructability and cost.

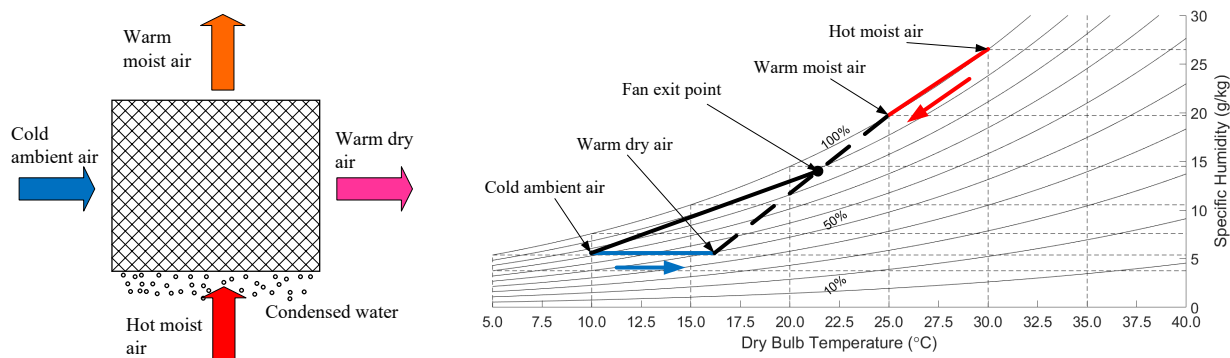


Figure 2.11: [Color] (a): Schematic of an Air2AirTM heat exchanger (Mortensen, 2009). (b): Psychrometric processes of Air2AirTM technology for plume abatement.

Recently Wang *et al.* (2019) evaluated the plume abatement and water conservation performances of the Air2AirTM heat exchanger. The parameters of particular interest were the

number of heat exchanger units (n) and the circulating water flowrate (G). They found that the optimized operating conditions were $n = 8$ and $G < 3000 \text{ m}^3/\text{h}$. Moreover, they found that water savings increased significantly under ambient conditions of low temperature and high RH. By choosing several typical months for reference and specifying certain operating parameters (see their table 4), they revealed that the amount of condensed water was 1.105 kg/s . Assuming the cooling tower operates 7200 h per year, the annual water savings by using Air2AirTM can therefore exceed $2.8 \times 10^7 \text{ kg}$.

Mantelli (2016) proposed a passive water vapor recovery technology that consists of thermosyphons and porous media as illustrated in figure 2.12. The basic idea is to locate the cooled porous media just downstream of the drift eliminator in a crossflow tower so as to condense and recover the water vapor from the hot, humid air exiting the fill. Meanwhile, the (mostly latent) heat was transferred to the ambient by the condenser part of the thermosyphon. Even without optimization, their device showed the ability to recover 10% of the water that would otherwise be lost to the atmosphere in the form of water vapor.

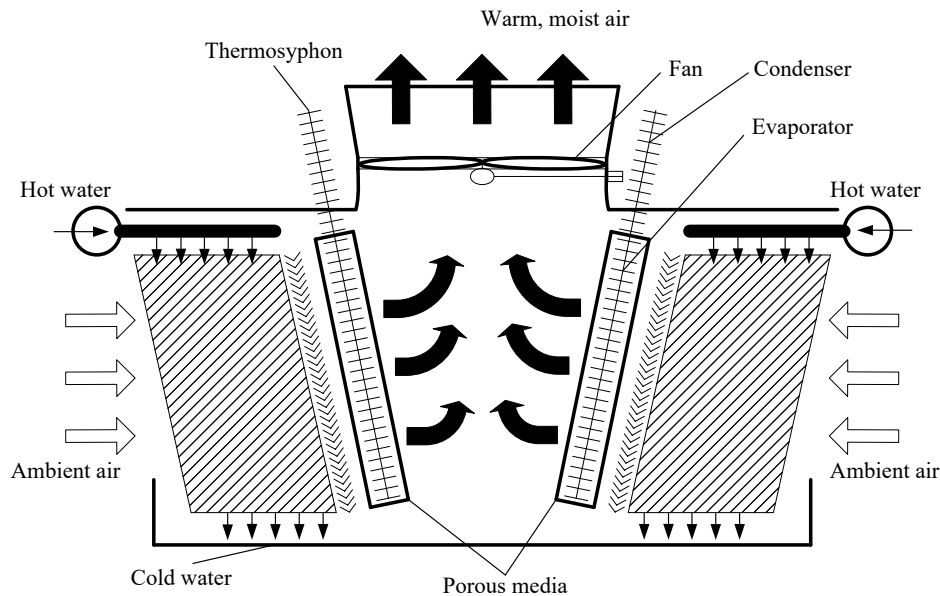


Figure 2.12: Schematic of the passive vapor recovery technology consisting of a thermosyphon and porous media in a crossflow cooling tower (Mantelli, 2016).

Libert & Nevins (2011) proposed a dual-coil closed circuit cooling tower which consists of two separate spiral fin coils and two independent water spraying systems. The fin coils have dual purposes of sensible and latent heat transfer, the latter of which occurs mainly in the fill zone within a wet cooling tower. Instead of using conventional round tube coils with spiral fins, they proposed instead elliptical tubes with extended fins. The advantages of their elliptical design are twofold: (i) form drag as air passes through the coils is reduced compared to round coils, and, (ii) heat transfer is enhanced since the elliptical designs allow a closer spacing for neighboring tubes. A similar oval coiled heat exchanger was proposed by Shin (2013) to improve the dry section cooling efficiency. Because the dual coils are in horizontal alignment, the tower height is reduced compared to a conventional PPWD tower. Nonetheless, the plume abatement mechanisms for both are similar.

Libert *et al.* (2015) compared three hybrid wet-dry cooling technologies for water conservation and plume abatement, i.e. PPWD, wet/wet-dry cooling and, the dual-coil design in Libert & Nevins (2011), which was termed as the “eco-hybrid” design by Libert *et al.* (2015). The wet/wet-dry cooling design replaces some portion of the cooling tower fill with coils made of elliptical tubes and extended fins. These coils also have the dual purpose of sensible and latent cooling, thus allowing a flexible shift from a pure wet cooling mode to a wet/dry cooling mode. The pros and cons of using the three technologies are summarized in table 2.2.

Table 2.2: Three hybrid cooling technologies compared to a typical counterflow wet cooling tower.

	PPWD	Wet/wet-dry	Eco-hybrid
Water conservation	5-20%	20-30% or more	$\geq 60\%$
Wet-dry alignment	Vertical (coil height ≤ 36 ft)	Horizontal	Horizontal
Power penalty increase	10-20%	None	Reduced
Pump head	Increased	Same	Same
Plume abatement control	Air dampers	Water valves	Dry mode dominated
Water treatment	Same	Same	Reduced
Capital cost	Wet/wet-dry < PPWD < Eco-hybrid (same plume performance)		
Footprint	None	increased (Wet/wet-dry < Eco-hybrid)	

Following Libert *et al.* (2015), Scholl *et al.* (2018) discussed the EvapDri wet/wet-dry cooling technology as a retrofit to abate the visible plume produced by an existing counterflow wet cooling tower. The plume abatement test was performed in accordance with the 150 code. By a sensitivity analysis, they revealed that high winds and recirculation have the largest effects on the uncertainties of measurements of exhaust dry-bulb and wet-bulb temperatures. In addition to the advantages indicated in table 2.2, the wet/wet-dry tower exhibits some unexpected advantages, such as unchanged pump head, reduced ice formation and diminished noise as compared to the original wet cooling tower.

Chan (2015) proposed the so-called water shedding approach to mitigate the severity and frequency of visible plumes. Instead of using alternative heat sources or adding a dry section, the water shedding approach reduces the rate of evaporation by minimizing the water flow rate, thus decreasing the amount of moisture in the effluent air. Based on the climatic data in Hong Kong, a plume abatement evaluation, performed for a commercial building using the water shedding approach, showed that the duration of fog formation and its severity are both effectively reduced.

Macedonio *et al.* (2019) tested the performance of a membrane condenser for recovering water from cooling tower plumes. Their main goal was to identify the critical operating conditions for effective water recovery. In their test, the cooling tower plume was simulated using an airstream saturated with ammonia. They found that the amount of water recovery increases with increasing temperature difference between the plume and the membrane, the plume relative humidity and the ratio of the plume source flow rate to the membrane area. In addition to water recovery, membrane condensers are capable of recovering chemicals and microparticles (Frappa *et al.*, 2020).

2.5 Plume modeling

2.5.1 Analytical models

The analytical modeling of moist plumes dates back to the seminal work of Morton (1957), which describes a vertically ascending thermal plume in a stationary ambient on the basis of the MTT model. In Morton’s formulation, the potential temperature⁴ and density, which are conserved during adiabatic mixing processes, are used in the governing equations. G.I. Taylor’s entrainment hypothesis (Taylor, 1945), which relates the entrainment velocity to the mean vertical velocity of the plume, is the closure condition. Importantly, Morton’s analysis assumes a still atmosphere, but this restriction is relaxed in subsequent work that includes wind forcing. To this end, Slawson & Csanady (1967) summarize the three distinct stages in the evolution of a plume subject to wind forcing where, in each case, a different entrainment assumption must be adopted. Specifically, mixing in the initial, intermediate and final stages is respectively governed by the plume’s self-generated turbulence, environmental turbulence in the inertial subrange and energy containing eddies. The MTT model is only valid in the initial phase wherein the plume’s own turbulence is dominant. The bent-over assumption, which states that the plume becomes quasi-horizontal rapidly upon discharge, was adapted by Slawson & Csanady (1967) to formulate a modified set of plume rise equations.

On the basis of the work by Morton (1957) and Slawson & Csanady (1967), Csanady (1971) studied bent-over moist plumes and found that an initially saturated plume will begin to re-evaporate upon release, provided that the ambient is unsaturated and the excess temperature of the plume is below a given threshold. Meanwhile, he argued that the influence of condensation and evaporation on the plume trajectory is minor. The subsequent study of bent-over plumes of Wigley & Slawson (1971) indicated that condensation always occurs close to the plume source. Slawson & Csanady (1971) examined the effect of atmospheric stability⁵ on plume rise. Wigley & Slawson (1972) compared the behavior of wet (condensed) and dry (uncondensed) plumes under different atmospheric conditions. Later Wigley (1975*a*) included the dynamics of droplet growth in the condensation phase.

These early attempts to model plume rise and condensation typically apply two key assumptions. The former is the bent-over assumption. The latter is an entrainment assumption (for the initial phase), $v_e = \beta |w|$, where v_e is the entrainment velocity, w is the vertical component of the mean streamwise velocity of the plume and β is an empirical entrainment coefficient – see figure 2.13. For the case of nontrivial ambient turbulence, three different entrainment assumptions are summarized in table 2 of Briggs (1975) – see section 2.5.4. Briggs (1984) presented a comprehensive review of plume modeling under various ambient conditions, and a detailed formulation of the relevant conservation equations was given. As

⁴The potential temperature, θ , of an air parcel is the temperature the parcel would have if it were brought adiabatically to the standard pressure. In symbols, we write $\theta = T \left(\frac{P_0}{P}\right)^{R/c_{pa}}$, where T is the thermodynamic temperature at pressure P , P_0 is the standard pressure, R is the gas constant of air and c_{pa} is the heat capacity of air at constant pressure.

⁵The stability of atmosphere is parameterized by the buoyancy frequency, $N = \sqrt{-\frac{g}{\rho_a} \frac{d\rho_a}{dz}} \simeq \sqrt{\frac{g}{\theta_a} \frac{d\theta_a}{dz}}$, which is the natural frequency of oscillation of a fluid parcel if disturbed from its equilibrium position. The atmosphere can be either stable ($N^2 > 0$), neutral ($N^2 = 0$) or unstable ($N^2 < 0$).

a starting point, it is appropriate to discuss Briggs’s “two-thirds” law of plume rise. Then step by step, we review the improvements upon this simplest analytical model and outline the more sophisticated plume models that have been derived since the publication of Briggs’s seminal work.

2.5.1.1 Foundational theoretical models

The classic Briggs’s formula (Briggs, 1969) for bent-over buoyant plume rise in a neutral crossflow reads

$$z = 1.6F_b^{1/3}U_a^{-1}x^{2/3}, \quad (2.2)$$

where z is the height of the plume centerline above the stack exit, U_a is the mean horizontal wind velocity and x is the horizontal distance downstream of the plume source. The source specific buoyancy flux is $F_b = g\frac{\rho_a - \rho_0}{\rho_a}U_0r_0^2$, in m^4/s^3 , where $\rho_a = \rho_a(z)$ is the density of ambient air, ρ_0 is the plume source density and r_0 is the actual plume source radius. Briggs’s equation was later revised to include the effects of finite source radius and source momentum (Briggs, 1984; Davidson, 1989):

$$z = \left[\frac{3}{2\beta^2} \left(\frac{F_b}{U_a^3}x^2 + 2\frac{F_m}{U_a^2}x \right) + \left(\frac{R_0}{\beta} \right)^3 \right]^{1/3} - \frac{R_0}{\beta}, \quad (2.3)$$

where $\beta = 0.6$ is the entrainment coefficient and the source specific momentum flux is $F_m = \frac{\rho_0}{\rho_a}U_0^2r_0^2$. The equivalent source radius, $R_0 = r_0\sqrt{\frac{U_0\rho_0}{U_a\rho_a}}$, is determined by matching the source mass flux of the plume to an equivalent flow of density ρ_a and velocity U_a (Davidson, 1982). The plume radius is given by $R = R_0 + \beta z$. Moreover, Briggs (1975) argued that the rise enhancement due to the release of latent heat is rather modest. More precisely, the plume rises to a height only 10% to 20% greater than would be the case in the absence of latent effects. Plume behaviors under neutrally and stably stratified crosswinds are sketched in figure 2.13. In a stably stratified crosswind, the plume first reaches its maximum rise height then tends to a terminal rise height at a greater downwind distance. The approach to the terminal rise is not necessarily monotone; rather, some oscillation about the terminal rise height may occur – see also figure 2.19 below. The plume trajectory from the source to its maximum rise is described by

$$z = \left[\frac{3F_b}{N^2\beta^2U_a} \left(1 - \cos \left(\frac{Nx}{U_a} \right) \right) + \frac{3F_m}{N\beta^2U_a} \sin \left(\frac{Nx}{U_a} \right) + \frac{R_0^3}{\beta^3} \right]^{1/3} - \frac{R_0}{\beta}. \quad (2.4)$$

The counterpart plume trajectory in an unstably stratified ambient where $N^2 < 0$ is expressed as

$$z = \left[\frac{3}{\beta^2U_a^2} \left(\frac{F_mU_a}{\sqrt{-N^2}} \sinh \frac{\sqrt{-N^2}}{U_a}x + \frac{F_bU_a}{-N^2} \left(\cosh \frac{\sqrt{-N^2}}{U_a}x - 1 \right) \right) + \frac{R_0^3}{\beta^3} \right]^{1/3} - \frac{R_0}{\beta}. \quad (2.5)$$

Davidson (1989) argued that the above analytical solution yields predictions of the plume trajectory that are in good agreement with measurements, however, the dilution rate is overestimated and thus the visible plume length may be underestimated. By comparing the

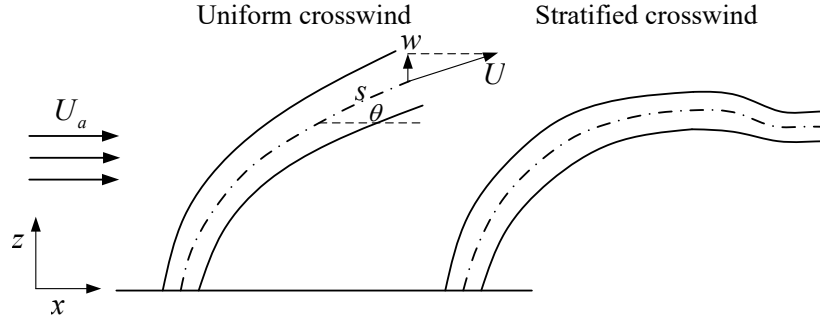


Figure 2.13: Plumes under neutral (left) and stably stratified (right) crosswinds.

predictions of the analytical formulation with a set of sophisticated plume models e.g. Schatzmann (1978, 1979), Davidson revealed that the inclusion of an added mass factor or a drag term⁶ in the momentum equation allows for accurate modeling of both the plume rise height and dilution rate. The added mass assumption derives from potential flow theory, which assumes that a plume accelerating through the ambient fluid can be regarded as having added mass attached its boundary. The amount of added mass is taken to be proportional to the core plume mass. Alton *et al.* (1993) measured the trajectory and dilution rate of a hot water plume discharged into a crossflow in a water flume. They compared the experimental data with integral model predictions and verified Davidson’s conclusion for simple analytical models.

2.5.1.2 Advanced theoretical models

For improved predictions of plume behavior, integral models of greater complexity have been proposed. Instead of using a single entrainment term in the entrainment hypothesis, refined models incorporating two entrainment terms have been proposed by various researchers – see e.g. Hoult *et al.* (1969) and Hoult & Weil (1972). The two-entrainment-coefficient assumption incorporates entrainment due to velocity differences both parallel and normal to the plume axis, i.e. $v_e = \gamma_1|U - U_a \cos \theta| + \gamma_2|U_a \sin \theta|$ where $U - U_a \cos \theta = w \sin \theta$ and γ_1 and γ_2 are the corresponding entrainment coefficients – see Tohidi & Kaye (2016). A modification to the above entrainment formulation was made by Abraham (1970), i.e. $v_e = \gamma_1|U - U_a \cos \theta| + \gamma_2|U_a \sin \theta| \cos \theta$; the addition of $\cos \theta$ in the latter right-hand side term shuts off line thermal-type entrainment in the near source region. A more general entrainment relation proposed by Devenish *et al.* (2010b) reads $v_e = \sqrt[n]{(\gamma_1|U - U_a \cos \theta|)^n + (\gamma_2|U_a \sin \theta|)^n}$ where $n \geq 1$. The entrainment assumption is further complicated by including the effect of ambient turbulence and a so-called drag hypothesis – see e.g. Winiarski & Frick (1976), Wu & Koh (1978) and Ooms & Mahieu (1981).

⁶Briggs (1975) preferred the added mass assumption over the inclusion of a drag term. The flow outside the plume is assumed to be irrotational thus the drag force term drops out in the momentum equation. Moreover, the assumption underlying the drag term is that there exists a turbulent wake on the leeward side of the “no-slip” surface of a solid object. By contrast, a plume consists of fluid so that its boundary with the ambient is more appropriately modeled as “free-slip”. Briggs also listed some evidence that demonstrates the non-existence of the wake for bent-over plumes.

Schatzmann (1979) developed a model to predict the spreading and rising of buoyant jets in a stratified crosswind. A Gaussian profile was assumed for plume velocity, temperature and humidity. In contrast to the two-entrainment-coefficient models, four empirical constants were involved in the entrainment hypothesis. Schatzmann & Policastro (1984) further advanced the aforementioned model by carefully quantifying the plume thermodynamics and the effects of stack downwash⁷. The pressure field around a bent-over plume in a crosswind is so complex that deriving a generic expression for the dynamic pressure gradient is extremely difficult. The error of assuming a zero dynamic pressure gradient is compensated by imposing a drag force normal to the plume axis (Schatzmann, 1978). To account for the downwash effects, additional terms are added to the drag force and the entrainment function to provide more bending and mixing due to the plume-wake interference. Schatzmann & Policastro (1984) also include a shape factor in the drag coefficient (cf. their equation 18) to account for the non-circular plume cross section e.g. shown in figure 2.22 below. List (1982) argued that Schatzmann’s model is “probably the most appropriate technique for engineering design purposes”. Schatzmann’s model was further discussed by Davidson (1986*a*) using a parallel control volume formulation, and by Teixeira & Miranda (1996) using a first-order turbulence closure in place of the entrainment assumption to improve the performance. Many integral models such as Hoult *et al.* (1969) and Wu & Koh (1978) produce unphysical results in some extreme cases, e.g. a momentum jet in a uniform co-flow (see the discussion in Schatzmann 1978), which Schatzmann’s model avoids.

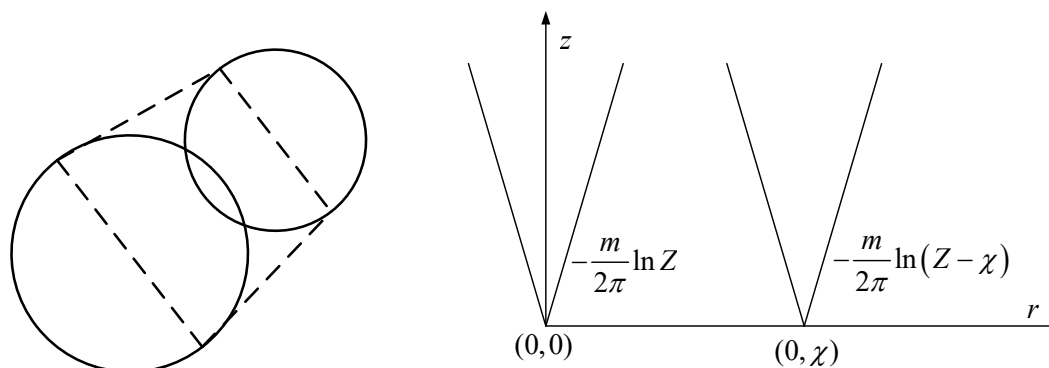
There are several other models that can be classified as advanced integral models. Carhart & Policastro (1991) developed the Argonne National Laboratory and University of Illinois (ANL/UI) model to resolve some deficiencies of previous integral models e.g. the inability to correctly and simultaneously predict plume trajectory and dilution. Janicke & Janicke (2001) proposed an integral plume rise model that is applicable for a three-dimensional wind profile and arbitrary source conditions. The added mass concept, rather than the drag hypothesis, was adapted in their formulation. Jirka (2004) validated his four empirical entrainment coefficient model by comparison with experimental data for five distinct regime of buoyant jet flow i.e. pure jet, pure plume, pure wake, advected line puff and advected line thermal. More importantly, Jirka (2004) pointed out the conditions beyond which integral models become invalid, e.g. the transition to a passive turbulent mixing plume, the final stage alluded to by Slawson & Csanady (1967). Jirka (2006) further extended his model to describe two dimensional buoyant jet flows.

Briggs (1984) argued that most of the analytical models of plumes are based on conservation of mass, momentum and buoyancy and at least one closure assumption. Some models employ conservation of mean kinetic energy (cf. Priestley & Ball 1955), which is actually an alternative form of the momentum conservation equation. Various closure assumptions can be found in table I of Briggs (1975), which correspond to different conservation equations. In short, integral models provide a quick and efficient means of estimating the plume trajectory and dilution rate. However, a key restriction, as stated by Jirka (2004), lies in the assumed unboundedness of the environment. For instance, and when the crosswind is sufficiently strong, cooling tower plumes may be drawn into the turbulent wake on the leeward side of the tower; such phenomena lie beyond the predictive capability of integral models.

⁷Downwash describes the downward motion of effluent in the leeward wake zone. As a consequence of downwash, high-concentration, possibly harmful effluents can be transported to ground level (Canepa, 2004).

2.5.1.3 Multiple sources and plume merger

For multiple sources in close proximity, several plumes may merge into a single plume with increased momentum and buoyancy. Following the “two-thirds” law, Briggs (1984) argued that the maximum rise enhancement factor for n stacks was $n^{1/3}$, assuming all the buoyancies were combined completely. In fact, plume merger depends on many geometric and dynamic parameters that include the wind speed, wind direction and level of ground turbulence. To this end, Briggs’s model for rise enhancement adapted results from available analytical models such as Murphy (1975) and Anfossi *et al.* (1978). Wu & Koh (1978) proposed a merging criterion for multiple plumes that emanate from adjacent cooling tower cells. They argued that the merged plume can be approximated by a central slot plume plus two half round plumes at the two ends. The effect of wind direction with respect to the tower arrangement was also included. Their predictions were in good agreement with the corresponding laboratory data on dry plumes. It should be emphasized that the merging criteria of Wu & Koh (1978) is based entirely on geometrical considerations (figure 2.14 a), and unfortunately, no physical justification is involved. Nonetheless, the conceptual simplicity offered by their model has led to its adoption in numerous studies of cooling tower plumes e.g. the ANL/UI model (Carhart & Policastro, 1991). Modeling the induced flow into a turbulent plume using the complex potential of a line sink, Kaye & Linden (2004) studied the coalescence of two pure axisymmetric plumes with equal and unequal source strengths (figure 2.14 b). The point of coalescence is defined as the point where a single peak appears in the horizontal buoyancy profile. The distance between plume centers diminishes with height due to the passive advection of one line sink towards the other. The theoretically predicted merging height is somewhat larger than the value measured in analogue laboratory experiments; as Kaye & Linden (2004) proposed, this mismatch is due to the sensitivity of the entrainment coefficient. Following the work of Kaye & Linden (2004), Cenedese & Linden (2014) proposed a piecewise model of plume merger accounting for various stages of plume interaction.



(a) Merging criteria by Wu & Koh (1978)

(b) Approach of line sink by Kaye & Linden (2004)

Figure 2.14: (a): Plume merger occurs when the area of the central trapezoid bounded by dashed lines is the sum of the areas of the two half round plumes on both sides. (b): The induced flows into the two adjacent plumes are represented by line sinks $\Omega = -\frac{m}{2\pi} \ln Z$ and $\Omega = -\frac{m}{2\pi} \ln(Z - \chi)$, where m is the line sink strength and $Z = x + iy$.

Lai & Lee (2012) proposed a general semi-analytical model to account for the merging of an array of closely spaced buoyant jets. The induced flow was modeled using a distribution of point sinks. The velocity and concentration profiles in the merged jet (or plume) flow were obtained by momentum (or kinetic energy) and concentration superposition, and the corresponding results were validated by CFD simulation. Their predicted merging height for two pure plumes of unequal strength was compared with that anticipated by Kaye & Linden (2004) – see figure 10 b of Lai & Lee (2012). The method of Lai & Lee (2012) yields better agreement with experimental data than does that of Kaye & Linden (2004), especially when the buoyancy flux ratio between the two plumes is small. Moreover, their model can be extended to describe plume merger in a weak crosswind.

Rooney (2015, 2016) adapted the physical interpretation of velocity potential to approximate the plume-ambient boundary of single and multiple plumes. The model in Rooney (2015), using an infinite row of line sinks, approached the limiting similarity solutions of axisymmetric and two-dimensional plumes or jets below and above the merging height. Further in Rooney (2016), he studied the merging of plumes with sources placed along the perimeter of a circle; the theoretical predictions agree satisfactorily with the experimental results of Cenedese & Linden (2014). One restriction of Rooney’s models is that the plume source is assumed to be small compared to the separation distance between neighboring plume centers. However, industrial cooling towers typically have large diameters (~ 10 m) and they are usually closely spaced. Recently Li & Flynn (2020*b*) modified Rooney’s theory to consider the merger of non-ideal plumes with arbitrary source diameter. Li and Flynn’s theoretical predictions of merging height agree well with the earlier predictions of Wu & Koh (1978). In case of a crosswind, the bent-over plume can be simulated as a line doublet (Wooler *et al.*, 1967) so that Rooney’s theory may be extended to a windy environment.

2.5.2 CFD models (single and multiple sources)

CFD simulation can describe almost all aspects of cooling tower plumes, including recirculation, downwash, plume merger and condensation/evaporation. Like their integral model counterparts, CFD models require closure, i.e. in the form of a turbulence model. A quick comparison between the different kinds of turbulence models that have been applied to atmospheric plumes is summarized in table 4.4 of Andersson *et al.* (2011). The CFD models reviewed here are mainly Reynolds-averaged Navier-stokes (RANS) models.

Demuren & Rodi (1987) used a 3D computational model to resolve the complex flow field past a cylindrical cooling tower whereby the downwash effects under strong crosswinds was modeled. Their pioneering work used a k - ϵ turbulence model (Launder & Spalding, 1974) and reproduced flow patterns in the vicinity of the tower. They modeled plume downwash and the formation and decay of longitudinal vortices – see their figure 2.22. One shortcoming of their model is the underestimation of the buoyancy effect on plume rise in the near field.

Becker *et al.* (1989) proposed a unique numerical model of cooling tower plume recirculation. The flow inside the tower was treated as a porous media flow whereby each of the cooling tower components, e.g. fill racks and drift eliminators, was modeled as a different porous medium of a different hydraulic mass conductivity. Meanwhile, the wake zone downstream of the tower was resolved using the Navier-Stokes equations. The flow fields inside and outside the cooling tower were coupled by matching the pressures and mass flow rates

at the louvers. The amount of recirculation⁸ was defined as

$$\text{Recirculation} = \frac{\bar{t}_{\text{in}} - t_a}{t_{\text{out}} - t_a}, \quad (2.6)$$

where t denotes temperature, the overbar denotes mass average and the subscripts ‘in’ and ‘out’, denote, respectively, the flows entering the louvers and leaving the cooling tower (the subscript ‘a’ indicates the ambient). As the wind speed increases, the plume is quickly bent towards the leeward side of the tower and is subsequently entrained into the wake zone thus enhancing recirculation. There results a decrease in the effluent temperature before it is discharged into the wake zone, which has the effect of then diminishing the recirculation. The findings of Becker *et al.* (1989) confirmed these two opposing effects and predicted an increasing then decreasing trend of recirculation with increasing wind speed. Later Ge *et al.* (2012) studied the effects of recirculation on the visible plume potential using CFD modeling. Their results showed that recirculation can increase the fogging frequency, which subsequently increases the heating demand for plume abatement. The heating demand for a recirculation ratio (defined by (2.6)) of 20% is 80-90% greater than that without recirculation.

Bornoff & Mokhtarzadeh-Dehghan (2001) investigated the interaction of two adjacent plumes in tandem and side-by-side arrangements in a crosswind. The turbulence model was a low Reynolds number k - ϵ model; the eddy viscosity was damped in the energy dissipation (ϵ) equation when the local Reynolds number was low. Their simulations indicated that the tandem configuration leads to rapid merging and a corresponding rise enhancement. Conversely, when the plumes are located side-by-side, their interaction is dominated by counter-rotating vortex pairs. König & Mokhtarzadeh-Dehghan (2002) used the standard k - ϵ turbulence model and a finite volume method to simulate multiple plumes emitted by a four-flue chimney. By comparing the results of multiple plumes with those of a single plume of the same overall source volume flow rate, they revealed that significant differences of velocity, temperature and turbulent energy occur only in the early stages of plume rise and spread. Notably, the multiple plumes merge into a single plume within ten stack diameters of the chimney. Mokhtarzadeh-Dehghan *et al.* (2006) modeled two interacting field-scale dry plumes in a neutral crosswind using three different turbulence models, i.e. the standard k - ϵ model, the renormalization group (RNG) k - ϵ model (Yakhot *et al.*, 1992) and the Differential Flux Model (DFM). The constants in the turbulence models and the discretization schemes are summarized in their tables 1 and 2, respectively. The numerical results of Mokhtarzadeh-Dehghan *et al.* (2006) showed general agreement in the plume rise height for all three models, of which DFM obtained temperature profiles in better agreement with experimental results.

Takata *et al.* (1996) used an RNG k - ϵ model to study the visible plume behavior above a mechanical draft wet cooling tower. The turbulent Prandtl number and Schmidt number were both set to 0.9. Moreover, the measured average velocities in three directions and the turbulent energy at the fan exit were used as the boundary conditions for the simulation. Results showed that the predicted length, width and volume of the visible plume agree with the corresponding measured values within 20%. Later Takata *et al.* (2016) adapted the same CFD model to predict the visible plume region above a hybrid crossflow wet/dry cooling tower. The initial and boundary conditions are exhibited schematically in figure 2.15. Their results showed that the fan can completely mix the wet and dry air streams, and

⁸A summary of different definitions to recirculation can be found in Liu & Bao (2014).

the predicted dimensions of the visible plume agree with observations with an error range of 15% to 20%. Furthermore, their CFD analysis revealed that the effect of the ambient wind on the dimension of the visible plume is significant – see figure 2.16.

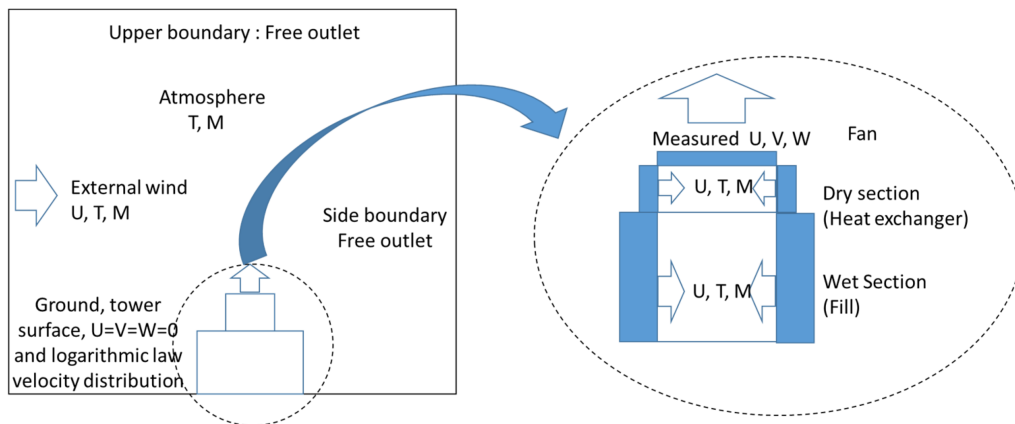


Figure 2.15: [Gray scale] Initial and boundary conditions used in the CFD simulation of Takata *et al.* (2016). The fan exit velocity distributions (U , V and W) measured in Takata *et al.* (1996) are used as the velocity boundary conditions. Measured ambient dry- and wet-bulb temperatures and the wind speed are also used as the boundary conditions. The exiting air velocity, temperature and moisture of the wet and dry sections are determined from design calculations. (Figure taken from Takata *et al.* 2016)

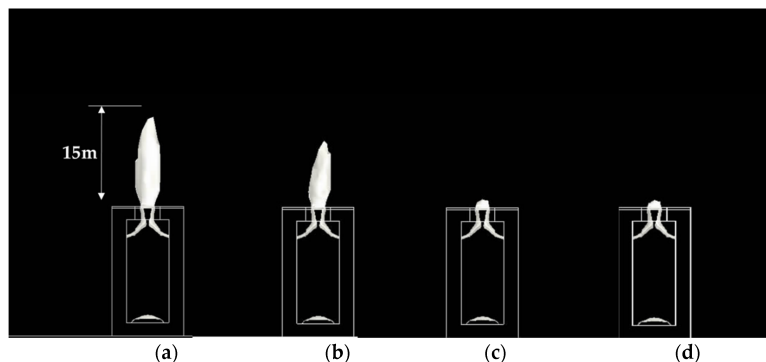


Figure 2.16: [Gray scale] Effect of wind speed on the scale of the visible plume produced above a hybrid wet/dry cooling tower; wind speeds of (a) 0, (b) 1 m/s, (c) 3 m/s and (d) 5 m/s are considered. (Figure taken from Takata *et al.* 2016)

Brown & Fletcher (2005) investigated the effect of condensation on plume rise. A buoyancy-corrected $k-\epsilon$ turbulence model was adapted. Meanwhile, a separate algorithm was developed to model the evaporation/condensation process. Consistent with Briggs (1975), their results showed that condensation does not affect significantly plume rise and ground level odour.

A full 3D CFD model on natural draft wet cooling towers is detailed in Klimanek (2013). The dispersed RNG $k-\epsilon$ model, which is a type of multiphase $k-\epsilon$ model, was selected for turbulence closure. Whereas Takata *et al.* (2016) did not specifically simulate cooling tower processes, Klimanek studied such processes in detail. For instance, heat and mass transfer

processes within the fill zone were modeled using proper orthogonal decomposition coupled with radial basis function networks, which is characterized as a simplified and reduced order model (Klimanek *et al.*, 2010). The slight contraction of the plume near the stack exit seems to indicate that the plume is initially lazy with an excess volume flow rate vs. a pure plume (Hunt & Kaye, 2005). Later Klimanek *et al.* (2015) used the 3D model of Klimanek (2013) to simulate a natural draft wet cooling tower with flue gas injection which included the effect of crosswind on rising plumes. Figure 2.17 shows that a recirculation zone forms at the windward side of the tower outlet, which leads to a possible reduction in the air flowrate through the tower.

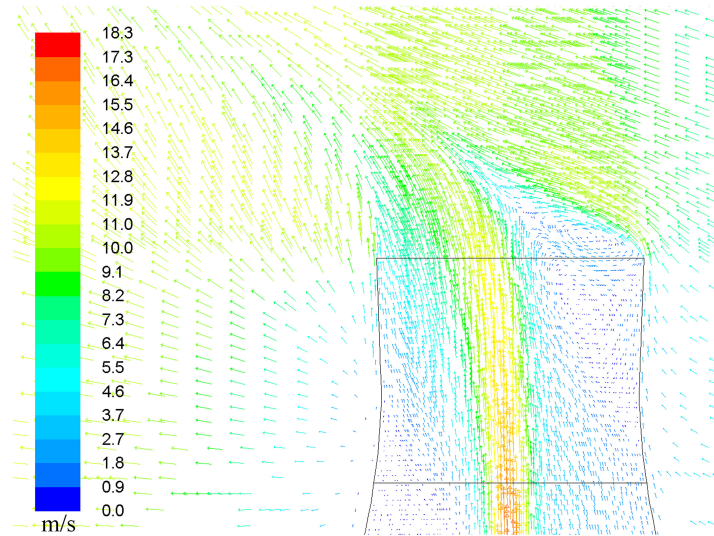


Figure 2.17: Plume velocity vector map near the tower exit in a crosswind. (Figure taken from Klimanek *et al.* 2015)

Chahine *et al.* (2015) also modeled the effect of wind on cooling performance and plume behavior above natural draft wet cooling towers, however, using a different numerical approach compared to Klimanek *et al.* (2015). The heat, mass and momentum transfer processes within the fill zone were parameterized using a source term approach. Specifically, the heat gain of air, mass loss of water and momentum loss of air through the fill zone were expressed as source terms in the conservation equations of thermal energy, mass and momentum, respectively. Moreover, the liquid potential temperature was used in the thermal energy conservation equation at the scale of the atmospheric boundary layer. Their predicted vertical profiles of plume temperature, velocity and liquid water content agreed well with field measurements.

Hargreaves *et al.* (2012) proposed a simplified CFD analysis of plumes in a quiescent atmosphere using a realizable $k-\epsilon$ model. The accuracy of their model was demonstrated by comparison with the theory of MTT and the empirical profiles of vertical velocity and reduced gravity by Rouse *et al.* (1952). Notably, their model predictions showed that MTT applies only at a distance well above the source – see their figure 17 for a comparison of plume centerline velocity predicted by the respective CFD and MTT models. The model of Hargreaves *et al.* (2012) is much less computationally expensive compared to large-eddy simulation (LES) while maintaining a reasonably good description of the flow.

2.5.3 Similitude laboratory experiments (single and multiple sources)

To corroborate the predictions of analytical and numerical models, a number of similitude experiments of cooling tower plumes have been completed. Laboratory experiments enjoy a number of advantages. For example, wind tunnel experiments can easily simulate the impact of neighboring and complex terrain. Andreopoulos (1989a, 1989b) conducted wind tunnel experiments on cooling tower plumes considering both uniform and non-uniform crossflows. In the former case, strong interactions between the bending plume and the wake zone of the cooling tower were found, which served as the main reason for stack downwash. Downwash was observed to be relatively strong at low velocity ratio (stack exit velocity to crossflow velocity) and high Reynolds numbers (defined based on the crossflow velocity and stack exit diameter). Michioka *et al.* (2007) proposed a novel method of using wind tunnel experiments to predict the visible plume region above a wet cooling tower. A tracer gas was used to model the effluent emitted from the cooling tower and the subsequent dispersion of water vapor in the atmosphere. The validity of this method was confirmed by the fact that the predicted visible plume length and height are in good agreement with field observations (Meyer, 1974). On the basis of Michioka *et al.*'s approach, Guo *et al.* (2014) performed wind tunnel experiments to study plume rise and the visible plume region of a natural draft cooling tower. Their predictions of plume rise agree with Briggs's two thirds law for downstream distances of 50 m to 200 m. Furthermore, their measurements of the visible plume region are consistent with the simulation results of Policastro & Wastag (1981).

Contini *et al.* (2014) used wind tunnel measurements to analyze the variance, skewness, kurtosis, intermittency, probability density function and power spectrum of the concentration field in two merging plumes. Consistent, broadly speaking, with Slawson & Csanady (1967), their results identified three distinct phases of plume development. In sequence, the three phases are dominated by turbulence self-generated within the plume near the stack, by both internal and external turbulence at somewhat greater distances and by external turbulence at further downwind distances.

Liu & Bao (2014) extended the above studies by considering, in the wind tunnel context, not only plume rise and ambient turbulence but also recirculation. Their set-up is illustrated in figure 2.18. Flow visualization was made possible by putting dry ice within the cooling towers; the water vapor in the air flow was quickly cooled to the dew point causing condensation. Separately, carbon monoxide (CO) was released into the central region of the cooling tower; from measurements of the CO concentration at the tower inlet and outlet, estimates of the recirculation ratio were made. As a result of their experimental findings, Liu & Bao (2014) proposed an empirical formula that expresses the recirculation ratio as a function of the following parameters: the length of the cooling tower row, the angle between the tower array and wind direction, the distance between two neighboring tower arrays, the height of the air intake and the wind speed. To minimize the recirculation ratio, several recommendations are made, such as to align the long axis of the tower array parallel to the dominant summertime wind direction (a practice common in industry), to shorten the length of tower array and to maintain a distance between tower arrays that is four to five times the air intake height.

Another powerful experimental tool is the water tank experiment. Here, flow visualization can be achieved using colored dyes and an ambient stratification may be realized

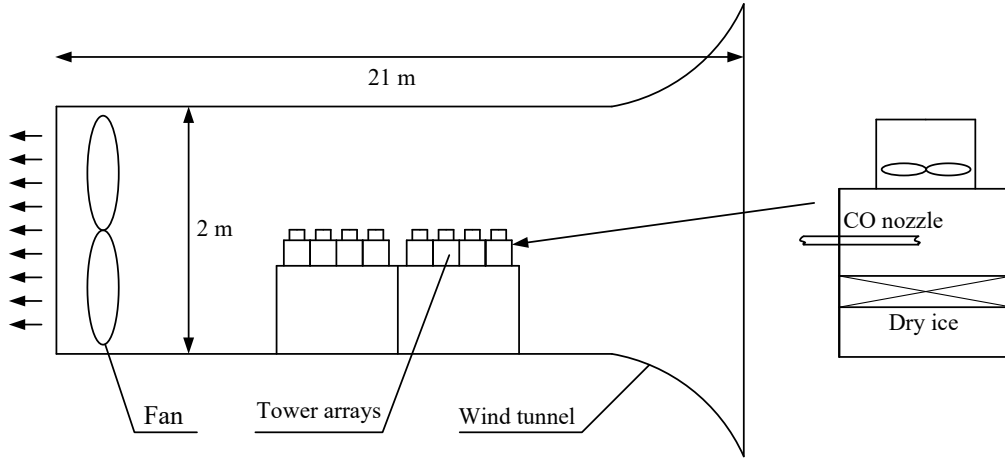


Figure 2.18: Wind tunnel experimental set-up of Liu & Bao (2014). Dry ice is put inside each cooling tower cell for flow visualization. Carbon monoxide is used as a tracer whose concentrations at the inlet and outlet of the tower are measured to determine the recirculation ratio.

using salinity gradients. Using a water tank, Davis *et al.* (1978) investigated the dilution characteristics of single and multiple buoyant discharges in a stationary ambient. Their simultaneous measurements of velocity and salinity within the plumes indicate that entrainment is greatly increased by reducing the source densimetric Froude number (defined as $Fr = U_0 / \sqrt{g \frac{\Delta\rho}{\rho_a} D_0}$ where U_0 is the nozzle exit discharge velocity, g is gravitational acceleration, $\Delta\rho$ is the density difference between the jet centerline and ambient whose density is ρ_a and D_0 is the nozzle diameter). Contini & Robins (2001) studied the rise and evolution of a single buoyant plume and a pair of in-line plumes in neutral crossflows using a towing tank apparatus. Flow visualization and local concentration measurements were used to investigate the plume trajectory and plume interactions particularly for two in-line plumes. A later study also by Contini & Robins (2004) considered two adjacent buoyant plumes while imposing various wind directions. More recently, Contini *et al.* (2011) provided a detailed comparison between several plume rise models and water tank experimental data for neutral and linearly stratified crossflows. The measured plume trajectory (see e.g. figure 2.19) was used to find, using statistical means, the appropriate entrainment coefficients in various plume models – see their tables 3 and 4. Furthermore, Contini *et al.* (2011) found that the added mass concept generates improved predictions of the maximum rise height and subsequent oscillation frequency. Another finding was that the measured plume oscillation was more significantly damped than was predicted theoretically. This may, in fact, speak to the influence of radiating internal gravity waves – see e.g. the LES study of Devenish *et al.* (2010b).

Instead of using the tow tank technique that mimics the effect of a laminar crossflow, Macdonald *et al.* (2002) conducted water flume experiments to study the rise behavior of a pair of merging plumes. The advantage of a water flume compared to a tow tank set-up is that the atmospheric boundary layer flow can be simulated properly only in the former case. The key result revealed by Macdonald *et al.* (2002) is that the best tower arrangement is in-line with the wind direction for the maximum rise enhancement; the worst tower arrangement is perpendicular to the wind direction wherein there is little or no rise enhancement compared

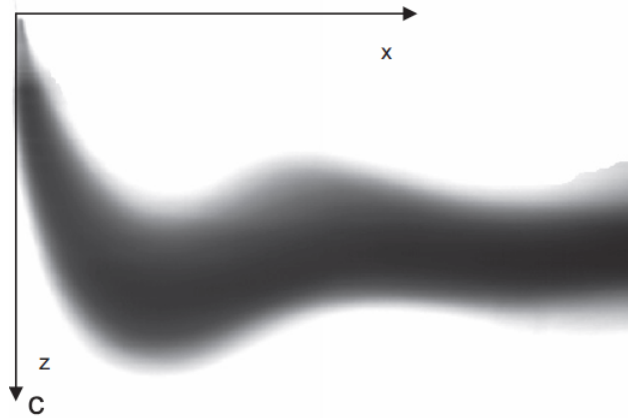


Figure 2.19: A water channel experimental image of a plume in a stably stratified cross-flow (Contini *et al.*, 2011). The plume starts to oscillate after reaching its maximum rise height. (Figure taken from Contini *et al.* 2011)

to the single source case. As discussed in Hensley (2009), the perpendicular configuration is also more likely to induce motions like recirculation and/or downwash.

2.5.4 Plume in a turbulent environment

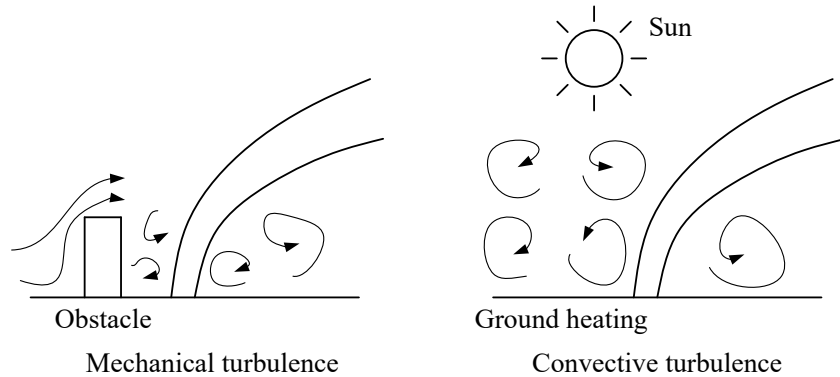


Figure 2.20: Schematics of mechanical and convective turbulence.

Ambient turbulence (if present) becomes dominant over the plume’s self-generated turbulence only at some further downstream distance from the source. Briggs (1984) proposed two patterns of turbulence, i.e. mechanical and convective turbulence as illustrated schematically in figure 2.20. Figure 2.20 a illustrates mechanical turbulence created by wind flowing around roughness elements, whose size is one of two key factors in setting the turbulence intensity. (The flow speed is the other.) Figure 2.20 b illustrates convective turbulence due to ground heating. The intensity of convective turbulence depends on the sensible heat transfer rate from the ground to the air and the depth over which an overturning of the air takes place. Briggs (1984) argued that the large scale turbulent eddies can push plume segments down to the ground and the small scale eddies can enhance mixing between the plume and the ambient. Simple analytical models of plume rise affected by mechanical and

convective turbulence were proposed and discussed in section 8-5 of Briggs (1984). Three different forms of entrainment velocity due to ambient turbulence are summarized in table 2 of Briggs (1975), of which the one preferred by Briggs is given by

$$v_e \propto (\epsilon r)^{1/3}, \quad (2.7)$$

where ϵ is the turbulent energy dissipation rate and r is the plume radius. Equation (2.7) is based on the assumption that the effective eddies are in the inertial sub-range of the turbulence spectrum where the turbulence statistics depends only on ϵ . Also implied by (2.7) is the fact that $r \ll l$ where l is the dominant eddy size associated with ambient turbulence.

Turner (1963) formulated a theoretical model to account for both the inflow of ambient air by turbulent entrainment into the plume and the outflow of plume fluid due to turbulence in the environment. Specifically, his theory followed MTT but introduced a constant mean outflow (extrainment) velocity. Theoretical results showed that the plume width first increases then decreases and finally disappears within a certain downstream distance. The physics of the decreasing profile is questionable, thus the model of Priestley (1953) was adapted by Turner (1963) after the plume reaches its maximum width. (At this maximum width, the turbulence within the plume or thermal is regarded as a part of the environmental turbulence). The laboratory experiments of Turner (1963) simulating a neutral environment revealed that the outflow velocity is of the same order of magnitude but somewhat less than the r.m.s. turbulent velocity. As stated later by Netterville (1990), Turner’s novel contribution was the stringent definition of the “active” radius of the plume or thermal to include only that portion governed by the buoyancy force and exhibiting a systematic upward motion.

Hamza & Golay (1981) constructed a model of moist plumes in the atmosphere whereby atmospheric turbulence is accounted for by incorporating a one-dimensional planetary boundary layer (PBL) model. As sketched in figure 2.21, the plume was modeled using the integral model of Winiarski & Frick (1976) and a numerical (k - ϵ turbulence) model, with the dividing line (vertical dashed line in figure 2.21) representing the point of model crossover. Given vertical profiles of temperature, humidity and wind speed, the one-dimensional PBL model yielded the vertical Reynolds stress and turbulent heat flux distribution, which served as inputs into the numerical plume model. The test results demonstrated their model strength in complex atmospheric conditions under which integral models may have difficulty.

Netterville (1990) proposed a two-way entrainment model for plumes in turbulent winds, which combines the methods of Priestley (1953) and Turner (1963). A characteristic frequency is introduced to quantify the decay rate of the vertical momentum and buoyancy, which justifies the governing equations introduced by Djurfors (1977). The new model outperforms the “laminar” plume model at downwind distances beyond 1 km where the effect of atmospheric turbulence (assumed homogeneous and isotropic by Netterville 1990) is dominant. Later Gangoiti *et al.* (1997) adapted Netterville’s parameterization of entrainment but argued that a wind-sheared atmosphere makes more sense than a flat wind profile, because atmospheric turbulence must be fed by wind shear to maintain its stationarity.

Huq & Stewart (1996) compared the plume evolution in laminar and weakly turbulent crossflows by laboratory experiments. The turbulent environment was produced by locating a turbulence generating grid upstream of the plume source. They found that the decaying, grid-generated turbulence enhanced the dilution of the buoyant plume core by up to 33%,

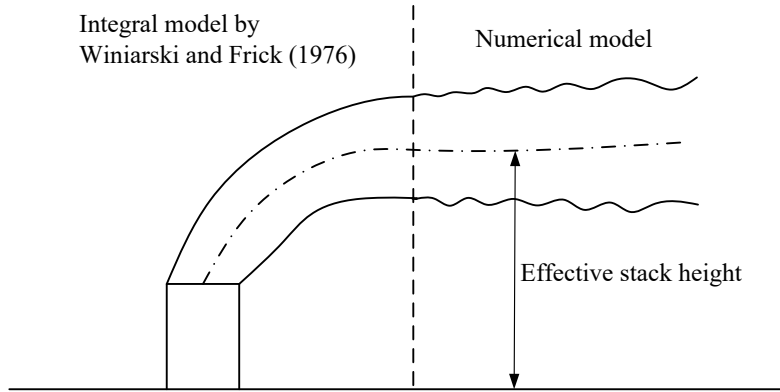


Figure 2.21: Division of plume modeling suggested by Hamza & Golay (1981). The effective stack height, $h_{\text{eff}} = h_{\text{stack}} + l_{\text{b}}$, where h_{stack} is the stack height measured from the ground and l_{b} is a so-called buoyancy length defined as the radius of curvature of a pure plume at the stack exit.

even though the associated dissipation rates were approximately two orders of magnitude smaller than the plume turbulence dissipation rates. Not surprisingly, the turbulent crossflow was also found to decrease the plume rise height, which can be accounted for by adopting a modified entrainment coefficient, i.e. β in (2.3).

Hübner (2004) conducted comprehensive experiments of a buoyant plume in a turbulent environment, where the ambient turbulence was created using an oscillating grid. Such a turbulent environment is nearly isotropic, horizontally homogeneous and exhibits intensity that increases closer to the grid. Two processes, plume meandering⁹ and plume spreading (see his figures 5.9 b and c), are modeled distinctly.

Witham & Phillips (2008) studied the dynamics of turbulent plumes under convective turbulence. Their theoretical model adapted the theoretical approach of Turner (1963) and complemented the theory of Netterville (1990). Meanwhile in their experiments, a negatively buoyant saline plume was initially seeded with hydrochloric acid of $\text{pH} = 1.2$ vs. an ambient pH of $\text{pH} = 7.1$. For relatively small ambient velocities, their measurements showed that the pH of the plume boundary drops rapidly below 6.3 approximately four nozzle diameters downstream, which demonstrates that plume fluid is entrained into the turbulent surroundings. A quantitative comparison between the theoretical plume length (defined as the vertical distance where the plume radius diminishes to zero) vs. its experimental counterpart showed good agreement. The comparison also yields the best-fit entrainment and extrainment coefficients. Extended study of plumes in finite convecting environments reveals the importance of convective mixing at the density interface that forms in filling-box type flows, e.g. of the type considered by Baines & Turner (1969), Baines (1983) and Kaye *et al.* (2010).

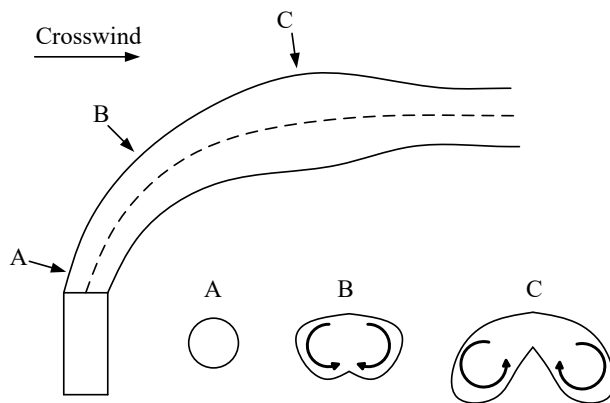


Figure 2.22: Vortex motion at different elevations of a plume in a crosswind. At cross section A, the plume behaves like a jet that has a circular cross section. At this stage, the plume’s self-generated turbulence is dominant in the dilution process. At cross section B, the edge of the plume is sheared off by the wind thus resulting in a kidney-shaped cross section. Thereafter at cross section C where the plume is fully bent-over, the dilution process is dominated by the interaction between the two counter-rotating line vortices and the ambient crossflow. (Fanaki, 1975)

2.5.5 Plume bifurcation

As shown in figure 2.22, Scorer (1958*a*, 1968) argued that bifurcation results from counter-rotating vortex pairs of equal strength but opposite sign within a bent-over plume. Some qualitative results by Scorer are: (i) bifurcation is always clearly present in cases of hot plumes rising in smooth winds, and, (ii) bifurcation can be induced by cooling at the plume boundary. The latter case occurs when the plume is visible, and the mixing between the ambient (unsaturated) air with the supersaturated air at the plume boundary evaporates and disperses the liquid moisture. Thus the cold flow at the plume edge falls due to its negative buoyancy. The associated baroclinic torque can enhance both the peripheral circulation exhibited schematically in figure 2.22 (points B and C) and also the tendency to plume bifurcation. In discussing Scorer’s conclusions, Briggs (1969) stated “it is not clear under what conditions the two vortices can separate, however, bifurcation is rare and appears to occur only in light winds”.

In analogue laboratory experiments conducted in a water channel, Hayashi (1971) found that the plume tends to bifurcate as it approaches the free water surface, which corresponds to the bottom of a temperature inversion in the context of atmospheric convection. A subsequent reanalysis of Hayashi’s experimental data by Khandekar & Murty (1975) determined that the free water surface creates an “image effect” (Kundu, 1990), which leads to the lateral separation of the vortex pair (see figure 2.23). Khandekar & Murty (1975) proposed that the image effect depends on the location and strength of the inversion layer and the buoyancy flux of the plume. Overall, and in agreement with the assertion of Briggs (1969), bifurcation caused by a separation of vortices may be considered as a rare phenomenon. Abdelwahed & Chu (1978) extended Hayashi’s experiments and found that a bifurcated jet follows the same generic scaling law as its non-bifurcated counterpart. Jirka & Fong (1981) proposed a

⁹Meandering describes the process by which the buoyant plume centerline deviates from the perfect vertical when discharged into a turbulent environment.

theoretical model that superimposes the internal vortex dynamics upon an integral model of buoyant jets in crossflows, the integral model being similar to that described in the follow-up study by Jirka (2004). The interaction of the counter-rotating motion with a fluid boundary and/or density interface was modeled by Jirka & Fong (1981) as a repulsive force that leads to bifurcation.

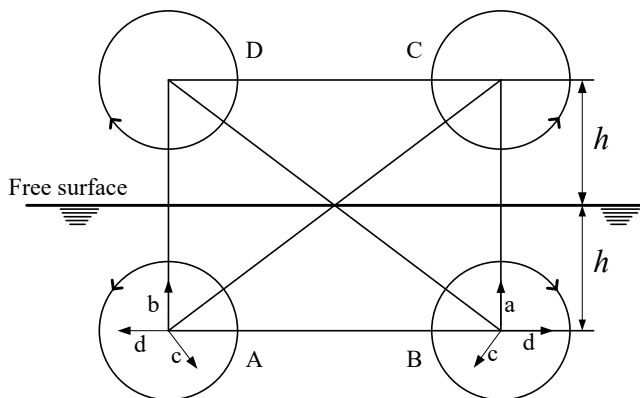


Figure 2.23: Image effect of the free surface on the vortex pairs A–B. The free surface acts as an image plane in which the vortex pairs A–B are mirrored, thus creating the image vortex pairs C–D. The velocity induced at vortex A (or B) by the other vortices B, C and D (or A, C and D) is vectorially represented using the corresponding lower-case letters. Note that the resultant horizontal velocity vectors at vortex A are opposite to those of vortex B, which leads to the separation of the vortex pairs. (Ernst *et al.*, 1994)

Turner (1960) treated the flow within a bent-over plume in a uniform ambient as a vortex pair. He assumed that the circulation, Γ , around one line vortex, is constant, thus the momentum (or impulse) of the vortex pair is proportional to the separation distance of the pair. In this way, any increase of momentum due to buoyancy leads to separation of the vortices. Furthermore, his theoretical result showed that the separation distance is linearly related to the downwind distance, which agrees well with experimental observations. It is, however, expected that Turner’s theory may not apply for stratified environments.

Bennett *et al.* (1992) used a scanning-Lidar system to measure the plume rise height, temperature profile, wind speed and direction, and the measured plume rise height is compared with Briggs’ formula. They found that plume bifurcation is favored in case of low ambient turbulence in a stable boundary layer. Moreover, and in contrast to Abdelwahed & Chu (1978), their measurements showed that bifurcation leads to a reduction in plume rise height due to the reduced buoyancy flux after plume splitting.

Ernst *et al.* (1994) analyzed bifurcation using ideal flow theory and thereby concluded that it is an induced lateral lift force that causes the vortices to separate. Their complementary laboratory experiments showed that bifurcation occurs for bent-over and straight-edged (i.e. slightly bent-over) buoyant jets for initial jet-to-crossflow velocity ratios of between two and six. For even larger jet-to-crossflow velocity ratios, bifurcation is blurred by the spreading gravity current that forms as the buoyant jet approaches the free water surface.

Huq & Dhanak (1996) studied experimentally the conditions under which the bifurcation of a circular jet in crossflow arises. They concluded that bifurcation occurs at some finite

distance from the source if the initial mean jet-to-crossflow velocity ratio is greater or equal to four. In turn, the distance from the source where bifurcation initiates increases with the jet-to-crossflow velocity ratio.

Arakeri *et al.* (2000) investigated the occurrence of bifurcation in case of horizontal injection of a laminar water jet into a brine solution. They found that bifurcation occurs in jets of relatively high Schmidt number and is caused by the slow moving fluid at the edges of the jets.

Cintolesi *et al.* (2018) performed LES simulations of buoyant jets in a neutral crossflow. Their simulations reproduced the counter-rotating vortex pair in the entrainment region where crossflow dominates over the initial momentum and buoyancy. Notably, a sausage-like turbulent structure develops at the top boundary of the plume. Moreover, these structures appear only in buoyant plumes but not in non-buoyant jets, which indicates that buoyancy tends to supply energy for the rotational motion within the plume.

In general, it seems that the mechanism of bifurcation is incompletely understood. Although the pressure distribution of the vortices proposed by Ernst *et al.* (1994) gives a reasonable hypothesis, rigorously speaking, a plume cannot be regarded as a rigid body. Scorer (1968) argued that bifurcation is due to a buoyancy induced circulation, however, buoyancy must obviously be omitted in the context of jet bifurcation (Abdelwahed & Chu, 1978; Huq & Dhanak, 1996). Lavelle (1997) argued that the large number of potential factors, such as background stratification, rotation and boundary layer shear, make difficult the task of determining exactly when plume bifurcation will arise. In terms of atmospheric dispersion, plume bifurcation enhances the dilution rate, albeit at the cost of possibly reducing the plume rise height.

2.5.6 Cooling tower drift

Cooling tower drift consists of water droplets mechanically entrained into the air flow through a wet cooling tower and discharged along with the moisture-laden buoyant plume. The US EPA considers cooling tower drift as a particulate emission (Lindahl & Mortensen, 2010). In this vein, it is important to highlight that only $\sim 1\%$ of the drift exhausted by a cooling tower is of respirable size i.e. has a diameter less than $5\ \mu\text{m}$ (Bugler *et al.*, 2010).

Roffman & Van Vleck (1974) and Chen (1977) reviewed the measurement techniques and theoretical models concerning drift deposition. In general, drift deposition is influenced by several physical processes, i.e. the dynamics and thermodynamics (evaporation) of droplets, droplets falling from a rising plume and dispersal by atmospheric turbulence. Chen (1977) compared 10 published theoretical models of drift deposition and found that the predicted maximum deposition and the corresponding downwind location deviate by two and one order of magnitude, respectively. These discrepancies, as argued by Chen (1977), are due to the different assumptions concerning the plume's vertical velocity as a function of height, and the effective height of emission i.e. the maximum rise height of droplets. A complete database for model validation can be found in Laulainen *et al.* (1979), which encompasses the simultaneous measurements of cooling tower source characteristics, e.g. drift rate, drift droplet size distribution, and meteorological conditions.

Meroney (2006) developed a CFD code to predict cooling tower drift deposition downwind of a cooling tower. The advantage of Meroney's CFD model as compared to previous

analytical methods is that it accounts for the effect of downwash. The turbulence model was the standard k - ϵ model, but Meroney (2006) also argued that the RNG or realizable k - ϵ models (Shih *et al.*, 1995) might be preferred in cases of shorter mechanical draft cooling towers and/or surrounding structures. The source droplet size distribution was modeled using a Rosin-Rammler particle distribution through the fitting of published data – see table 1 of Meroney (2006). The trajectories of drift droplets as a discrete phase were resolved using a Lagrangian stochastic approach. Later Meroney (2008) tested the CFD model of Meroney (2006) for urban cooling towers with surrounding buildings. One deficiency of Meroney’s CFD model is that the effect of droplet evaporation was not accounted for. This particular deficiency was corrected in the follow-up CFD model developed by Lucas *et al.* (2010). They investigated the influence of ambient conditions on the drift deposition of a natural draft cooling tower. A k - ϵ turbulence closure was employed to model the plume flow as a continuous phase, whereas a Lagrangian formulation derived from momentum and energy conservation was employed to describe the drift droplets as a discrete phase. Model performance was validated by comparison with other analytical, CFD and observational results as illustrated in figure 2.24. A key result from their study is that the drift deposition rate decreases with decreasing ambient humidity ratio, increasing droplet exit temperature and, most especially, increasing ambient dry-bulb temperature. Later Consuegro *et al.* (2014) adapted a similar CFD model but considered mechanical draft cooling towers in urban areas. Their study revealed that buildings downstream of the tower impose negligible influence on the area affected by drift deposition.

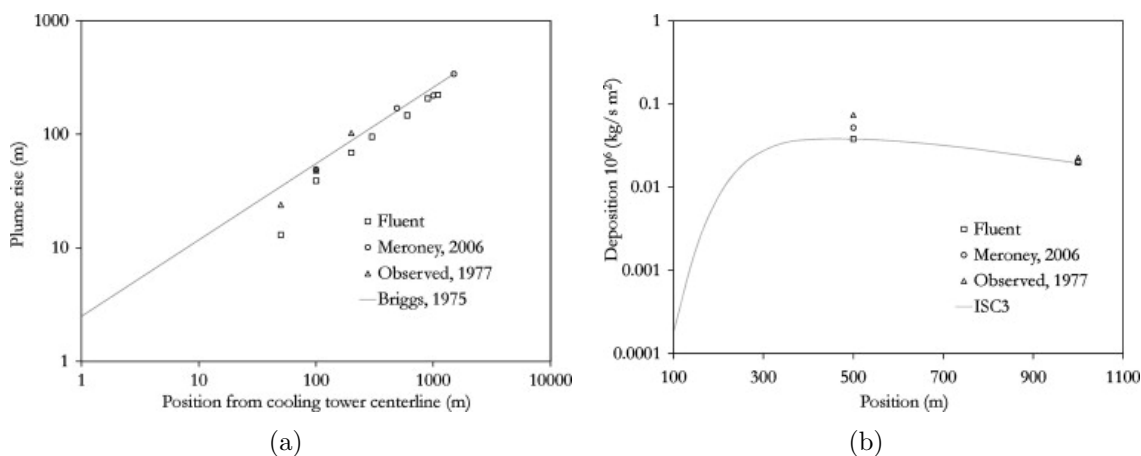


Figure 2.24: (a): Plume trajectories from Lucas *et al.* (2010), Meroney (2006), the 1977 Chalk Point Dye Tracer Experiment and Briggs’ plume rise formulae. (b): Drift deposition rates (mass/area/time) from Lucas *et al.* (2010), Meroney (2006), the 1977 Chalk Point Dye Tracer Experiment and the Industrial Source Complex (ISC3) Dispersion Models. The definition of drift deposition rate in CFD simulations is given in Meroney (2006). (Figure taken from Lucas *et al.* 2010)

Sánchez *et al.* (2015) studied the lifetime of drift with the combined effects of atmospheric conditions and droplet size distribution. If the lifetime experienced by the droplets is less than the time necessary to reach ground level, there is obviously less risk of Legionella bacteria. Their CFD model is similar to the modeling of continuous and discrete phases by Lucas *et al.* (2010). On the other hand, they measured the meteorological conditions and

droplet size distribution and temperature from a pilot mechanical draft cooling tower as the boundary conditions for their numerical model. Meanwhile, the measured deposition was used for validating their numerical model. Results from the study of Sánchez *et al.* (2015) were broadly consistent with those of Lucas *et al.* (2010); they revealed that a short lifetime is favored under conditions with high ambient temperature, low relative humidity and small droplet size.

2.6 Conclusions

The present manuscript gives a summary of plume abatement approaches and the modeling of buoyant moist plumes. Both traditional and novel plume abatement approaches are reviewed. Sensibly heating the hot, humid air so as to reduce the exhaust relative humidity has been studied by several researchers on cooling towers used in HVAC systems. Solar collectors and heat pumps are considered as potential heat sources, however, the intermittency of solar energy (and its complete absence at nighttime) poses obviously challenges. Also important is to consider the added space, capital and operational costs. A conventional PPWD tower adds a dry section through which the ambient air is sensibly heated and thereafter mixed with the hot, humid air from the wet section, thus the resulting air mixture is discharged with lowered relative humidity. For PPWD counterflow towers, static mixers are usually inserted within the plenum chamber to promote the mixing of the wet and dry airstreams. These static mixers range from simple baffles to vortex generators. The latter can achieve good mixing efficiency with moderate pressure drop. On the other hand, flow deflectors, though they increase the pressure drop and hence fan power, are generally more suitable for back-to-back cooling towers. A further option is to enhance mixing using a stirring device. These employ an axial flow fan and intense mixing is anticipated just below and above the fan. Another approach, originally found in PPWD crossflow towers, is to allow mixing to occur post-atmospheric discharge thereby reducing the pressure drop through the plenum space. In this scheme, the cooling tower plume assumes a coaxial structure with less humid air shielding the more humid air in the plume core.

Plume abatement can be a side effect of water conservation cooling towers, but not necessarily *vice versa*. Condensing module technology and thermosyphon systems are intended for water conservation by means of cooling the hot, moist air and collecting the condensed water. These designs have shown great advantages including improved water quality, absence of a dry section and, correspondingly, reduced pump head. The more recent invention of the dual dry and wet coil system has good flexibility for transition among different cooling modes. On the other hand, membrane-assisted condensers exhibit competing strength because they can recover not only water vapor but also chemicals and microparticles.

The review of plume modeling is the more substantial contribution of this work; it starts with the classic Briggs's two thirds law, then focuses on more advanced integral modeling. Several different entrainment assumptions are examined. The model of Schatzmann & Policastro (1984) is described in detail as an example illustrating the formulation, capability and limitation of integral models. Several theoretical attempts to model plume merger yield good agreement with experimental data, however, these models are, by necessity, associated with restrictive assumptions e.g. of a still ambient or weak crossflow. CFD simulations are

able to describe some complex phenomena, such as recirculation, downwash, plume merger and drift deposition, however, this comes at an elevated computational cost. In case of complex cooling tower structures or topography, similitude laboratory experiments may yield equally valuable insights. Wind tunnel, water tank and water flume experiments have been performed to account for different plume source and environmental conditions.

Several topics of greater complication are ambient turbulence, plume bifurcation and drift deposition. The effect of ambient turbulence has been incorporated by adding into previous integral models an extrainment velocity. Some plausible hypotheses from potential flow theory have been made to describe the mechanism of bifurcation, however, no firm conclusion has been made regarding the conditions that define its onset. Finally, the drift deposition rate, its area of effect and the lifetime of emitted water droplets have all been predicted by using various CFD algorithms. These studies show that the same factors that aid in plume abatement e.g. a high ambient dry-bulb temperature are also conducive to reducing drift deposition.

This review can motivate future research in a number of different areas. In terms of plume abatement, the utility of the solar collectors can and should be further explored. For instance, the dry section e.g. depicted in figure 3.4 can be replaced by solar absorbing material through which the ambient air, to be mixed with the moist air from the cooling tower fill, is driven by the fan. Such a design is expected to reduce the capital cost, although the dry heating performance and, by extension, the dimension of solar absorber material must be tailored specifically to achieve plume abatement. Another idea is to extend the thermosyphon design in Mantelli (2016) into hybrid cooling towers, possibly by locating the porous media structure in the plenum chamber. Here again, dry coils are avoided. In these designs, a coaxial plume structure occurs above the cooling tower. There are also designs, e.g. the wet/wet-dry design of Libert *et al.* (2015), that result in a plume source that is half wet and half dry. Plumes that are non-uniform at the source are yet to be fully understood. In a similar spirit, the buoyancy flux of a cooling tower plume may vary according to the time-dependent cooling demand of the power plant; the behavior (rise height and dilution) of such an unsteady source plume in a crosswind has not been thoroughly studied.

Chapter 3

Cooling tower plume abatement using a coaxial plume structure

3.1 Abstract

The traditional approach of cooling tower plume abatement is supposed to result in an unsaturated, well-mixed plume with a “top-hat” structure in the radial direction, but this is an idealization that is rarely achieved in practice. Meanwhile, previous analyses have shown that there may be an advantage in specifically separating the wet and dry air streams whereby the corresponding plume is of the coaxial variety with dry air enveloping (and thereby shielding) an inner core of wet air. Given that a detailed understanding of the evolution of coaxial plumes is presently lacking, we derive an analytical model of coaxial plumes in the atmosphere, which includes the effects of possible condensation. Of particular concern is to properly parameterize the entrainment (by turbulent engulfment) of fluid from the inner to the outer plume and vice-versa. We also present and discuss the two different body force formulations that apply in describing the dynamics of the inner plume. Based on the resulting model predictions, we introduce a so-called *resistance factor*, which is defined as the ratio of the average non-dimensional velocity to the average relative humidity. In the context of visible plume abatement, the resistance factor so defined specifies the likelihood of fog formation and/or a recirculation of moist air into the plenum chamber. On the basis of this analysis, we can identify the region of the operating-environmental condition parameter space where a coaxial plume might offer advantages over its uniform counterpart.

3.2 Introduction

A visible plume is a column of microscopic droplets of condensed water. Hot, moist air emitted from a wet cooling tower cools by entraining cold ambient air and a visible plume, or fog, forms if the plume temperature falls below the dew-point temperature. Though containing no pollutants except in entrained water droplets, which are, in any event, few in number, a visible plume is oftentimes regarded as a nuisance, which is better avoided. This need has led to various strategies for plume abatement (see below) whereas the need to model the fluid- and thermodynamical behavior of cooling tower plumes has produced

a voluminous literature on the topic. Indeed, the analytical description of atmospheric plumes, cooling tower and otherwise, dates back to Morton (1957), who formulated a one-dimensional, “top-hat” model of vertically ascending thermal plumes in a moist ambient based on the integral approach of Morton *et al.* (1956) (hereafter referred to as MTT). In the work of Morton (1957) (but not MTT), the potential temperature and density, which are conserved during adiabatic processes, are used in the governing equations. Morton’s model, which can predict the height at which fog will begin to form within the ascending plume, was improved upon by Csanady (1971), who included an ambient wind and was the first to note that condensation might occur only over some intermediate range of heights. The subsequent numerical results of Wigley & Slawson (1971) support this conclusion but indicate that whatever condensation does occur must do so relatively close to the stack/plume source. Wigley and Slawson further showed (Wigley & Slawson 1972 – see also Hanna 1972, Weil 1974 and Wigley 1975*b*) that plumes that include condensation rise to greater heights than do plumes in which no fog is formed. Wu & Koh (1978) proposed a merging criteria for the multiple plumes that emanate from adjacent cooling tower cells. Their predictions are in good agreement with corresponding laboratory data on dry plumes (without moisture). Carhart & Policastro (1991) developed the Argonne National Laboratory and University of Illinois (ANL/UI) model (a so-called second-generation model) to resolve select deficiencies of previous integral models e.g. their inability to correctly and simultaneously predict plume bending and dilution. Furthermore, Janicke & Janicke (2001) proposed an integral plume rise model which can be applied to arbitrary wind fields and source conditions.

Based on the above quick review, we now focus on the (hybrid) cooling tower configurations associated with different plume abatement strategies. Arguably the most popular configuration is the so-called parallel path wet/dry or PPWD configuration, which has been deployed commercially for more than 40 years. Lindahl & Jameson (1993) present a detailed description of PPWD towers, for both counter- and crossflow operation. In the former case, wet air exiting the fill section is co-mingled with comparatively dry air exiting heat exchanger bundle(s) (see figure 3.1 below). The two air streams mix in a plenum chamber and are then discharged to the atmosphere by a fan. Although perfect mixing is never achieved in practice, such an idealization serves as a convenient starting point for the development of plume dispersion models. In the crossflow configuration, the strategy is quite different. Here, air flows horizontally through the fill (see figure 3.5 below). Once in the plenum, this wet air stream has a velocity approximately twice that of the dry air and so the opportunity for mixing is (deliberately) limited. As a result, the plumes generated by PPWD crossflow cooling towers tend to be of the co-axial variety with dry air enveloping (and thereby shielding) an inner core of wet air. As illustrated in Figure 10 of Lindahl & Jameson (1993), the coaxial wet/dry plume above a PPWD crossflow tower results in a cone shaped visible plume that disappears at a vertical distance of about two to three fan stack diameters. Alas, a more detailed understanding of the evolution of coaxial plumes is presently lacking. Given this deficit of knowledge, our present goals are twofold: (i) to adapt ideas from Morton (1957), Wu & Koh (1978) and many others and thereby derive an analytical model for coaxial plumes in the atmosphere, and, (ii) to identify that region of the operating condition-environmental condition parameter space for PPWD where a coaxial plume might offer an advantage over its uniform counterpart. Of course, one might prefer a crossflow PPWD tower for other reasons: the lack of static mixing devices within the plenum chamber signifies a smaller

pressure drop to be overcome by the fan. Such design- and operation-specific details are not of principal concern here. Rather, our primary focus is on the buoyant convection that occurs above the cooling tower.

The manuscript is arranged as follows. In section 3.3 we recapitulate the theoretical model germane to uniform plumes encountered in PPWD counterflow towers. Following a discussion of coaxial plume structures in the open literature in section 3.3.3, we formulate in section 3.4 the theory for coaxial plumes above PPWD crossflow towers. Thereafter, in section 3.5, we study the range of process/ambient conditions where a coaxial plume structure offers some advantage with respect to plume abatement. Finally section 3.6 provides conclusions for the work as a whole and also identifies ideas for future research.

3.3 Theory for uniform plumes and its application to counterflow cooling towers

Figure 3.1 is a simplified sketch of a PPWD counterflow cooling tower. A dry section that consists of finned tube heat exchangers is added above the wet section, which consists of a spray zone, fill zone and rain zone. Thus warm, less humid air from the dry section and hot, saturated air from the wet section flow into the plenum chamber located just upstream of the axial fan. The two air streams are mixed thoroughly then discharged to the atmosphere with an average relative humidity below saturation. Streng (1998) suggests that the PPWD counterflow cooling tower, with its series connection of the dry and wet sections on the water side and parallel connection of these sections on the air side, produces the most effective overall cooling performance.

To describe the uniform plume that forms above the PPWD counterflow cooling tower illustrated in figure 3.1, we adapt the integral model of Wu & Koh (1978), which allows prediction of the plume temperature, moisture (vapor and liquid phases), vertical velocity, width, and density as well as the visible plume length in case of condensation. The main assumptions are:

- (i) Molecular transport is negligible compared to turbulent transport as a result of which
 - (a) model output is independent of the Reynolds number, and, (b) the Lewis number, defined as the ratio of thermal to mass diffusivity, is unity (Kloppers & Kröger, 2005). Because $Le = 1$, the dilution curve that appears in the psychrometric chart connecting the cooling tower exit to the far field ambient is a straight line.
- (ii) The cross-sectional profiles of the plume vertical velocity, temperature, density, vapor and liquid phase moistures are all self-similar. More specifically, plume properties are assumed to exhibit “top-hat” profiles (Davidson, 1986*b*).
- (iii) The variation of the plume density is small, i.e. no more than 10%. As such, the Boussinesq approximation can be applied.
- (iv) The pressure is hydrostatic throughout the flow field.
- (v) The plumes emitted from adjacent cooling tower cells are initially axisymmetric and propagate vertically upwards. At larger elevations, plume merger may occur as a result

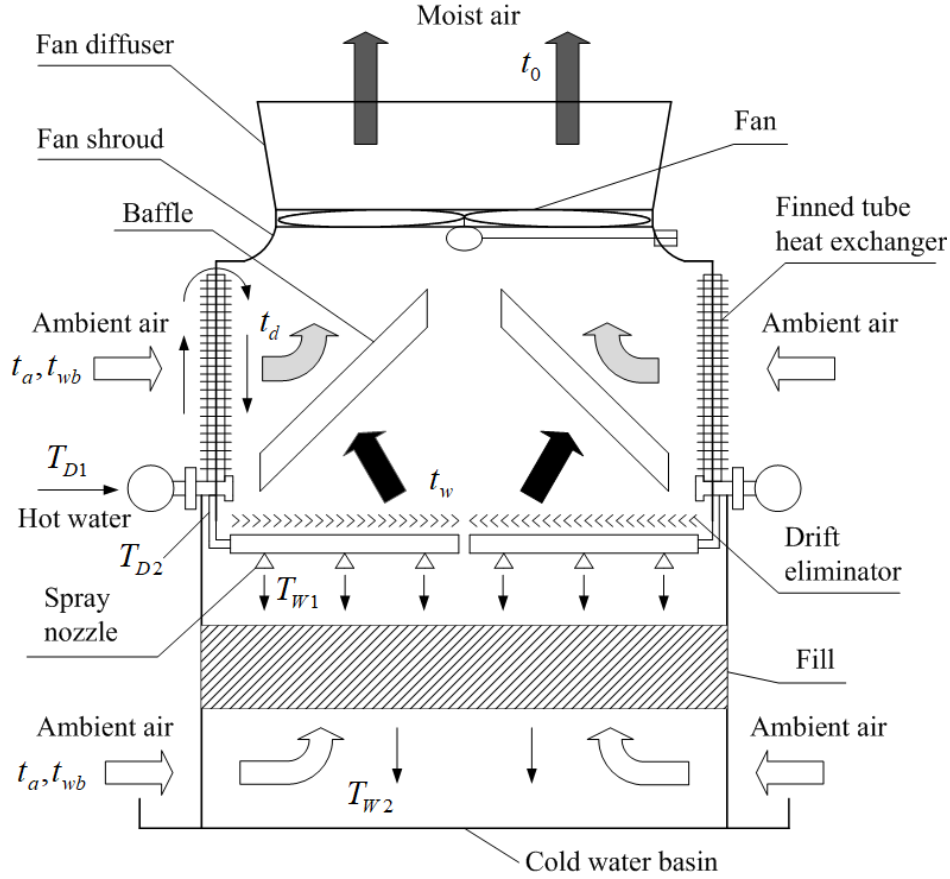


Figure 3.1: Schematic of a PPWD counterflow cooling tower. The white arrows denote the ambient air. The black and light gray arrows denote, respectively, the hot, saturated air from the wet section and the warm, dry air from the dry section. The dark gray arrows at the top of fan shroud denote the resulting well-mixed air stream (We assume complete mixing within the plenum chamber.). In the dry section, t_a is the ambient dry-bulb temperature, t_{wb} is the ambient wet-bulb temperature, t_d is the temperature of the sensibly heated air from the dry section (also called the dry cooling temperature), T_{D1} is the dry section inlet water temperature, T_{D2} is the dry section outlet water temperature, $R_D = T_{D1} - T_{D2}$ is the range temperature in the dry section and $A_D = T_{D2} - t_a$ is the approach temperature in the dry section. For the wet section, t_w is the temperature of the saturated moist air discharged from the drift eliminator, T_{W1} is the wet section inlet water temperature where, ideally, $T_{W1} = T_{D2}$. Moreover, T_{W2} is the wet section outlet water temperature, $R_W = T_{W1} - T_{W2}$ is the range temperature in the wet section and $A_W = T_{W2} - t_{wb}$ is the approach in the dry section. Finally, t_0 is the temperature of the well-mixed air at the top of the fan shroud/base of the (uniform) plume.

of which the shape of the combined plume is assumed to be a combination of a finite line plume in the central part and two half axisymmetric plumes at either end. The criterion for plume merger follows from Wu & Koh (1978) and is summarized in section 3.7.

- (vi) The ambient is, to a first approximation, assumed to be uniform in temperature and humidity. It is also devoid of liquid phase moisture.

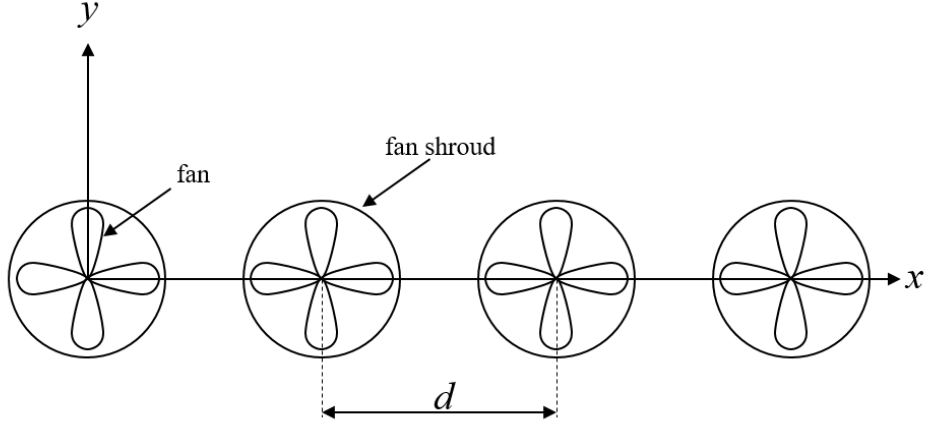


Figure 3.2: The coordinate system associated with a (four cell) cooling tower in a still ambient. The z axis points upwards, i.e. out of the page.

3.3.1 Formulation

The plan-view schematic of figure 3.2 shows the coordinate system chosen for a typical array of (equidistant) cooling towers. The x -axis is parallel to the line connecting the centers of the cells whereas the z -axis is the vertical axis with $z = 0$ corresponding to the top of the fan shroud.

The conservation equations for mass, momentum, energy and (vapor and liquid phase) moisture are written symbolically as

$$\frac{d}{dz} \left\{ \int_A \rho_p U_p dA \right\} = \rho_a E, \quad (3.1)$$

$$\frac{d}{dz} \left\{ \int_A \rho_p U_p^2 dA \right\} = g \int_A (\rho_a - \rho_p) dA, \quad (3.2)$$

$$\frac{d}{dz} \left\{ \int_A (t_p - t_a) U_p dA \right\} = \int_A \frac{L_v}{c_{pa}} \sigma_p U_p dA, \quad (3.3)$$

$$\frac{d}{dz} \left\{ \int_A [(q_p - q_a) + \sigma_p] U_p dA \right\} = 0, \quad (3.4)$$

where ρ_p , U_p and A are, respectively, the plume density, vertical velocity, and cross-sectional area. Moreover, q is the specific humidity, t is the air dry-bulb temperature¹, σ is the specific liquid moisture, E specifies the rate of entrainment of external ambient air, g is gravitational acceleration, $L_v(t) = 4.1868 \times 10^3 [597.31 - 0.57t]$ J/g is the latent heat of condensation in which t is measured in °C, and $c_{pa} = 1.006$ J/g °C is the specific heat capacity of air at constant pressure. The subscripts p and a indicate values in the plume and in the ambient, respectively. According to Taylor's entrainment hypothesis (Morton *et al.*, 1956)

$$E = S\alpha U_p, \quad (3.5)$$

¹Below the plume origin and consistent with figure 3.1, we use a lowercase t to indicate the temperature of a gas stream and an uppercase T to indicate the temperature of a liquid stream. Above the plume origin, the lowercase t is retained for the temperature of the moist plume and ambient air.

where α is an entrainment coefficient whose value is typically 0.117 for axisymmetric plumes and 0.147 for line-source plumes (Bloomfield & Kerr, 2000). Moreover, S is the plume perimeter.

For convenience, we use the virtual temperature when calculating plume densities. The virtual temperature, t_v , corresponds to the temperature of dry air having the same density as a parcel of moist air at an identical pressure (Curry & Webster 1998; cf. Monteiro & Torlaschi 2007). For purposes of including condensation, we adopt the virtual temperature for foggy air² and use the following expression, presented by Emanuel (1994):

$$t_v = t(1 + 0.608q - \sigma) , \quad (3.6)$$

$$P = \rho_p R_a t_v , \quad (3.7)$$

where t and t_v are measured in Kelvin, P is the total pressure inside/outside the plume and $R_a = 287.058 \text{ J/kg K}$ is the gas constant of air. Note that the above definition for t_v incorporates liquid moisture to express the change in bulk density as a result of condensed water.

Applying the Boussinesq approximation and the definition of the virtual temperature, (3.1)–(3.2) can be simplified as,

$$\frac{d}{dz} \left\{ \int_A U_p dA \right\} = E , \quad (3.8)$$

$$\frac{d}{dz} \left\{ \int_A U_p^2 dA \right\} = \int_A g' dA , \quad (3.9)$$

where $g' = g \left(1 - \frac{t_{v,a}}{t_{v,p}} \right)$ in which $t_{v,p}$ and $t_{v,a}$ are the virtual temperatures of the plume and ambient, respectively.

To simplify the conservation equations, it is helpful to define the plume volume flux Q , momentum flux M , temperature deficiency flux Θ , specific humidity deficiency flux H , and specific liquid moisture deficiency flux W as follows:

$$Q = \int_A U_p dA , \quad (3.10)$$

$$M = \int_A U_p^2 dA , \quad (3.11)$$

$$\Theta = \int_A (t_p - t_a) U_p dA , \quad (3.12)$$

$$H = \int_A (q_p - q_a) U_p dA , \quad (3.13)$$

$$W = \int_A (\sigma_p - \sigma_a) U_p dA . \quad (3.14)$$

Recall that, consistent with the top-hat approximation, ρ_p , U_p , t_p , q_p , and σ_p are all constant inside the plume. Note also that assumption (vi) demands that $\sigma_a = 0$. Rewriting the

²Moist air can be regarded as a limiting case of foggy air where the liquid moisture content is zero, i.e. $\sigma = 0$.

conservation equations using the above variables yields

$$\frac{dQ}{dz} = E, \quad (3.15)$$

$$\frac{dM}{dz} = g \frac{Q^2}{M} \left(1 - \frac{t_{v,a}}{t_{v,p}} \right), \quad (3.16)$$

$$\frac{d}{dz} \left(\Theta - \frac{L_v}{c_{pa}} W \right) = 0, \quad (3.17)$$

$$\frac{d}{dz} (H + W) = 0, \quad (3.18)$$

where $t_{v,p} = \left(t_a + 273.15 + \frac{\Theta}{Q} \right) \left[1 + 0.608 \left(q_a + \frac{H}{Q} \right) - \frac{W}{Q} \right]$ in (3.16).

The system of equations (3.15)–(3.18) constitutes four ordinary differential equations in five unknowns. Model closure is achieved by noting that

$$\begin{aligned} \sigma_p &= 0, & \text{for } q_p < q_{sp} \text{ (dry plume)} \\ q_p &= q_{sp}(t, P), & \text{for } q_p \geq q_{sp} \text{ (wet plume)} \end{aligned} \quad (3.19)$$

where q_{sp} is the saturation specific humidity and P is the total pressure. The former quantity is given by

$$q_{sp}(t, P) = \frac{M_v P_{sv}(t)}{M_a [P - P_{sv}(t)] + M_v P_{sv}(t)}, \quad (3.20)$$

where $M_v = 18.02 \times 10^{-3}$ kg/mol is the water molar mass, $M_a = 28.966 \times 10^{-3}$ kg/mol is the air molar mass, and P_{sv} is the saturated vapor pressure. Within the temperature range of 0 to 200°C, P_{sv} , measured in Pa, is given by (ASHRAE, 2013b)

$$P_{sv} = e^{C_1/t + C_2 + C_3 t + C_4 t^2 + C_5 t^3 + C_6 \ln t}, \quad (3.21)$$

$$\begin{aligned} C_1 &= -5.8002206 \times 10^3 \text{ K}, & C_2 &= 1.3914993, \\ C_3 &= -4.8640239 \times 10^{-2} \text{ K}^{-1}, & C_4 &= 4.1764768 \times 10^{-5} \text{ K}^{-2}, \\ C_5 &= 1.4452093 \times 10^{-8} \text{ K}^{-3}, & C_6 &= 6.5459673. \end{aligned}$$

Meanwhile assumption (iv) requires that the total pressure inside the plume changes hydrostatically with elevation, i.e.

$$P = P_0 - \rho_a g z. \quad (3.22)$$

Here, P_0 denotes the pressure at the top of the cooling tower and ρ_a can be calculated using (3.7).

The system of equations (3.15)–(3.18) with the additional constraint (3.19) can be integrated forward in z starting from known (or, in the design stage, estimated) conditions at the cooling tower exit, i.e. $z = 0$. These so-called source conditions can be computed using the following formulas:

$$\begin{aligned} Q_0 &= \frac{\pi}{4} D_0^2 U_0, \\ M_0 &= \frac{\pi}{4} D_0^2 U_0^2, \\ \Theta_0 - \frac{L_{v,0}}{c_{pa}} W_0 &= \frac{\pi}{4} D_0^2 U_0 (t_0 - t_a), \\ H_0 + W_0 &= \frac{\pi}{4} D_0^2 U_0 (q_0 - q_a), \end{aligned} \quad (3.23)$$

where a subscript 0 denotes a value measured at the tower exit so that, for instance, D_0 is the initial plume diameter which corresponds to the inner diameter of the fan shroud.

Due to the complexity of the governing equations, no analytical solution can be obtained. The ordinary differential equations (3.15) to (3.18) are instead solved numerically using MATLAB's `ode45` function.

3.3.2 Representative solutions

We consider a single cooling tower cell and a line array of $n = 9$ cooling tower cells with representative operating and ambient conditions as specified in table 3.1. For reference, the temperatures described in this table are defined in figure 3.1.

Table 3.1: Representative operating and environmental conditions for a single cooling tower cell and a line array of $n = 9$ cells.

Variable name and symbol	Value (unit)
Ambient pressure at the top of the cooling tower, P_a	101325 (Pa)
Ambient temperature, t_a	5 ($^{\circ}\text{C}$)
Ambient relative humidity, RH_a	60 (%)
Wet cooling temperature, t_w	30 ($^{\circ}\text{C}$)
Dry cooling temperature, t_d	25 ($^{\circ}\text{C}$)
Stack exit velocity, U_0	6 (m/s)
Stack exit area, A_0	71.3 (m^2)
Distance between cell centers, d	14.3 (m)
Ratio of the dry air mass flux to the wet air mass flux, $\frac{\dot{m}_d}{\dot{m}_w}$	0.6 0.3

Numerical results showing the solution of (3.15)–(3.18) are indicated by the curves of figure 3.3. Note the plume excess temperature and height are non-dimensionalized by the source excess temperature ($t_0 - t_a$) and source plume diameter D_0 , respectively. In the case of the black curves, which assume a dry air mass flux to wet air mass flux of $\frac{\dot{m}_d}{\dot{m}_w} = 0.6$, figure 3.3 b confirms that there is no condensation during plume dilution; correspondingly the dilution lines on the psychrometric chart never intersect the saturation curve. Rather, the maximum relative humidity of 90.07% occurs at an elevation of $Z = 2.26$ for both single and multiple cell towers. In the multiple cell case, plume merger begins at $Z = 2.90$. The temperature and relative humidity in the merged plume decay more slowly with elevation because merger is associated with a lesser volume of entrained ambient fluid. The vertical velocity (not shown) is therefore greater in the merged plume, a manifestation of the “buoyant enhancement” described by Briggs (1975).

Although condensation is absent when $\frac{\dot{m}_d}{\dot{m}_w} = 0.6$, figure 3.3 shows that fog will form when this mass flow ratio is reduced to 0.3 corresponding to more limited dry cooling. (Of course, fog may also appear if the ambient temperature or relative humidity are respectively decreased and increased.) As illustrated by the red curves in figure 3.3 b, the plume undergoes three stages, i.e. invisible, visible and invisible again. In the single cell case, the plume is visible when $1.21 < Z < 3.22$. By contrast, in the $n = 9$ case, the plumes/merged plume is visible when $1.21 < Z < 3.36$. (Plume merger begins at $Z = 2.94$.)

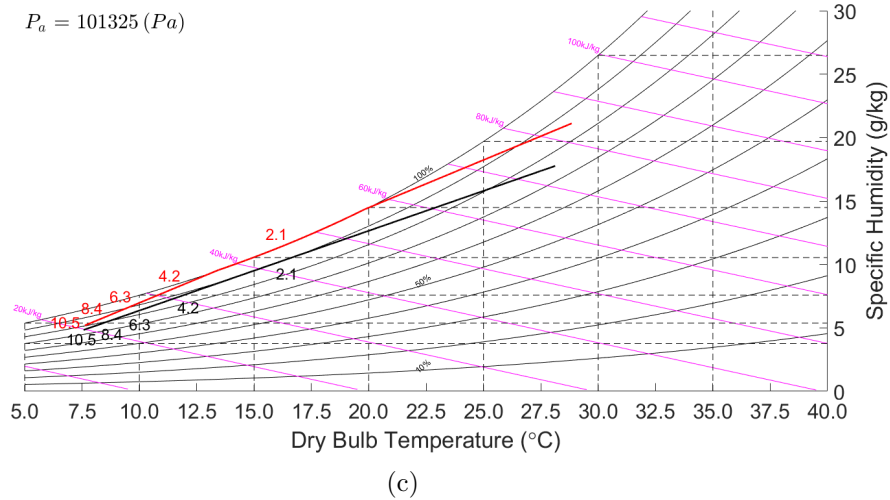
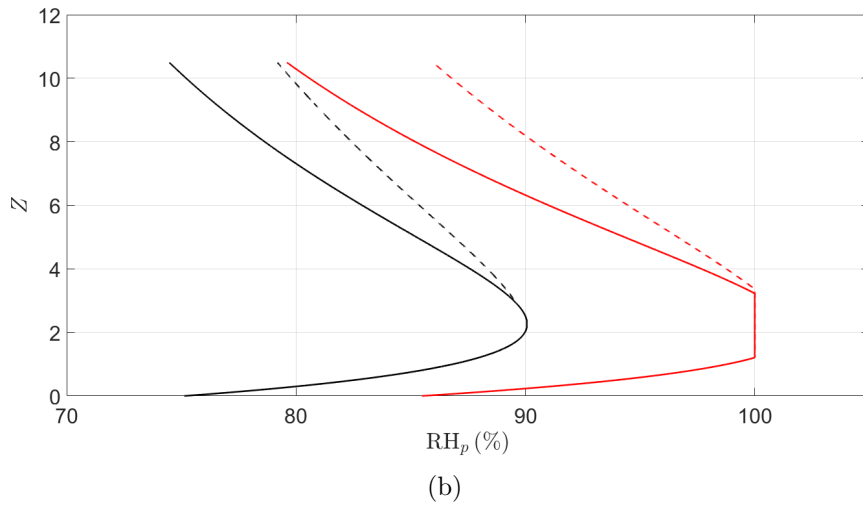
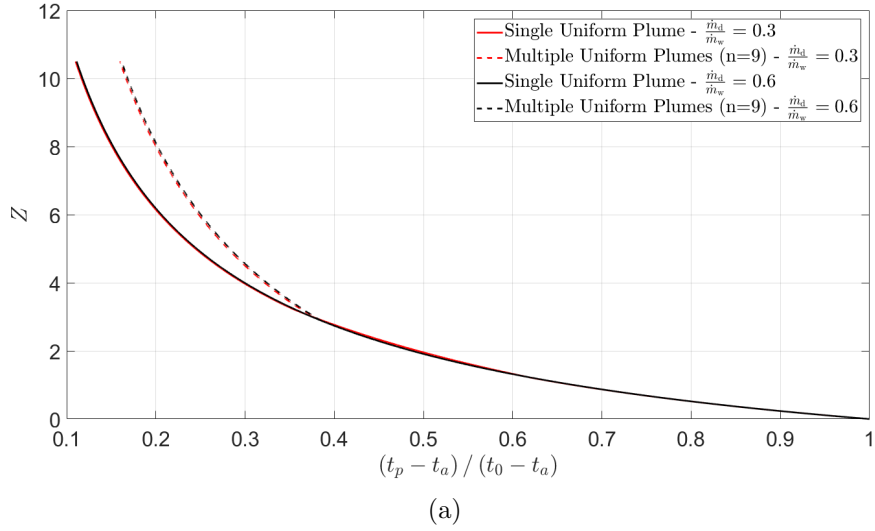


Figure 3.3: [Color] Non-dimensional plume excess temperature (panel a) and relative humidity (panel b) as functions of height where $Z \equiv z/D_0 = 0$ corresponds to the top of the fan diffuser. Panel c shows the plume temperature, specific humidity and the corresponding non-dimensional elevations on the psychrometric chart. Ambient and operating conditions are specified in table 3.1.

3.3.3 Discussion

The aforementioned PPWD counterflow towers are supposed to result in a well-mixed plume with a “top-hat” structure in the radial direction, but this is an idealization that is rarely achieved in practice. Generally, mixing is incomplete in the context of hybrid cooling because this mixing, even if aided by static mixing devices, must occur over short vertical distances i.e. the height of the plenum plus fan shroud and fan diffuser. Moreover, the mixing efficacy of the fan from figure 3.1 remains unclear. Whereas the recent numerical study by Takata *et al.* (2016) concludes that the fan could yield complete mixing of the wet and dry airstreams, this finding is contradicted by observation. For instance, Hensley (2009) notes that “the wet and dry air masses tend to follow flow paths through the fan and the combined flow exits the fan cylinder in streamlines”. This finding is corroborated by Kinney Jr *et al.* (1999) who state that “surprisingly little air stream mixing occurs at fan”.

Of course, there may be instances in which there is an advantage to specifically separate the wet and dry air streams. Cooling towers based on this idea are often called water conservation cooling towers (Houx Jr *et al.*, 1978; Lindahl & Jameson, 1993; Hensley, 2009). In this configuration, hot water is first sensibly cooled in the dry section, then if additional cooling is needed, the water is then directed to the wet section where evaporative cooling occurs. If no additional cooling is required, the water is instead bypassed directly to the cold water basin thus water conservation is achieved. Houx Jr *et al.* (1978) proposed a water-conserving hybrid cooling tower according to which the ascending plume of wet air is surrounded (or enveloped) by four plumes of ascending dry air. Provided the ambient air temperature is not too low, this configuration is expected to avoid fog formation because the dry air shields the wet air from directly contacting the external ambient. Another benefit associated with this design is that the wet air can rise quickly because its buoyancy is more slowly eroded. Thus the likelihood of recirculating this wet air through the cooling tower is decreased (Kröger, 2004). A similar kind of coaxial wet/dry plume structure can be achieved without the operational headache of running five fans simultaneously by modifying the fan shroud in the manner suggested schematically by figure 3.4 (Koo, 2016*a*, 2016*b*). Here, external dry air is drawn into the space between the fan stack and the outer shroud, then mixed with the hot, saturated air discharged by the fan.

Sitting between the cooling tower designs shown in figure 3.1 vs. those of Houx Jr *et al.* (1978), Koo (2016*a*, 2016*b*), are, of course, PPWD crossflow towers of the type shown schematically in figure 3.5. According to PPWD crossflow design, the degree of mixing in the plenum chamber is modest and, therefore, the emitted plume is again of coaxial type with (buoyant) wet air occupying the center core.

Motivated by the above summary, we shall, in the sections to follow, develop and apply a theory for coaxial plumes. Although specific reference will be made to PPWD crossflow towers, it should be understood that our governing equations can easily be generalized to cooling towers of the type studied by Houx Jr *et al.* (1978), Koo (2016*a*, 2016*b*). Our analysis is motivated by the lack of a robust model for coaxial plumes and will discuss possible advantages of this configuration in the cooling tower/visible plume abatement context. In addition to the reduced probability of recirculation already described, these include, for instance, possibly delaying the onset of condensation.

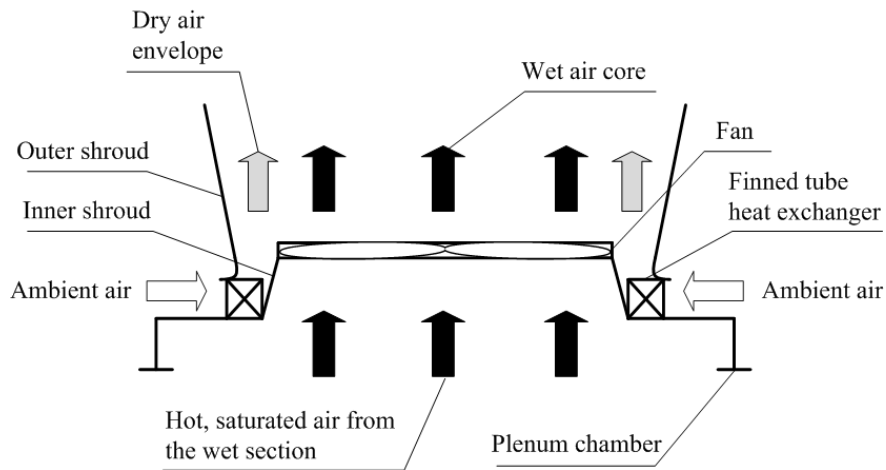


Figure 3.4: The hybrid cooling tower design of Koo (2016a, 2016b). Visible plume abatement is achieved by enveloping the wet air stream within a sheath of drier air.

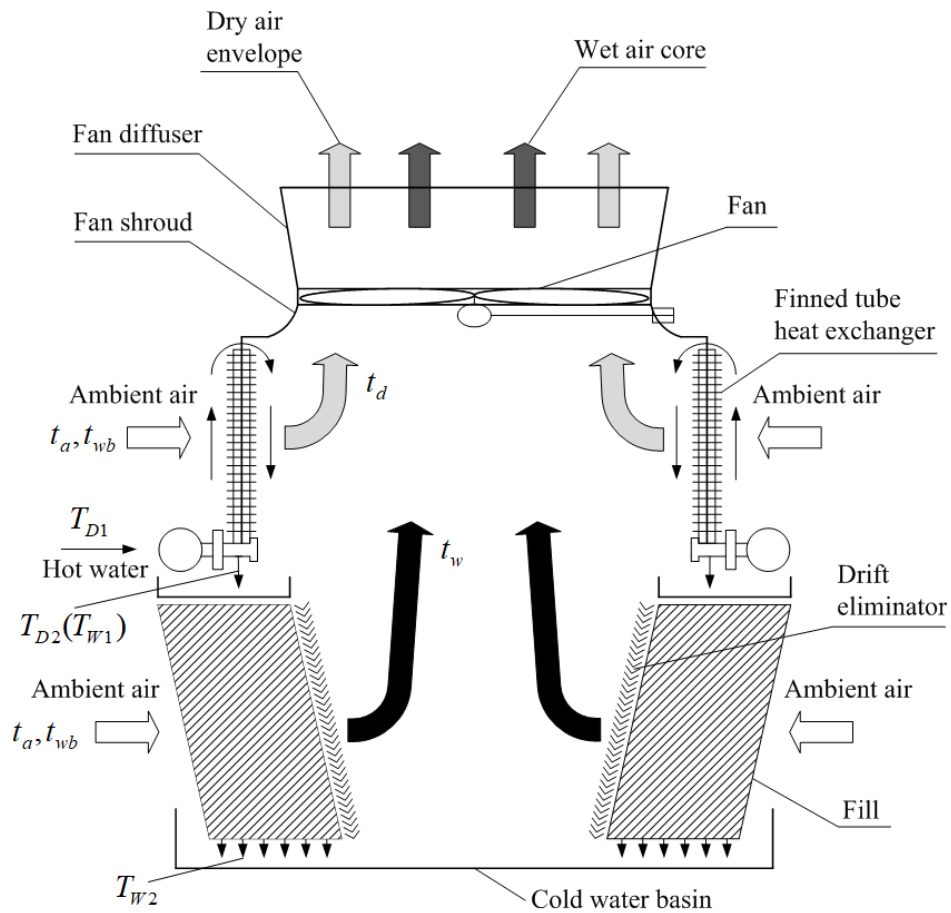


Figure 3.5: As in Figure 3.1 but with a different fill configuration and internal structure inside the plenum chamber. A limited amount of dry air is mixed into the wet air inside the plenum. The remaining fraction is assumed to leave the tower without mixing so that it envelopes the core of wetter air upon discharge to the atmosphere.

3.4 Theory for coaxial plumes and its application to crossflow cooling towers

3.4.1 Formulation

The theory of coaxial plumes is developed by analogy with turbulent fountain theory as proposed by McDougall (1981) and subsequently adapted by Bloomfield & Kerr (2000). Before elaborating on this analogy, it is important to note that all previously stated assumptions with the possible exception of assumption (iv) from section 3.3.1 continue to apply. We further assume that adjacent plumes still merge according to the dynamics described in section 3.7. An important point of difference with the analysis of section 3.3.1 concerns the body force calculation for the inner plume. Studying a similar coaxial flow problem, McDougall (1981) concluded that there exist two reasonable approaches as outlined below.

The former body force formulation (referred to as BFI by Bloomfield & Kerr, 2000) retains the assumption of a hydrostatic flow. The latter formulation (referred to as BFII by Bloomfield & Kerr, 2000) evaluates the body force of the inner plume relative to the buoyancy of the outer plume, not the ambient. In other words, the body force is determined by computing the density difference between the inner and outer plumes and by considering the acceleration of the outer plume. As a matter of fact, the solutions produced using BFI and BFII are very similar in many respects. Moreover, in their careful study of turbulent fountains, Bloomfield & Kerr (2000) determined that formulation BFII provides a moderately better agreement with experimental data than does BFI. As such, we shall apply BFII in the discussion to follow. To resolve the choice of body force formulation more decisively, we plan, in the near future, to report upon the results of new laboratory experiments that focus specifically on coaxial plumes. Inclusion of the material in question here is outside of the scope of the present inquiry.

A further complication associated with coaxial plumes concerns the entrainment of fluid from the inner to the outer plume and vice-versa. In his investigation of coaxial jets, Morton (1962) argued that the turbulence in the inner jet arose from mean velocity differences between the inner and outer jets, whereas turbulence in the outer jet was due to mean velocity differences between the outer jet and ambient. Adopting the same idea here, and further to figure 3.6, entrainment processes are expressed mathematically as follows:

$$\omega_\alpha = \alpha|U_1 - U_2|, \quad \omega_\beta = \beta U_2, \quad \omega_\gamma = \gamma U_2. \quad (3.24)$$

Here ω_α , ω_β and ω_γ are the entrainment velocities³ from the outer plume to the inner plume, from the inner plume to the outer plume and from the ambient to the outer plume, respectively. Furthermore, U_1 and U_2 are the respective mean velocities of the inner and outer plumes. Equation (3.24) is expected to apply for Reynolds number that is large enough to generate a turbulent plume flow. Meanwhile, we assume that the entrainment coefficients, i.e. α , β and γ , are independent of the buoyancy in the plumes. Regarding the values of the entrainment coefficients in figure 3.6, we refer to Bloomfield & Kerr (2000) and assume that $\alpha = 0.085$ and $\beta = \gamma = 0.117$. These values are considered to apply up to the point

³Here we assume that α is non-zero, whereas in later chapters we may treat α differently, e.g. $\alpha = 0$ is assumed in Chapter 4.

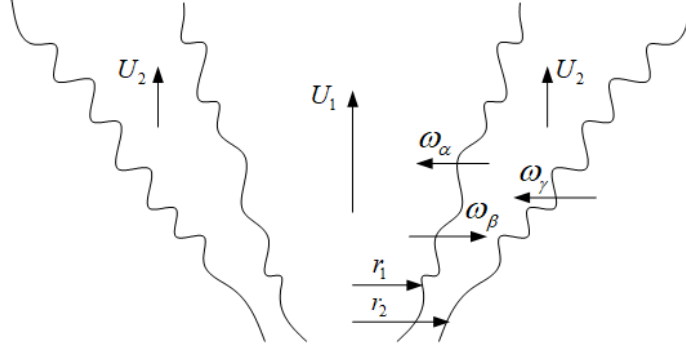


Figure 3.6: Coaxial plume structure. Entrainment from the outer plume to the inner plume, from the inner to the outer plume and from the ambient to the outer plume are parameterized by entrainment velocities ω_α , ω_β and ω_γ , respectively. Meanwhile, r_1 and r_2 are the respective characteristic radii for the inner and outer plumes. ω_α , ω_β and ω_γ are defined by equation (3.24).

of (outer) plume merger, above which γ is increased to 0.147 corresponding to a pure line plume (List, 1982).

Given (3.24), the conservation of volume, energy and moisture for the inner and outer plumes are respectively expressed as follows:

$$\frac{d}{dz} \left\{ \int_{A_1} \rho_1 U_1 dA \right\} = \rho_2 c_1 \omega_\alpha - \rho_1 c_1 \omega_\beta, \quad (3.25)$$

$$\frac{d}{dz} \left\{ \int_{A_2} \rho_2 U_2 dA \right\} = \rho_1 c_1 \omega_\beta - \rho_2 c_1 \omega_\alpha + \rho_a c_2 \omega_\gamma, \quad (3.26)$$

$$\begin{aligned} \frac{d}{dz} \left\{ \int_{A_1} (t_1 - t_a) U_1 dA \right\} &= c_1 \omega_\alpha \left(t_2 - t_a - \sigma_2 \frac{L_{v,2}}{c_{pa}} \right) - c_1 \omega_\beta \left(t_1 - t_a - \sigma_1 \frac{L_{v,1}}{c_{pa}} \right) \\ &+ \frac{d}{dz} \left\{ \int_{A_1} \frac{L_{v,1}}{c_{pa}} \sigma_1 U_1 dA \right\}, \end{aligned} \quad (3.27)$$

$$\begin{aligned} \frac{d}{dz} \left\{ \int_{A_2} (t_2 - t_a) U_2 dA \right\} &= c_1 \omega_\beta \left(t_1 - t_a - \sigma_1 \frac{L_{v,1}}{c_{pa}} \right) - c_1 \omega_\alpha \left(t_2 - t_a - \sigma_2 \frac{L_{v,2}}{c_{pa}} \right) \\ &+ \frac{d}{dz} \left\{ \int_{A_2} \frac{L_{v,2}}{c_{pa}} \sigma_2 U_2 dA \right\}, \end{aligned} \quad (3.28)$$

$$\frac{d}{dz} \left\{ \int_{A_1} (q_1 - q_a + \sigma_1) U_1 dA \right\} = c_1 \omega_\alpha (q_2 - q_a + \sigma_2) - c_1 \omega_\beta (q_1 - q_a + \sigma_1), \quad (3.29)$$

$$\frac{d}{dz} \left\{ \int_{A_2} (q_2 - q_a + \sigma_2) U_2 dA \right\} = c_1 \omega_\beta (q_1 - t_a + \sigma_1) - c_1 \omega_\alpha (q_2 - q_a + \sigma_2). \quad (3.30)$$

Here, the geometric parameters c_1 , c_2 , A_1 and A_2 are defined as $c_1 = 2\pi r_1$ and $c_2 = 2\pi r_2$, $A_1 = \pi r_1^2$ and $A_2 = \pi (r_2^2 - r_1^2)$.

Equations (3.25)–(3.30) must be coupled with equations describing momentum conservation. Under the BFII formulation, the momentum conservation equation for the inner plume

is

$$\frac{d}{dz} \left\{ \int_{A_1} \rho_1 U_1^2 dA \right\} = A_1 \left[g(\rho_2 - \rho_1) + \rho_1 U_2 \frac{dU_2}{dz} \right] + c_1 \rho_2 \omega_\alpha U_2 - c_1 \rho_1 \omega_\beta U_1, \quad (3.31)$$

where $U_2 \frac{dU_2}{dz}$ is the acceleration of the outer plume. To derive the analogue expression for the outer plume, it is helpful to first consider momentum conservation for the coaxial plume as a whole, by which we write

$$\frac{d}{dz} \left\{ \int_{A_1} \rho_1 U_1^2 dA + \int_{A_2} \rho_2 U_2^2 dA \right\} = gA_1(\rho_a - \rho_1) + gA_2(\rho_a - \rho_2). \quad (3.32)$$

Subtracting (3.31) from (3.32) then yields

$$\begin{aligned} \frac{d}{dz} \left\{ \int_{A_2} \rho_2 U_2^2 dA \right\} &= A_1 \left[g(\rho_a - \rho_2) - \rho_1 U_2 \frac{dU_2}{dz} \right] + gA_2(\rho_a - \rho_2) \\ &\quad + c_1 \rho_1 \omega_\beta U_1 - c_1 \rho_2 \omega_\alpha U_2. \end{aligned} \quad (3.33)$$

Analogous to section 3.3.1, it is helpful to define an equivalent set of integral parameters as follows:

$$Q_1 = \int_{A_1} U_1 dA, \quad Q_2 = \int_{A_2} U_2 dA, \quad (3.34)$$

$$M_1 = \int_{A_1} U_1^2 dA, \quad M_2 = \int_{A_2} U_2^2 dA, \quad (3.35)$$

$$\Theta_1 = \int_{A_1} (t_1 - t_a) U_1 dA, \quad \Theta_2 = \int_{A_2} (t_2 - t_a) U_2 dA, \quad (3.36)$$

$$H_1 = \int_{A_1} (q_1 - q_a) U_1 dA, \quad H_2 = \int_{A_2} (q_2 - q_a) U_2 dA, \quad (3.37)$$

$$W_1 = \int_{A_1} \sigma_1 U_1 dA, \quad W_2 = \int_{A_2} \sigma_2 U_2 dA, \quad (3.38)$$

where, consistent with figure 3.6, subscripts 1 and 2 refer to the inner and outer plumes, respectively.

The aforementioned conservation equations for volume, energy and moisture then become

$$\frac{dQ_1}{dz} = c_1(\omega_\alpha - \omega_\beta), \quad (3.39)$$

$$\frac{dQ_2}{dz} = c_1(\omega_\beta - \omega_\alpha) + c_2 \omega_\gamma, \quad (3.40)$$

$$\frac{d}{dz} \left(\Theta_1 - \frac{L_{v,1}}{c_{pa}} W_1 \right) = c_1 \omega_\alpha \left(t_2 - t_a - \sigma_2 \frac{L_{v,2}}{c_{pa}} \right) - c_1 \omega_\beta \left(t_1 - t_a - \sigma_1 \frac{L_{v,1}}{c_{pa}} \right), \quad (3.41)$$

$$\frac{d}{dz} \left(\Theta_2 - \frac{L_{v,2}}{c_{pa}} W_2 \right) = c_1 \omega_\beta \left(t_1 - t_a - \sigma_1 \frac{L_{v,1}}{c_{pa}} \right) - c_1 \omega_\alpha \left(t_2 - t_a - \sigma_2 \frac{L_{v,2}}{c_{pa}} \right), \quad (3.42)$$

$$\frac{d}{dz} (H_1 + W_1) = c_1 \omega_\alpha (q_2 - q_a + \sigma_2) - c_1 \omega_\beta (q_1 - q_a + \sigma_1), \quad (3.43)$$

$$\frac{d}{dz} (H_2 + W_2) = c_1 \omega_\beta (q_1 - q_a + \sigma_1) - c_1 \omega_\alpha (q_2 - q_a + \sigma_2). \quad (3.44)$$

Similarly, the momentum conservation equations assuming a BFII formulation are rewritten

$$\frac{dM_1}{dz} = A_1 \left(g'_1 - g'_2 + U_2 \frac{dU_2}{dz} \right) + c_1 (\omega_\alpha U_2 - \omega_\beta U_1) , \quad (3.45)$$

$$\frac{dM_2}{dz} = A_1 \left(g'_2 - U_2 \frac{dU_2}{dz} \right) + g'_2 A_2 + c_1 (\omega_\beta U_1 - \omega_\alpha U_2) , \quad (3.46)$$

where $g'_1 = g \left(1 - \frac{P_1 t_{v,a}}{P_a t_{v,1}} \right)$ and $g'_2 = g \left(1 - \frac{P_2 t_{v,a}}{P_a t_{v,2}} \right)$, in which $t_{v,1}$ and $t_{v,2}$ are the virtual temperatures of the inner and outer plumes, respectively. Mathematically, the total pressure, P_1 , of the inner plume can be computed from

$$\frac{dP_1}{dz} = -g\rho_2 - \rho_a U_2 \frac{dU_2}{dz} . \quad (3.47)$$

Meanwhile, the (hydrostatic) pressure of the outer plume, P_2 , can be determined by trivial adaptation of (3.22).

As before, (3.19) must be used to close the governing equations. Finally, the source conditions for the coaxial plume are as follows:

$$\begin{aligned} Q_{10} &= A_{10} U_{10} , & Q_{20} &= A_{20} U_{20} , \\ M_{10} &= A_{10} U_{10}^2 , & M_{20} &= A_{20} U_{20}^2 , \\ \Theta_{10} - \frac{L_{v,10}}{c_{pa}} W_{10} &= A_{10} U_{10} (t_{10} - t_a) , & \Theta_{20} - \frac{L_{v,20}}{c_{pa}} W_{20} &= A_{20} U_{20} (t_{20} - t_a) , \\ H_{10} + W_{10} &= A_{10} U_{10} (q_{10} - q_a) , & H_{20} + W_{20} &= A_{20} U_{20} (q_{20} - q_a) . \end{aligned} \quad (3.48)$$

3.4.2 Representative solutions

Further to the discussion in section 3.3.3, we consider in this section a PPWD crossflow tower such as that shown schematically in figure 3.5. As described previously, only modest mixing is supposed to occur in the plenum. The degree of mixing shall be varied in the calculations to follow. More precisely, we shall allow either 5%, 50% or 95% of the dry air to be mixed into the wet air stream below the top of the fan shroud⁴. To make a fair comparison with the results of section 3.3, we consider the same operating and ambient conditions as shown in table 3.1. We further assume that vertical velocities are spatially-uniform at the top of the fan shroud. As a result, and in comparing the source volume flux of the inner vs. the outer plume, one must consider the proportion of the cross section occupied by each air stream. This proportion is, of course, directly related to the aforementioned mixing fraction.

For the case with $\frac{\dot{m}_d}{\dot{m}_w} = 0.6$, we present in figure 3.7 plume radii, vertical velocities and reduced gravities for both the inner and outer plumes. For ease of interpretation, we limit ourselves in figure 3.7 to two bookend values for the dry air mixing fraction, namely 5% and 95%. These values correspond to a thick and thin outer plume, respectively. Attention

⁴Throughout our analysis, we assume that some fraction of the dry air is mixed into the wet air, but not vice versa. This assumption is based on the fact that the wet air stream at the center of the cooling tower is supposed to have a comparatively low pressure. As a consequence, this wet air stream naturally entrains some dry air into its core.

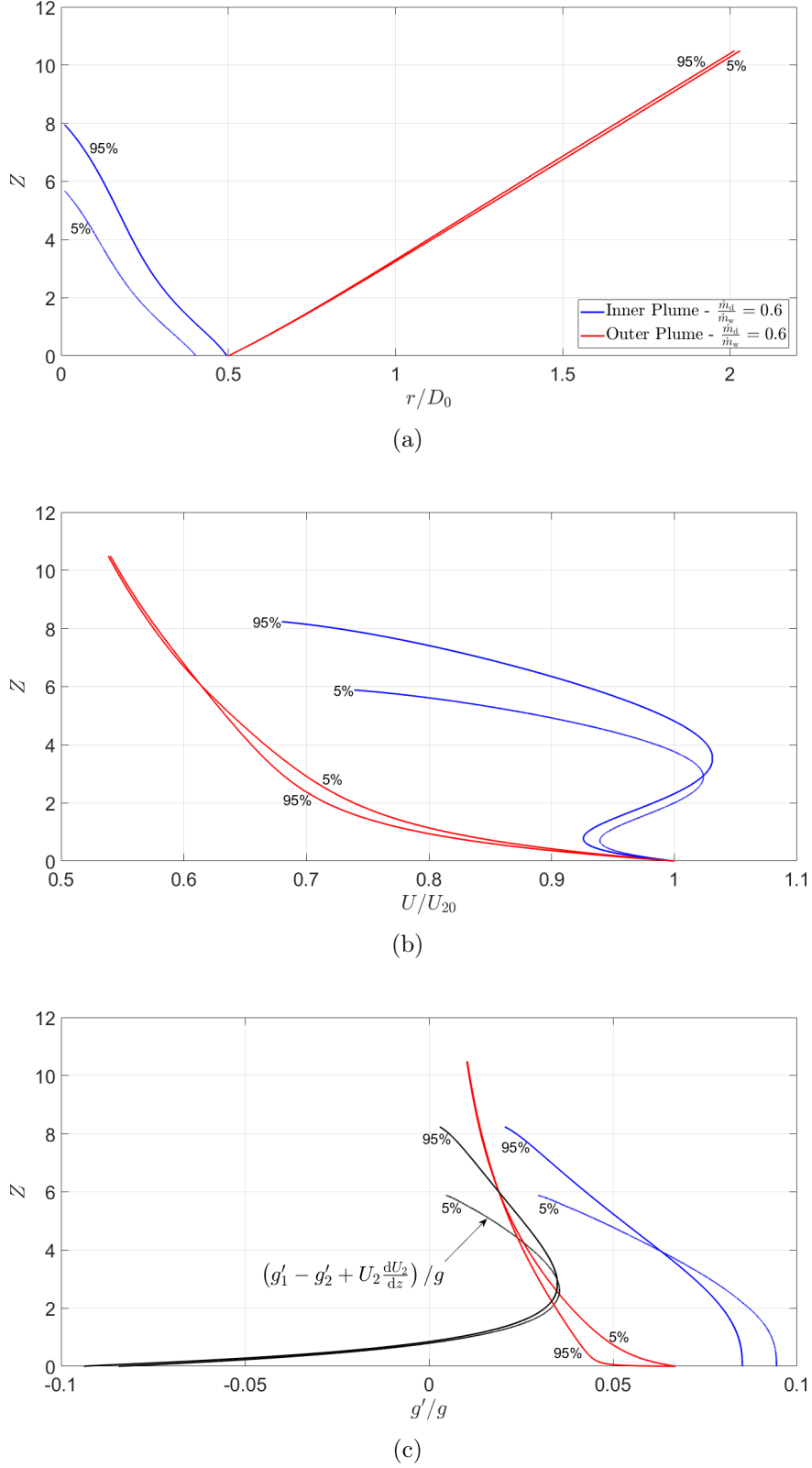


Figure 3.7: [Color] Non-dimensional plume radii (panel a), vertical velocities (panel b) and reduced gravities (panel c) as functions of height. The solid black curves in panel c denote the non-dimensional body force $(g'_1 - g'_2 + U_2 \frac{dU_2}{dz}) / g$ in the inner plume. Labels of 5% and 95% denote the dry air mixing fraction (DAMF).

is likewise restricted to a single cooling tower cell; the scenario of multiple cells and the concomitant complication of plume merger shall be investigated later.

Figure 3.7 a indicates that the outer plume expands continuously whereas the inner plume shrinks until it vanishes at some point above the source. For instance, for a dry air mixing fraction (DAMF) of 5%, the inner plume is totally engulfed by the outer plume at an elevation of $Z_{c,5\%} = 5.67$. Analogous to the coaxial turbulent jets studied by Morton (1962), below this critical (or “cut-off”) height, the inner and outer plumes exhibit considerable differences of velocity (figure 3.7 b) and density (figure 3.7 c). The inner and outer plumes are therefore expected to be demonstrably different one from the other. For the opposite limiting case having a DAMF of 95%, the outer plume starts off very thin, but progressively expands as a result of fluid entrainment. The inner plume again diminishes in radius, but does so over a comparatively large vertical distance.

Because α , β and γ are derived from a study of turbulent fountains (Bloomfield & Kerr, 2000), a sensitivity analysis of the results to variations in the values of the entrainment coefficients is warranted. As shown in table 3.2, we use as reference values $\alpha = 0.085$, $\beta = 0.117$ and $\gamma = 0.117$ then investigate the effect of changing each entrainment coefficient one-by-one. The trends of the data from table 3.2 are as expected with by far the greatest sensitivity arising in the case of the numerical value of β . To wit, $Z_{c,5\%}$ increases by a factor of 2.6 when β decreases from 0.117 (axisymmetric plume) to 0.076 (axisymmetric jet). By contrast, increasing β from 0.117 to 0.147 (line plume) causes $Z_{c,5\%}$ to decrease from 5.67 to 3.84. Increasing β causes more hot, humid air from the inner plume to be mixed into the outer plume. This has the effect of hastening the disappearance of the inner plume while slowing the dilution and deceleration of the outer plume.

Table 3.2: Sensitivity of $Z_{c,5\%}$ to variations in the values of the entrainment coefficients α , β and γ .

Entrainment coefficients	$Z_{c,5\%}$
$\alpha = 0.085, \beta = 0.117 \ \& \ \gamma = 0.117$	5.67 (reference)
$\alpha = 0.076, \beta = 0.117 \ \& \ \gamma = 0.117$	5.56
$\alpha = 0.117, \beta = 0.117 \ \& \ \gamma = 0.117$	6.07
$\alpha = 0.085, \beta = 0.076 \ \& \ \gamma = 0.117$	14.82
$\alpha = 0.085, \beta = 0.147 \ \& \ \gamma = 0.117$	3.84
$\alpha = 0.085, \beta = 0.117 \ \& \ \gamma = 0.076$	4.47
$\alpha = 0.085, \beta = 0.117 \ \& \ \gamma = 0.147$	6.80

A distinguishing feature of figure 3.7 b is that the inner plume velocity first decreases then increases then decreases again. This behavior speaks, in part, to the influence of the source conditions and is qualitatively different from that documented by Morton (1962) who studied coaxial jets but did not observe the initial decrease of velocity – see his figure 3. As illustrated by the black dashed curves of figure 3.7 c, $g'_1 - g'_2 + U_2 \frac{dU_2}{dz}$, which appears on the right-hand side of (3.45), is initially negative, but increases rapidly owing to the deceleration of the outer plume. When $Z = 0.72$, $g'_1 - g'_2 + U_2 \frac{dU_2}{dz}$ changes sign and the inner plume velocity begins gradually to increase. Finally, for $Z \geq 2.96$, the inner plume velocity falls rapidly until such time as the inner plume disappears. This is due to the fact that the entrainment of outer plume and, by extension, ambient fluid come to dominate the dynamics of the

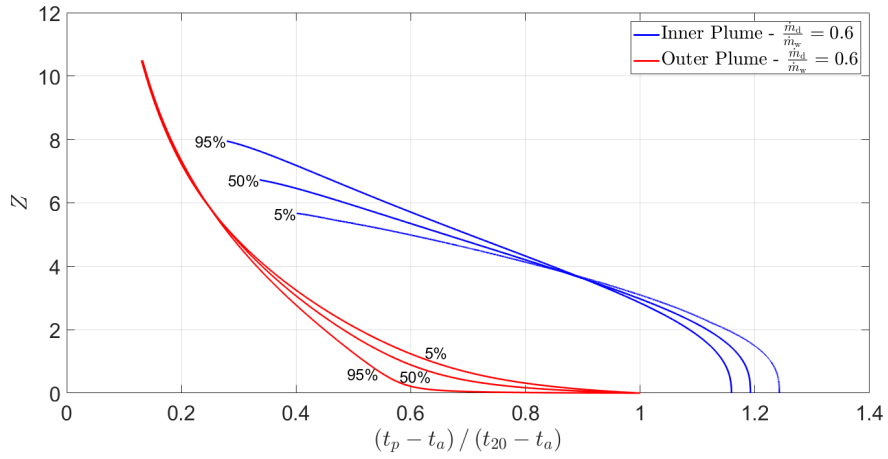
inner plume. As further evidence of the importance of entrainment, note that differences of velocity and buoyancy between the inner and outer plumes diminish significantly just before the disappearance of the inner plume. As noted above, this disappearance is significantly delayed when the outer plume is initially very thin (95% DAMF). Of course, whatever the initial sizes of the inner and outer plumes, there remains a considerable transport of mass into the latter, which is consistent with the results of coaxial turbulent jets by Morton (1962).

Figure 3.8 considers the evolution of the plumes in terms of dynamics and psychrometrics and now also includes a DAMF of 50%. To be consistent with figure 3.7 and the operating and ambient conditions studied in section 3.3.2, figure 3.8 again assumes $\frac{\dot{m}_d}{\dot{m}_w} = 0.6$. Figure 3.8 a shows that initially the non-dimensional excess temperature $(t_p - t_a) / (t_{20} - t_a)$ of the outer plume drops sharply because the outer plume becomes diluted by ambient fluid; a much slower initial decrease is noted in the case of the inner plume. Figure 3.8 b indicates that, as expected, the inner plume relative humidity (RH) decreases with increasing DAMF. When the mixing of the dry and wet air streams is severely curtailed i.e. the DAMF is only 5%, condensation is anticipated. Consistent with the blue curves of figure 3.8 a, the relative humidity of the inner plume remains approximately constant below $Z = 1$, then begins to increase as the relative humidity of the outer plume rises sharply. The subsequent decrease in the inner plume relative humidity results from the fact that the outer plume eventually becomes quite dry, i.e. it approaches the psychrometric condition of the ambient air. With respect to the outer plumes there exist below $Z = 2$ considerable deviations in the relative humidities between the 5% and 95% DAMF cases. For instance, at an elevation of $Z = 0.5$, the corresponding relative humidities of the outer plumes are 57.9% (5% DAMF), 67.1% (50% DAMF) and 86.7% (95% DAMF).

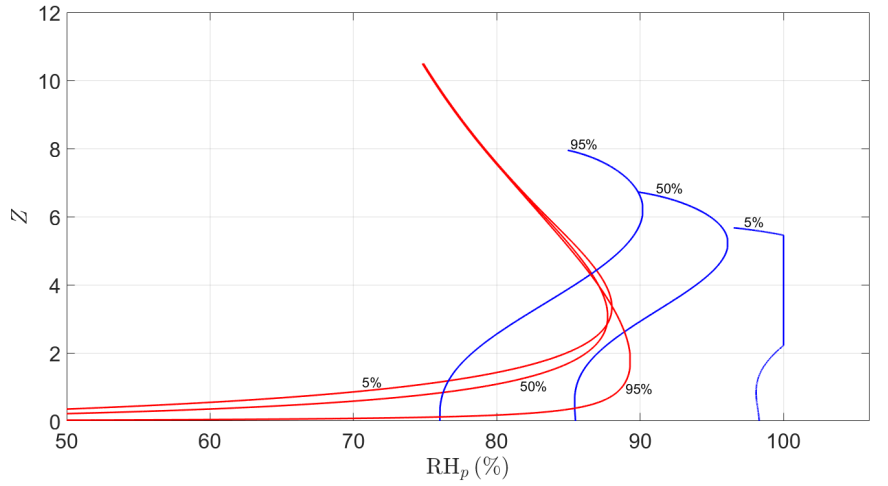
Figure 3.8 c presents a very different dilution process on the psychrometric chart compared to the single straight line characteristic of the uniform plume case. Within a short distance above the cooling tower, the outer plume gains humidity because of the entrainment of large volumes of inner plume fluid. Obviously, this process cannot continue indefinitely and the effect of this humidity gain is soon outweighed by the dilution of ambient air. In a similar fashion, the inner plume is gradually consumed rather than diluted by the outer plume. As a result, any fog that is produced in the inner plume will become entrained into the outer plume where evaporation of these water droplets will very quickly occur.

For the case with $\frac{\dot{m}_d}{\dot{m}_w} = 0.3$, figure 3.9 illustrates the non-dimensional plume radii, vertical velocities and reduced gravities as functions of height. In contrast to figures 3.7 and 3.8, here we consider only a single value for the DAMF (of 5%), but now specifically investigate differences between the single and multiple cooling tower cell cases. While the single cell results are similar to those in figure 3.7, the results of figure 3.9 c with multiple cells ($n = 9$) show clearly that merged plumes are more buoyant than individual (axisymmetric) plumes. As such, there is an increase in the outer plume rise velocity when $Z = 2.99$ (figure 3.9 b). When the inner plumes disappear ($Z \simeq 6.5$ in figure 3.9 b), the rise velocity of the outer plumes begins to fall.

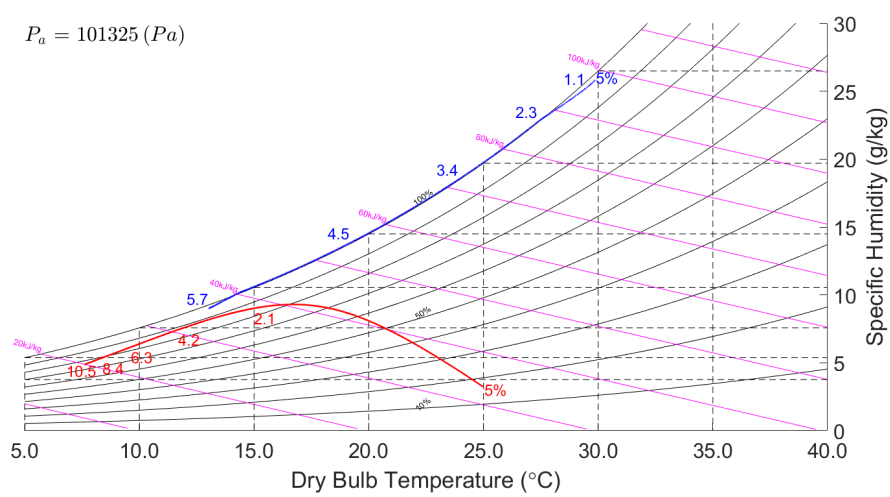
Figure 3.10 a shows the same decreasing profiles as those in figure 3.8 a now with a smaller dry to wet air mass flux ratio: the differences among the 5%, 50% and 95% DAMF cases are now less distinguishable. Figure 3.10 b illustrates that, with 95% DAMF, the outer plume begins to condense at an elevation of $Z = 0.59$, which is less than what is observed in figure 3.3 where condensation is delayed till $Z = 1.21$. However, with 5% or 50% DAMF, there is



(a)

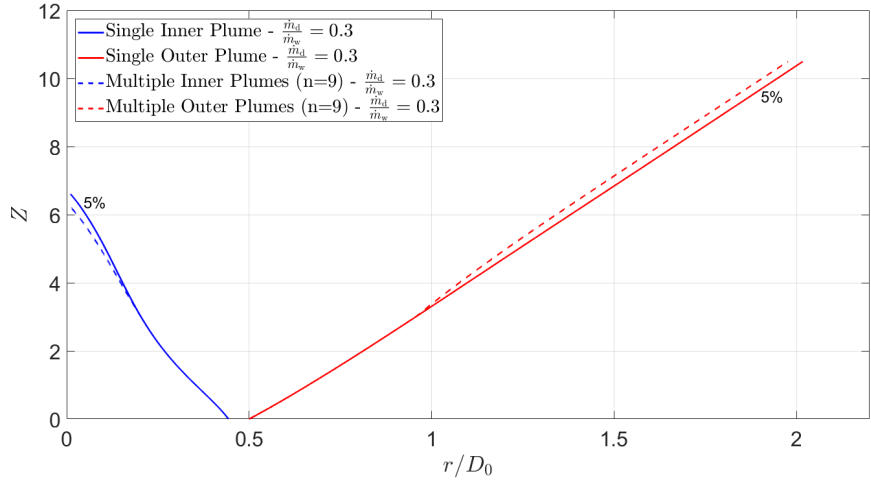


(b)

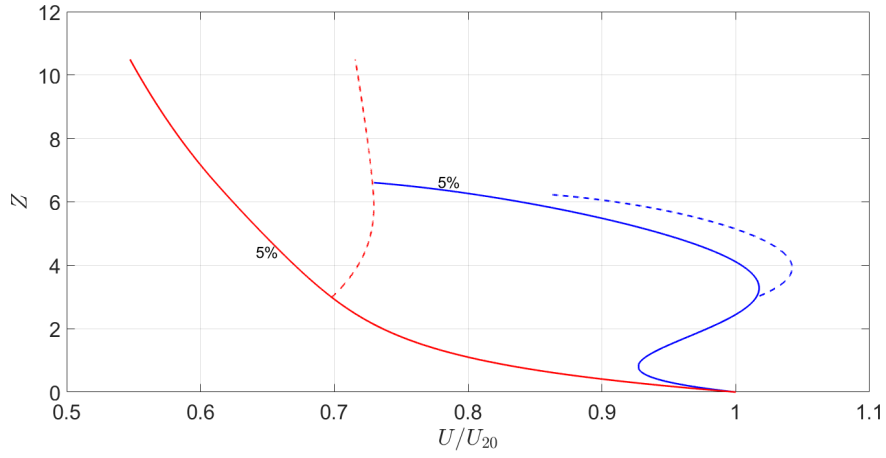


(c)

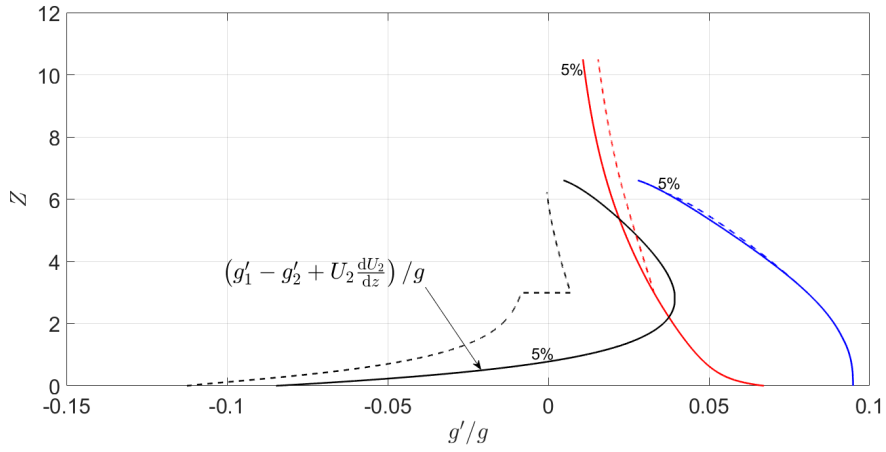
Figure 3.8: [Color] Non-dimensional plume temperature (panel a) and relative humidity (panel b) as functions of height. Solid curves show the results of a single cooling tower cell, with blue for the inner plume and red for the outer plume. Labels of 5%, 50% and 95% denote the dry air mixing fraction (DAMF).



(a)



(b)



(c)

Figure 3.9: [Color] As in figure 3.7 but with $\frac{\dot{m}_d}{\dot{m}_w} = 0.3$ and 5% DAMF.

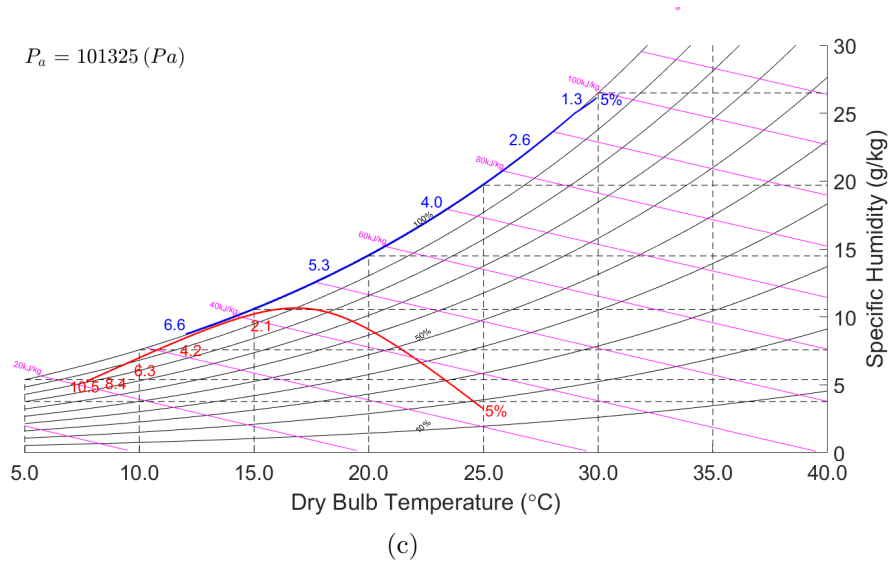
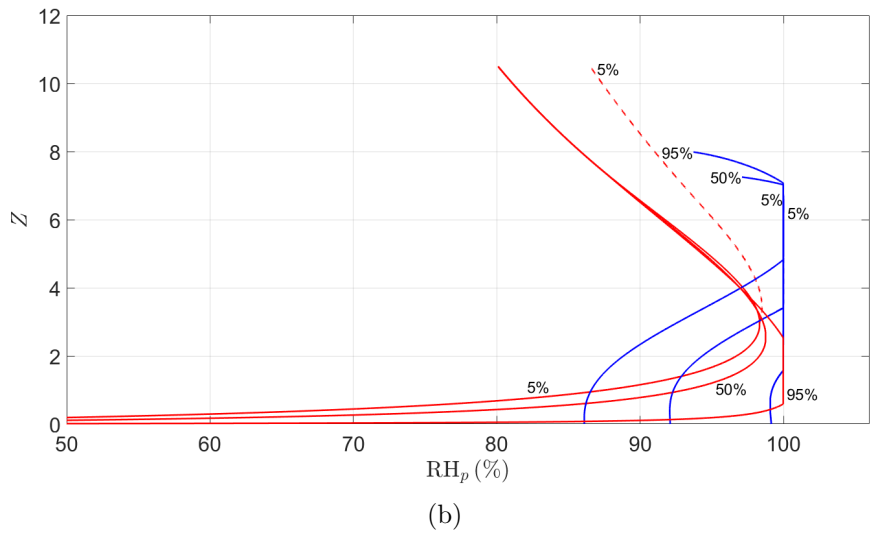
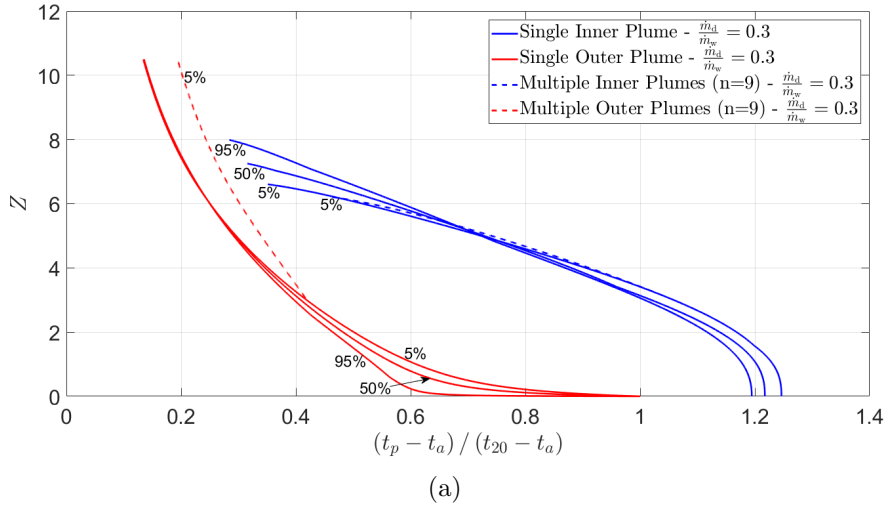


Figure 3.10: [Color] As in figure 3.8 but with $\frac{\dot{m}_d}{\dot{m}_w} = 0.3$.

no condensation in the outer plume throughout the dilution process because the outer plume is relatively thick and the moisture is concentrated in the inner (visible) plume. Besides, visible inner plumes with 5% and 50% DAMF start at $Z = 1.58$ and $Z = 3.42$ respectively, which are both larger than the threshold elevation from figure 3.3.

3.5 How much mixing should occur in the plenum of a crossflow cooling tower?

3.5.1 Hybrid cooling tower calculations – the effectiveness-NTU method

Similar to uniform plumes, the behavior of coaxial plumes depends on conditions measured at the source. In assessing the parametric regimes where a coaxial plume may prove advantageous, it is necessary to first understand how the source conditions are influenced by environmental and operating conditions. In this spirit, reference is made to the Examples 8.1.3 and 9.4.1 of Kröger (2004), which respectively consider the wet and dry sections of a PPWD crossflow cooling tower. Using the input parameters summarized in table 3.3, we adapt Kröger’s effectiveness-NTU solution methodology along the lines presented in section 3.8. In so doing, we introduce the dry cooling energy fraction or DCEF as the ratio of the dry to wet section range temperatures. Symbolically, $DCEF = (T_{D1} - T_{D2}) / (T_{W1} - T_{W2})$ where the temperatures are defined in figure 3.1. As indicated in table 3.3, and consistent with Kröger (2004), we assume $DCEF = 20\%$. Accordingly, our effectiveness-NTU calculations yield output as summarized in table 3.4 from which the coaxial plume equations of section 3.4 may be integrated forward in Z .

Table 3.3: Input parameters for a hybrid cooling tower calculation.

Variable name and symbol	Value (unit)
Ambient pressure at the top of the cooling tower, P_a	101325 (Pa)
Range temperature in the wet section, R_W	10 (°C)
Dry cooling energy fraction (DCEF)	20 (%)
Ambient dry-bulb temperature, t_a	5 (°C)
Ambient relative humidity, RH_a	60 (%)
Water mass flow rate, L	1000 (kg/s)
Liquid-to-air ratio in the wet section, $\frac{L}{G_W}$	1.0
Fill height, H	11 (m)
Fill depth (air travel distance), ATD	4.57 (m)

3.5.2 Visible plume resistance and recirculation

The “two-thirds” law of Briggs (1969) implies that buoyant inner plumes having large rise velocities are less likely to be deflected by the wind and are therefore less likely to lead to ground level fog and/or a recirculation of moist air through the dry or wet sections of the

Table 3.4: Output parameters for a hybrid cooling tower calculation.

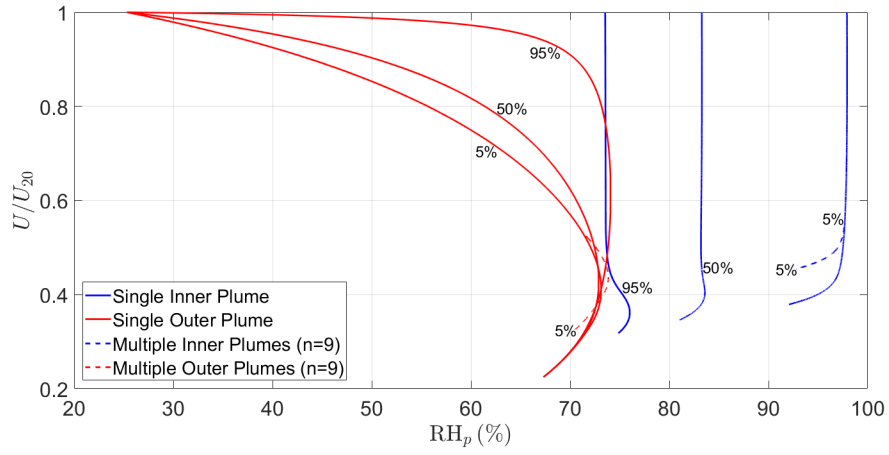
Variable name and symbol	Value (unit)
Approach temperature in the wet section, A_W	14.2 (°C)
Approach temperature in the dry section, A_D	20.7 (°C)
Wet cooling temperature, t_w	19.0 (°C)
Dry cooling temperature, t_d	18.8 (°C)
Liquid-to-air ratio in the dry section, $\frac{L}{G_D}$	1.66

cooling tower. Efforts have been made to determine empirically the resistance of a (uniform) plume to deflection by the wind – see e.g. figure 9.4.1 of Kröger (2004). Here we follow an alternative approach based on the numerical solutions developed in section 3.4. First, and whether we wish to consider the inner plume, the outer plume or both, it is necessary to combine the vertical velocity, U , and relative humidity, RH, into a single (non-dimensional) parameter. For this purpose, we define the ratio $\mathcal{R} = \mathcal{R}(Z) = \frac{U/U_{20}}{\text{RH}}$ as the height-dependent *resistance factor*⁵. The name stems from the fact that, as \mathcal{R} increases, the local resistance of the (coaxial) plume to both fog formation and recirculation also increases. Of course, \mathcal{R} does not, in and of itself, indicate when a visible plume will occur. In the event of fog formation, the air is supersaturated with water vapor and for this particular case an equivalent relative humidity must be defined as $\text{RH} = \frac{q_{sp} + \sigma}{q_{sp}}$ (Monjoie & Libert, 1994).

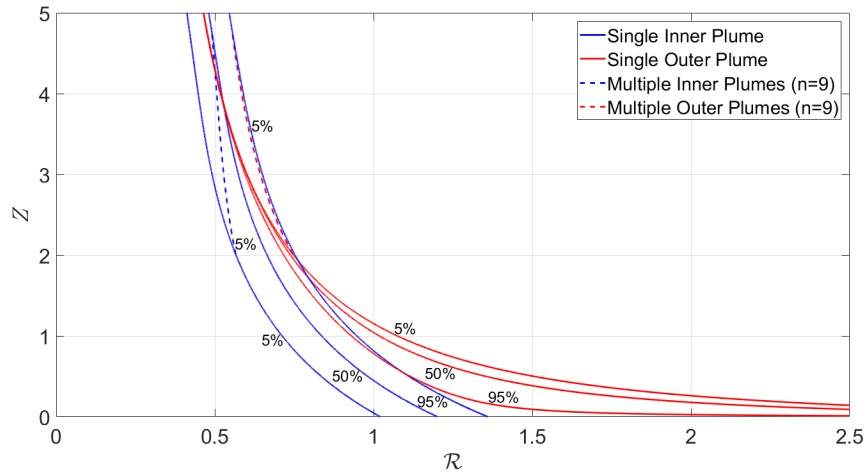
The above ideas are illustrated with reference to the curves of figure 3.11, which derive from the input parameters of table 3.3. The plume velocity and relative humidity are shown in figure 3.11 a. Note that in contrast to figures 3.8 b and 3.10 b, the inner plume relative humidity is here nearly constant with height. Obviously the combination of high vertical velocity and low relative humidity is desired in terms of avoiding condensation and recirculation. Figure 3.11 a confirms that, as expected, the inner (outer) plume becomes less (more) susceptible to fog formation as the DAMF increases. On the other hand, the non-monotone character of the blue and red curves shown in figure 3.11 a make it somewhat difficult to make more precise statements. As a result, we instead draw attention to figure 3.11 b, which shows the vertical variation of \mathcal{R} for the inner and outer plumes for a range of different DAMF. Figure 3.11 b reveals that for the outer plume, \mathcal{R} drops sharply for $0 \leq Z \leq 2$, which is mainly due to the rapid increase in the relative humidity. Thereafter, the rate of change of the resistance factor is more moderate. A similar profile is observed in the inner plume in that \mathcal{R} falls rapidly for $Z < 1$ as a result of the loss of momentum of the inner plume close to the source (cf. figures 3.7 b and 3.9 b). For $Z \geq 1$, the resistance factor decreases less rapidly. Here, changes of vertical velocity are accompanied by positive or negative changes of relative humidity (cf. figure 3.8).

Although figures 3.11 a and 3.11 b present a quantitative characterization of the visible plume resistance, the relative dimensions of the inner and outer plumes are not taken into consideration. Such geometric details are important because the continuously expanding

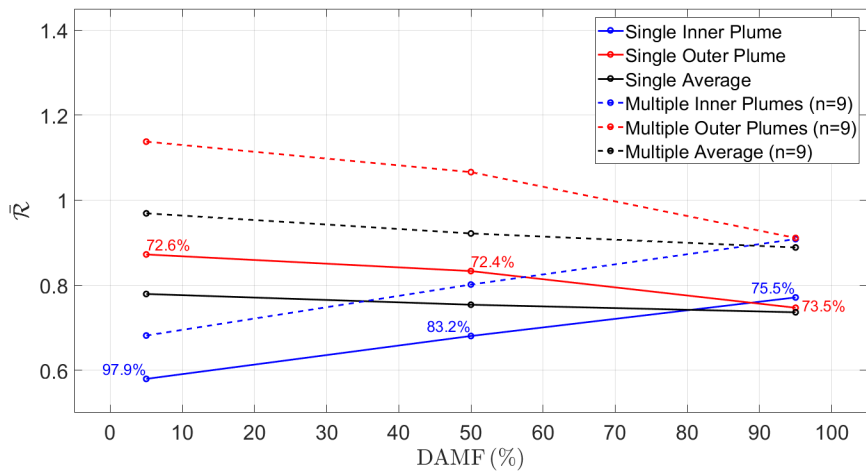
⁵The more appropriate velocity scale on which to nondimensionalize the plume vertical velocity may be the wind speed. Note that, however, our goal is not to characterize the actual deflection of the plume in a crosswind, but rather to identify a means of rigidifying the plume that should be applicable for arbitrary wind speed. In this respect, our analysis applies even in the limit of small wind speed for which any speed nondimensionalized by this wind speed would become very large.



(a)



(b)



(c)

Figure 3.11: [Color] (a) plume velocity vs. relative humidity. (b) resistance factor vs. height. (c) resistance factor, averaged over height, vs. DAMF. For the single cell case, 5%, 50% and 95% DAMFs are presented, while for multiple cells only 5% DAMF is shown in panels (a) and (b). In panel (c), the maximum relative humidities are specified for select DAMF.

outer plume is supposed to make a greater contribution to $\bar{\mathcal{R}}$ than the decaying inner plume. Taking this consideration into account, we define the plume-average resistance factor as

$$\bar{\mathcal{R}} = \frac{1}{Z_{c,5\%}} \int_0^{Z_{c,5\%}} \left[\frac{Q_1}{Q_1 + Q_2} \frac{U_1/U_{20}}{\text{RH}_1} + \frac{Q_2}{Q_1 + Q_2} \frac{U_2/U_{20}}{\text{RH}_2} \right] dZ, \quad (3.49)$$

where $Z_{c,5\%}$ is a characteristic reference height and RH_1 and RH_2 are the relative humidities of the inner and outer plumes, respectively. Where necessary, we may also compute average resistance factors for the inner and outer plumes separately. The corresponding equations read

$$\bar{\mathcal{R}}_1 = \frac{1}{Z_{c,5\%}} \int_0^{Z_{c,5\%}} \frac{U_1/U_{20}}{\text{RH}_1} dZ, \quad (3.50)$$

$$\bar{\mathcal{R}}_2 = \frac{1}{Z_{c,5\%}} \int_0^{Z_{c,5\%}} \frac{U_2/U_{20}}{\text{RH}_2} dZ. \quad (3.51)$$

Figure 3.11 c illustrates the variation of $\bar{\mathcal{R}}$, $\bar{\mathcal{R}}_1$ and $\bar{\mathcal{R}}_2$ with the DAMF for both single and multiple cell cooling towers. The increase (decrease) of the inner (outer) plume resistance with increasing DAMF has been justified in figure 3.11 a. More importantly, and less intuitively, the black curves of figure 3.11 c indicate that $\bar{\mathcal{R}}$ decreases with the DAMF. This observation is significant because it suggests that, for the plume as a whole, there is a moderate but not inconsequential advantage to limiting the degree of mixing of the wet and dry air streams in the plenum chamber. Of course, this strategy should not be applied absolutely: in the limit of no mixing, the inner plume would be saturated and condensation would occur immediately upon discharge to the atmosphere. As a consequence, it is important when interpreting curves such as those presented in figure 3.11 c to separately evaluate the relative humidities of the inner (and outer) plumes. Such data are presented in blue (and red) text in figure 3.11 c. From the information so provided, we confirm that a maximum (inner plume) relative humidity of 97.9% is realized when, as expected, the DAMF is a minimum. Note finally that figure 3.11 c indicates that merged plumes exhibit larger resistance factors than do individual (axisymmetric) plumes. Insofar as visible plume abatement is concerned, a single plume corresponds to a worse case scenario.

Whereas figure 3.11 is limited to an invisible plume, figure 3.12 extends the previous analysis to the case of a visible plume consisting of supersaturated air. Note that the results of figure 3.12 are obtained by decreasing the ambient temperature t_a in table 3.3 from 5 °C to -10 °C. The relatively low dry-bulb temperature tends to increase the dry cooling efficiency, which results in a low dry air mass flow rate in the dry section, G_D . Correspondingly the inner plume may become saturated, or supersaturated, which is clearly evident in figure 3.12 a. Despite the presence of fog, figures 3.12 b and 3.12 c show qualitatively similar trends to figures 3.11 b and 3.11 c, respectively. In particular, the black curves of figure 3.12 c still show a decreasing trend of $\bar{\mathcal{R}}$ vs. the DAMF. Notwithstanding this observation, it may in this case be disadvantageous to limit the mixing of the wet and dry air streams owing to the large inner plume relative humidities that result. Formalizing this last statement, we propose that the following two criteria must be satisfied in order for a coaxial plume structure to be considered advantageous from the point of view of avoiding fog formation and recirculation:

- (i) The relative humidity of the outer plume should not exceed 95% for intermediate DAMF, say 50% DAMF. For the inner plume, it may be tolerable to set a less stringent

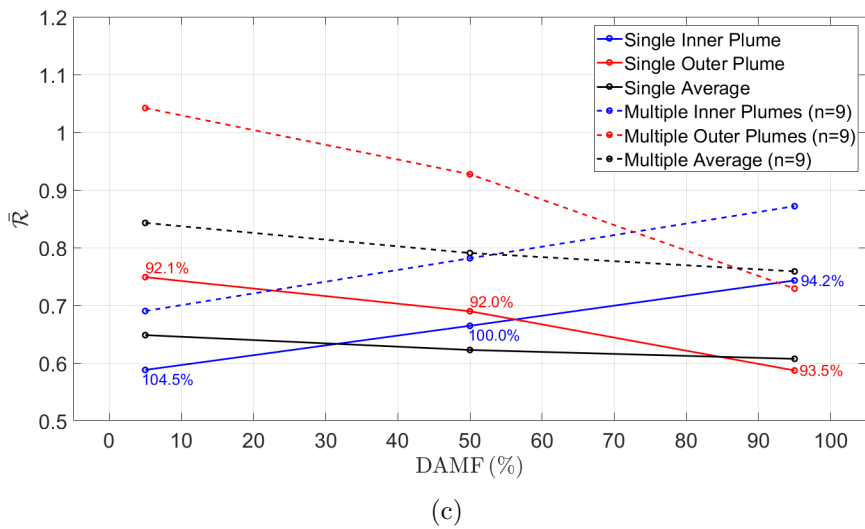
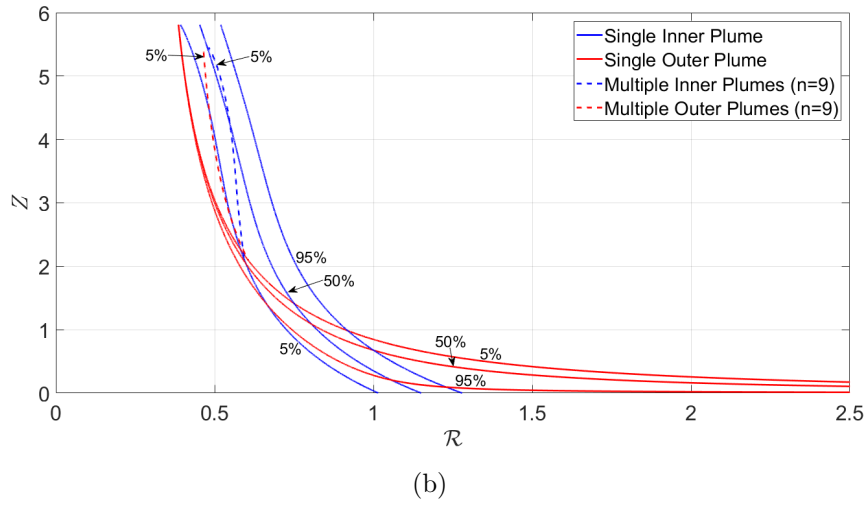
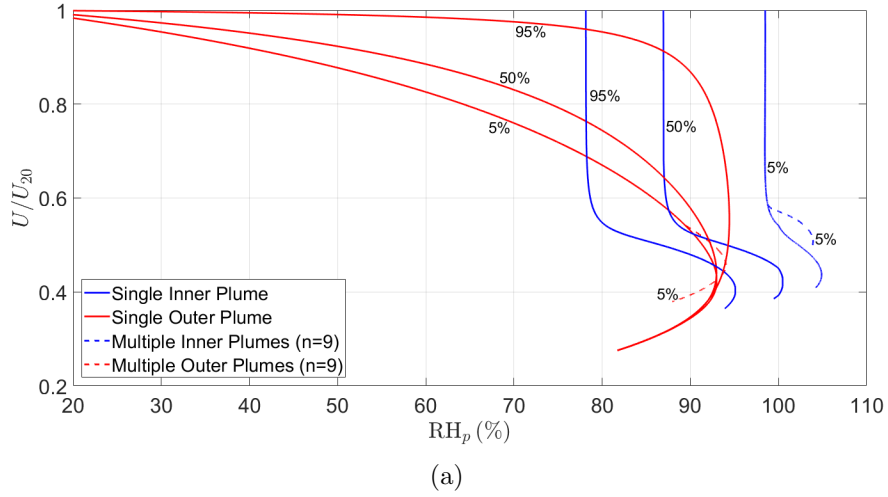


Figure 3.12: [Color] As with figure 3.11 but with ambient temperature $t_a = -10^\circ\text{C}$, and other input parameters remain the same in table 3.3.

requirement (e.g. $RH_1 < 100\%$ for 50% DAMF) owing to the smaller dimension of the inner compared to the outer plume. (Note that the specific numbers used above i.e. 50% DAMF, 100% and 95% RH may be adjusted according to site-specific constraints and the severity of local regulations.)

- (ii) $\bar{\mathcal{R}}$ should be a monotone decreasing function of the DAMF (as it is in figures 3.11 c and 3.12 c).

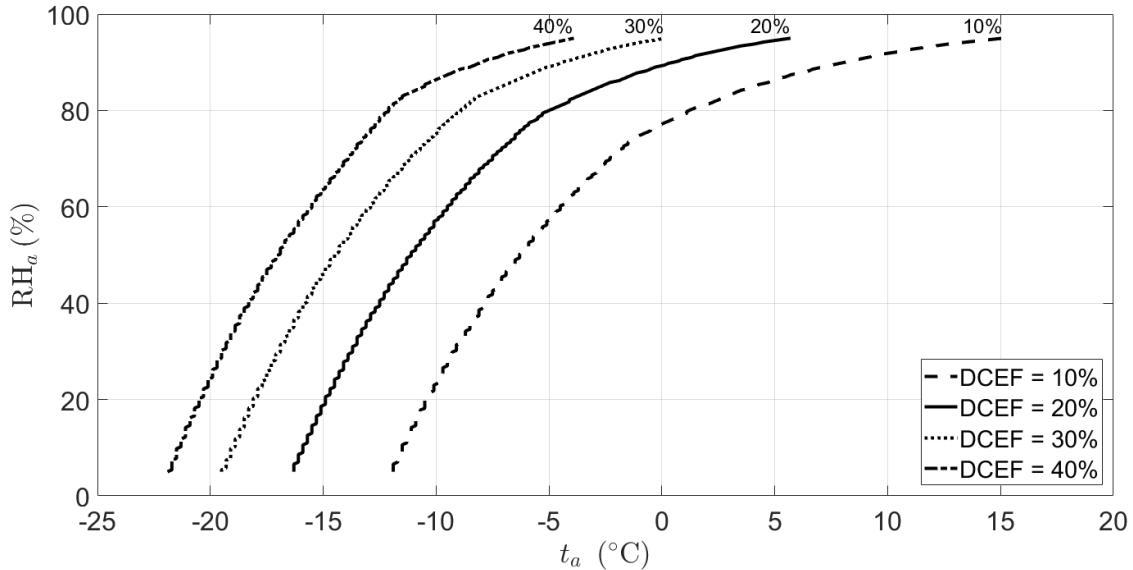


Figure 3.13: Regime diagram indicating the combinations of ambient temperature and relative humidity for which a coaxial plume structure is (to the right of the curves) and is not (to the left of the curves) advantageous. Only single cell results are presented; results for multiple cells are qualitatively similar.

The two design criteria summarized at the end of section 3.5.2 form the basis for figure 3.13, which shows a regime diagram in the (t_a, RH_a) parameter space. Figure 3.13 can be used to determine where a coaxial plume is or is not advantageous; it suggests that for low ambient temperatures and/or high relative humidities, a relatively high DCEF is required to achieve visible plume abatement.

3.6 Conclusion and future work

Based on the coaxial jet model of Morton (1962) and the turbulent fountain theory proposed by McDougall (1981) and Bloomfield & Kerr (2000), an analytical model describing coaxial plumes is herein developed. This model assumes “top-hat” profiles for the plume velocity, temperature and humidity. Morton’s entrainment assumption is used in which the entrainment into the inner plume scales with the velocity difference between the inner and outer plumes.

Our study is motivated by the possible advantage of using coaxial plumes in the context of visible plume abatement from cooling towers, a topic previously investigated by Houx Jr *et al.*

(1978), Lindahl & Jameson (1993), Hensley (2009) and Koo (2016*a*, 2016*b*). Central to our investigation is the notion of partial mixing in the plenum chamber between the wet and dry air streams – see figure 3.5. Our results of section 3.5.2 are based on the effectiveness-NTU calculations summarized in section 3.8 and make reference to a resistance factor $\mathcal{R} = \frac{U/U_{20}}{\text{RH}}$, which characterizes the decreased likelihood of fog formation and/or recirculation. Based on this resistance factor, two criteria are proposed to determine whether a coaxial plume is indeed advantageous as compared to its uniform counterpart. To wit, (i) with 50% DAMF, the respective maximum relative humidities in the inner and outer plume should not exceed 100% and 95%, and, (ii) the resistance factor, averaged over height, should be a monotone decreasing function of the DAMF. On the basis of the aforementioned analyses and criteria, regime diagrams such as figure 3.13 can be drawn in a straightforward fashion. For fixed ambient conditions, such regime diagrams specify whether or not a coaxial plume is likely to be advantageous.

This study opens the door for numerous adaptations and future endeavors. Most immediately, the effectiveness-NTU method summarized in section 3.8 is predicated on a number of simplifying assumptions e.g. the humid air exiting the wet section is just saturated i.e. $\text{RH} = 100\%$. Relaxing these assumptions could provide a more detailed description of the interior dynamics and, by extension, the plume source conditions and their relationship to key environmental and operational variables. Moreover, laboratory experiments e.g. using a water channel ought to be performed so that the most appropriate values for the entrainment coefficients i.e. α , β and γ may be determined. Indeed, table 3.2 confirms that model output may be sensitive to the value of these entrainment coefficients (β most especially) and so careful estimation of the values seems to us important. Finally, all of the above analysis assumes a still (and, for that matter, uniform-density) ambient. Whereas incorporating the effect of wind is nontrivial from an analytical point of view, good progress might again be possible using laboratory experiment. Of particular interest would be to estimate the threshold wind speed for which the coaxial structure becomes very heavily distorted so that the inner plume is directly exposed to ambient fluid. It is also worthwhile mentioning the differences between the current coaxial plume structure vs. a forced i.e. relatively high velocity (dry) air curtain, the latter of which can lift the wet plume to some nontrivial extent (Veldhuizen & Ledbetter, 1971). Whether, from the point of view of fluid mechanics, economics, etc., one approach is generally favorable to the other remains to be investigated carefully.

3.7 Appendix A: Plume merger

3.7.1 Uniform plumes

A number of different approaches for describing plume merger have been proposed in the literature. For example, and using ideas summarized in Kaye & Linden (2004), Rooney (2015) adapted the physical interpretation of velocity potential to approximate the plume-ambient boundaries of single or multiple plumes. Here we follow a more traditional approach to plume merger i.e. that suggested by Wu & Koh (1978) in which, as we describe below, the merged plume is approximated by a slot plume in the central part and two half-round

plumes at the two ends. Although we do not pursue these ideas here, Wu & Koh's approach, which has been adapted by Policastro *et al.* (1980, 1994) among others, has the advantage that ambient wind effects can be included.

According to Wu & Koh (1978), and in the absence of an ambient wind, the (vertically ascending) plumes discharged from cooling tower cells are assumed to be axisymmetric. When, as is typical, there are multiple cooling tower cells, adjacent axisymmetric plumes merge relatively quickly, where the precise vertical distance obviously depends on the cell spacing. As shown in figure 3.14, the cross-sectional area of the resulting merged plume tends to be elliptical. Here, we adopt the merging criteria used by Wu & Koh (1978). Accordingly, plume merger is assumed to initiate once the area of the central rectangle from figure 3.14 equals the areas of the two half round circles indicated by the dashed lines.

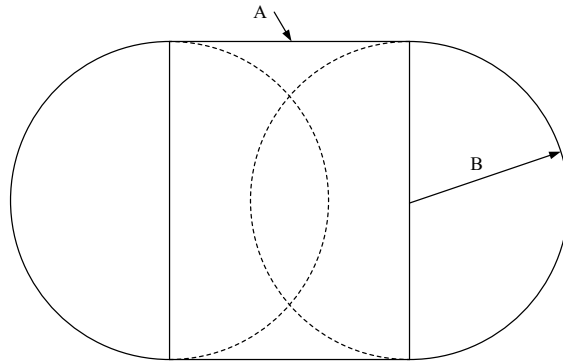


Figure 3.14: A cross-sectional view of the merged plume shape. The dashed circles represent the individual plumes at the moment that the merging criterion is satisfied and the solid curve shows the geometry of the merged plume.

Up to the point of merger, the equations for individual round plumes are applied to calculate relevant properties such as the plume temperature, moisture, vertical velocity and width. Once merging occurs we then determine the new centroid and shape of the merged plume, the latter being necessary to estimate the perimeter, S , and the rate of ambient entrainment – see (3.5). Moreover, the fluxes of the merged plumes are summed in order to respect e.g. conservation of mass.

The merged plume is characterized by the width, A , of the central rectangle and the radii, B , of the half circles – see figure 3.14. Whereas the radii of the half circles are the same as the radii of the individual plumes, A can be calculated based on geometric considerations, i.e.

$$A = \frac{\pi B}{2}. \quad (3.52)$$

Once the shape of the merged plume is determined, solutions for the half-round and line plumes are separately integrated forward by one spatial step. The cross-sectional area, A_r (A_l), and entrainment rate, E_r (E_l), for the half-round (line) plume is as follows:

$$\begin{aligned} A_r &= \frac{1}{2}\pi B^2, & E_r &= \alpha_r \pi B U, \\ A_l &= 2AB, & E_l &= 2\alpha_l A U, \end{aligned} \quad (3.53)$$

where $\alpha_r = 0.117$ and $\alpha_l = 0.147$. U is the velocity of the modified merged plume shape defined by the geometric parameters B and A . Thereafter, the calculations of the properties of the half-round and line plumes follow equations (3.15) to (3.18) using E_r and E_l , respectively, in place of E . Because of the different entrainment rates for the line and half-round plumes, the new radii, b , of the half round plumes and the width, a , of the central line plume may be inconsistent in that a non-smooth shape is predicted for the plume cross-section (see the dashed line of figure 3.15). In order to correct this model deficiency, the following equations are proposed:

$$\pi b^2 U_r + 2ba U_l = (\pi B^2 + 2AB) U, \quad (3.54)$$

$$a + 2b = A + 2B, \quad (3.55)$$

where U_r , U_l are, respectively, the plume velocities corresponding to the half-round plumes with radii b , the line plume with width a . Equation (3.54) describes a redistribution of the volume flux from the calculated merged plume to the modified merged plume indicated by the solid line in figure 3.15. Conversely, (3.55) ensures the same plume width between the calculated and modified plumes.

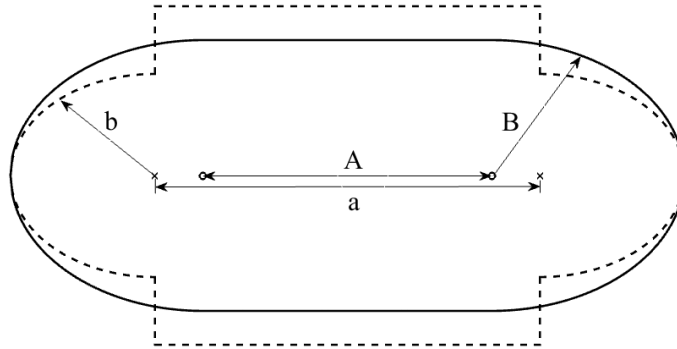


Figure 3.15: A cross-sectional view of the modified shape of the merged plume. The calculated plume cross-section shape (dashed line), defined by a and b , shows discontinuities at the junctions of the slot and round plumes. A modified smooth plume cross-section (solid line), defined by A and B , is proposed according to equations (3.54) and (3.55).

3.7.2 Coaxial plumes

Plume merger involving coaxial plumes is more complicated than in section 3.7.1; nonetheless, similar principles can be applied. Upon merger, and as illustrated schematically in figure 3.16, the outer plumes coalesce with each other to become a single plume characterized by a slot plume in the center and two half round plumes at the two ends. The inner plumes (if they still exist) remain discrete because the radii of inner plumes shrink with elevation. For computational tractability, we manually shift the two terminal inner plumes inwards so as to avoid an uneven division between the central slot plume and two half round plumes. This assumption seems to be justified based on expectations of flows characterized by entrainment. Moreover, it applies only to the two end member inner plumes; no such translation is required for those inner plumes (seven in the case of figure 3.5) that are not adjacent to an end of the line plume.

Analogous to the calculation of uniform plume merger, the merged coaxial plume is divided into two parts of which the former is the coaxial plume consisting of n inner round plumes with corresponding outer slot plume, and the latter consists of the two half-round plumes at the two ends. Separate solutions are obtained for these two parts at each spatial step, and a smooth, merged outer plume is then resolved using the methodology outlined in figure 3.15.

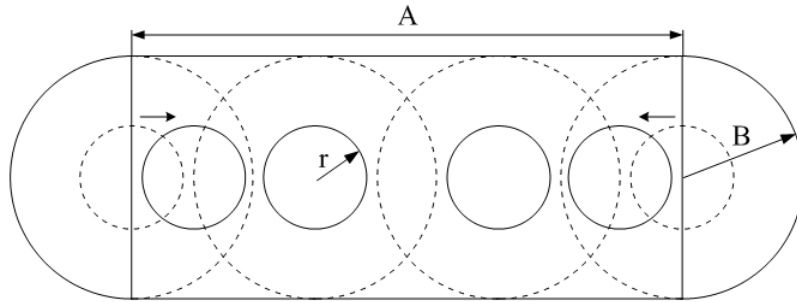


Figure 3.16: A cross-sectional view of four coaxial plumes upon merging. The solid curves or circles represent the merged coaxial structure.

3.8 Appendix B: Hybrid wet/dry cooling tower calculation

This section gives a description of the effectiveness-NTU method for crossflow dry and wet sections, and illustrates how the hybrid cooling tower calculation is implemented.

3.8.1 Effectiveness-NTU method for a crossflow dry section

The geometric parameters in the dry section are drawn from Example 9.4.1 of Kröger (2004). The heat capacity rates are defined as

$$[C_{\min}, C_{\max}] = \begin{cases} [Lc_{pw}, G_Dc_{pa}] & \text{if } Lc_{pw} < G_Dc_{pa} \\ [G_Dc_{pa}, Lc_{pw}] & \text{otherwise} \end{cases}$$

and the heat capacity ratio is $C_R = C_{\min}/C_{\max}$. The maximum heat transfer rate is

$$Q_{\max} = C_{\min} (T_{D1} - t_a) . \quad (3.56)$$

Given the range temperature in the dry section, R_D , the effectiveness in demand, ϵ_d , is given by

$$\epsilon_d = Lc_{pw}R_D/Q_{\max} . \quad (3.57)$$

Meanwhile, the number of transfer units per pass is

$$\text{NTU}_p = \frac{U_i A_i}{C_{\min} n_p} , \quad (3.58)$$

where n_p is the number of water passes, U_i is the overall heat transfer coefficient based on the total inside area, A_i , of the tubes. Note that U_i and A_i are calculated primarily based on the dry section geometrical parameters. If, as recommended by Jaber & Webb (1989), we assume that both streams i.e. air and water flows are unmixed⁶, the effectiveness per pass is

$$\epsilon_p = 1 - \exp \left[\text{NTU}_p^{0.22} \left(\exp(-C_R \text{NTU}_p^{0.78}) - 1 \right) / C_R \right]. \quad (3.59)$$

From ϵ_p , it is straightforward to compute the total effectiveness in supply from

$$\epsilon_s = \left[\left(\frac{1 - \epsilon_p C_R}{1 - \epsilon_p} \right)^{n_p} - 1 \right] / \left[\left(\frac{1 - \epsilon_p C_R}{1 - \epsilon_p} \right)^{n_p} - C_R \right]. \quad (3.60)$$

The operating point is determined by equating ϵ_s and ϵ_d using the iteration process outlined in figure 3.17.

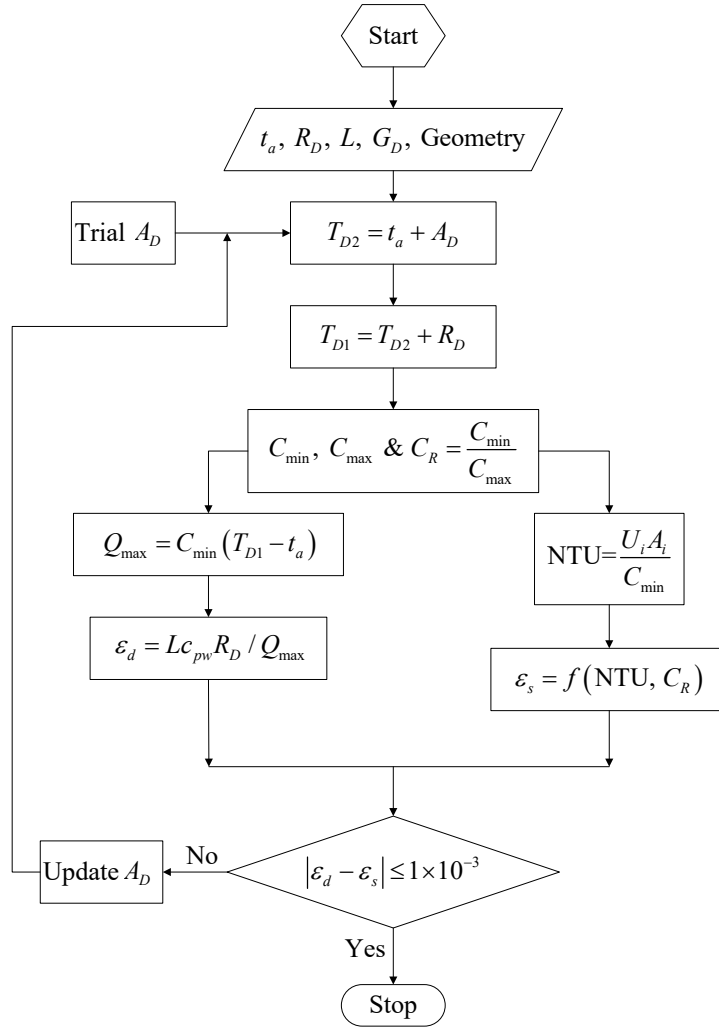


Figure 3.17: The dry section calculation diagram.

⁶As stated in Kröger (2004), unmixed flow indicates that the temperature variations within the fluid in at least one direction normal to the flow can exist but no flux of heat occurs.

3.8.2 Effectiveness-NTU method for a crossflow wet section

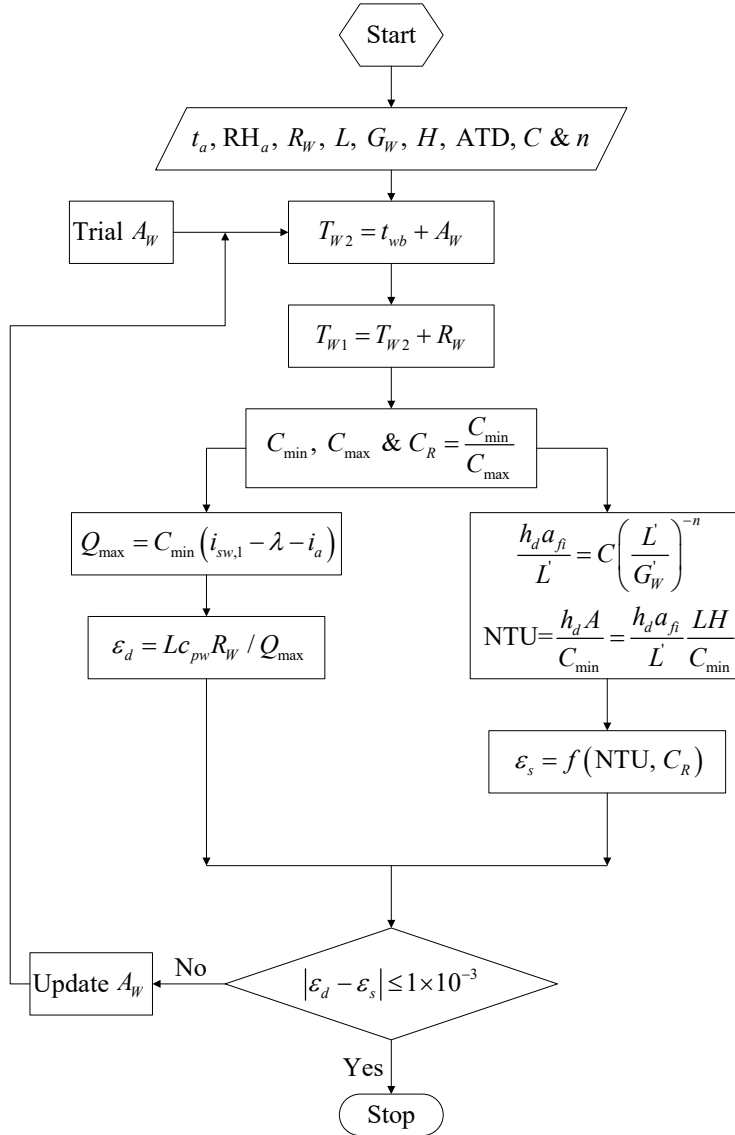


Figure 3.18: The wet section calculation diagram.

The detailed derivation of effectiveness-NTU theory for the wet section is outlined in Chapter 4 of Kröger (2004), where canonical fill characteristics are drawn from Kröger's Example 8.1.3. The enthalpy-temperature gradient is approximated as

$$\frac{di_{sw}}{dT_W} = \frac{i_{sw,1} - i_{sw,2}}{T_{W1} - T_{W2}}, \quad (3.61)$$

where $i_{sw,1}$ and $i_{sw,2}$ are the respective saturated air enthalpies at water temperatures T_{W1} and T_{W2} . Consistent with the dry heat exchanger design process, the heat capacity rates are defined as

$$[C_{min}, C_{max}] = \begin{cases} [Lc_{pw} / (di_{sw}/dT_W), G_W] & \text{if } Lc_{pw} / (di_{sw}/dT_W) < G_W \\ [G_W, Lc_{pw} / (di_{sw}/dT_W)] & \text{otherwise} \end{cases}$$

and the evaporative capacity rate ratio is given as $C_R = C_{\min}/C_{\max}$. The maximum enthalpy transfer is

$$Q_{\max} = C_{\min} (i_{sw,1} - \lambda - i_a) , \quad (3.62)$$

where the correction factor λ is defined as $\lambda = (i_{sw,1} + i_{sw,2} - 2i_{sw,m})/4$, and $i_{sw,m}$ is the saturated air enthalpy at the mean water temperature $(T_{W1} + T_{W2})/2$. Given the range temperature in the wet section, R_W , the effectiveness in demand, ϵ_d , is expressed as

$$\epsilon_d = Lc_{pw}R_W/Q_{\max} , \quad (3.63)$$

Meanwhile, the fill transfer coefficient per meter of fill height (H) is given as

$$\frac{h_d a_{fi}}{L'} = C \left(\frac{L'}{G'_W} \right)^{-n} , \quad (3.64)$$

where h_d is the mass transfer coefficient, a_{fi} is the wetted surface area divided by the volume of the fill, $L' = L/A_{fr,h}$ is the mean water mass flow rate through the fill with $A_{fr,h}$ the horizontal frontal area of the fill, $G'_W = G_W/A_{fr,v}$ is the mean air mass flow rate with $A_{fr,v}$ the vertical frontal area of the fill, and C and n are empirical constants here set to 0.268 and 0.56, respectively (Table 4.3.2a of Kröger, 2004). The number of transfer units (NTU) is given as

$$\text{NTU} = \frac{h_d A}{C_{\min}} , \quad (3.65)$$

where $A = a_{fi}V$ is the total wetted surface area in the fill and V is the volume of the fill. By simple rearrangement, (3.65) can be expressed as $\text{NTU} = \frac{h_d a_{fi}}{L'} \frac{LH}{C_{\min}}$, thus the fill transfer coefficient can be related to the NTU. The effectiveness-NTU equation for crossflow with both streams unmixed is given as

$$\epsilon_s = 1 - \exp \left[\text{NTU}^{0.22} (\exp(-C_R \text{NTU}^{0.78}) - 1) / C_R \right] . \quad (3.66)$$

The determination of the wet section operating point is similar to that of the dry section in that ϵ_s and ϵ_d must be matched. The corresponding calculation flowchart is shown in figure 3.18.

3.8.3 The PPWD crossflow cooling tower calculation

The calculations to be performed for a hybrid PPWD crossflow cooling tower must obviously incorporate those from the previous two subsections. Accordingly, the flowchart of figure 3.19 makes reference to both figures 3.17 and 3.18. Because the water flows in both the dry and wet sections are in series, the restriction, $T_{D2} = T_{W1}$, must be invoked in the PPWD crossflow calculation. Therefore, if the dry air mass flow rate in the wet section, G_W , is fixed, the dry air mass flow rate in the dry section, G_D , is supposed to be solved using a trial-and-error approach suggested in figure 3.19.

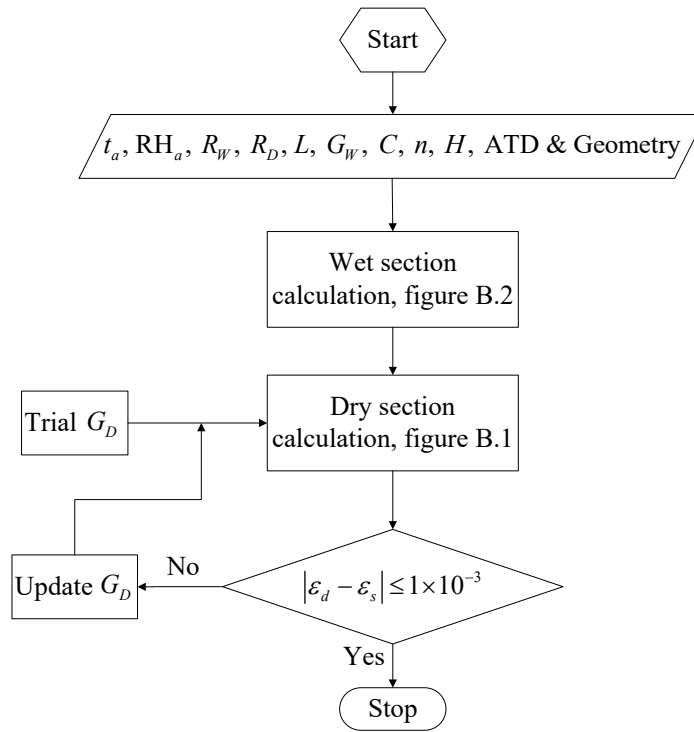


Figure 3.19: The PPWD crossflow tower calculation diagram. Figures B.1 and B.2 corresponds to figures 3.17 and 3.18, respectively.

Chapter 4

Coaxial plumes: theory and experiment

4.1 Abstract

Boussinesq, turbulent plume flows have been successfully described by the well-established model of Morton *et al.* (1956), however, the more complicated case of a coaxial plume consisting of an inner circular plume and an outer annular plume is more challenging to describe theoretically. The difficulties in question arise because of the turbulent exchange of mass, momentum and buoyancy between the inner plume, the outer plume and the ambient. The present study explores the possibility of using a double plume model for coaxial plumes. Model predictions are compared against analogue experimental measurements where, in the latter case, we employ a planar laser-induced fluorescence technique for purposes of visualizing the flow and for measuring concentrations of coaxial plumes. The plumes in question issued from a specially-designed coaxial nozzle, are of moderate Reynolds number (approximately 500) and are of intermediate flux-balance parameter indicating a plume that is either slightly lazy or slightly forced. A whole-field comparison of the scalar concentration between theory and experiment is conducted to obtain the optimal entrainment coefficients. The advantage and limitation of using coaxial plumes to abate the visible plume discharged by cooling towers is discussed.

4.2 Introduction

Turbulent mixing resulting from coaxial jets has received extensive investigation because of its widespread application in combustion processes. Detailed experimental and numerical studies of coaxial jets can be found in Champagne & Wygnanski (1971), Dahm *et al.* (1992), Buresti *et al.* (1994), Rehab *et al.* (1997) and Villermaux & Rehab (2000), with the conventional configuration that the outer flow has much greater source velocity than the inner flow. Select investigations consider density (or buoyancy) effects on coaxial jet mixing. Favre-Marinet *et al.* (1999) and Favre-Marinet & Schettini (2001) studied coaxial jets with large (non-Boussinesq) density differences. They argued that the effects of velocity and density can be combined by considering the outer to inner jet momentum flux ratio. Theoretical in-

vestigations are less numerous, the seminal work being that of Morton (1962) for coaxial jets, which follows from the classical plume model of Morton *et al.* (1956) (MTT56 hereafter). In a coaxial turbulent flow structure, Morton (1962) assumes that the entrainment from the outer to the inner jet scales with the velocity difference between the inner and outer jets, and the entrainment from the inner jet and from the ambient into the outer jet scales with the outer jet velocity. Of course, it is more straightforward to distinguish between inner and outer jet fluid in an integral theoretical model like that of Morton (1962) than it is in an experiment characterized by turbulent transport over different time- and length-scales. In a similar vein, integral flow models do not consider the modified mixing that may arise in the flow development zone (Champagne & Wygnanski, 1971). These points aside, the comparative simplicity and reasonable accuracy of integral coaxial jet models serves as a motivation to extend this analysis in describing a new category of flow, namely coaxial plumes or highly-buoyant jets where buoyancy quickly dominates over momentum post-discharge.

Motivating the extension described above, it is worthwhile highlighting examples from industry where coaxial plume-type flows arise. These include industrial burners (Oefelein, 2006), personalized ventilation (Makhoul *et al.*, 2015), thermal mixing devices (Kok *et al.*, 2017) and strategies for cooling tower plume abatement (Li *et al.*, 2018). Depending on the requisite amount of mixing, the parameters of interest vary for each of the examples just cited. For example, in personalized ventilation, the aim is to lengthen the inner potential core region so as to increase the penetration of fresh air into the breathing zone. In the case of the cooling tower plume, the coaxial wet/dry plume structure is expected to reduce the frequency and/or severity of fog formation, i.e. the steam present in the inner, wet plume is shielded by the outer, dry plume from interacting directly with the relatively cold ambient air.

Others have used Morton (1962) as a springboard for studying related kinds of coaxial flows. For instance, McDougall (1978) proposed a double plume model for bubble plumes which includes an inner circular plume (dispersed gas phase) and an outer annular plume (continuous liquid phase). Two different body force formulations for the inner plume were proposed in McDougall (1978). Later Socolofsky *et al.* (2008) developed a more general double plume model for bubble plumes in a stratified ambient wherein the inner flow consists of a multi-phase plume and the outer flow is a counter-flowing plume. Bloomfield & Kerr (2000) (BK00 hereafter) gave theoretical formulations of a turbulent fountain in a uniform and in a stratified ambient. These formulations span two different entrainment assumptions (one of which is Morton’s entrainment assumption for coaxial jets) and two body force formulations (McDougall, 1978, 1981). The double plume equations are also used to describe a single uniform plume in an otherwise turbulently convecting environment as studied by Turner (1963) and Witham & Phillips (2008). In such cases, the uniform turbulent plume detrains its fluid into the turbulent environment.

For the present theoretical modeling of co-flowing, single phase, coaxial plumes, Morton’s coaxial jet model is extended to include the effect of buoyancy. In this context, McDougall’s two body force assumptions are formulated and discussed. A nontrivial contribution of our study is to determine, with reference to laboratory experimental measurements, which of these body force formulations is more appropriate to the coaxial plume case. In like fashion, we estimate values for the entrainment coefficients. This is done through an analysis of images collected using planar laser-induced fluorescence (PLIF), the same laboratory

technique used in the earlier coaxial jet study of Villermaux & Rehab (2000). By this technique, the spatial evolution of a passive scalar within a coaxial plume may be visualized and this, in turn, gives insights into the mixing behavior more generally.

The manuscript is organized as follows. In section 4.3 we derive the coaxial plume theory. Because entrainment is an essential model component, section 4.3 also reviews the choice of entrainment coefficients from related investigations. In section 4.4 we describe the experimental set-up and present some representative experimental results. Thereafter, in section 4.5 we compare the experimental results to the theory. A major impetus to our work is to provide strategies to reduce the length and severity of the visible plumes produced by cooling towers. To this end, section 4.6 indicates how our results might be applied in this particular context. Finally in section 7.7 we draw conclusions.

4.3 Theory of coaxial plumes in a homogeneous ambient

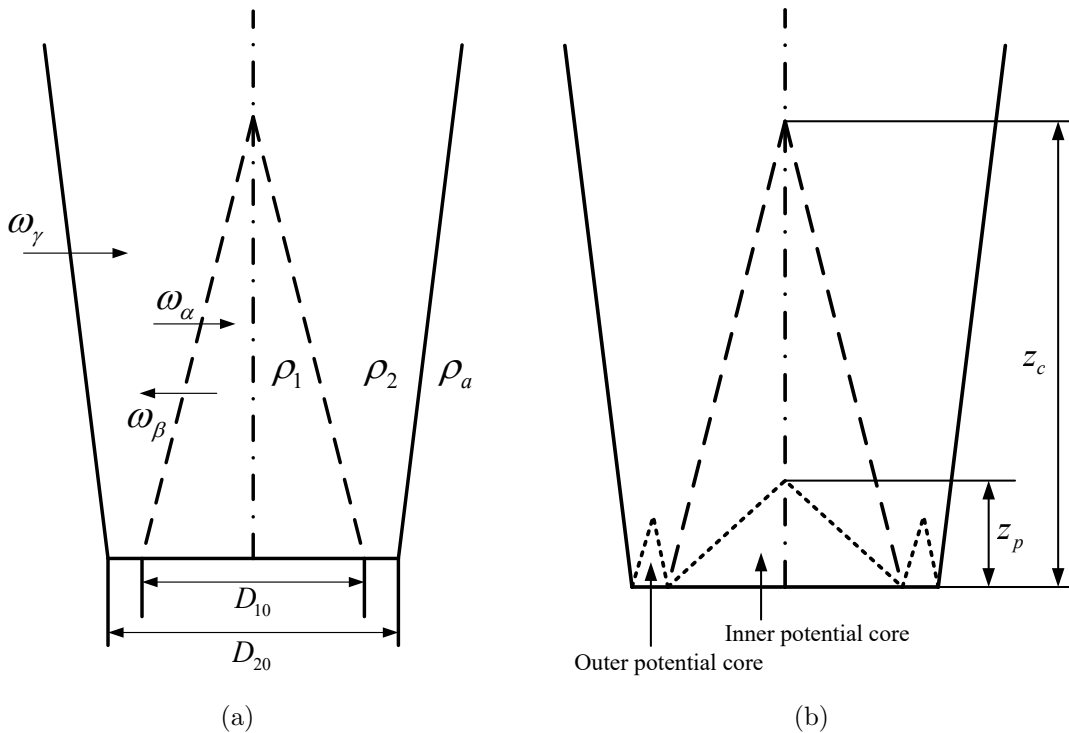


Figure 4.1: (a): Schematic of a coaxial plume in a stationary ambient. The cone-shaped region bounded by the dashed black line is the inner plume. $D_{10} = 2r_{10}$ and $D_{20} = 2r_{20}$ are the respective source diameters for the inner and outer plumes. ρ_a , ρ_1 and ρ_2 are the densities of the ambient fluid, the inner and outer plumes, respectively. The entrainment velocities (ω_α , ω_β and ω_γ) are labeled and the corresponding directions are indicated by the solid arrows. (b): The cone-shaped regions bounded by the dotted lines are the inner and outer potential cores, respectively. z_p and z_c are, respectively, the inner potential core height and the cut-off height of the inner plume; these are defined in section 4.4.3.

4.3.1 Coaxial plumes

A sketch of the coaxial plume structure is given in figure 4.1. “Top-hat” profiles of plume velocity, buoyancy and passive scalar concentration are assumed for simplicity. For the inner plume, the volume flux is given by $Q_1 = \pi r_1^2 U_1$ where r_1 and U_1 are the radius and vertical velocity of the inner plume, respectively, the kinematic momentum flux is given by $M_1 = \pi r_1^2 U_1^2$, the buoyancy flux is given by $F_1 = \pi r_1^2 U_1 g'_1$ where $g'_1 = g \frac{\rho_a - \rho_1}{\rho_a}$ and the passive scalar concentration flux is given by $C_1 = \pi r_1^2 U_1 c_1$ where c_1 is the scalar concentration in the inner plume. The counterpart fluxes for the outer plume are $Q_2 = \pi (r_2^2 - r_1^2) U_2$ where r_2 and U_2 are the outer radius and vertical velocity of the outer plume, respectively, $M_2 = \pi (r_2^2 - r_1^2) U_2^2$, $F_2 = \pi (r_2^2 - r_1^2) U_2 g'_2$ where $g'_2 = g \frac{\rho_a - \rho_2}{\rho_a}$ and $C_2 = \pi (r_2^2 - r_1^2) U_2 c_2$ where c_2 is the scalar concentration in the outer plume. Entrainment of fluid between the inner and outer plumes and from the ambient to the outer plume follow Morton’s entrainment assumption for coaxial jets (Morton, 1962). Symbolically, we write

$$\omega_\alpha = \alpha |U_1 - U_2|, \quad \omega_\beta = \beta U_2, \quad \omega_\gamma = \gamma U_2. \quad (4.1)$$

Previous theoretical studies of coaxial plumes, e.g. Li *et al.* (2018) and Li & Flynn (2020a), have indicated that model predictions are much less sensitive to the precise value of α than they are to the values of β and γ . For simplicity, we shall assume that $\alpha = 0$ thus $\omega_\alpha = 0$, which signifies that there is no entrainment from the outer to the inner plume. This assumption may seem counter-intuitive, especially when the inner plume is considered to be much “stronger” than the outer plume. Nonetheless, the coaxial jet model of Morton (1962) has indicated that, in most cases, the inner flow is absorbed entirely by the outer flow whereas the outer flow is never extinguished by the inner flow. Assuming $\alpha = 0$ greatly simplifies the model development to follow and the problem of determining the entrainment coefficients using the PLIF experiments as described in section 4.4 below. This assumption also avoids the ambiguity of other possible forms of entrainment assumption, e.g. $\omega_\alpha = \alpha U_1$ where ω_α is related to the inner plume velocity only. Nonetheless, we note that when the outer plume is extremely “weak” compared to the inner plume, e.g. $r_2 - r_1 \ll r_1$ (r_1 and r_2 are the respective radii of the inner and outer plumes) and $U_1 \ll U_2$, the $\omega_\alpha = 0$ assumption is unlikely to be valid especially near the source. Note that this zero α should not be confused with the non-zero α in the model of Chapter 5, which focuses on coaxial plumes in a crosswind.

In measuring the buoyancy of the inner plume, McDougall (1981) suggested that such an evaluation may be made with respect to either the ambient or the outer plume fluid. If the reference density is chosen to be ρ_a , we consider body force formulation one or BFI; if the reference density is chosen to be ρ_2 , we instead refer to body force formulation two or BFII. In the former case, and assuming an ambient that is neither density-stratified nor windy, the governing equations read as follows:

$$\frac{dQ_1}{dz} = -2\pi r_1 \omega_\beta, \quad (4.2)$$

$$\frac{dQ_2}{dz} = 2\pi r_1 \omega_\beta + 2\pi r_2 \omega_\gamma, \quad (4.3)$$

$$\frac{dM_1}{dz} = \pi r_1^2 g'_1 - 2\pi r_1 \omega_\beta U_1, \quad (4.4)$$

$$\frac{dM_2}{dz} = \pi (r_2^2 - r_1^2) g'_2 + 2\pi r_1 \omega_\beta U_1, \quad (4.5)$$

$$\frac{dF_1}{dz} = -2\pi r_1 \omega_\beta g'_1, \quad (4.6)$$

$$\frac{dC_1}{dz} = -2\pi r_1 \omega_\beta c_1, \quad (4.7)$$

where $F_1 + F_2 = F_{10} + F_{20} = \pi r_{10}^2 U_{10} g'_{10} + \pi (r_{20}^2 - r_{10}^2) U_{20} g'_{20}$ and $C_1 + C_2 = C_{10} + C_{20} = \pi r_{10}^2 U_{10} c_{10} + \pi (r_{20}^2 - r_{10}^2) U_{20} c_{20}$ where the subscripts 10 and 20 are used to denote the source conditions for the inner and outer plumes, respectively. (On account of these last relations, no separate evolution equations need to be given for F_2 or C_2 .) Conversely, if we adopt BFII, then the momentum equation for the inner plume is instead written as

$$\frac{dM_1}{dz} = \pi r_1^2 \left(g'_1 - g'_2 + U_2 \frac{dU_2}{dz} \right) - 2\pi r_1 \omega_\beta U_1, \quad (4.8)$$

where the term $U_2 \frac{dU_2}{dz}$ is the acceleration of the frame of reference of the outer plume. Considering the inner plume and outer plume as a whole, the momentum equation for either of BFI or BFII reads

$$\frac{d(M_1 + M_2)}{dz} = \pi r_1^2 g'_1 + \pi (r_2^2 - r_1^2) g'_2. \quad (4.9)$$

Subtracting (4.8) from (4.9) then yields

$$\frac{dM_2}{dz} = \pi r_1^2 \left(g'_2 - U_2 \frac{dU_2}{dz} \right) + \pi (r_2^2 - r_1^2) g'_2 + 2\pi r_1 \omega_\beta U_1. \quad (4.10)$$

Equations (4.8) and (4.10) along with (4.2)-(4.3) and (4.6)-(4.7) complete the BFII formulation, i.e. the volume, momentum, buoyancy and scalar concentration conservation equations for the inner and outer plumes. The derivation of the momentum equations using the BFI and BFII formulations is given in section 4.8.

A shortcoming of e.g. (4.2)-(4.7) is that this set of equations does not leverage the connection between, for instance, Q_1 , U_1 and r_1 . Correcting this deficiency, (4.2)-(4.7) can be written so as to only ever refer to flux variables. After some straightforward algebra, we find that

$$\frac{dQ_1}{dz} = -2\pi^{1/2} \beta \frac{Q_1}{M_1^{1/2}} \frac{M_2}{Q_2}, \quad (4.11)$$

$$\frac{dQ_2}{dz} = 2\pi^{1/2} \left[\beta \frac{Q_1}{M_1^{1/2}} \frac{M_2}{Q_2} + \gamma \left(\frac{Q_1^2}{M_1} + \frac{Q_2^2}{M_2} \right)^{1/2} \frac{M_2}{Q_2} \right], \quad (4.12)$$

$$\frac{dM_1}{dz} = \frac{Q_1 F_1}{M_1} - 2\pi^{1/2} \beta M_1^{1/2} \frac{M_2}{Q_2}, \quad (4.13)$$

$$\frac{dM_2}{dz} = \frac{Q_2 (F_{10} + F_{20} - F_1)}{M_2} + 2\pi^{1/2} \beta M_1^{1/2} \frac{M_2}{Q_2}, \quad (4.14)$$

$$\frac{dF_1}{dz} = -2\pi^{1/2} \beta \frac{Q_1}{M_1^{1/2}} \frac{M_2}{Q_2} \frac{F_1}{Q_1}, \quad (4.15)$$

$$\frac{dC_1}{dz} = -2\pi^{1/2} \beta \frac{Q_1}{M_1^{1/2}} \frac{M_2}{Q_2} \frac{C_1}{Q_1}. \quad (4.16)$$

Meanwhile in the BFII case, the momentum equations may be written as

$$\frac{dM_1}{dz} = \frac{Q_1^2}{M_1} \left(\frac{F_1}{Q_1} - \frac{F_{10} + F_{20} - F_1}{Q_2} + \frac{M_2}{Q_2^2} \frac{dM_2}{dz} - \frac{M_2^2}{Q_2^3} \frac{dQ_2}{dz} \right) - 2\pi^{1/2}\beta M_1^{1/2} \frac{M_2}{Q_2}, \quad (4.17)$$

$$\frac{dM_2}{dz} = \frac{Q_2^2 M_1}{Q_1^2 M_2 + Q_2^2 M_1} \left[\left(\frac{Q_1^2}{M_1} + \frac{Q_2^2}{M_2} \right) \frac{F_2}{Q_2} + \frac{Q_1^2 M_2^2}{Q_2^3 M_1} \frac{dQ_2}{dz} + 2\pi^{1/2}\beta M_1^{1/2} \frac{M_2}{Q_2} \right]. \quad (4.18)$$

The above governing equations assume implicitly that the profiles of vertical velocity, buoyancy and scalar concentration are self-similar. On the other hand, the theory also predicts that the inner plume shrinks until it disappears, which is, strictly-speaking, a violation of self-similarity. For instance, self-similarity in a uniform plume results in power law scalings for the plume radius and volume flux, i.e. $r \propto z$ and $Q \propto F^{1/3} z^{5/3}$; such kinds of scalings do not apply for the shrinking inner plume. Note that a similar assumption of self-similarity has been questioned in the context of turbulent fountains (cf. Mizushima *et al.* 1982). Nonetheless, Hunt & Debugne (2016) argued that self-similar integral plume models can be successfully applied to flows that are not fully self-similar, such as the near source region of forced and lazy plumes. With this auspicious record in mind, we proceed to evaluate the accuracy of the models formulated above. Before doing so, some discussion of BFI vs. BFII is necessary as is a consideration of the flow evolution following the disappearance of the inner plume.

4.3.2 Body force formulation

Whereas in the previous subsection, equations corresponding to BFI and BFII are presented for completeness, we find, as a result of contrasting with the experimental data to be described in sections 4.4 and 4.5, that BFI gives a more consistent comparison. Consequently, from this point forward, we will focus exclusively on the BFI solution. It is important to highlight, however, that the differences between the predictions made using a BFI vs. BFII formulation are comparatively small, as already noted by Devenish *et al.* (2010a).

4.3.3 The merged single plume

Once the inner plume disappears, the resulting flow is expected to behave like a single uniform plume. The corresponding governing equations are then

$$\frac{dQ}{dz} = 2\alpha_p \pi^{1/2} M^{1/2}, \quad (4.19)$$

$$\frac{dM}{dz} = \frac{FQ}{M}, \quad (4.20)$$

$$\frac{dF}{dz} = 0, \quad (4.21)$$

$$\frac{dC}{dz} = 0, \quad (4.22)$$

where the volume flux is given by $Q = \pi r^2 U$, the kinematic momentum flux is given by $M = \pi r^2 U^2$, the buoyancy flux is given by $F = \pi r^2 U g'$ where $g' = g \frac{\rho_a - \rho}{\rho_a}$ and the passive scalar concentration flux is given by $C = \pi r^2 U c$. The pure plume entrainment coefficient,

$\alpha_p = 0.117$, is used for the merged single plume (List, 1982). The “source” conditions (Q_0 , M_0 , F_0 and C_0) for the merged single plume are evaluated from the properties of the outer plume computed at the “cut-off” height z_c , the elevation where the inner plume disappears.

4.3.4 Nondimensionalization and reformulation to solve for \hat{r}_1 , \hat{r}_2 , \hat{U}_1 , \hat{U}_2 and Γ_1

Following the studies of Hunt & Kaye (2005) and Hunt & Debugne (2016), we attempt to express the BFI governing equations in terms of the local flux-balance parameter, Γ , which is defined as (Hunt & Van den Bremer, 2011)

$$\Gamma = \frac{5}{8\alpha_p\pi^{1/2}} \frac{Q^2 F}{M^{5/2}}, \quad (4.23)$$

where the flux parameters Q , M and F are defined in the same way as for the single merged plume in section 4.3.3. Note that Γ is proportional to the plume Richardson number, Ri , defined as

$$\text{Ri} = \frac{g'r}{U^2}, \quad (4.24)$$

i.e.

$$\text{Ri} = \frac{8\alpha_p}{5} \Gamma. \quad (4.25)$$

For the inner plume, the dimensionless radius, dimensionless vertical velocity and Richardson number are respectively given by

$$\hat{r}_1 = \frac{r_1}{r_{20}}, \quad \hat{U}_1 = \frac{U_1}{U_{20}}, \quad \text{Ri}_1 = \frac{g'_1 r_1}{U_1^2}, \quad \hat{z} = \frac{z}{r_{20}}, \quad (4.26)$$

where the hatted variables are dimensionless. The counterpart radius, vertical velocity and Richardson number for the outer plume are

$$\hat{r}_2 = \frac{r_2}{r_{20}}, \quad \hat{U}_2 = \frac{U_2}{U_{20}}, \quad \text{Ri}_2 = \frac{g'_2 (r_2^2 - r_1^2)^{1/2}}{U_2^2}, \quad (4.27)$$

respectively. The dimensionless flux parameters are

$$\hat{Q}_1 = \hat{r}_1^2 \hat{U}_1, \quad \hat{M}_1 = \hat{r}_1^2 \hat{U}_1^2, \quad \hat{F}_1 = \frac{r_{00} \text{Ri}_1 \hat{r}_1 \hat{U}_1^3}{\text{Ri}_{20}}, \quad (4.28)$$

$$\hat{Q}_2 = (\hat{r}_2^2 - \hat{r}_1^2) \hat{U}_2, \quad \hat{M}_2 = (\hat{r}_2^2 - \hat{r}_1^2) \hat{U}_2^2, \quad \hat{F}_2 = \frac{F_{10} + F_{20}}{\pi r_{20}^2 U_{20} g'_{20}} - \hat{F}_1, \quad (4.29)$$

where $r_{00} = \frac{(r_{20}^2 - r_{10}^2)^{1/2}}{r_{20}}$ and $\text{Ri}_{20} = \frac{g'_{20} (r_{20}^2 - r_{10}^2)^{1/2}}{U_{20}^2}$. Thus the set of equations (4.11)-(4.15) can be rearranged and written in nondimensional form as

$$\frac{d\hat{Q}_1}{d\hat{z}} = -2\hat{r}_1 \beta \hat{U}_2, \quad (4.30)$$

$$\frac{d\hat{Q}_2}{d\hat{z}} = 2 \left(\hat{r}_1 \beta \hat{U}_2 + \gamma \hat{r}_2 \hat{U}_2 \right), \quad (4.31)$$

$$\frac{d\hat{M}_1}{d\hat{z}} = \text{Ri}_1 \hat{r}_1 \hat{U}_1^2 - 2\hat{r}_1 \beta \hat{U}_1 \hat{U}_2, \quad (4.32)$$

$$\frac{d\hat{M}_2}{d\hat{z}} = \text{Ri}_2 \hat{r}_a \hat{U}_2^2 + 2\hat{r}_1 \beta \hat{U}_1 \hat{U}_2, \quad (4.33)$$

$$\frac{d\hat{F}_1}{d\hat{z}} = -\frac{2r_{00} \text{Ri}_1}{\text{Ri}_{20}} \beta \hat{U}_2 \hat{U}_1^2, \quad (4.34)$$

where $\hat{r}_a = (\hat{r}_2^2 - \hat{r}_1^2)^{1/2}$.

To obtain the variation of the nondimensional plume radius, vertical velocity and Richardson number, we differentiate $\hat{r}_1 = \frac{\hat{Q}_1}{\hat{M}_1^{1/2}}$, $\hat{r}_2 = \left(\frac{\hat{Q}_1^2}{\hat{M}_1} + \frac{\hat{Q}_2^2}{\hat{M}_2} \right)^{1/2}$, $\hat{U}_1 = \frac{\hat{M}_1}{\hat{Q}_1}$, $\hat{U}_2 = \frac{\hat{M}_2}{\hat{Q}_2}$ and $\text{Ri}_1 = \frac{\text{Ri}_{20} \hat{Q}_1^2 \hat{F}_1}{r_{00} \hat{M}_1^{5/2}}$ with respect to \hat{z} . Accordingly, we find that

$$\frac{d\hat{r}_1}{d\hat{z}} = \frac{1}{\hat{r}_1 \hat{U}_1} \frac{d\hat{Q}_1}{d\hat{z}} - \frac{1}{2\hat{r}_1 \hat{U}_1^2} \frac{d\hat{M}_1}{d\hat{z}}, \quad (4.35)$$

$$\frac{d\hat{r}_2}{d\hat{z}} = \frac{\hat{r}_1}{\hat{r}_2} \frac{d\hat{r}_1}{d\hat{z}} + \frac{1}{2\hat{r}_2} \left(\frac{2}{\hat{U}_2} \frac{d\hat{Q}}{d\hat{z}} - \frac{1}{\hat{U}_2^2} \frac{d\hat{M}_2}{d\hat{z}} \right), \quad (4.36)$$

$$\frac{d\hat{U}_1}{d\hat{z}} = \frac{1}{\hat{r}_1^2 \hat{U}_1} \frac{d\hat{M}_1}{d\hat{z}} - \frac{1}{\hat{r}_1^2} \frac{d\hat{Q}_1}{d\hat{z}}, \quad (4.37)$$

$$\frac{d\hat{U}_2}{d\hat{z}} = \frac{1}{\hat{r}_a^2} \left(\frac{1}{\hat{U}_2} \frac{d\hat{M}_2}{d\hat{z}} - \frac{d\hat{Q}_2}{d\hat{z}} \right), \quad (4.38)$$

$$\frac{d\text{Ri}_1}{d\hat{z}} = \frac{2\text{Ri}_1}{\hat{r}_1^2 \hat{U}_1} \frac{d\hat{Q}_1}{d\hat{z}} - \frac{5\text{Ri}_1}{2\hat{r}_1^2 \hat{U}_1^2} \frac{d\hat{M}_1}{d\hat{z}} + \frac{\text{Ri}_{20}}{r_{00} \hat{r}_1 \hat{U}_1^3} \frac{d\hat{F}_1}{d\hat{z}}. \quad (4.39)$$

Using the above equations and letting $\zeta = 4\alpha_p \hat{z}$, $\alpha_\beta = \beta/\alpha_p$, $\alpha_\gamma = \gamma/\alpha_p$ and $\Gamma = \frac{5}{8\alpha_p} \text{Ri}$, (4.30)-(4.34) can be rewritten as

$$\frac{d\hat{r}_1}{d\zeta} = -\frac{\Gamma_1}{5} + J_1, \quad (4.40)$$

$$\frac{d\hat{r}_2}{d\zeta} = -\frac{\hat{r}_1 \Gamma_1 + \hat{r}_a \Gamma_2}{5\hat{r}_2} + J_2, \quad (4.41)$$

$$\frac{d\hat{U}_1}{d\zeta} = \frac{2\hat{U}_1 \Gamma_1}{5\hat{r}_1}, \quad (4.42)$$

$$\frac{d\hat{U}_2}{d\zeta} = \frac{2\hat{U}_2 \Gamma_2}{5\hat{r}_a} + J_3, \quad (4.43)$$

$$\frac{d\Gamma_1}{d\zeta} = -\frac{\Gamma_1^2}{\hat{r}_1} + J_4, \quad (4.44)$$

where the interaction terms J_1 to J_4 are given by

$$J_1 = -\frac{\alpha_\beta \hat{U}_2}{4 \hat{U}_1}, \quad J_2 = \frac{\alpha_\gamma}{2} + \frac{\hat{r}_1}{4\hat{r}_2} \alpha_\beta \left(2 - \frac{\hat{U}_1}{\hat{U}_2} - \frac{\hat{U}_2}{\hat{U}_1} \right),$$

$$J_3 = \frac{1}{2\hat{r}_a^2} \left[\alpha_\beta \hat{r}_1 (\hat{U}_1 - \hat{U}_2) - \alpha_\gamma \hat{r}_2 \hat{U}_2 \right], \quad J_4 = -\frac{\Gamma_1}{4\hat{r}_1} \alpha_\beta \frac{\hat{U}_2}{\hat{U}_1}. \quad (4.45)$$

The source conditions necessary for solving the set of ODEs presented by (4.40)-(4.44) are

$$\begin{aligned} \hat{r}_{10} &= \frac{r_{10}}{r_{20}}, \quad \hat{U}_{10} = \frac{U_{10}}{U_{20}}, \quad \Gamma_{10} = \Gamma_1(\zeta = 0), \\ \hat{r}_{20} &= 1, \quad \hat{U}_{20} = 1. \end{aligned} \quad (4.46)$$

Note that the constraint linking Γ_1 and Γ_2 reads as

$$\hat{r}_1 \hat{U}_1^3 \Gamma_1 + (\hat{r}_2^2 - \hat{r}_1^2)^{1/2} \hat{U}_2^3 \Gamma_2 = \hat{r}_{10} \hat{U}_{10}^3 \Gamma_{10} + (1 - \hat{r}_{10}^2)^{1/2} \Gamma_{20}, \quad (4.47)$$

where $\Gamma_{20} = \Gamma_2(\zeta = 0)$. Equation (4.47) results from a rearrangement of the buoyancy conservation equation, i.e. $\frac{d}{d\zeta} (\hat{F}_1 + \hat{F}_2) = 0$. For the inner plume, an analytical solution for the vertical velocity can be obtained from

$$\hat{U}_1 = \hat{U}_{10} \left(1 + \frac{4\Gamma_{10}}{5\hat{r}_{10}} \zeta \right)^{1/2}. \quad (4.48)$$

Meanwhile, \hat{r}_1 and Γ_1 follow

$$\frac{\hat{r}_1}{\Gamma_1} = \frac{4}{5} \zeta + \frac{\hat{r}_{10}}{\Gamma_{10}}. \quad (4.49)$$

If the inner plume is cut off by the outer plume so that $\hat{r}_1 = \hat{U}_1 = \Gamma_1 = 0$, the conservation equations for the outer plume read as follows:

$$\frac{d\hat{r}_2}{d\zeta} = \frac{1}{5} \left(\frac{5}{2} - \Gamma_2 \right), \quad (4.50)$$

$$\frac{d\hat{U}_2}{d\zeta} = \frac{2\hat{U}_2}{5\hat{r}_2} \left(\Gamma_2 - \frac{5}{4} \right), \quad (4.51)$$

$$\frac{d\Gamma_2}{d\zeta} = \frac{\Gamma_2(1 - \Gamma_2)}{\hat{r}_2}, \quad (4.52)$$

which is identical to equation (24) of Hunt & Van den Bremer (2011). The governing equations, (4.40)-(4.44) and (4.50)-(4.52) are solved using a fourth order Runge-Kutta finite difference method.

4.3.5 Representative solutions

To gain more insights into the governing equations for coaxial plumes, we illustrate the coaxial plume dynamics under representative source conditions. Specifically, we fix the ratio of inner to outer source radius as $\hat{r}_{10} = 0.7$ and choose a pure plume balance for the inner plume at the source i.e. $\Gamma_{10} = 1$. For simplicity, the dimensionless entrainment coefficients are fixed as $\alpha_\beta = \alpha_\gamma = 1$; we will discuss the choice of entrainment coefficients in section 4.3.6. The effects of changing Γ_{20} and \hat{U}_{10} on the coaxial plume dynamics are illustrated in figure 4.2. As Γ_{20} increases from 0.05, 1 to 20, the outer plume varies from a forced

to a pure to a lazy plume, respectively. Figure 4.2a show that the cut-off height of the inner plume decreases as Γ_{20} increases. This is illustrated by the sharp increase in the outer plume velocity for $\Gamma_{20} = 20$ – see the red dotted curve in figure 4.2c. Figure 4.2e shows that, regardless of Γ_{20} , all the outer plumes approach pure plume balance (i.e. $\Gamma = 1$) at $\zeta \approx 4$. On the other hand, figure 4.2b shows that, as expected, the inner plume cut-off height increases with increasing \hat{U}_{10} . For large \hat{U}_{10} , e.g. $\hat{U}_{10} = 2$, figure 4.2d shows that the outer plume experiences an increase in the vertical velocity near the source due to the entrainment from the inner to the outer plume. For this latter case, the outer plume shows a transition from slightly lazy to slightly forced then approaches a pure plume balance in the far field.

4.3.6 Entrainment coefficients

The determination of the (top-hat) entrainment coefficients β and γ is of key importance in this study. It should be emphasized, however, that there is not even a consensus regarding the appropriate value of the entrainment coefficient in the simpler case of a single uniform plume. Carazzo *et al.* (2006) summarized that, between different experimental studies, the measured entrainment coefficients in the case of a uniform plume fall between 0.10 and 0.16 (see their table 1). This effort of reviewing the relevant turbulent plume literature was later extended by Kaye (2008). Evidence shows that the constant-entrainment-coefficient assumption fails in some cases such as lazy ($\Gamma > 1$) or highly-lazy ($\Gamma \gg 1$) plumes (Hunt & Kaye, 2005) and the jet in a coflow (Lee & Chu, 2003). For lazy plumes, the experimental results of Kaye & Hunt (2009) indicate that the analytical formulations due to List & Imberger (1973) and Kaminski *et al.* (2005) that relate the entrainment coefficient to Γ are unrealistic due to the particular vertical mixing process that occur as the plume contracts near the source. Marjanovic *et al.* (2017) studied the near source entrainment of lazy plumes; their direct numerical simulation results showed that the entrainment processes in the near field are more properly modeled using large values for the entrainment coefficient. Recently Ciriello & Hunt (2020) have summarized previous work on uniform plumes and referred to the linear dependence of entrainment coefficient on the local plume Richardson number as a universal entrainment assumption.

In selecting the values for β and γ in a double plume structure, it is helpful to revisit how the entrainment coefficients are determined in the context of turbulent fountain flow (e.g. BK00) – see figure 4.3. By comparing the theoretical and experimental results of the initial fountain height, $\alpha = 0.085$ was chosen as the effective value for the entrainment coefficient from the downflow to the upflow (Bloomfield & Kerr, 1998). As for β and γ i.e. the entrainment coefficients defined implicitly by the corresponding entrainment velocities ω_β and ω_γ in the right sketch of figure 4.3, BK00 chose entrainment values for a line source plume i.e. $\beta = \gamma = 0.147$. McDougall (1981) argued that there is no *a-priori* reason to assume that $\beta = \gamma$, however, BK00 argue that the details of the solution are comparatively insensitive to the precise value of β : choosing $\beta = 0.076$ (corresponding to a point source jet value) has only a small effect on the prediction of the final fountain height. Fountain-type behavior also occurs for a buoyant plume in stably stratified ambient between its heights of neutral buoyancy and maximum rise. Using Large-eddy simulations (LES), Devenish *et al.* (2010a) compared the volume and momentum fluxes of the upward and downward flows

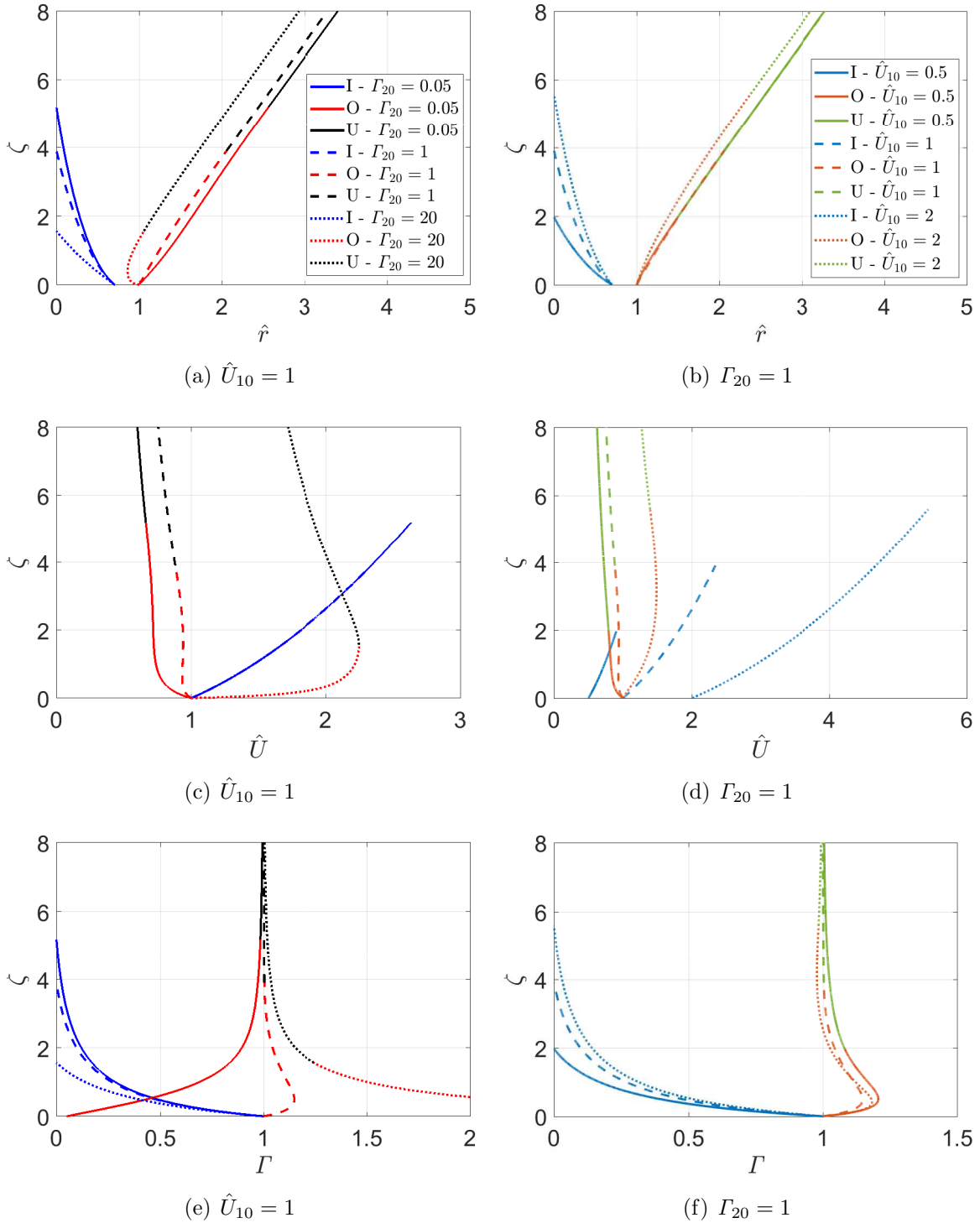


Figure 4.2: [Color] Effects of varying Γ_{20} (a, c and e) and \hat{U}_{10} (b, d and f) on plume radii, vertical velocities and flux-balance parameters. The letters I, O and U represent the inner and outer plumes and the merged uniform plume, respectively.

with the counterpart fluxes predicted by BK00. It was found that a revised BK00 model that allows for plume-top entrainment and has entrainment coefficients $\alpha = 0.05$, $\beta = 0.8$

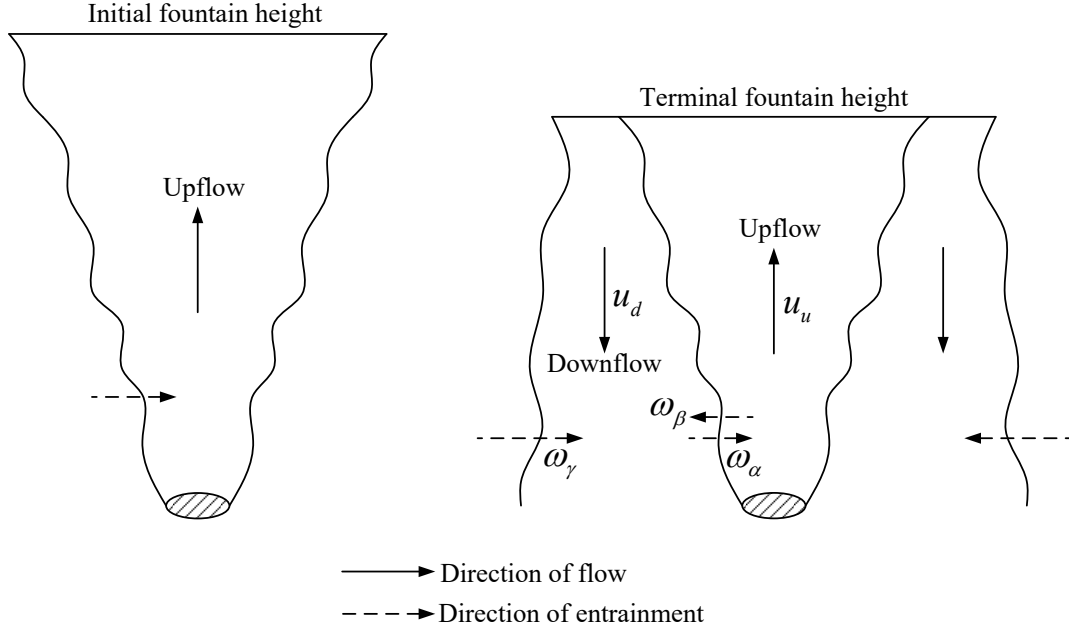


Figure 4.3: Schematic of a turbulent fountain. The flow is initiated by a negatively buoyant jet, which grows in size and slows down due to its negative buoyancy (left sketch). After reaching the initial (or maximum) fountain height, the flow reverses its direction and a plume-like downflow surrounds the jet-like upflow (right sketch).

and $\gamma = 0.01$ results in better agreement with the LES results. Plume-top entrainment was also included in the analysis of Hunt & Debugne (2016), which investigated turbulent fountain flow of high source densimetric Froude number. They chose as reference entrainment coefficients $\alpha = 0.06$ (midway between Williamson *et al.*, 2011 and Burrige & Hunt, 2013), $\gamma = 0.15$, and $\beta = 0$ because they assumed there is negligible entrainment from the upflow to the downflow.

In light of all of this previous research, we herein focus on determining, by carefully comparing experimental images with analogue theoretical predictions, the two key entrainment coefficients, i.e. β and γ in the context of coaxial plumes. This process is guided by the range of entrainment values reported above, whether these consider uniform or coaxial flows.

4.4 Laboratory experiments

4.4.1 Experimental set-up

A side-view schematic image of the PLIF experimental set-up is shown in figure 4.4. The experiments were conducted in a glass tank measuring $5.5 \text{ m} \times 0.6 \text{ m} \times 0.6 \text{ m}$ (length \times width \times height). Source fluid for the inner and outer plumes was supplied by a pair of overhead buckets. Ball valves and precision flow adjustment valves were used to regulate the flow rate in either case. Simple flow straighteners were inserted within the nozzle shell to avoid any swirling motion at the nozzle exit. Moreover, wire crosshairs were added within the nozzle and at the nozzle exit to enhance flow disturbances and thereby hasten the transition from a laminar to a tur-

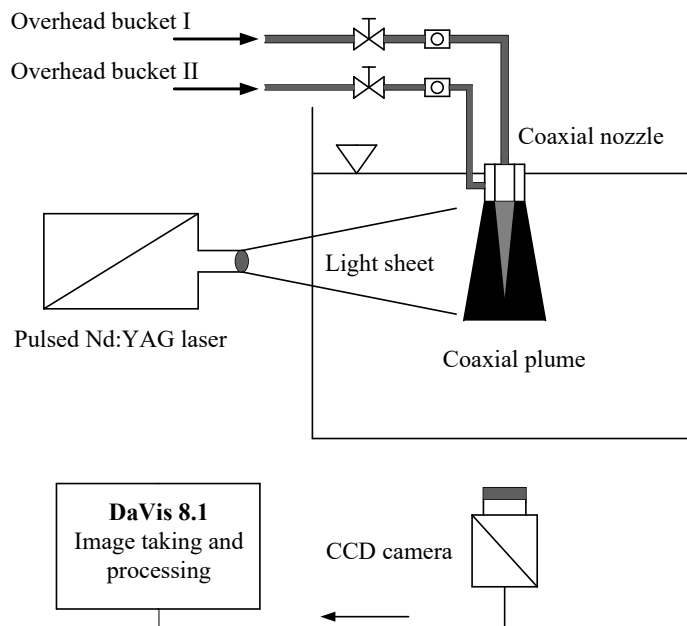


Figure 4.4: Schematic of the PLIF experimental set-up including the laser optics. The coaxial plumes consist of an inner circular plume (shaded gray) and an outer annular plume (shaded black).

bulent state (figure 4.5). Rhodamine 6G was seeded in the outer plume in a concentration of 0.30 mg/L. Note that the molecular diffusion coefficient for Rhodamine 6G is similar to that of salt¹ and both coefficients are, in any event, negligible compared to turbulent diffusion.

The light source was a Q-switched, repetitive pulsed Nd:YAG laser (Nano 560-20, LaVision) which had a maximum repetition rate of 20 Hz. The laser power was 0.6 W and the pulse energy was 0.03 J with a duration of 7 ns. The flashed laser light sheet was green and its wavelength was 532 nm. Two divergent lenses (focal length $f = -10$ mm and $f = -20$ mm) were used to give an aperture angle of 35°. The light sheet thickness was adjusted to be about 1.5 mm by turning the telescope inside the sheet optics. Experimental images were recorded using a CCD camera having a resolution of 1392 pixels (horizontal) \times 1040 pixels (vertical). The CCD camera (Imager E-lite 1.4M, Part # 1101131, LaVision) was 12 bit and had a maximum frame rate 17 fps at full resolution and a spectral range 400-850 nm. A Nikon 60 mm lens was fitted to the CCD camera. An optical filter (Part # 1108573, LaVision) having a cut-off wavelength of 540 nm was used to block the laser light and allow most of the light fluoresced by the Rhodamine 6G to pass to the CCD chip. After performing a perspective calibration, the resolution for the images was about 0.14 mm per pixel. An energy correction was not performed due to the fact that the shot-to-shot variation of laser light intensity was estimated to be only $\sim 5\%$. Further details regarding the post-processing of PLIF images can be found in section 4.9.

Experimental parameters are presented in table 4.1. Although we consider a variety of

¹At 25°C, the molecular diffusivities of Rhodamine 6G and salt in water are $D_{\text{Rh.6G}} = (4.0 \pm 0.3) \times 10^{-10} \text{ m}^2/\text{s}$ (Gendron *et al.*, 2008) and $D_{\text{salt}} \approx 1.6 \times 10^{-9} \text{ m}^2/\text{s}$ (Vitagliano & Lyons, 1956), respectively.

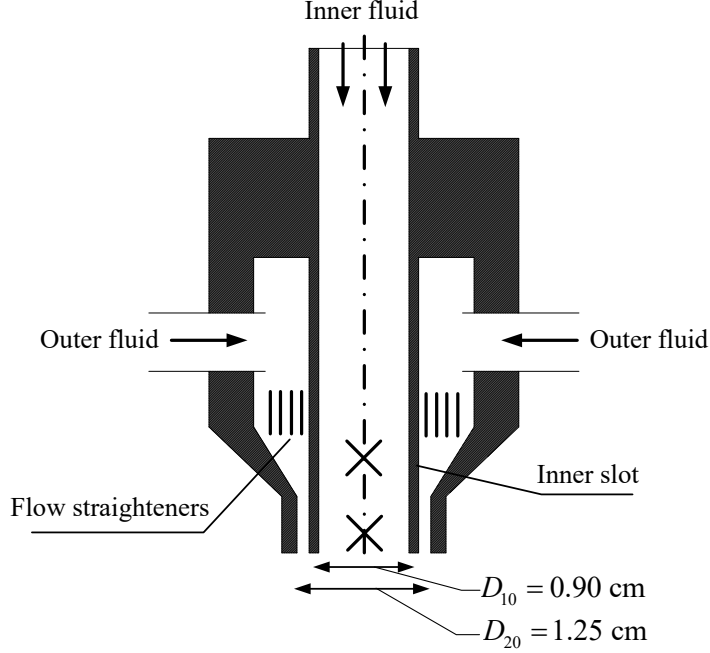


Figure 4.5: A cross-cut view of the coaxial nozzle. The inner nozzle and outer shell were connected by a threaded connection and were 3D printed using PLA and ABS plastics, respectively. The locations labeled with crosses show where the wire crosshairs were inserted. Note that the inner diameter of the inner nozzle is 8 mm and the inner slot has a thickness of 0.1 cm. As a first approximation, the source diameter for the inner fluid is $D_{10} = 0.9$ cm.

source densities and volume flow rates for each of the inner and outer plumes, experiments are typically classified as $g'_{10} \leq g'_{20}$. The $g'_{10} > g'_{20}$ cases are not considered because, as observed in the experiments, there is elongated flow development zone in such cases. Density contrasts fall into the range $\frac{\rho_{i0} - \rho_a}{\rho_a} < 10\%$ where $i = 1$ (inner plume) or 2 (outer plume). Thus the Boussinesq approximation is valid and the descending coaxial plumes produced in the water tank were dynamically equivalent to ascending coaxial plumes. The baseline case (experiment A3) has almost equal volume fluxes and densities for the inner and outer plumes, i.e. $Q_{10}, Q_{20} = 3.33 \text{ cm}^3/\text{s}$ and $\rho_{10}, \rho_{20} \approx 1.01 \text{ g/cm}^3$. Accordingly, the source Reynolds number, densimetric Froude number and flux-balance parameter of the inner plume are $Re_{10} = \frac{U_{10} D_{10}}{\nu} \approx 470$ where ν is the kinematic viscosity of pure water, $Fr_{10} = \frac{U_{10}}{\sqrt{g'_{10} D_{10}}} = 1.60$ and $\Gamma_{10} = 1.04$, which indicate an (inner) plume in near pure plume balance and having a modest Reynolds number. For the inner plume, the jet length is defined as $l_{j,1} = \frac{M_{10}^{3/4}}{F_{10}^{1/2}} \simeq 1.5 \text{ cm}$, which we regard as acceptably moderate. For the outer plume, the Reynolds number and flux-balance parameter are defined in section 4.10. Also summarized in this appendix are experimental data complementary to those data reported in table 1.

A virtual origin correction is not performed at the source because the (non-ideal) inner and outer plumes would give rise to two virtual origins at different locations on the coaxial plume axis (Morton, 1962). The inner and outer plumes start to interact before the inner plume and/or outer plume are fully developed and fully turbulent, i.e. there is a potential core zone. This region of laminar flow, though small in vertical extent, still requires careful

Table 4.1: Summary of the source conditions for the inner and outer plumes. The experiments consider an outer plume that is dyed with Rhodamine 6G. Densities are considered accurate to within ± 0.00005 g/cm³, volume flow rates to within ± 0.083 cm³/s and velocities to within ± 0.14 cm/s. The background fresh water density is $\rho_a = 0.9982$ g/cm³. The source velocities U_{10} and U_{20} are fixed whereas the source densities ρ_{10} and ρ_{20} are variable. The combination of Q_{10} and Q_{20} are chosen to ensure that the total source volume flux and momentum flux are approximately the same for all experimental categories.

Experiment	ρ_{10} (g/cm ³)	ρ_{20} (g/cm ³)	Q_{10} (cm ³ /s)	Q_{20} (cm ³ /s)	U_{10} (cm/s)	U_{20} (cm/s)
A1	1.0103	1.0102	2.50	4.17	3.93	7.06
A2			2.92	3.75	4.59	6.34
A3			3.33	3.33	5.23	5.63
A4			3.75	2.92	5.89	4.94
A5			4.17	2.50	6.55	4.23
B1	1.0101	1.0200	2.50	4.17	3.93	7.06
B2			2.92	3.75	4.59	6.34
B3			3.33	3.33	5.23	5.63
B4			3.75	2.92	5.89	4.94
B5			4.17	2.50	6.55	4.23
C1	1.0102	1.0398	2.50	4.17	3.93	7.06
C2			2.92	3.75	4.59	6.34
C3			3.33	3.33	5.23	5.63
C4			3.75	2.92	5.89	4.94
C5			4.17	2.50	6.55	4.23
D1	1.0102	1.0784	2.50	4.17	3.93	7.06
D2			2.92	3.75	4.59	6.34
D3			3.33	3.33	5.23	5.63
D4			3.75	2.92	5.89	4.94
D5			4.17	2.50	6.55	4.23

attention when setting the numerical values of β and γ – see e.g. (4.53) and the discussion thereof.

4.4.2 Experimental results (qualitative)

Sample instantaneous images are shown upside-down in figure 4.6. Kelvin-Helmholtz-type instabilities form in the outer plume just downstream of the source. Subsequently, the unstable vortex sheet rolls up into a succession of discrete vortices. The axisymmetric vortex roll-up is associated with an increase of vortex diameter in the downstream direction. Consistent with figure 7 of Dahm *et al.* (1992) illustrating the near-field vortex structure of coaxial jets, the near-field dynamics are governed by the pairing of vortex rings. Through this pairing process, the irrotational ambient fluid is brought into the core of the coaxial plume. Notice that for a very buoyant (i.e. lazy) outer plume as shown in figure 4.6 d, the vortices are significantly stretched and break up into finer vortex structures.

The mean concentration maps corresponding to the snapshot images of figure 4.6 are

shown in the four panels of figure 4.7. Each panel of figure 4.7 shows the average of 500 snapshot images collected over a time interval of 255 s. From figure 4.7 a to 4.7 d, we find that the lazier the outer plume, the thinner is its diameter near the source.

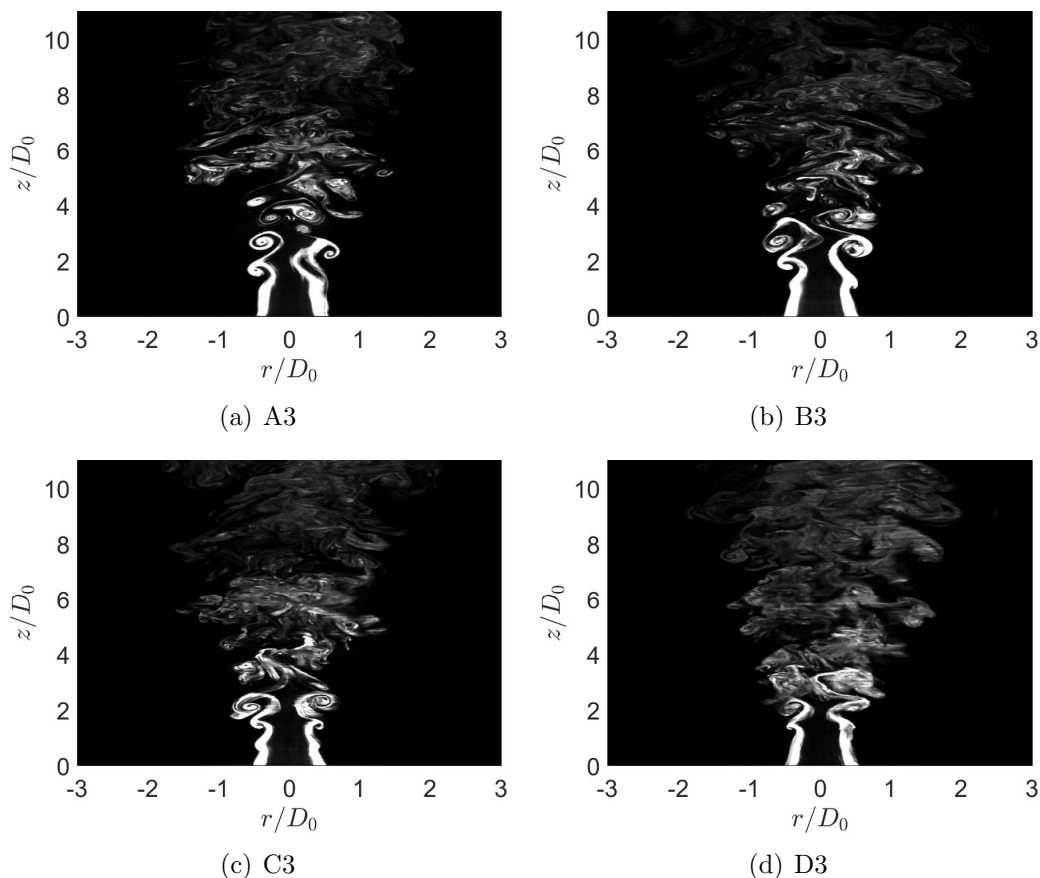


Figure 4.6: [Gray scale] Instantaneous images showing vortex roll-up for the coaxial plumes of experiments A3, B3, C3 and D3.

4.4.3 Experimental results (quantitative)

The evolution of coaxial plumes can be roughly evaluated by estimating the inner potential core height, z_p , and the cut-off height, z_c , of the inner plume. The two distances in question are defined respectively as follows:

1. The inner potential core height is defined as the elevation where the outer plume pinches the inner plume on the plume centerline (Rehab *et al.*, 1997).
2. The inner plume cut-off height is defined as the elevation where a single peak (rather than a pair of peaks) appears in the radial concentration distribution.

Or *et al.* (2007) argued that the potential core height can be measured in PLIF experiments as the distance where the centerline standard deviation of scalar concentration starts to rise sharply from the low level close to the source. Likewise, we adapt this definition here. Meanwhile, the definition for the cut-off height is analogous to the onset height of plume merger in the case of two coalescing axisymmetric plumes (Kaye & Linden, 2004).

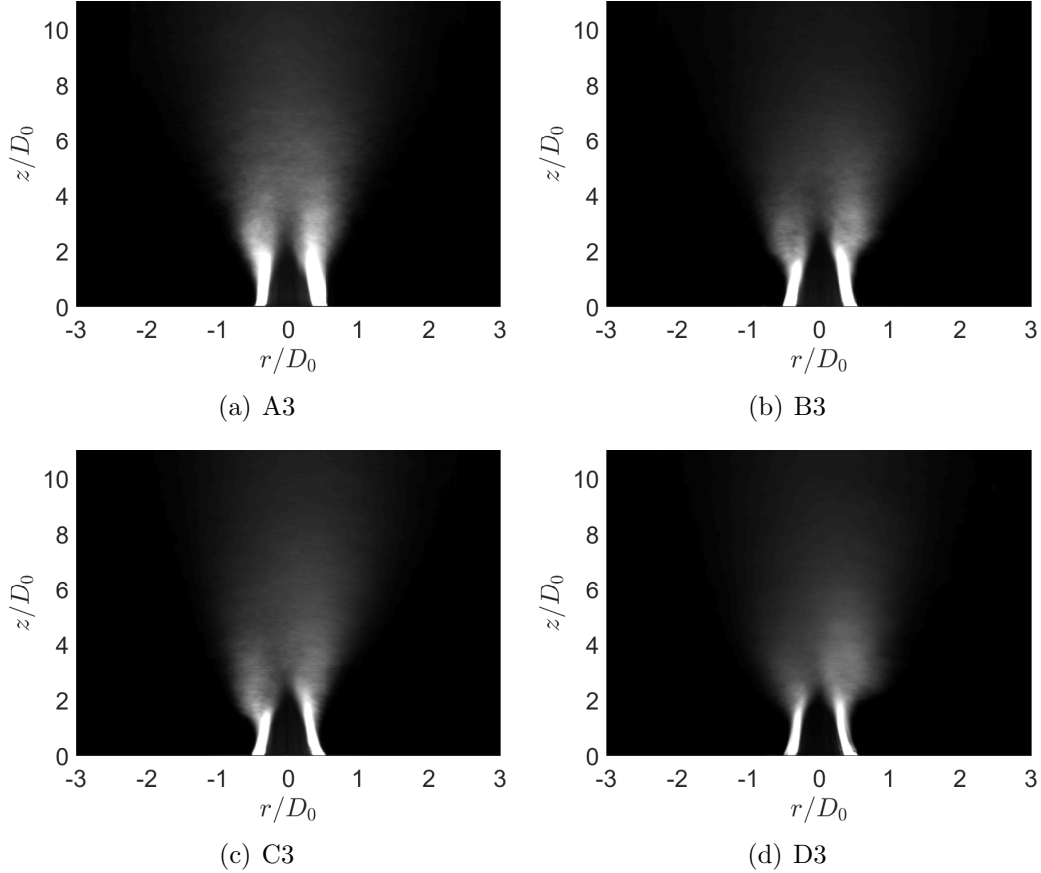


Figure 4.7: [Gray scale] As in figure 4.6 but showing time-averaged rather than instantaneous images. In each case, images are generated by averaging together 500 snapshot images, collected over a time interval of 255 s.

4.4.3.1 Two end-member cases: A3 and D3

For experiments A3 and D3, figures 4.8 a,b show that the centerline concentration approaches the uniform plume self-similar solution within a downstream distance of $z/D_0 = 10$. The peak centerline concentration occurs prior to the self-similar state being achieved. Specifically, D3 reaches its peak concentration at $z/D_0 = 3.3$, which is less than the counterpart $z/D_0 = 4.4$ for A3. Figures 4.8 c,d show that the centerline turbulent fluctuations for both cases exhibit similar trends characterized by an increase and subsequent decrease for larger values of z . With reference to these data, and using the definition of Or *et al.* (2007), the potential core height is estimated as $Z_p \equiv z_p/D_0 = 1.8$ for experiment A3 and $Z_p = 1.6$ for experiment D3. For experiment A3, the radial concentration profiles at successive downstream distances are shown in figure 4.9. Figure 4.9 clearly shows that the coaxial plumes evolve from a bimodal distribution near the source to a unimodal distribution at greater downstream distances. The onset of a single peak in the radial concentration profile of experiment A3 is estimated to occur at $Z_c = z_c/D_0 = 4.3 \pm 0.1$. The counterpart cut-off height for D3 is estimated as $Z_c = 3.4 \pm 0.1$.

Building on figure 4.9, figures 4.10 a,b illustrate more clearly the process of plume broadening in the radial direction with figures 4.10 c,d providing the corresponding turbulent fluc-

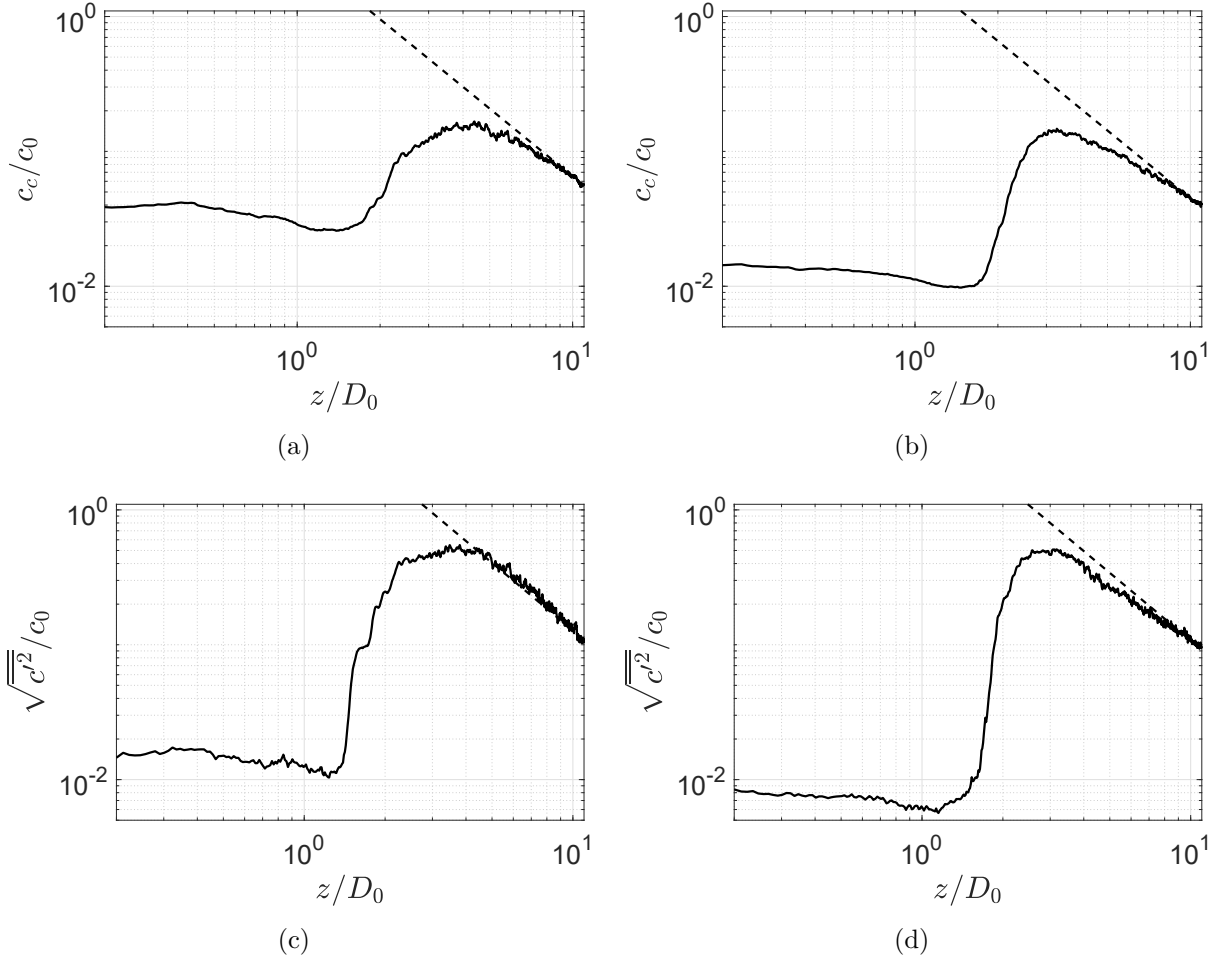


Figure 4.8: Log-log mean centerline concentration with corresponding “-5/3” dashed line (panels a and b) and log-log centerline standard deviation with corresponding “-5/3” dashed line (panels c and d) of coaxial plumes in experiments A3 (left) and D3 (right), respectively. The “-5/3” relationship is anticipated from the work of Papanicolaou & List (1987, 1988).

tuation profiles. Figures 4.10 a,b show that the peaks in the distribution are located along the outer plume where the shear is expected to be intense. However, and with increasing distance from the source, there is again a shift from a bimodal to a unimodal distribution as boundary layers broaden and more of the shear concentrates in the neighborhood of the centerline. Similar looking profiles of the radial concentration standard deviation are observed in figures 4.10 c,d. Figure 4.10 shows some mild asymmetries in the profiles of radial concentration and its standard deviation. Here and below, these suggest that the velocity profile near the source is not perfectly symmetric. Similar asymmetries can also be found in the near field velocity profiles of thin, annular jets as studied by Padhani *et al.* (2018), for instance. The above observations reinforce the fact that producing a truly uniform annular flow is difficult in laboratory settings.

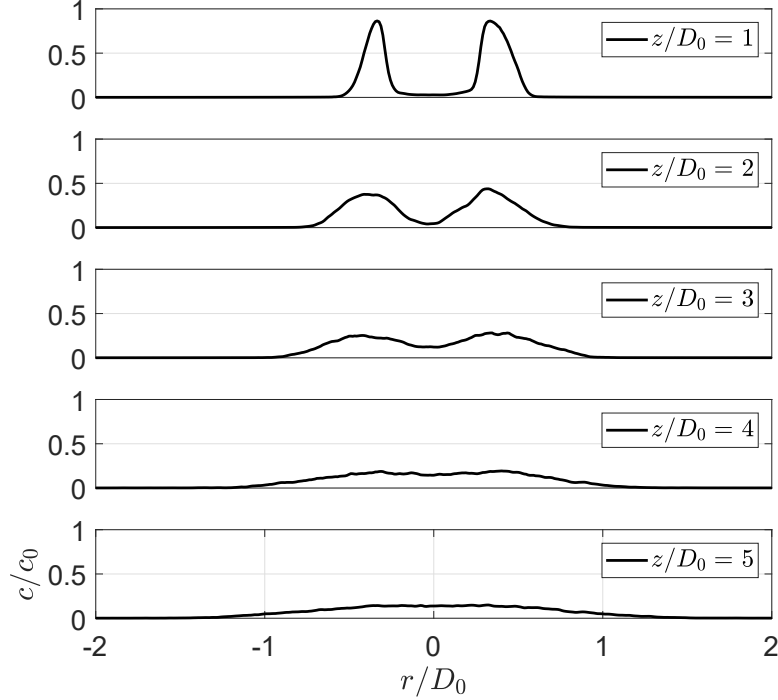


Figure 4.9: Radial concentration profiles at successive downstream distances for experiment A3.

4.5 Theory vs. experiment

4.5.1 Pixel-by-pixel comparison

The methodology to determine the optimal entrainment coefficients β and γ is analogous to that of Witham & Phillips (2008). A misfit function that sums up all the discrepancies in the passive scalar concentration between theory (t) and experiment (e), is defined mathematically as

$$\Phi(\beta, \gamma) = \frac{1}{nm} \sum_{i=1}^n \sum_{j=1}^m |c_t(r_i, z_j) - c_e(r_i, z_j)|, \quad (4.53)$$

where (r_i, z_j) is the pixel location in a time-averaged concentration image such as any one of those shown in figure 4.7. The lateral and vertical ranges for comparison are, respectively, $-2.25 \leq r/D_0 \leq 2.25$ and $Z_p \leq z/D_0 \leq 11$, where the inner potential core height, Z_p , is determined from the analysis of section 4.4.3. The vertical range starts from $z/D_0 = Z_p$ instead of $z = 0$ because, as noted above, the flow in the immediate neighborhood of the source is not fully turbulent and so is not well-represented by (4.1). Moreover, close to the source, the turbulent Schmidt number² may be affected by the molecular Schmidt number (Kaminski *et al.*, 2005). These points notwithstanding, figure 4.6 shows that the mixing in the flow development zone is non-negligible. We therefore propose two scenarios in constructing the theoretical solutions for inclusion in (4.53), i.e.

²The turbulent Schmidt number is defined as the ratio of the turbulent transport of momentum to the turbulent transport of a passive scalar, mathematically expressed as $Sc_T = \frac{\nu_T}{D_T}$ where ν_T is the eddy viscosity and D_T is the turbulent mass diffusivity.

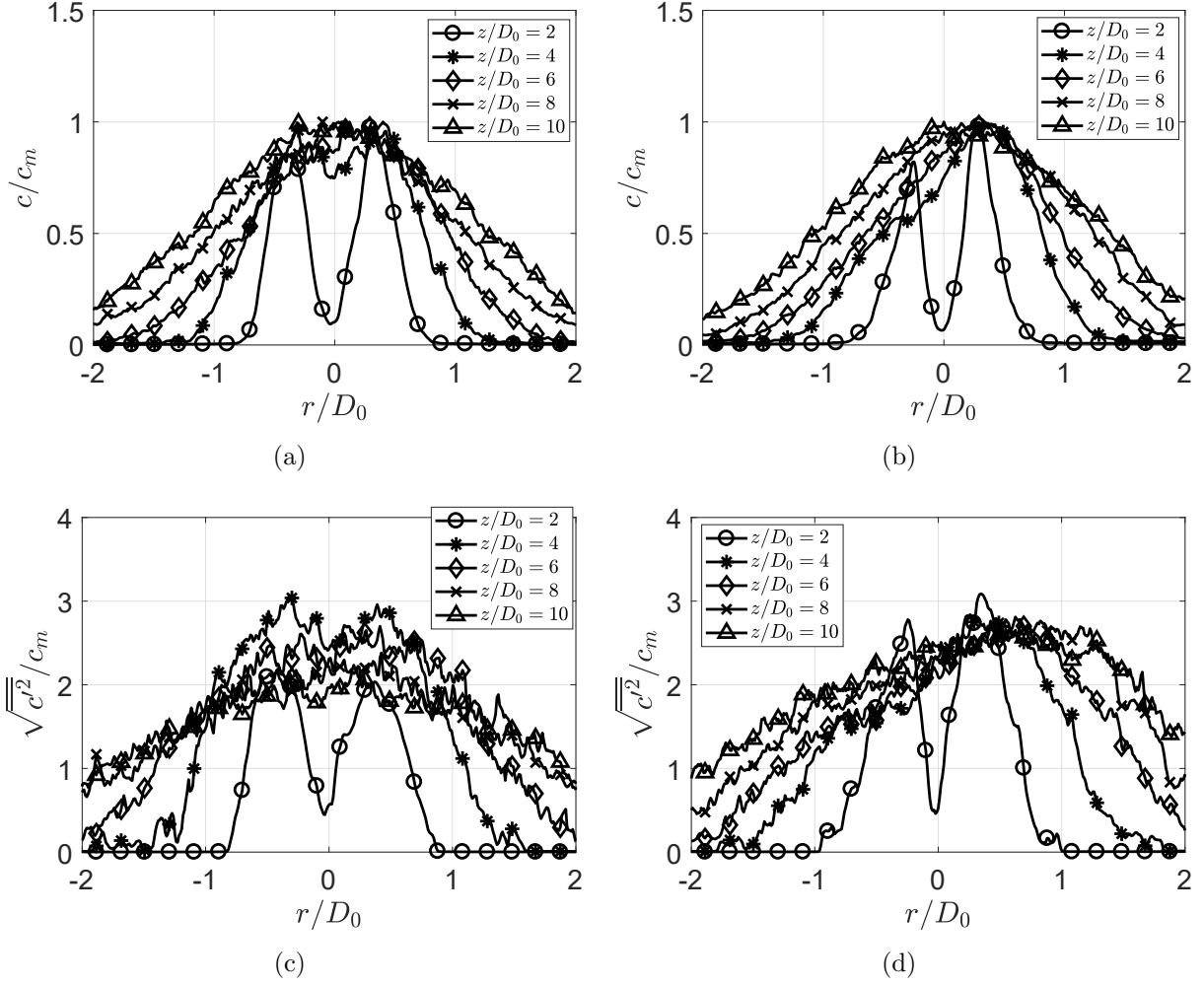


Figure 4.10: Radial concentration profiles (panels a and b) and radial standard deviation profiles (panels c and d) for experiments A3 (left) and D3 (right) at successive downstream distances, i.e. $z/D_0 = 2, 4, 6, 8$ and 10 . The radial mean concentration and standard deviation are non-dimensionalized by the corresponding maximum radial mean concentration, c_m .

- (i) Entrainment starts from the source. To wit, β and γ are non-zero everywhere in the flow development zone.
- (ii) Entrainment is negligible close to the source and begins, in earnest, only at some larger elevation. In what follows, we shall consider this elevation to be $Z_p/2$ respecting the fact that some mixing must occur within the potential core, e.g. between the outer plume and the ambient.

In the analysis to follow, we consider both of the above possibilities, which respectively yield lower (β_{lb} and γ_{lb}) and upper bounds (β_{ub} and γ_{ub}) for the entrainment coefficients. We thereby seek the unique combination of β and γ that minimizes the misfit function, Φ . To this end, β and γ are respectively varied between 0.01 and 0.3, both with the same increment i.e. 0.01.

The methodology described in the previous paragraph (and, more specifically, the notion

of minimizing a misfit function defined as in equation (4.53)) was tested with reference to a uniform plume. As described in more detail in section 4.11, this approach yielded estimates for the entrainment coefficient that were in good agreement with the results of previous experimental investigations.

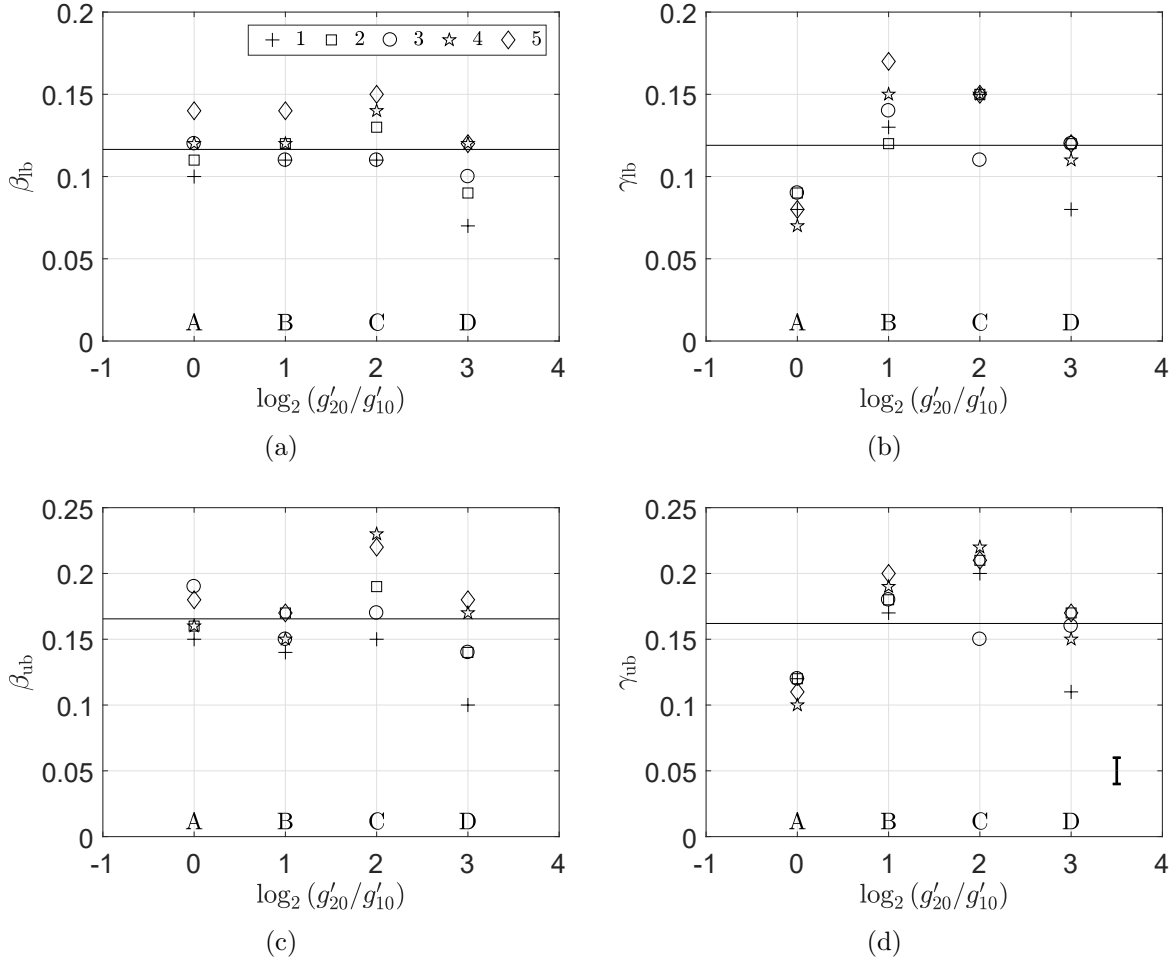


Figure 4.11: Φ -minimizing values of β_{lb} (panel a), γ_{lb} (panel b), β_{ub} (panel c) and γ_{ub} (panel d) for experiments A, B, C and D. The legend indicates the number within each experimental category, e.g. A1, A2, A3, A4 and A5. The different symbols thereby show the effect of changing the source velocities of the inner vs. the outer plume. The horizontal lines denote the mean entrainment coefficients in each panel. A representative error bar is shown in panel d.

For each of the experiments reported in table 4.1, the Φ -minimizing set of entrainment coefficients are plotted in figure 4.11. Consistent with (4.53), these entrainment coefficients are mean values and do not depend on height or, by extension, the local flux-balance parameter Γ . Although the data of figure 4.11 show some scatter, not altogether surprising given the turbulent nature of the flow, the entrainment coefficients generally fall within a reasonable range. Figure 4.11 presents lower and upper bounds for β and γ as a function of g'_{20}/g'_{10} and U_{20}/U_{10} (represented by different symbols). Measured values for β show little variation with g'_{20}/g'_{10} . Although β generally increases as U_{20}/U_{10} decreases, the effect is comparatively minor, particularly when considering the scatter within the data set. Because

similar comments apply for γ , we consider, as a first approximation, average values for the entrainment coefficients, which are indicated in the four panels of figure 4.11 by the thin horizontal lines. Specifically, we obtain $\beta_{\text{lb}} = \gamma_{\text{lb}} \approx 0.12$ and $\beta_{\text{ub}} = \gamma_{\text{ub}} \approx 0.16$. In the theory vs. experiment comparisons to follow, we shall split the difference between these lower and upper bounds and thereby select $\beta = \gamma = 0.14$.

4.5.2 Centerline and radial concentration profiles

With particular values for β and γ to hand, comparisons can now be made with respect to the mean centerline and radial concentration profiles for theory vs. experiment. The centerline concentration profiles for experiments A1, A5, B1, B5, C1, C5, D1 and D5 are shown in the eight panels in figure 4.12. For any of the experimental results, the centerline concentration at the source is small but non-zero; the concentration decreases slightly before progressively increasing to a maximum value, which is often realized at about $z/D_0 \simeq 4$. This non-monotonic variation of the concentration through the flow development zone is most likely due to laser light reflection near the nozzle exit and/or some premixing of the inner and outer plume fluid within the nozzle. In other words, the decrease of centerline concentration immediately upon discharge is unlikely to be a real physical effect. By contrast, the theoretical solution shows a sudden jump from zero to the point of maximum centerline concentration. To this end, note that the theoretical centerline concentration initially follows the inner plume concentration (the solid blue curve) but then adjusts to the uniform plume concentration (the solid red curve) when the inner plume disappears. A generally robust match of the centerline concentration profiles between theory and experiment is observed in figure 4.12. Specifically, the location at which the maximum centerline concentration occurs in theory and experiment agree to reasonable accuracy. The counterpart radial concentration profiles at successive downstream distances are shown in figure 4.13. Here again, generally good agreement can be seen from the radial peaks and troughs in theory vs. experiment. Notice, however, that the unimodal profile observed in experiments does not always correspond to a single top-hat profile in theory – see the black curves in figures 4.13e and 4.13g. In these cases, the outer plumes possess significantly more momentum and buoyancy than do the inner plumes, thus theory predicts that inner plumes may be cut off relatively quickly. Whereas comparable behavior is not seen in the experimental profiles, this is most likely due to an elongated flow development zone for the outer plume, which is a consequence of the greater momentum at the source. By contrast, and with a smaller outer plume source momentum, figures 4.13 b,d,f,h show that the double peak profiles in experiments match (in a qualitative sense) the bimodal profiles predicted theoretically. Shifting to a quantitative comparison, the theoretical peaks of figure 4.13 d match closely with the counterpart experimental peaks when $z/D_0 = 2$. In other instances, figure 4.13 b most especially, there is a larger difference between the black solid and dashed curves. For these cases, there is a greater deviation between the experiment-specific value for γ vs. the average value determined for all 20 experiments from table 4.1. To this end, recall from figures 4.11 b,d that the γ values measured in experiments of categories A and B respectively lie below and above the mean values indicated, in figure 4.11, by the horizontal solid lines.

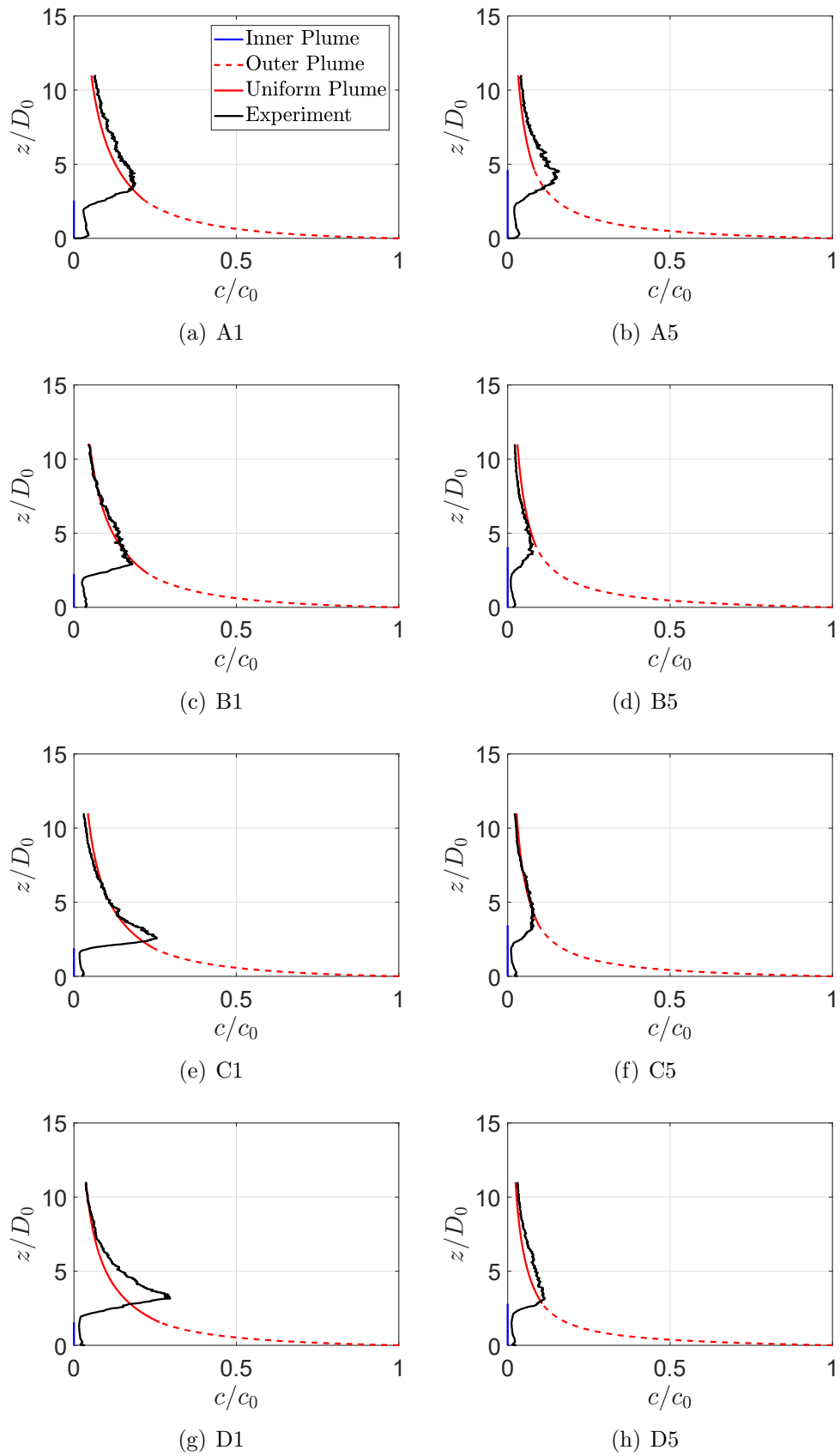


Figure 4.12: [Color] Comparison of the centerline concentration profiles in experiments A1, A5, B1, B5, C1, C5, D1 and D5.

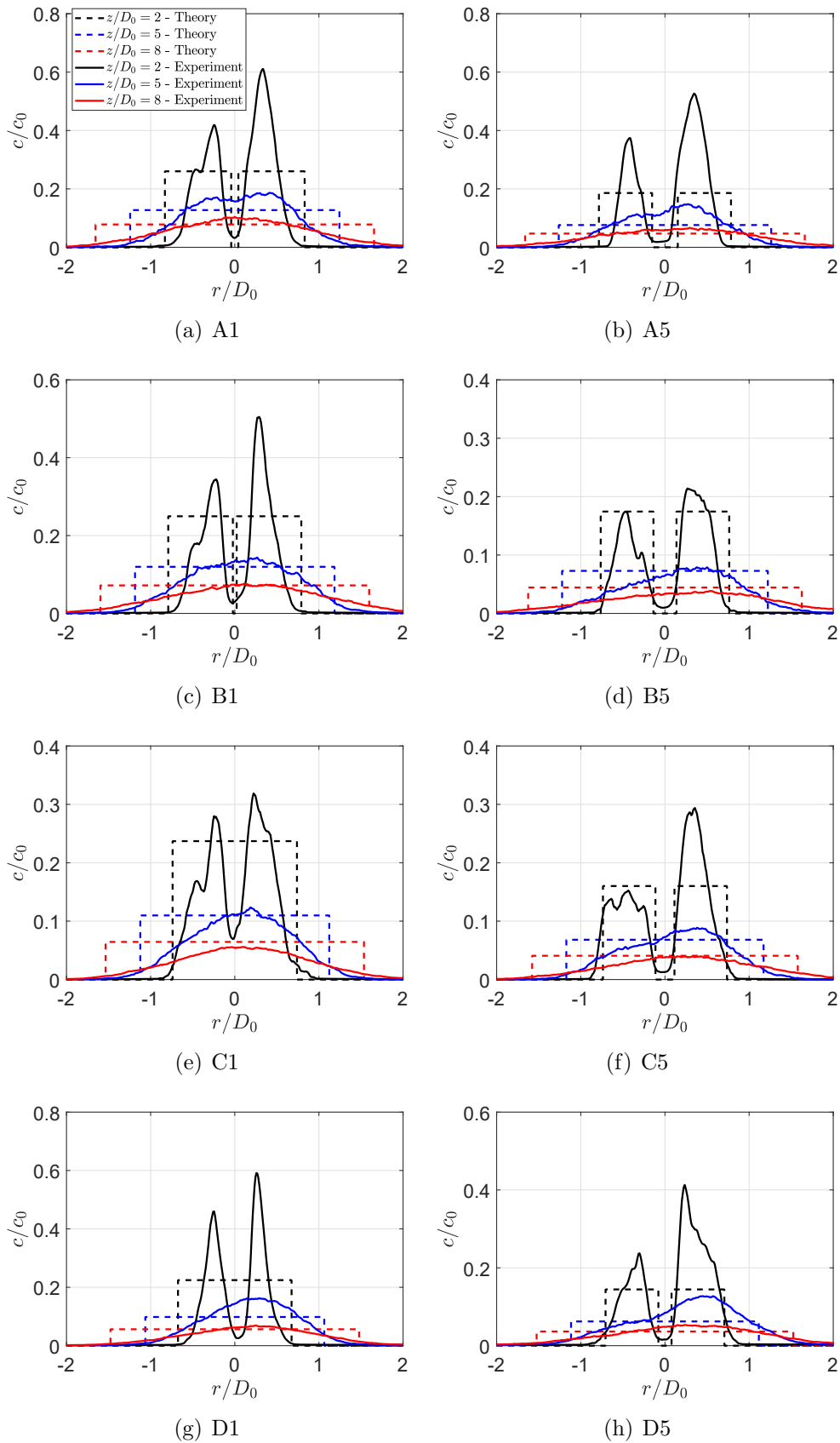


Figure 4.13: [Color] Comparison of the radial concentration profiles in experiments A1, A5, B1, B5, C1, C5, D1 and D5 with the same sequence as in figure 4.12.

4.6 Applications to cooling tower plume abatement

To illustrate a possible application of the above concepts and our experimentally-augmented analytical model more specifically, we illustrate below how knowledge of coaxial plumes may inform cooling tower design decisions. Of particular interest are hybrid wet/dry crossflow cooling towers, which make use of both latent (wet) and sensible (dry) heat transfer. In the wet section, the hot water is cooled mainly by evaporation, thus the crossflowing air gains moisture and becomes more humid (wet air). In the dry section, the hot water flows within heat exchangers (e.g. of the finned-tube variety) across which the incoming air is heated without adding moisture (dry air). The wet and dry airstreams join and mix in the plenum chamber as shown in figure 4.14. Although the plenum chamber allows for some mixing, residence times are short and the degree of mixing varies by design. When the plenum chamber is relatively tall so that vigorous mixing takes place, a uniform plume may be assumed – see figure 4.14 a. On the other hand, if the plenum chamber is short (or altogether absent – see e.g. Houx Jr *et al.*, 1978), a coaxial plume of the type indicated in figure 4.14 b will result. Compared to a uniform plume regime, the potential advantage of using a coaxial plume structure is that visible plume abatement can be realized with little plenum chamber mixing. Rather, the mixing occurs above the plenum chamber and fan via turbulent entrainment and so necessitates less fan power than in the case where the wet and dry airstreams are thoroughly homogenized within the plenum chamber. Li *et al.* (2018) studied the dynamics of a coaxial wet/dry plume in a stationary ambient, however, the optimal values for the entrainment coefficients were left unspecified in their (purely analytical) study. The present work resolves this ambiguity thus allowing more reliable predictions than those summarized in Li *et al.* (2018).

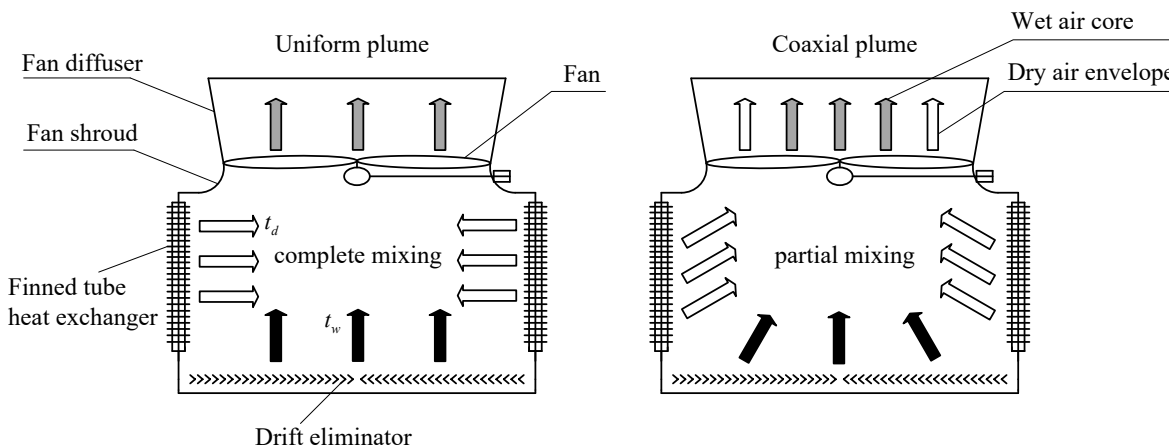


Figure 4.14: Uniform and coaxial plumes in the cooling tower context. The black arrows (above the drift eliminator) and white arrows (close to the heat exchangers) denote the hot, humid air from the wet section and the warm, dry air from the dry section, respectively. The light gray arrows at the fan exit denote the air mixture formed by complete or partial mixing within the plenum chamber. The variables t_w and t_d denote the respective temperatures of the wet and dry airstreams. We consider $z = 0$ as coinciding with the top of the fan diffuser.

For the cases illustrated schematically in figure 4.14, we suppose that the cooling tower is located close to some critical piece of infrastructure (e.g. an airport runway) and so specify

Table 4.2: Environmental and operating conditions for the cooling tower example considered in section 4.6.

Variable name and symbol	Value (unit)
Ambient pressure at the top of the cooling tower, P_a	101325 (Pa)
Ambient temperature, t_a	5 ($^{\circ}\text{C}$)
Ambient relative humidity, RH_a	40 (%)
Wet cooling temperature, t_w	30 ($^{\circ}\text{C}$)
Dry cooling temperature, t_d	15 ($^{\circ}\text{C}$)
Stack exit velocity, U_0	6 (m/s)
Stack exit area, A_0	71.3 (m^2)
Number of cooling tower cells	1

the maximum relative humidity (RH) as 90%, this according to the uniform plume strategy as sketched in figure 4.14 a. From RH_{\max} , we can determine the ratio, $\frac{\dot{m}_d}{\dot{m}_w}$, of the dry to wet air mass flow rates using psychrometric principles and the dry cooling temperature, t_d . This temperature and other cooling tower specifications are listed in table 4.2. With $t_d = 15^{\circ}\text{C}$, $\frac{\dot{m}_d}{\dot{m}_w} = 0.889$. We assume that only 5% of the dry air is mixed into the wet air within the plenum chamber. Setting $\beta = \gamma = 0.14$, we can predict the relative humidity, excess temperature, radius and vertical velocity of the associated atmospheric coaxial plume – see figure 4.15. For the combination of parameters examined here, figures 4.15 a,c reveal that a visible plume will form but only in the shrinking inner plume and over a limited range of heights.

A benefit associated with coaxial plumes is that the vertical velocity (figure 4.15 d) of the inner plume is expected to be larger than that of the corresponding uniform plume. This larger velocity gives a better likelihood of avoiding the immediate deposition of drift, the small water droplets that may be carried over from the cooling tower spray zone. Drift deposition is associated with numerous negative effects among them enhanced corrosion of, or ice accumulation on, industrial infrastructure and the possible spread of the Legionella bacteria (Lucas *et al.*, 2010). A potential disadvantage of using a coaxial plume structure is that, under strong crosswinds, the coaxial structure may be broken and the hot, humid air comprising the inner plume may suddenly become exposed to the relatively cold ambient air leading to rapid condensation. On the other hand, wind tends to enhance mixing and significantly narrow the visible plume region (cf. figure 11 of Takata *et al.*, 2016).

Although latent heat release associated with condensation can increase the buoyancy in moist plumes, this contribution is comparatively modest (cf. Briggs 1975; Janicke & Janicke 2001). This is the basis on which we use the laboratory-derived values $\beta = \gamma = 0.14$ for the above example. There is, of course, a more fundamental assumption with this association, i.e. that once the flow is turbulent, the entrainment values very little with the Reynolds number, Re . To this end, $\text{Re}_{\text{expt}} = \mathcal{O}(10^2)$ vs. the case of an industrial-scale cooling tower for which $\text{Re} = \mathcal{O}(10^7)$ (Takata *et al.*, 1996). By way of comparison, the MTT56 model, originally verified using small-scale laboratory experiments at relatively low Re , has been successfully applied at much larger geophysical scales such as volcanic plumes (Woods, 2010) and subglacial plumes (Hewitt, 2020). Moreover, and although MTT56 strictly assumes that the flow is fully developed, self-similar and that the vertical extent is much greater than the

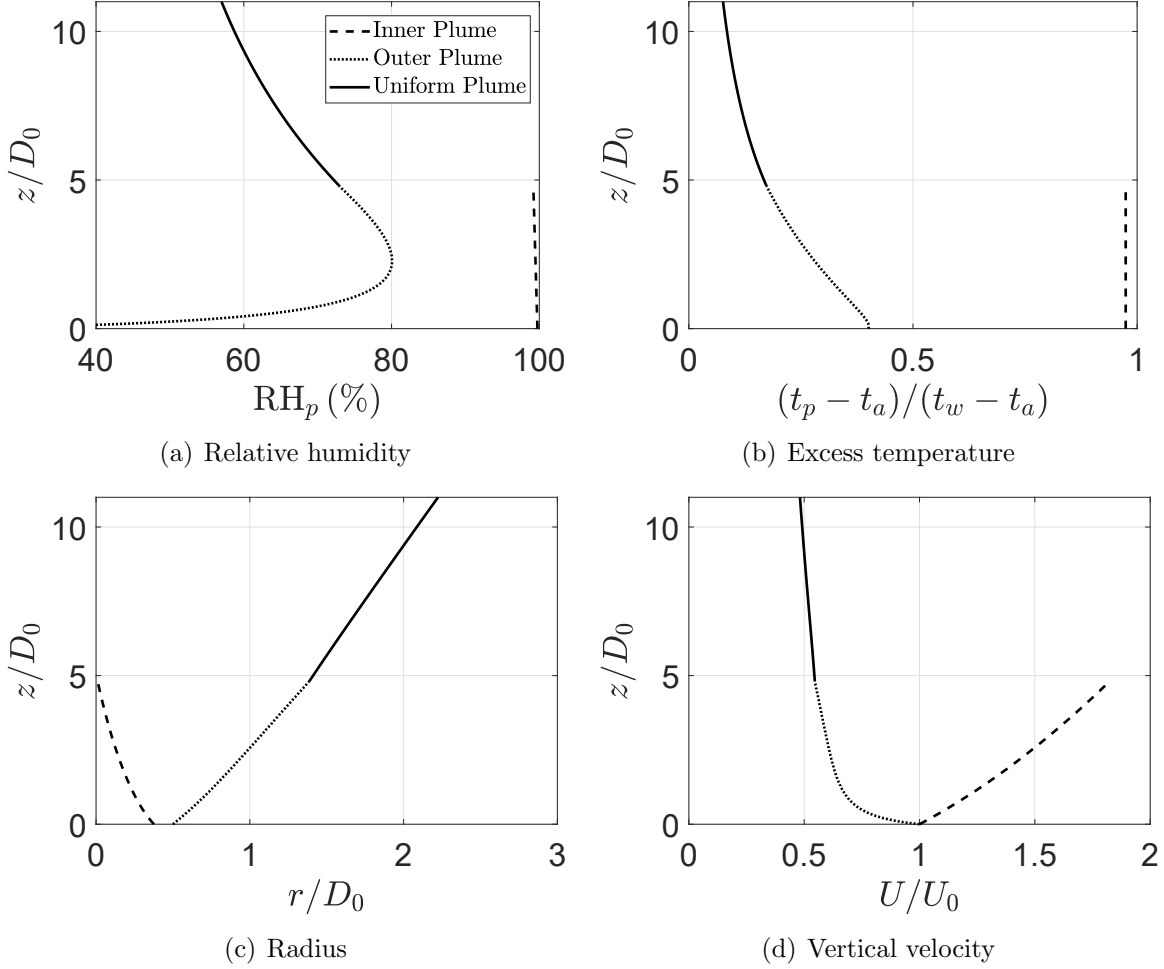


Figure 4.15: Theoretical prediction of the relative humidity, excess temperature, radius and vertical velocity of the inner and outer plumes for the example considered in section 4.6. Note that the inner plume disappears when $z/D_0 = 4.8$.

lateral extent, it can also generate realistic predictions of the near-field region in case of turbulent fountains (cf. BK00). Given these auspicious records and the similarities between our formulation and that of MTT56, we argue that $\beta = \gamma = 0.14$ should provide some reasonable estimates even in the case of coaxial plumes of much larger scale.

4.7 Conclusions

The current manuscript presents theoretical and experimental studies of coaxial plumes in a stationary ambient. In the theoretical modeling, we implement Morton’s entrainment assumption for coaxial jets and McDougall’s body force formulations (BFI and BFII). The momentum conservation equations assuming BFI and BFII are formulated, which evaluate the buoyancy-driven acceleration of the inner plume (1) using the ambient fluid (0) and the outer plume (2) as the respective reference fluids.

To validate the theoretical model and to determine the value of the entrainment coefficients, complementary laboratory experiments were performed using PLIF. Rhodamine 6G

is seeded in the outer plume to allow flow visualization and quantification of the passive scalar concentration as a function of the radial (r) and vertical (z) coordinates. In the PLIF experiments (figure 4.6), vortex roll-up is evident with an increase in vortex diameter in the downstream direction. Quantitatively, two characteristic length scales, the inner potential core height and the cut-off height of the inner plume, are defined to describe the downstream evolution of a coaxial plume. The measured mean centerline concentration in the relative far field approaches the “-5/3” law anticipated by Papanicolaou & List (1987, 1988). The radial concentration and standard deviation profiles in the experiments show bimodal distributions close to the source and unimodal distributions for greater downstream distances.

A pixel-by-pixel comparison between the passive scalar concentration maps in theory and experiment is conducted for determining the optimal values of the entrainment coefficients β and γ , which are defined implicitly in figure 4.1. The vertical extent for the comparison is between the inner potential core height and 11 nozzle diameters in the downstream direction. Strictly-speaking, the plume dynamics are somewhat different than what is anticipated over the height of the flow development zone. We therefore propose that, in the context of the theory, turbulent entrainment occurs starting from either the source or half of the potential core height. These two regimes produce the respective lower and upper bounds for β and γ . Results from this process of comparison are presented in figure 4.11 on which basis, we select $\beta = \gamma = 0.14$, which represents the arithmetic average of the lower and upper bounds.

In section 4.6, we explore the application of coaxial plume theory to visible plume abatement in the cooling tower context. For realistic environmental and cooling tower operating conditions, figure 4.15 shows that fog appears only in the shrinking inner plume and then over a limited span of height and breadth.

The main weakness in the experimental study is the single value of the ratio of the inner to outer source diameter, D_{10}/D_{20} . The effect of varying D_{10}/D_{20} is left for future study. Several other topics of possible interest can be proposed. For instance, different types of flow may occur considering a negatively buoyant source. Unclear, for instance, is what will happen if the coflowing inner and outer flows have opposite buoyancies so that $F_{10} + F_{20} = 0$, say. The outer plume will behave like a turbulent fountain if it is negatively buoyant at the source; if this fountain is sufficiently weak, it may be possible for the inner plume to avoid being cut off. Such a coaxial flow regime may arise in flexible building ventilation types (displacement ventilation and mixing ventilation or a hybrid mode ventilation) – see e.g. Lin & Linden (2005). Another special case of a coaxial plume is the annular plume for which there is no forced inner plume flow. Rather the inner flow is due solely to the action of the outer plume (Padhani *et al.*, 2018). Finally, the behavior of coaxial plumes in a windy and/or stratified environment is also of great interest because wind tends to enhance turbulent mixing whereas ambient stratification tends to suppress it.

4.8 Appendix A: BFI and BFII formulations

In this section, we use a control volume method to derive the momentum conservation equations assuming the BFI and BFII formulations. By choosing a control volume of height dz around the inner flow, and assuming that the pressure is hydrostatic throughout the

coaxial plumes i.e. a BFI formulation, conservation of momentum reads

$$\left[\pi\rho_1r_1^2U_1^2\right]_{z+dz} - \left[\pi\rho_1r_1^2U_1^2\right]_z = 2\pi\rho_2r_1\omega_\alpha w_2 dz - 2\pi\rho_1r_1\omega_\beta w_1 dz + \pi\rho_a r_1^2 g'_1 dz, \quad (4.54)$$

where the first and second terms on the left-hand side denote the momentum fluxes exiting and entering the control volume, the first term on the right-hand side denotes the outer plume momentum flux entrained into the inner plume which is assumed to be zero, the second term on the right-hand side denotes the inner plume momentum flux entrained into the outer plume, and the third term on the right-hand side denotes the buoyancy force acting on the inner plume. For Boussinesq plumes, (4.54) can be simplified as

$$\frac{dM_1}{dz} = -2\pi r_1 \omega_\beta w_1 + \pi r_1^2 g'_1. \quad (4.55)$$

The momentum equation for the outer plume can be derived in a similar fashion.

For a BFII formulation, we switch to a non-inertial frame of reference, i.e. that of the outer plume, which moves with a vertical acceleration $U_2 \frac{dU_2}{dz}$. With this new frame of reference, the reduced gravity of the inner plume is given by

$$g \frac{\rho_2 - \rho_1}{\rho_a} = g'_1 - g'_2, \quad (4.56)$$

thus the momentum equation for the inner plume reads

$$\frac{dM_1}{dz} = \pi r_1^2 \left(g'_1 - g'_2 + U_2 \frac{dU_2}{dz} \right) - 2\pi r_1 \omega_\beta w_1, \quad (4.57)$$

where the positive sign for the acceleration term i.e. $U_2 \frac{dU_2}{dz}$ should not be confused with the counterpart negative sign in (2.7) of Bloomfield & Kerr (2000). Bloomfield and Kerr's result describes the upflow in a turbulent fountain with the frame of reference fixed to the downward flowing counterflow.

4.9 Appendix B: Post-processing of PLIF images

Once collected, PLIF images were corrected for various influences including camera dark current noise (the influence of background light can be neglected because the laboratory was dark except for the flashing laser), the pulse-to-pulse variation of the laser intensity, spatial inhomogeneities of the laser sheet, attenuation of the laser sheet due to absorption effects, image distortion and a vignetting effect. To these ends, we followed the procedures outlined in LaVision's product manual "LIF in liquid fluids" (LaVision, 2011). First we built the laser set-up and camera set-up to ensure that the laser light sheet (about 1.5 mm in thickness) was perpendicular to the camera view. Then a length scale calibration was conducted using a plate having a series of regularly-spaced holes, which allowed us to easily convert between pixel and world coordinates. Thereafter, we recorded in sequence the background images, sheet images, concentration calibration images and then finally experimental images. For the concentration calibration images, we recorded images for different Rhodamine 6G concentrations i.e. 0 (fresh water) and 20% of maximum where the maximum concentration was typically set to be $c_0 = 0.30$ mg/L.

The camera dark noise was corrected by subtracting the average of 300 background images with the camera lens closed. Image distortions due to parallax were corrected by a perspective calibration that, in turn, referenced the aforementioned grid consisting of uniformly spaced round holes. Spatial inhomogeneities of the laser sheet were corrected by taking so-called “sheet” images using a thin calibration tank that contained $c_{\text{cal}} = 0.06 \text{ mg/L}$ of Rhodamine 6G. Built-in functions in LaVision’s DaVis 8.1 were employed for each of the above three calibration steps.

The pulse-to-pulse variation in laser energy was quantified by measuring the variation of the mean intensity within a mask in the calibration images, which were recorded within a tank having a homogeneous mixture of Rhodamine 6G. A plot showing the representative fluctuation in intensity is illustrated in figure 4.16. The maximum variation normalized by the average intensity over the time period of interest is approximately 5%.

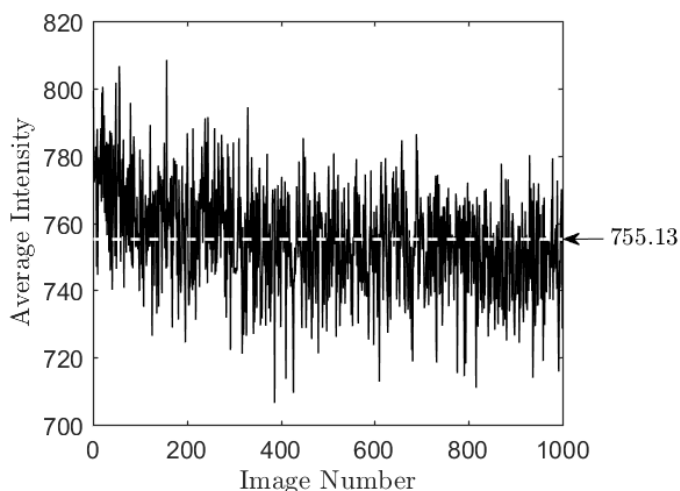


Figure 4.16: Variation of the mean pixel intensity within a mask from 1000 calibration images taken in a duration of approximately 8.5 mins. The dashed white line denotes the time-averaged intensity over the time interval in question.

The Beer-Lambert law is used to estimate the attenuation of the laser power flux (I) over a length Δx within a uniform concentration (c) and is expressed mathematically by (Tian & Roberts, 2003)

$$I(\Delta x) = I \exp(-\epsilon c \Delta x), \quad (4.58)$$

where ϵ is the absorption coefficient. The difference between the triangular laser sheet and the rectangular camera view makes the correction complicated (see the discussions in Smith, 1996 and Getsinger, 2012), however, we expect that to be a minor effect owing to the slender geometry of the coaxial plume. To derive a more precise attenuation estimate, we made reference to calibration images collected by inserting a thin (6 cm by 6 cm cross section) tank into the much larger flow tank – see figure 4.17. By measuring the intensity of laser light at the right- and left-hand sides of the indicated mask, the right- and left-hand side intensities were related to the corresponding concentrations, using the following equation derived from (4.58):

$$\frac{I_r}{I_l} = \frac{c_r}{c_l} = \exp(-\epsilon c \Delta x). \quad (4.59)$$

Here the subscripts r and l denote the right- and left-hand sides of the thin mask in figure 4.17. The above equation assumes that $c_l \simeq c$. Applying exponential curve fitting (see figure 4.18 a), it was estimated that the absorption coefficient was approximately $5 \text{ m}^{-1}(\text{mg/L})^{-1}$, which is consistent with the Rhodamine 6G value of $4 \pm 1 \text{ m}^{-1}(\text{mg/L})^{-1}$ reported in Vanderwel & Tavoularis (2014). Thus the mean attenuation over a laser pathline of length 0.1 m in a Rhodamine 6G solution that had concentration of 0.06 mg/L was approximately 3.0%. Note also that the maximum attenuation occurred at the plume source because attenuation is determined by the scale and intensity of concentration filaments (Crimaldi & Koseff, 2001). Replacing Δx and c in (4.58) with $D_{20} - D_{10}$ and $c_s = 0.30 \text{ mg/L}$, respectively, the maximum attenuation that occurred at the source was estimated as 0.52%. Figure 4.18 b confirmed that the laser energy was below the saturation energy of Rhodamine 6G so that a linear relationship between the intensity and dye concentration could be safely assumed.

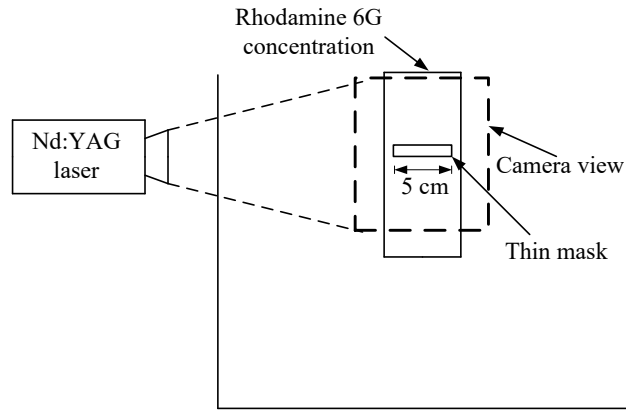


Figure 4.17: Schematic of the calibration tank that contains a homogeneous concentration of Rhodamine 6G. The dimensions of the tank were $6 \text{ cm} \times 6 \text{ cm} \times 20 \text{ cm}$ (length \times width \times height). The incremental dye concentrations were 0, 0.01, 0.02, 0.03, 0.04, 0.05, 0.06, 0.07, 0.08, 0.09, 0.10, 0.12, 0.14, 0.16, 0.18, 0.20, 0.22, 0.24, 0.26, 0.28 and 0.30 mg/L.

Although refractive index matching was not performed, we note that no shadows or blurs in the experimental images was observed or reported in our records of the dyed experiments. We also note that the range for comparison of theory vs. experiment went beyond the near source potential core region, where the density contrast between the plume and ambient (and thus the refractive index difference) was significant.

4.10 Appendix C: Complimentary data to table 4.1

The source Reynolds number and flux-balance parameter of the outer plume are defined, respectively, as

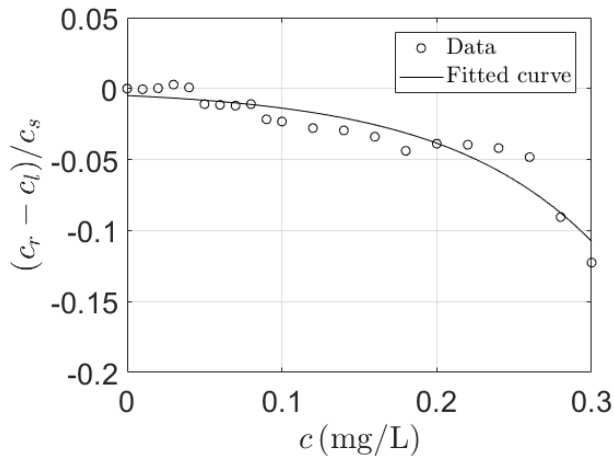
$$\text{Re}_{20} = \frac{U_{20} (D_{10} + D_{20})}{2\nu}, \quad (4.60)$$

$$\Gamma_{20} = \frac{5}{8\alpha_p \pi^{1/2}} \frac{Q_{20}^2 F_{20}}{M_{20}^{5/2}}. \quad (4.61)$$

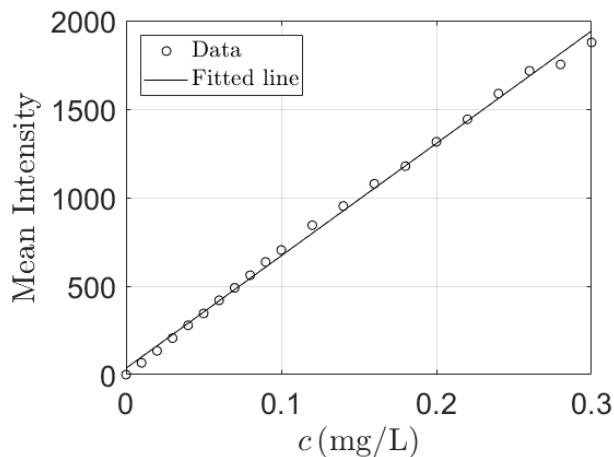
The complementary data to table 4.1 are given in table 4.3.

Table 4.3: Source Reynolds number, flux-balance parameter, inner potential core height, cut-off height of the inner plume and optimal entrainment coefficients (β and γ) for experimental categories A, B, C and D.

Experiment	Re_{10}, Re_{20}	Γ_{10}, Γ_{20}	Z_p	Z_c	β_{lb}, β_{ub}	γ_{lb}, γ_{ub}
A1	352, 755	1.85, 0.55	2.0	5.4	0.10, 0.15	0.08, 0.12
A2	411, 680	1.36, 0.68	1.9	4.8	0.11, 0.16	0.09, 0.12
A3	470, 604	1.04, 0.86	1.8	4.3	0.12, 0.19	0.09, 0.12
A4	529, 529	0.82, 1.12	1.8	4.4	0.12, 0.16	0.07, 0.10
A5	587, 453	0.66, 1.52	1.9	4.2	0.14, 0.18	0.08, 0.11
B1	352, 755	1.81, 1.00	1.7	3.8	0.11, 0.14	0.13, 0.17
B2	411, 680	1.33, 1.23	1.7	4.0	0.12, 0.17	0.12, 0.18
B3	470, 604	1.02, 1.56	1.7	4.4	0.11, 0.15	0.14, 0.18
B4	529, 529	0.81, 2.03	1.7	4.4	0.12, 0.15	0.15, 0.19
B5	587, 453	0.65, 2.77	1.7	4.1	0.14, 0.17	0.17, 0.20
C1	352, 755	1.83, 1.90	1.5	2.7	0.11, 0.15	0.15, 0.20
C2	411, 680	1.34, 2.35	1.5	2.8	0.13, 0.19	0.15, 0.21
C3	470, 604	1.03, 2.97	1.7	4.0	0.11, 0.17	0.11, 0.15
C4	529, 529	0.81, 3.88	1.7	3.9	0.14, 0.23	0.15, 0.22
C5	587, 453	0.66, 5.28	1.9	4.1	0.15, 0.22	0.15, 0.21
D1	352, 755	1.83, 3.66	1.8	3.2	0.07, 0.10	0.08, 0.11
D2	411, 680	1.34, 4.52	1.6	3.5	0.09, 0.14	0.12, 0.17
D3	470, 604	1.02, 5.72	1.6	3.4	0.10, 0.14	0.12, 0.16
D4	529, 529	0.81, 7.47	1.7	3.7	0.12, 0.17	0.11, 0.15
D5	587, 453	0.66, 10.17	1.9	3.9	0.12, 0.18	0.12, 0.17



(a) Attenuation as a function of Rhodamine 6G concentration. The maximum concentration is $c_s = 0.30$ mg/L.



(b) Mean intensity of the thin mask in the attenuation calibration images.

Figure 4.18: Laser light attenuation in the calibration tank of figure 4.17.

4.11 Appendix D: Pixel-by-pixel comparison for uniform plumes

To confirm that the entrainment coefficients obtained using the pixel-by-pixel comparison methodology are reasonable estimates, we performed PLIF experiments of uniform plumes for validation. Relevant source conditions are specified in table 4.4. A special nozzle was used to excite a turbulent plume near the source, i.e. that originally designed by Dr. Paul Cooper – see Hunt & Kaye (2001). For each experimental category, i.e. U1 to U4, we obtain the mean concentration image by averaging 400 snapshot images collected over a period of 204s. We specified the lateral and vertical ranges for the pixel-by-pixel comparison as

$-5 \leq r/D_0 \leq 5$ and $0 \leq z/D_0 \leq 30$, respectively³. To compute the misfit function, we allowed the uniform plume entrainment coefficient, α_u , to vary between 0.01 and 0.2 with an increment of 0.001.

Table 4.4: Source conditions for the uniform plume experiments. The nozzle diameter was $D_0 = 0.4$ cm. The ambient fresh water density was measured as $\rho_a = 0.9983$ g/cm³.

Experiment	ρ_0 (g/cm ³)	Q_0 (cm ³ /s)	Re_0	Γ_0	Z_p	$L_j (= l_j/D_0)$
U1	1.0201	1.17	371.10	0.26	1.1±0.05	3.00
U2		1.00	317.23	0.36	1.2±0.05	2.56
U3		0.83	264.36	0.52	1.8±0.05	2.13
U4		0.67	211.49	0.81	2.0±0.05	1.71

The optimal entrainment coefficient as a function of Γ_0 is shown in figure 4.19. For the vertical range of interest, all the optimal entrainment coefficients fall within the range ($0.095 \leq \alpha_u \leq 0.15$) reported in previous experimental studies – see table 3 of van Reeuwijk & Craske (2015). Moreover, the average entrainment coefficient is 0.106, which is close to $\alpha_u = 0.11 \pm 0.01$ as determined recently by Burrige *et al.* (2017). Note that figure 4.19 incorporates a constant maximum vertical length scale, i.e. $Z_{\max} \equiv z_{\max}/D_0 = 30$. To gain more insight into how α_u varies with this maximum height of the mask image, we shall consider a range of Z_{\max} . Measured values of α_u vs. Z_{\max} are illustrated in figure 4.20, which indicates that α_u begins to approach a constant value for $Z_{\max} > 20$. The relatively low α_u observed for small Z_{\max} (if not too close to the source) is most likely a reflection of entrainment suppression in the flow development zone.

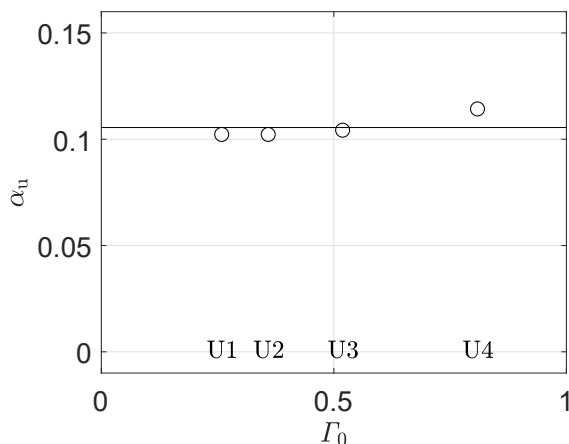


Figure 4.19: Φ -minimizing entrainment coefficient as a function of Γ_0 . The horizontal line denotes the average entrainment coefficient of 0.106. Error bars are of a size comparable to the marker symbols and are therefore omitted.

³We found that replacing $0 \leq z/D_0 \leq 30$ with $Z_p \leq z/D_0 \leq 30$ only slightly increases the calibrated entrainment coefficient α_u .

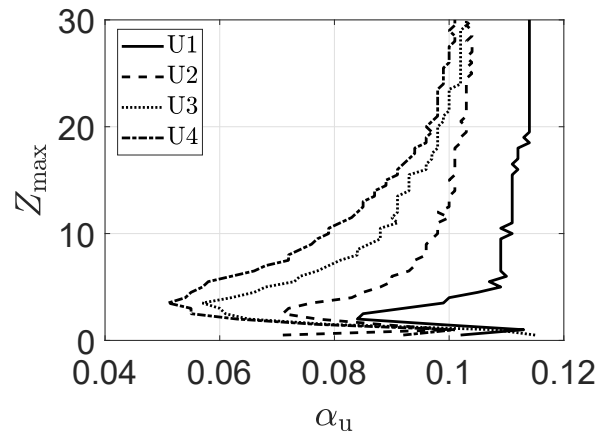


Figure 4.20: Φ -minimizing entrainment coefficient as a function of varying Z_{\max} .

Chapter 5

Coaxial plumes in a windy ambient with applications to cooling towers

5.1 Abstract

The dynamics of coaxial plumes that consist of an inner, humid plume and an outer, less humid plume has been studied analytically, however, only for the case of a stationary ambient. The present study extends the previous theoretical model by incorporating the effect of a windy ambient for both single and multiple cooling tower cell cases. Of particular concern is the choice of an appropriate entrainment assumption associated with wind shear and the modeling of entrainment between the inner and outer plumes. Two entrainment formulations are proposed regarding the entrainment from the inner to the outer plume. Meanwhile, two body force formulations for the inner plume are discussed. In terms of plume abatement, a visible plume length, defined on the basis of the predicted plume trajectory and relative humidity, is used to evaluate the severity of visible plumes under different operating and environmental conditions. By extension, and with fixed wind speed and cooling tower operating conditions, the parameter range of environmental conditions where fog is restricted to the inner plume is determined.

5.2 Introduction

The behavior of buoyant plumes in a windy ambient has been studied for more than half a century. Early attempts to model the plume rise and dilution have made good use of dimensional analysis. Batchelor (1954) pioneered the use of dimensional analysis in buoyant convection, this on the basis of assuming self-similarity. Whereas Batchelor only considered convection in a stationary ambient, Scorer (1958*b*) studied buoyant plumes in a laminar, neutral crosswind. Later Briggs (1965) generalized the dimensional analysis to include the effect of atmospheric stability. Specifically, and for a neutral crosswind, Briggs (1965) argued that the dominant terms are the wind speed, U_a , and the buoyancy flux¹, F . Thus on

¹According to Batchelor (1954), the buoyancy flux is defined as $F = \frac{g Q_H}{c_p \rho_0 T_0}$ where Q_H is the heat flux of the plume, c_p is the specific heat at constant pressure, g is the gravitational acceleration, ρ_0 is a reference density and T_0 is a reference absolute temperature.

dimensional grounds, the bent-over plume rise height was argued to satisfy

$$z \propto F^{1/3} U_a^{-1} x^{2/3}, \quad (5.1)$$

where x is the downwind distance. Equation (5.1) is commonly termed as Briggs’s “two thirds” law. The two thirds law was later modified and generalized in Briggs (1984) and Davidson (1989) to include the additional effects of source momentum flux and finite source size.

Davidson (1989) pointed out that a deficiency of analytical models, such as Slawson & Csanady (1971) and Briggs (1984), is their inability to accurately predict both the plume trajectory and dilution rate. This deficiency is, however, avoided in the more advanced theoretical models of Weil (1974), Winiarski & Frick (1976), Wu & Koh (1978) and Schatzmann & Policastro (1984). In general, the main differences between various integral models lie in the forms of the entrainment assumption and of the force due to dynamic pressure in the momentum equation. Regarding entrainment, most models incorporate one or two empirical coefficients with a few exceptions that consider four empirical coefficients – see Schatzmann & Policastro (1984) and Jirka (2004). Meanwhile, a force due to dynamic pressure may be added either via an added mass term or a drag term. The added mass is, according to Briggs (1975), presumed to both surround and exert a pressure on the plume body. By contrast, the drag term is expressed in a form similar to the drag experienced by a rigid body in crossflow and is adopted in studies such as Wu & Koh (1978) and Ooms & Mahieu (1981). This dynamic pressure correction, however, introduces more empirical parameters like the added mass correction factor or drag coefficient. To avoid this deficiency, there are also models, e.g. Devenish *et al.* (2010*b*), that try to improve the entrainment assumption without adding the dynamic pressure term. More recently, Tohidi & Kaye (2016) discussed the choice of entrainment assumption and the associated entrainment coefficients; they focused particularly on highly buoyant wildfire plumes and the effect of a non-uniform velocity distribution within the atmospheric boundary layer.

The aforementioned models are generally categorized as Eulerian in that they combine integral forms for the conservation of mass, momentum (and/or mean kinetic energy) and buoyancy with an entrainment assumption as the closure condition. There are also models based on a Lagrangian method, e.g. the Lagrangian particle models (LPM), to describe plume rise. The nontrivial part of LPM is to describe the buoyancy of each particle, which, in any event, depends on turbulent entrainment. Webster & Thomson (2002) proposed an integral model to calculate the plume rise², which is based on predictions of each particle subject to local conditions. Beyond plume rise, dispersion due to ambient turbulence is described by random walk models. Unlike the “hybrid” Eulerian and Lagrangian frameworks in Webster & Thomson (2002), Alessandrini *et al.* (2011, 2013) put forward a “pure” Lagrangian method that introduced a fictitious scalar, i.e. the temperature difference between the plume and the ambient fluid, transported by particles, to simulate the effect of entrainment. Generally, LPM shows some advantages in describing e.g. plume merger, however, it also introduces an empirical drag coefficient that is similar to the entrainment coefficient in Eulerian models. Another Lagrangian approach different from LPM has been detailed in Lee & Chu (2003);

²As argued by Weil (1988), the evolution of an atmospheric plume can be divided into two stages: (i) a plume rise phase where self-generated turbulence dominates over ambient turbulence, and, (ii) a dispersion phase where ambient turbulence dominates.

the analogue assumption therein is a spreading hypothesis associated with some spreading coefficients. As argued by Jirka (2004), Lagrangian approaches are suitable for plumes in the far field where advection and dispersion is governed primarily by ambient wind/turbulence, whereas Eulerian models are simple and computationally-inexpensive for calculating the near field plume rise. Therefore, and for a better evaluation of plume dilution and deflection in the near field region, we hereafter focus exclusively on integral plume models in an Eulerian framework.

Compared to the numerous studies concerning uniform plumes, coaxial plumes in a windy ambient are far less well understood. Li & Flynn (2020a) studied coaxial plumes using both theoretical modeling and similitude laboratory experiments, however, the ambient was assumed to be both unstratified and still except for small radial inflows due to entrainment. The purposes of this study are therefore twofold. First, and most obviously, to extend the theory of a coaxial plume in a stationary ambient as developed by Li & Flynn (2020a) with earlier contributions by Morton (1962) and Li *et al.* (2018). Second, and with particular reference to the coaxial plumes produced by crossflow cooling towers (Lindahl & Jameson, 1993), to identify the range of environmental conditions where fog formation is either altogether avoided or, at the very least, restricted to the inner plume.

This manuscript is structured as follows. Section 5.3 reviews the theory for uniform plumes in a crosswind in cases of single and multiple cooling tower cells. The counterpart theory for coaxial plumes is formulated and discussed in section 5.4. In section 5.4.5 the effects of varying ambient and source conditions on the visible plume length are discussed. Conclusions are drawn in section 5.5.

5.3 Theory for uniform plumes in a windy ambient

5.3.1 Formulation

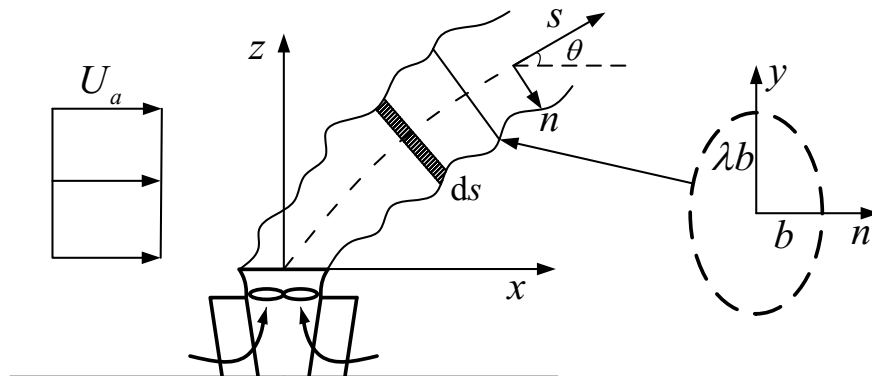


Figure 5.1: Definition sketch. s and n are the streamwise and normal coordinates, respectively. x and z are the horizontal and vertical coordinate axes, respectively. λb ($\lambda \geq 1$) and b are the respective major and conjugate radii of the elliptical cross section.

Figure 5.1 shows a schematic of a single, uniform cooling tower plume in a uniform crossflow. In modeling the associated dynamics, we invoke a number of assumptions, namely

- (i) The plume is fully turbulent, Boussinesq and slender. The slender plume assumption requires that the longitudinal length scale is much greater than the plume radius so that the streamwise pressure gradient is significantly greater than the normal pressure gradient, i.e. $\frac{\partial P}{\partial s} \gg \frac{\partial P}{\partial n}$. Although this is not strictly valid near the source, the plume theory derived from this assumption has been successfully applied to the near source region of a forced plume (Morton, 1959).
- (ii) Plume properties, such as velocity, temperature and humidity, satisfy “top-hat” profiles.
- (iii) The plume cross section is elliptical as shown in figure 5.1. Laboratory experimental evidence, such as Savory *et al.* (1996) and Contini & Robins (2001) have revealed a stable twin vortex structure that develops in case of low ambient turbulence. The twin vortex structure does not initiate immediately upon discharge from a (circular) source, but rather establishes over certain downwind distances³. Thereafter, we anticipate a significant increase in the entrainment rate. The assumption of an elliptical cross section is adopted to account for both the plume deflection and the twin vortex structure (Cintolesi *et al.*, 2019).
- (iv) The ambient wind is uniform in time and space and there is no atmospheric stratification. With the assumption of a uniform (i.e. shear-free) wind profile, the turbulent shear stresses outside the plume can be ignored (Hirst, 1972). An otherwise turbulent environment would compete with the turbulence of the buoyant plume thereby causing extrainment from the plume to the ambient (Witham & Phillips, 2008).
- (v) The longitudinal turbulent transport is only a small fraction of the mean longitudinal transport. In turn, the mean longitudinal flux can be decomposed into two parts, one due to advection and the other due to turbulent fluctuation. Adopting standard notation, we write,

$$\int_A \overline{U_p f} \, dA = \int_A \overline{U_p} \overline{f} \, dA + \int_A \overline{U'_p f'} \, dA, \quad (5.2)$$

where f is a generic property of the plume. For example, the left-hand side of (5.2) with $f = \rho_p$ and $f = U_p$ denote, respectively, the density and kinematic momentum fluxes. By a Reynolds decomposition, $U_p = \overline{U_p} + U'_p$ and $f = \overline{f} + f'$ where an overbar denotes a time-averaged quantity and a prime denotes the fluctuating component. Experimental measurements, as summarized in table 1 of Linden (2000), have shown that the turbulent flux term, i.e. the latter term on the right-hand side of (5.2), comprises a small proportion of the mean flux.

- (vi) There exists a state of thermal equilibrium between saturated moist air and liquid moisture.

³The numerical simulation of Cintolesi *et al.* (2019) revealed that the counter-rotating vortex pairs are dominant beyond $x/D_0 > 17$ where D_0 is the source diameter. Note that their simulations focus on very small wind to plume source velocity ratio (1/8) and large source Froude number (10), which results in relatively large momentum-buoyancy region and deflection region.

Based on the aforementioned assumptions, we choose a small control volume having height ds and corresponding to the shaded region illustrated in figure 5.1. We then formulate the conservation equations of volume, horizontal and vertical momentum, thermal energy and moisture. The set of governing equations are as follows:

$$\frac{d}{ds} \left\{ \int_A \rho_p U_p dA \right\} = \rho_a E, \quad (5.3)$$

$$\frac{d}{ds} \left\{ \int_A \rho_p U_p^2 \cos \theta dA \right\} = \rho_a E U_a, \quad (5.4)$$

$$\frac{d}{ds} \left\{ \int_A \rho_p U_p^2 \sin \theta dA \right\} = g \int_A (\rho_a - \rho_p) dA, \quad (5.5)$$

$$\frac{d}{ds} \left\{ \int_A (t_p - t_a) U_p dA \right\} = \int_A \frac{L_v}{c_{pa}} \sigma_p U_p dA, \quad (5.6)$$

$$\frac{d}{ds} \left\{ \int_A [(q_p - q_a) + \sigma_p] U_p dA \right\} = 0, \quad (5.7)$$

$$\frac{dx}{ds} = \cos \theta, \quad (5.8)$$

$$\frac{dz}{ds} = \sin \theta, \quad (5.9)$$

where θ is the plume angle to the horizontal, $E \approx 2\pi b \sqrt{\frac{\lambda^2+1}{2}} v_e$ is the rate of entrainment from the ambient to the plume, v_e is the entrainment velocity and λ is defined as the ratio of the major to conjugate radii in the plume cross section that is assumed to be constant. Meanwhile, t is temperature measured in °C, c_{pa} is the specific heat capacity of air at constant pressure, $L_v(t) = 4.1868 \times 10^3 [597.31 - 0.57 t]$ J/g is the latent heat of condensation and q and σ are the specific humidity and liquid moisture, respectively. The plume cross-sectional area is $A = \pi \lambda b^2$. Flux parameters may be defined as the volume flux $Q = \pi \lambda b^2 U_p$, the kinematic momentum flux $M = \pi \lambda b^2 U_p^2$, the temperature deficiency flux $\Theta = \pi \lambda b^2 U_p (t_p - t_a)$, the specific humidity deficiency flux $H = \pi \lambda b^2 U_p (q_p - q_a)$ and the liquid moisture flux $W = \pi \lambda b^2 U_p \sigma_p$. Thus (5.3) to (5.7) may be rewritten in terms of flux parameters and the entrainment velocity, v_e , as follows:

$$\frac{dQ}{ds} = I_s \sqrt{\frac{Q^2}{M}} v_e, \quad (5.10)$$

$$\frac{d}{ds} (M \cos \theta) = I_s \sqrt{\frac{Q^2}{M}} v_e U_a, \quad (5.11)$$

$$\frac{d}{ds} (M \sin \theta) = g' \frac{Q^2}{M}, \quad (5.12)$$

$$\frac{d}{ds} \left(\Theta - \frac{L_v}{c_{pa}} W \right) = 0, \quad (5.13)$$

$$\frac{d}{ds} (H + W) = 0, \quad (5.14)$$

where $I_s = \sqrt{\frac{2\pi(\lambda^2+1)}{\lambda}}$ is a geometrical constant associated with the elliptical cross section and $g' = g \left(1 - \frac{t_{v,a}}{t_{v,p}} \right)$ is the reduced gravity where $t_{v,a}$ and $t_{v,p}$ are the virtual temperatures of

the ambient air and of the plume, respectively. The above theoretical formulation is similar to that of Tohidi & Kaye (2016), which is based on the assumption that the trajectory of the bent-over plume is mainly determined by the rate of entrainment (i.e. the drag term is excluded). Alternatively, the momentum equations (5.11) and (5.12) can be rewritten as evolution equations for M and θ , i.e.

$$\frac{dM}{ds} = I_s \sqrt{\frac{Q^2}{M}} v_e U_a \cos \theta + g' \frac{Q^2}{M} \sin \theta, \quad (5.15)$$

$$M \frac{d\theta}{ds} = g' \frac{Q^2}{M} \cos \theta - I_s \sqrt{\frac{Q^2}{M}} v_e U_a \sin \theta. \quad (5.16)$$

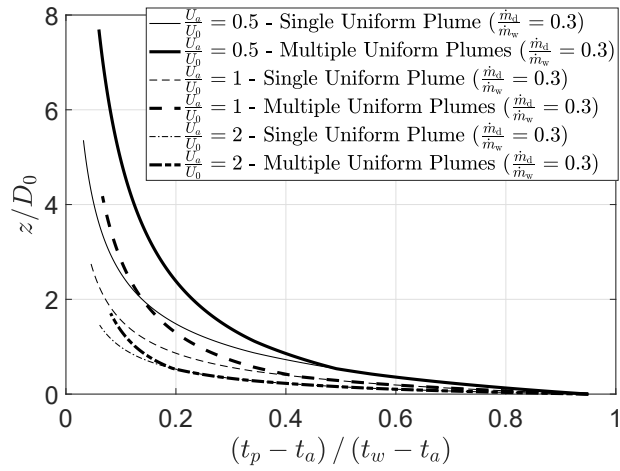
The closure condition for the governing equations (5.10) to (5.14) is the entrainment formulation. To this end, we adapt the most general form of the entrainment formulation proposed by Devenish *et al.* (2010b), which is mathematically expressed by

$$v_e = \sqrt[m]{(\gamma_1 |U_p - U_a \cos \theta|)^m + (\gamma_2 |U_a \sin \theta|)^m}, \quad (5.17)$$

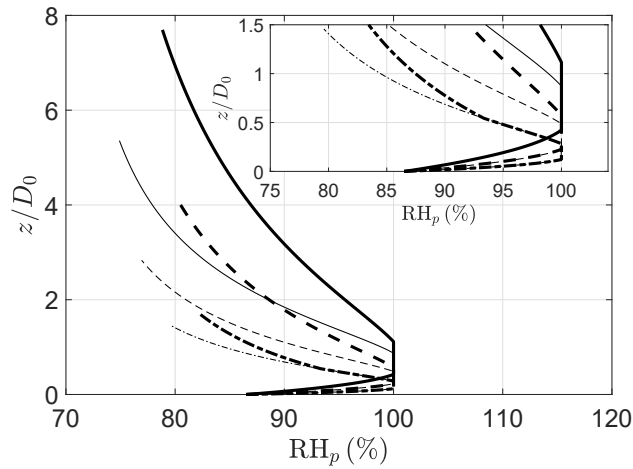
where $m = 3/2$ agrees well with their large-eddy simulation results and observations. Note that (5.17) is empirical and has no rigorous theoretical basis. The two entrainment terms in (5.17), i.e. $v_{e,l} = \gamma_1 |U_p - U_a \cos \theta|$ and $v_{e,t} = \gamma_2 |U_a \sin \theta|$ are the longitudinal and transverse entrainment velocities, respectively. The respective longitudinal and transverse shears⁴ are $|U_p - U_a \cos \theta|$ and $|U_a \sin \theta|$. Entrainment coefficients of $\gamma_1 = 0.1$ and $\gamma_2 = 0.6$ are assigned. The former value corresponds to the approximate mean of the entrainment coefficients for a vertical jet (0.076) and a vertical plume (0.117) – see List (1982). Meanwhile, the latter value corresponds to the entrainment coefficient associated with a cylindrical thermal (Turner, 1973). The ratio of the major to conjugate radii is assigned a value $\lambda = 1.2$ according to the laboratory measurements of uniform plumes in neutral crossflows by Contini *et al.* (2011). Moreover, the source value for the conjugate radius is obtained by equating $\frac{1}{4}\pi D_0^2$ and $\pi \lambda b_0^2$ where D_0 is the source diameter. Thus $b_0 = \frac{D_0}{2\lambda^{1/2}}$.

For brevity, and for the case of multiple cooling tower cells in a line array, only circumstances where the wind direction is perpendicular to the line array are considered. Macdonald *et al.* (2002) argued that this tower orientation represents the worst case for plume rise enhancement. A perpendicular arrangement may also give rise to the undesirable phenomena of downwash and plume recirculation, but such considerations are beyond the predictive capabilities of integral-type models.

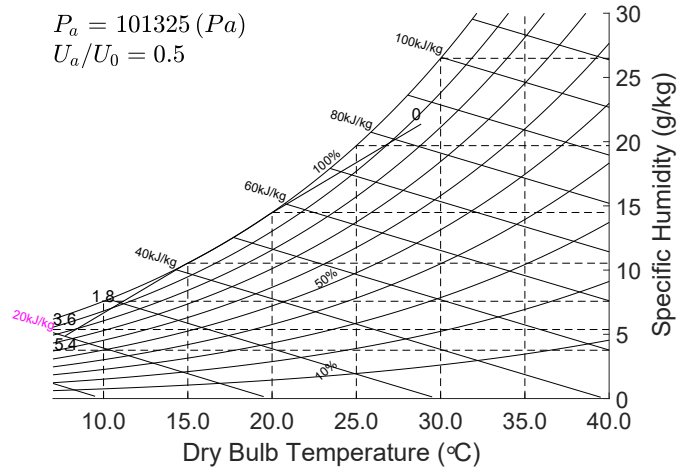
The introduction of multiple adjacent plumes brings into play the eventuality of plume merger. The algorithm used for describing this process mathematically is outlined in section 5.6. Merger is an essential step in the evolution of the plume when multiple axisymmetric plumes combine to form a single line plume and there is a step decrease in the surface-area-to-volume ratio. As a consequence, the entrainment of ambient fluid is curtailed. This, in turn, has important consequences for the mixing of ambient and buoyant fluids and for the likelihood of fog formation.



(a) Excess temperature

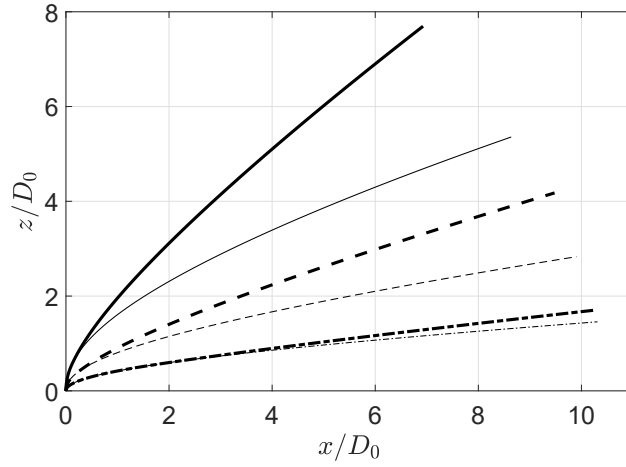


(b) Relative humidity

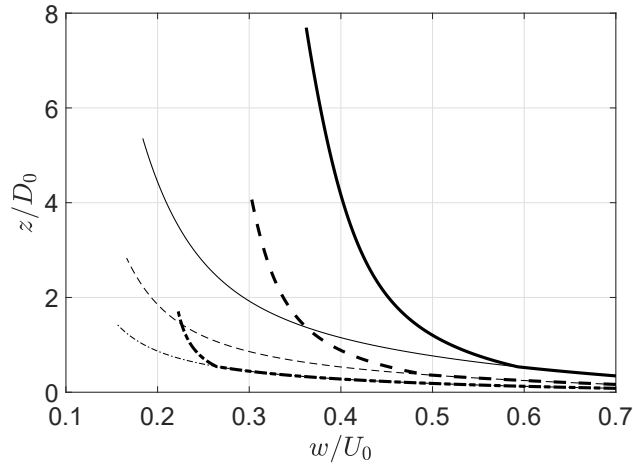


(c) Psychrometric chart

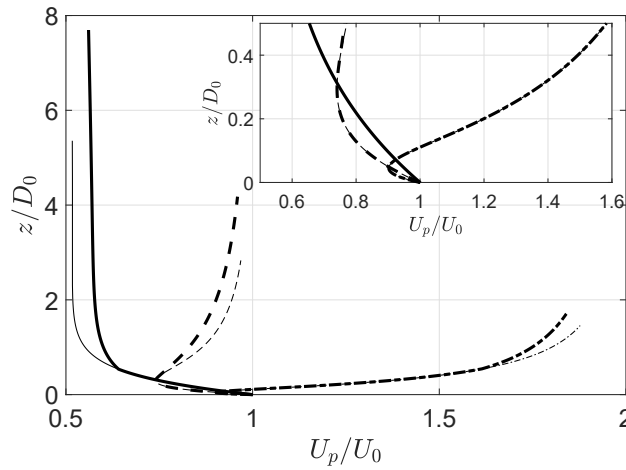
Figure 5.2: Non-dimensional plume excess temperature (panel a) and relative humidity (panel b) as functions of plume rise height. Panel (c) illustrates the plume temperature, specific humidity and the corresponding non-dimensional vertical elevations on the psychrometric chart for the case of single cell with $U_a/U_0 = 0.5$. The environmental and operating conditions are specified in table 5.1.



(a) Centerline trajectory



(b) Vertical velocity



(c) Streamwise velocity

Figure 5.3: Non-dimensional plume centerline trajectories (panel a), vertical velocities (panel b) and streamwise velocities (panel c) as functions of plume rise height. The source conditions are the same as in figure 5.2.

Table 5.1: Representative operating and environmental conditions for a single cooling tower cell and a single row of $n = 9$ cells.

Variable name and symbol	Value (unit)
Ambient pressure at the top of the cooling tower, P_a	101325 (Pa)
Ambient temperature, t_a	7 ($^{\circ}\text{C}$)
Ambient relative humidity, RH_a	70 (%)
Wet cooling temperature, t_w	30 ($^{\circ}\text{C}$)
Dry cooling temperature, t_d	25 ($^{\circ}\text{C}$)
Wind to plume source velocity ratio, U_a/U_0	0.5, 1 and 2
Stack exit velocity, U_0	6 (m/s)
Stack exit area, A_0	71.3 (m^2)
Distance between cell centers, d	14.3 (m)
Ratio of the dry to wet air mass flow rate, $\frac{\dot{m}_d}{\dot{m}_w}$	0.6 0.3

5.3.2 Representative solutions

Because plume visibility is of particular concern, we shall first discuss qualitatively the mechanism by which condensation occurs. The moist plume cools as a result of mixing, by turbulent entrainment, with the comparatively colder ambient air. Condensation ensues if the plume temperature falls below its dew-point temperature. This is, of course, a simplified picture. In fact, the mixing process occurs by way of a cascade, ranging from the largest eddies that give rise to turbulent engulfment to the smallest eddies that regularize velocity and/or scalar fluctuations by molecular diffusion. The mixing process is further complicated with the presence of a crosswind. To make a tractable prediction of plume visibility, we deemphasize any one particular mixing event and instead consider the time-averaged temperature and moisture profiles.

Table 5.1 lists the reference input parameters that are, for the most part, derived from Example 9.4.1 of Kröger (2004). These parameters are considered representative because, as in the current study, the ratio of dry cooling to wet cooling is set to be small (around 10%). Of particular interest is the ratio of dry to wet air mass flow rate, i.e. $\frac{\dot{m}_d}{\dot{m}_w}$, which is a variable that depends on the plume abatement requirement and, by extension, seasonal conditions. For large velocity ratios i.e. U_a/U_0 , stack-tip downwash is always a concern. In the towing-tank experiment of Contini & Robins (2001), they found no evidence of stack downwash when $U_a/U_0 \approx 0.9$. Later Contini *et al.* (2011) expanded this ratio up to $U_a/U_0 \approx 1.7$ and still no stack downwash was reported. On the other hand, a very small velocity ratio e.g. $U_a/U_0 < 0.25$ has the risk of inducing bifurcation (Huq & Dhanak, 1996). The theoretical model of Schatzmann & Policastro (1984) incorporates the effect of stack downwash via the entrainment assumption and an extra drag term, however, only in an empirical way. Due to these complications, we do not attempt to model the effect of stack downwash in the present study. Another downwash effect due to the interaction between plumes is briefly discussed in section 5.6.

Theoretical results obtained by solving Eqs. (5.10)–(5.14) are shown in figures 5.2 and

⁴The absolute value is retained to guarantee that shear is always positive.

5.3. These two figures consider the thermodynamic and kinematic properties of the plume, respectively. We assume a single dry to wet air mass flow rate ratio $\frac{\dot{m}_d}{\dot{m}_w} = 0.3$, nevertheless, a larger ratio i.e. $\frac{\dot{m}_d}{\dot{m}_w} = 0.6$ produces similar results. Note the scaling parameters for excess temperature, vertical and horizontal length and velocity are the wet air excess temperature, $t_w - t_a$, the stack diameter, D_0 and the plume source velocity, U_0 . Some of the solutions from figure 5.2a admit plume merger and, in these cases, we find that the merged plume in case of multiple cell towers is more buoyant than the individual plume from a single cell. This buoyant enhancement results from a reduced surface-area-to-volume ratio thus reduced entrainment after plume merger. Figure 5.2b confirms fog may form as the plume rises, which is also anticipated by the overlap of the dilution curve with the saturation curve in the psychrometric chart of figure 5.2c. The inset to figure 5.2b shows the visible plume regions for $U_a/U_0 = 0.5, 1$ and 2 , being respectively $0.42 < z/D_0 < 0.87$, $0.23 < z/D_0 < 0.49$ and $0.12 < z/D_0 < 0.28$ in the single cell case. Noticeably, under relatively large wind speeds e.g. $U_a/U_0 = 2$, plume merger is predicted to occur (at $z/D_0 = 0.54$) after condensation terminates.

Buoyant enhancement in the case of merged plumes can be evaluated from the trajectory profiles shown in figure 5.3a. More specifically, and shortly after plume merger, figure 5.3a shows an approximately linear relationship between the plume rise height, z , and downwind distance, x . This observation can be rationalized by dimensional analysis where we consider as key parameters the buoyancy flux, F , the length of the merged (line) plume, L , and the wind speed, U_a . Thus

$$z \propto \left(\frac{F}{L}\right)^{1/3} U_a^{-1} x. \quad (5.18)$$

Further combining figures 5.2b and 5.3a, we notice that merged plumes result in a longer visible plume length, but they are less deflected by the wind. An increase in vertical velocity is observed after plume merger – see figure 5.3b. Meanwhile, differences in the streamwise velocity of plumes from single and multiple cells are shown in figure 5.3c. For the single cell case, all plumes approach the respective wind speed in the very far field (not shown); this asymptotic behavior, i.e. $U_p \sim U_a$, is a direct consequence of the continuous deflection illustrated by the thin curves in figure 5.3a. By contrast, the influence of the wind is smaller (though by no means insignificant) when considering the streamwise velocity of the merged plume in case of multiple cells. However, and even when $U_a/U_0 = 0.5$, say, note that this merged plume will, in the far field, be highly deflected and have a streamwise velocity very close to the wind speed.

To evaluate the visible plume length under various ambient conditions, we define the visible plume length as $\Delta s = \int_{s_s}^{s_t} ds$ where s_s and s_t denote the streamwise locations at which the condensation starts and terminates, respectively. For fixed velocity ratios, i.e. $U_a/U_0 = 0.25, 0.5, 1$ and 2 , the corresponding surface plots of the visible plume length ($\Delta s/D_0$) for different ambient temperatures and relative humidities are shown in the four panels of figure 5.4. The breadth of the environmental parameter range that guarantees no visible plume (the “flat” region) increases with the wind speed. Under the most adverse ambient conditions, i.e. low temperature and high relative humidity, the visible plume length initially decreases with wind speed ($U_a/U_0 = 0.25$ to 0.5), but thereafter increases ($U_a/U_0 = 0.5$ to 2) as plume advection by the wind dominates over internal buoyancy. This non-monotonic variation of the visible plume length is reflected in the evolution of the entrainment velocity

and entrainment flux per unit height illustrated in figure 5.5. For $U_a/U_0 = 0.25$ to 2, figure 5.5 a indicates that the larger the wind speed, the greater the near source entrainment velocity, though differences all but disappear for $s/D_0 \geq 4.0$. A larger wind speed also results in a larger near-source entrainment flux as shown in figure 5.5 b. In the far field, by contrast, the smallest wind speed corresponds to the largest entrainment flux. In other words, and when the wind speed is high, external ambient fluid is entrained in large volumes close to the source, but, owing to plume bending, the entrainment flux decreases sharply with increasing downstream distance. The profiles exhibited in figure 5.5, drawn assuming $t_a = 2^\circ\text{C}$ and $\text{RH}_a = 60\%$, help to interpret figure 5.4. The flat regions in figure 5.4 increase in extent with increasing wind speed due to the larger near source entrainment. Where condensation is predicted to occur, however, the visible plume length is largest for the highest wind speed: for sufficiently large s , large U_a is associated with a comparatively minor, not robust, entrainment flux. Analogously, short visible plumes are anticipated when $U_a/U_0 = 0.5$ – see figure 5.4 b. From figure 5.5 b, we see that $U_a/U_0 = 0.5$ is associated with the largest overall entrainment flux, at least over the range of s of interest here. In interpreting figure 5.4, we caution that the visible plume length is, of course, not the only criterion to consider when assessing the severity of fog formation. Other parameters, such as the visible plume elevation and radius, may also be examined. For example, $U_a/U_0 = 2$ exhibits the smallest far field visible plume radius, which can be inferred from figure 5.5 and the relation, $E \approx 2\pi b \sqrt{\frac{\lambda^2+1}{2}} v_e$.

5.4 Theory for coaxial plumes in a windy ambient

5.4.1 Formulation

When the plume is assumed to be coaxial in structure, we consider that the inner plume is, up to the point of its disappearance, symmetrically bounded by the outer plume. In the theoretical formulation to follow, the entrainment between the inner and outer plumes follows Morton’s entrainment assumption for coaxial jets (Morton, 1962). Meanwhile, Devenish’s entrainment formulation is retained to describe the entrainment from the ambient to the outer plume. The entrainment velocities from the outer to the inner plume and from the inner plume and the ambient to the outer plume are, respectively, expressed as follows:

$$\omega_\alpha = \alpha|U_1 - c_1 U_2|, \quad \omega_\beta = \beta U_2, \quad \omega_\gamma = \sqrt[3/2]{(\gamma_1|U_2 - U_a \cos \theta|)^{3/2} + (\gamma_2|U_a \sin \theta|)^{3/2}}, \quad (5.19)$$

where the entrainment coefficients in ω_γ , i.e. γ_1 and γ_2 , are assumed to be the same as those in case of uniform plumes. The coefficient, c_1 , gives rise to two entrainment assumptions. For $c_1 = 1$, the entrainment velocity, ω_α , scales with the velocity difference between the inner and outer plumes. Hereafter, we refer to this entrainment assumption as EI. By contrast, when $c_1 = 0$, the entrainment velocity scales with the inner plume velocity only and we then refer to an entrainment assumption EII. Both EI and EII have been adapted in the context of turbulent fountains (Bloomfield & Kerr, 2000) and bubble plumes (Socolofsky *et al.*, 2008).

The flux parameters are defined as follows:

$$Q_1 = \pi \lambda b_1^2 U_1, \quad Q_2 = \pi \lambda (b_2^2 - b_1^2) U_2, \quad (5.20)$$

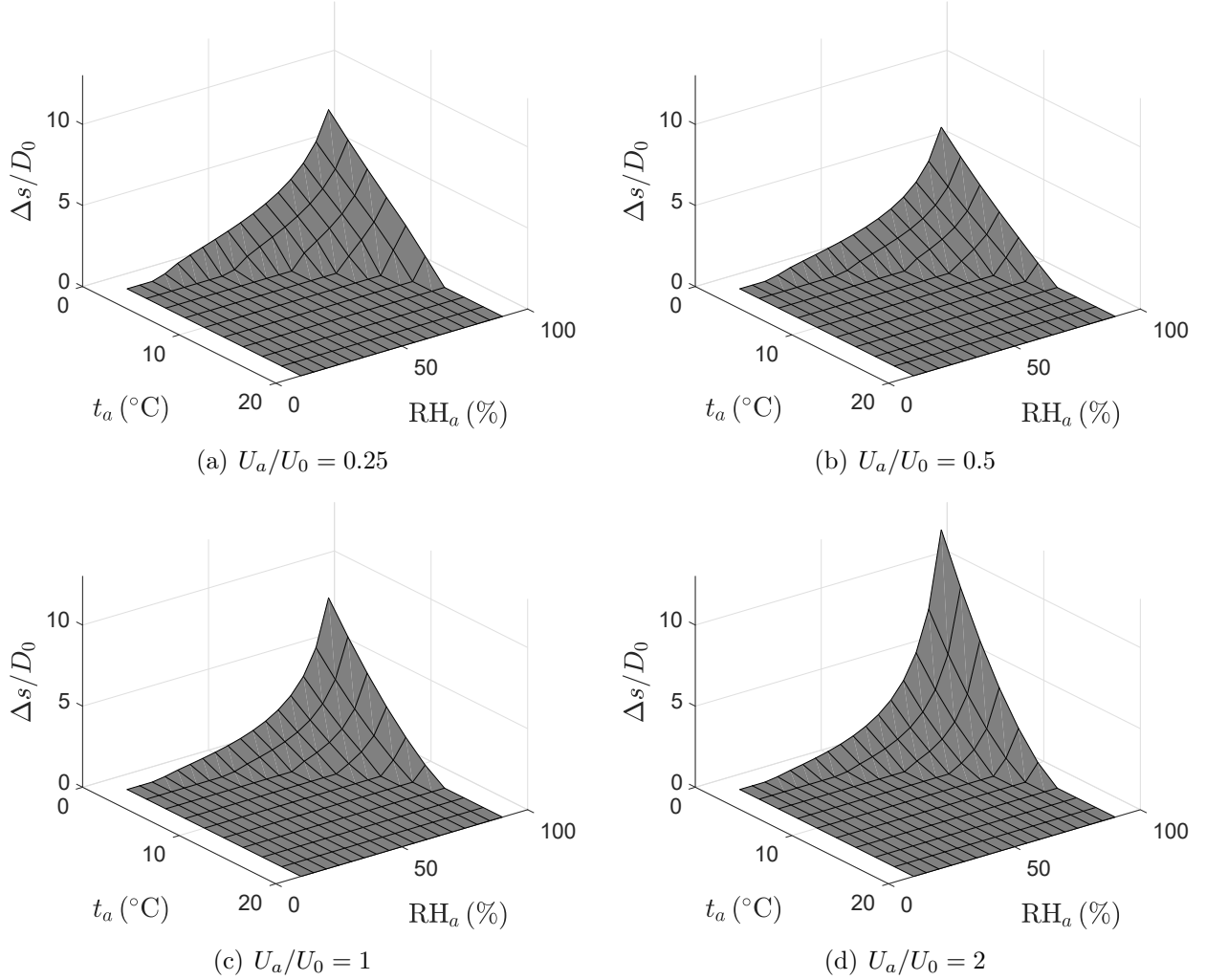


Figure 5.4: Surface plots of visible plume length for different ambient temperatures, relative humidities and wind speeds.

$$M_1 = \pi \lambda b_1^2 U_1^2, \quad M_2 = \pi \lambda (b_2^2 - b_1^2) U_2^2, \quad (5.21)$$

$$\Theta_1 = \pi \lambda b_1^2 U_1 (t_1 - t_a), \quad \Theta_2 = \pi \lambda (b_2^2 - b_1^2) U_2 (t_2 - t_a), \quad (5.22)$$

$$H_1 = \pi \lambda b_1^2 U_1 (q_1 - q_a), \quad H_2 = \pi \lambda (b_2^2 - b_1^2) U_2 (q_2 - q_a), \quad (5.23)$$

$$W_1 = \pi \lambda b_1^2 U_1 \sigma_1, \quad W_2 = \pi \lambda (b_2^2 - b_1^2) U_2 \sigma_2, \quad (5.24)$$

where t is the plume temperature, q is the specific humidity, σ is the specific liquid moisture and subscripts 1 and 2 respectively indicate the inner and outer plumes. With the aforementioned entrainment velocities and flux parameters defined, the volume, thermal energy and moisture conservation equations for the inner and outer plumes are given as

$$\frac{dQ_1}{ds} = I_s \sqrt{\frac{Q_1^2}{M_1}} (\omega_\alpha - \omega_\beta), \quad (5.25)$$

$$\frac{dQ_2}{ds} = I_s \sqrt{\frac{Q_1^2}{M_1}} (\omega_\beta - \omega_\alpha) + I_s \sqrt{\left(\frac{Q_1^2}{M_1} + \frac{Q_2^2}{M_2}\right)} \omega_\gamma, \quad (5.26)$$

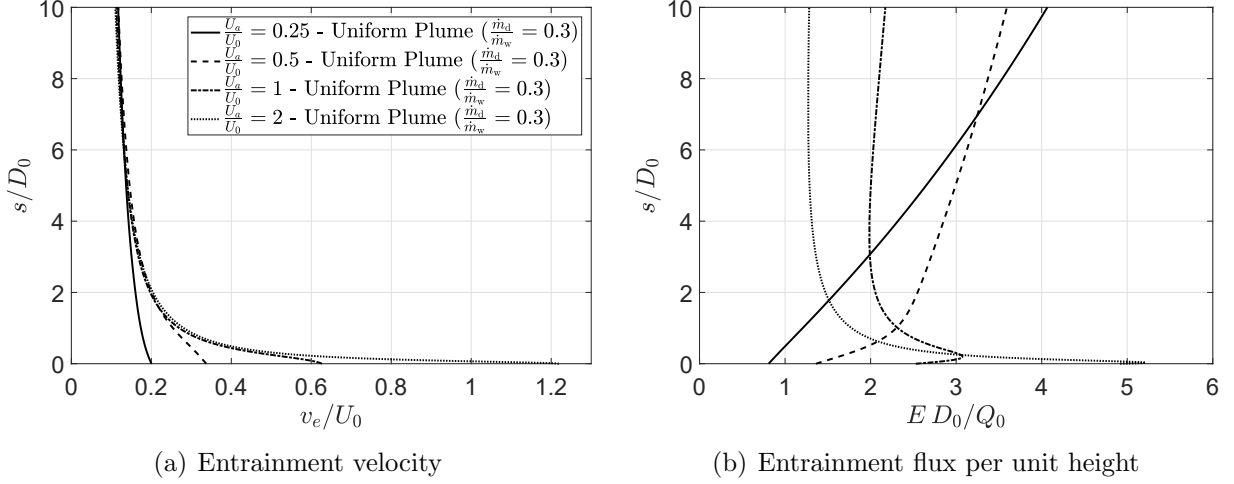


Figure 5.5: Variations of entrainment velocity (left panel) and entrainment flux per unit height (right panel) with streamwise distance for different wind speeds. The ambient temperature and relative humidity are $t_a = 2^\circ\text{C}$ and $\text{RH}_a = 60\%$, respectively.

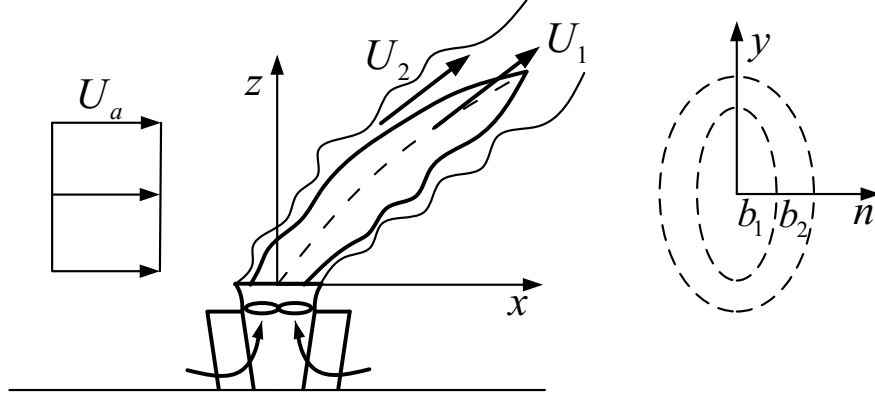


Figure 5.6: Schematic of a coaxial plume in a windy ambient. b_1 and b_2 are the conjugate radii of the inner and outer plumes, respectively. The respective streamwise velocities for the inner and outer plumes are U_1 and U_2 .

$$\frac{d}{ds} \left(\Theta_1 - \frac{L_{v,1} W_1}{c_{pa}} \right) = I_s \sqrt{\frac{Q_1^2}{M_1}} \left[\omega_\alpha \left(\frac{\Theta_2}{Q_2} - \frac{L_{v,2} W_2}{c_{pa} Q_2} \right) - \omega_\beta \left(\frac{\Theta_1}{Q_1} - \frac{L_{v,1} W_1}{c_{pa} Q_1} \right) \right], \quad (5.27)$$

$$\frac{d}{ds} \left(\Theta_2 - \frac{L_{v,2} W_2}{c_{pa}} \right) = I_s \sqrt{\frac{Q_2^2}{M_2}} \left[\omega_\beta \left(\frac{\Theta_1}{Q_1} - \frac{L_{v,1} W_1}{c_{pa} Q_1} \right) - \omega_\alpha \left(\frac{\Theta_2}{Q_2} - \frac{L_{v,2} W_2}{c_{pa} Q_2} \right) \right], \quad (5.28)$$

$$\frac{d}{ds} (H_1 + W_1) = I_s \sqrt{\frac{Q_1^2}{M_1}} \left[\omega_\alpha \left(\frac{H_2}{Q_2} + \frac{W_2}{Q_2} \right) - \omega_\beta \left(\frac{H_1}{Q_1} + \frac{W_1}{Q_1} \right) \right], \quad (5.29)$$

$$\frac{d}{ds} (H_2 + W_2) = I_s \sqrt{\frac{Q_2^2}{M_2}} \left[\omega_\beta \left(\frac{H_1}{Q_1} + \frac{W_1}{Q_1} \right) - \omega_\alpha \left(\frac{H_2}{Q_2} + \frac{W_2}{Q_2} \right) \right], \quad (5.30)$$

where the velocities in the entrainment terms can be expressed as $U_1 = \frac{M_1}{Q_1}$ and $U_2 = \frac{M_2}{Q_2}$.

Meanwhile, the momentum equations for the composite inner/outer plume are

$$\frac{d}{ds} (M_1 + M_2) = I_s \sqrt{\left(\frac{Q_1^2}{M_1} + \frac{Q_2^2}{M_2}\right)} \omega_\gamma U_a \cos \theta + \left(g'_1 \frac{Q_1^2}{M_1} + g'_2 \frac{Q_2^2}{M_2}\right) \sin \theta, \quad (5.31)$$

$$(M_1 + M_2) \frac{d\theta}{ds} = \left(g'_1 \frac{Q_1^2}{M_1} + g'_2 \frac{Q_2^2}{M_2}\right) \cos \theta - I_s \sqrt{\left(\frac{Q_1^2}{M_1} + \frac{Q_2^2}{M_2}\right)} \omega_\gamma U_a \sin \theta, \quad (5.32)$$

where the reduced gravities are defined as $g'_1 = g \frac{\rho_a - \rho_1}{\rho_a} = g \left(1 - \frac{P_1}{P_a} \frac{t_{v,a}}{t_{v,1}}\right)$ and $g'_2 = g \frac{\rho_a - \rho_2}{\rho_a} = g \left(1 - \frac{P_2}{P_a} \frac{t_{v,a}}{t_{v,2}}\right)$ with P_a , P_1 and P_2 denoting the static pressures within the ambient, and the inner and outer plumes, respectively. Assuming a body force formulation that regards the ambient fluid as the reference fluid when evaluating the buoyancy of the inner plume (McDougall, 1981), the streamwise momentum equations for the inner and outer plumes are respectively given as

$$\frac{dM_1}{ds} = \frac{Q_1^2}{M_1} g'_1 \sin \theta + I_s \sqrt{\frac{Q_1^2}{M_1}} (\omega_\alpha U_2 - \omega_\beta U_1), \quad (5.33)$$

$$\frac{dM_2}{ds} = \frac{Q_2^2}{M_2} g'_2 \sin \theta - I_s \sqrt{\frac{Q_1^2}{M_1}} (\omega_\alpha U_2 - \omega_\beta U_1) + I_s \sqrt{\left(\frac{Q_1^2}{M_1} + \frac{Q_2^2}{M_2}\right)} \omega_\gamma U_a \cos \theta. \quad (5.34)$$

If instead, outer plume fluid is considered as the reference, then the above equation for M_1 must be modified to read

$$\frac{dM_1}{ds} = \frac{Q_1^2}{M_1} \left[(g'_1 - g'_2) \sin \theta + U_2 \frac{dU_2}{ds} \right] + I_s \sqrt{\frac{Q_1^2}{M_1}} (\omega_\alpha U_2 - \omega_\beta U_1). \quad (5.35)$$

Subtracting (5.35) from (5.31) yields the analogue streamwise momentum equation for the outer plume

$$\begin{aligned} \frac{dM_2}{ds} &= I_s \sqrt{\left(\frac{Q_1^2}{M_1} + \frac{Q_2^2}{M_2}\right)} \omega_\gamma U_a \cos \theta - I_s \sqrt{\frac{Q_1^2}{M_1}} (\omega_\alpha U_2 - \omega_\beta U_1) \\ &\quad + \frac{Q_1^2}{M_1} \left(g'_2 \sin \theta - U_2 \frac{dU_2}{ds} \right) + \frac{Q_2^2}{M_2} g'_2 \sin \theta. \end{aligned} \quad (5.36)$$

We refer to the equation pairs (5.33)/(5.34) and (5.35)/(5.36) as respectively corresponding to the first and second body force formulations and write BFI and BFII for short. In the former case, pressure is hydrostatic everywhere, thus

$$\frac{dP_1}{ds} = \frac{dP_2}{ds} = -g\rho_a \sin \theta. \quad (5.37)$$

The static pressures within the inner and outer plumes assuming a BFII formulation are given respectively as follows:

$$\frac{dP_1}{ds} = -g\rho_2 \sin \theta - \rho_a U_2 \frac{dU_2}{ds}, \quad (5.38)$$

$$\frac{dP_2}{ds} = -g\rho_a \sin \theta. \quad (5.39)$$

The set of governing equations to be solved consists of (5.25)–(5.30) and (5.32)–(5.34) for the BFI formulation. The counterpart governing equations for BFII are (5.25)–(5.30), (5.32), (5.35) and (5.36).

5.4.2 Entrainment coefficient and body force formulation

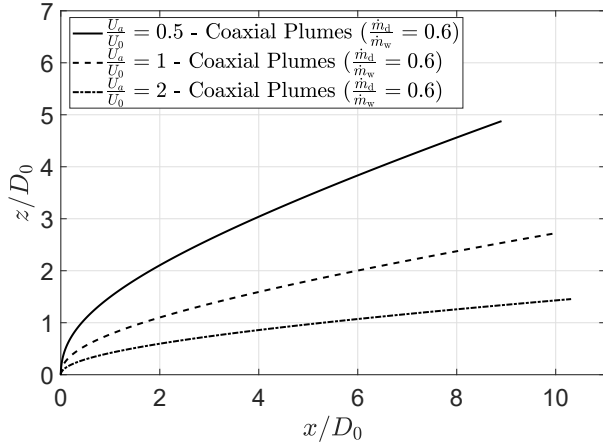
The values to choose for the entrainment coefficients, α and β , are not immediately obvious when considering a windy ambient. For simplicity, we assume that α and β deviate little from their values when $U_a = 0$. However, as shown by Li & Flynn (2020a) in this stationary ambient case, it is inappropriate to assume a single universal value for either of the entrainment coefficients, which are, in fact, functions of source reduced gravity ratio i.e. g'_{10}/g'_{20} . Thus, by applying (4.2) and (4.3) of Li & Flynn (2020a) in conjunction with the source conditions specified in table 5.1, we estimate that $\alpha = 0.039$ and $\beta = 0.065$. These entrainment coefficients, though calibrated specifically for EI in the study of Li & Flynn (2020a), are also adopted for EII. By doing so, we focus specifically on the differences of model predictions that arise from the choice of entrainment assumption. Note that the sensitivity of α and β on the modeling results is discussed in section 5.4.4. Note also that as the wind speed increases, the entrainment between the inner and outer plumes is expected to play a less important role compared to the case of a stationary ambient.

Regarding equations (5.33)/(5.34) vs. (5.35)/(5.36), Devenish *et al.* (2010a) argued that there is only a moderate difference between the BFI and BFII formulations. Although Devenish *et al.*'s study focused on turbulent fountains, their conclusion was supported by later work (i.e. Li & Flynn 2020a), which examined coaxial plumes and which likewise found only moderate differences between BFI and BFII. Because Li & Flynn's study suggests slightly better agreement between theory and experiment when using BFI, we shall henceforth consider this formulation here too. However, to reiterate, we would expect only minor variations if BFII were to be selected instead.

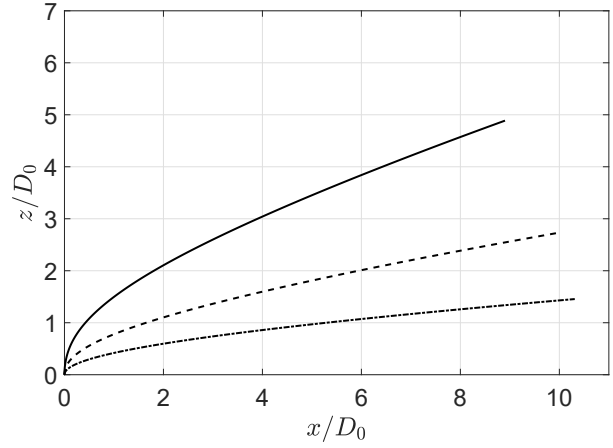
5.4.3 Representative solutions

Further to the discussion in section 5.3.2, we now consider a non-uniform distribution of temperature and humidity in the plume radial direction. Specifically, we allow a moderate amount (e.g. 30%) of dry air to be mixed into the wet air within the cooling tower plenum chamber; the resulting air mixture and the remaining dry air respectively comprise the inner and outer portions of the coaxial plume post atmospheric discharge. As a realistic approximation, we assume a top-hat velocity profile at the fan exit, which neglects the low velocity region immediately above the central hub of the fan – see figure 3 of Davis (1975) or figure 23 of Winiarski & Frick (1977). Furthermore, the source velocities of the inner and outer plumes satisfy $U_{10} = U_{20} \approx U_0$. As with the uniform plume case, plume merger in the context of coaxial plumes is briefly described in section 5.6.

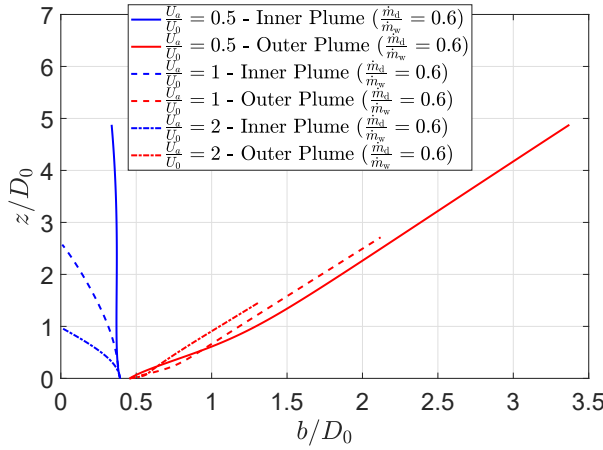
In interpreting our model predictions, attention is first paid to coaxial plumes emanating from a single cooling tower cell; the more complicated case involving multiple cells shall be described later. Considering as inputs the data of table 5.1 and assuming $\frac{\dot{m}_d}{\dot{m}_w} = 0.6$,



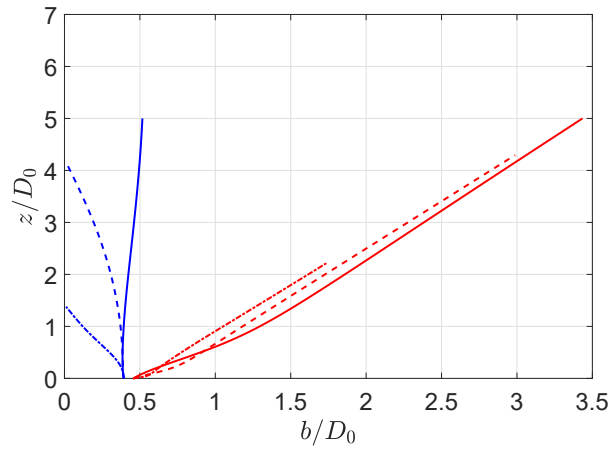
(a) Centerline trajectory (EI)



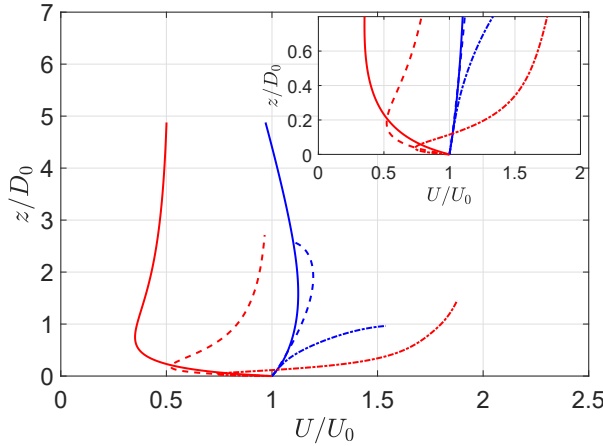
(b) Centerline trajectory (EII)



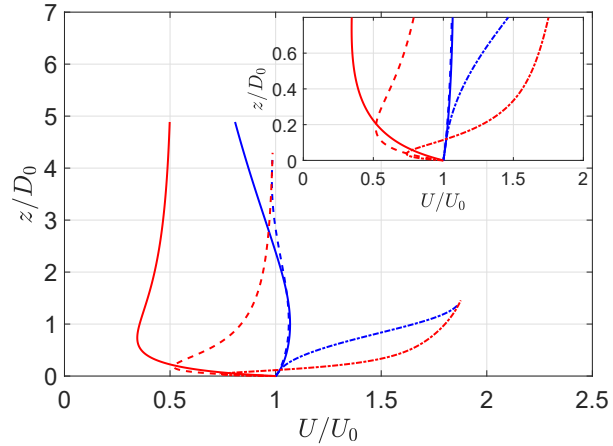
(c) Conjugate radius (EI)



(d) Conjugate radius (EII)

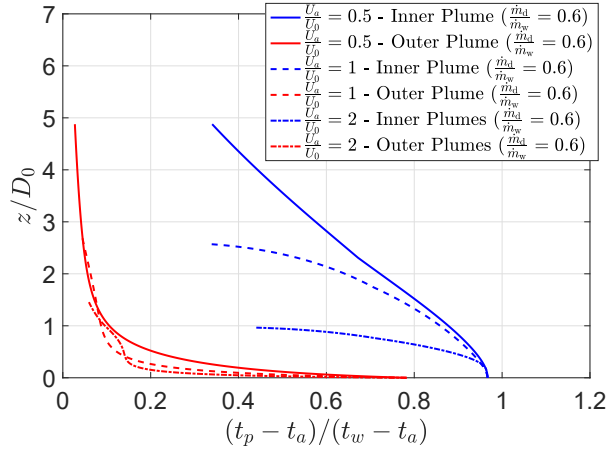


(e) Streamwise velocity (EI)

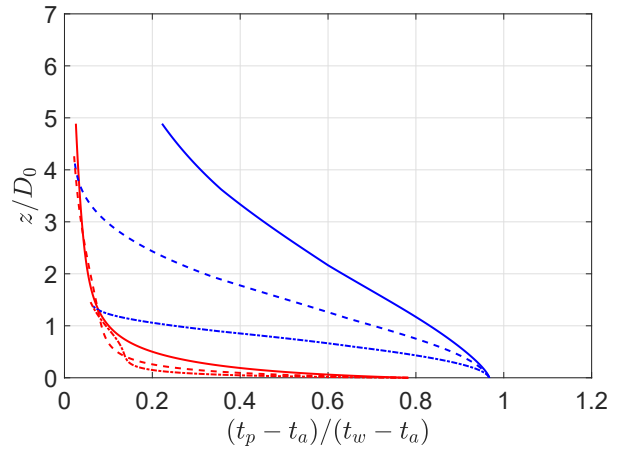


(f) Streamwise velocity (EII)

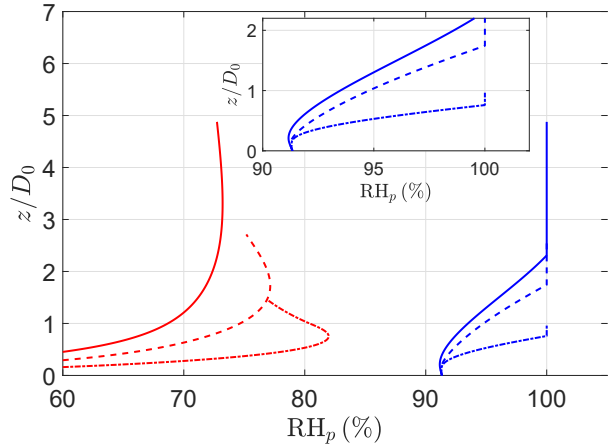
Figure 5.7: [Color] Non-dimensional plume centerline trajectories (panels a and b), conjugate radii (panels c and d) and streamwise velocities (panels e and f) as functions of plume rise height. Panels a, c and e correspond to an EI entrainment formulation whereas panels b, d and f correspond to an EII entrainment formulation.



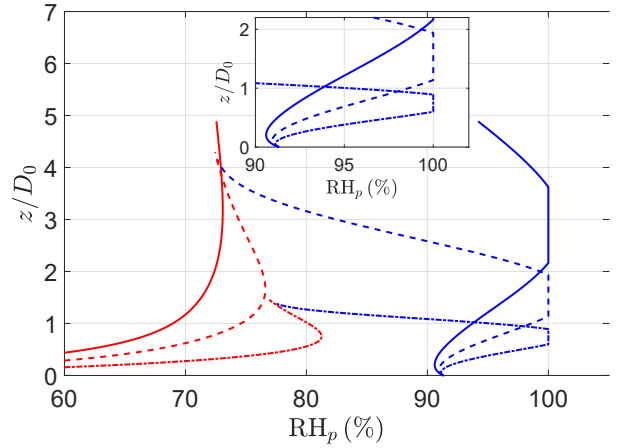
(a) Excess temperature (EI)



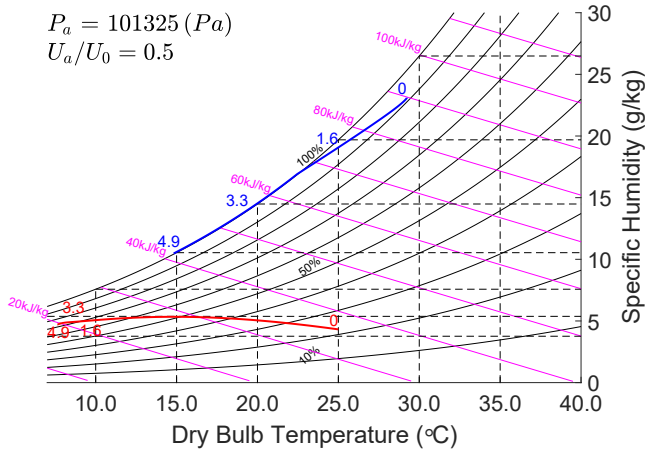
(b) Excess temperature (EII)



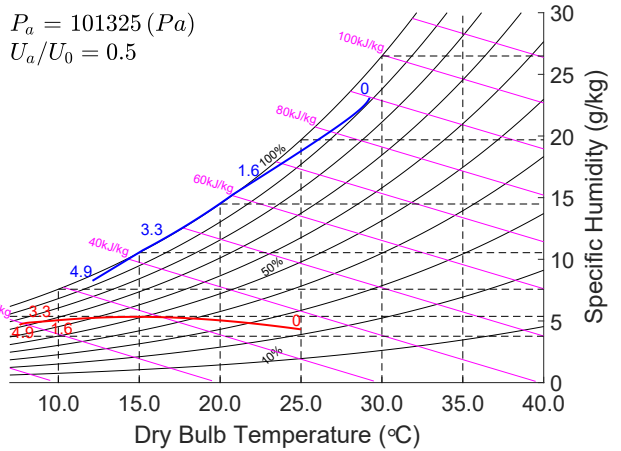
(c) Relative humidity (EI)



(d) Relative humidity (EII)



(e) Psychrometric chart (EI)



(f) Psychrometric chart (EII)

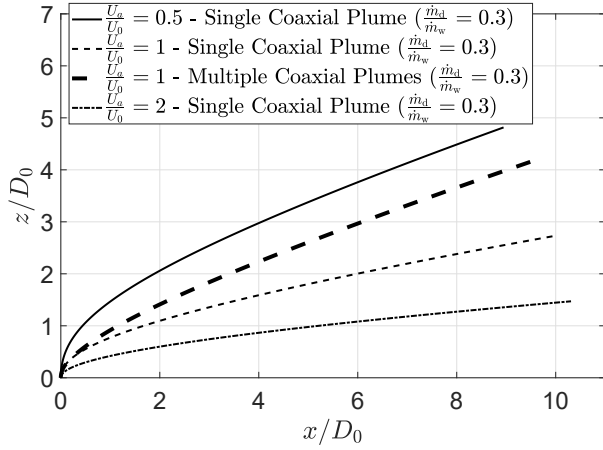
Figure 5.8: [Color] Non-dimensional plume excess temperature (panels a and b) and relative humidity (panels c and d) as functions of plume rise height. Panels e and f illustrate the dilution curves for the inner (blue) and outer (red) plumes on the psychrometric charts.

we present in figure 5.7 plume trajectories, conjugate radii and streamwise velocities for the inner and outer plumes assuming entrainment formulations of type EI (panels a, c and e) and EII (panels b, d and f). The coaxial plume trajectories illustrated in figures 5.7a and 5.7b are similar to those (thin curves) in figure 5.3a. This is unsurprising because the plume trajectory in a neutrally-stratified atmosphere is determined by the total source momentum and buoyancy fluxes, as indicated by the general form of Briggs’ “two-thirds” law (Davidson, 1989). Figure 5.7c shows the general trend that the outer plume increases in size continuously whereas the inner plume shrinks and/or disappears somewhere above the source. Nonetheless, a clear difference in the breadth of the inner plumes is observed as the wind speed increases with larger U_a being associated with smaller b_2 and, more especially, b_1 . The wind speed also modifies the cut-off heights, defined as the height where the inner plume disappears. For instance, and still considering EI, these are $Z_c \equiv z/D_0 = 2.57$ and 0.96 for $U_a/U_0 = 1$ and 2 , respectively. The rapid decrease in the breadth of the inner plume with increasing U_a is due to the momentum transfer from the wind to the outer plume, which, in turn, increases the entrainment from the inner to the outer plume. Similar profiles of plume radii are illustrated in figure 5.7d with some differences in the inner plume radius. As expected, and provided $U_1 \geq U_2$, EII prescribes a greater entrainment from the outer to the inner plume than does EI. Therefore, the inner plumes with EII tend to persist for greater downstream distances.

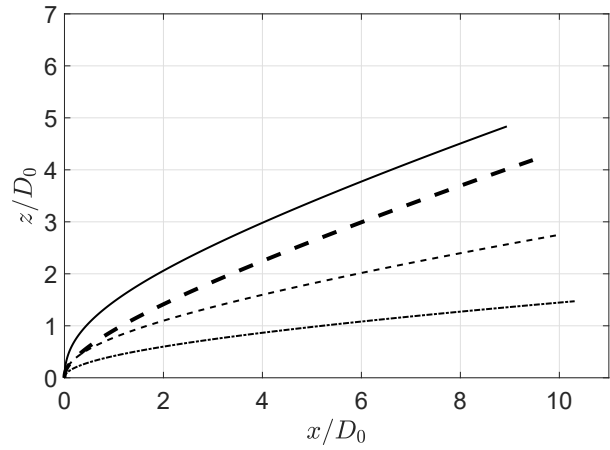
As shown in figure 5.7e, the streamwise velocities of the outer plumes (red curves) initially drop sharply and then rise and eventually approach the wind speed asymptotically. For moderate wind speeds, i.e. $U_a/U_0 = 0.5$ and 1 , the inner plume always propagates faster than the outer plume because of its larger buoyancy. However, a larger wind speed of $U_a/U_0 = 2$ tends to quickly deflect and drag the outer plume. As a result, the streamwise velocity of the outer plume rapidly exceeds that of the inner plume – see the inset to figure 5.7e. Similar trends are, of course, evident in figure 5.7f though here the velocity difference between the inner and outer plumes is slightly less pronounced.

Complementing figure 5.7, figure 5.8 shows temperatures, relative humidities and the dilution processes on a psychrometric chart. Figures 5.8a and 5.8b illustrate that the inner and outer plumes are rapidly diluted as the wind speed increases. This trend of dilution is also reflected in the corresponding relative humidity profiles presented in figures 5.8c and 5.8d. Shown in the inset to figure 5.8c are the onset heights of condensation for the inner plumes, these being $z/D_0 = 2.31$, 1.74 and 0.76 for $U_a/U_0 = 0.5$, 1 and 2 , respectively. By contrast, and although the relative humidities of the outer plumes increase relatively quickly at first, the peak values are always well below saturation. Compared to figure 5.8c, figure 5.8d indicates that fog first forms at slightly lower heights for EII vs. EI. Also, the inner plumes persist even after condensation terminates. The psychrometric chart, figure 5.8e, shows a curve for the outer plume that cuts across lines of constant humidity. In physical terms, the outer plume respectively gains and loses humidity from the inner plume and from the ambient. Because the outer plume temperature is all the while dropping, there is, as noted above, a rise (followed later by a fall) in the relative humidity. Also included in figure 5.8e is a curve corresponding to the inner plume. Here, of course, the variation of relative humidity with height is less pronounced. Little difference is observed between the psychrometric charts in figures 5.8e and 5.8f.

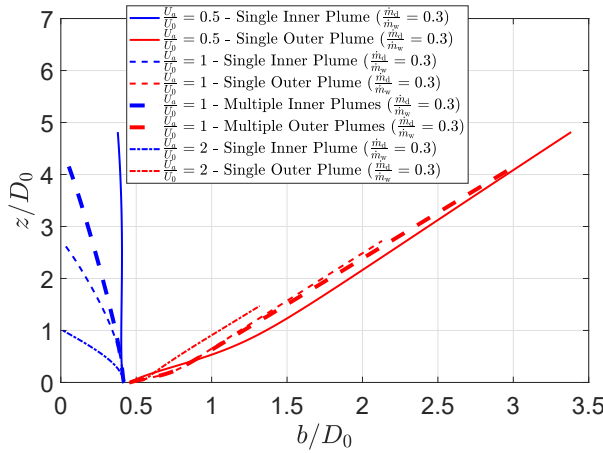
For the case of $\frac{\dot{m}_d}{\dot{m}_w} = 0.3$, figure 5.9 shows the centerline trajectories, conjugate radii and



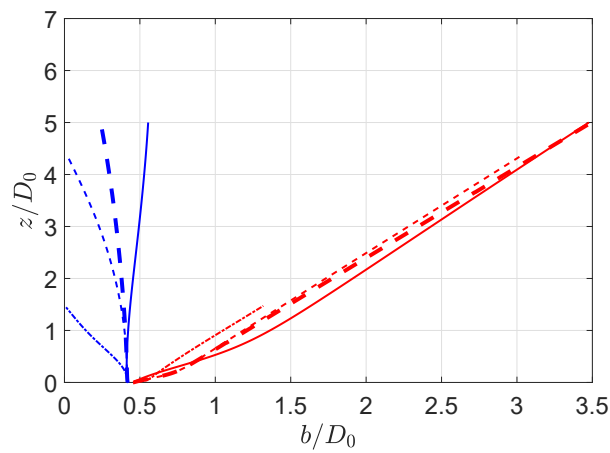
(a) Centerline trajectory (EI)



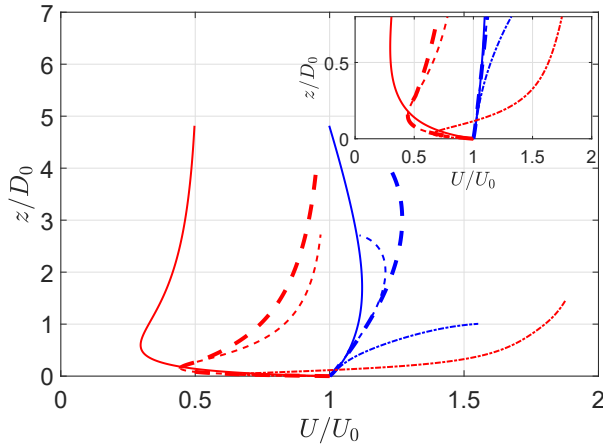
(b) Centerline trajectory (EII)



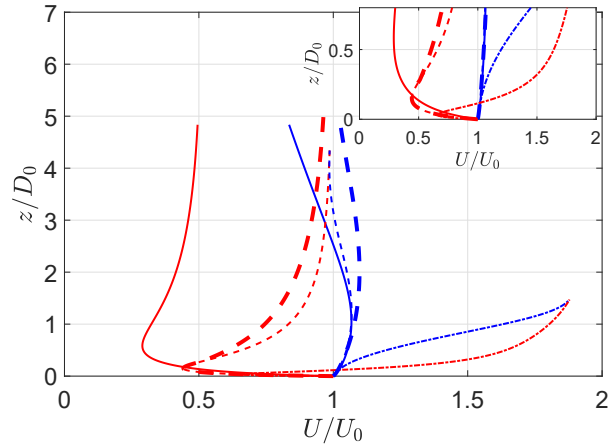
(c) Conjugate radius (EI)



(d) Conjugate radius (EII)

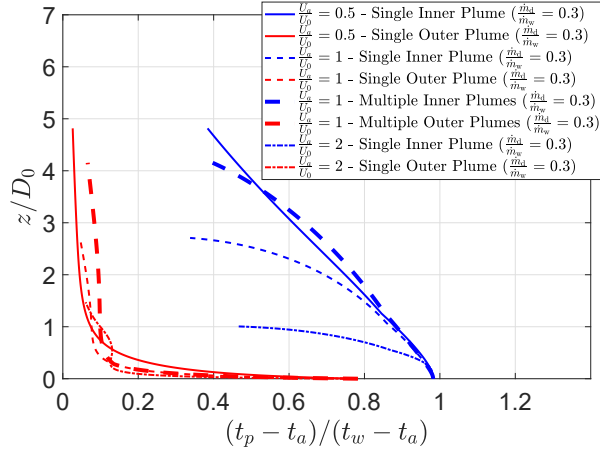


(e) Streamwise velocity (EI)

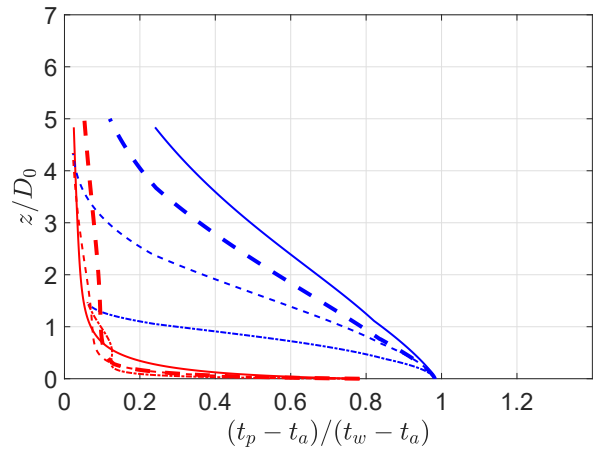


(f) Streamwise velocity (EII)

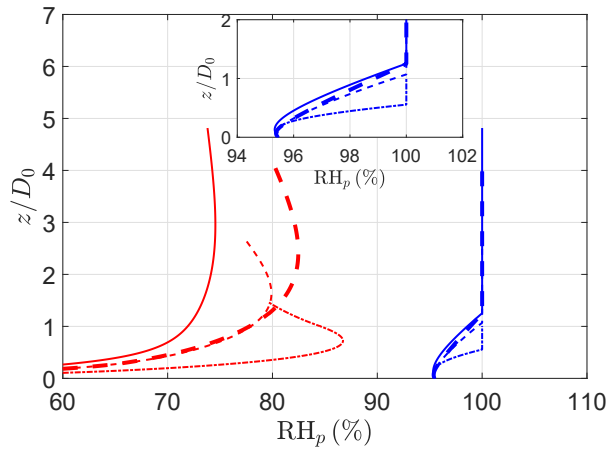
Figure 5.9: [Color] Non-dimensional plume centerline trajectories (panels a and b), conjugate radii (panels c and d) and streamwise velocities (panels e and f) as functions of plume rise height. The thick dashed curves denote the results for multiple cooling tower cells.



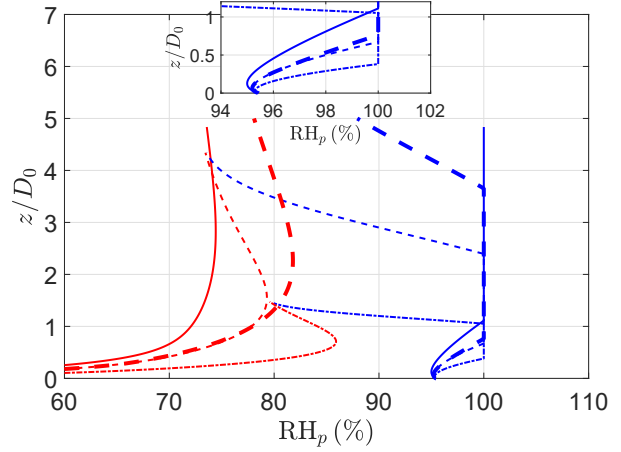
(a) Excess temperature (EI)



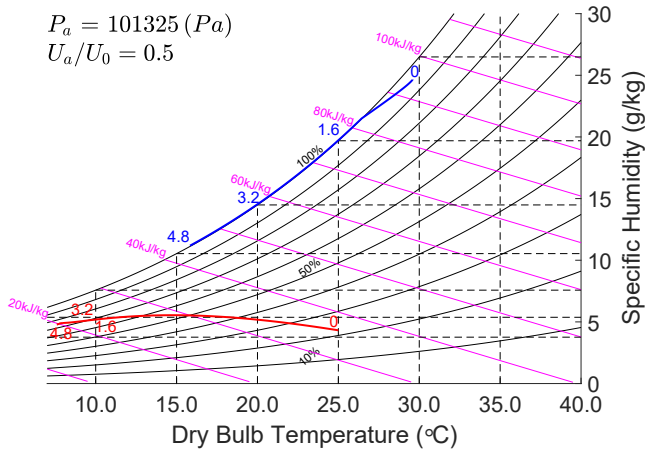
(b) Excess temperature (EII)



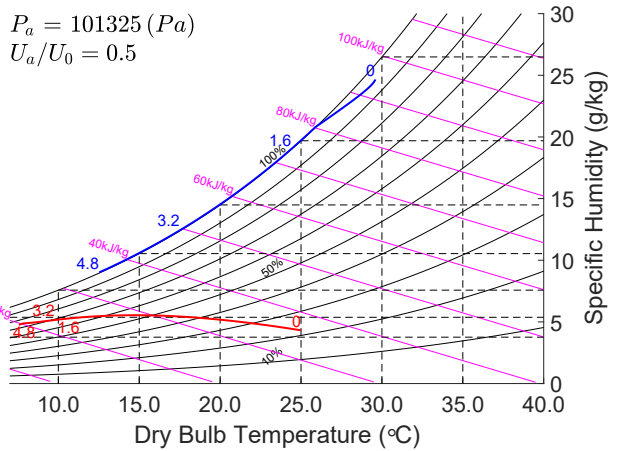
(c) Relative humidity (EI)



(d) Relative humidity (EII)



(e) Psychrometric chart (EI)



(f) Psychrometric chart (EII)

Figure 5.10: [Color] Non-dimensional plume excess temperature (panels a and b) and relative humidity (panels c and d) as functions of plume rise height. Panels e and f illustrate the dilution curves for the inner (blue) and outer (red) plumes on the psychrometric charts. The thick dashed curves denote the results for multiple cooling tower cells.

streamwise velocities as functions of plume rise height assuming entrainment formulations of type EI (panels a, c and e) and EII (panels b, d and f). The results are similar to figure 5.7, but now we add multiple cooling tower cells ($n = 9$) and the possibility of plume merger specifically for the case where $U_a/U_0 = 1$. The trajectories of single cell plumes in figures 5.9 a and 5.9 b are almost identical to those in figures 5.7 a and 5.7 b, which implies that moisture plays only a small role in plume rise. For multiple cells, the coaxial plume trajectory with $U_a/U_0 = 1$ is similar to the counterpart uniform plume trajectory shown in figure 5.3 a. Moreover, the cut-off height of the inner plume for the multiple cell case is greater than that for a single cell, i.e. $Z_c = 4.15$ vs. $Z_c = 2.71$ in figure 5.9 c. This observation also applies for figure 5.9 d, though the cut-off heights (not shown) therein are predicted to be much greater. Analogous to the streamwise velocity profiles in figure 5.3 c, figures 5.9 e and 5.9 f illustrate that the streamwise velocities of the inner and outer plumes for multiple cells are less quickly influenced by the wind than the counterpart velocity for a single cell.

Figure 5.10 illustrates the corresponding excess temperatures, relative humidities and dilution curves of the inner and outer plumes shown in figure 5.9. Figures 5.10 a and 5.10 b confirm that the inner and outer plumes for multiple cells are more buoyant than their single plume counterparts; similar enhancements can be seen in the relative humidity profiles in figures 5.10 c and 5.10 d. Comparing the insets to figures 5.8 c and 5.8 d, figures 5.10 c and 5.10 d indicate that the onset height for condensation decreases for smaller $\frac{\dot{m}_a}{\dot{m}_w}$. Nonetheless, the dilution curves of both cases are similar, as indicated by the similar shapes of the red curves from figures 5.8 e,f and figures 5.10 e,f.

5.4.4 Sensitivity of theoretical results to entrainment coefficients

Further to the brief discussion on entrainment coefficients in section 5.4.2, we now examine the sensitivity of our model predictions to the precise values of α and β . Due to the qualitatively similar results for EI and EII described in section 5.4.3, we only consider the variation of the EI results in the brief analysis to follow. The parameter of reference is the inner visible plume length, i.e. $\Delta S_1 \equiv \Delta s_1/D_0$. For the source conditions specified in table 5.1 with $\frac{\dot{m}_a}{\dot{m}_w} = 0.3$, ΔS_1 is presented as a function of α and β in figure 5.11 a with $U_a/U_0 = 0.25$ and in figure 5.11 b with $U_a/U_0 = 2$. Consistent with Carazzo *et al.* (2006), we consider as the maximum possible value for α and β the top-hat entrainment coefficient of 0.160. Figure 5.11 indicates that wind significantly alters the sensitivity of ΔS_1 to variations in α and β . More specifically, and as the wind speed increases from $U_a/U_0 = 0.25$ to $U_a/U_0 = 2$, the sensitivity of ΔS_1 with respect to α greatly reduces whereas the sensitivity with respect to β increases. This is because the inner plume is more rapidly absorbed by the outer plume for large wind speeds (cf. figure 5.9 c).

5.4.5 Coaxial plumes under various ambient and source conditions

The analysis of section 5.4.3 is limited to a single dry air mixing fraction (DAMF) of 30%; here we relax this restriction and allow DAMF to vary. For fixed ambient temperature, t_a , and relative humidity, RH_a , we study the effect of DAMF and wind speed on the visible plume length. Moreover, to avoid the complication of condensation in both the inner and outer plumes, cases wherein fog forms only within the inner plume are considered first. The

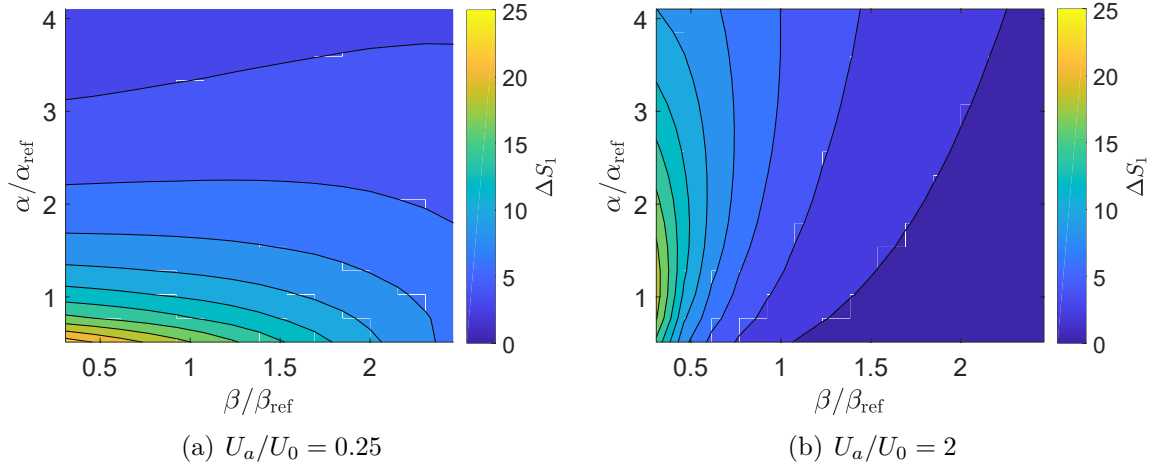


Figure 5.11: [Color] Contour plots of the inner visible plume length (ΔS_1) as a function of α and β assuming an EI formulation. The reference entrainment coefficients are $\alpha_{\text{ref}} = 0.039$ and $\beta_{\text{ref}} = 0.065$.

inner visible plume lengths are shown as a function of DAMF and wind speed in the six panels of figure 5.12 where, in all cases, $\frac{\dot{m}_d}{\dot{m}_w} = 0.3$ and we consider an EI entrainment formulation. In general, the portion of the DAMF – U_a/U_0 parameter space where no fog forms (deep blue) increases as t_a rises (figures 5.12 a,b,d,f) or RH_a drops (figures 5.12 a,c,e). Meanwhile, the maximum visible plume lengths occur for small DAMF and wind speed ratios of between 0 and 1. Noticeably, by fixing DAMF = 20% in e.g. figure 5.12 a, the visible plume length varies non-monotonically with increasing wind speed, experiencing a peak then a trough, the latter being coincident with a wind speed of $U_a/U_0 \approx 1.4$.

To gain more insight into this non-intuitive behavior, we plot the velocity difference, $(U_1 - U_2)/U_0$, as a function of downwind streamwise distance for different wind speeds – see figure 5.13. At $U_a/U_0 = 1.4$, the dashed curve in figure 5.13 indicates that the shear, $|U_1 - U_2|$, becomes comparatively small over a relatively broad range of streamwise distances. As a result, and referring back to (5.19), ω_β far outweighs ω_α and thereby the inner plume is easily cut off before it begins to condense. When $U_a/U_0 \neq 1.4$, we expect a more nuanced competition between ω_α and ω_β . For small but non-zero wind speed, e.g. $U_a/U_0 = 0.5$, the near source dilution increases compared to cases with smaller wind speed (e.g. $U_a/U_0 = 0.25$) – see figure 5.5 b. This enhanced dilution decreases U_2 and results in an increase in $U_1 - U_2$. Therefore, the ambient fluid initially entrained into the outer plume is rapidly entrained into the inner plume, leading to a higher risk of condensation. As the wind speed increases from $U_a/U_0 = 0.5$ to $U_a/U_0 = 1.4$, U_2 increases (cf. figure 5.9 e) whereas $|U_1 - U_2|$ decreases, thus more inner plume fluid is entrained into the outer plume. For still larger wind speeds with $U_a/U_0 > 1.4$, on the other hand, both U_2 and $|U_1 - U_2|$ tend to increase. Notice from figure 5.13, however, that the cut-off height for the inner plume decreases for sufficiently large wind speed. Thus, in case of very large U_a/U_0 , the inner plume tends to be cut off and thereby the visible plume length is reduced, which is corroborated by the contours in figure 5.12. To conclude, we argue that the non-monotonic variation in the visible plume length (figure 5.12) is a direct consequence of the EI entrainment assumption, in particular the ω_α term in (5.19). To this end, it is helpful to draw a comparison with EII and its different equation

for ω_α .

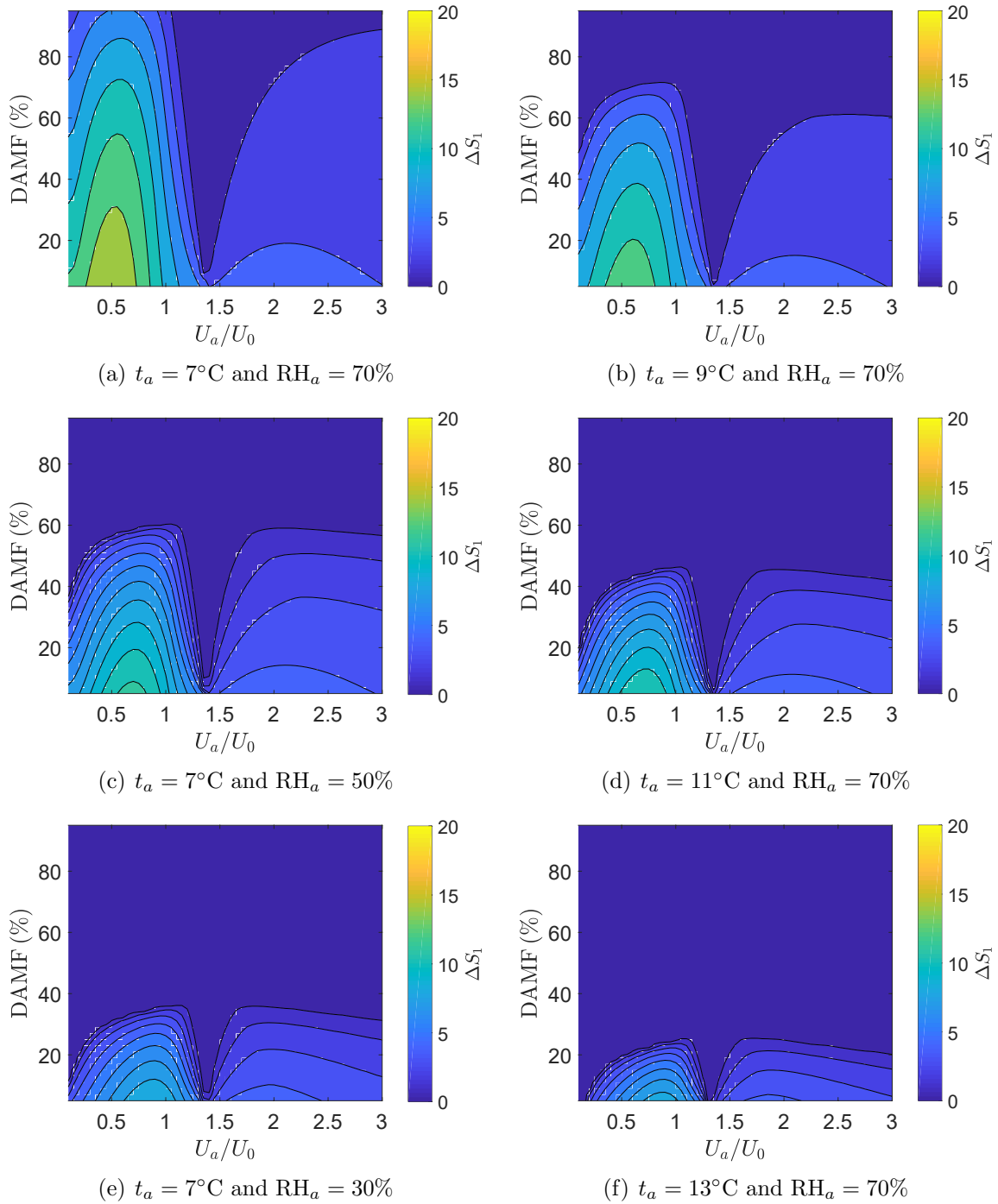


Figure 5.12: [Color] Contour plots of visible plume length (ΔS_1) under various dry air mixing fractions (DAMFs) and for different wind speeds assuming an EI entrainment formulation. Panels a, c and e correspond to the same t_a but different RH_a , whereas panels a, b, d and f correspond to the same RH_a but different t_a .

The contour plots of the inner visible plume length assuming an EII entrainment formulation are illustrated in figure 5.14. Analogous to figure 5.12, figure 5.14 shows an increase

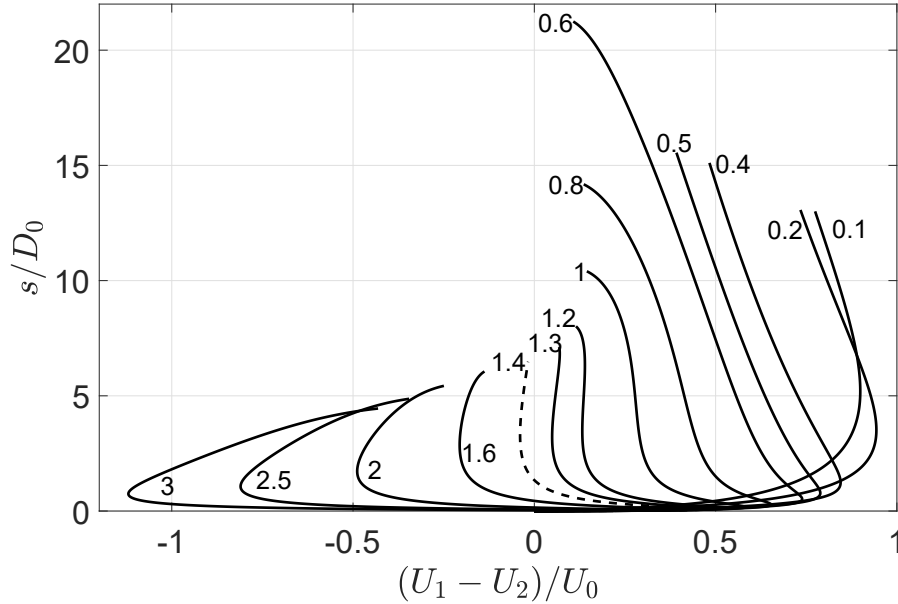


Figure 5.13: The velocity differences between the inner and outer plumes as functions of streamwise distance for different wind speeds. The solid curves are labeled with values of U_a/U_0 with the dashed curve corresponding to the special case $U_a/U_0 = 1.4$. The other parameters are $t_a = 7^\circ\text{C}$, $\text{RH}_a = 70\%$ and $\text{DAMF} = 30\%$.

in the portion of deep blue region with increasing t_a or decreasing RH_a . However, in contrast to figure 5.12, figure 5.14 shows a greater regularity as the wind speed increases. For instance, by fixing the DAMF (say, 20%) in figure 5.14 a and allowing the wind speed to increase, the visible plume length initially increases then decreases with a single peak located at $U_a/U_0 \approx 0.5$. With EII in other words, we avoid a local minimum at $U_a/U_0 \approx 1.4$. This observation, can be justified by comparing the entrainment velocities into the inner plume in the EI and EII entrainment formulations, i.e. $\omega_\alpha = \alpha |U_1 - U_2|$ vs. $\omega_\alpha = \alpha U_1$, particularly when $|U_1 - U_2| \ll U_1$. In this limit, $U_1 \approx U_2$, and the composite plume may be more appropriately characterized by a uniform plume rather than a coaxial plume. EI then prescribes an asymmetric process whereby fluid is entrained from the inner to the outer plume in greater volumes than from the outer to the inner plume. By contrast, EII prescribes a two-way entrainment process, which seems more physically reasonable in the $U_1 \approx U_2$ limit. Extending this conclusion to other combinations of the inner and outer plume velocities, we argue that EII exhibits a greater realism than does EI. Nonetheless, a definite verdict on EI vs. EII can only be drawn from a careful analysis of future experimental data.

To further investigate the environmental condition parameter space where fog forms only in the inner plume, if at all, we generate surface plots of the inner visible plume length. Results are summarized in figure 5.15 wherein we consider the EII entrainment formulation with $\frac{\dot{m}_d}{\dot{m}_w} = 0.3$ and $\text{DAMF} = 30\%$. Considering the most adverse environmental conditions, figure 5.15 shows that the maximum inner visible plume length decreases rapidly with increasing wind speed (figures 5.15 a to d), a consequence of enhanced dilution. Note also that the enhanced mixing associated with large wind speeds does not significantly expand the parameter space for which no fog forms, as can be inferred by comparing the breadth of the flat regions in the four panels of figure 5.15. On the other hand, figures 5.15 b,c,d

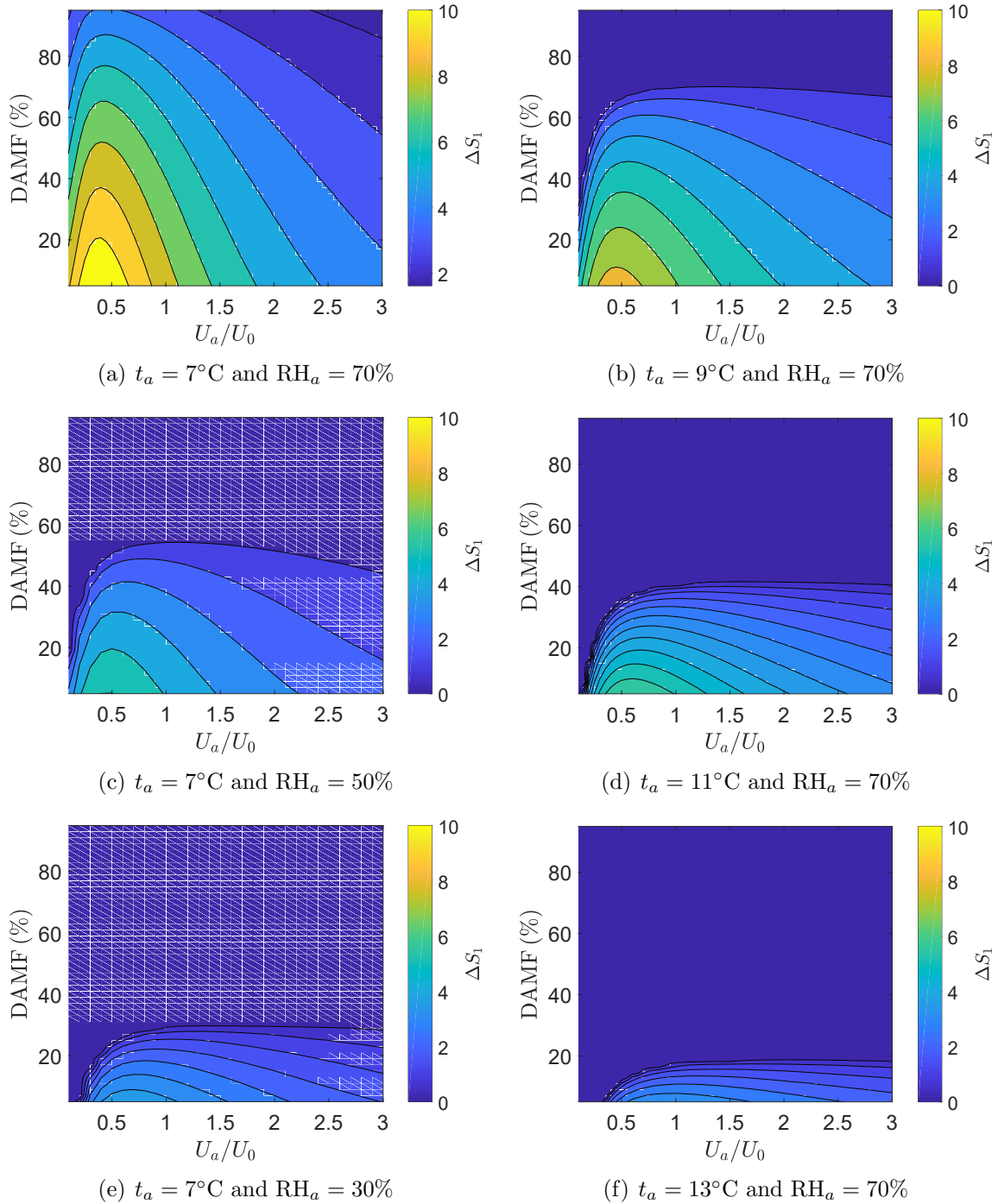


Figure 5.14: [Color] As in figure 5.12 but assuming an EII entrainment formulation.

anticipate a region above the upper “sawtooth” where fog also forms in the outer plume. This indicates that for especially low ambient temperature and high relative humidity, the coaxial plume offers no material advantage over its uniform counterpart, at least insofar as plume abatement is concerned. On this topic, note that the region where fog forms in the outer plume expands as the wind speed increases from figures 5.15 b to d. This is most likely due to the more rapid blending of the inner and outer plume fluid in case of larger wind speeds.

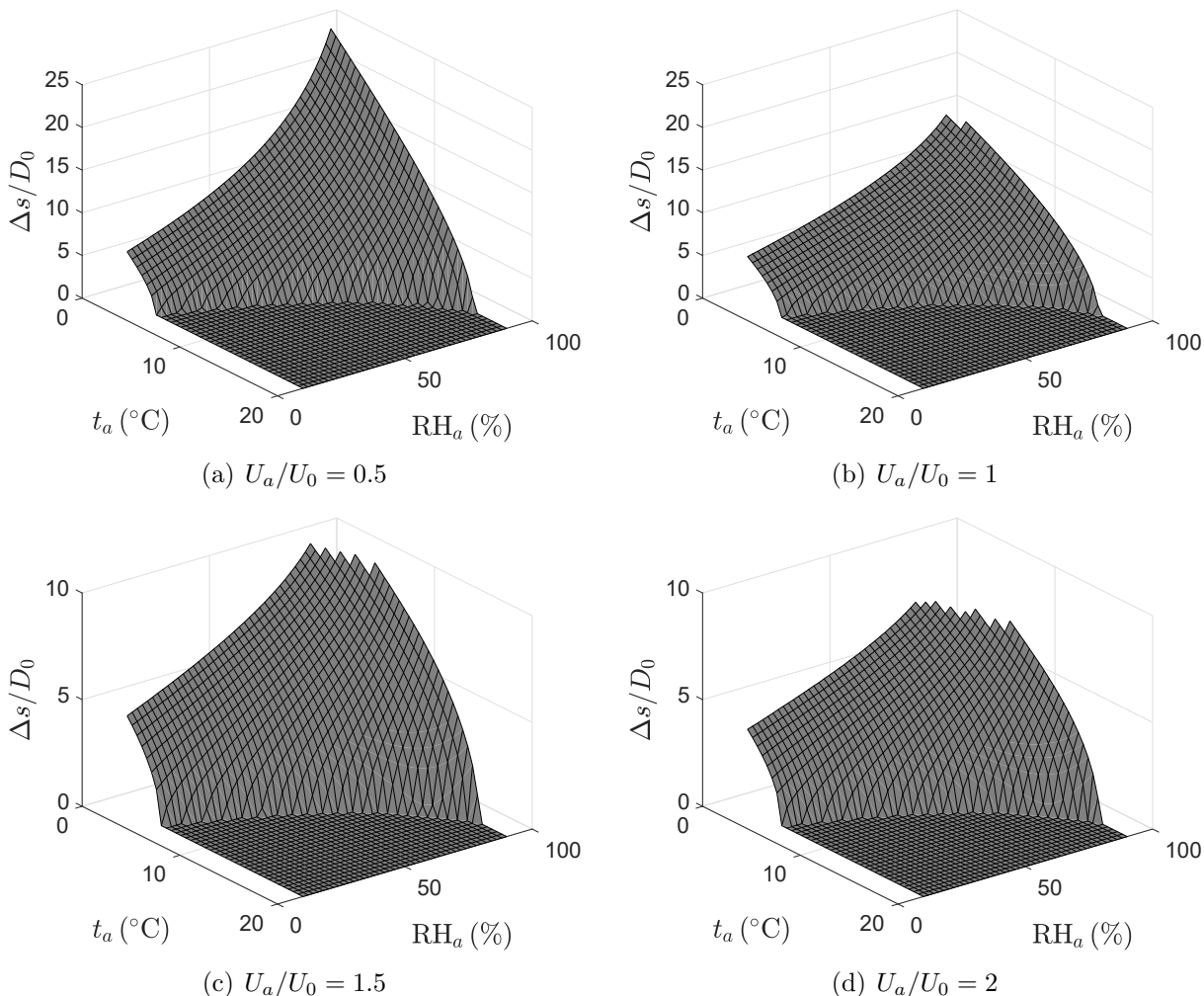


Figure 5.15: Surface plots of visible plume length under varying ambient temperature and relative humidity with $\frac{\dot{m}_a}{\dot{m}_w} = 0.3$ and DAMF = 30%. The regions above the upper sawteeth in panels b, c and d correspond to conditions where fog forms in the outer plume. Note the difference of vertical axis limits between the top and bottom panels.

5.5 Conclusions

The current manuscript presents theoretical modeling of coaxial plumes in a windy ambient. The entrainment from the inner to the outer plume follows the formulations derived by Morton (1962) and Li *et al.* (2018), whereas the entrainment from the ambient to

the outer plume follows analyses from Devenish *et al.* (2010*b*). Regarding the entrainment from the outer to the inner plume, we follow the two entrainment assumptions proposed by Bloomfield & Kerr (2000), using either the velocity difference between the inner and outer plumes (EI) or only the inner plume velocity (EII) as the scaling velocity. Two body force formulations for the inner plume are discussed, which regard either the ambient fluid (BFI) or outer plume (BFII) as the reference fluid when evaluating the inner plume buoyancy.

Representative results show that for coaxial plumes, fog is not completely eliminated, however, it typically forms only in the inner plume. As the wind speed increases, the inner plume is more rapidly cut off by the outer plume. Meanwhile, the moisture transferred from the inner to the outer plume is quickly diluted by the wind. In the very far field, the outer plume (or the uniform plume after the inner plume disappears) approaches the wind speed asymptotically, which is consistent with the analogue case of a uniform plume. The two entrainment formulations, EI and EII, produce qualitatively similar results of coaxial plume dynamics.

The visible plume length is used to evaluate the severity of fog formation, a generally undesirable attribute of cooling towers. For uniform plumes, figure 5.4 reveals a non-monotonic variation of the visible plume length with increasing wind speed. Qualitatively similar observations apply to the case of coaxial plumes though here the analysis is more involved. Consider, for example, figures 5.12 and 5.14, which respectively consider the EI and EII entrainment formulations and which show the visible plume length vs. the wind speed and the dry air mixing fraction (DAMF). Nontrivial differences between the contour plots with EI and EII are noted. For an EI entrainment formulation, by fixing DAMF, the visible plume length oscillates as the wind speed increases, with a local minimum (and possibly no condensation at all) when $U_a/U_0 \approx 1.4$. This non-monotonic behavior is, as revealed in figure 5.13, due to the combined effect of the entrainment between the inner and outer plumes and the dilution of the outer plume by the wind. By contrast, an EII entrainment formulation results in a more regular, though still non-monotonic, evolution of the visible plume length, as reflected by the contours of figure 5.14. In light of this observation, and by special consideration of the limit of nearly equal inner and outer plume speeds, we argue that EII provides more realistic results than does EI. On the basis of the above analysis, the severity of the visible plume is assessed in regime diagrams e.g. figure 5.15, which specifically consider the influence of environmental conditions, i.e. the ambient temperature, t_a , and the relative humidity, RH_a .

The key limitation of this study is the lack of an experimental verification, especially vis-à-vis the entrainment assumptions EI vs. EII. Performing such (nontrivial) experiments is a task that we defer to future studies. Another limitation is related to the restrictions of integral plume models, which are only capable of describing time-averaged, boundary layer type flows in an unbounded environment as indicated by the parabolic nature of the governing equations (Jirka, 2004). As far as recirculation is concerned, a future experimental test of interest is to determine whether a coaxial plume structure helps reduce the recirculation ratio – see e.g. the wind tunnel experiment in Liu & Bao (2014). In their test, carbon monoxide was released into the central region of a model-scale cooling tower, and thus the recirculation ratio could be determined by measuring the carbon monoxide concentrations at the tower inlet. One may also consider a turbulent windy environment to see whether the inner-outer plume structure is easily broken by external turbulence. To this end, a water flume (Yuan

et al., 2011) or wind tunnel (Michioka *et al.*, 2007; Contini *et al.*, 2009) experiment may be considered where, in either case, we expect a turbulent boundary layer to develop much like in the real atmosphere. Moreover, and given the simplified treatment of the merging criteria used in this study, the process of plume merger deserves more detailed attention. For instance, a question of particular concern is how exactly the merging process modifies entrainment and hence influences the visible plume length. Recently, Rooney (2015, 2016) proposed a sound theoretical analysis of plume merger on the basis of potential flow theory. The idea of using a velocity potential to represent the mean plume-ambient boundary of a merged plume could be fruitfully extended to cooling tower plume rise in either a stationary or windy environment.

5.6 Appendix A: Plume merger in a crosswind

As illustrated in figure 5.16 a, the wind is assumed normal to the tower array i.e. $\varphi = 90^\circ$ in figure 5.16 b, which is expected to represent a worst case scenario for plume rise enhancement (Macdonald *et al.*, 2002). In such a configuration, the interior individual plumes are expected to have almost identical trajectories, cross sections and buoyancy and momentum fluxes until the onset of merging. With this “symmetry”, it is appropriate to use the merging criteria based on the geometrical principles suggested by Wu & Koh (1978).

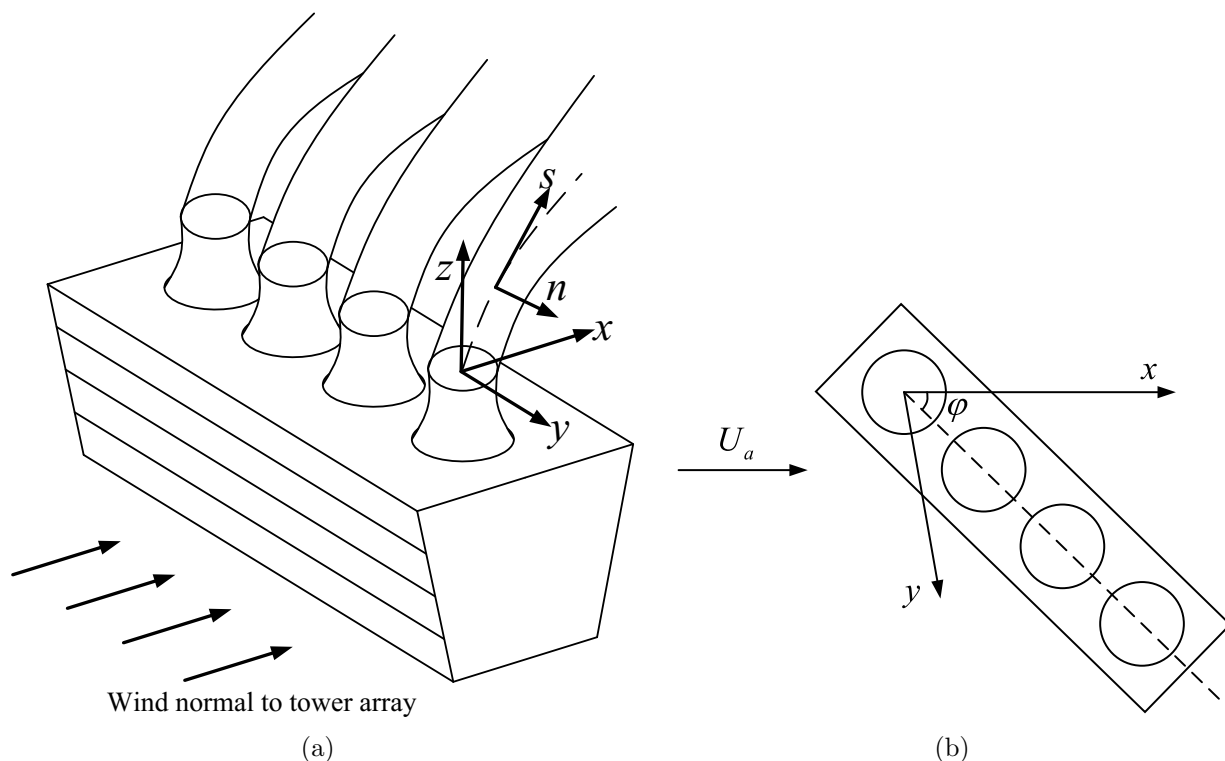


Figure 5.16: (a): Schematic of a line array of four tower cells that is perpendicular to the wind direction. (b): Top view of the cooling tower configuration with ϕ denoting the angle between the wind direction and the cooling tower axis.

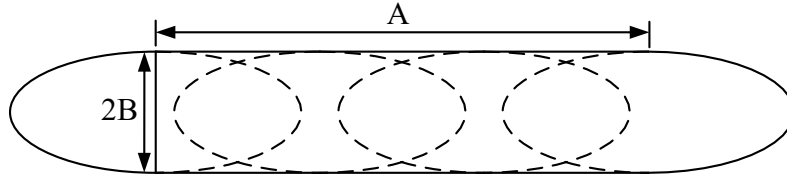


Figure 5.17: A cross-sectional view of the merged plume in a crosswind. The dashed ellipses show the cross sections of individual plumes. The solid curve shows the geometry of the merged uniform plume.

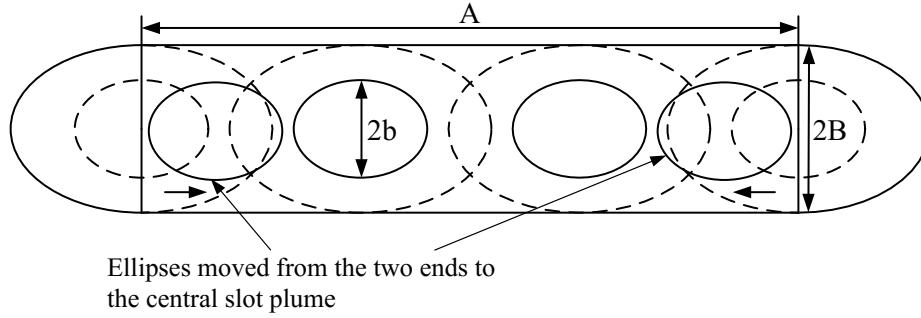


Figure 5.18: A cross-sectional view of four coaxial plumes upon merging in a crosswind. The solid curves and ellipses show the geometry of the merged plume.

The cross sections of merged uniform and coaxial plumes are sketched in figures 5.17 and 5.18, respectively. For uniform plumes, the cross section of the merged plume consists of a central slot plume and two half elliptical plumes at the two ends. With reference to figure 5.17, plume merger is deemed to occur once the area of the central rectangle equals the sum of the areas of the interior ellipses. Thus figure 5.17 shows a circumstance post-merger. With reference to this schematic and the length scales defined therein, the geometric condition defining merger reads $A = \frac{\pi\lambda B(n-1)}{2}$ where $n = 4$. After plume merger, solutions for the half-elliptical and line plumes are separately integrated forward by one spatial step. The cross-sectional area, $A_e(A_l)$, and entrainment flux, $E_e(E_l)$, for the half-elliptical (line) plume is as follows:

$$\begin{aligned}
 A_e &= \frac{1}{2}\pi\lambda B^2, & E_e &\approx \pi\sqrt{\frac{\lambda^2+1}{2}}B^{3/2}\sqrt{(\gamma_{1,e}|U_p - U_a \cos \theta|)^{3/2} + (\gamma_2|U_a \sin \theta|)^{3/2}}, \\
 A_l &= 2AB, & E_l &= 2A^{3/2}\sqrt{(\gamma_{1,l}|U_p - U_a \cos \theta|)^{3/2} + (\gamma_2|U_a \sin \theta|)^{3/2}},
 \end{aligned} \tag{5.40}$$

where the entrainment coefficient for the two terminal half-elliptical plumes is $\gamma_{1,e} = \gamma_1 = 0.1$ and the entrainment coefficient for the central slot plume is given as $\gamma_{1,l} \simeq 0.2$ (Wu & Koh, 1978). For the counterpart coaxial plumes, we manually shift the two inner plumes at the two ends into the central slot plume for ease of computation. Thus the central, coaxial plume consists of n inner elliptical plumes and an outer slot plume. The entrainment coefficient for the two terminal half-elliptical plumes is, by assumption, the same as in the uniform plume case. More details on the calculation of the merged uniform and coaxial plumes can be found in Appendix A of Li *et al.* (2018).

Because the present study only considers a single wind direction that is normal to the tower array, we briefly review the effect of varying the wind direction i.e. of changing φ .

Contini & Robins (2001) considered two in-line plumes with $\varphi = 0^\circ$, i.e. a crosswind parallel to the tower array. Their experimental results show that the resulting twin plume exhibits a rise height that is up to 30% larger than the counterpart single plume. Meanwhile, the interaction between the two plumes results in the nontrivial development of an internal vortex structure that is different from the single plume case – see their figure 6. Later Macdonald *et al.* (2002) confirmed the rise enhancement for the in-line arrangement, which approaches $2^{1/3}$ i.e. the limit according to Briggs’ two-thirds law. On the other hand, and for the perpendicular arrangement with $\varphi = 90^\circ$, they typically found a slight decrease in plume rise height. Macdonald *et al.* (2002) argued that this decrease is partially due to a downwash effect associated with an opposing vortex structure in the perpendicular arrangement. Considering the more general case of $0^\circ \leq \varphi \leq 90^\circ$, Contini & Robins (2004) found that the rise enhancement of two identical plumes decreases linearly with $\sin\varphi$ with increasing φ until $\varphi = 20^\circ$ to 30° . Thereafter, and consistent with Macdonald *et al.* (2002), reductions in plume rise occur due to the so-called “induced downwash” effect. In a follow-up study, Contini *et al.* (2006) investigated the mixing of two identical plumes in a turbulent boundary layer rather than in a laminar crossflow. They found that for $\varphi \geq 45^\circ$, there is an average downward velocity in the middle of the plume that stretches the plume and results in a negative rise enhancement. Of course, the interaction between the counter-rotating vortices and the associated negative rise enhancement are not accounted for in the present study, which focuses instead on integral plume formulations.

Chapter 6

Merging of two plumes from area sources with applications to cooling towers

6.1 Abstract

Velocity potential contours have been used to demarcate the boundary between the interior and exterior of a plume, this for the case of adjacent plumes subject to merger (Rooney 2015, *J. Fluid Mech.*, vol. 771, R1). Whereas Rooney's theory is restricted to cases where the plume source is much smaller than the distance between neighboring plume centers, the modification suggested herein allows individual plumes to originate from an area source of arbitrary size. In the present theory, the height at which two plumes fully merge is defined as the location where the combined plume boundary is no longer concave. Referencing the plume boundary curvature, we introduce an alternative, simpler entrainment formulation that does not involve the flux-balance parameter used in Rooney's revised model. The present model is applied to adjacent cooling tower plumes and generates satisfactory agreement with previous model predictions, including those that adopt a quite different criterion for plume merger.

6.2 Introduction

The merging of jets or plumes is observed in many situations, such as multiport diffusers (Abessi & Roberts, 2014), natural ventilation (Linden, 1999) and cooling tower plumes (Wu & Koh, 1978). In case of natural ventilation, Linden & Kaye (2006) argued that the merging of co-flowing plumes can be important in tall, naturally ventilated rooms of high occupancy. For industrial cooling towers commonly arranged in inline or back-to-back configurations (Lindahl & Mortensen, 2010), plume merger influences the amount of entrainment and, by extension, the dilution rate and the visible plume length. In turn, a correct estimation of the visible plume length is crucial in evaluating possible risks to nearby infrastructure e.g. due to ice accretion as well as strategies for plume abatement.

The process of plume merger is illustrated in figure 6.1. A number of theoretical models

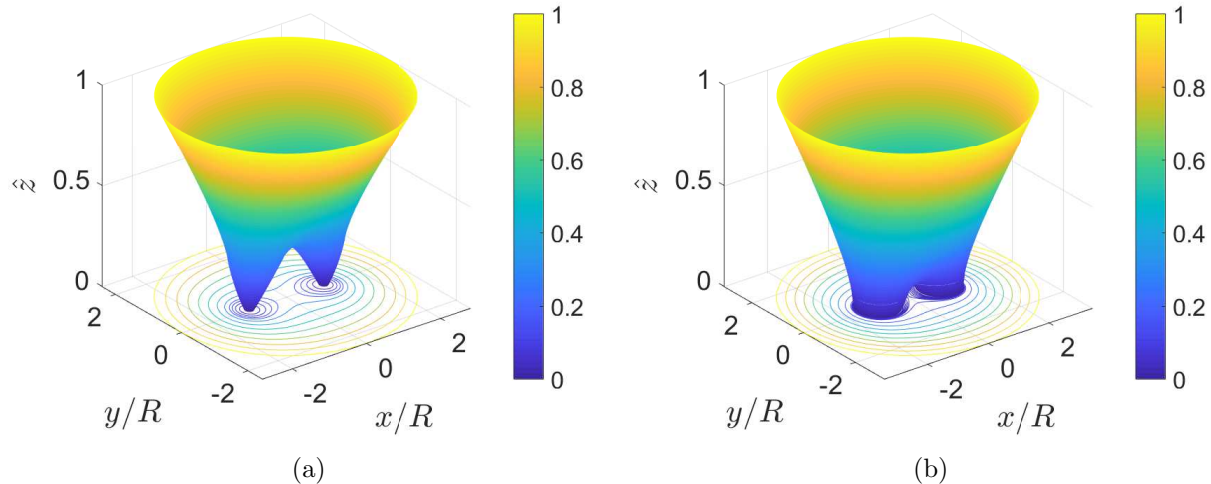


Figure 6.1: [Color online] Surface plots illustrating plume merger from small (panel a, $\rho_0 = 0.1$) and large (panel b, $\rho_0 = 0.6$) sources with $\Gamma_0 = 1$. The parameters, ρ_0 , Γ_0 , x/R , y/R and \hat{z} , are defined in section 6.3 below. The plume boundaries are shaded according to the height between 0 and 1, and these contours are also projected onto the bottom plane. Note that these results are produced using a so-called curvature method, which is outlined in section 6.4.

on plume merger, starting with Taylor (1958), are based on the idea that the external flow field can be approximated as irrotational. Because irrotational flow is governed by Laplace’s equation, which is linear, it is straightforward to superpose two different sinks corresponding to two different entraining plumes. Kaye & Linden (2004) investigated the merging of two axisymmetric plumes of equal and unequal strengths using a combination of theory and experiment. Their model assumes that each plume is passively advected by the entrainment flow field of the opposite plume, ambient entrainment being the mechanism responsible for drawing the plumes together. Meanwhile, the merging height in their laboratory experiments is defined as the height where there first appears a single maximum in the transverse buoyancy profile. Following the work of Kaye & Linden (2004), Cenedese & Linden (2014) proposed a model that parameterizes the mutual entrainment of side by side plumes over a vertical range spanning first contact to full plume merger. Over this range of heights, they found that the plume volume flux varies linearly with height. Their novel contribution was to use a single equation (i.e. their 2.12) to represent the evolution of volume flux of two merging plumes. Unlike the small initial momentum and buoyancy fluxes studied by Kaye & Linden (2004) and Cenedese & Linden (2014), which, in turn, suggest source conditions close to those of an ideal plume, Lai & Lee (2012) investigated the merging of buoyant jets with an excess of momentum compared to pure plumes. Before merger, the individual jet elements are represented by a distribution of point sinks and the dynamic pressure field can be described using Bernoulli’s equation. This pressure calculation is used in conjunction with the integral governing equations to derive an updated jet trajectory. A revised pressure field is then computed and the process is repeated until the solution converges – see their figure 4. After merger, the velocity and scalar concentration fields are resolved by superposition of momentum or kinetic energy and scalar mass flux, respectively. The validity of Lai and Lee’s model was verified by comparison with the output from a RANS-based numerical

model employing a k - ϵ turbulence closure (Shih *et al.*, 1995). A similar superposition method was adapted by Yannopoulos (2010) to predict the mean vertical velocity and concentration of a finite number of interacting buoyant jets.

More recently, Rooney (2015) (hereafter R15) proposed using the contours of velocity potential to represent the mean flow boundaries for a long row of plumes or jets. Previous models (e.g. Yannopoulos (2010)) assume that the plumes are deflected but that their cross sections remain circular and overlap when merging occurs. By contrast, R15 allows the plume cross section to distort as a result of reduced entrainment. His model prediction generates good agreement with the experimental results of Bush & Woods (1998) regarding the depth of the two-dimensional outflow resulting from plume rise in a restricted channel. Later Rooney (2016) (hereafter R16) applied the same approach to study the merging of a number of plumes equally spaced along the perimeter of a circle. The other novel contribution in R16 compared to R15 is the introduction of a modified entrainment assumption, which considers the effect of a so-called flux-balance parameter, Γ (defined and discussed in section 6.3.3.2). The R16 model, referred to below as Rooney’s revised model to distinguish it from the original model presented in R15, matches satisfactorily with the experimental measurements of the total volume flux of two merging plumes made by Cenedese & Linden (2014). R16 has been recently employed by He & Lou (2019) to study the interaction of multiple forced plumes in a linearly stratified ambient. One possible limitation of Rooney’s work is that the plume source is assumed to be small compared to the separation distance between neighboring plume centers. In many cases of practical interest (e.g. cooling towers), however, the plume source diameter is nontrivial and the plumes are relatively closely spaced. Under such conditions, a virtual origin correction cannot be applied because the cross section of an individual plume arising from the virtual source is expected to be highly distorted by the time it reaches the level of the actual (circular) source.

In the context of cooling tower plumes, a number of merging criteria have been proposed. Davis (1975) assumed that the plumes originating from middle cells are affected only slightly by the total number of cells, i.e. end effects can be ignored. In coming to this conclusion, Davis (Davis, 1975) assumed *a-priori* a smooth temperature profile along the axis of the merging plumes (see his figure 7). As illustrated schematically in figure 6.2, Wu & Koh (1978) (hereafter WK78) proposed a merging criterion on the basis of purely geometrical considerations; their criterion has been employed in various follow-up studies (e.g. Policastro *et al.* (1994); Li *et al.* (2018)). Unfortunately, the interaction between plumes and the associated reduced entrainment due to plume merger are not accounted for, which possibly underestimates the visible plume length.

In the current study, we extend the potential flow theory of R15 and R16 to model the merging of two plumes rising from arbitrary area sources. An alternate entrainment assumption, which considers only the evolution of the plume boundary, is proposed. On this basis, we apply our theory to the merging of two industrial cooling tower plumes. Comparisons with the complementary theory of WK78 are then drawn.

Our manuscript is organized as follows: In section 6.3, we review Rooney’s potential flow theories. A novel entrainment formulation that relates the entrainment coefficient to the plume boundary curvature is proposed in section 6.4. In section 6.5, we modify Rooney’s analysis to include finite source effects. Thereafter, in section 6.6 we adapt the present model to cooling tower plumes. Finally, in section 7.7 we draw conclusions.

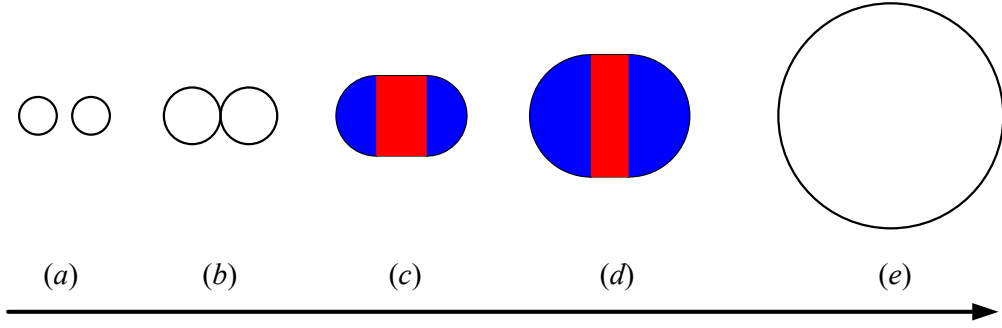


Figure 6.2: [Color online] Evolution of the plume cross section as described by Wu & Koh (1978). Panel (a) denotes the initial stage of two individual plumes. Panel (b) denotes the stage of first contact, however, no plume interaction occurs until full merger, which is depicted in panel (c) and which is defined as the elevation where the area of the central rectangle (shaded red) equals the sum of the areas of the two half round plumes (shaded blue). Panel (d) denotes a stage of the combined plume post merger. Panel (e) shows an axisymmetric plume in the very far field.

6.3 Rooney's theory

6.3.1 Complex potential

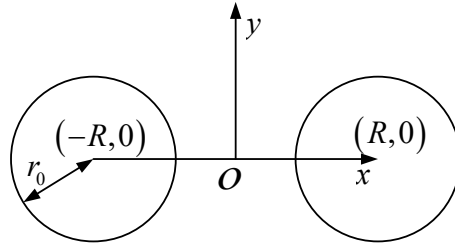


Figure 6.3: Sketch of two plumes from an area source of radius r_0 . As $r_0 \rightarrow 0$, the flow becomes identical to the $n = 2$ case exhibited in figure 1 of R16.

Following R16, the complex potential due to two equal line sinks (figure 6.3 with $\rho_0 \rightarrow 0$) reads

$$\Omega = -\frac{m}{2\pi} \ln(Z'^2 - 1) - \frac{m}{2\pi} \ln R^2, \quad (6.1)$$

where $-m(Z)$ is the strength of each line sink with $Z = x+iy = r e^{i\theta}$, $Z' = x/R+iy/R = \rho e^{i\theta}$. Here R is half of the distance between the line sink sources. Due to the symmetry of the flow field, only the sector for which $-\pi/2 \leq \theta \leq \pi/2$ is considered. The contours of velocity potential are given by $|Z'^2 - 1| = k$ where $k > 0$ is a constant. Stated in terms of radius and polar angle, the velocity potential contours satisfy

$$\rho^4 - 2\rho^2 \cos 2\theta + 1 = (\rho^2 + 2\rho \cos \theta + 1) (\rho^2 - 2\rho \cos \theta + 1) = k^2. \quad (6.2)$$

Solving for ρ and θ yields

$$\rho = \left(\cos 2\theta \pm (k^2 - \sin^2 2\theta)^{1/2} \right)^{1/2}, \quad (6.3)$$

$$\theta = \pm \frac{1}{2} \cos^{-1} \left(\frac{\rho^4 + 1 - k^2}{2\rho^2} \right), \quad (6.4)$$

where the negative square root in (6.3) is to be considered only when $k \leq 1$. Meanwhile, $k^2 - \sin^2 2\theta \geq 0$ ($k \leq 1$) specifies the limit of polar angle to be determined in (6.9). Sample contours of velocity potential are illustrated in figure 6.4.

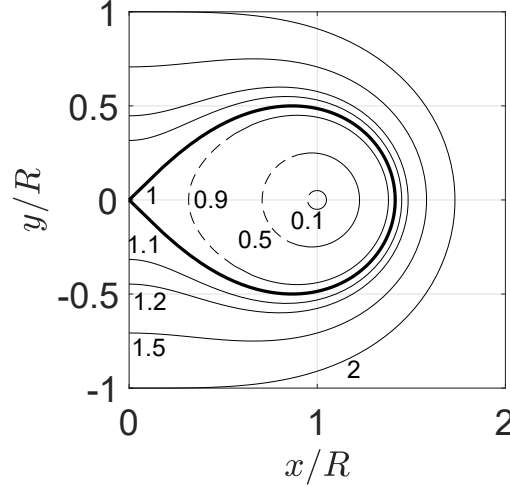


Figure 6.4: Contours of velocity potential in Z' -space. The numerical values of k are labeled. For closed contours with $k \leq 1$, the dashed (solid) curves represent the negative (positive) square root in (6.3).

Differentiating (6.2) with respect to θ yields

$$\frac{d\rho}{d\theta} = \frac{\rho \sin 2\theta}{\cos 2\theta - \rho^2}, \quad (6.5)$$

thus ρ_{\max} occurs at $\theta = 0$, which corresponds to the positive square root in (6.3), i.e.

$$\rho_{\max} = (k + 1)^{1/2}. \quad (6.6)$$

Analogous to ρ_{\max} , it is helpful to consider the minimum radial length, ρ_{\min} . When $k < 1$, ρ_{\min} is determined by setting $\theta = 0$ and considering the negative square root in (6.3). When $k = 1$, $\rho_{\min} = 0$. Finally, when $k > 1$, we consider $\theta = \pm\pi/2$ and the positive square root in (6.3). Altogether

$$\rho_{\min} = \begin{cases} (1 - k)^{1/2}, & k \leq 1 \\ (k - 1)^{1/2}. & k > 1 \end{cases} \quad (6.7)$$

For $k \leq 1$, the contours are closed and bounded by a polar angle $|\theta_{\lim}| < \pi/2$. The contour coordinates at θ_{\lim} , $(\rho_{\lim}, \theta_{\lim})$, are determined by setting $\frac{d\theta}{d\rho} = 0$. Thus, it may be shown from (6.5) that $\rho_{\lim}^2 = \cos 2\theta_{\lim}$. Applying (6.3), we find that

$$\rho_{\lim} = (1 - k^2)^{1/4}, \quad (6.8)$$

$$\pm\theta_{\lim} = \pm \frac{1}{2} \sin^{-1} k. \quad (6.9)$$

The maximum closed contour occurs when $k = 1$ with an angular range $-\pi/4 \leq \theta \leq \pi/4$. Note also that $k = 1$ represents the point of first contact. Accordingly, we define the height of first contact as the height corresponding to $k = 1$.

6.3.2 Flow speed, flux and area integrals

The complex velocity can be obtained from (6.1) as

$$u - iv = \frac{d\Omega}{dZ} = -\frac{m}{2\pi R} \frac{2\rho [(\rho^2 \cos \theta - \cos \theta) - i(\rho^2 \sin \theta + \sin \theta)]}{\rho^4 - 2\rho^2 \cos 2\theta + 1}. \quad (6.10)$$

With this result in hand, the orthogonality between the streamlines and the contours of velocity potential can be confirmed by noting that

$$\frac{dy}{dx} = \frac{(1 - \rho^2) \cos \theta}{(1 + \rho^2) \sin \theta} = -\frac{u}{v}. \quad (6.11)$$

The square of the flow speed is given by

$$q^2 = \left| \frac{d\Omega}{dZ} \right|^2 = \frac{m^2}{4\pi^2 R^2} \frac{4\rho^2}{\rho^4 - 2\rho^2 \cos 2\theta + 1}. \quad (6.12)$$

Thus, using (6.2),

$$q = \frac{m}{2\pi R} \frac{2\rho}{k}. \quad (6.13)$$

At $\rho = \rho_{\max}$, the flow speed is

$$q_e = \frac{m}{2\pi R} \frac{2(k+1)^{1/2}}{k}, \quad (6.14)$$

which is the maximum speed of the entrained flow along a velocity potential contour. Finally, the cross-sectional area enclosed by a velocity potential contour is calculated as follows:

$$A' \equiv \frac{A}{R^2} = \begin{cases} 2 \int_{\rho_{\min}}^{\rho_{\max}} \theta_+ \rho \, d\rho, & k \leq 1 \\ \frac{1}{2} \int_{-\pi/2}^{\pi/2} \rho_+^2 \, d\theta, & k > 1 \end{cases} \quad (6.15)$$

where ρ_+ and θ_+ refer to the different solutions in (6.3) and (6.4).

6.3.3 Plume theory

6.3.3.1 Generalized plume equations

According to R15 and R16, the plume governing equations are given by

$$A \frac{d}{dz} \left(\frac{1}{2} w^2 \right) = Ag' - wE, \quad (6.16)$$

$$\frac{d}{dz} (Aw) = E, \quad (6.17)$$

$$\frac{d}{dz}(Awg') = -N^2Aw, \quad (6.18)$$

Though written in terms of the plume cross-sectional area, A , vertical velocity, w , reduced gravity, g' , and the buoyancy frequency, $N = \left(-\frac{g}{\rho_a} \frac{d\rho_a}{dz}\right)^{1/2}$ where ρ_a is the ambient density and g is gravitational acceleration, the above equations could just as well be expressed using the volume flux, $Q = Aw$, the momentum flux, $M = Aw^2$, the buoyancy flux, $F = Awg'$. In contrast to the novel approach of He & Lou (2019), we consider, for simplicity, a neutrally-stratified ambient so that the governing equation for buoyancy is trivial and can be omitted. The closure condition to (6.16)-(6.18) is G.I. Taylor's entrainment assumption (Morton *et al.*, 1956), which relates the entrainment velocity to the vertical velocity of the plume, i.e.

$$q_e = \alpha w, \quad (6.19)$$

where α is an entrainment coefficient¹ and q_e is assumed to be the maximum speed of the entrained flow as specified by (6.14). The flux of ambient fluid entrained into the rising plume is given as

$$E = m = \alpha w R f_e, \quad (6.20)$$

where

$$f_e = \frac{\pi k}{(k+1)^{1/2}}. \quad (6.21)$$

6.3.3.2 Modified entrainment assumption

To further characterize the plume, we follow Morton (1959) and introduce a parameter Γ that describes how forced or lazy a plume is, defined as

$$\Gamma(z) = \frac{5}{8\alpha\pi^{1/2}} \frac{Q^2 F}{M^{5/2}}. \quad (6.22)$$

Γ is equivalent to the local plume Richardson number, and its value indicates the departure of the plume from pure plume balance, a state defined mathematically as $\Gamma(z=0) \equiv \Gamma_0 = 1$ (Hunt & Van den Bremer, 2011). For $\Gamma_0 \neq 1$, plumes can be classified as forced ($0 < \Gamma_0 < 1$) or lazy ($\Gamma_0 > 1$). In the forced and lazy cases, respectively, there is an excess and deficit of momentum at the source compared to a pure plume. When two plumes merge, according to R16, the flux-balance parameter becomes, $\Gamma_m(z) = 2^{1/2}\Gamma(z)$. Accordingly, (6.19) is revised to read

$$q_e = \alpha f_m w, \quad (6.23)$$

in which

$$f_m = \frac{Sk + 2^{1/2}}{Sk + \Gamma_m}, \quad (6.24)$$

where S is an arbitrary constant with $S = 0.1$ in R16. The two entrainment formulations, (6.19) and (6.23), correspond to Rooney's original and revised models, respectively.

¹Note that previously-measured values for α presume that the plume is either axisymmetric or two-dimensional. Here, consistent with figure 6.3, we focus on the former geometry and assume a value for α that is z -independent. For a comprehensive discussion on the choice of entrainment coefficient, see Refs. Kaye (2008) and Van den Bremer & Hunt (2010).

6.3.3.3 Nondimensionalization

Following R16, (6.16) and (6.17) can be nondimensionalized using the buoyancy flux F and the distance, $d = 2R$, between plume sources. On this basis, we write

$$w = \alpha^{-1/3} F^{1/3} d^{-1/3} \hat{w}, \quad Q = \alpha^{-1/3} F^{1/3} d^{5/3} \hat{Q}, \quad z = \alpha^{-1} d \hat{z}, \quad (6.25)$$

where hatted variables carry no units. The flux-balance parameter can be expressed as $\Gamma = \frac{5}{8\pi^{1/2}} \hat{A}^{-1/2} \hat{w}^{-3}$. Thus the non-dimensional form of the governing equations read

$$\frac{d\hat{w}}{d\hat{z}} = \frac{1}{\hat{w}\hat{Q}} - \frac{\hat{w}^2}{2\hat{Q}} f_e, \quad (6.26)$$

$$\frac{d\hat{Q}}{d\hat{z}} = \frac{1}{2} \hat{w} f_e. \quad (6.27)$$

The non-dimensional cross-sectional area is $\hat{A} = \hat{Q}/\hat{w} = A/d^2 = A'/4$ where A' is defined in (6.15). Equations (6.26) and (6.27) are solved using a fourth-order Runge-Kutta finite difference method whereby the range of integration is $0.001 \leq \hat{z} \leq 5$ with a step size of 0.001. Specifically, we first assign an initial guess of small k , e.g. $k = 0.1$, then the (small) source cross-sectional area, A' , is obtained from (6.15). The source value for \hat{w} is obtained by selecting a value for Γ_0 depending on the nature of the plume under examination (i.e. forced vs. pure vs. lazy). After each numerical integration step in \hat{z} , the value of k can be updated by inverting (6.15) using root-finding. It is expected that k increases with z , albeit in a nonlinear fashion. Note that (6.26) and (6.27) are based on the original model of R15; for the revised model we can simply multiply the term f_e (from (6.21)) with f_m (from (6.24)) on the right-hand side of both (6.26) and (6.27).

Because the plume at $\hat{z} = 0.001$ and $k = 0.1$ is not strictly ideal ($\rho_0 \approx 0.05$), a virtual origin correction, i.e. \hat{z}_{vn} , is made to better match the numerical solution with the corresponding near-source similarity scaling. For $\Gamma_0 > 0.5$, we follow the formula for \hat{z}_{vn} proposed by Hunt & Kaye (2001). In case of pure plume balance at the source, i.e. $\Gamma_0 = 1$, the location of the virtual origin below the actual source is estimated as $\hat{z}_{vn} \approx 0.02$.

6.3.3.4 Representative results

Considering $\Gamma_0 = 1$, the evolution of vertical velocity (\hat{w}) and flux-balance parameter (Γ_m) using both the original and revised models is illustrated in figure 6.5. As shown in figure 6.5 a, the original model predicts a greater vertical velocity than does the revised model with $S = 0.1$. Notably, and for $\hat{z} \gtrsim 0.32$, the vertical velocity using the original model overshoots the far-field similarity solution then approaches it asymptotically. Over this range of heights, figure 6.5 b reveals that the plume is in a forced plume regime, i.e. $\Gamma_m < 1$, which is a direct consequence of the reduced entrainment associated with the simple entrainment assumption (6.19). Conversely, the introduction of f_m tends to increase entrainment when Γ_m is low. For the revised models illustrated in figure 6.5 b, Γ_m with $S = 1$ decreases to a level slightly below unity, whereas Γ_m with $S = 0.1$ remains above unity over the entire range of heights. In general, for the original model and revised model with $S = 1$, the plume follows a relatively non-smooth “lazy – forced – pure” regime transition. By contrast, for the revised model with $S = 0.1$, the plume follows a more monotone “lazy – pure” regime transition.

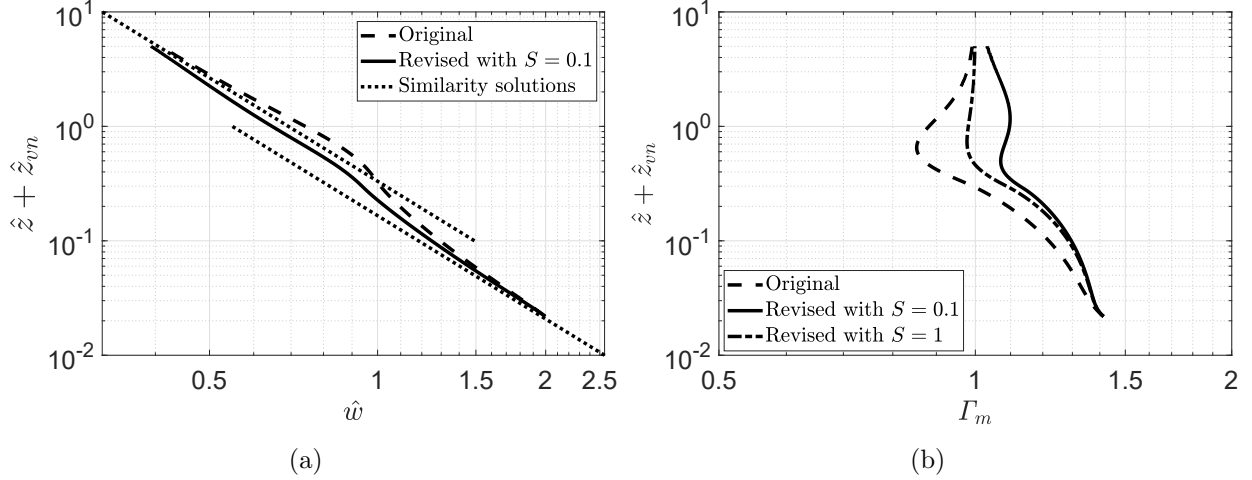


Figure 6.5: Evolution of \hat{w} (panel a) and Γ_m (panel b) as predicted by the original model (dashed curve), revised model with $S = 0.1$ (solid curve) and with $S = 1$ (dash-dotted curve). The dotted lines in (a) denote the near- and far-field self-similarity solutions.

6.4 Alternate form for f_m

6.4.1 Plume-boundary curvature

R15 argued that it should be possible to devise an entrainment assumption that relates the rate of entrainment to the curvature of the plume boundary. This curvature is indicated by the shape of the velocity potential contours in e.g. figure 6.4. On the other hand, R16 introduced a correction factor, f_m in (6.24), with a different goal in mind, i.e. to increase the entrainment when Γ_m decreases and *vice versa*. The revised entrainment assumption proposed by R16 produces good agreement with Cenedese & Linden (2014) vis-à-vis the volume flux of two merging plumes. However, it is not altogether obvious whether Γ_m maps straightforwardly to the plume boundary curvature except in the near- and far-field limits where the individual and the merged plumes are axisymmetric. In light of the above, and returning to the suggestion made in R15, we propose that the rate of entrainment, rather than depending on Γ_m , depends instead on the shape of the plume boundary as represented by the shape of the velocity potential contours defined by (6.2). Below, we explore this possibility in quantitative detail and thereby derive a new entrainment formulation that is different from the well-established formulations presented in R15 (Rooney’s original model) and R16 (Rooney’s revised model).

The contour curvature is expressed as

$$\kappa(\theta) = \frac{\left| 2 \left(\frac{d\rho}{d\theta} \right)^2 + \rho^2 - \rho \frac{d^2\rho}{d\theta^2} \right|}{\left[\left(\frac{d\rho}{d\theta} \right)^2 + \rho^2 \right]^{3/2}}. \quad (6.28)$$

At $\rho = \rho_{\max}$, the curvature simplifies to

$$\kappa_c = \frac{2 + k}{k(1 + k)^{1/2}}. \quad (6.29)$$

We measure the departure of the contour from a circular shape using a parameter P , defined as

$$P = \begin{cases} \frac{1}{2} (\rho_{\max} - \rho_{\min}) \kappa_c, & k \leq 1 \\ \rho_{\max} \kappa_c. & k > 1 \end{cases} \quad (6.30)$$

The near- and far-field limits whereby $P \rightarrow 1$ as $k \rightarrow 0$ and $k \rightarrow \infty$ also apply. Even so, there is a discontinuity in P at $k = 1$ because $k = 1$ marks the beginning of the transition from individual plumes to a merged plume. By comparison with (6.24), we find in figure 6.6 that the following simple formulation for f_m in terms of P generates equally-acceptable behavior:

$$f_m = \begin{cases} P^{n'}, & k \leq 1 \\ P^{n''}. & k > 1 \end{cases} \quad (6.31)$$

By an empirical trial-and-error process, and favoring a fractional representation for the exponents n' and n'' , we propose that $n' = 1/2$ and $n'' = 1/4$. Note that He & Lou (2019) also discussed the plume-boundary curvature but did not propose a functional form like (6.31) for f_m . Instead, they proposed a simpler function that reads, for the two plume case,

$$f_m = k^2 \exp(-k^2) + 1. \quad (6.32)$$

The above formulation also achieves near- and far-field limits of unity; moreover, f_m reaches its maximum value at $k = 1$. Note, however, that for $k > 1$ (6.32) converges to unity much more rapidly than do the formulations illustrated in figure 6.6 a. This implies that (6.32) may lead to relatively low entrainment post-merger.

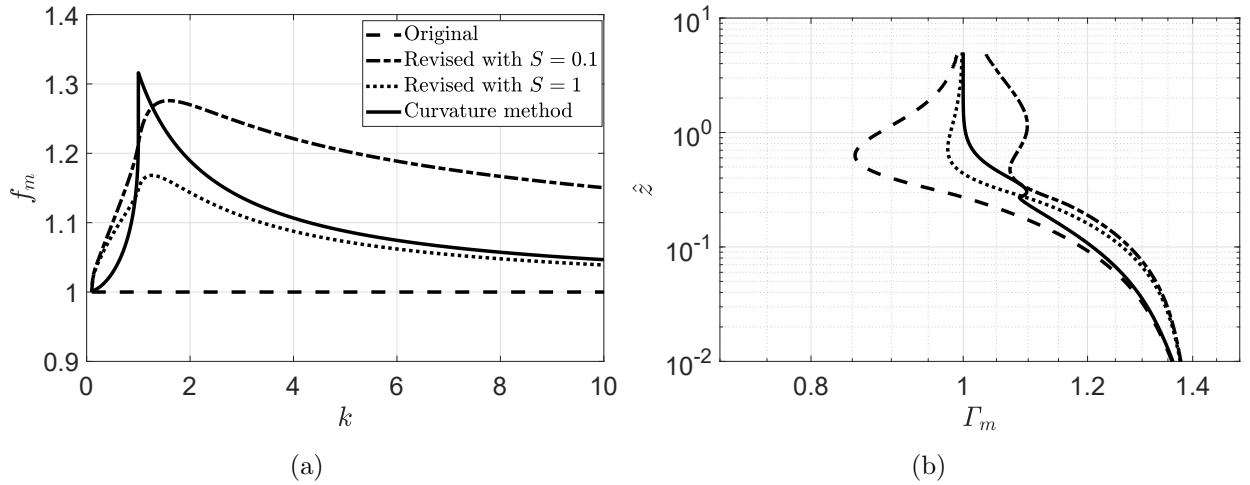


Figure 6.6: The evolution of f_m and Γ_m in the original model (dashed line or curve), revised model with $S = 0.1$ (dash-dotted curve) and with $S = 1$ (dotted curve) and the curvature method using (6.31) (solid curve). In contrast to figure 6.5 b, a virtual origin correction is not included because the small offset by \hat{z}_{vn} does not significantly alter the positions of the curves.

Shown in figure 6.6 a is the correction factor, f_m vs. k . For $k \gtrsim 1$, the value of f_m computed using the curvature method lies slightly above that obtained by the revised model with $S = 1$. One advantage of the curvature method is that, as shown in figure 6.6 b, it

avoids the oscillation about unity that characterizes both the original model (dashed curve) and the revised model with $S = 1$ (dotted curve). Moreover, Γ_m using the curvature method approaches the far-field similarity solution more rapidly than is the case with the other models considered. This accelerated similarity seems more consistent with the observation of two merging plumes made by Baines (1983). He found that the total volume flux of the two merging plumes rapidly approached the similarity solution once the two plumes began to interact.

6.4.2 Height of full merger

As mentioned at the end of section 6.3.1, R16 defined the height of first contact, \hat{z}_{fc} , which corresponds to $k = 1$. R16 also determined the far-field virtual origin correction, \hat{z}_{vf} , which is defined as the height below the actual source where a virtual pure plume with an identical total buoyancy flux can achieve the same far-field similarity solution for the merged plume. What is left unspecified is the height of full merger. Unfortunately, the definition proposed by Kaye & Linden (2004), i.e. the height where a single maximum in the transverse buoyancy profile appears, is difficult to apply in the present analysis. For a more straightforward prediction, we shall define the height of full merger on the basis of the velocity potential contours. For $1 \leq k < 2$, as illustrated in figure 6.4, the combined plume boundary always exhibits concavity close to $x = 0$. The height of full merger, \hat{z}_{fm} , is defined as the height at which the boundary of the combined plume is no longer concave. Stated in mathematical terms, we look for the elevation (or k value) satisfying

$$\kappa(\theta = \pi/2) = \frac{|1 - 2/k|}{(k - 1)^{1/2}} = 0, \quad (6.33)$$

which yields $k = 2$. Therefore, \hat{z}_{fm} is defined as the height corresponding to $k = 2$.

6.4.3 Comparison with previous theoretical and experimental results

To test the validity of the definition for the height of full merger, we compare \hat{z}_{fm} predicted by the original and revised models and the curvature method with the theoretical and experimental results of Kaye & Linden (2004) in table 6.1. The non-dimensional height of full merger in Kaye & Linden (2004) is sensitive to the choice of entrainment coefficient, although $\alpha = 0.09$ was selected therein. We shall instead choose $\alpha \approx 0.12$, as validated by Cenedese & Linden (2014). Meanwhile, Kaye & Linden (2004) predicted theoretically that $\hat{z}_{fm} = 0.44$. Table 6.1 shows that \hat{z}_{fm} predicted by the revised models and the curvature method match well with this measured result.

Table 6.1: Height of full merger predicted by R15, R16, the present analysis and measured/predicted in Kaye & Linden (2004).

	Original	Revised with $S = 0.1$ (1)	Curvature	Kaye & Linden (2004)	
\hat{z}_{fm}	0.61	0.51 (0.54)	0.52	0.49 ± 0.03 ($\alpha = 0.12$)	0.44 (theory)

R16 compared his original and revised models with the experimental results of Cenedese & Linden (2014). Details of the associated “filling-box” experiment are presented in section 3 of Cenedese & Linden (2014) and in section 6 of R16. By reproducing figures 6 and 9 of R16 (not shown here) but adding solutions derived from the curvature method, we find, consistent with figure 6.6 a, that the curvature method produces results very close to those derived from the revised model with $S = 1$. From these comparisons with previous theoretical and experimental results, we conclude that the curvature method exhibits comparable performance vis-à-vis Rooney’s revised model. It is worth reiterating that the curvature model is simpler than the revised model because the former requires specification only of k whereas the latter requires specification of both k and Γ_m .

6.5 Finite source effect

6.5.1 Modified contours approximating plume boundaries

We now introduce $\rho_0 = r_0/R > 0$, defined as the ratio of the plume source radius to half of the distance between the plume centers – see figure 6.3. Our analysis proceeds on the basis of the following two assumptions: (i) the complex potential is still given by (6.1), and, (ii) non-point source plumes distort in a manner similar to their point source counterparts. Technical details associated with this latter assumption are briefly summarized in section 6.8. Therefore, and incorporating a finite ρ_0 into (6.2), we ultimately arrive at the following analogue expression:

$$\rho^4 - 2\rho^2 (\cos 2\theta + \rho_0^2) + (\rho_0^2 - 1)^2 = (\rho^2 + 2\rho \cos \theta + 1 - \rho_0^2) (\rho^2 - 2\rho \cos \theta + 1 - \rho_0^2) = k^2. \quad (6.34)$$

Solutions to (6.34) are presented in figure 6.7 for a pair of ρ_0 values. On the basis of this figure and (6.34), we make two important observations. Firstly, (6.34) does not admit any contours within the cross section of the plume source. Secondly, (6.34) applies for the case of two adjacent plumes. Results similar to (6.34) for cases with $n > 2$ are provided in section 6.9.

Analytical solutions to (6.34) are as follows:

$$\rho = \left(\cos 2\theta + \rho_0^2 \pm (k^2 - \sin^2 2\theta + 2\rho_0^2 (1 + \cos 2\theta))^{1/2} \right)^{1/2}, \quad (6.35)$$

$$\theta = \pm \frac{1}{2} \cos^{-1} \left(\frac{\rho^4 + (\rho_0^2 - 1)^2 - k^2}{2\rho^2} - \rho_0^2 \right), \quad (6.36)$$

where the negative square root in (6.35) applies for $k < 1 - \rho_0^2$. Analogous to (6.3), $k^2 - \sin^2 2\theta + 2\rho_0^2 (1 + \cos 2\theta) \geq 0$ ($k < 1 - \rho_0^2$) determines the range of polar angles occupied by the closed contours in figure 6.7.

Differentiating (6.34) yields

$$\frac{d\rho}{d\theta} = \frac{\rho \sin 2\theta}{\cos 2\theta - \rho^2 + \rho_0^2}, \quad (6.37)$$

and so the maximum radial extent, now defined as

$$\rho_{\max} = \left(1 + \rho_0^2 + (k^2 + 4\rho_0^2)^{1/2} \right)^{1/2}, \quad (6.38)$$

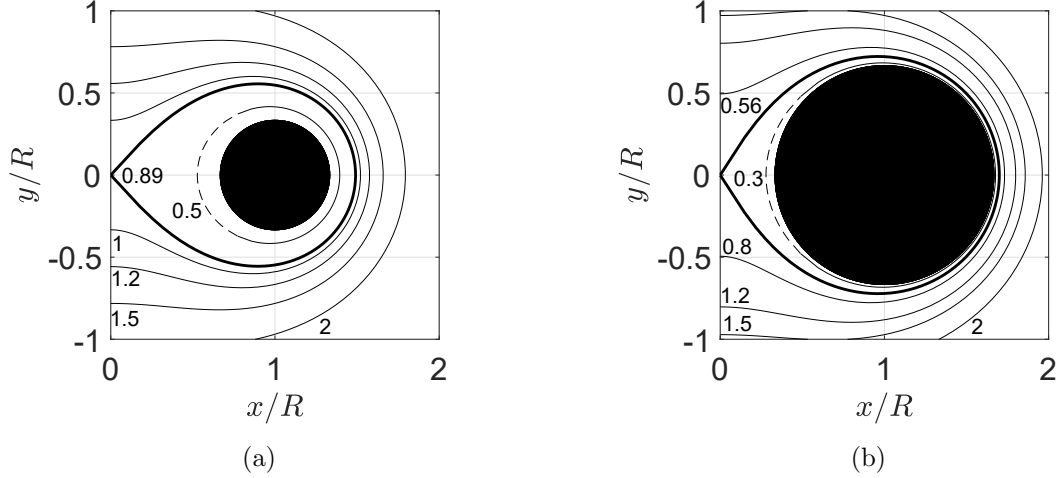


Figure 6.7: As in figure 6.4, but with $\rho_0 > 0$. (a) $\rho_0 = 1/3$, (b) $\rho_0 = 2/3$. The closed black circles in both panels denote the plume source.

still occurs at $\theta = 0$. On the other hand, the minimum radial length is given as

$$\rho_{\min} = \begin{cases} \left(1 + \rho_0^2 - (k^2 + 4\rho_0^2)^{1/2}\right)^{1/2}, & k \leq 1 - \rho_0^2 \\ (k - 1 + \rho_0^2)^{1/2}. & k > 1 - \rho_0^2 \end{cases} \quad (6.39)$$

For $k \leq 1 - \rho_0^2$, the positions of the limits $(\rho_{\lim}, \theta_{\lim})$ are determined from $d\theta/d\rho = 0$, which gives $\rho_{\lim}^2 = \cos 2\theta_{\lim} + \rho_0^2$. Substituting into (6.34) yields, as the respective analogues of (6.8) and (6.9),

$$\rho_{\lim} = \left((1 - \rho_0^2)^2 - k^2\right)^{1/4}, \quad (6.40)$$

$$\pm\theta_{\lim} = \pm\frac{1}{2} \cos^{-1} \left[-\rho_0^2 + \left((1 - \rho_0^2)^2 - k^2\right)^{1/2} \right]. \quad (6.41)$$

Note, in particular, that the maximum closed contour when $k = 1 - \rho_0^2$ corresponds to an angular range $-\frac{1}{2} \cos^{-1}(-\rho_0^2) \leq \theta \leq \frac{1}{2} \cos^{-1}(-\rho_0^2)$.

Analogous to the approach outlined in section 6.4.2, the plume curvature at the level of full merger should satisfy

$$\kappa(\theta = \pi/2) = \frac{|1 - 2/k|}{(k - 1 + \rho_0^2)^{1/2}} = 0, \quad (6.42)$$

which again yields $k = 2$ as the height of full merger. Meanwhile, and consistent with the $\rho_0 \rightarrow 0$ case, $k = 1 - \rho_0^2$ represents the point of first contact.

Under the assumption that the complex potential defined by (6.1) applies also to the non-point source case, the contours illustrated in figure 6.7 are not, strictly-speaking, curves of equi-(velocity) potential. The velocity potential, ϕ , associated with (6.1) is expressed for the $\rho_0 > 0$ case as

$$\phi = -\frac{m}{2\pi R} \ln \left(k^2 + 2\rho_0^2\rho^2 - \rho_0^4 + 2\rho_0^2 \right)^{1/2}. \quad (6.43)$$

For small ρ_0 , ϕ is approximately constant on each of the contours defined by (6.34). For large ρ_0 , it can be inferred from (6.38) and (6.39) that greater variations in ϕ arise, but these are most prominent in the near source region with small k values. In the context of the self-similar model prescribed by (6.16)-(6.18), this near source region is of less interest than the regions of greater distances from the source. Moreover, and as we explain in greater detail in section 6.5.7 below, the contours defined by (6.34), which we consider to define the plume boundary when $\rho_0 > 0$, yield good agreement with previous theoretical results of Cenedese & Linden (2014) even in the extreme case of $\rho_0 = 1$.

6.5.2 Flow speed and cross-sectional area

To be consistent with the $\rho_0 \rightarrow 0$ case, and following the justification given in section 6.10, we require that $E = m$ also applies for non-ideal line sinks. Accordingly, and with $\rho_0 > 0$, the complex velocity normal to the plume boundary reads

$$u_{\perp} - iv_{\perp} = -\frac{m}{2\pi R} \frac{2\rho(k^2 + \rho_0^2\rho^2 - \rho_0^4 + 2\rho_0^2 + \rho_0^2 \cos 2\theta) [(\rho^2 - \rho_0^2 - 1) \cos \theta - i(\rho^2 - \rho_0^2 + 1) \sin \theta]}{(k^2 + 2\rho_0^2\rho^2 - \rho_0^4 + 2\rho_0^2) [k^2 + 2\rho_0^2(1 + \cos 2\theta)]}. \quad (6.44)$$

The flow speed normal to the plume boundary is given by

$$q_{\perp} = \frac{m}{2\pi R} \frac{2\rho(k^2 + \rho_0^2\rho^2 - \rho_0^4 + 2\rho_0^2 + \rho_0^2 \cos 2\theta)}{(k^2 + 2\rho_0^2\rho^2 - \rho_0^4 + 2\rho_0^2) [k^2 + 2\rho_0^2(1 + \cos 2\theta)]^{1/2}}. \quad (6.45)$$

Thus at $\rho = \rho_{\max}$, the speed of the flow entrained across the plume boundary is

$$q_e = \frac{m}{2\pi R} \frac{2 \left[1 + \rho_0^2 + (k^2 + 4\rho_0^2)^{1/2}\right]^{1/2} \left[k^2 + 4\rho_0^2 + \rho_0^2 (k^2 + 4\rho_0^2)^{1/2}\right]}{\left[k^2 + \rho_0^4 + 4\rho_0^2 + 2\rho_0^2 (k^2 + 4\rho_0^2)^{1/2}\right] (k^2 + 4\rho_0^2)^{1/2}}, \quad (6.46)$$

which is used to represent the bulk entrainment velocity.

Note finally that plume cross-sectional areas are still defined by (6.15). The cross-sectional area as a function of k for different ρ_0 is shown in figure 6.8. In general, A' grows approximately linearly for $k \gtrsim 1$.

6.5.3 Entrainment flux

With reference to the original entrainment assumption i.e. (6.19), the entrainment flux with $\rho_0 \geq 0$ is given by

$$E = m = \alpha\omega R f_e, \quad (6.47)$$

where

$$f_e = \frac{\pi \left[k^2 + \rho_0^4 + 4\rho_0^2 + 2\rho_0^2 (k^2 + 4\rho_0^2)^{1/2}\right] (k^2 + 4\rho_0^2)^{1/2}}{\left[1 + \rho_0^2 + (k^2 + 4\rho_0^2)^{1/2}\right]^{1/2} \left[k^2 + 4\rho_0^2 + \rho_0^2 (k^2 + 4\rho_0^2)^{1/2}\right]}, \quad (6.48)$$

which reduces to (6.21) in the limit $\rho_0 \rightarrow 0$. In the near- and far-field limits, (6.48) reduces to

$$f_e \rightarrow \begin{cases} \frac{\pi\rho_0(\rho_0 + 2)}{\rho_0 + 1}, & k \rightarrow 0 \\ \pi k^{1/2}, & k \rightarrow \infty \end{cases} \quad (6.49)$$

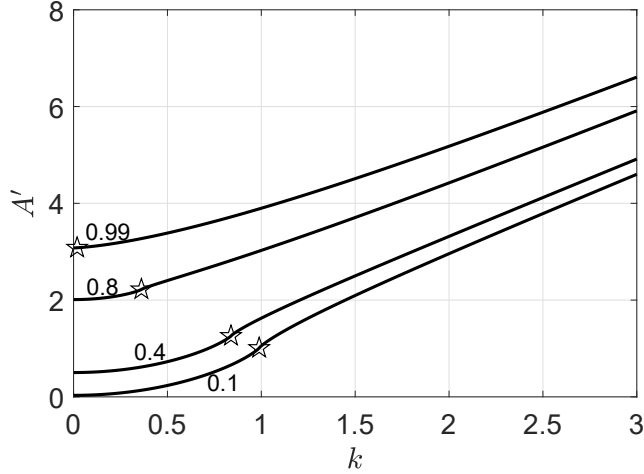


Figure 6.8: Plume cross-sectional area as a function of k for different source radii, i.e. $\rho_0 = 0.1, 0.4, 0.8$ and 0.99 . The stars indicate where $k = 1 - \rho_0^2$.

respectively. In the latter case, we reproduce the limit associated with $\rho_0 = 0$. In the former case, Rf_e tends to the plume source perimeter ($2\pi R\rho_0$) times $\frac{\rho_0+2}{2(\rho_0+1)}$. The term $\frac{\rho_0+2}{2(\rho_0+1)}$ decreases monotonically as ρ_0 increases, which, as expected, indicates less entrainment associated with a large plume source.

We retain the governing equations described in sections 6.3.3.1 and 6.3.3.3, however, with entrainment fluxes given by (6.47) and (6.48). The procedure for solving the original model with (6.20), the revised model with (6.23) and the curvature method with (6.31), by replacing (6.21) with (6.48), is similar to that described in section 6.3.3.3. A slight difference is that the initial guess for k is now vanishingly small, e.g. 10^{-12} , and the range of integration is $0 \leq \hat{z} \leq 5$.

6.5.4 Representative results

Representative solutions showing the vertical velocities (panels a and b) and volume fluxes (panels c and d) with $\rho_0 = 0.1$ and 0.6 and $\Gamma_0 = 1$ are illustrated in figure 6.9. In general, both the revised model and the curvature method predict a smaller vertical velocity but a greater volume flux (and therefore greater breadth) compared to the original model. For $\rho_0 = 0.1$, the vertical velocity predicted by the original model (figure 6.9 a) overshoots the far-field similarity solution, which is consistent with figure 3 a of R16. This overshoot is however absent in figure 6.9 b for which $\rho_0 = 0.6$.

Table 6.2 lists the characteristic heights, i.e. \hat{z}_{fc} , \hat{z}_{fm} and \hat{z}_{vf} , for the flows considered in figure 6.9. The method of determining the far-field virtual origin is identical to that in R16, with a positive value denoting a distance below the actual source. Due to the enhanced entrainment considered in the revised model and the curvature method, both (6.24) and (6.31) predict somewhat lower elevations for full merger than does the original model.

The evolution of $\Gamma_m = 2^{1/2}\Gamma(z)$ for the original, revised and curvature models is illustrated in figure 6.10. Figure 6.10 a shows that for plumes with $\rho_0 = 0.1$ and $\Gamma_0 = 1$, Γ_m oscillates about unity using the original model and the revised model with $S = 1$. For the original model, a similar oscillation is observed in figure 6.10 b where, consistent with figure

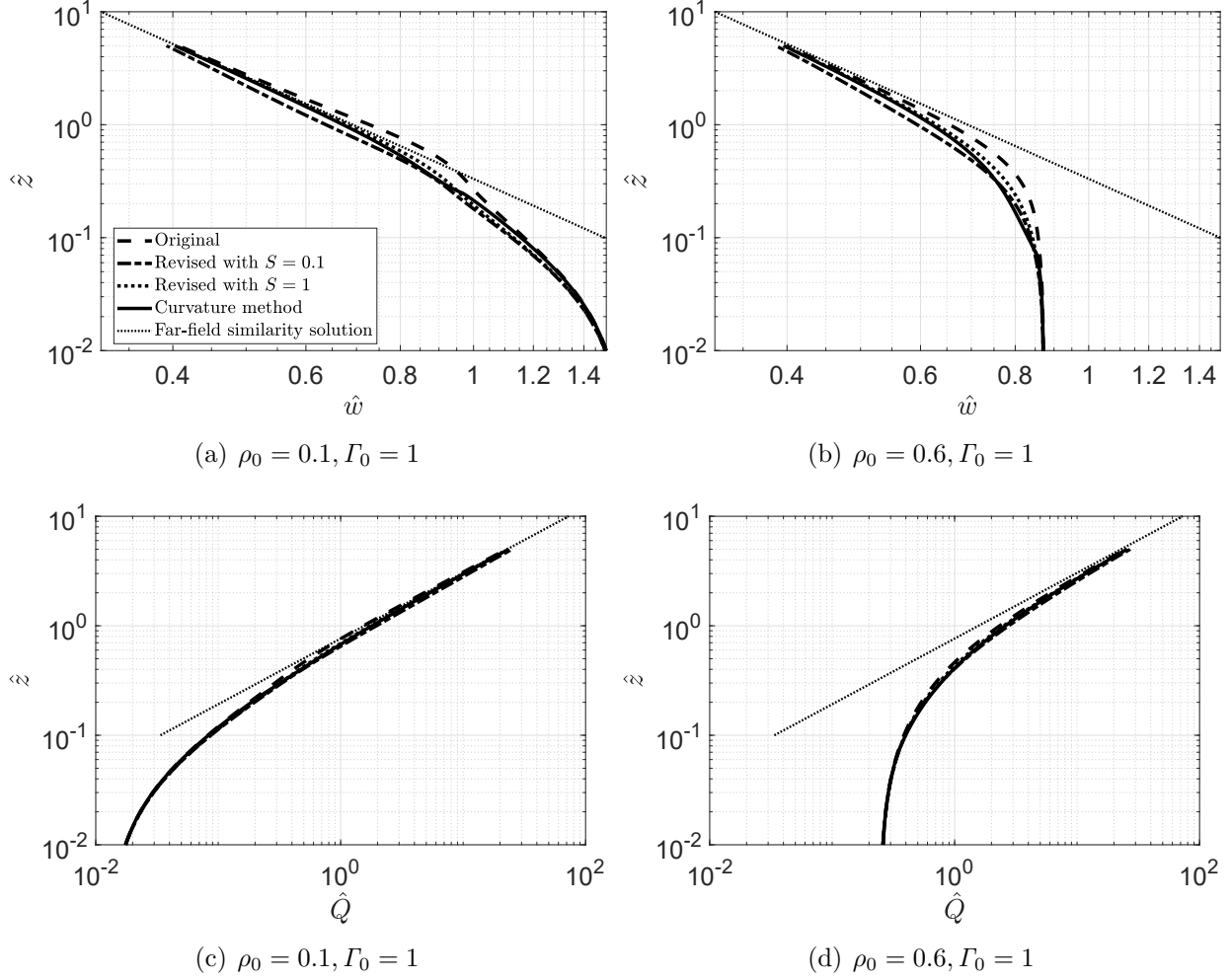


Figure 6.9: Non-dimensional vertical velocity (panels a and b) and volume flux (panels c and d) as functions of height for the original model (dashed curve), the revised model with $S = 0.1$ (solid curve) and with $S = 1$ (dotted curve) and the curvature method (solid curve). The thin dotted lines denote the far-field similarity solutions for \hat{w} and \hat{Q} , respectively.

Table 6.2: Heights of first contact and full merger and the far-field virtual origin correction for the source conditions considered in figure 6.9. Values correspond, in sequence, to the original model (6.19), the revised model (6.24) with $S = 0.1$ and with $S = 1$, and the curvature method (6.31).

Source parameters	\hat{z}_{fc}	\hat{z}_{fm}	\hat{z}_{vf}
$\rho_0 = 0.1, \Gamma_0 = 1$	0.27, 0.23, 0.24, 0.25	0.56, 0.46, 0.49, 0.48	-0.05, 0.19, 0.06, 0.09
$\rho_0 = 0.6, \Gamma_0 = 1$	0.08, 0.07, 0.07, 0.07	0.34, 0.28, 0.30, 0.28	0.24, 0.45, 0.33, 0.36

6.9, ρ_0 is increased from 0.1 to 0.6. According to R16, the pronounced dip to $\Gamma_m < 1$ using the original model (figures 6.10 a,b) indicates that entrainment is relatively low around \hat{z}_{fm} . As a result, the plume is forced to accelerate to the far-field limit, which is reflected by the overshooting of the far-field similarity solution in figure 6.9 a. By contrast, the curvature method and the revised model with $S = 0.1$ tend more smoothly to the far-field similarity

Another parameter of interest is the effective entrainment, which is defined as the ratio of the volume flux of two merging (non-ideal) plumes to the total volume flux of the same two plumes, now isolated (Cenedese & Linden, 2014). For a single isolated axisymmetric plume, the entrainment rate is expressed as

$$E = 2\pi b\alpha w, \quad (6.50)$$

where b is the mean plume radius. Following the non-dimensionalization in section 6.3.3.3, the governing equations for an isolated plume are given as

$$\frac{d\hat{w}_1}{d\hat{z}} = \frac{1}{\hat{w}_1\hat{Q}_1} - \frac{2\pi^{1/2}\hat{w}_1^{3/2}}{\hat{Q}_1^{1/2}}, \quad (6.51)$$

$$\frac{d\hat{Q}_1}{d\hat{z}} = 2\pi^{1/2}\hat{w}_1^{1/2}\hat{Q}_1^{1/2}, \quad (6.52)$$

where the subscript 1 denotes a single isolated plume. Figure 6.12 shows the evolution of the effective entrainment, expressed as $(\hat{Q}/\hat{Q}_1)^{3/4}$, for $\Gamma_0 = 1$ and different ρ_0 . It is evident from figure 6.12 that the larger the plume source, the greater the effective entrainment. This result seems counter-intuitive: two plumes are deemed to be less affected by each other if they are set apart by a greater distance (i.e. ρ_0 is small). This paradoxical behavior arises because small plumes tend to be more heavily distorted in terms of their cross-sectional area and this, in turn, depresses ambient entrainment. By contrast, a comparison between figures 6.7 a and 6.7 b reveals that larger plume sources suffer from less distortion, i.e. departure from the original circular shape. As a consequence, they admit more (effective) ambient entrainment than their small ρ_0 counterparts.

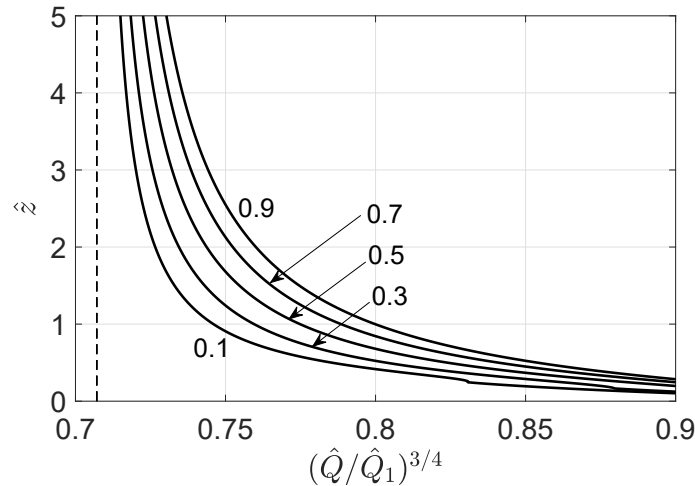


Figure 6.12: Effective entrainment with $\Gamma_0 = 1$ and $\rho_0 = 0.1, 0.3, 0.5, 0.7$ and 0.9 . The thin dashed vertical line denotes the far-field limit, $2^{-1/2}$.

6.5.6 Comparison with the saline plume experiment of Davis *et al.* (1977)

Davis *et al.* (1977) studied the dilution characteristics of single and multiple plumes using water tank experiments. In their experiments, the densimetric Froude number is defined as

$\text{Fr}_0 = w_0 / (g'_0 D)^{1/2}$ where D is the plume source diameter, thus we can relate Fr_0 to Γ_0 as follows:

$$\Gamma_0 = \frac{5}{16\alpha} \text{Fr}_0^{-2}. \quad (6.53)$$

With $\alpha = 0.12$, $\text{Fr}_0 = 6$ corresponds to $\Gamma_0 = 0.072$, which represents a highly forced plume at the source. A single spacing ratio corresponding to $\rho_0 = 0.75$ is considered by Davis *et al.* (1977). The comparison between their experimental measurements and the curvature method is shown in figure 6.13 where we plot the variation of the plume volume flux with elevation. Although only limited experimental data are available, the agreement between theory and experiment is robust.

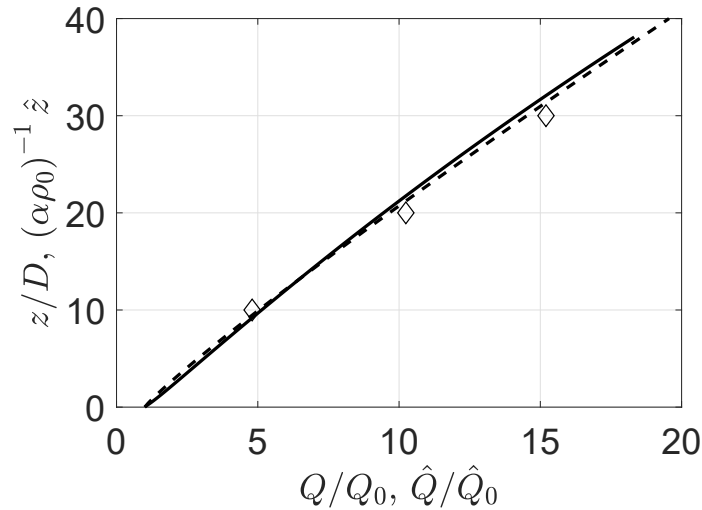


Figure 6.13: Comparison of the curvature method with the experimental data of Davis *et al.* (1977). The solid curve denotes the curvature method with $\alpha = 0.14$. The open diamonds correspond to volume flux measurements made at $z/D_0 = 10, 20$ and 30 . The dashed curve is a curve fit to all the experimental data of Davis *et al.* (1977).

6.5.7 Extreme case of $\rho_0 = 1$

The extreme case with $\rho_0 = 1$ is of interest because the plumes start to contact at the source, whilst the plume sources are circular. A similar situation is, of course, the merger of two plumes whose cross-sections remain circular, which is assumed in the models of Kaye & Linden (2004) and Cenedese & Linden (2014). Therefore, and for $\rho_0 = 1$, we argue that the merging plume is likely to be approximated by the region above the “touching height” (a.k.a. the height of first contact) in the piecewise model of Cenedese & Linden (2014). Note that the characteristic length scale is the centerline distance between the two plume centers at the touching height not at the level of the near-field virtual source. Following (2.5) and (2.10) in Cenedese & Linden (2014), we first give the piecewise model and its prediction for

half of the total volume flux of the two plumes, i.e.

$$\hat{Q} = \begin{cases} \left(\frac{9}{10}\right)^{1/3} \frac{3}{5} \pi^{2/3} (1.643\hat{z} + 0.465), & \hat{z} \leq 0.107 \\ \left(\frac{9}{5}\right)^{1/3} \frac{3}{5} \pi^{2/3} (\hat{z} + 0.560)^{5/3}, & \hat{z} > 0.107 \end{cases} \quad (6.54)$$

where $\hat{z} = 0$ now represents the touching height at which point the two plumes are expected to be fully self-similar, i.e. $\Gamma(\hat{z} = 0) = 1$ and $\hat{z} = 0.107$ represents the height of full merger. The evolution of the volume flux obtained from the models of sections 6.3, 6.4 and 6.5 and Cenedese and Linden's piecewise counterpart (6.54) is shown in figure 6.14. In all cases, excellent overlap is noted.

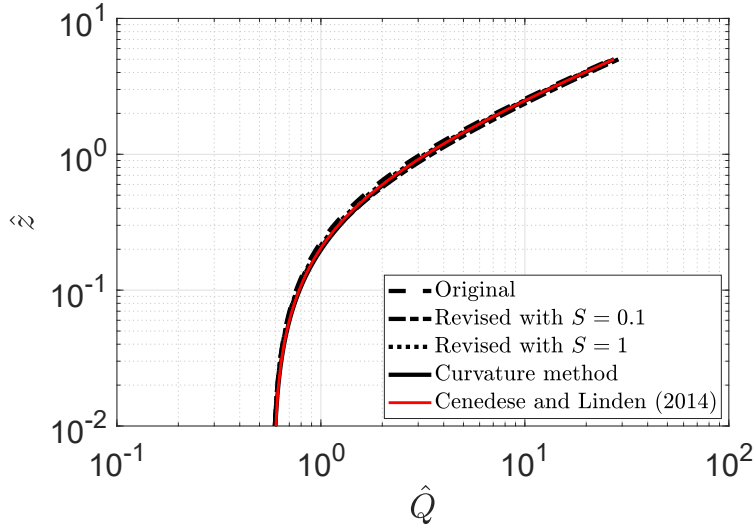


Figure 6.14: [Color online] Plume volume flux for the limiting case of $\rho_0 = 1$ and $\Gamma_0 = 1$.

6.6 Applications to cooling towers

6.6.1 Governing equations

For cooling tower plumes, buoyancy derives from temperature and humidity. As such, and in addition to the volume and momentum fluxes defined respectively as $Q = Aw$ and $M = Aw^2$, we must also define an excess temperature flux, $\Theta = Aw(t_p - t_a)$ where t denotes the air dry-bulb temperature, an excess specific humidity flux, $H = Aw(q_p - q_a)$ where q denotes the specific humidity, and an excess specific liquid moisture flux, $W = Aw(\sigma_p - \sigma_a)$ where σ denotes the specific liquid moisture. Subscripts p and a denote the plume and the ambient, respectively. The buoyancy flux is defined as

$$F = Awg' = Awg \left(1 - \frac{t_{v,a}}{t_{v,p}}\right), \quad (6.55)$$

where the plume virtual temperature and ambient virtual temperature, $t_{v,p}$ and $t_{v,a}$, are respectively defined as follows (Emanuel, 1994):

$$t_{v,p} = \left(t_a + 273.15 + \frac{\Theta}{Q} \right) \left[1 + 0.608 \left(q_a + \frac{H}{Q} \right) - \frac{W}{Q} \right], \quad (6.56)$$

$$t_{v,a} = (t_a + 273.15) (1 + 0.608q_a - \sigma_a). \quad (6.57)$$

Here we consider t_a values measured in degrees Celsius and $\sigma_a = 0$ signifying an ambient devoid of liquid moisture. Note that even in a stationary and unstratified ambient, the buoyancy flux of a moist plume is not always constant due to the possibility of condensation. We consider the dimensional form of the governing equations, which read as follows:

$$\frac{dQ}{dz} = E, \quad (6.58)$$

$$\frac{dM}{dz} = Ag', \quad (6.59)$$

$$\frac{d}{dz} \left(\Theta - \frac{L_v}{c_{pa}} W \right) = 0, \quad (6.60)$$

$$\frac{d}{dz} (H + W) = 0, \quad (6.61)$$

where the latent heat of condensation, measured in J/g, is $L_v = L_v(t) = 4.1868 [597.31 - 0.57 t]$ with t measured in degrees Celsius, and $c_{pa} = 1.006$ J/(g K) representing the specific heat of air at constant pressure (Wu & Koh, 1978). The set of equations (6.58)-(6.61) is consistent with the governing equation for moist plumes specified by (19) of Morton (1957). Some authors, e.g. Woods (1993), have used the full form of the energy conservation equation including enthalpy, kinetic energy and potential energy (cf. Woods's equation 4). When the mixing process is adiabatic, the full form equation reduces to the conservation equation for thermal energy, i.e. (6.60).

6.6.2 Representative results

Table 6.3 lists the input parameters to be used in assessing the heights of full merger for the present model and also for the WK78 model. According to (7.23), and assuming $\alpha = \alpha_p = 0.117$ (List, 1982), the source flux-balance parameters are, respectively, $\Gamma_0 = 0.52$ and $\Gamma_0 = 0.57$ for $\frac{\dot{m}_d}{\dot{m}_w} = 0.6$ and $\frac{\dot{m}_d}{\dot{m}_w} = 0.3$ where, in both cases, we have assumed a stack exit velocity of $w_0 = 6$ m/s. The counterpart values for Γ_0 with $w_0 = 10$ m/s are 0.19 and 0.20, respectively. Here $\frac{\dot{m}_d}{\dot{m}_w}$ specifies the ratio between dry (sensible) cooling to wet (evaporative) cooling in a hybrid wet/dry cooling tower – see Li & Flynn (2020a) for additional details. In WK78, the composite plume post-merger is a combination of a central slot plume and two half round plumes at the two ends – see figure 6.2c. The entrainment coefficient for the central slot plume is $\alpha_l = 0.147$ and the counterpart coefficient for the two half round plumes is, consistent with the above discussion, $\alpha_p = 0.117$. Therefore, the effective entrainment coefficient for the plume post merger is, on average, between α_p and α_l .

To examine the difference between the WK78 model, Rooney's original and revised models and the curvature method, we plot the height of full merger, $\hat{z}_{fm} = \alpha_p z_{fm}/d$, using the

Table 6.3: Representative operating and environmental conditions for cooling towers (Kröger, 2004).

Variable symbol	Variable name	Value (unit)
P_a	Ambient pressure at the top of the cooling tower	101325 (Pa)
t_a	Ambient temperature	6 (°C)
RH_a	Ambient relative humidity	65 (%)
t_w	Wet cooling temperature	30 (°C)
t_d	Dry cooling temperature	20 (°C)
w_0	Stack exit velocity	6 and 10 (m/s)
A_0	Stack exit area	71.3 (m ²)
d	Distance between cell centers	14.3 (m)
$\frac{\dot{m}_d}{\dot{m}_w}$	Ratio of the dry to wet air mass flow rate	0.3 and 0.6
n	Number of cooling tower cells	2

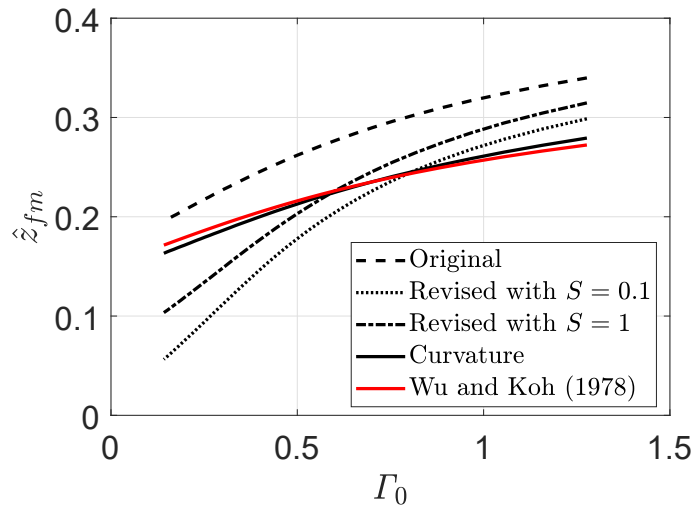


Figure 6.15: [Color online] Height of full merger, \hat{z}_{fm} , as a function of the source flux-balance parameter, Γ_0 , with $\frac{\dot{m}_d}{\dot{m}_w} = 0.3$. Note that the variation in Γ_0 corresponds to the variation in the cooling tower exit velocity, w_0 . Meanwhile all other parameters correspond to the values given in table 6.3.

four aforementioned approaches as functions of the source flux-balance parameter, Γ_0 , for $\frac{\dot{m}_d}{\dot{m}_w} = 0.3$ – see figure 6.15. The range for Γ_0 is 0.13 to 1.22 (w_0 is 4 to 12 m/s) to ensure that the source flow spans the range between forced and slightly lazy. Similar profiles are predicted in case of $\frac{\dot{m}_d}{\dot{m}_w} = 0.6$ (not shown), which indicates that the moisture effect on plume dynamics is modest. For $\Gamma_0 \lesssim 0.7$, the WK78 model predicts slightly greater \hat{z}_{fm} than does the curvature method although the difference is small. The original model always predicts the greatest \hat{z}_{fm} among the five models. On the other hand, and for $\Gamma_0 \approx 1$, the revised models predict somewhat greater \hat{z}_{fm} than does the WK78 model. This reduced entrainment in the revised model is consistent with (6.23) and (6.24) which require entrainment to decrease as Γ_m increases. For smaller Γ_0 , the revised models, with their increased entrainment, predict smaller \hat{z}_{fm} than does the WK78 model.

The strong agreement between the curvature method and the WK78 model evident in

figure 6.15 is all the more encouraging given the prevalence of the latter in atmospheric dispersion models (Policastro *et al.*, 1994; Davis, 1998). Unfortunately, and whereas the red and (solid) black curves show strong overlap when considering \hat{z}_{fm} , greater differences arise when examining other metrics. For example, figure 6.16 shows the plume reduced gravity, vertical velocity and relative humidity (RH) of the WK78 vs. original and revised models and the curvature method where we consider $w_0 = 6$ m/s. Similar results but with $w_0 = 10$ m/s, are presented in figure 6.17. Figures 6.16 a,b,c,d indicate that the WK78 (original) model predicts the greatest (smallest) dilution rate. Accordingly, figure 6.16 e shows that the WK78 (original) model predicts the shortest (longest) visible plume. For a larger exit velocity, i.e. $w_0 = 10$ m/s, on the other hand, figure 6.17 shows that the revised model with $S = 0.1$ produces the greatest dilution rate, even compared to the WK78 model. By contrast, the curvature method always predicts a greater visible plume length thus less dilution rate compared to WK78. It should be emphasized that the WK78 model overestimates the entrainment rate in the near field because it does not properly account for plume interaction and the corresponding reduced entrainment that follows therefrom. Consequently, and in contrast to Rooney’s revised model, we see that there exists a consistent offset between the curvature method and WK78, this because the curvature method predicts a lower rate of dilution than does WK78. In spite of this, the overall comparison, accounting for the data of figures 6.15 to 6.17, is satisfactorily robust.

6.7 Conclusions

The present manuscript extends the theory in Rooney (2015, 2016) to describe the merging of two area source plumes in an unstratified ambient. The plume boundary is defined by the contours defined by (6.34); these contours grow from the circumference of a circular source of arbitrary size. The height of full merger is here defined as the height at which the combined plume boundary is no longer concave. Another contribution of this work is to compare this height of full merger with the alternative definition (and model predictions) due to Wu & Koh (1978). In adapting the turbulent plume equations of Morton *et al.* (1956), Wu & Koh (1978) argued that the point of merger should be regarded as that elevation where the area of the central rectangle equals the sum of areas of the two half round plumes – see figure 6.2 c.

Rooney’s revised model incorporates a correction factor (6.24) that depends on the velocity potential contour (k), flux-balance parameter (Γ_m) and a free parameter (S). To generalize and simplify the correction factor, an alternate entrainment assumption, i.e. the so-called curvature method, is herein proposed. It allows one to specify the rate of entrainment exclusively from the geometry of the plume boundary. In turn, predictions of the height of full merger derived from the curvature method and from Rooney’s revised model are broadly consistent with the experimental results of Kaye & Linden (2004). Similarly positive agreement is also noted upon comparing the curvature method and the experimental data collected by Davis *et al.* (1977).

For small, forced and pure plume sources, plume merger allows the plume to transition to a lazy plume regime then approach the far-field pure plume limit. By contrast, and for larger and highly forced plume sources, the merging plume directly approaches the far-field

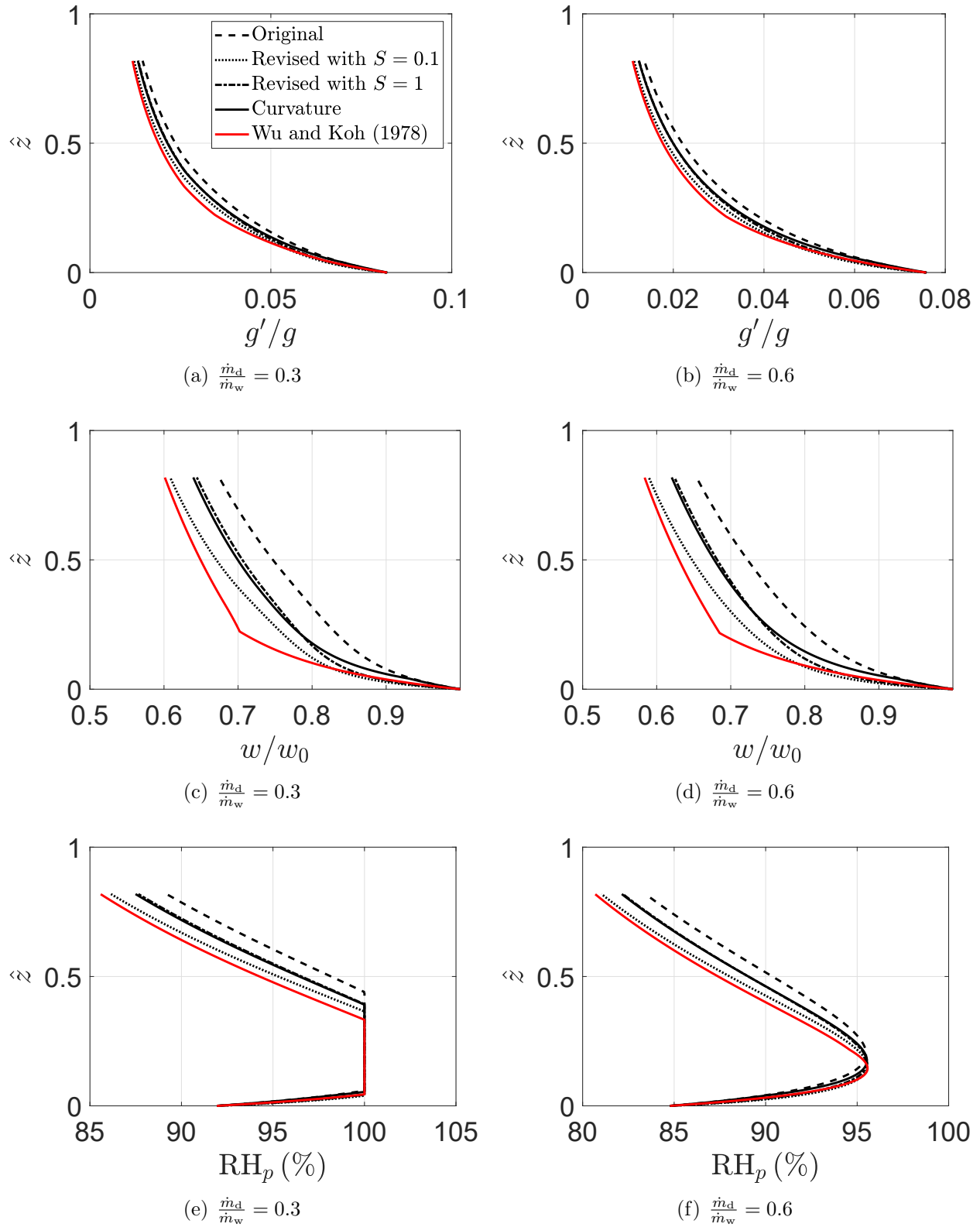


Figure 6.16: [Color online] Non-dimensional plume reduced gravity (panels a and b), vertical velocity (panels c and d) and relative humidity (panels e and f) as functions of height above the stack exit. The stack exit velocity is $w_0 = 6$ m/s.

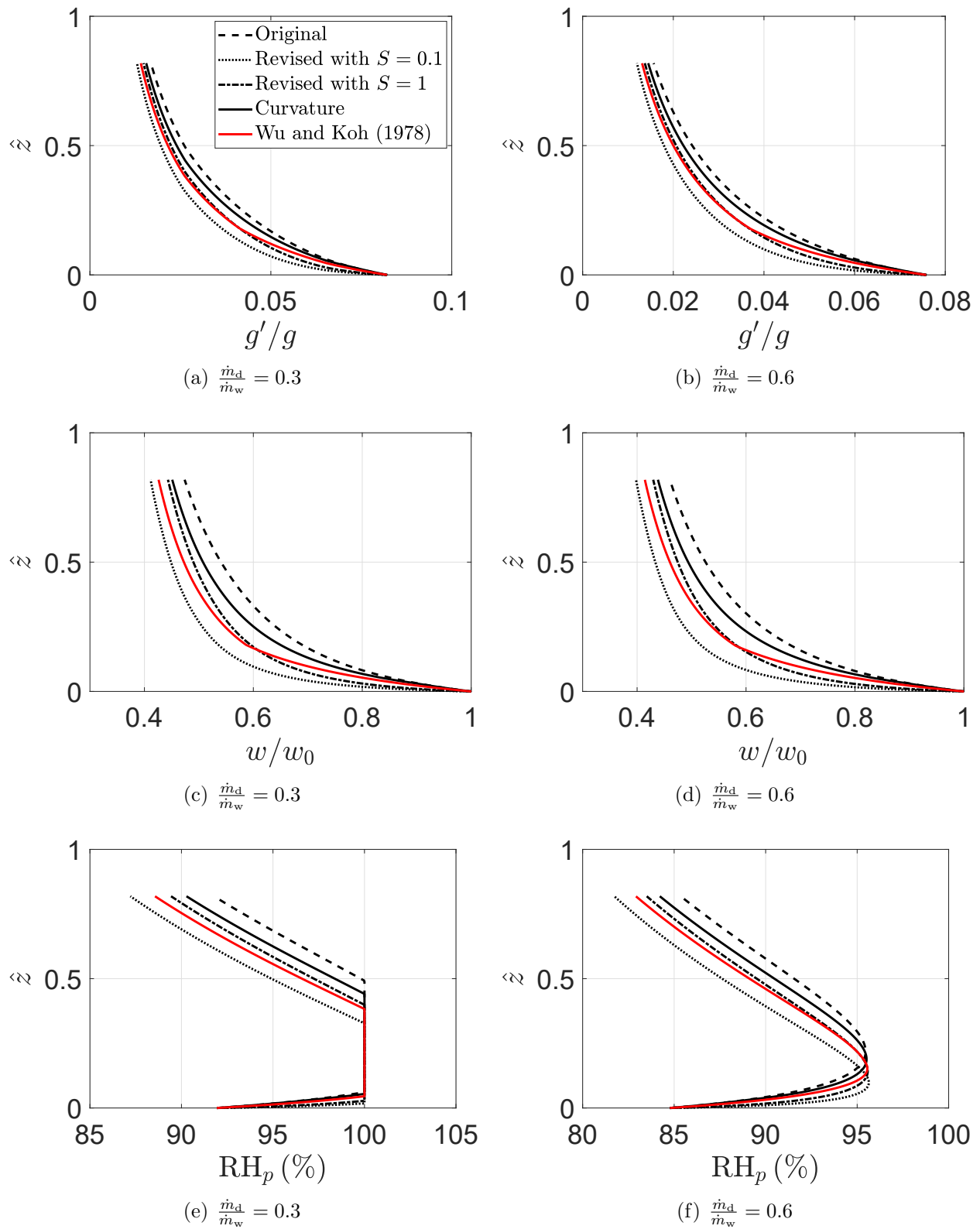


Figure 6.17: [Color online] As in figure 6.16 but with a stack exit velocity of $w_0 = 10$ m/s.

limit, dynamics that are similar to an isolated plume. For fixed T_0 , small plume sources yield less effective entrainment as compared to larger sources, this as a result of the entrainment-inhibiting distortion of the plume cross-sectional area that is experienced for small z .

The application of the curvature method to adjacent cooling tower plumes yields good agreement with predictions of the merger height made by Wu & Koh (1978). Meanwhile, representative results (figures 6.16 and 6.17) show that the curvature method consistently predicts a slightly greater visible plume length than does the model of Wu & Koh (1978), the latter exhibiting generally good agreement with independently-collected laboratory and field data (Fan, 1967; Carpenter *et al.*, 1968).

The present model is restricted to two plumes with the same source height, source size and source strength. Even with this restriction, the model cannot describe the contraction above a lazy plume with $T_0 > 5/2$. Nonetheless, as a first approximation, lazy plumes may be assumed to interact only above the necking zone. Topics of future research interest are to apply the present model to merging plumes in case of ambient stratification and to merging turbulent fountains. For adjacent forced plumes in a linearly stratified ambient, He & Lou (2019) directly applied Rooney's theory whereas the finite source effect and the fountain-like behavior at the plume top were not considered. For moderately spaced turbulent fountains, the downflowing outer plumes are expected to merge thus influencing the fountain rise height.

6.8 Appendix A: A note on the derivation of (6.34)

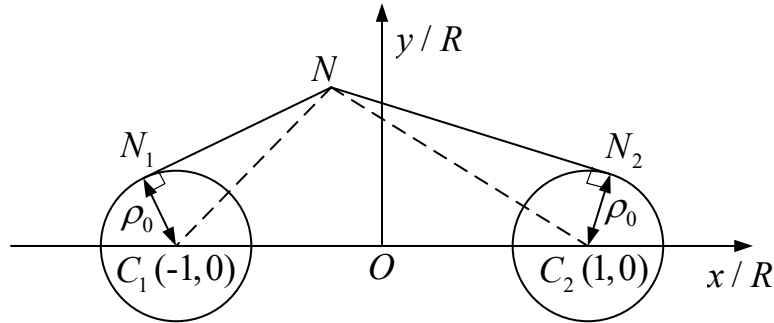


Figure 6.18: Schematic illustrating the geometric details associated with (6.34). The left and right circles are centered at $C_1(-1, 0)$ and $C_2(1, 0)$, respectively and both have radius ρ_0 . From the point N , the straight lines NN_1 and NN_2 are tangent to the circles centered at C_1 and C_2 , respectively; N_1 and N_2 are the respective tangent points.

Underpinning (6.34) are some geometrical details, which we highlight in figure 6.18. The lengths of the straight lines, $|NC_1|$, $|NC_2|$, $|NN_1|$ and $|NN_2|$, are given as follows:

$$|NC_1| = |Z' + 1|, \quad |NC_2| = |Z' - 1|, \quad (6.62)$$

$$|NN_1| = \left(|Z' + 1|^2 - \rho_0^2\right)^{1/2}, \quad |NN_2| = \left(|Z' - 1|^2 - \rho_0^2\right)^{1/2}, \quad (6.63)$$

where $Z' = x/R + iy/R$ corresponds to the position N . The product $|NC_1||NC_2| = k$ is consistent with (6.2). A set of curves resulting from this latter equality are called Cassini ovals

(Karataş, 2013); these curves are shown in the right-half plane in figure 6.4. For $\rho_0 > 0$, and to avoid any curves within the two circles shown in figure 6.18, we consider not $|NC_1| |NC_2|$ but rather $|NN_1| |NN_2|$. Doing so yields $(|Z' + 1|^2 - \rho_0^2)^{1/2} (|Z' - 1|^2 - \rho_0^2)^{1/2} = k$, which is consistent with (6.34). As observed in figures 6.4 and 6.7, a half lemniscate is realized in the right-half plane when $k = 1$ and $k = 1 - \rho_0^2$ using (6.2) and (6.34), respectively.

6.9 Appendix B: Note on $n \geq 3$ area source plumes

According to R16, the velocity potential contours for n ideal source plumes spaced equally around a circle of radius R are specified by

$$\rho^{2n} - 2\rho^n \cos n\theta + 1 = k^2. \quad (6.64)$$

The left-hand side of (6.64) can be decomposed as follows:

$$\rho^{2n} - 2\rho^n \cos n\theta + 1 = \prod_{m=1}^n \left(\rho^2 - 2\rho \cos \left(\theta + \frac{2(m-1)\pi}{n} \right) + 1 \right). \quad (6.65)$$

To introduce a source of finite radius, we must now include a factor of ρ_0 . Doing so after first combining (6.64) and (6.65) yields

$$\prod_{m=1}^n \left(\rho^2 - 2\rho \cos \left(\theta + \frac{2(m-1)\pi}{n} \right) + 1 - \rho_0^2 \right) = k^2. \quad (6.66)$$

On substituting $\rho = 0$ in (6.66), we find that $k = (1 - \rho_0^2)^{n/2}$, which corresponds to the point of first contact. This implies that first contact between adjacent plumes is accelerated if ρ_0 and/or n increases. Unfortunately, it is not straightforward to obtain analytical solutions to (6.66) with $n \geq 3$.

6.10 Appendix C: Entrainment flux for sources with $\rho_0 > 0$

From (6.34) and (6.12), we can determine the flow speed as

$$q = \frac{m}{2\pi R} \frac{2\rho}{(k^2 + 2\rho_0^2\rho^2 - \rho_0^4 + 2\rho_0^2)^{1/2}}. \quad (6.67)$$

Analogous to R16, the volume of fluid entrained across any velocity potential contour C is

$$E = \int_C q \, dl = \frac{mI}{2\pi}, \quad (6.68)$$

where

$$I = \int_C \frac{2\rho}{(k^2 + 2\rho_0^2\rho^2 - \rho_0^4 + 2\rho_0^2)^{1/2}} \, dl', \quad (6.69)$$

and

$$dl' = \frac{2 \left[\rho^4 + (-\rho^4 + \rho_0^2 \rho^2) \left((1 - \rho_0^2)^2 - k^2 - \rho_0^2 \rho^2 \right) \right]^{1/2}}{\left[4\rho^4 - \left(\rho^4 - 2\rho_0^2 \rho^2 + (1 - \rho_0^2)^2 - k^2 \right) \right]^{1/2}} d\rho \quad (6.70)$$

$$= \frac{[k^2 + 2\rho_0^2(1 + \cos 2\theta)]^{1/2} \left[\rho_0^2 + \cos 2\theta \pm (k^2 - \sin^2 2\theta + 2\rho_0^2(1 + \cos 2\theta))^{1/2} \right]^{1/2}}{[k^2 - \sin^2 2\theta + 2\rho_0^2(1 + \cos 2\theta)]^{1/2}} d\theta. \quad (6.71)$$

Using (6.35) or (6.36), the right-hand side of (6.69) can be expressed as a function of ρ or θ , respectively. Note that (6.68) does not account for the non-orthogonality between the streamlines and the plume boundary defined by (6.34). For $\rho_0 > 0$, the velocity component that is normal to the contours defined by (6.34) satisfies

$$\frac{dy}{dx} = \frac{(1 + \rho_0^2 - \rho^2) \cos \theta}{(1 - \rho_0^2 + \rho^2) \sin \theta} = -\frac{u_\perp}{v_\perp}. \quad (6.72)$$

Note that (6.72) reduces to (6.11) in the limit of vanishingly small ρ_0 . By incorporating the angle, θ' , between the velocity vectors (\mathbf{u} and \mathbf{u}_\perp) expressed respectively by (6.11) and (6.72), (6.68) can be rewritten as

$$E = \int_C q_\perp dl = \int_C q \cos \theta' dl = \frac{mI}{2\pi}, \quad (6.73)$$

where q_\perp is the flow speed normal to the plume boundary and

$$\cos \theta' = \frac{\mathbf{u}}{\|\mathbf{u}\|} \cdot \frac{\mathbf{u}_\perp}{\|\mathbf{u}_\perp\|} = \frac{k^2 + \rho_0^2 \rho^2 - \rho_0^4 + 2\rho_0^2 + \rho_0^2 \cos 2\theta}{(k^2 + 2\rho_0^2 \rho^2 - \rho_0^4 + 2\rho_0^2)^{1/2} (k^2 + 2\rho_0^2(1 + \cos 2\theta))^{1/2}}. \quad (6.74)$$

Of course, (6.74) reduces to $\cos \theta' = 1$ when $\rho_0 = 0$.

Solutions for I determined respectively by (6.68) and (6.73) are presented as functions of k in figure 6.19. Note that, once the speed normal to the plume boundary (q_\perp) is adopted, $I = 2\pi$ and therefore $E = m$. When the total speed (q) is applied instead, we find from the dashed curves of figure 6.19 a deviation from $I = 2\pi$ for small k . Not surprisingly, the deviation grows with ρ_0 .

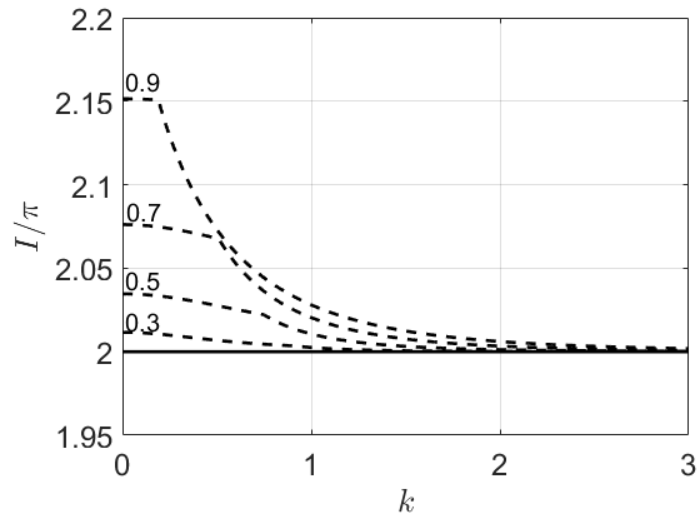


Figure 6.19: Flux integral as a function of k for various ρ_0 . Dashed curves follow (6.68) whereas the solid line follows (6.73).

Chapter 7

Merging of long rows of plumes: Crosswinds, multiple rows and applications to cooling towers

7.1 Abstract

The merging of a single row of plumes in a quiescent environment has been studied using irrotational flow theory (Rooney 2015, *J. Fluid Mech.*, vol. 771, R1). The present study extends this theory by considering (i) two parallel rows of plumes in a quiescent environment, and, (ii) a single row of plumes in a crosswind. For plumes in two rows with and without offset, the effect of varying the ratio of the vertical to horizontal spacing on the plume dynamics is investigated. Two definitions of the contact height are suggested according to the shape of the velocity potential contours. For a single row of plumes in a crosswind, the governing equations are closed using an entrainment flux evaluated by the irrotational flow theory. This novel theory predicts the correct near- and far-field similarity solutions in both modest and strong crosswinds. A comparison of the theory in question to previous towing tank experiments yields satisfactory agreement in terms of plume trajectory. The present theory of single and dual rows of plumes is applied to long rows of cooling tower plumes.

7.2 Introduction

Plume merger has been studied under different configurations, including pairs (Kaye & Linden, 2004; Cenedese & Linden, 2014), rows (Yannopoulos & Noutsopoulos, 2006a; Rooney, 2015) and rosette groups (Lai & Lee, 2012) of plumes. In case of a pair of plumes, a deflection of the plume axes is expected to occur as plumes draw closer together, this a result of restricted entrainment. By contrast for a long row of plumes, the plumes located far from the ends are not significantly deflected, due to the approximately equal but opposite pull exerted by the neighboring plumes. Yannopoulos & Noutsopoulos (2006a,b) formulated the theories of the so-called entrainment restriction approach (ERA) and of the superposition method (SM), respectively. For two or more buoyant jets, ERA assumes Gaussian profiles of velocity and concentration as a result of which the differential equations describing momen-

tum and concentration conservation are integrated over a reduced cross-sectional area – see their figure 2. Based on the same set of governing equations as in ERA, SM developed the superposition solution for any sets of pure jets or pure plumes. Later Yannopoulos (2010) combined ERA and SM to propose an advanced and more general integral model of plume merger. Unlike Yannopoulos’s models, Rooney (2015) proposed a theoretical model whereby the boundaries of a long row of plumes are approximated by the velocity potential contours due to an infinite row of line sinks. Rooney’s model predicts the correct near-field (far-field) axisymmetric (two-dimensional) plume similarity solutions. Compared to earlier theoretical models e.g. Yannopoulos (2010) and Lai & Lee (2012), Rooney’s model is simpler and less computationally expensive. Rooney’s theory presumes a smooth and gradual transition from an axisymmetric plume to a line plume, which is reflected by the evolution of the velocity potential contours – see e.g. figure 7.1.

In the case of multiple plumes in a crosswind, the dynamics of any individual plume is influenced by both wind forcing and the entrainment flow field due to the other plumes. Yannopoulos (1996) proposed a superposition method to study the merging of a finite row of n plumes in a perpendicular wind. In the $n \rightarrow \infty$ limit, Yannopoulos (1996) revealed that the ratio of centerline concentrations between n plumes and an isolated plume is $n^{2/3}$, which is consistent with the simple enhancement model of Briggs (1975) (cf. figure 4 of Yannopoulos 1996). For a rosette group of plumes in a crossflow, Lai & Lee (2012) applied a semi-analytical model whereby the entrainment field is represented by a distribution of point sinks along the plume centerline trajectory; they found that the interaction between plumes weakens in the presence of a crossflow. Despite the neglect of vortex entrainment in the far field, the model prediction of Lai & Lee (2012) is found to be consistent with the experimental results of Lai *et al.* (2011). For multiple tandem plumes in a crossflow, Lai & Lee (2010) modeled the blockage and sheltering effect of the leading plume on the rear plume using a distribution of doublets.

Most of the previous studies on plume merger have focused on a single row of plumes; the interactions between two neighboring rows of plumes have not been thoroughly investigated. In the context of cooling towers, a so-called back-to-back configuration, which gives rise to the merging of two rows of plumes, is a popular design alternative because of its ability to dissipate comparatively large amounts of low-grade heat without requiring a large footprint (Lindhahl & Mortensen, 2010). On the other hand, back-to-back towers may further reduce the rate of entrainment as compared to a single row of towers. This reduced entrainment tends to increase the visible plume length under adverse ambient conditions (i.e. low ambient temperatures and high relative humidities). To this end, insights into the merging of two rows of plumes may benefit cooling tower designs in terms of plume abatement. Of similar importance is to explore a fast and efficient model for describing the merging of a single row of plumes in a crosswind. These twin needs provide the motivation for the present investigation. As such, and following the study of Rooney (2015) (R15 hereafter), we shall (i) apply R15 to the case of two parallel rows of plumes arranged with and without offset, and, (ii) to extend R15 to model a single row of plumes in a windy environment. This latter analysis considers specifically a wind direction that is perpendicular to the row axis so that symmetry is not broken. More generally, goals (i) and (ii) aim to explore the ability of simple irrotational flow theory to describe more complicated plume source conditions and/or ambient conditions.

The manuscript is organized as follows. Section 7.3 reviews the original R15 model. Section 7.4 formulates the irrotational flow theory for two rows of plumes with and without offset. Section 7.5 develops the theory for a single row of plumes in a crosswind. Section 7.6 applies the present theory to long rows of cooling tower plumes. Conclusions are drawn in section 7.7.

7.3 Single row of infinite line sinks (Rooney's theory)

7.3.1 Irrotational flow theory for entrainment flow

R15 considers a single infinite row of equally-spaced line sinks spaced at positions na ($n \in \mathbb{Z}$) on the real axis. Here a is the distance between neighboring plumes. The complex potential due to the whole row of line sinks is

$$\Omega = -\frac{m}{2\pi} \ln \left(\sin \frac{\pi Z}{a} \right), \quad (7.1)$$

where $Z = x + iy$, m is the strength of a line sink. The velocity potential associated with Ω is

$$\phi = -\frac{m}{2\pi} \ln \left| \sin \frac{\pi Z}{a} \right| = -\frac{m}{2\pi} \ln |\sin x' \cosh y' + i \cos x' \sinh y'|, \quad (7.2)$$

where $x' + iy' = \pi Z/a$. Thus the contours of constant velocity potential contours are described by

$$\left| \sin \frac{\pi Z}{a} \right| = |\sin(x' + iy')| = p, \quad (7.3)$$

where $p > 0$ is a constant. Equation (7.3) can be simplified as

$$\cosh 2y' = \cos 2x' + 2p^2. \quad (7.4)$$

Expressing y' in terms of x' and p yields

$$y' = \frac{1}{2} \ln \left(2p^2 + \cos 2x' + \left[(2p^2 + \cos 2x')^2 - 1 \right]^{1/2} \right). \quad (7.5)$$

Velocity potential contours are plotted in figure 7.1 for a range of p . For $0 \leq p \leq 1$, the roots of y' are $x' = \pm \frac{1}{2} \cos^{-1}(1 - 2p^2)$ whereas for $p > 1$, the roots are $x' = \pm \pi/2$. The area under any velocity potential contour, $A' = \pi^2 A/a^2$, is given by

$$A' = \int_{x'_-}^{x'_+} y' dx', \quad (7.6)$$

where $x'_\pm = \pm \frac{1}{2} \cos^{-1}(1 - 2p^2)$ for $0 < p \leq 1$ and $x'_\pm = \pm \pi/2$ for $p > 1$.

The complex velocity is obtained by $\frac{d\Omega}{dZ} = u - iv$, thus

$$\frac{d\Omega}{dZ} = -\frac{m \sin 2x' - i \sinh 2y'}{2a \cosh 2y' - \cos 2x'}. \quad (7.7)$$

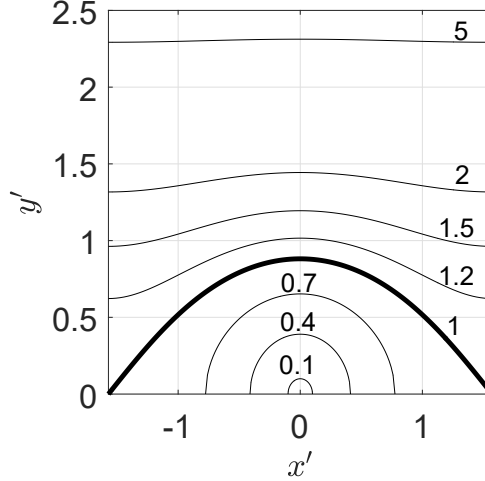


Figure 7.1: Velocity potential contours for a range of p , i.e. $p = 0.1, 0.4, 0.7, 1, 1.2, 1.5, 2$ and 5 . The thick curve, which corresponds to $p = 1$, represents the height of first contact.

Hence, the entrainment flow speed, $q = (u^2 + v^2)^{1/2}$, is given by

$$q = \frac{m}{2a} \left(\frac{\cosh 2y' + \cos 2x'}{\cosh 2y' - \cos 2x'} \right)^{1/2} = \frac{m(p^2 + \cos 2x')^{1/2}}{2ap} = \frac{m(\cosh 2y' - p^2)^{1/2}}{2ap}. \quad (7.8)$$

The speed, q_e , of the fluid entrained at $x' = 0$ is given by

$$q_e = \frac{m(p^2 + 1)^{1/2}}{2ap}. \quad (7.9)$$

Note that q_e is the maximum entrainment speed on a velocity potential contour. The entrainment flux, E , across any velocity potential contour, is defined as

$$E = \int_{x_-}^{x_+} q \, dl, \quad (7.10)$$

and the contour length is given by

$$l' = \frac{\pi}{a} l = \int_{x'_-}^{x'_+} dl'. \quad (7.11)$$

It is shown in section 7.8 that the entrainment flux across any velocity potential contour equals half of the strength of the line sink¹, i.e. $E = m/2$.

7.3.2 Plume equations and entrainment closure

The generalized plume equations (for a half-plume) are given by

$$A \frac{d}{dz} \left(\frac{1}{2} w^2 \right) = Ag' - wE, \quad (7.12)$$

¹This result is not stated explicitly in Rooney (2015) due to a possible rounding error. Changes resulting from $E = m/2$ have been made in the following sections.

$$\frac{d}{dz}(Aw) = E, \quad (7.13)$$

$$\frac{d}{dz}(Awg') = -AwN^2, \quad (7.14)$$

where w is the mean vertical velocity, g' is the reduced gravity and N is the ambient buoyancy frequency. Equations (7.13)-(7.14) can be obtained by reorganizing the original plume equations from the seminal work of Morton *et al.* (1956).

Recognizing the need for an entrainment closure, R15 suggested relating q_e with w , i.e. $q_e = \alpha w$, where α is an entrainment coefficient. Applying this last result in (7.9), the strength of the line sink can be expressed as

$$m = 2a\alpha w \frac{p}{(p^2 + 1)^{1/2}}. \quad (7.15)$$

Because we have shown that $E = m/2$, the entrainment flux is given by

$$E = m/2 = a\alpha w \frac{p}{(p^2 + 1)^{1/2}}, \quad (7.16)$$

which serves as the closure condition for (7.12)-(7.14).

7.3.3 Merging plumes in an unstratified ambient

For an unstratified ambient with $N = 0$, the buoyancy flux, $F = Awg'$, is constant – see (7.14). On this basis, (7.12) and (7.13) can be rewritten as

$$\frac{dw}{dz} = \frac{F}{Qw} - \frac{a\alpha w^2}{Q} f, \quad (7.17)$$

$$\frac{dQ}{dz} = a\alpha w f, \quad (7.18)$$

where $Q = Aw$ is plume volume flux and

$$f = \frac{p}{(p^2 + 1)^{1/2}} \rightarrow \begin{cases} p, & p \ll 1 \\ 1, & p \gg 1. \end{cases} \quad (7.19)$$

In the limit $p \ll 1$, $y'_0 \equiv y'(x' = 0) = \ln \left[p + (p^2 + 1)^{1/2} \right] \approx \ln(p + 1) \approx p$. The product af tends to π times the plume radius, ap/π , in the limit $p \ll 1$ and tends to the constant value a in the limit $p \gg 1$.

The dimensionless vertical velocity, \hat{w} , volume flux, \hat{Q} , and vertical distance, \hat{z} , are as follows:

$$w = \alpha^{-1/3} F^{1/3} a^{-1/3} \hat{w}, \quad Q = \alpha^{-1/3} F^{1/3} a^{5/3} \hat{Q}, \quad z = \alpha^{-1} a \hat{z}, \quad (7.20)$$

where the hatted variables are dimensionless. Therefore, (7.17) and (7.18) can be nondimensionalized as

$$\frac{d\hat{w}}{d\hat{z}} = \frac{1}{\hat{Q}\hat{w}} - \frac{\hat{w}^2}{\hat{Q}} f, \quad (7.21)$$

$$\frac{d\hat{Q}}{d\hat{z}} = \hat{w}f. \quad (7.22)$$

The dimensionless cross-sectional area is $\hat{A} = \hat{Q}/\hat{w} = A'/\pi^2 = A/a^2$.

In the near-source region of small p , the plume is approximately axisymmetric and thus can be characterized by a flux-balance parameter, Γ , which is defined as

$$\Gamma = \frac{5}{8\pi^{1/2}\alpha} \frac{(2Q)^2(2F)}{(2M)^{5/2}} = \frac{5}{2^{5/2}\pi^{1/2}} \hat{A}^{-1/2} \hat{w}^{-3}, \quad (7.23)$$

where $M = Qw$ is the momentum flux. To solve (7.21) and (7.22), we first choose a small p , e.g. 0.05, then the corresponding cross-sectional area, \hat{A} , can be determined from (7.6). Subsequently, we set the source value of Γ (i.e. $\Gamma_0 = \Gamma(z = 0)$) thus the source value of \hat{w} is determined by (7.23).

7.3.4 Representative solution

Representative results showing the dimensionless vertical velocity and volume flux with $\Gamma_0 = 1$ are illustrated in figure 7.2. Note that we neglect a near-field virtual origin correction which does not significantly change the overall profiles. The height of first contact, $\hat{z}_{fc} = 0.340$, is defined as the point where p is closest to unity. This height is slightly lower than the height of first contact of 0.350 for two axisymmetric plumes (Cenedese & Linden, 2014). Linearly extrapolating the \hat{Q} data on a Cartesian grid over $4 < \hat{z} \leq 5$ yields the far-field line plume virtual origin, $\hat{z}_{vf} = -0.149$, where the volume flux is “zero”. To help with visualization, the surface plot illustrating plume merger is shown in figure 7.3.

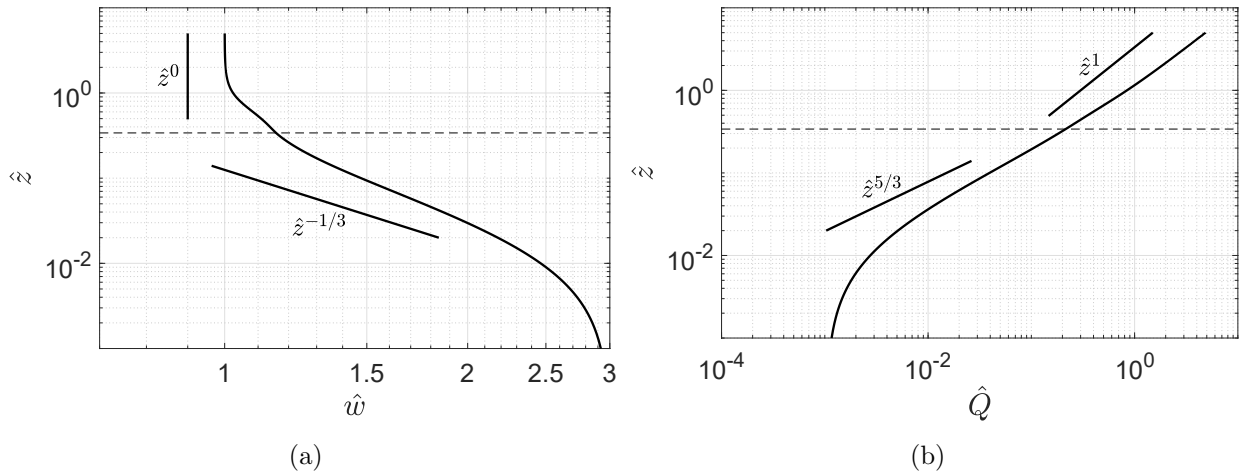


Figure 7.2: Evolution of \hat{w} and \hat{Q} as a function of \hat{z} . The horizontal dashed lines denote the height of first contact, $\hat{z}_{fc} = 0.340$. The solid straight lines denote the near-field ($p < 1$) and far-field ($p > 1$) similarity scalings.

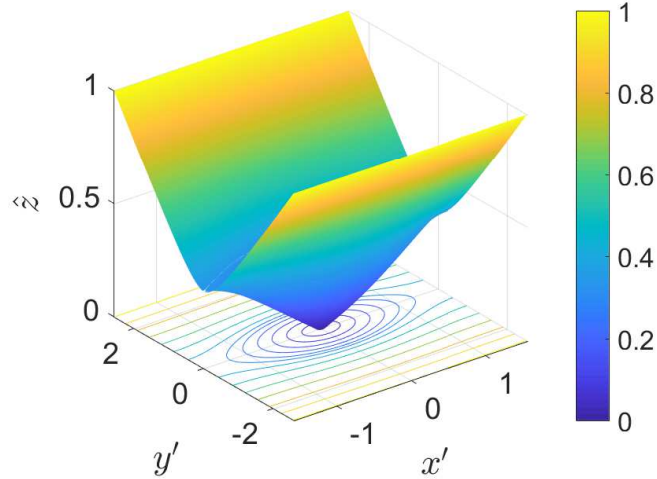


Figure 7.3: [Color] Surface plot illustrating plume merger in a long row of plumes. The plume boundaries are shaded according to the height between 0 and 1, and these contours are also projected onto the bottom plane.

7.4 Two rows of infinite line sinks

7.4.1 Non-offset parallel line sinks

7.4.1.1 Complex potential

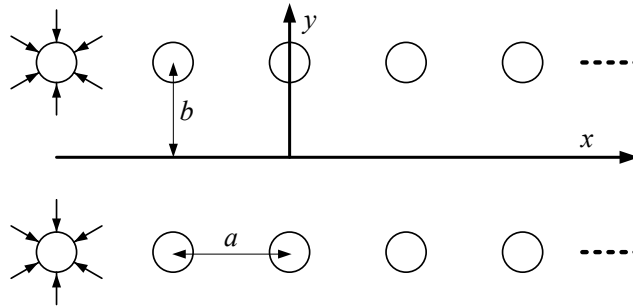


Figure 7.4: Schematic of two non-offset parallel rows of an infinite number of line sinks.

As shown in figure 7.4, we consider two rows of line sinks spaced $2b$ apart in the y -direction. Each row consists of an infinite line of sinks at positions $x = na$ ($n \in \mathbb{Z}$). The total complex potential is

$$\Omega = -\frac{m}{2\pi} \left[\ln \left(\sin \frac{\pi (Z - ib)}{a} \right) + \ln \left(\sin \frac{\pi (Z + ib)}{a} \right) \right]. \quad (7.24)$$

The velocity potential is

$$\phi = -\frac{m}{2\pi} \left[\ln \left| \sin \frac{\pi (Z - ib)}{a} \right| + \ln \left| \sin \frac{\pi (Z + ib)}{a} \right| \right] \quad (7.25)$$

$$= -\frac{m}{2\pi} \ln \left| \frac{1}{2} (\cosh 2b' - \cos 2x' \cosh 2y' + i \sin 2x' \sinh 2y') \right|, \quad (7.26)$$

where $x' + iy' = \pi Z/a$ and $b' = \pi b/a$. The contours of constant velocity potential are described by

$$\left| \sin \frac{\pi (Z - ib)}{a} \sin \frac{\pi (Z + ib)}{a} \right| = p/2, \quad (7.27)$$

where $p > 0$ is an arbitrary constant. Expanding (7.27) in terms of x' and y' yields

$$\cosh^2 2y' - 2 \cosh 2b' \cos 2x' \cosh 2y' + \cos^2 2x' + \sinh^2 2b' = p^2. \quad (7.28)$$

Solving for y' yields

$$\cosh 2y' = \cosh 2b' \cos 2x' \pm (p^2 - \sinh^2 2b' \sin^2 2x')^{1/2}, \quad (7.29)$$

$$y' = \frac{1}{2} \ln \left[\cosh 2y' + (\cosh^2 2y' - 1)^{1/2} \right]. \quad (7.30)$$

We can alternatively solve for x' , i.e.

$$\cos 2x' = \cosh 2b' \cosh 2y' - (p^2 + \sinh^2 2b' \sinh^2 2y')^{1/2}. \quad (7.31)$$

The negative square root in (7.29) is applicable for $p < \sinh 2b'$. Equations (7.29) and (7.30) indicate that y' is periodic in x' with period π . The roots of y' are $x' = \pm (1/2) \cos^{-1} (\cosh 2b' - p)$ for $\cosh 2b' - 1 \leq p \leq \cosh 2b' + 1$. For $p < \cosh 2b' - 1$, the horizontal range is $-\frac{1}{2} \sin^{-1} (p/\sinh 2b') \leq x' \leq \frac{1}{2} \sin^{-1} (p/\sinh 2b')$. Sample velocity potential contours for $b' = \pi/2$ (i.e. $a = 2b$) are illustrated in figure 7.5.

The maximum vertical extent, y'_{\max} , of each contour occurs at $x' = 0$ where

$$y'_{\max} = \frac{1}{2} \ln \left(\cosh 2b' + p + [(\cosh 2b' + p)^2 - 1]^{1/2} \right). \quad (7.32)$$

The corresponding minimum vertical extent is a piecewise function of p , which reads

$$y'_{\min} = \begin{cases} \frac{1}{2} \ln \left(\cosh 2b' - p + [(\cosh 2b' - p)^2 - 1]^{1/2} \right), & p \leq \cosh 2b' - 1 \\ 0, & \cosh 2b' - 1 < p \leq \cosh 2b' + 1 \\ \frac{1}{2} \ln \left(-\cosh 2b' + p + [(-\cosh 2b' + p)^2 - 1]^{1/2} \right), & p > \cosh 2b' + 1. \end{cases} \quad (7.33)$$

The complex velocity can be obtained from the complex derivative, i.e.

$$\begin{aligned} \frac{d\Omega}{dZ} &= u - iv \\ &= -\frac{m}{2a} \left(\cot \frac{\pi (Z - ib)}{a} + \cot \frac{\pi (Z + ib)}{a} \right) \\ &= -\frac{m}{a} \frac{\cosh 2b' \sin 2x' \cosh 2y' - \frac{1}{2} \sin 4x' + i (\cosh 2b' \cos 2x' \sinh 2y' - \frac{1}{2} \sinh 4y')}{\cosh^2 2b' - 2 \cosh 2b' \cos 2x' \cosh 2y' + \frac{1}{2} (\cos 4x' + \cosh 4y')}. \end{aligned} \quad (7.34)$$

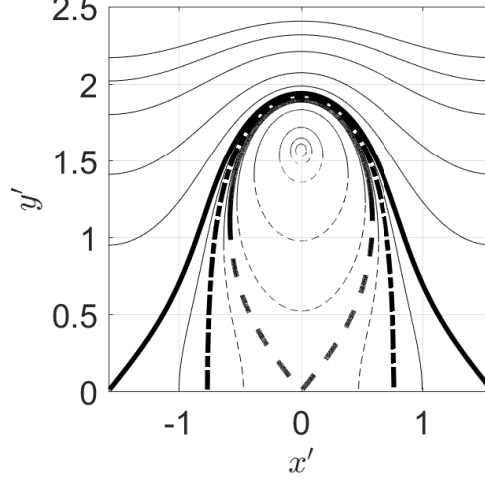


Figure 7.5: Velocity potential contours for $b' = \pi/2$. The contours start from $(0, \pi/2)$ and expand outward with p selected from the set $\{1, 2, 4, 8, 10, \cosh 2b' - 1, 11, \sinh 2b', 12, \cosh 2b' + 1, 15, 20, 30, 40, 50\}$. The thick half solid and half dashed contour corresponds to $p = \cosh 2b' - 1$, the thick dash-dotted contour corresponds to $p = \sinh 2b'$ and the thick solid contour that extends into the corners corresponds to $p = \cosh 2b' + 1$. Within the dash-dotted contour ($p < \sinh 2b'$), the solid and dashed parts of the contours correspond, respectively, to the positive and negative roots in (7.29).

The flow speed can be obtained from $q = \left| \frac{d\Omega}{dz} \right|$ and is given by

$$q^2 = \frac{m^2 \left(\cosh 2b' \sin 2x' \cosh 2y' - \frac{1}{2} \sin 4x' \right)^2 + \left(\cosh 2b' \cos 2x' \sinh 2y' - \frac{1}{2} \sinh 4y' \right)^2}{a^2 \left[\cosh^2 2b' - 2 \cosh 2b' \cos 2x' \cosh 2y' + \frac{1}{2} (\cos 4x' + \cosh 4y') \right]^2}. \quad (7.35)$$

Using (7.28), (7.35) is simplified as

$$q^2 = \frac{m^2 \sin^2 2x' + \sinh^2 2y'}{a^2 p^2} = \frac{m^2 \sin^2 2x' + \cosh^2 2y' - 1}{a^2 p^2}. \quad (7.36)$$

At $x' = 0$ and $y' = y'_{\max}$, the characteristic entrainment flow speed is

$$q_e = \frac{m \sinh 2y'}{a p} = \frac{m \left[(\cosh 2b' + p)^2 - 1 \right]^{1/2}}{a p}. \quad (7.37)$$

7.4.1.2 Flux and area

Differentiating (7.28) with respect to x' yields

$$\left(\frac{dy'}{dx'} \right)^2 = \frac{(1 - \cos^2 2x') (\cos 2x' - \cosh 2b' \cosh 2y')^2}{(\cosh^2 2y' - 1) (\cosh 2y' - \cosh 2b' \cos 2x')^2}. \quad (7.38)$$

Using (7.29) and (7.31), respectively, the right-hand side of (7.38) can be expressed as a function of x' and p or y' and p . In turn, the contour length, l' , is calculated from

$$dl' = (dx'^2 + dy'^2)^{1/2} = \left(1 + \left(\frac{dy'}{dx'} \right)^2 \right)^{1/2} dx' = \left(1 + \left(\frac{dy'}{dx'} \right)^{-2} \right)^{1/2} dy'. \quad (7.39)$$

For $p \geq \cosh 2b' + 1$, l' and the area, A' , are given by

$$l' = \int_{x'_-}^{x'_+} \left(1 + \left(\frac{dy'_+}{dx'} \right)^2 \right)^{1/2} dx', \quad (7.40)$$

$$A' = \int_{x'_-}^{x'_+} y'_+ dx', \quad (7.41)$$

where $x'_\pm = \pm\pi/2$ and y'_+ corresponds to the positive root in (7.29). For $\sinh 2b' \leq p < \cosh 2b' + 1$, l' and A' are resolved by replacing $x'_\pm = \pm\pi/2$ with $x'_\pm = \pm(1/2) \cos^{-1}(\cosh 2b' - p)$ in both (7.40) and (7.41). Conversely when $\cosh 2b' - 1 \leq p < \sinh 2b'$, the length and area are evaluated from

$$l' = 2 \int_0^{y'_{\max}} \left(1 + \left(\frac{dy'}{dx'} \right)^{-2} \right)^{1/2} dy', \quad (7.42)$$

$$A' = 2 \int_0^{y'_{\max}} x' dy'. \quad (7.43)$$

Finally for $p < \cosh 2b' - 1$, the length and area are calculated by

$$l' = \int_{x'_{\min}}^{x'_{\max}} \left[\left(1 + \left(\frac{dy'_+}{dx'} \right)^2 \right)^{1/2} + \left(1 + \left(\frac{dy'_-}{dx'} \right)^2 \right)^{1/2} \right] dx', \quad (7.44)$$

$$A' = \int_{x'_{\min}}^{x'_{\max}} (y'_+ - y'_-) dx', \quad (7.45)$$

where $x'_{\min} = -\frac{1}{2} \sin^{-1}(p/\sinh 2b')$, $x'_{\max} = \frac{1}{2} \sin^{-1}(p/\sinh 2b')$ and y'_- corresponds to the negative root in (7.29). Figure 7.6 shows l' and A' as a function of p .

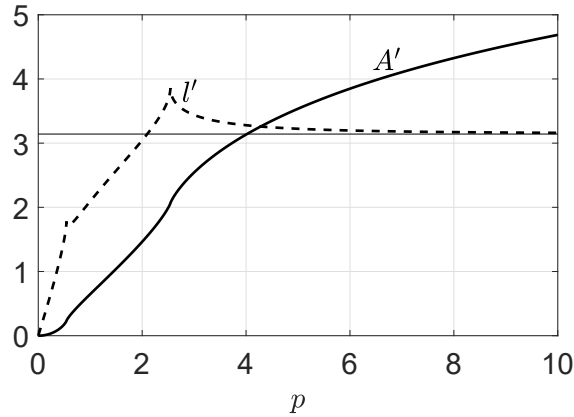


Figure 7.6: l' and A' as a function of p for $b/a = 0.5$. The horizontal line denotes a constant value of π .

Analogous to (7.10), the entrainment flux across an arbitrary velocity potential contour, C , is

$$E = \int_C q dl = \int_C \frac{aq}{\pi} dl' = m, \quad (7.46)$$

where the latter equality applies for all values of p – see section 7.8. In turn, the strength of the line sink can be determined by inverting (7.37), i.e.

$$m = E = a\alpha w \frac{p}{[(\cosh 2b' + p)^2 - 1]^{1/2}}. \quad (7.47)$$

Thus the f parameter in (7.21) and (7.22) is given by

$$f = \frac{p}{[(\cosh 2b' + p)^2 - 1]^{1/2}}. \quad (7.48)$$

7.4.1.3 Representative solutions

For $b/a = 0.25, 0.5$ and 1 and $\Gamma_0 = 1$, the plume vertical velocity and volume flux are illustrated in figure 7.7. Figure 7.7 a shows that the evolution of vertical velocity in case of a small vertical spacing i.e. $b/a = 0.25$ is similar to the counterpart evolution for a single row of plumes as shown in figure 7.2 a. By contrast, and for larger values of b/a e.g. $b/a = 1$, there appears a transition zone of almost constant vertical velocity before the far-field limit is approached. Figure 7.7 b shows similar profiles of volume flux for all values of b/a .

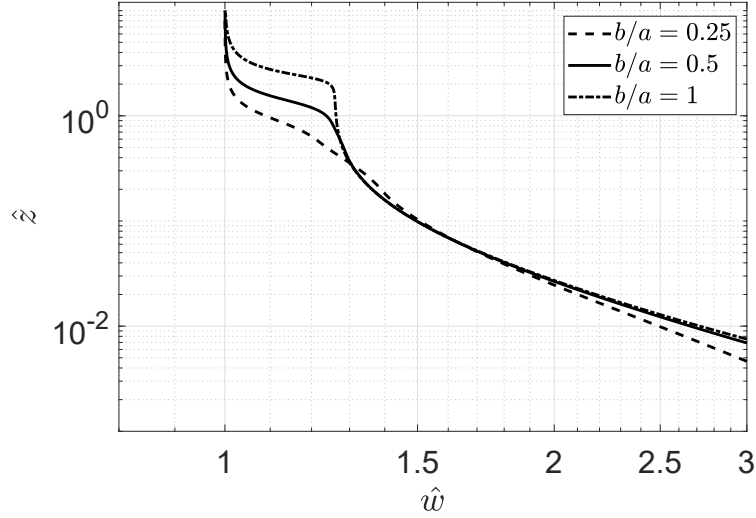
Two different contact height are defined: the first contact height, $\hat{z}_{c,1}$, is defined as the elevation where the two opposite plumes first contact one another. This elevation is determined as the point where p is closest to $\cosh 2b' - 1$. The second contact height, $\hat{z}_{c,2}$, is defined as the elevation where the combined plume (post-merger of the two opposite plumes) extends to the corners (see e.g. the thick solid curve in figure 7.5). This second contact height is determined as the point where p is closest to $\cosh 2b' + 1$. Interestingly, from $\hat{z}_{c,1}$ to $\hat{z}_{c,2}$ the velocity potential contours move from the stagnation point located at the origin to a stagnation point located in either one of the two corners – see figure 7.5. Note that $\hat{z}_{c,1}$ is similar to the height of first contact for two neighboring axisymmetric plumes. Figure 7.9 indicates that $\hat{z}_{c,1}$ and $\hat{z}_{c,2}$ increase in an approximately linear fashion with b/a . In case of a small b/a , e.g. $b/a = 0.05$, $\hat{z}_{c,2} = 0.338$, which is close to the counterpart merger height $\hat{z}_c = 0.340$ for a single row of plumes. In the case of two axisymmetric plumes spaced $2b$ apart, the height of first contact is $z = 0.35 (2b/\alpha)$ thus $\hat{z}_c = 0.7b/a$ (Cenedese & Linden, 2014); this height is somewhat lower than the first contact height for two infinite rows of plumes, i.e. $\hat{z}_{c,1} \approx 0.9b/a$ as inferred from figure 7.9. This difference is likely because, in the latter case, plume distortion is driven by restricted entrainment from two orthogonal directions, i.e. between plumes opposite one another and between neighboring plumes within the same row.

7.4.2 Offset parallel line sinks

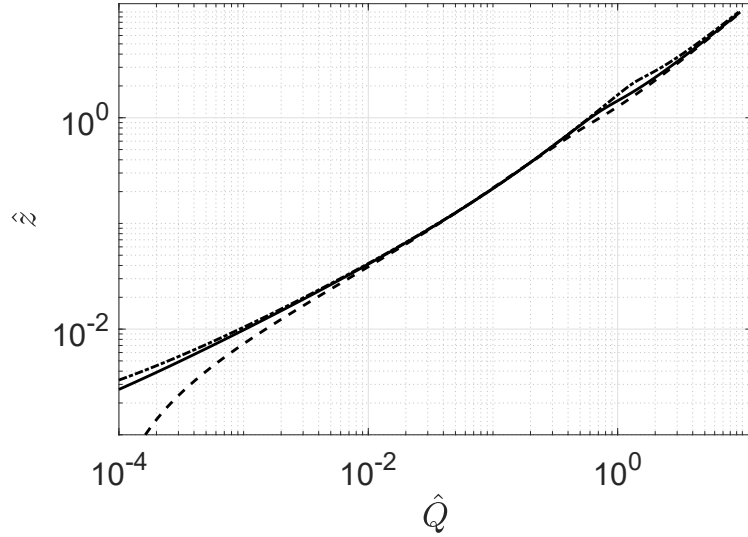
7.4.2.1 Complex potential

Another typical configuration is two parallel rows of line sinks with an offset ($a/2$) as shown in figure 7.10. With this configuration, the complex potential reads

$$\Omega = -\frac{m}{2\pi} \left[\ln \left(\sin \frac{\pi (Z - ib)}{a} \right) + \ln \left(\cos \frac{\pi (Z + ib)}{a} \right) \right]. \quad (7.49)$$



(a)



(b)

Figure 7.7: Evolution of \hat{w} and \hat{Q} as a function of \hat{z} for $b/a = 0.25, 0.5$ and 1 . In all cases, $\Gamma_0 = 1$.

The velocity potential is given by

$$\phi = -\frac{m}{2\pi} \left[\ln \left| \sin \frac{\pi (Z - ib)}{a} \right| + \ln \left| \cos \frac{\pi (Z + ib)}{a} \right| \right] \quad (7.50)$$

$$= -\frac{m}{2\pi} \ln \left| \frac{1}{2} (\sin 2x' \cosh 2y' + i(\cos 2x' \sinh 2y' - \sinh 2b')) \right|. \quad (7.51)$$

Constant velocity potential contours are given by

$$\left| \sin \frac{\pi (Z - ib)}{a} \cos \frac{\pi (Z + ib)}{a} \right| = p/2, \quad (7.52)$$

which is simplified as

$$\cosh^2 2y' - 2 \sinh 2b' \cos 2x' \sinh 2y' - \cos^2 2x' + \sinh^2 2b' = p^2. \quad (7.53)$$

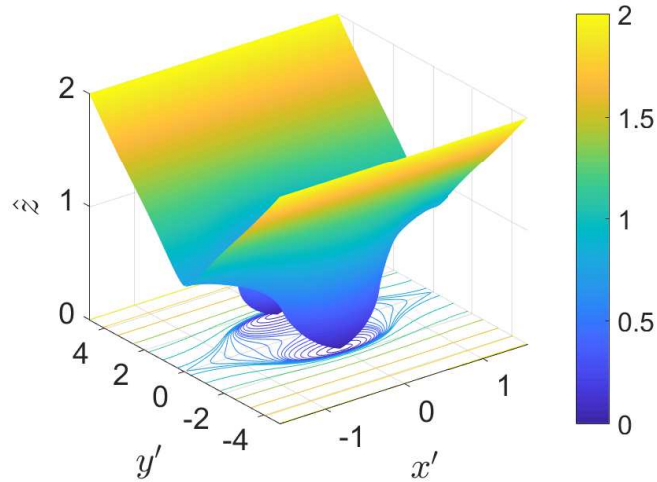


Figure 7.8: [Color] Surface plot illustrating plume merger in case of two parallel rows of non-offset plumes with $b/a = 0.5$. The plume boundaries are shaded according to the height between 0 and 2, and these contours are also projected onto the bottom plane.

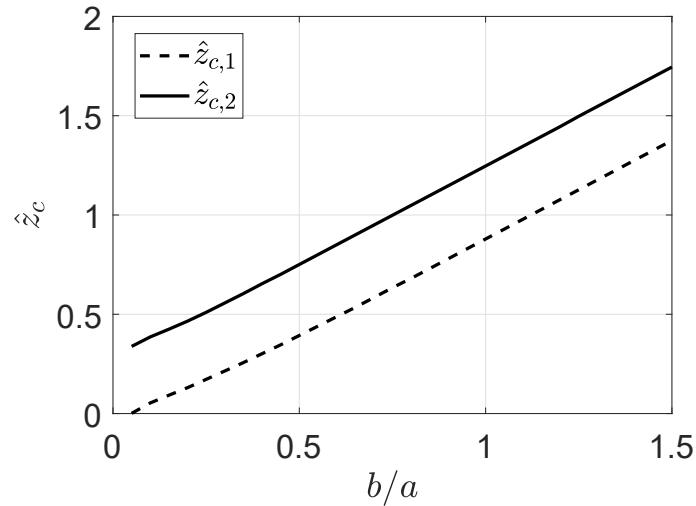


Figure 7.9: The contact heights $\hat{z}_{c,1}$ and $\hat{z}_{c,2}$ plotted as a function of b/a . In all cases, $\Gamma_0 = 1$.

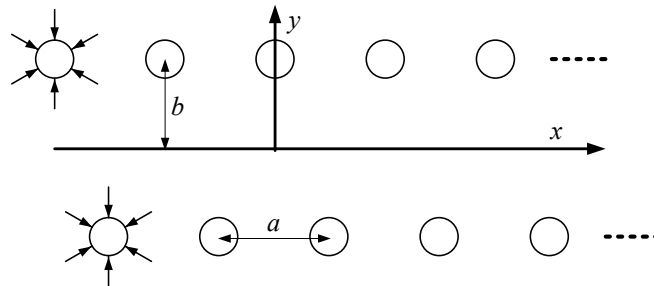


Figure 7.10: Schematic of two parallel rows of an infinite number of line sinks with an offset.

Solving for y' yields

$$\sinh 2y' = \sinh 2b' \cos 2x' \pm (p^2 - \cosh^2 2b' \sin^2 2x')^{1/2}, \quad (7.54)$$

$$y' = \frac{1}{2} \ln \left(\sinh 2y' + (\sinh^2 2y' + 1)^{1/2} \right), \quad (7.55)$$

or solving for x' yields

$$\cos 2x' = -\sinh 2b' \sinh 2y' + (\cosh^2 2b' \cosh^2 2y' - p^2)^{1/2}. \quad (7.56)$$

The positive/negative square roots in (7.54) are applicable for all values of p . Due to the symmetry of the configuration shown in figure 7.10, the analysis is restricted to $-\pi/4 \leq x' \leq \pi/4$. For $\sinh 2b' \leq p \leq \cosh 2b'$, the roots of y' are $x' = \pm 1/2 \cos^{-1} (\cosh^2 2b' - p^2)^{1/2}$. For $p \leq \cosh 2b'$, the horizontal range is $-\frac{1}{2} \sin^{-1} (p/\cosh 2b') \leq x' \leq \frac{1}{2} \sin^{-1} (p/\cosh 2b')$. Sample velocity potential contours with $b' = \pi/4$ are illustrated in figure 7.11.

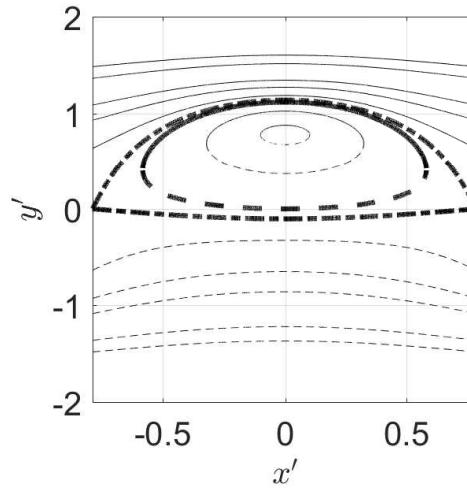


Figure 7.11: Velocity potential contours for $b' = \pi/4$. The contours start from $(0, \pi/4)$ and expand outward with p selected from the set $\{0.5, 1.5, \sinh 2b', \cosh 2b', 3, 4, 5, 8, 10\}$. The thick half solid and half dashed contour corresponds to $p = \sinh 2b'$ and the dash-dotted contour corresponds to $p = \cosh 2b'$. The solid and dashed curves correspond, respectively, to the positive and negative roots in (7.54).

The maximum and minimum vertical extents are given by

$$y'_{\max} = \frac{1}{2} \ln \left[\sinh 2b' + p + \left((\sinh 2b' + p)^2 + 1 \right)^{1/2} \right], \quad (7.57)$$

$$y'_{\min} = \frac{1}{2} \ln \left[\sinh 2b' - p + \left((\sinh 2b' - p)^2 + 1 \right)^{1/2} \right], \quad (7.58)$$

respectively. The complex velocity is obtained from

$$\begin{aligned} u - iv &= -\frac{m}{2a} \left(\cot \frac{\pi(Z - ib)}{a} - \tan \frac{\pi(Z + ib)}{a} \right) \\ &= -\frac{m}{2a} \frac{\sin 4x' \cosh 4y' - 2 \sinh 2b' \sin 2x' \sinh 2y' + i (\cos 4x' \sinh 4y' - 2 \sinh 2b' \cos 2x' \cosh 2y')}{\cosh^2 2y' - 2 \sinh 2b' \cos 2x' \sinh 2y' - \cos^2 2x' + \sinh^2 2b'} \end{aligned} \quad (7.59)$$

thus the flow speed is

$$q^2 = \frac{m^2 \cosh^2 2y' - \sin^2 2x'}{p^2} = \frac{m^2 \sinh^2 2y' + \cos^2 2x'}{p^2}. \quad (7.60)$$

At $x' = 0$ and y' reaches its maximum and the characteristic entrainment speed is given by

$$q_e = \frac{m}{a} \frac{[(\sinh 2b' + p)^2 + 1]^{1/2}}{p}. \quad (7.61)$$

Differentiation of (7.53) with respect to x' yields

$$\left(\frac{dy'}{dx'}\right)^2 = \frac{\sin^2 2x' (\sinh 2b' \sinh 2y' + \cos 2x')^2}{\cosh^2 2y' (\sinh 2b' \cos 2x' - \sinh 2y')^2}. \quad (7.62)$$

The contour length and cross-sectional area can be calculated using a similar approach as in section 7.4.1. Specifically, l' and A' are given by

$$l' = \int_{x'_-}^{x'_+} \left[\left(1 + \left(\frac{dy'_+}{dx'}\right)^2\right)^{1/2} + \left(1 + \left(\frac{dy'_-}{dx'}\right)^2\right)^{1/2} \right] dx' \quad (7.63)$$

$$A' = \int_{x'_-}^{x'_+} (y'_+ - y'_-) dx' \quad (7.64)$$

where $x'_\pm = \pm\pi/4$ for $p > \cosh 2b'$, $x'_\pm = \pm\frac{1}{2} \sin^{-1}(p/\cosh 2b')$ for $p \leq \cosh 2b'$ and y'_\pm correspond to the positive and negative roots in (7.54). Figure 7.12 shows l' and A' as a function of p .

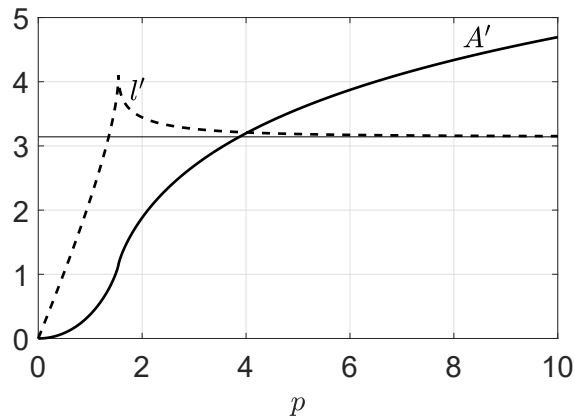


Figure 7.12: l' and A' as a function of p for $b/a = 0.5$. The horizontal line denotes a constant value of π .

Adopting the simple entrainment relation $q_e = \alpha w$, the strength of the line sink, m , is thus given by

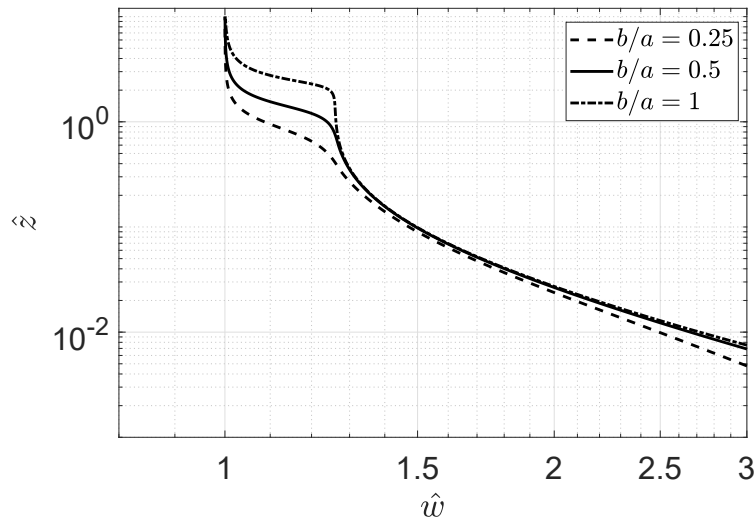
$$m = a\alpha w \frac{p}{[(\sinh 2b' + p)^2 + 1]^{1/2}}, \quad (7.65)$$

where, consistent with (7.46) and (7.47), $m = E$ – see section 7.8. Correspondingly, the parameter, f in (7.21) and (7.22), is expressed by

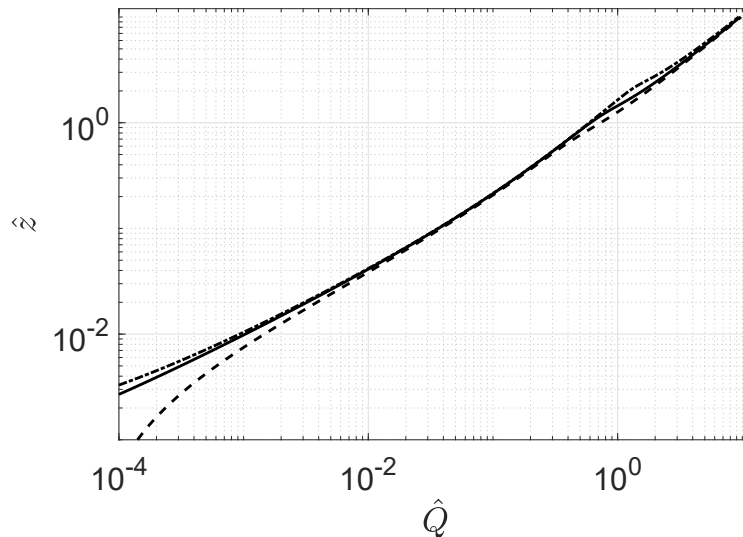
$$f = \frac{p}{[(\sinh 2b' + p)^2 + 1]^{1/2}}, \quad (7.66)$$

which reduces to (7.19) in the limit $b' \rightarrow 0$.

7.4.2.2 Representative solutions



(a)



(b)

Figure 7.13: Evolution of \hat{w} and \hat{Q} as a function of \hat{z} . In all cases, $\Gamma_0 = 1$.

For $b/a = 0.25, 0.5$ and 1 and $\Gamma_0 = 1$, figure 7.13 shows that the vertical velocity and volume flux for the offset case are similar to the counterpart results for the non-offset case

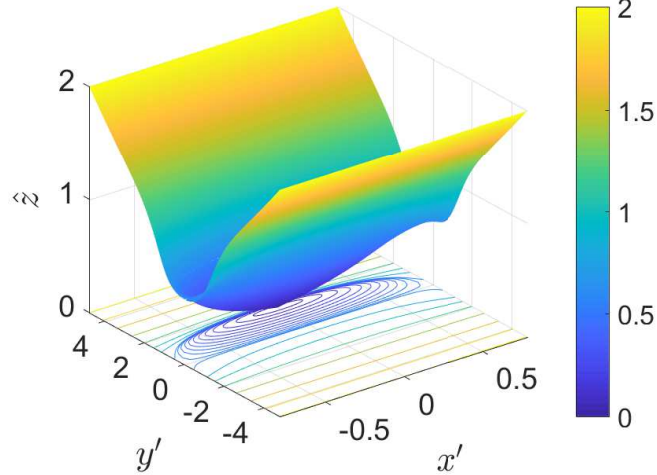


Figure 7.14: [Color] Surface plot illustrating plume merger in case of two offset parallel rows of plumes with $b/a = 0.5$. The plume boundaries are shaded according to the height between 0 and 2, and these contours are also projected onto the bottom plane.

from figure 7.7. The vertical velocity profiles are consistent with the shape of velocity potential contours, i.e. the plume boundaries, for different b/a values. Thus for small b/a , e.g. $b/a = 0.25$, the contour at the contact height ($p = \cosh 2b'$) is “short and fat”; subsequently this contour evolves like a line plume with a horizontal axis that persists into the very far field (figure 7.11). By contrast, the counterpart contour for larger b/a e.g. $b/a = 1$ is expected to be relatively “long and thin”, i.e. before approaching its far-field limiting shape, the contour is analogous to a line plume with a vertical axis before approaching the far-field limit. The surface plot illustrated in figure 7.14 shows the velocity potential contours at different heights for the case $b/a = 0.5$. We define two different contact heights, $\hat{z}_{c,1}$ and $\hat{z}_{c,2}$, as follows: $\hat{z}_{c,1}$ ($\hat{z}_{c,2}$) is given as the vertical distance where p is closest to $\sinh 2b'$ ($\cosh 2b'$). Physically, $\hat{z}_{c,1}$ is the elevation where an individual plume first touches the center plane (i.e. the horizontal axis in figure 7.10) and $\hat{z}_{c,2}$ is the elevation where individual plumes contact one another. The contact heights $\hat{z}_{c,1}$ and $\hat{z}_{c,2}$ are illustrated in figure 7.15; differences between $\hat{z}_{c,1}$ and $\hat{z}_{c,2}$ are most apparent for $b/a < 0.5$. Thereafter, and to very good approximation, $\hat{z}_{c,1} \simeq \hat{z}_{c,2}$.

7.4.3 Effective entrainment perimeter

Consistent with He & Lou (2019) who studied the merger of two adjacent plumes, we have shown in figures 7.6 and 7.12 that the contour length l' is a nonmonotonic function of p , with a “kinky” peak value at the contact height, $\hat{z}_{c,2}$. Due to the discontinuity in $\partial l'/\partial p$, it is expected that the spatial derivative (with respect to p) of the entrainment per unit plume perimeter exhibits a singular point at $\hat{z}_{c,2}$. It should be emphasized that the contour length is not directly included in the plume modeling except in the definition of the entrainment flux, i.e. (7.10). Instead of the plume perimeter, we may consider an “effective entrainment perimeter” to account for the reduced entrainment due to plume merger. The entrainment closure (7.16) implicitly defines the effective entrainment perimeter, denoted by P_e , which is

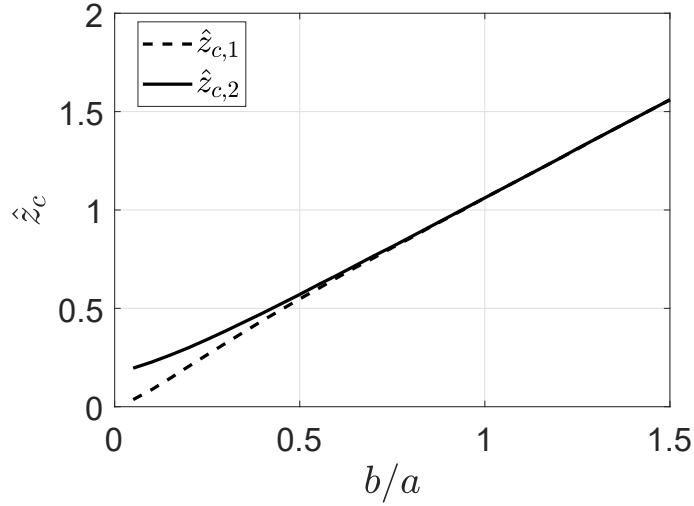


Figure 7.15: As in figure 7.9 but in case of offset plumes with an offset distance of $a/2$. In all cases, $I_0 = 1$.

given by

$$P_e = af, \quad (7.67)$$

where f can be specified by either (7.19), (7.48) or (7.66). For single and dual rows of plumes, the evolution of $f = P_e/a$ as a function of p is shown in figure 7.16. The lower value of f for the case of two rows is indicative of the reduced entrainment compared to the single row case. For a modest spacing ratio of $b/a = 0.2$, figure 7.16 shows that the effective entrainment perimeters for two rows with and without offset are extremely close, which is consistent with the similar profiles shown in figures 7.7 and 7.13.

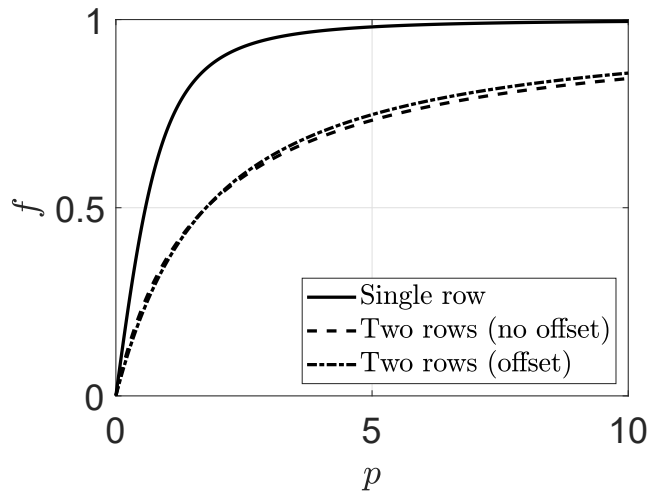


Figure 7.16: Effective entrainment perimeter as a function of p . For two rows of plumes, the vertical to horizontal spacing ratio is fixed as $b/a = 0.2$.

7.5 Plume merger in a neutral crosswind

7.5.1 Formulation

In case of a crosswind, we assume based on the experimental study of Jordinson (1956) that the main mechanism for bending a plume is the rate of entrainment from the ambient to the plume core. Thus each individual plume in a crosswind can still be regarded as a line sink, whose strength is now related to the wind speed. Considering a wind direction that is perpendicular to the axis of a single row of line sinks, the symmetry between individual plumes is not broken. The governing equations are then as follows:

$$\frac{d}{ds} (AU_p) = E, \quad (7.68)$$

$$\frac{d}{ds} (AU_p u) = EU_a, \quad (7.69)$$

$$\frac{d}{ds} (AU_p w) = g' A, \quad (7.70)$$

$$\frac{d}{ds} (AU_p g') = 0, \quad (7.71)$$

$$\frac{dx}{ds} = \cos \theta, \quad (7.72)$$

$$\frac{dz}{ds} = \sin \theta, \quad (7.73)$$

where U_p is the mean streamwise velocity, $u = U_p \cos \theta$ and $w = U_p \sin \theta$ are the horizontal and vertical components of U_p , respectively, and U_a is the ambient wind velocity that is assumed to be everywhere uniform. Defining the volume flux, $Q = AU_p$, and buoyancy flux, $F = AU_p g'$, (7.68)-(7.70) can be rewritten as

$$\frac{dQ}{ds} = E, \quad (7.74)$$

$$\frac{du}{ds} = \frac{E(U_a - u)}{Q}, \quad (7.75)$$

$$\frac{dw}{ds} = \frac{F}{Q(u^2 + w^2)^{1/2}} - \frac{wE}{Q}. \quad (7.76)$$

The above set of equations is closed with an entrainment assumption. Consistent with the irrotational flow theory described in section 7.3, we relate a characteristic entrainment velocity (q_e) to the shear between plume and crosswind. One of the simplest forms of entrainment closure has been proposed by Hoult & Weil (1972), which reads

$$q_e = \gamma_1 |U_p - U_a \cos \theta| + \gamma_2 U_a \sin \theta, \quad (7.77)$$

where γ_1 and γ_2 are entrainment coefficients associated with the longitudinal and transverse shear, respectively. Equation (7.77) assumes that the longitudinal and transverse entrainments are linearly additive. The rate of entrainment, E , is evaluated as

$$E = 2af (\gamma_1 |U_p - U_a \cos \theta| + \gamma_2 U_a \sin \theta). \quad (7.78)$$

where f is to be specified later. Note that the plume in question is a whole plume with $E = m$ rather than the half plume considered in section 7.3. This $E = m$ outcome is consistent with the plume equations (7.68)-(7.71) and (7.74)-(7.76) which implicitly assume a whole plume. Hereafter, the variables are nondimensionalized using a buoyancy length scale, $L_B = FU_a^{-3}$, and the wind speed, U_a , as follows:

$$\begin{aligned} s &= L_B \bar{s}, & z &= L_B \bar{z}, & x &= L_B \bar{x}, & a &= L_B \bar{a}, \\ u &= U_a \bar{u}, & w &= U_a \bar{w}, & U_p &= U_a \bar{U}_p = (\bar{u}^2 + \bar{w}^2)^{1/2}, \\ Q &= F^2 U_a^{-5} \bar{Q} = L_B^2 U_a \bar{Q}. \end{aligned} \quad (7.79)$$

On this basis, (7.74)-(7.76) are nondimensionalized as

$$\frac{d\bar{Q}}{d\bar{s}} = 2\bar{a}f (\gamma_1 |\bar{U}_p - \cos \theta| + \gamma_2 \sin \theta), \quad (7.80)$$

$$\frac{d\bar{u}}{d\bar{s}} = 2\bar{a}f \frac{1 - \bar{u}}{\bar{Q}} (\gamma_1 |\bar{U}_p - \cos \theta| + \gamma_2 \sin \theta), \quad (7.81)$$

$$\frac{d\bar{w}}{d\bar{s}} = \frac{1}{\bar{Q}\bar{U}_p} - 2\bar{a}f \frac{\bar{w}}{\bar{Q}} (\gamma_1 |\bar{U}_p - \cos \theta| + \gamma_2 \sin \theta), \quad (7.82)$$

where $\cos \theta = \frac{\bar{u}}{(\bar{u}^2 + \bar{w}^2)^{1/2}}$, $\sin \theta = \frac{\bar{w}}{(\bar{u}^2 + \bar{w}^2)^{1/2}}$ and f is given by (7.19). Note that the f of (7.19) is originally derived for an infinite row of plumes in a quiescent environment. In a weak or moderate crosswind, plume interactions are not expected to be significantly influenced by the crosswind so that (7.19) remains a reasonable approximation. In a strong crosswind, by contrast, the plumes are rapidly bent-over and significant vortex entrainment is anticipated (Lai & Lee, 2012). Such vortex entrainment is not modeled explicitly in the present study. Despite this limitation, the present theory will be shown to compare satisfactorily with the experimental data of Kannberg & Davis (1976) – see figure 7.19 below. In a similar spirit, drawing comparisons between the present theory and the plume merger model of Wu & Koh (1978) also yields satisfactory agreement – see section 7.9.

The flux-balance parameter is expressed as

$$\Gamma = \frac{5}{8\pi^{1/2}\alpha} \frac{Q^2 F}{M^{5/2}} = \frac{5}{8\pi^{1/2}\alpha} \bar{a}^{-1} A^{*-1/2} \bar{w}^{-3}, \quad (7.83)$$

where $A^* = A/a^2$ is only a function of p . To solve (7.80)-(7.82), we first assign a small value of p , e.g. $p = 0.05$, thus A^* can be determined from (7.6) (twice the area because we now consider a whole plume). Then we assign a constant value for \bar{a} and a source value for Γ (i.e. Γ_0), thus the source value of \bar{w} , i.e. $\bar{w}_0 \equiv \bar{w}(z = 0)$, can be determined from (7.83). The source value for \bar{Q} can then be specified from $\bar{Q} = \bar{a}^2 A^* \bar{w}$. The entrainment coefficients are specified as $\alpha = 0.117$, $\gamma_1 = 0.1$ and $\gamma_2 = 0.6$ (Tohidi & Kaye, 2016; Li & Flynn, 2020a).

7.5.2 Near- and far-field similarity scalings

For simplicity, it is assumed that there is no relative motion between the plume and crosswind in the horizontal direction, i.e. $u = U_a$ (Devenish *et al.*, 2010b). Thus, (7.81) reduces to $\frac{d\bar{u}}{d\bar{s}} = 0$. Moreover, (7.72) and (7.73) imply that

$$\bar{w} \equiv \frac{w}{U_a} = \frac{w}{u} = \frac{dz}{dx} = \frac{d\bar{z}}{d\bar{x}}. \quad (7.84)$$

7.5.2.1 Modest crosswind

In a modest crosswind, the plume trajectory is expected to be quasi-vertical, which implies that $ds \approx dz$, $U_p \approx w$ and $w \gg U_a$. Moreover, the entrainment in this case is similar to the entrainment in a quiescent environment, thus the entrainment velocity is approximated by

$$q_e = \gamma_1 |U_p - U_a \cos \theta| \approx \gamma_1 U_p \approx \gamma_1 w. \quad (7.85)$$

With the above simplification, (7.80) and (7.82) reduce, respectively, to the following equations:

$$\frac{d\bar{Q}}{d\bar{z}} = 2\gamma_1 \bar{a} f \frac{\bar{M}}{\bar{Q}}, \quad (7.86)$$

$$\frac{d\bar{M}}{d\bar{z}} = \frac{\bar{Q}}{\bar{M}}, \quad (7.87)$$

where $\bar{M} = \bar{Q} \bar{w} = L_B^{-2} U_a^{-2} M$. In the limit $p \ll 1$, $2af$ tends to 2π times the plume radius, ap/π . Thus the cross-sectional area, $A = \pi (ap/\pi)^2 = \pi (af/\pi)^2 = Q^2/M$. Then (7.86) reduces to

$$\frac{d\bar{Q}}{d\bar{z}} = 2\gamma_1 (\pi \bar{M})^{1/2}. \quad (7.88)$$

Solving (7.87) and (7.88) yields

$$\bar{Q} = \frac{6\gamma_1}{5} \left(\frac{9\gamma_1}{10} \right)^{1/3} \pi^{2/3} \bar{z}^{5/3}, \quad \bar{M} = \left(\frac{9\gamma_1}{10} \right)^{2/3} \pi^{1/3} \bar{z}^{4/3}, \quad (7.89)$$

and thus

$$\bar{w} = \frac{5}{6\gamma_1} \left(\frac{9\gamma_1}{10} \right)^{1/3} \pi^{-1/3} \bar{z}^{-1/3}. \quad (7.90)$$

Equations (7.88)-(7.90) are consistent with the classic plume theory of Morton *et al.* (1956). Using (7.84), \bar{z} is given by

$$\bar{z} = \left(\frac{10}{9\gamma_1} \right)^{1/2} \pi^{-1/4} \bar{x}^{3/4}. \quad (7.91)$$

In the limit $p \gg 1$, $f \rightarrow 1$, thus the solution to (7.86) and (7.87) can be obtained as

$$\bar{Q} = (2\gamma_1 \bar{a})^{2/3} \bar{z}, \quad \bar{M} = (2\gamma_1 \bar{a})^{1/3} \bar{z}, \quad \bar{w} = (2\gamma_1 \bar{a})^{-1/3}, \quad \bar{z} = (2\gamma_1 \bar{a})^{-1/3} \bar{x}. \quad (7.92)$$

7.5.2.2 Strong crosswind

In case of a strong crosswind, the plume is a bent-over plume, which implies that $ds \approx dx$, $U_p \approx U_a$ and $w \ll U_a$. The entrainment of a bent-over plume is similar to the entrainment due to a line thermal, which is given by

$$q_e = \gamma_2 U_a \sin \theta \approx \gamma_2 w, \quad (7.93)$$

thus (7.80) and (7.82) can be simplified, respectively, as

$$\frac{d\bar{Q}}{d\bar{x}} = 2\gamma_2 \bar{a} f \frac{\bar{M}}{\bar{Q}}, \quad (7.94)$$

$$\frac{d\bar{M}}{d\bar{x}} = 1. \quad (7.95)$$

In the limit $p \ll 1$, the cross-sectional area, $A = \pi (ap/\pi)^2 = \pi (af/\pi)^2 = Q/U_a$. Thus, (7.94) reduces to

$$\frac{d\bar{Q}}{d\bar{x}} = 2\gamma_2\pi^{1/2}\bar{Q}^{-1/2}\bar{M}. \quad (7.96)$$

The solution to (7.95) and (7.96) is

$$\bar{Q} = \left(\frac{3\gamma_2}{2}\right)^{2/3} \pi^{1/3}\bar{x}^{4/3}, \quad \bar{M} = \bar{x}, \quad \bar{w} = \left(\frac{2}{3\gamma_2}\right)^{2/3} \pi^{-1/3}\bar{x}^{-1/3}. \quad (7.97)$$

Using (7.84), the plume trajectory is given by

$$\bar{z} = \frac{3}{2} \left(\frac{2}{3\gamma_2}\right)^{2/3} \pi^{-1/3}\bar{x}^{2/3}, \quad (7.98)$$

which is consistent with Briggs's classic two-thirds law (Briggs, 1984). Using (7.98), (7.97) can be rewritten in terms of \bar{z} as

$$\bar{Q} = \gamma_2^2\pi\bar{z}^2, \quad \bar{M} = \left(\frac{2}{3}\right)^{1/2} \gamma_2\pi^{1/2}\bar{z}^{3/2}, \quad \bar{w} = \left(\frac{2}{3}\right)^{1/2} \gamma_2^{-1}\pi^{-1/2}\bar{z}^{-1/2}. \quad (7.99)$$

In the limit $p \gg 1$, the counterpart solution is given by

$$\bar{Q} = (2\gamma_2\bar{a})^{1/2}\bar{x}, \quad \bar{M} = \bar{x}, \quad \bar{w} = (2\gamma_2\bar{a})^{-1/2}, \quad \bar{z} = (2\gamma_2\bar{a})^{-1/2}\bar{x}. \quad (7.100)$$

Note from (7.97) and (7.100) that \bar{M} has an identical scaling in the near and far fields.

7.5.3 Representative results

For $\bar{a} = 0.2$ and 1 and $\Gamma_0 = 1$, representative results of plume trajectory, volume flux and horizontal and vertical velocities are illustrated in figure 7.17. The contact height with $\bar{a} = 0.2$ and 1 are $\bar{z}_c = 0.210$ and 0.621 , respectively. Figure 7.17 a shows that the plume trajectories for $\bar{a} = 0.2$ and 1 approach the respective near-field scalings $\bar{z} \sim \bar{x}^{3/4}$ and $\bar{z} \sim \bar{x}^{2/3}$, respectively. Nonetheless, the far-field trajectories for both cases follow $\bar{z} \sim \bar{x}$. Analogous near- and far-field similarity scalings for the volume flux and vertical velocity are shown in figure 7.17 b and 7.17 d, respectively. Notably, figure 7.17 b shows that the plume volume flux increases from $\bar{a} = 0.2$ to $\bar{a} = 1$, which is expected because a larger distance between neighboring plumes allows more entrainment. Shown in figure 7.17 c is that \bar{u} becomes close to unity at small \bar{z} , thus the approximation used in (7.84) is self-consistent. Figure 7.18 shows that \bar{z}_c increases monotonically with \bar{a} .

7.5.4 Comparison with the towing tank experiments of Kannberg & Davis (1976)

Kannberg & Davis (1976) studied the dilution and trajectory of multi-port diffusers in a flowing environment. Although a finite row of diffusers was used in their experiments, image

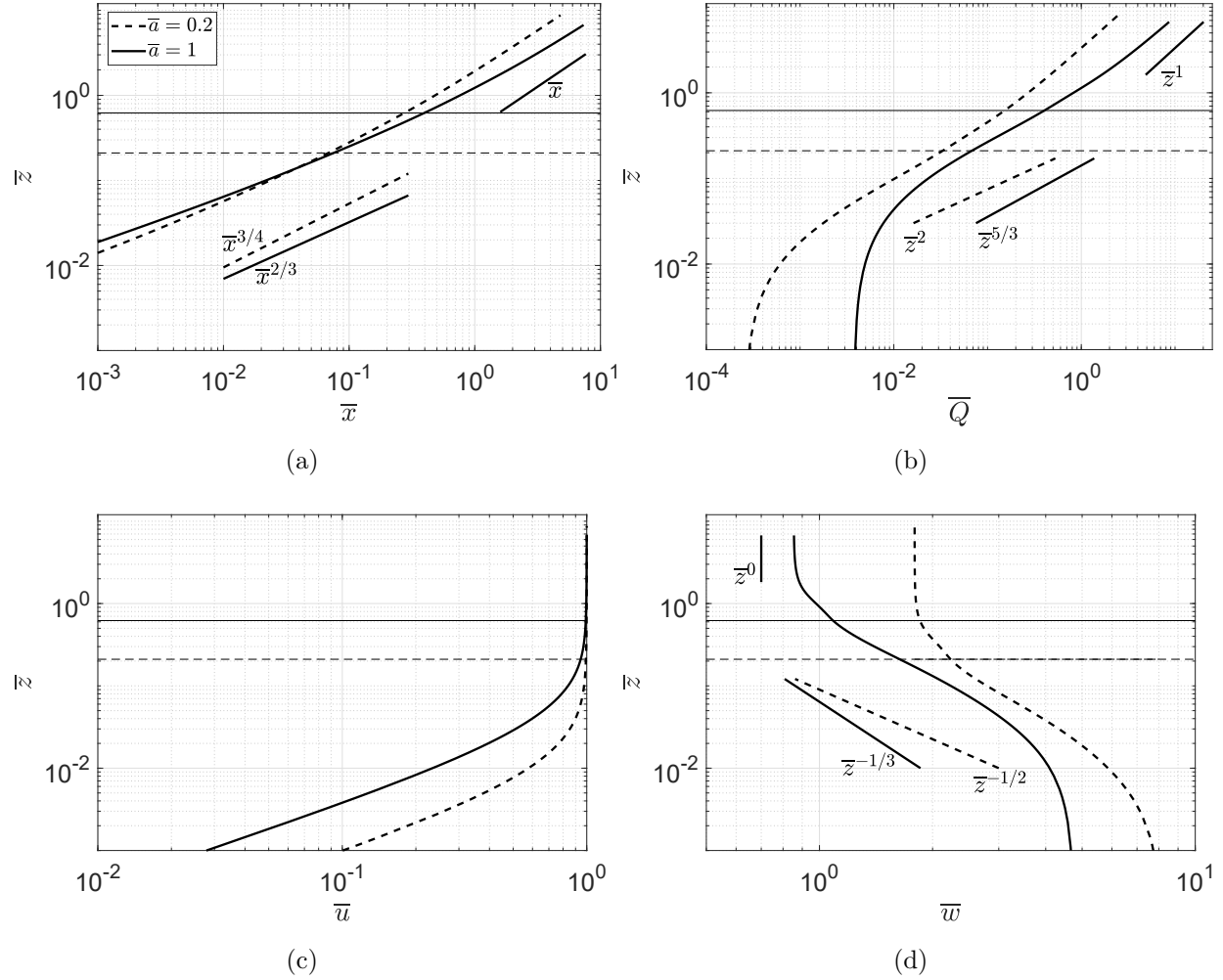


Figure 7.17: Evolution of plume trajectory (a), volume flux (b), horizontal (c) and vertical (d) velocities. The horizontal dashed (solid) line denotes the height of first contact for $\bar{a} = 0.2$ ($\bar{a} = 1$). In both cases, $\Gamma_0 = 1$.

walls were added to emulate the effect of an infinite row of plumes in a crosswind. The main control parameters were as follows: source densimetric Froude number, $\text{Fr}_0 = w_0 / (g'_0 D)^{1/2}$, where D is the port diameter; ratio of the ambient velocity to the plume source velocity, $R = U_a / w_0$ and ratio of port spacing to port diameter, a/D . Kannberg & Davis (1976) considered different angles (denoted by θ_0) between the plume source velocity and the ambient current velocity, however, we shall only consider the perpendicular configuration i.e. $\theta_0 = \pi/2$ for a comparison between theory and experiment. The measured parameter of particular interest is the plume centerline trajectory, which consists of a set of points $(X/D, Y/D)$ where X and Y are the respective horizontal and vertical distances from the port source. A goal of their experiments was to study the effects of Froude number (Fr_0), velocity ratio (R) and port spacing (a/D) on the plume trajectory. The main parameters in Kannberg & Davis (1976) can be related to the variables in section 7.5.1 as follows:

$$\Gamma_0 = \frac{5}{16\alpha} \text{Fr}_0, \quad \bar{a} = \frac{4}{\pi} \frac{a}{D} \text{Fr}_0^2 R^3, \quad A_0^* \equiv A^*(z=0) = \frac{\pi}{4} \left(\frac{a}{D} \right)^{-2},$$

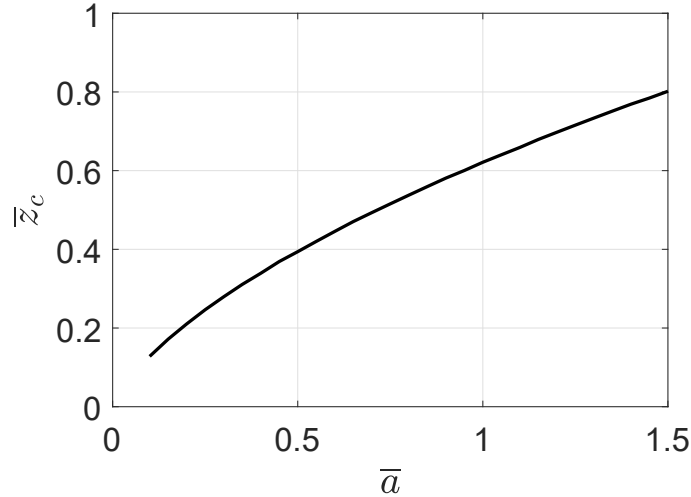


Figure 7.18: Contact height as a function of \bar{a} . In all cases, $\Gamma_0 = 1$.

$$X/D = \frac{a \bar{x}}{D \bar{a}}, \quad Y/D = \frac{a \bar{z}}{D \bar{a}}. \quad (7.101)$$

A comparison of the present theory to Kannberg and Davis’s experiment with respect to plume trajectory is shown in figure 7.19. Satisfactory agreement is observed in most of the panels. Note that a nontrivial difference between theory and experiment occurs for the $a/D = 2.5$ case shown in figure 7.19 d. This difference is most likely due to (i) the lower entrainment coefficient (especially γ_1) used in the theory, (ii) the inability of the theory to reproduce the twin vortex structure in the plume cross section as observed in experiments, and, (iii) a plume downwash effect due to the blockage of the ambient flow post-merger.

7.6 Applications to cooling towers

A major motivation for this study stems from evaluating the visible plume length in cases of back-to-back cooling towers vs. a single row of tower cells. Typical ambient condition and cooling tower operating conditions are listed in table 7.1. Specifically, each row contains a finite number of $n = 15$ cooling tower cells – see the top-view schematic shown in figure 7.20. Among these cooling tower cells, those of particular concern are the cells at the center and the end points. For a single row, the axis of the plume at the center is not deflected due to symmetry, which is analogous to a plume in an infinite row of plumes. Thus the plume at the center, if not in the very far field, can be modeled using the analysis in section 7.3. The half plumes at the two ends are, on the other hand, exempt from plume merger and they entrain ambient fluid like an isolated plume. Therefore, the center plume and the plumes at the two sides lead to the least and largest amount of entrainment, respectively; they also represent the “worst” and “best” scenarios in case of visible plumes. For the counterpart dual rows of plumes, the two center plumes are similar to plumes in the two infinite row configuration. By contrast, the two half round plumes on each side may be approximated by the merging of two adjacent axisymmetric plumes. Using the same terminology as above, the worst scenarios are to be estimated using the irrotational flow theory described in sections 7.3 and 7.4. The best scenario, corresponding to the merger of two adjacent plumes, is

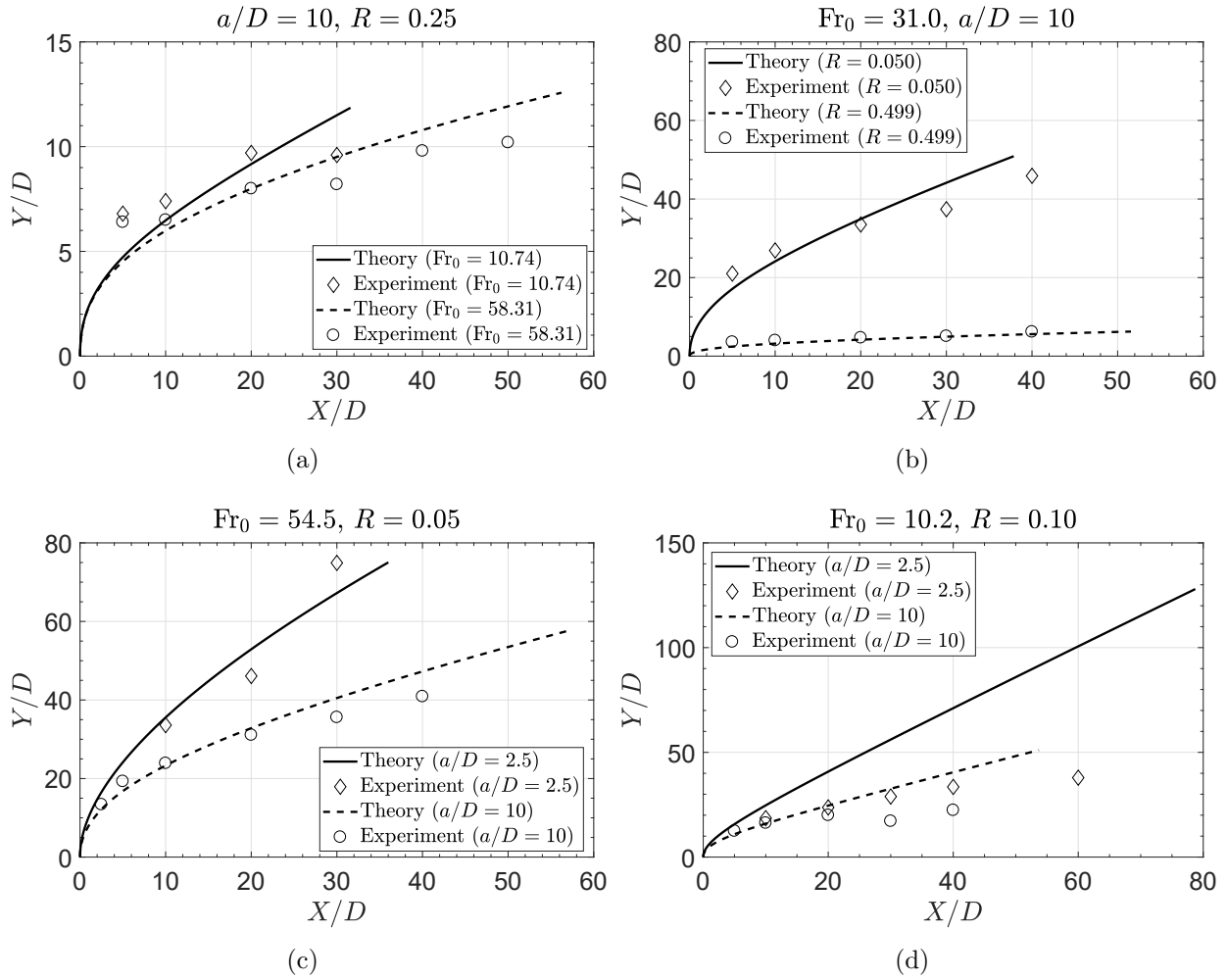


Figure 7.19: Effects of varying Fr_0 (a), R (b) and a/D (c and d) on the plume trajectory. The experimental data are taken from Appendix A of Kannberg & Davis (1976).

modeled using the geometrical merging criterion proposed by Wu & Koh (1978) (cf. figure 2 of Li & Flynn 2020b).

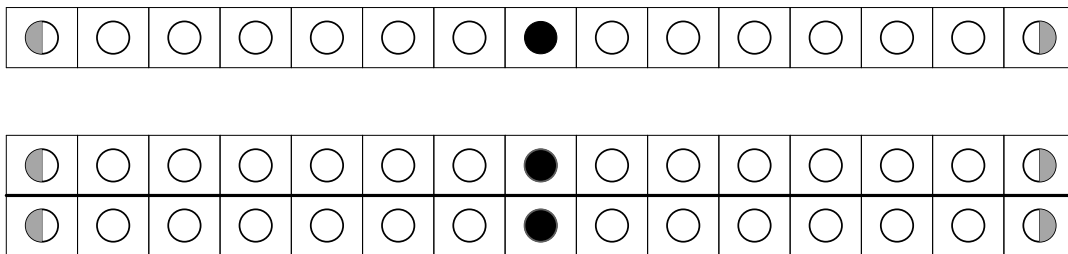


Figure 7.20: Top view of single and dual rows of cooling tower cells. The black circles denote cells at the center and the gray half circles denote the half cells at the two ends.

We follow the governing equations for moist plumes presented in Li & Flynn (2020b) and evaluate the relative humidity (RH) of plumes discharged from cooling tower cells at

Table 7.1: Representative operating and environmental conditions for the back-to-back and single row cooling towers illustrated in figure 7.20 (Kröger, 2004).

Variable symbol	Variable name	Value (unit)
P_a	Ambient pressure at the top of the cooling tower	101325 (Pa)
t_a	Ambient temperature	10 (°C)
RH_a	Ambient relative humidity	80 (%)
t_w	Wet cooling temperature	30 (°C)
t_d	Dry cooling temperature	25 (°C)
w_0	Stack exit velocity	6 (m/s)
D_0	Stack exit diameter	8 (m)
a	Horizontal distance between cell centers	15 (m)
b	Half of the vertical distance between cell centers	7 (m)
$\frac{\dot{m}_d}{\dot{m}_w}$	Ratio of the dry to wet air mass flow rate	0.2 and 0.4
n	Number of cooling tower cells in a single row	15

the center and at the end points. Figures 7.21 a and 7.21 c show that, as expected and as concerns fog formation, the visible plume length at the center is greater than that at the end points. This difference is more pronounced for two rows of plumes whereby entrainment is more heavily curtailed. In case of no fog formation, figures 7.21 c and 7.21 d show that a maximum RH is achieved at a higher elevation for the plume at the center than for the plumes at the end points. This latter case indicates that less entrainment does not necessarily lead to fog formation, but rather slows down the rate of decrease of RH. Note that the model calculation leading to figure 7.21 presumes that the dry and wet air are completely mixed thus resulting in a radially uniform plume at the source. If complete mixing is not achieved, but neither is a coaxial wet/dry plume structure (Houx Jr *et al.*, 1978; Li *et al.*, 2018), the visible plume length can be greatly enhanced – see figure 7.21 c. Therefore, relatively stringent mixing criteria must be assured within the plenum chamber of back-to-back cooling towers.

7.7 Conclusions

The present manuscript has extended a previous formulation of Rooney (2015) to model two parallel rows of plumes in a quiescent environment and a single row of plumes in a crosswind. We first note that for all symmetric plume configurations considered so far, the entrainment flux is found to be equal to the strength of the line sink, i.e. $E = m$. For two parallel rows of plumes, we consider both configurations with and without offset. Similar profiles of vertical velocity and volume flux are predicted for those two configurations. In contrast to a single row of plumes, the vertical velocity of plumes in two rows levels off before approaching the far-field limit under a relatively large vertical to horizontal spacing ratio – see figures 7.7 a and 7.13 a. Two different contact heights are defined and these heights are found to increase approximately linearly with the vertical to horizontal spacing ratio – see figures 7.9 and 7.15. For both single and dual rows of plumes, it is found that an effective entrainment perimeter, proportional to the f parameter specified e.g. in (7.19), accounts for the reduced entrainment

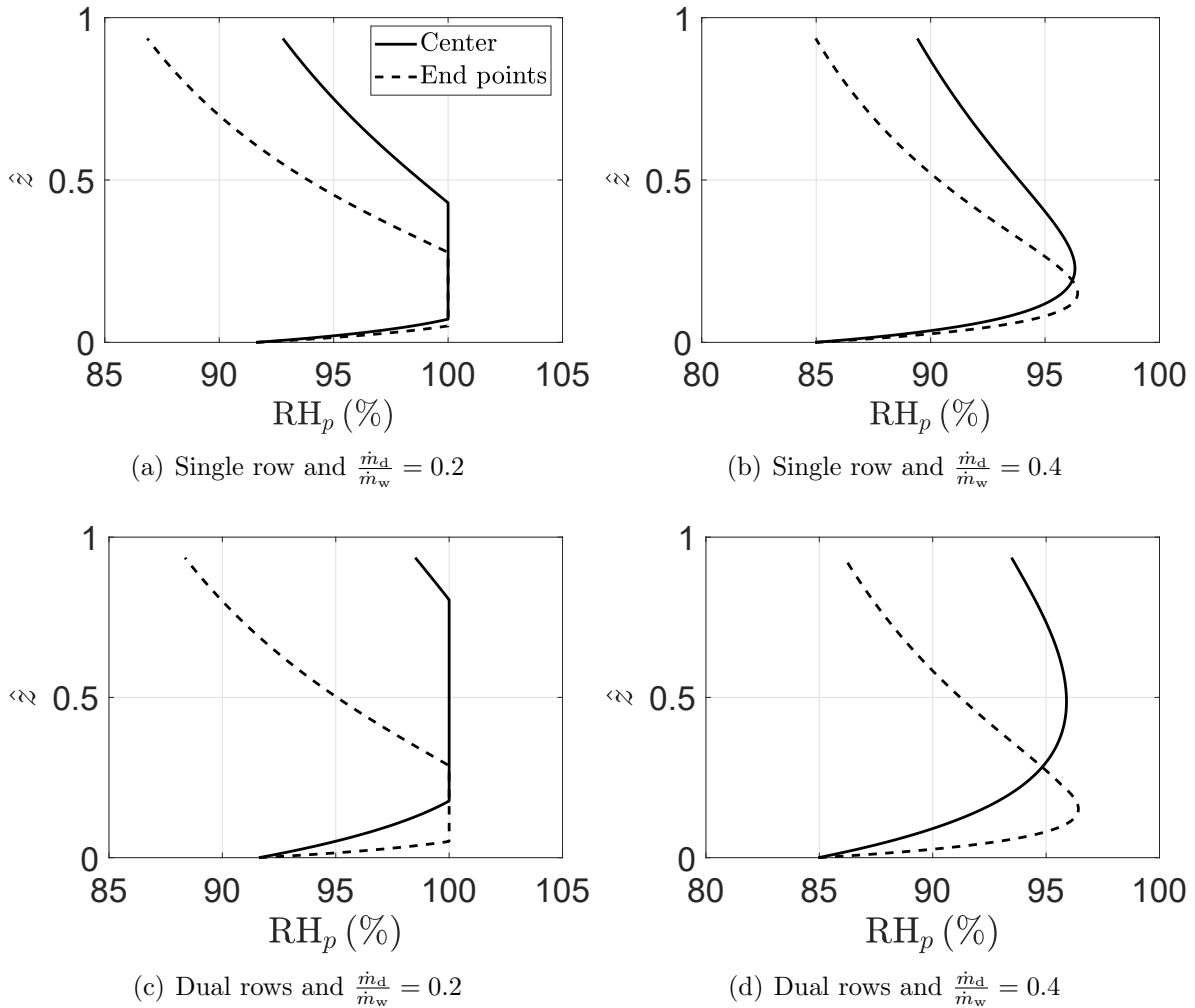


Figure 7.21: Relative humidity profiles for single (a and b) and dual (c and d) rows of plumes. The model input parameters are specified in table 7.1.

due to plume merger.

Another major contribution of this study is the integral modeling of an infinite row of plumes in a crosswind. In particular, the velocity potential contours remain identical to those in Rooney (2015), whereas the modified entrainment closure includes both longitudinal and transverse entrainment. For both modest and strong crosswinds, the theoretical solutions approach the corresponding near- and far-field similarity limits – see figures 7.17 a,b,d. A comparison of the present theory to the experimental data collected by Kannberg & Davis (1976) vis-à-vis the centerline plume trajectory yields satisfactory agreement as shown in figure 7.19.

The theory of single and dual rows of plumes in a quiescent environment has been applied to cooling tower plumes arising from long rows containing multiple cooling tower cells. The aforementioned theory only applies to plumes discharged from cells at the center, where a minimum of ambient entrainment is expected. A comparison of the relative humidity profiles for plumes at the center vs. plumes at the end points has been made – see figure 7.21. Results drawing from this comparison indicate that a back-to-back configuration may

greatly enhance the visible plume length.

Given the rather complicated nature of plume-plume interactions, the coupling presented here between the irrotational flow theory and the integral plume equations may be improved. Key to this coupling is an entrainment closure that incorporates the nonuniform distribution of the entrainment flow speed along the velocity potential contours. Accounting for such an effect also requires a presumed nonuniform vertical velocity profile that deviates from the “top-hat” profiles considered in the present model.

7.8 Appendix A: Entrainment flux calculation using the stream function

For two-dimensional and incompressible flows, the flux of fluid between two streamlines equals the difference in the stream function. For a single row of line sinks, the stream function is given as

$$\psi = \text{Im}(\Omega) = -\frac{m}{2\pi} \tan^{-1} \left(\frac{\cos x' \sinh y'}{\sin x' \cosh y'} \right). \quad (7.102)$$

Using the physical interpretation of the stream function, the rate of entrainment across any contour in figure 7.1 is

$$E = \psi(x'_+, y') - \psi(x'_-, y'). \quad (7.103)$$

For $p \leq 1$, $y'(x'_+) = y'(x'_-) = 0$, thus $E = -\frac{m}{2\pi}(0 - \pi) = m/2$. For $p > 1$, $\cos x'_\pm = 0$ so that $E = -\frac{m}{2\pi}(0 - \pi) = m/2$.

For the case of dual rows of non-offset line sinks, the stream function is given as

$$\psi = -\frac{m}{2\pi} \tan^{-1} \left(\frac{\sin 2x' \sinh 2y'}{\cosh 2b' - \cos 2x' \cosh 2y'} \right). \quad (7.104)$$

For $p \leq \cosh 2b' - 1$, the rate of entrainment across any closed contour is

$$E = 2 \left(\psi_{(0, y'_{\max})} - \psi_{(0, y'_{\min})} \right) = -\frac{m}{\pi} (0 - \pi) = m. \quad (7.105)$$

where y'_{\max} and y'_{\min} are given by (7.32) and (7.33), respectively. For $\cosh 2b' - 1 < p \leq \cosh 2b' + 1$,

$$E = 2 \left(\psi_{(0, y'_{\max})} - \psi_{(x'_-, 0)} \right) = -\frac{m}{\pi} (0 - \pi) = m. \quad (7.106)$$

For $p > \cosh 2b' + 1$,

$$E = 2 \left(\psi_{(0, y'_{\max})} - \psi_{(-\pi/2, y')} \right) = -\frac{m}{\pi} (0 - \pi) = m. \quad (7.107)$$

For the case of dual rows of line sinks with an offset $a/2$, the stream function is given as

$$\psi = -\frac{m}{2\pi} \tan^{-1} \left(\frac{\cos 2x' \sinh 2y' - \sinh 2b'}{\sin 2x' \cosh 2y'} \right). \quad (7.108)$$

For $p \leq \cosh 2b'$,

$$E = 2 \left(\psi_{(0, y'_{\max})} - \psi_{(0, y'_{\min})} \right) = -\frac{m}{\pi} (-\pi/2 - \pi/2) = m. \quad (7.109)$$

where y'_{\max} and y'_{\min} are given by (7.57) and (7.58), respectively. For $p > \cosh 2b'$,

$$E = \left(\psi_{(\pi/4, y'_+)} - \psi_{(-\pi/4, y'_+)} \right) + \left(\psi_{(-\pi/4, y'_-)} - \psi_{(\pi/4, y'_-)} \right) = -\frac{m}{2\pi} (-\pi) - \frac{m}{2\pi} (-\pi) = m. \quad (7.110)$$

On the basis of the above results, we conclude that $E = m/2$ and $E = m$ for the single and dual rows of plumes, respectively.

7.9 Appendix B: Comparison between the present theory and Wu & Koh (1978)

In a strong crosswind, the plume-plume interactions become less intense than those in a weak crosswind. For a rosette buoyant jet group with a jet-to-riser diameter ratio of the order of 0.1, Lai *et al.* (2011) revealed that the dynamic interactions between buoyant jets are negligible even in a moderate crossflow. Therefore, and in cases of moderate to strong crosswinds, we may treat multiple plumes the same as an isolated plume pre-merger, which is consistent with the model of Wu & Koh (1978) (hereafter WK78). WK78 assumes that the plume cross section is perfectly round pre-merger, the rate of entrainment is given as

$$E = 2\pi r (\gamma_1 |U_p - U_a \cos \theta| + \gamma_2 U_a \sin \theta), \quad (7.111)$$

where r is the mean plume radius. Once merger is initiated, the round plume transitions to a slot plume with a rectangular cross section. Thus, the counterpart entrainment rate post-merger is evaluated from

$$E = 2a (\gamma_1 |U_p - U_a \cos \theta| + \gamma_2 U_a \sin \theta). \quad (7.112)$$

On this basis, and following the nondimensionalization given by (7.79), (7.74)-(7.76) can be nondimensionalized to the identical form as (7.80)-(7.82) but with f given instead by

$$f = \begin{cases} \pi^{1/2} \frac{\bar{Q}^{1/2}}{\bar{a} \bar{U}_p^{1/2}}, & \text{(pre-merger)} \\ 1, & \text{(post-merger)}. \end{cases} \quad (7.113)$$

WK78 assumes that merging occurs on the basis of a geometrical criterion, which requires that $r = a/2$. The equivalent nondimensional relation is given as

$$\bar{r} \equiv \left(\frac{\bar{Q}}{\pi \bar{U}_p} \right)^{1/2} = \bar{a}/2, \quad (7.114)$$

where \bar{r} denotes the nondimensional plume radius. At the merger height, the round plume evolves to a two-dimensional plume while the plume cross-sectional area remain unchanged.

Figure 7.22 shows the comparison between the present irrotational flow theory and the WK78 theory in terms of plume trajectory and vertical velocity for $\bar{a} = 0.2, 1$ and 10 . The gap between the heights of first contact for the present theory and WK78 increases as \bar{a} increases. This is consistent with the fact that the effect of plume merger weakens with

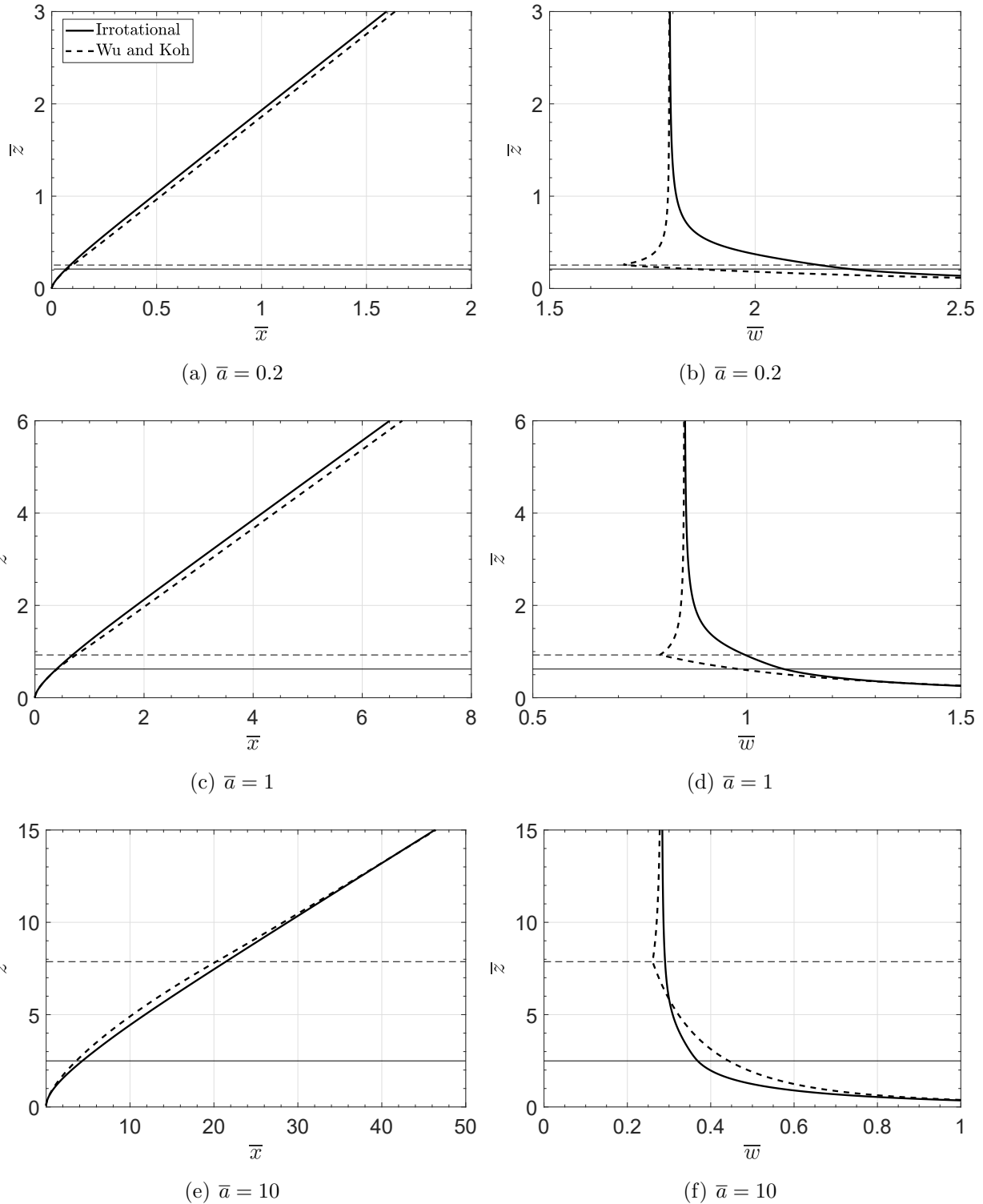


Figure 7.22: Comparison between the present irrotational flow theory and the theory of Wu & Koh (1978). The horizontal solid and dashed lines denote the respective heights of first contact for the above theories. In all cases, $\Gamma_0 = 1$.

increasing \bar{a} . Overall good agreement is observed vis-à-vis the plume trajectory – see figures

7.22 a,c,e. It is intuitive that the present theory should predict greater plume rise than does WK78 because the former theory admits less entrainment than the latter. The above argument applies for the cases $\bar{a} = 0.1$ and 1. However, and in the case of large \bar{a} , e.g. $\bar{a} = 10$, figure 7.22 e shows greater plume rise for WK78 than for the present theory, at least in the near-field region. Correspondingly, the vertical velocity predicted by WK78 is larger in the range $0 < \bar{z} \lesssim 5$. This nonintuitive result is due to the large near-source entrainment experienced at large wind speeds, which rapidly expands the plume cross section using the irrotational flow theory. By contrast, and for a single plume (pre-merger using WK78), the entrainment rate actually decreases near the source as the plume is bent-over rapidly by a strong wind (cf. figure 5 b of Li & Flynn 2020*a*). Reassuringly, the present irrotational flow theory avoids the kinks that characterize the vertical velocity profiles as computed using WK78 – see figures 7.22 b,d,f.

Chapter 8

Conclusions and future work

8.1 Conclusions

8.1.1 Coaxial plumes

Whereas cooling towers have been considered as efficient cooling devices used in e.g. large power plants, the visible plume or fog formed above the towers can be a nuisance in terms of aesthetics and potential traffic safety hazards. One of the most successful plume abatement designs is a parallel path wet/dry (PPWD) tower. A PPWD allows the dry air to mix with the wet air in the plenum chamber thus the discharged air mixture is unsaturated. This method is often thought to be efficient only when internal mixing devices are added to achieve the desired mixing quality. On the other hand, a number of designs (Houx Jr *et al.*, 1978; Koo, 2016a) and some industrial observations (Lindahl & Jameson, 1993; Kinney Jr *et al.*, 1999) have found a coaxial wet/dry plume structure above the tower exit. This coaxial plume structure is expected to (i) reduce the possibility of condensation because the hot, humid air is surrounded by the warm, dry air envelope, and, (ii) the core of humid air rises more quickly before it is significantly diluted.

The analysis of Chapter 3 explores the dynamics of coaxial plumes in a stationary ambient and shows a delay in the onset of condensation under some operating conditions. An important conclusion drawn from this theoretical analysis is that, a so-called resistance factor, which is defined as the ratio of the vertical velocity to the relative humidity, is a monotonic decreasing function of the dry air mixing fraction (DAMF). In other words, the likelihood of recirculation and/or condensation decreases as the plume source condition varies from a uniform plume with DAMF of 100% to coaxial plumes with smaller DAMF. On this basis, we propose the plume abatement criterion for coaxial plumes, which lies between the two levels of plume abatement for uniform plumes in ATC (2011). To make an informed choice about the size of the dry section for plume abatement, we further plot the regime diagrams that specify whether a coaxial plume is likely to be advantageous compared to the counterpart uniform plume.

A deficiency of the preceding theory is that the empirical entrainment coefficients remain undetermined. This situation is further complicated by the choice of body force formulation for the inner plume (McDougall, 1981; Bloomfield & Kerr, 2000). To fill these gaps, we perform planar laser-induced fluorescence (PLIF) experiments of coaxial plumes in a large

water tank. The PLIF experimental images exhibit expanding and wider vortices in the near source flow. Quantitatively, we define two length scales, i.e. the inner potential core height and the cut-off height of the inner plume, to characterize the evolution of coaxial plumes. Note that the current experimental study is restricted to moderate source Reynolds number of $300 < \text{Re}_0 < 800$ and source flux-balance parameter of $0.5 < \Gamma_0 < 11$ – see the detailed data in table 4.3 of Chapter 4.

The major contribution of Chapter 4 is the approach to determine the entrainment coefficients by a comparison of theory vs. experiment. We propose a pixel-by-pixel comparison between the concentration images from theory and experiment. Specifically, the minimum error associated with this comparison determines the optimal combination of entrainment coefficients, i.e. β and γ . Moreover, theoretical model with these optimal entrainment coefficients produce centerline and radial concentration profiles in satisfactory agreement with laboratory experimental results, which in turn confirms the validity of the pixel-by-pixel comparison. In particular, this type of whole field comparison avoids the difficulty of detecting the inner/outer plume interface, which, as argued by Morton (1962), does not have a proper physical meaning. An application of the pixel-by-pixel comparison to uniform plumes also yields reasonable estimates for the entrainment coefficient. To conclude, the theoretical and laboratory experimental work described in Chapters 3 and 4 demonstrate the applicability of double plume models in the dynamics of coaxial plumes in a stationary ambient.

Previous analyses assume the absence of extraneous wind forcing that is commonly observed in the real atmosphere. For uniform plumes in a crosswind, the visible plume length varies non-monotonically with increasing wind speed; the most adverse condition is light to moderate wind speed. The counterpart coaxial plumes exhibit more departure from monotonicity. To wit, the inner visible plume length oscillates as the wind speed increases using the entrainment assumption of Morton (1962) and McDougall (1981). Therefore, we further apply an alternate entrainment assumption proposed by Bloomfield & Kerr (2000), which results in a more regular, but still non-monotonic variation of visible plume length. In the absence of ambient density stratification and turbulence, theoretical results indicate that wind, in most cases, avoids condensation in the outer plume. This latter conclusion can be considered as an advantage of coaxial plumes in the context of plume abatement.

8.1.2 Plume merger

Plume merger has been considered in the theoretical analyses of uniform and coaxial plumes (cf. Chapters 3 and 5), however, using exclusively the merging criteria of Wu & Koh (1978). Whereas this merging criteria can provide tractable computation of the evolving plume boundaries, the merging process from where the plumes become in contact to where they fully merge is virtually neglected. The novel contribution of Chapter 6 is to extend the irrotational flow analysis of Rooney (2016) to describe the merging of two plumes arising from area sources. Although the analysis in Chapter 6 follows the procedures in Rooney (2015, 2016), the height of full merger is defined and more importantly, an alternate entrainment formulation is proposed. Notably, the present entrainment correction factor is only a function of the plume boundary curvature. By contrast, the correction factor (f_m) of Rooney (2016) includes the flux-balance parameter (Γ), which is closely related to plume dynamics. The novel plume merger theory of nonpoint source plumes yields good agreement with the theory

of Wu & Koh (1978) in terms of mean vertical velocity, temperature and relative humidity profiles.

Using a similar irrotational flow analysis in Chapter 6, Chapter 7 studied (i) the merging of dual rows of plumes in a quiescent environment and (ii) a single row of plumes in a crosswind. For dual rows of plumes with and without offset, we reveal that, under a moderate or large vertical to horizontal spacing ratio, there appears an intermediate region wherein the plume vertical velocity levels off. This intermediate line plume scaling is consistent with the evolution of the corresponding velocity potential contours. For a single row of plumes in a crosswind, we attempt to couple the irrotational flow theory of Rooney (2015) with the plume equations whereby wind forcing is included. The plume theory in question is found to predict the correct near- and far-field similarity scalings under both modest and strong crosswinds. Moreover, the theory in question agrees satisfactorily with previous experimental data in terms of plume trajectories. A further application of the dual row plume theory to back-to-back cooling towers suggests that the back-to-back configuration may greatly enhance the visible plume length compared to the counterpart single row case.

8.1.3 Limitations

Several major limitations of the current work are listed as follows:

- (i) Cooling tower designs related to the coaxial plume structure are not discussed. In this regard, we may explore some passive designs that make use of e.g. the free solar energy. In Chapter 2 we review several passive designs (e.g. the air-to-air heat exchanger of Lindahl & Mortensen 2010) that abandon the dry coils in conventional PPWD towers. In addition to those designs already put into practice, other innovative designs are discussed in section 8.2.1.
- (ii) Only a neutrally stratified ambient is considered in the study of coaxial plumes. Whereas ambient density stratification has been considered for the study of uniform plumes (cf. Chapter 2), coaxial plumes in a density-stratified (stationary or windy) environment are rarely studied except in the context of bubble plumes (McDougall, 1978; Socolofsky & Adams, 2002).
- (iii) A major deficiency in the theoretical study in Chapter 5 is the lack of experimental verification. Towing tank or water flume experiments are required to study the dynamics of coaxial plumes in a crosswind.
- (iv) The present theory of plume merger only includes $n = 2$ and $n = \infty$ of plumes. Further work is needed to describe the merging of $n \geq 3$ of plumes. The $n \geq 3$ case may be resolved by an interpolation of the $n = 2$ and $n = \infty$ cases.
- (v) Merging of two plumes from unequal strengths and source diameters has not been fully conquered using Rooney's theory. This requires a generalized plume merger theory for the two plume case.
- (vi) In the entrainment models described in Chapters 3 to 7, the entrainment coefficient is assumed to be independent of the flux-balance parameter, Γ (see the definition in

e.g. Chapter 4). A variable-entrainment-coefficient model, e.g. the entrainment relation described by (1.79), may be adapted in future studies.

The aforementioned limitations open the door to a fruitful set of future topics that are proposed in section 8.2 below.

8.2 Future work

8.2.1 Plume abatement

8.2.1.1 Solar collectors

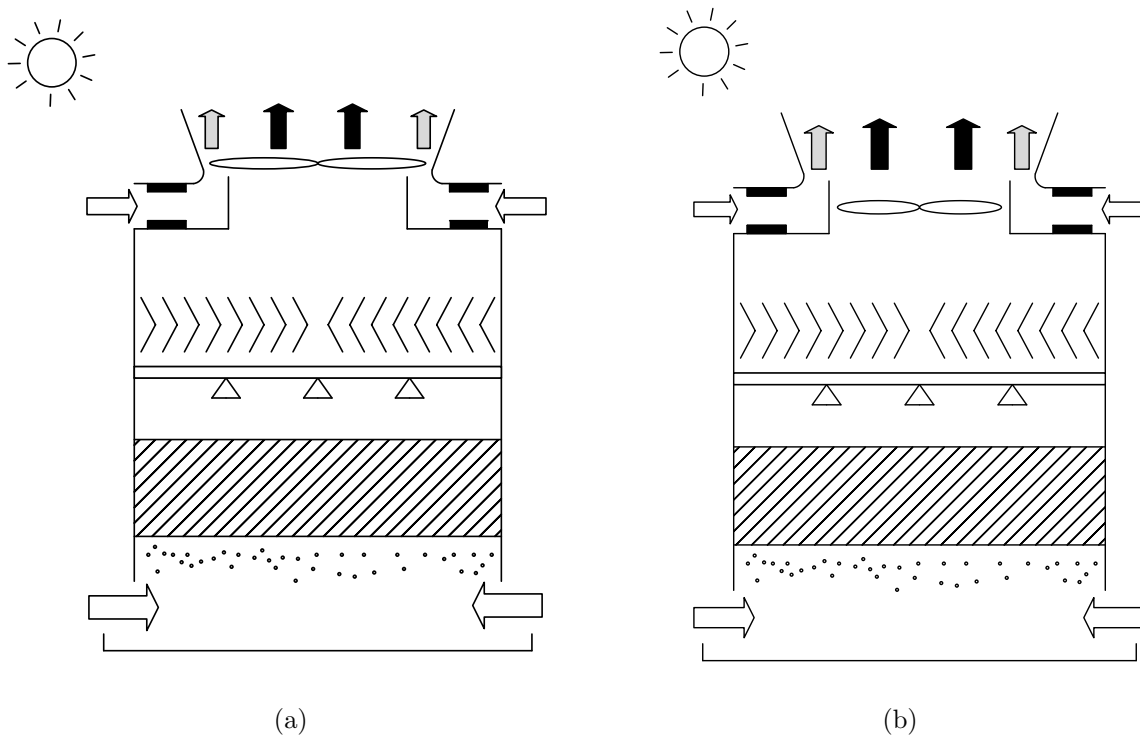


Figure 8.1: Solar collector assisted plume abatement in a PPWD cooling tower. The fan directly drives air through the solar collector (a) or induces air through the solar collector (b). The filled rectangles on the two sides of the fan shroud denote solar collectors.

As illustrated in figure 8.1, we replace the dry coils with solar collectors in a PPWD. In conventional PPWDs, the cost of the dry sections using finned tube coils usually exceeds the cost of the wet sections (Lindahl & Jameson, 1993). Thus the capital cost may be reduced if solar collectors are used. This idea is similar to but different from the concept of solar chimney (Schlaich, 1995) in the following respects:

- (i) A solar chimney drives the flow by a stack effect, which is similar to a natural draft cooling tower. By contrast, the driving force for air flow through the dry sections of the present design is primarily the fan.

- (ii) A solar chimney typically incorporates a electricity-generating turbine in the path of the buoyancy driven air flows, which allows the conversion of kinetic energy to electricity. The present design makes full use of the solar energy.

Due to the intermittent nature of solar energy, a few dry coils can be installed as backup dry cooling. In terms of modeling, the solar collector model must be coupled with the wet section model. Detailed analytical modeling of PPWD counterflow and crossflow towers can be found in Kröger (2004). Meanwhile, the analytical model of a solar chimney system by Chitsomboon (2001) may serve as a starting point for modeling the solar collector.

8.2.1.2 Thermosyphon system

The thermosyphon system in Mantelli (2016) can be modified as shown in figure 8.2. Instead of putting the condenser portion of the thermosyphon in the exterior ambient, we may locate the condenser portion within the plenum chamber. In this way, the ambient air is forced to pass through the condenser and baffles are incorporated to separate the air streams through the evaporators and condensers, respectively. With the present design, the plume abatement efficiency is expected to be enhanced at the cost of elevated overall tower height.

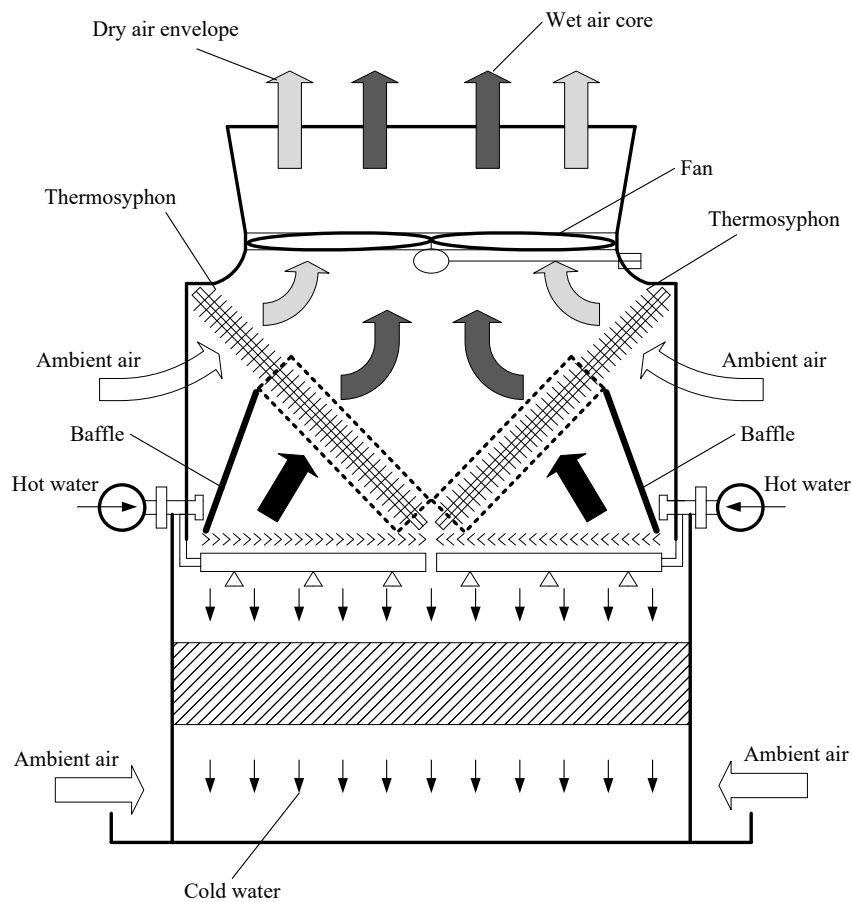


Figure 8.2: Thermosyphon system for plume abatement in a PPWD. The portion of the thermosyphon that is bounded by dashed rectangles denote the porous media structure.

8.2.2 Plume studies

8.2.2.1 Coaxial plumes in a stratified ambient

By considering a stratified ambient, a number of classifications with respect to stratification can be proposed as follows: (i) A constant density gradient; (ii) A two-layer density stratification; (iii) An inversion layer and (iv) A non-uniform density profile, e.g. a power law profile of density considered by Caulfield & Woods (1998). Each category can be combined with either stationary or windy environments. For category (i), the conservation equations of buoyancy for the inner and outer plumes in a stratified ambient read respectively

$$\frac{dF_1}{dz} = 2\pi r_1 (\omega_\alpha g'_2 - \omega_\beta g'_1) - \pi N^2 r_1^2 U_1, \quad (8.1)$$

$$\frac{dF_2}{dz} = 2\pi r_1 (\omega_\beta g'_1 - \omega_\alpha g'_2) - \pi N^2 (r_2^2 - r_1^2) U_2, \quad (8.2)$$

where $N = \left(-\frac{g}{\rho_a} \frac{d\rho_a}{dz}\right)^{1/2}$ is the buoyancy frequency (ρ_a is the ambient density). Conservation equations of volume and momentum remain unchanged as those in Chapter 4. The sum of (8.1) and (8.2) is

$$\frac{d(F_1 + F_2)}{dz} = -\pi N^2 r_1^2 U_1 - \pi N^2 (r_2^2 - r_1^2) U_2 = -N^2 (Q_1 + Q_2), \quad (8.3)$$

which is consistent with the buoyancy conservation equation for a uniform plume. Two situations may occur depending upon the strength of the buoyancy frequency N , which are sketched respectively in figure 8.3.

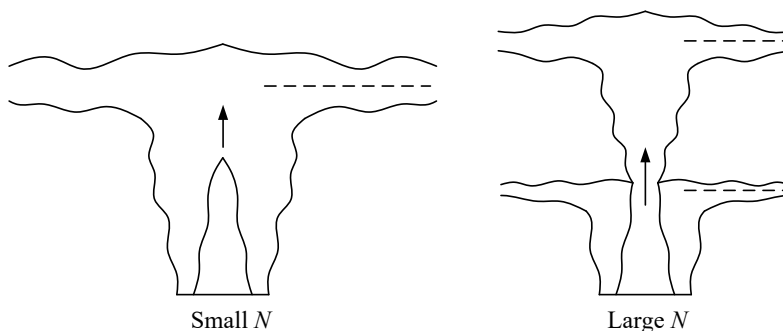


Figure 8.3: Coaxial plumes in a stratified ambient. For small values of N , coaxial plumes behave like a uniform plume and the merged uniform plume spreads out horizontally at a height above the cut-off height. By contrast, and for large values of N , the peeling height of the outer plume may be below the cut-off height thus the inner plume rises continuously to its own maximum height then falls to the neutral buoyancy height.

To verify the qualitative picture of coaxial plumes in a linearly stratified ambient, laboratory experiments may be conducted. The ambient density stratification can be realized by a double-tank method – see e.g. Economidou & Hunt (2009). Moreover, the inner plume source fluid is always more buoyant than the outer plume source fluid thus different peeling heights of the inner and outer plumes may occur.

8.2.2.2 Annular plumes

Annular jet flows issued from closed cores (unventilated source) have been extensively investigated experimentally (cf. Ko & Chan 1978; Patte-Rouland *et al.* 2001; Vanierschot & Van den Bulck 2008) and numerically (cf. Chattopadhyay 2004). By contrast, there are far fewer studies on open core annular jets (cf. Warda *et al.* 1999; Padhani *et al.* 2018). Padhani *et al.* (2018) is probably the first comprehensive study on annular jets issuing from an open core. They found that the volume flux induced through the open core is 1.2 times the source volume flux, which results in enhanced dilution compared to a typical round plume in the near field. Moreover, they argued that the annular open core source configuration is advantageous in case of pollution discharge where enhanced near-field dilution is desirable.

Previous studies focus primarily on high momentum jet flows and the effect of buoyancy (if density variation exists) is only important in the very far field. In case of a highly buoyant flow produced by e.g. a circular ring fire, buoyancy is the main driving force which gives rise to the study of annular plumes. Analogous to the experimental study of coaxial plumes, we propose as a fruitful area of investigation the study of the unventilated and ventilated annular plumes as might be produced by the nozzles illustrated schematically in figure 8.4.

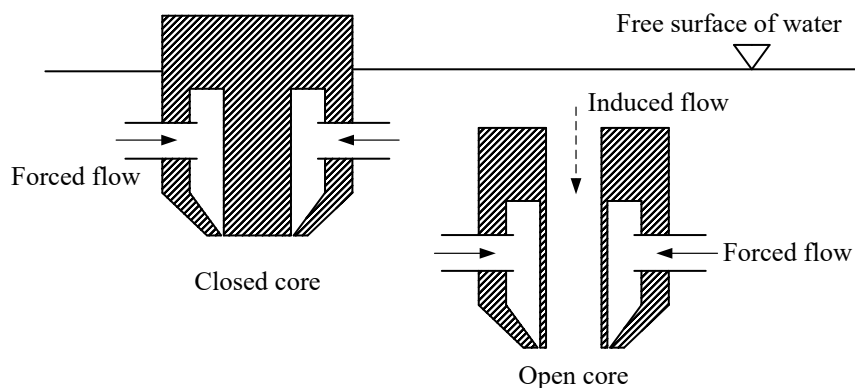


Figure 8.4: Cross-cut view of the nozzles needed to produce the closed core and open core annular plumes. Solid and dashed lines denote forced and induced flows, respectively.

8.2.2.3 Merging of two plumes with unequal strengths

Recently Rooney (2019) studied the merging of a pair of unequal line sinks. Specifically, the complex potential for the two line sinks, located respectively at $(0, 0)$ and $(a, 0)$, reads

$$\Omega = -\frac{m_1}{2\pi} \ln z - \frac{m_2}{2\pi} \ln(z - a), \quad (8.4)$$

where $z = x + iy = re^{i\theta}$, m_1 and m_2 are the respective strengths of the two line sinks. Letting $M = m_1/m_2$, constant velocity potential contours are described by $|z^M(z - a)| = k^2$ (k is a constant), which can be expressed using polar coordinates as follows:

$$r^{2M} (r^2 - 2ar \cos \theta + a^2) = k^4. \quad (8.5)$$

Note that M can be an arbitrary positive constant. In the special case of $M = 1/2$, i.e. the so-called “cubic” case, Rooney (2019) gave the simple analytical solution to (8.5). For the

general case, Rooney (2019) proposed a parametric solution to (8.5) by mapping from the cubic case.

On the basis of Rooney (2019), we can draw the velocity potential contours for the general case with arbitrary M . However, and due to the asymmetry when $M \neq 1$, the link between irrotational flow theory and the plume equations is not straightforward. We may speculate that the flux of entrained fluid across any velocity potential contour is given by $E = m_1 + m_2$. Nonetheless, we expect to treat the two plumes as separate plumes pre-merger and as a single plume post-merger. Note that the point of full merger for the asymmetric case remains to be specified.

8.2.2.4 Plume merger with applications to natural ventilation

The irrotational flow theory of plume merger by Rooney (2016) has not been applied to the standard natural ventilation model of Linden *et al.* (1990). For the merging of two co-flowing ideal source plumes, Linden & Kaye (2006) found that plume merger only affects the internal stratification provided the height of merger is below the interface height expected for two non-interacting plumes. Following the work of Linden & Kaye (2006), we propose another two cases for future study: (i) Merging of $n \geq 3$ (n is an integer) ideal source plumes equally spaced around a circle in a naturally ventilated enclosure, and (ii) merging of two non-ideal source plumes in a naturally ventilated enclosure.

Case (i) seems to be straightforward in the fact that we may simply replace $n \geq 3$ in the theoretical analysis in section 3.1 of Linden & Kaye (2006). By contrast, case (ii) can be complicated if the plume source is relatively large, e.g. a distributed heat source by a sun patch, and the plumes are highly lazy. Whereas most of previous models consider perfectly symmetric configurations which require n to be integer, the evolution of a plume in corners of arbitrary angle $2\pi/n$ where n is non-integer merits better understanding (Rooney, 2016).

References

- ABDELWAHED, M. S. & CHU, V. H. 1978 Bifurcation of buoyant jets in a crossflow. In *Verification of Mathematical and Physical Models in Hydraulic Engineering*, pp. 819–826. ASCE.
- ABESSI, O. & ROBERTS, P. J. 2014 Multiport diffusers for dense discharges. *Journal of Hydraulic Engineering* **140** (8), 04014032.
- ABRAHAM, G. 1970 Round buoyant jet in cross-flow. In *5th International Conf. Water Pollut. Res. San Francisco, USA*.
- ALESSANDRINI, S., ANFOSSI, D. & FERRERO, E. 2011 A new method for buoyant plume rise computation in Lagrangian particle models. In *Air Pollution Modeling and its Application XXI*, pp. 45–50. Springer.
- ALESSANDRINI, S., FERRERO, E. & ANFOSSI, D. 2013 A new Lagrangian method for modelling the buoyant plume rise. *Atmospheric Environment* **77**, 239–249.
- ALTON, B., DAVIDSON, G. & SLAWSON, P. 1993 Comparison of measurements and integral model predictions of hot water plume behaviour in a crossflow. *Atmospheric Environment. Part A. General Topics* **27** (4), 589–598.
- ANDERSSON, B., ANDERSSON, R., HÅKANSSON, L., MORTENSEN, M., SUDIYO, R. & VAN WACHEM, B. 2011 *Computational Fluid Dynamics for Engineers*. Cambridge University Press.
- ANDREOPOULOS, J. 1989a Wind tunnel experiments on cooling tower plumes: Part I – in uniform crossflow. *Journal of Heat Transfer* **111** (4), 941–948.
- ANDREOPOULOS, J. 1989b Wind tunnel experiments on cooling tower plumes: Part II – in nonuniform cross flow of boundary layer type. *NASA STI/Recon Technical Report N* **111** (4), 949–955.
- ANFOSSI, D., BONINO, G., BOSSA, F. & RICHIARDONE, R. 1978 Plume rise from multiple sources: a new model. *Atmospheric Environment (1967)* **12** (9), 1821–1826.
- ARAKERI, J. H., DAS, D. & SRINIVASAN, J. 2000 Bifurcation in a buoyant horizontal laminar jet. *Journal of Fluid Mechanics* **412**, 61–73.
- ASHRAE 2013a *Fundamentals handbook. SI Edition* .
- ASHRAE 2013b *Fundamentals, SI ed. American Society of Heating, Refrigerating and Air Conditioning Engineers: Atlanta, GA, USA* .
- ATC, C. 2011 Acceptance test procedure for wet-dry plume abatement cooling towers. *Cooling Tower Institute, Houston* .
- BAILLY, C. & COMTE-BELLOT, G. 2015 Homogeneous and isotropic turbulence. In *Turbulence*, pp. 129–177. Springer.

- BAINES, P. G. 2014 Plumes, entrainment and B.R. Morton. *Australian Meteorology* .
- BAINES, W. & TURNER, J. 1969 Turbulent buoyant convection from a source in a confined region. *Journal of Fluid mechanics* **37** (1), 51–80.
- BAINES, W. D. 1983 A technique for the direct measurement of volume flux of a plume. *Journal of Fluid Mechanics* **132**, 247–256.
- BATCHELOR, G. 1954 Heat convection and buoyancy effects in fluids. *Quarterly Journal of the Royal Meteorological Society* **80** (345), 339–358.
- BECKER, B., STEWART, W., WALTER, T. & BECKER, C. 1989 A numerical model of cooling tower plume recirculation. *Mathematical and Computer Modelling* **12** (7), 799–819.
- BENNETT, M., SUTTON, S. & GARDINER, D. 1992 Measurements of wind speed and plume rise with a rapid-scanning lidar. *Atmospheric Environment. Part A. General Topics* **26** (9), 1675–1688.
- BLOOMFIELD, L. J. & KERR, R. C. 1998 Turbulent fountains in a stratified fluid. *Journal of Fluid Mechanics* **358**, 335–356.
- BLOOMFIELD, L. J. & KERR, R. C. 2000 A theoretical model of a turbulent fountain. *Journal of Fluid Mechanics* **424**, 197–216.
- BORNOFF, R. & MOKHTARZADEH-DEGHAN, M. 2001 A numerical study of interacting buoyant cooling-tower plumes. *Atmospheric Environment* **35** (3), 589–598.
- BRIGGS, G. A. 1965 A plume rise model compared with observations. *Journal of the Air Pollution Control Association* **15** (9), 433–438.
- BRIGGS, G. A. 1969 Plume rise usaec critical review series tid-25075. *National Technical Information Service, Springfield, Virginia* **22161**.
- BRIGGS, G. A. 1975 Plume rise predictions. In *Lectures on Air Pollution and Environmental Impact Analyses*, pp. 59–111. American Meteorological Society, Boston.
- BRIGGS, G. A. 1984 Plume rise and buoyancy effects. *Atmospheric science and power production* **850**, 327–366.
- BROWN, G. & FLETCHER, D. 2005 CFD prediction of odour dispersion and plume visibility for alumina refinery calciner stacks. *Process Safety and Environmental Protection* **83** (3), 231.
- BUGLER, T., LANE, J., FIELDS, B. & MILLER, R. D. 2010 Cooling towers, drift and legionellosis. *Journal of the Cooling Tower Institute* **31** (1), 30–47.
- BURESTI, G., TALAMELLI, A. & PETAGNA, P. 1994 Experimental characterization of the velocity field of a coaxial jet configuration. *Experimental Thermal and Fluid Science* **9** (2), 135–146.
- BURRIDGE, H. & HUNT, G. 2013 The rhythm of fountains: the length and time scales of rise height fluctuations at low and high froude numbers. *Journal of Fluid Mechanics* **728**, 91–119.
- BURRIDGE, H., PARKER, D., KRUGER, E., PARTRIDGE, J. L. & LINDEN, P. F. 2017 Conditional sampling of a high Péclet number turbulent plume and the implications for entrainment. *Journal of Fluid Mechanics* **823**, 26–56.

- BUSH, J. W. & WOODS, A. W. 1998 Experiments on buoyant plumes in a rotating channel. *Geophysical & Astrophysical Fluid Dynamics* **89** (1-2), 1–22.
- CANEPA, E. 2004 An overview about the study of downwash effects on dispersion of airborne pollutants. *Environmental Modelling & Software* **19** (12), 1077–1087.
- CARAZZO, G., KAMINSKI, E. & TAIT, S. 2006 The route to self-similarity in turbulent jets and plumes. *Journal of Fluid Mechanics* **547**, 137–148.
- CARBONARO, M. G. 1983 Air channeling device for mixing dry and humid air streams of a combined wet and dry atmospheric cooler. US Patent 4,367,183.
- CARHART, R. & POLICASTRO, A. 1991 A second-generation model for cooling tower plume rise and dispersion—i. single sources. *Atmospheric Environment. Part A. General Topics* **25** (8), 1559–1576.
- CARPENTER, S., LEAVITT, J., THOMAS, F. W., FRIZZOLA, J. A. & SMITH, M. E. 1968 Full-scale study of plume rise at large coal-fired electric generating stations. *Journal of the Air Pollution Control Association* **18** (7), 458–465.
- CAULFIELD, C. & WOODS, A. W. 1998 Turbulent gravitational convection from a point source in a non-uniformly stratified environment. *Journal of Fluid Mechanics* **360**, 229–248.
- CENEDESE, C. & LINDEN, P. F. 2014 Entrainment in two coalescing axisymmetric turbulent plumes. *Journal of Fluid Mechanics* **752**.
- CHAHINE, A., MATHARAN, P., WENDUM, D., MUSSON-GENON, L., BRESSON, R. & CARISSIMO, B. 2015 Modelling atmospheric effects on performance and plume dispersal from natural draft wet cooling towers. *Journal of Wind Engineering and Industrial Aerodynamics* **136**, 151–164.
- CHAMPAGNE, F. & WYGNANSKI, I. 1971 An experimental investigation of coaxial turbulent jets. *International Journal of Heat and Mass Transfer* **14** (9), 1445–1464.
- CHAN, M.-H. 2015 Cooling tower performance analysis and visible air plume abatement in buildings situated in temperate climate zone. PhD thesis, Cardiff University.
- CHATTOPADHYAY, H. 2004 Numerical investigations of heat transfer from impinging annular jet. *International journal of heat and mass transfer* **47** (14-16), 3197–3201.
- CHEN, N. C. 1977 Review of cooling tower drift deposition models. *Tech. Rep.*. Oak Ridge National Lab., TN (USA).
- CHITSOMBOON, T. 2001 A validated analytical model for flow in solar chimney. *International Journal of Renewable Energy Engineering* **3** (2), 339–346.
- CHU, V. H. 1994 Lagrangian scaling of turbulent jets and plumes with dominant eddies. In *Recent research advances in the fluid mechanics of turbulent jets and plumes*, pp. 45–72. Springer.
- CINTOLESI, C., PETRONIO, A. & ARMENIO, V. 2018 Turbulent structures of buoyant jet in cross-flow studied through large-eddy simulation. *Environmental Fluid Mechanics* pp. 1–33.
- CINTOLESI, C., PETRONIO, A. & ARMENIO, V. 2019 Turbulent structures of buoyant jet in cross-flow studied through large-eddy simulation. *Environmental Fluid Mechanics* **19** (2), 401–433.

- CIRIELLO, F. & HUNT, G. 2020 Analytical solutions and virtual origin corrections for forced, pure and lazy turbulent plumes based on a universal entrainment function. *Journal of Fluid Mechanics* **893**.
- CIZEK, J. & NOZICKA, J. 2016 Cooling tower plume. In *AIP Conference Proceedings*, , vol. 1768, p. 020001. AIP Publishing.
- CONSUEGRO, A., KAISER, A., ZAMORA, B., SÁNCHEZ, F., LUCAS, M. & HERNÁNDEZ, M. 2014 Numerical modeling of the drift and deposition of droplets emitted by mechanical cooling towers on buildings and its experimental validation. *Building and Environment* **78**, 53–67.
- CONTINI, D., CESARI, D., DONATEO, A. & ROBINS, A. 2009 Effects of Reynolds number on stack plume trajectories simulated with small scale models in a wind tunnel. *Journal of Wind Engineering and Industrial Aerodynamics* **97** (9-10), 468–474.
- CONTINI, D., DONATEO, A., CESARI, D. & ROBINS, A. 2011 Comparison of plume rise models against water tank experimental data for neutral and stable crossflows. *Journal of Wind Engineering and Industrial Aerodynamics* **99** (5), 539–553.
- CONTINI, D., HAYDEN, P. & ROBINS, A. 2006 Concentration field and turbulent fluxes during the mixing of two buoyant plumes. *Atmospheric Environment* **40** (40), 7842–7857.
- CONTINI, D. & ROBINS, A. 2001 Water tank measurements of buoyant plume rise and structure in neutral crossflows. *Atmospheric Environment* **35** (35), 6105–6115.
- CONTINI, D. & ROBINS, A. 2004 Experiments on the rise and mixing in neutral crossflow of plumes from two identical sources for different wind directions. *Atmospheric Environment* **38** (22), 3573–3583.
- CONTINI, D., ROBINS, A. & HAYDEN, P. 2014 Statistical properties of concentration fluctuations in two merging plumes. *Environmental Fluid Mechanics* **14** (4), 919–942.
- CRIMALDI, J. 2008 Planar laser induced fluorescence in aqueous flows. *Experiments in fluids* **44** (6), 851–863.
- CRIMALDI, J. & KOSEFF, J. 2001 High-resolution measurements of the spatial and temporal scalar structure of a turbulent plume. *Experiments in Fluids* **31** (1), 90–102.
- CSANADY, G. 1971 Bent-over vapor plumes. *Journal of Applied Meteorology* **10** (1), 36–42.
- CURRY, J. A. & WEBSTER, P. J. 1998 *Thermodynamics of Atmospheres and Oceans*, , vol. 65. Elsevier.
- DAHM, W. J., FRIELER, C. E. & TRYGGVASON, G. 1992 Vortex structure and dynamics in the near field of a coaxial jet. *Journal of Fluid Mechanics* **241**, 371–402.
- DAVIDSON, G. 1982 Source flux corrections in analytical vapor plume models. *Journal of Applied Meteorology* **21** (12), 1792–1797.
- DAVIDSON, G. 1986a A discussion of schatzmann’s integral plume model from a control volume viewpoint. *Journal of Climate and Applied Meteorology* **25** (6), 858–867.
- DAVIDSON, G. 1986b Gaussian versus top-hat profile assumptions in integral plume models. *Atmospheric Environment (1967)* **20** (3), 471–478.
- DAVIDSON, G. 1989 Simultaneous trajectory and dilution predictions from a simple integral plume model. *Atmospheric Environment (1967)* **23** (2), 341–349.

- DAVIS, L., SHIRAZI, M. & SIEGEL, D. 1978 Measurement of buoyant jet entrainment from single and multiple sources. *Journal of Heat Transfer* **100** (3), 442–447.
- DAVIS, L., SHIRAZI, M. A. & SLEGEL, D. L. 1977 *Experimental simulation of single and multiple cell cooling tower plumes*, , vol. 1. Environmental Protection Agency, Office of Research and Development.
- DAVIS, L. R. 1975 *Analysis of multiple cell mechanical draft cooling towers*. US Environmental Protection Agency.
- DAVIS, L. R. 1998 *Fundamentals of Environmental Discharge Modeling*. CRC Press.
- DEMUREN, A. O. & RODI, W. 1987 Three-dimensional numerical calculations of flow and plume spreading past cooling towers. *Journal of Heat Transfer* **109** (1), 113–119.
- DEVENISH, B., ROONEY, G. & THOMSON, D. 2010a Large-eddy simulation of a buoyant plume in uniform and stably stratified environments. *Journal of Fluid Mechanics* **652**, 75–103.
- DEVENISH, B., ROONEY, G., WEBSTER, H. & THOMSON, D. 2010b The entrainment rate for buoyant plumes in a crossflow. *Boundary-Layer Meteorology* **134** (3), 411–439.
- DIEZ, F., BERNAL, L. & FAETH, G. 2005 PLIF and PIV measurements of the self-preserving structure of steady round buoyant turbulent plumes in crossflow. *International journal of heat and fluid flow* **26** (6), 873–882.
- DJURFORS, S. 1977 On the rise of buoyant plumes in turbulent environments .
- ECONOMIDOU, M. & HUNT, G. R. 2009 Density stratified environments: the double-tank method. *Experiments in fluids* **46** (3), 453–466.
- EMANUEL, K. A. 1994 *Atmospheric Convection*. Oxford University Press on Demand.
- ERNST, G. G., DAVIS, J. P. & SPARKS, R. S. J. 1994 Bifurcation of volcanic plumes in a crosswind. *Bulletin of Volcanology* **56** (3), 159–169.
- FAN, L.-N. 1967 Turbulent buoyant jets into stratified or flowing ambient fluids. PhD thesis, California Institute of Technology.
- FANAKI, F. 1975 Experimental observations of a bifurcated buoyant plume. *Boundary-Layer Meteorology* **9** (4), 479–495.
- FAVRE-MARINET, M., CAMANO, E. & SARBOCH, J. 1999 Near-field of coaxial jets with large density differences. *Experiments in Fluids* **26** (1-2), 97–106.
- FAVRE-MARINET, M. & SCHETTINI, E. C. 2001 The density field of coaxial jets with large velocity ratio and large density differences. *International journal of heat and mass transfer* **44** (10), 1913–1924.
- FERNANDES, J. H. 1979 Vortex cooling tower. US Patent 4,157,368.
- FISCHER, H., LIST, E., KOH, R., IMBERGER, J. & BROOKS, N. 1979 *Mixing in Inland and Coastal Waters*.
- FISHER, B. 1997 Predicting cooling tower plume dispersion. *Proceedings of the Institution of Mechanical Engineers, Part A: Journal of Power and Energy* **211** (4), 291–297.
- FOX, D. G. 1970 Forced plume in a stratified fluid. *Journal of Geophysical Research* **75** (33), 6818–6835.

- FRAPPA, M., BRUNETTI, A., DRIOLI, E., CUI, Z., PAN, J. & MACEDONIO, F. 2020 Membrane condenser for particulate abatement from waste-gaseous streams. *Journal of Membrane Science and Research* **6** (1), 81–89.
- GANGOITI, G., SANCHO, J., IBARRA, G., ALONSO, L., GARCIA, J., NAVAZO, M., DURANA, N. & ILARDIA, J. 1997 Rise of moist plumes from tall stacks in turbulent and stratified atmospheres. *Atmospheric Environment* **31** (2), 253–269.
- GE, G., XIAO, F., WANG, S. & PU, L. 2012 Effects of discharge recirculation in cooling towers on energy efficiency and visible plume potential of chilling plants. *Applied Thermal Engineering* **39**, 37–44.
- GENDRON, P.-O., AVALTRONI, F. & WILKINSON, K. 2008 Diffusion coefficients of several rhodamine derivatives as determined by pulsed field gradient–nuclear magnetic resonance and fluorescence correlation spectroscopy. *Journal of fluorescence* **18** (6), 1093.
- GETSINGER, D. 2012 Shear layer instabilities and mixing in variable density transverse jet flows. PhD thesis, UCLA.
- GOLUBOVIC, M. N., HETTIARACHCHI, H. M. & WOREK, W. M. 2007 Evaluation of rotary dehumidifier performance with and without heated purge. *International Communications in Heat and Mass Transfer* **34** (7), 785–795.
- GUO, D.-P., YAO, R.-T. & FAN, D. 2014 Wind tunnel experiment for predicting a visible plume region from a nuclear power plant cooling tower. *Journal of Applied Meteorology and Climatology* **53** (2), 234–241.
- HAMZA, R. & GOLAY, M. 1981 *Behavior of buoyant moist plumes in turbulent atmospheres*. [Cambridge, Mass.]: Massachusetts Institute of Technology, Energy Laboratory.
- HANNA, S. R. 1972 Rise and condensation of large cooling tower plumes. *Journal of Applied Meteorology* **11** (5), 793–799.
- HARGREAVES, D. M., SCASE, M. M. & EVANS, I. 2012 A simplified computational analysis of turbulent plumes and jets. *Environmental Fluid Mechanics* **12** (6), 555–578.
- HAYASHI, T. 1971 Turbulent buoyant jets of effluent discharged vertically upwards from an orifice in a cross-current in the ocean. In *Proc. 14th Congress, Int. Assoc. Hydr. Res., Paris, Aug*, pp. 157–165.
- HE, Z. & LOU, Y. 2019 Integral model for multiple forced plumes arranged around a circle in a linearly stratified environment. *Physical Review Fluids* **4** (12), 123501.
- HE, Z., ZHANG, W., JIANG, H., ZHAO, L. & HAN, X. 2018 Dynamic interaction and mixing of two turbulent forced plumes in linearly stratified ambience. *Journal of Hydraulic Engineering* **144** (12), 04018072.
- HENSLEY, J. C. 2009 Cooling tower fundamentals. compiled from the knowledge and experience of the entire SPX cooling technologies staff. SPX cooling technologies. *Inc. Overland Park, Kansas USA* .
- HEWITT, I. J. 2020 Subglacial plumes. *Annual Review of Fluid Mechanics* **52**, 145–169.
- HIRST, E. 1972 Buoyant jets with three-dimensional trajectories. *Tech. Rep.*. Oak Ridge National Lab., TN.
- HOLIDAY, R. A. & ALSAYED, S. 2015 Sustainability in cooling system operation. *Journal of the Cooling Tower Institute* **36** (1), 74–78.

- HOULT, D. P., FAY, J. A. & FORNEY, L. J. 1969 A theory of plume rise compared with field observations. *Journal of the Air Pollution Control Association* **19** (8), 585–590.
- HOULT, D. P. & WEIL, J. C. 1972 Turbulent plume in a laminar cross flow. *Atmospheric Environment (1967)* **6** (8), 513–531.
- HOUX JR, J. R., LANDON, R. D. & LINDAHL JR, P. A. 1978 Bottom vented wet-dry water cooling tower. US Patent 4,076,771.
- HUBBARD, B. J., MOCKRY, E. F. & KINNEY JR, O. 2003 Air-to-air atmospheric exchanger for condensing cooling tower effluent. US Patent 6,663,694.
- HÜBNER, J. 2004 Buoyant plumes in a turbulent environment. PhD thesis, University of Cambridge.
- HUNT, G. & VAN DEN BREMER, T. 2011 Classical plume theory: 1937–2010 and beyond. *IMA journal of applied mathematics* **76** (3), 424–448.
- HUNT, G. & BURRIDGE, H. 2015 Fountains in industry and nature. *Annual Review of Fluid Mechanics* **47**, 195–220.
- HUNT, G. & KAYE, N. 2001 Virtual origin correction for lazy turbulent plumes. *Journal of Fluid Mechanics* **435**, 377–396.
- HUNT, G. & KAYE, N. 2005 Lazy plumes. *Journal of Fluid Mechanics* **533**, 329–338.
- HUNT, G. R. & DEBUGNE, A. L. 2016 Forced fountains. *Journal of Fluid Mechanics* **802**, 437–463.
- HUQ, P. & DHANAK, M. 1996 The bifurcation of circular jets in crossflow. *Physics of Fluids* **8** (3), 754–763.
- HUQ, P. & STEWART, E. 1996 A laboratory study of buoyant plumes in laminar and turbulent crossflows. *Atmospheric Environment* **30** (7), 1125–1135.
- JABER, H. & WEBB, R. 1989 Design of cooling towers by the effectiveness-ntu method. *Journal of Heat Transfer* **111** (4), 837–843.
- JANICKE, U. & JANICKE, L. 2001 A three-dimensional plume rise model for dry and wet plumes. *Atmospheric Environment* **35** (5), 877–890.
- JIRKA, G. H. 2004 Integral model for turbulent buoyant jets in unbounded stratified flows. Part I: Single round jet. *Environmental Fluid Mechanics* **4** (1), 1–56.
- JIRKA, G. H. 2006 Integral model for turbulent buoyant jets in unbounded stratified flows Part II: Plane jet dynamics resulting from multiport diffuser jets. *Environmental Fluid Mechanics* **6** (1), 43–100.
- JIRKA, G. H. & FONG, H. L. 1981 Vortex dynamics and bifurcation of buoyant jets in crossflow. *Journal of the American Society of Civil Engineers* **107**, 479–499.
- JORDINSON, R. 1956 *Flow in a Jet Directed Normal to the Wind*. Ministry of Supply, Aeronautical Research Council.
- KAMINSKI, E., TAIT, S. & CARAZZO, G. 2005 Turbulent entrainment in jets with arbitrary buoyancy. *Journal of Fluid Mechanics* **526**, 361–376.
- KANNBERG, L. D. & DAVIS, L. 1976 *An experimental/analytical investigation of deep submerged multiple buoyant jets*. Environmental Protection Agency, Office of Research and Development.

- KARATAŞ, M. 2013 A multi foci closed curve: Cassini oval, its properties and applications. *Doğuş Üniversitesi Dergisi* **14** (2), 231–248.
- KAYE, N. 2008 Turbulent plumes in stratified environments: a review of recent work. *Atmosphere-Ocean* **46** (4), 433–441.
- KAYE, N., FLYNN, M., COOK, M. J. & JI, Y. 2010 The role of diffusion on the interface thickness in a ventilated filling box. *Journal of Fluid Mechanics* **652**, 195–205.
- KAYE, N. & HUNT, G. 2009 An experimental study of large area source turbulent plumes. *International Journal of Heat and Fluid Flow* **30** (6), 1099–1105.
- KAYE, N. & LINDEN, P. 2004 Coalescing axisymmetric turbulent plumes. *Journal of Fluid Mechanics* **502**, 41–63.
- KHANDEKAR, M. & MURTY, T. 1975 A note on bifurcation of buoyant bent-over chimney plumes. *Atmospheric Environment (1967)* **9** (8), 759–762.
- KINNEY JR, O. L., BRENNEKE, G. S. & BUGLER III, T. W. 1999 Dry-air-surface heat exchanger. US Patent 5,944,094.
- KLIMANEK, A. 2013 Numerical modelling of natural draft wet-cooling towers. *Archives of Computational Methods in Engineering* **20** (1), 61–109.
- KLIMANEK, A. & BIAŁECKI, R. 2009 Solution of heat and mass transfer in counterflow wet-cooling tower fills. *International Communications in Heat and Mass Transfer* **36** (6), 547–553.
- KLIMANEK, A., BIAŁECKI, R. A. & OSTROWSKI, Z. 2010 CFD two-scale model of a wet natural draft cooling tower. *Numerical Heat Transfer, Part A: Applications* **57** (2), 119–137.
- KLIMANEK, A., CEDZICH, M. & BIAŁECKI, R. 2015 3D CFD modeling of natural draft wet-cooling tower with flue gas injection. *Applied Thermal Engineering* **91**, 824–833.
- KLOPPERS, J. C. & KRÖGER, D. G. 2005 The Lewis factor and its influence on the performance prediction of wet-cooling towers. *International Journal of Thermal Sciences* **44** (9), 879–884.
- KLOPPERS, J. C. & KRÖGER, D. G. 2005a Cooling tower performance evaluation: Merkel, poppe, and e-ntu methods of analysis. *Journal of Engineering for Gas Turbines and Power* **127** (1), 1–7.
- KLOPPERS, J. C. & KRÖGER, D. G. 2005b A critical investigation into the heat and mass transfer analysis of counterflow wet-cooling towers. *International Journal of Heat and Mass Transfer* **48** (3-4), 765–777.
- KO, N. & CHAN, W. 1978 Similarity in the initial region of annular jets: three configurations. *Journal of Fluid Mechanics* **84** (4), 641–656.
- KOK, B., VAROL, Y., AYHAN, H. & OZTOP, H. F. 2017 Experimental and computational analysis of thermal mixing characteristics of a coaxial jet. *Experimental Thermal and Fluid Science* **82**, 276–286.
- KÖNIG, C. & MOKHTARZADEH-DEGHAN, M. 2002 Numerical study of buoyant plumes from a multi-flue chimney released into an atmospheric boundary layer. *Atmospheric Environment* **36** (24), 3951–3962.
- KOO, J. B. 2016a Plume abatement cooling tower. KR Patent 20160007843.

- KOO, J. B. 2016*b* Plume abatement cooling tower. KR Patent 20160109975.
- KRÖGER, D. G. 2004 *Air-cooled heat exchangers and cooling towers*, , vol. 1. PennWell Books.
- KUNDU, P., COHEN, I., HU, G. & DOWLING, D. 2015 Fluid mechanics 6th ed., waltham, ma.
- KUNDU, P. K. 1990 *Fluid Mechanics*, 1st edn. San Diego, USA: Academic Press.
- LAI, A. C. & LEE, J. H. 2010 Multiple tandem jet interaction in a crossflow. *Journal of Hydrodynamics* **22** (1), 616–620.
- LAI, A. C. & LEE, J. H. 2012 Dynamic interaction of multiple buoyant jets. *Journal of Fluid Mechanics* **708**, 539–575.
- LAI, A. C., YU, D. & LEE, J. H. 2011 Mixing of a rosette jet group in a crossflow. *Journal of Hydraulic Engineering* **137** (8), 787–803.
- LATIMER, D. & SAMUELSEN, G. 1978 Visual impact of plumes from power plants: A theoretical model. *Atmospheric Environment (1967)* **12** (6-7), 1455–1465.
- LAULAINEN, N., WEBB, R., WILBER, K. & ULANSKI, S. 1979 Comprehensive study of drift from mechanical draft cooling towers. final report. *Tech. Rep.*. Battelle Pacific Northwest Labs., Richland, WA (USA).
- LAUNDER, B. & SPALDING, D. 1974 The numerical computation of turbulent flows. *Computer Methods in Applied Mechanics and Engineering* **3** (2), 269–289.
- LAVELLE, J. 1997 Buoyancy-driven plumes in rotating, stratified cross flows: Plume dependence on rotation, turbulent mixing, and cross-flow strength. *Journal of Geophysical Research: Oceans* **102** (C2), 3405–3420.
- LAVISION 2011 LIF in Liquid Fluids.
- LEE, J. 2018 Evaluation of impacts of cooling tower design properties on the near-field environment. *Nuclear Engineering and Design* **326**, 65–78.
- LEE, J. H.-W. & CHU, V. 2003 *Turbulent Jets and Plumes: A Lagrangian Approach*. Springer Science & Business Media.
- LEE, Y. S. 2017 An air mixer for vapor reduction. KR Patent 101763629 (B1).
- LI, S. & FLYNN, M. 2020*a* Coaxial plumes in a windy ambient with applications to cooling towers. *Journal of Wind Engineering and Industrial Aerodynamics* **196**, 104054.
- LI, S. & FLYNN, M. 2020*b* Merging of two plumes from area sources with applications to cooling towers. *Physical Review Fluids* **5** (5), 054502.
- LI, S., MORADI, A., VICKERS, B. & FLYNN, M. 2018 Cooling tower plume abatement using a coaxial plume structure. *International Journal of Heat and Mass Transfer* **120**, 178–193.
- LIBERT, J.-P., HAMILTON, J. & BUGLER, T. 2015 Advanced cooling solutions for water conservation. *Journal of the Cooling Tower Institute* **36** (1), 66–72.
- LIBERT, J.-P. & NEVINS, S. 2011 Cooling tower plume. *Journal of the Cooling Tower Institute* **32** (2), 14–30.

- LIN, Y.-J. P. & LINDEN, P. 2005 A model for an under floor air distribution system. *Energy and Buildings* **37** (4), 399–409.
- LINDAHL, P. & JAMESON, R. W. 1993 Plume abatement and water conservation with the wet/dry cooling tower. *Tech. Rep.*. Electric Power Research Inst., Palo Alto, CA (United States); Yankee Scientific, Inc., Medfield, MA (United States).
- LINDAHL, P. & MORTENSEN, K. 2010 Plume abatement—the next generation. *Journal of the Cooling Tower Institute* **31** (2), 8–24.
- LINDEN, P., LANE-SERFF, G. & SMEED, D. 1990 Emptying filling boxes: the fluid mechanics of natural ventilation. *Journal of Fluid Mechanics* **212**, 309–335.
- LINDEN, P. F. 1999 The fluid mechanics of natural ventilation. *Annual review of fluid mechanics* **31** (1), 201–238.
- LINDEN, P. F. 2000 Convection in the environment. Perspectives in fluid dynamics: A collective introduction to current research (ed. Batchelor, GK and Moffatt, HK and Worster, MG). Cambridge University Press.
- LINDEN, P. F. & KAYE, N. B. 2006 Interacting turbulent plumes in a naturally ventilated enclosure. *International Journal of Ventilation* **4** (4), 301–310.
- LIST, E. 1982 *Turbulent Buoyant Jets and Plumes: HMT: The Science & Applications of Heat and Mass Transfer. Reports, Reviews & Computer Programs*, , vol. 6. Elsevier.
- LIST, E. J. & IMBERGER, J. 1973 Turbulent entrainment in buoyant jets and plumes. *Journal of the Hydraulics Division* **99** (9), 1461–1474.
- LIU, Z. & BAO, B. 2014 Research on reducing recirculation influence of warm and saturated air discharged from cooling towers. *Journal of the Cooling Tower Institute* **35** (1), 48–56.
- LOU, Y., HE, Z., JIANG, H. & HAN, X. 2019 Numerical simulation of two coalescing turbulent forced plumes in linearly stratified fluids. *Physics of Fluids* **31** (3), 037111.
- LUCAS, M., MARTINEZ, P. J., RUIZ, J., KAISER, A. S. & VIEDMA, A. 2010 On the influence of psychrometric ambient conditions on cooling tower drift deposition. *International Journal of Heat and Mass Transfer* **53** (4), 594–604.
- MACDONALD, R., STROM, R. & SLAWSON, P. 2002 Water flume study of the enhancement of buoyant rise in pairs of merging plumes. *Atmospheric Environment* **36** (29), 4603–4615.
- MACEDONIO, F., FRAPPA, M., BRUNETTI, A., BARBIERI, G., DRIOLI, E., MACEDONIO, F., FRAPPA, M., BRUNETTI, A., BARBIERI, G. & DRIOLI, E. 2019 Recovery of water and contaminants from cooling tower plume. *Environmental Engineering Research* **25** (2), 222–229.
- MAKHOUL, A., GHALI, K. & GHADDAR, N. 2015 Low-mixing coaxial nozzle for effective personalized ventilation. *Indoor and Built Environment* **24** (2), 225–243.
- MANTELLI, M. H. 2016 Development of porous media thermosyphon technology for vapor recovering in cross-current cooling towers. *Applied Thermal Engineering* **108**, 398–413.
- MARJANOVIC, G., TAUB, G. & BALACHANDAR, S. 2017 On the evolution of the plume function and entrainment in the near-source region of lazy plumes. *Journal of Fluid Mechanics* **830**, 736–759.
- MCDUGALL, T. J. 1978 Bubble plumes in stratified environments. *Journal of Fluid Mechanics* **85** (4), 655–672.

- McDOUGALL, T. J. 1981 Negatively buoyant vertical jets. *Tellus* **33** (3), 313–320.
- MERKEL, F. 1925 *Verdunstungskühlung*. VDI-Verlag.
- MERONEY, R. N. 2006 CFD prediction of cooling tower drift. *Journal of Wind Engineering and Industrial Aerodynamics* **94** (6), 463–490.
- MERONEY, R. N. 2008 Protocol for CFD prediction of cooling-tower drift in an urban environment. *Journal of Wind Engineering and Industrial Aerodynamics* **96** (10-11), 1789–1804.
- MEYER, J. 1974 Mechanical-draft cooling tower visible plume behavior: measurements, models, prediction. *Cooling Tower Environment* pp. 307–352.
- MICHIOKA, T., SATO, A., KANZAKI, T. & SADA, K. 2007 Wind tunnel experiment for predicting a visible plume region from a wet cooling tower. *Journal of Wind Engineering and Industrial Aerodynamics* **95** (8), 741–754.
- MINGOTTI, N. & CARDOSO, S. 2019 Mixing and reaction in turbulent plumes: the limits of slow and instantaneous chemical kinetics. *Journal of Fluid Mechanics* **861**, 1–28.
- MISHRA, H. & PHILIP, J. 2018 Simultaneous velocity and density measurements using PIV and PLIF in turbulent axisymmetric buoyant plumes .
- MIZUSHINA, T., OGINO, F., TAKEUCHI, H. & IKAWA, H. 1982 An experimental study of vertical turbulent jet with negative buoyancy. *Wärme-und Stoffübertragung* **16** (1), 15–21.
- MOKHTARZADEH-DEHGHAN, M., KÖNIG, C. & ROBINS, A. 2006 Numerical study of single and two interacting turbulent plumes in atmospheric cross flow. *Atmospheric Environment* **40** (21), 3909–3923.
- MONJOIE, M. & LIBERT, J.-P. 1994 Testing procedures for wet/dry plume abatement cooling towers. *CTI JOURNAL* **15**, 56–56.
- MONTEIRO, E. & TORLASCHI, E. 2007 On the dynamic interpretation of the virtual temperature. *Journal of the Atmospheric Sciences* **72** (9).
- MOON, J. S. 2017 Vortex – cooling tower having an air mixer. KR Patent 101724128 (B1).
- MORTENSEN, K. 2009 Use of Air2Air technology to recover fresh-water from the normal evaporative cooling loss at coal-based thermoelectric power plants. *Tech. Rep.*. SPX Cooling Technologies Incorporated.
- MORTENSEN, K. 2011 Improvement to Air2Air technology to reduce fresh-water evaporative cooling loss at coal-based thermoelectric power plants. *Tech. Rep.*. SPX Cooling Technologies Incorporated.
- MORTON, B. 1957 Buoyant plumes in a moist atmosphere. *Journal of Fluid Mechanics* **2** (02), 127–144.
- MORTON, B. 1959 Forced plumes. *Journal of Fluid mechanics* **5** (1), 151–163.
- MORTON, B. 1962 Coaxial turbulent jets. *International Journal of Heat and Mass Transfer* **5** (10), 955–965.
- MORTON, B., TAYLOR, G. I. & TURNER, J. S. 1956 Turbulent gravitational convection from maintained and instantaneous sources. *Proceedings of the Royal Society of London. Series A. Mathematical and Physical Sciences* **234** (1196), 1–23.

- MORTON, B. R. 1971 The choice of conservation equations for plume models. *Journal of Geophysical Research* **76** (30), 7409–7416.
- MURPHY, B. 1975 Plume rise from a row of chimneys. In *68th Annual Meeting of the Air Pollution Control Association, Paper No.*, pp. 75–04.
- NETTERVILLE, D. D. 1990 Plume rise, entrainment and dispersion in turbulent winds. *Atmospheric Environment. Part A. General Topics* **24** (5), 1061–1081.
- OEFELIN, J. C. 2006 Mixing and combustion of cryogenic oxygen-hydrogen shear-coaxial jet flames at supercritical pressure. *Combustion Science and Technology* **178** (1-3), 229–252.
- OOMS, G. & MAHIEU, A. 1981 A comparison between a plume path model and a virtual point source model for a stack plume. *Applied Scientific Research* **36** (5-6), 339–356.
- OR, C., LAM, K. & POON, C. 2007 Flow establishment of concentration field in submerged round jets. In *Proc. 32nd IAHR Congress, Venice*, pp. 1–10.
- PADHANI, S. A., HUNT, G. R. & JUKES, T. N. 2018 Turbulent jet from a slender annular slot ventilated by a self-induced flow through the open core. *Physical Review Fluids* **3** (1), 014602.
- PALMER, B. 2006 Method and system for recovering vapor exhaust from processing equipment. US Patent App. 11/523,318.
- PAPANICOLAOU, P. N. & LIST, E. J. 1987 Statistical and spectral properties of tracer concentration in round buoyant jets. *International journal of heat and mass transfer* **30** (10), 2059–2071.
- PAPANICOLAOU, P. N. & LIST, E. J. 1988 Investigations of round vertical turbulent buoyant jets. *Journal of Fluid Mechanics* **195**, 341–391.
- PATTE-ROULAND, B., LALIZEL, G., MOREAU, J. & ROULAND, E. 2001 Flow analysis of an annular jet by particle image velocimetry and proper orthogonal decomposition. *Measurement Science and Technology* **12** (9), 1404.
- POLICASTRO, A., CARHART, R., WASTAG, M., ZIEMER, S., HAAKE, K., DUNN, W. & GAVIN, P. 1980 Improvement of mathematical models for plume rise and drift deposition from cooling towers. *Studies in Environmental Science* **8**, 43–48.
- POLICASTRO, A., DUNN, W. & CARHART, R. 1994 A model for seasonal and annual cooling tower impacts. *Atmospheric Environment* **28** (3), 379–395.
- POLICASTRO, A. & WASTAG, M. 1981 Studies on mathematical models for characterizing plume and drift behavior from cooling towers. Volume 1. Review of european research. *Tech. Rep.*. Argonne National Lab., IL (USA).
- POPE, S. B. 2001 *Turbulent Flows*. Cambridge University Press.
- POPPE, M. & RÖGENER, H. 1991 Berechnung von rückkühlwerken. *VDI Wärmeatlas*, pp. Mi .
- PRIESTLEY, C. 1953 Buoyant motion in a turbulent environment. *Australian Journal of Physics* **6** (3), 279–290.
- PRIESTLEY, C. & BALL, F. 1955 Continuous convection from an isolated source of heat. *Quarterly Journal of the Royal Meteorological Society* **81** (348), 144–157.

- RAFFEL, M., WILLERT, C. E., SCARANO, F., KÄHLER, C. J., WERELEY, S. T. & KOMPENHANS, J. 2018 *Particle Image Velocimetry: A Practical Guide*. Springer.
- VAN REEUWIJK, M. & CRASKE, J. 2015 Energy-consistent entrainment relations for jets and plumes. *Journal of Fluid Mechanics* **782**, 333–355.
- REHAB, H., VILLERMAUX, E. & HOPFINGER, E. 1997 Flow regimes of large-velocity-ratio coaxial jets. *Journal of Fluid Mechanics* **345**, 357–381.
- ROFFMAN, A. & VAN VLECK, L. D. 1974 The state-of-the-art of measuring and predicting cooling tower drift and its deposition. *Journal of the Air Pollution Control Association* **24** (9), 855–859.
- ROONEY, G. G. 2015 Merging of a row of plumes or jets with an application to plume rise in a channel. *Journal of Fluid Mechanics* **771**.
- ROONEY, G. G. 2016 Merging of two or more plumes arranged around a circle. *Journal of Fluid Mechanics* **796**, 712–731.
- ROONEY, G. G. 2019 Asymmetric Cassini Ovals. *Mathematics Today* **55** (2), 70–72.
- ROONEY, G. G. & LINDEN, P. F. 1996 Similarity considerations for non-Boussinesq plumes in an unstratified environment. *Journal of fluid mechanics* **318**, 237–250.
- ROUSE, H., YIH, C. S. & HUMPHREYS, H. 1952 Gravitational convection from a boundary source. *Tellus* **4** (3), 201–210.
- RUSCHEWEYH, H. 1984 A mixing system for gas flow. *Journal of Wind Engineering and Industrial Aerodynamics* **16** (2-3), 189–199.
- RUSCHEWEYH, H. 1985 Apparatus for uniformizing the parameters of a flow and/or for mixing together at least two individual streams which discharge into a main flow. US Patent 4,527,903.
- SÁNCHEZ, F., KAISER, A., ZAMORA, B., RUIZ, J. & LUCAS, M. 2015 Prediction of the lifetime of droplets emitted from mechanical cooling towers by numerical investigation. *International Journal of Heat and Mass Transfer* **89**, 1190–1206.
- SAVORY, E., TOY, N. & AHMED, S. 1996 Experimental study of a plume in a crossflow. *Journal of Wind Engineering and Industrial Aerodynamics* **60**, 195–209.
- SCHATZMANN, M. 1978 The integral equations for round buoyant jets in stratified flows. *Zeitschrift für angewandte Mathematik und Physik ZAMP* **29** (4), 608–630.
- SCHATZMANN, M. 1979 An integral model of plume rise. *Atmospheric Environment (1967)* **13** (5), 721–731.
- SCHATZMANN, M. & POLICASTRO, A. J. 1984 An advanced integral model for cooling tower plume dispersion. *Atmospheric Environment (1967)* **18** (4), 663–674.
- SCHLAICH, J. 1995 *The solar chimney: electricity from the sun*. Edition Axel Menges.
- SCHOLL, M., LIBERT, J.-P. & BAUGHER, D. 2018 Wet-dry technology to abate the visible plume from an existing cooling tower. *Journal of the Cooling Tower Institute* **39** (1), 34–42.
- SCHULZE, H. D. 2010 Hybrid cooling tower. EP2141429 (A2).
- SCORER, R. 1958a *Natural Aerodynamics*. London, Pergamon.

- SCORER, R. 1968 *Air Pollution*. Pergamon Press, Oxford.
- SCORER, R. S. 1958*b* *Natural Aerodynamics*. Pergamon Press, London.
- SHIH, T.-H., LIOU, W. W., SHABBIR, A., YANG, Z. & ZHU, J. 1995 A new k - ϵ eddy viscosity model for high reynolds number turbulent flows. *Computers & Fluids* **24** (3), 227–238.
- SHIN, H. M. 2013 Plume abatement system of exit saturated air with ellipse coil for cooling tower. KR Patent 20130018124 (A).
- SLAWSON, P. & CSANADY, G. 1967 On the mean path of buoyant, bent-over chimney plumes. *Journal of Fluid Mechanics* **28** (2), 311–322.
- SLAWSON, P. & CSANADY, G. 1971 The effect of atmospheric conditions on plume rise. *Journal of Fluid Mechanics* **47** (1), 33–49.
- SMITH, S. 1996 The scalar concentration field of the axisymmetric jet in crossflow. PhD thesis, Stanford University.
- SOCOLOFSKY, S. & ADAMS, E. 2002 Multi-phase plumes in uniform and stratified crossflow. *Journal of Hydraulic Research* **40** (6), 661–672.
- SOCOLOFSKY, S. A., BHAUMIK, T. & SEOL, D.-G. 2008 Double-plume integral models for near-field mixing in multiphase plumes. *Journal of Hydraulic Engineering* **134** (6), 772–783.
- STRENG, A. 1998 Combined wet/dry cooling towers of cell-type construction. *Journal of Energy Engineering* **124** (3), 104–121.
- TAKATA, K., MICHIOKA, T. & KUROSE, R. 2016 Prediction of a visible plume from a dry and wet combined cooling tower and its mechanism of abatement. *Atmosphere* **7** (4), 59.
- TAKATA, K., NASU, K. & YOSHIKAWA, H. 1996 *Prediction of the visible plume from a cooling tower*. Cooling Tower Institute.
- TALBOT, J. J. 1979 A review of potential biological impacts of cooling tower salt drift. *Atmospheric Environment (1967)* **13** (3), 395–405.
- TAYLOR, G. 1935 Statistical theory of turbulence: Parts i-iii. *Proceedings of the Royal Society of London. Series A, Mathematical and Physical Sciences* **151** (873), 421–464.
- TAYLOR, G. 1945 *Dynamics of a mass of hot gas rising in air*. U.S. Atomic Energy Commission MDDC 919. LADC 276.
- TAYLOR, G. I. 1958 Flow induced by jets. *Journal of the Aerospace Sciences* **25** (7), 464–465.
- TEIXEIRA, M. A. & MIRANDA, P. M. 1996 On the entrainment assumption in schatzmann’s integral plume model. *Applied Scientific Research* **57** (1), 15–42.
- TENNEKES, H. & LUMLEY, J. L. 1972 *A First Course in Turbulence*. MIT press.
- TIAN, X. & ROBERTS, P. J. 2003 A 3D LIF system for turbulent buoyant jet flows. *Experiments in Fluids* **35** (6), 636–647.
- TOHIDI, A. & KAYE, N. B. 2016 Highly buoyant bent-over plumes in a boundary layer. *Atmospheric Environment* **131**, 97–114.
- TURNER, J. 1960 A comparison between buoyant vortex rings and vortex pairs. *Journal of Fluid Mechanics* **7** (3), 419–432.

- TURNER, J. 1963 The motion of buoyant elements in turbulent surroundings. *Journal of Fluid Mechanics* **16** (1), 1–16.
- TURNER, J. 1986 Turbulent entrainment: the development of the entrainment assumption, and its application to geophysical flows. *Journal of Fluid Mechanics* **173**, 431–471.
- TURNER, J. S. 1973 *Buoyancy Effects in Fluids*. Cambridge university press.
- TYAGI, S., WANG, S. & MA, Z. 2007 Prediction, potential and control of plume from wet cooling tower of commercial buildings in hong kong: A case study. *International Journal of Energy Research* **31** (8), 778–795.
- VAN DEN BREMER, T. & HUNT, G. 2010 Universal solutions for Boussinesq and non-Boussinesq plumes. *Journal of Fluid Mechanics* **644**, 165–192.
- VANDERWEL, C. & TAVOULARIS, S. 2014 On the accuracy of PLIF measurements in slender plumes. *Experiments in Fluids* **55** (8), 1801.
- VANIERSCHOT, M. & VAN DEN BULCK, E. 2008 Influence of swirl on the initial merging zone of a turbulent annular jet. *Physics of fluids* **20** (10), 105104.
- VELDHUIZEN, H. & LEDBETTER, J. 1971 Cooling tower fog: control and abatement. *Journal of the Air Pollution Control Association* **21** (1), 21–24.
- VILLERMAUX, E. & REHAB, H. 2000 Mixing in coaxial jets. *Journal of Fluid Mechanics* **425**, 161–185.
- VITAGLIANO, V. & LYONS, P. A. 1956 Diffusion coefficients for aqueous solutions of sodium chloride and barium chloride. *Journal of the American Chemical Society* **78** (8), 1549–1552.
- WAITZ, I., QIU, Y., MANNING, T., FUNG, A., ELLIOT, J., KERWIN, J., KRASNODEBSKI, J., O’SULLIVAN, M., TEW, D., GREITZER, E. *et al.* 1997 Enhanced mixing with streamwise vorticity. *Progress in Aerospace Sciences* **33** (5-6), 323–351.
- WALSER, S. M., GERSTNER, D. G., BRENNER, B., HÖLLER, C., LIEBL, B. & HERR, C. E. 2014 Assessing the environmental health relevance of cooling towers—a systematic review of legionellosis outbreaks. *International journal of hygiene and environmental health* **217** (2-3), 145–154.
- WANG, H. & LAW, A. W.-K. 2002 Second-order integral model for a round turbulent buoyant jet. *Journal of Fluid Mechanics* **459**, 397–428.
- WANG, J., WANG, S., XU, X. & XIAO, F. 2009 Evaluation of alternative arrangements of a heat pump system for plume abatement in a large-scale chiller plant in a subtropical region. *Energy and Buildings* **41** (6), 596–606.
- WANG, S. & TYAGI, S. 2006 Report on the prediction, potential and control of plume from cooling towers of international commerce center. *The Hong Kong Polytechnic University, Hong Kong* .
- WANG, S., TYAGI, S., SHARMA, A. & KAUSHIK, S. 2007 Application of solar collectors to control the visible plume from wet cooling towers of a commercial building in hong kong: a case study. *Applied Thermal Engineering* **27** (8), 1394–1404.
- WANG, W., GE, X., ZHAO, S., ZHENG, H., XU, W., LV, J. & ZHU, G. 2019 A novel approach for water conservation and plume abatement in mechanical draft cooling towers. *Atmosphere* **10** (12), 734.

- WARDA, H., KASSAB, S., ELSHORBAGY, K. & ELSAADAWY, E. 1999 An experimental investigation of the near-field region of free turbulent round central and annular jets. *Flow Measurement and Instrumentation* **10** (1), 1–14.
- WEBSTER, H. & THOMSON, D. 2002 Validation of a Lagrangian model plume rise scheme using the Kincaid data set. *Atmospheric Environment* **36** (32), 5031–5042.
- WEIL, J. C. 1974 The rise of moist, buoyant plumes. *Journal of Applied Meteorology* **13** (4), 435–443.
- WEIL, J. C. 1988 Plume rise. In *Lectures on Air Pollution Modeling*, pp. 119–166. Springer.
- WESTERWEEL, J., FUKUSHIMA, C., PEDERSEN, J. M. & HUNT, J. 2009 Momentum and scalar transport at the turbulent/non-turbulent interface of a jet. *Journal of Fluid Mechanics* **631**, 199–230.
- WIGLEY, T. 1975*a* Condensation in jets, industrial plumes and cooling tower plumes. *Journal of Applied Meteorology* **14** (1), 78–86.
- WIGLEY, T. 1975*b* A numerical analysis of the effect of condensation on plume rise. *Journal of Applied Meteorology* **14** (6), 1105–1109.
- WIGLEY, T. & SLAWSON, P. 1971 On the condensation of buoyant, moist, bent-over plumes. *Journal of Applied Meteorology* **10** (2), 253–259.
- WIGLEY, T. & SLAWSON, P. 1972 A comparison of wet and dry bent-over plumes. *Journal of Applied Meteorology* **11** (2), 335–340.
- WILLIAMSON, N., ARMPFIELD, S. W. & LIN, W. 2011 Forced turbulent fountain flow behaviour. *Journal of Fluid Mechanics* **671**, 535–558.
- WINIARSKI, L. D. & FRICK, W. F. 1976 *Cooling Tower Plume Model*. US Environmental Protection Agency, Office of Research and Development.
- WINIARSKI, L. D. & FRICK, W. F. 1977 *Field Investigations of Mechanical Draft Cooling Tower Plumes*. US Environmental Protection Agency, Corvallis Environmental Research Laboratory, Office of Research and Development.
- WINTER, A. 1997 Control of visible plumes from cooling towers. *Proceedings of the Institution of Mechanical Engineers, Part A: Journal of Power and Energy* **211** (1), 67–72.
- WITHAM, F. & PHILLIPS, J. C. 2008 The dynamics and mixing of turbulent plumes in a turbulently convecting environment. *Journal of Fluid Mechanics* **602**, 39–61.
- WOODS, A. W. 1993 A model of the plumes above basaltic fissure eruptions. *Geophysical Research Letters* **20** (12), 1115–1118.
- WOODS, A. W. 2010 Turbulent plumes in nature. *Annual Review of Fluid Mechanics* **42**, 391–412.
- WOOLER, P., BURGHART, G. & GALLAGHER, J. 1967 Pressure distribution on a rectangular wing with a jet exhausting normally into an airstream. *Journal of Aircraft* **4** (6), 537–543.
- WU, F. H. & KOH, R. C. 1978 *Mathematical Model for Multiple Cooling Tower Plumes*, vol. 1. US Environmental Protection Agency, Office of Research and Development, Environmental Research Laboratory.

- YAKHOT, V., ORSZAG, S., THANGAM, S., GATSKI, T. & SPEZIALE, C. 1992 Development of turbulence models for shear flows by a double expansion technique. *Physics of Fluids A: Fluid Dynamics* **4** (7), 1510–1520.
- YANNOPOULOS, P. C. 1996 Superposition model for multiple plumes and jets predicting end effects. *Journal of Geophysical Research: Atmospheres* **101** (D10), 15153–15167.
- YANNOPOULOS, P. C. 2010 Advanced integral model for groups of interacting round turbulent buoyant jets. *Environmental Fluid Mechanics* **10** (4), 415–450.
- YANNOPOULOS, P. C. & NOUTSOPOULOS, G. C. 2006a Interaction of vertical round turbulent buoyant jets – Part I: Entrainment restriction approach. *Journal of Hydraulic Research* **44** (2), 218–232.
- YANNOPOULOS, P. C. & NOUTSOPOULOS, G. C. 2006b Interaction of vertical round turbulent buoyant jets – Part II: Superposition method. *Journal of Hydraulic Research* **44** (2), 233–248.
- YUAN, R., WU, X., LUO, T., LIU, H. & SUN, J. 2011 A review of water tank modeling of the convective atmospheric boundary layer. *Journal of Wind Engineering and Industrial Aerodynamics* **99** (10), 1099–1114.
- ZANDIAN, A. & ASHJAEI, M. 2013 The thermal efficiency improvement of a steam rankine cycle by innovative design of a hybrid cooling tower and a solar chimney concept. *Renewable Energy* **51**, 465–473.

Appendix A

Derivation of the integral form of governing equations for a uniform plume in stationary ambient

The following method of deriving governing equations, for a plume sketched in figure A.1, is to integrate the differential form of conservation equations with respect to the radial direction, based on some assumptions to be stated clearly below. The main references include Morton *et al.* (1956), Wu & Koh (1978), Fischer *et al.* (1979), Briggs (1975, 1984), Linden (2000) and Bailly & Comte-Bellot (2015).

A.1 Conservation of mass

For a point within the plume, the mass conservation equation reads

$$\frac{\partial \rho}{\partial t} + \frac{1}{r} \frac{\partial}{\partial r}(r\rho u) + \frac{1}{r} \frac{\partial}{\partial \theta}(\rho v) + \frac{\partial}{\partial z}(\rho w) = 0, \quad (\text{A.1})$$

where ρ is the local density, u , v and w are the respective radial, tangential and vertical (i.e. r , θ and z) components of the velocity. **Assume the flow is steady-state**¹, thus the derivative with respect to time is dropped. Invoking the **Boussinesq approximation**² which states that density variations can be neglected except where ρ is multiplied with gravitational acceleration, g , (A.1) can be rewritten as

$$\frac{1}{r} \frac{\partial}{\partial r}(ru) + \frac{1}{r} \frac{\partial v}{\partial \theta} + \frac{\partial w}{\partial z} = 0. \quad (\text{A.2})$$

¹On timescales long compared to the eddy turnover time, the plume flow and the entrainment process can be considered as steady-state (Woods, 2010).

²Boussinesq approximation is valid in the atmosphere provided that the velocity is small compared to the speed of sound and the vertical scale of motion is much less than the scale height of 10 km.

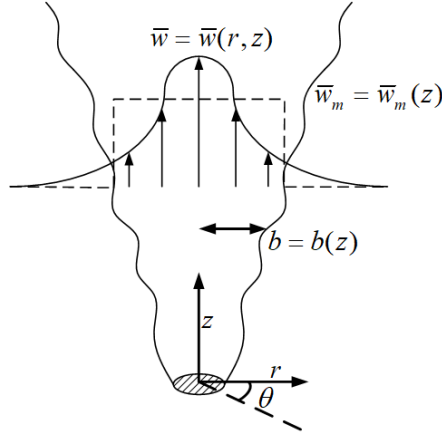


Figure A.1: Schematic of an axisymmetric plume in a homogeneous ambient. $b = b(z)$ is the plume radius and $\bar{w} = \bar{w}(r, z)$ is the time-averaged vertical velocity. $\bar{w}_m = \bar{w}_m(z)$ is the mean vertical velocity assuming a “top-hat” profile (the plume properties e.g. velocity and buoyancy are taken to be constant within the plume and zero outside).

By the Reynolds decomposition, u , v and w can be expressed as $u = \bar{u} + u'$, $v = \bar{v} + v'$ and $w = \bar{w} + w'$ where the primed variables denote the fluctuating components. Then the time-averaged (Reynolds averaged) volume conservation equation reads

$$\frac{1}{r} \frac{\partial(r\bar{u})}{\partial r} + \frac{1}{r} \frac{\partial\bar{v}}{\partial\theta} + \frac{\partial\bar{w}}{\partial z} = 0. \quad (\text{A.3})$$

Using the **assumption of plume axisymmetry** i.e. $\frac{\partial\bar{v}}{\partial\theta} = 0$, (A.3) is simplified as

$$\frac{1}{r} \frac{\partial(r\bar{u})}{\partial r} + \frac{\partial\bar{w}}{\partial z} = 0. \quad (\text{A.4})$$

Integrating (A.4) over a horizontal plane intersecting the plume at some point on the z -axis yields

$$\int_0^\infty 2\pi \frac{\partial(r\bar{u})}{\partial r} dr + \int_0^\infty 2\pi r \frac{\partial\bar{w}}{\partial z} dr = 0$$

The second term on the LHS can be written as follows:

$$\begin{aligned} \frac{d}{dz} \left(\int_0^\infty 2\pi r \bar{w} dr \right) &= - \int_0^\infty 2\pi \frac{\partial(r\bar{u})}{\partial r} dr \\ &= - [2\pi r \bar{u}]_0^\infty \\ &= - \lim_{r \rightarrow \infty} [2\pi r \bar{u}] \quad \leftarrow \text{entrainment from infinity} \\ &= 2\pi b \bar{u}_e \quad \leftarrow \text{entrainment at the plume edge} \\ \therefore \frac{d\bar{Q}}{dz} &= 2\pi b \bar{u}_e, \end{aligned} \quad (\text{A.5})$$

where $\bar{Q} = \int_0^\infty 2\pi r \bar{w} dr$ is the mean volume flux and \bar{u}_e is the entrainment velocity at the plume edge.

G.I. Taylor's entrainment hypothesis states that the entrainment velocity at the plume edge is proportional to the local mean vertical velocity at the corresponding height, i.e.

$$\bar{u}_e = \alpha \bar{w}_m, \quad (\text{A.6})$$

where α denotes the entrainment coefficient. Substituting (A.6) into (A.5) gives the integral form of the volume conservation equation as follows:

$$\frac{d\bar{Q}}{dz} = 2\pi b\alpha \bar{w}_m. \quad (\text{A.7})$$

A.2 Conservation of momentum

The Navier-Stokes equations for a plume flowing vertically upwards are as follows:

$$(\text{NS} - r) \rightarrow \frac{Du}{Dt} - \frac{v^2}{r} = -\frac{1}{\rho_0} \frac{\partial P}{\partial r} + \nu \left(\nabla^2 u - \frac{u}{r^2} - \frac{2}{r^2} \frac{\partial v}{\partial \theta} \right), \quad (\text{A.8})$$

$$(\text{NS} - \theta) \rightarrow \frac{Dv}{Dt} + \frac{uv}{r} = -\frac{1}{\rho_0 r} \frac{\partial P}{\partial \theta} + \nu \left(\nabla^2 v + \frac{2}{r^2} \frac{\partial u}{\partial \theta} - \frac{v}{r^2} \right), \quad (\text{A.9})$$

$$(\text{NS} - z) \rightarrow \frac{Dw}{Dt} = -g \frac{\rho}{\rho_0} - \frac{1}{\rho_0} \frac{\partial P}{\partial z} + \nu \nabla^2 w, \quad (\text{A.10})$$

where the operators $\frac{Df}{Dt} = \frac{\partial f}{\partial t} + \frac{1}{r} \frac{\partial(fr u)}{\partial r} + \frac{1}{r} \frac{\partial(f v)}{\partial \theta} + \frac{\partial(f w)}{\partial z}$ and $\nabla^2 f = \frac{1}{r} \frac{\partial}{\partial r} (r \frac{\partial f}{\partial r}) + \frac{1}{r^2} \frac{\partial^2 f}{\partial \theta^2} + \frac{\partial^2 f}{\partial z^2}$ with f denoting a generic scalar quantity, and ρ_0 is the reference density. Extending the Reynolds decomposition to the pressure ($P = \bar{P} + P'$) and density ($\rho = \bar{\rho} + \rho'$) and using the **assumption of plume axisymmetry** i.e. $\bar{v} = 0$, $\frac{\partial \bar{f}}{\partial \theta} = 0$ and $\overline{u'v'} = \overline{w'v'} = 0$ (the turbulence is homogeneous in the tangential direction, see Bailly & Comte-Bellot, 2015), the Reynolds averaged Navier-Stokes equations are given as follows:

$$(\text{RANS} - r) \rightarrow \frac{D\bar{u}}{Dt} = -\frac{1}{\rho_0} \frac{\partial \bar{P}}{\partial r} - \frac{1}{r} \frac{\partial(r \overline{u'^2})}{\partial r} - \frac{\partial \overline{u'w'}}{\partial z} + \frac{\overline{v'^2}}{r} + \nu \left(\nabla^2 \bar{u} - \frac{\bar{u}}{r^2} \right), \quad (\text{A.11})$$

$$(\text{RANS} - \theta) \rightarrow 0 = -\frac{1}{\rho_0 r} \frac{\partial \bar{P}}{\partial \theta}, \quad (\text{A.12})$$

$$(\text{RANS} - z) \rightarrow \frac{D\bar{w}}{Dt} = -g \frac{\bar{\rho}}{\rho_0} - \frac{1}{\rho_0} \frac{\partial \bar{P}}{\partial z} - \frac{1}{r} \frac{\partial(r \overline{u'w'})}{\partial r} - \frac{\partial \overline{w'^2}}{\partial z} + \nu \nabla^2 \bar{w}, \quad (\text{A.13})$$

where the operator $\frac{D\bar{f}}{Dt} = \frac{1}{r} \frac{\partial(r \bar{u} \bar{f})}{\partial r} + \frac{\partial(\bar{w} \bar{f})}{\partial z} = \bar{u} \frac{\partial \bar{f}}{\partial r} + \bar{w} \frac{\partial \bar{f}}{\partial z}$ (using (A.4)). Equation (A.12) implies that the time-averaged pressure $\bar{P} = \bar{P}(r, z)$.

Assume that the plume is relatively thin thus the boundary layer approximation can be applied. Characteristic length scales (b, L) and velocity scales (\bar{u}, \bar{w}) are

used for the radial and vertical directions, respectively. Only a single velocity scale, w' , is used to characterize the fluctuating velocity. A scaling analysis for the volume conservation equation i.e. (A.4) yields

$$\frac{1}{r} \frac{\partial(r\bar{u})}{\partial r} + \frac{\partial\bar{w}}{\partial z} = 0. \quad (\text{A.14})$$

$$\frac{\bar{u}}{b} \sim \frac{\bar{w}}{L}$$

Thus $\bar{u} \sim \frac{b}{L} \bar{w}$. The boundary layer approximation requires that $\frac{b}{L} \ll 1$, therefore we have $\frac{\bar{u}}{b} \ll 1$.

Analogously for the RANS equation in the z direction, a scaling analysis yields

$$\bar{u} \frac{\partial\bar{w}}{\partial r} + \bar{w} \frac{\partial\bar{w}}{\partial z} = -g \frac{\bar{\rho}}{\rho_0} - \frac{1}{\rho_0} \frac{\partial\bar{P}}{\partial z} - \frac{1}{r} \frac{\partial(r \overline{u'w'})}{\partial r} - \frac{\partial\overline{w'^2}}{\partial z} + \nu \nabla^2 \bar{w} \quad (\text{A.15})$$

$$\frac{\bar{u}\bar{w}}{b} \quad \frac{\bar{w}^2}{L} \quad \frac{w'^2}{b} \quad \frac{w'^2}{L} \quad \nu \left(\frac{\bar{w}}{b^2} + \frac{\bar{w}}{L^2} \right)$$

Because $\frac{b}{L} \ll 1$, we obtain $\frac{\bar{u}\bar{w}}{b} \sim \frac{\bar{w}^2}{L}$, $\frac{w'^2}{b} \gg \frac{w'^2}{L}$ and $\frac{\bar{w}}{b^2} \gg \frac{\bar{w}}{L^2}$. The viscous term therefore scales with $\nu \frac{\bar{w}}{b^2} = \frac{\bar{w}^2}{L} \frac{L}{b} \frac{\nu}{\bar{w}b} = \frac{1}{\text{Re}} \frac{\bar{w}^2}{L} \frac{L}{b}$, and for **fully turbulent flows with relatively large Reynolds number**, viscous effects can be neglected. Moreover, if we **assume that the rate of mean vertical momentum transfer due to the turbulent fluctuations is small compared to that due to advection**, the Reynolds stress term i.e. $\frac{1}{r} \frac{\partial(r \overline{u'w'})}{\partial r}$ can be dropped thus (A.15) becomes

$$\bar{u} \frac{\partial\bar{w}}{\partial r} + \bar{w} \frac{\partial\bar{w}}{\partial z} = -g \frac{\bar{\rho}}{\rho_0} - \frac{1}{\rho_0} \frac{\partial\bar{P}}{\partial z}, \quad (\text{A.16})$$

which implies that $\bar{P} \sim \rho_0 \bar{w}^2$.

For the RANS equation in the r direction, the scaling analysis is given as follows:

$$\bar{u} \frac{\partial\bar{u}}{\partial r} + \bar{w} \frac{\partial\bar{u}}{\partial z} = -\frac{1}{\rho_0} \frac{\partial\bar{P}}{\partial r} - \frac{1}{r} \frac{\partial(r \overline{u'^2})}{\partial r} - \frac{\partial\overline{u'w'}}{\partial z} + \frac{\overline{v'^2}}{r} + \nu \left(\nabla^2 \bar{u} - \frac{\bar{u}}{r^2} \right) \quad (\text{A.17})$$

$$\frac{\bar{u}\bar{u}}{b} \quad \frac{\bar{w}\bar{u}}{L} \quad \frac{\bar{w}^2}{b} \quad \frac{w'^2}{b} \quad \frac{w'^2}{L} \quad \frac{w'^2}{b} \quad \nu \left[\left(\frac{\bar{u}}{b^2} + \frac{\bar{u}}{L^2} \right); \frac{\bar{u}}{b^2} \right]$$

The scaling in question implies that the order of magnitude of the pressure gradient term i.e. $\frac{1}{\rho_0} \frac{\partial\bar{P}}{\partial r}$ is much greater than all the other terms, thus (A.17) can be simplified as $\frac{\partial\bar{P}}{\partial r} = 0$, which indicates $\bar{P} = \bar{P}(z)$. Therefore, we argue that the pressure within the plume is imposed by the external (hydrostatic) ambient $\bar{P}(z) = P_a(z)$.

Note that for the external ambient with $\rho_a = \rho_a(z)$ and $w = 0$, the pressure distribution must be hydrostatic such that

$$\frac{\partial \bar{P}}{\partial z} = -g\rho_a. \quad (\text{A.18})$$

Substituting (A.18) into (A.16) yields

$$\bar{u} \frac{\partial \bar{w}}{\partial r} + \bar{w} \frac{\partial \bar{w}}{\partial z} = \frac{g}{\rho_0}(\rho_a - \bar{\rho}) = \bar{g}'. \quad (\text{A.19})$$

Integrating (A.19) over a horizontal plane that slices the plume yields

$$\begin{aligned} \int_0^\infty 2\pi r \left(\bar{u} \frac{\partial \bar{w}}{\partial r} + \bar{w} \frac{\partial \bar{w}}{\partial z} \right) dr &= \int_0^\infty 2\pi r \bar{g}' dr \\ \int_0^\infty 2\pi r \bar{u} \frac{\partial \bar{w}}{\partial r} dr &= [2\pi r \bar{u} \bar{w}]_0^\infty - \int_0^\infty 2\pi \bar{w} \frac{\partial(r\bar{u})}{\partial r} dr \quad \leftarrow \text{integration by parts} \\ &= 0 + \int_0^\infty 2\pi r \bar{w} \frac{\partial \bar{w}}{\partial z} dr \quad \leftarrow \text{using (A.4)} \\ &= \int_0^\infty 2\pi r \bar{w} \frac{\partial \bar{w}}{\partial z} dr \\ \therefore \text{LHS} &= 2 \int_0^\infty 2\pi r \bar{w} \frac{\partial \bar{w}}{\partial z} dr \\ &= \frac{d}{dz} \int_0^\infty 2\pi r \bar{w}^2 dr \\ &= \text{RHS} = \int_0^\infty 2\pi r \bar{g}' dr \\ \therefore \frac{d\bar{M}}{dz} &= 2\pi g \int_0^\infty r \frac{\rho_a - \bar{\rho}}{\rho_0} dr, \end{aligned} \quad (\text{A.20})$$

where $\bar{M} = \int_0^\infty 2\pi r \bar{w}^2 dr$ is the mean momentum flux.

A.3 Conservation of any scalar component

Equation (A.20) introduces the density variation between the plume and the ambient fluid, which can be resolved by the conservation of temperature or moisture in the context of cooling tower plumes. The scalar conservation equation **assuming no sources, sinks or chemical reactions** reads

$$\frac{Dc}{Dt} = \kappa \nabla^2 c, \quad (\text{A.21})$$

where c denotes either temperature or humidity or any passive scalar concentration with κ as the corresponding transport coefficient. c can be decomposed as $c = \bar{c} + c'$, whereby the Reynolds averaged scalar transport equation is given as

$$\underbrace{\frac{1}{r} \frac{\partial(r \bar{c} \bar{u})}{\partial r}}_{\text{Advection}} + \underbrace{\frac{\partial(\bar{c} \bar{w})}{\partial z}}_{\text{Diffusion}} = \kappa \left[\underbrace{\frac{1}{r} \frac{\partial}{\partial r} \left(r \frac{\partial \bar{c}}{\partial r} \right)}_{\text{Diffusion}} + \frac{\partial^2 \bar{c}}{\partial z^2} \right] - \underbrace{\frac{1}{r} \frac{\partial(\overline{u' c'})}{\partial r}}_{\text{Turbulent transport}} - \frac{\partial(\overline{w' c'})}{\partial z}. \quad (\text{A.22})$$

Because **molecular diffusion is negligible compared to turbulent transport, and the turbulent (scalar) flux comprises only a small fraction of the mean (scalar) flux** (Linden, 2000), the diffusion and turbulent transport terms on the right-hand side of (A.22) can be dropped and to first order the scalar transport equation is rewritten as

$$\frac{1}{r} \frac{\partial(r \bar{c} \bar{u})}{\partial r} + \frac{\partial(\bar{c} \bar{w})}{\partial z} = 0. \quad (\text{A.23})$$

Integrating (A.23) over a horizontal plane yields

$$\int_0^\infty 2\pi \frac{\partial(r \bar{c} \bar{u})}{\partial r} dr + \int_0^\infty 2\pi r \frac{\partial(\bar{c} \bar{w})}{\partial z} dr = 0$$

The latter term on the LHS can be expressed as

$$\int_0^\infty 2\pi r \frac{\partial(\bar{c} \bar{w})}{\partial z} dr = \frac{d}{dz} \int_0^\infty 2\pi r \bar{c} \bar{w} dr$$

The former term on the LHS can be expressed as

$$\begin{aligned} \int_0^\infty 2\pi \frac{\partial(r \bar{c} \bar{u})}{\partial r} dr &= [2\pi r \bar{c} \bar{u}]_0^\infty \\ &= \lim_{r \rightarrow \infty} [2\pi r \bar{c} \bar{u}] \end{aligned}$$

$$\therefore \frac{d}{dz} \int_0^\infty 2\pi r \bar{c} \bar{w} dr = - \lim_{r \rightarrow \infty} [2\pi r \bar{c} \bar{u}]. \quad (\text{A.24})$$

To resolve the inflow of scalar flux term on the RHS of (A.24), we need to consider the scalar (concentration) in the ambient i.e. $c_a = c_a(z)$, which may vary with elevation. Multiply both sides of (A.4) with c_a and then integrate over a horizontal plane to give

$$\int_0^\infty 2\pi c_a \frac{\partial(r \bar{u})}{\partial r} dr + \int_0^\infty 2\pi r c_a \frac{\partial \bar{w}}{\partial z} dr = 0$$

The latter term on the LHS is given by

$$\begin{aligned} \int_0^\infty 2\pi r c_a \frac{\partial \bar{w}}{\partial z} dr &= \int_0^\infty 2\pi r \frac{\partial(c_a \bar{w})}{\partial z} dr - \int_0^\infty 2\pi r \bar{w} \frac{\partial c_a}{\partial z} dr \\ &= \frac{d}{dz} \int_0^\infty 2\pi r c_a \bar{w} dr - \frac{dc_a}{dz} \int_0^\infty 2\pi r \bar{w} dr \end{aligned}$$

The former term on the LHS is given by

$$\begin{aligned} \int_0^\infty 2\pi c_a \frac{\partial(r \bar{u})}{\partial r} dr &= [2\pi r c_a \bar{u}]_0^\infty \\ &= \lim_{r \rightarrow \infty} [2\pi r c_a \bar{u}] \end{aligned}$$

$$\therefore \frac{d}{dz} \int_0^\infty 2\pi r c_a \bar{w} dr = - \lim_{r \rightarrow \infty} [2\pi r c_a \bar{w}] + \frac{dc_a}{dz} \int_0^\infty 2\pi r \bar{w} dr. \quad (\text{A.25})$$

Subtracting (A.25) from (A.24) yields

$$\frac{d}{dz} \int_0^\infty 2\pi r \bar{w} (\bar{c} - c_a) dr = - \lim_{r \rightarrow \infty} [2\pi r \bar{w} (\bar{c} - c_a)] - \frac{dc_a}{dz} \int_0^\infty 2\pi r \bar{w} dr. \quad (\text{A.26})$$

As $r \rightarrow \infty$, $\bar{c} - c_a \rightarrow 0$, thus (A.26) is simplified as

$$\frac{d}{dz} \int_0^\infty 2\pi r \bar{w} (\bar{c} - c_a) dr = - \frac{dc_a}{dz} \int_0^\infty 2\pi r \bar{w} dr = 0, \quad (\text{unstratified ambient}) \quad (\text{A.27})$$

where $\frac{dc_a}{dz} = 0$ corresponds to an unstratified ambient.

In the context of cooling tower plumes, we consider separately the conservations of thermal energy and moisture. In the former case, we need to add the release of latent heat in case of condensation within the plume; the resulting equation reads

$$\frac{d}{dz} \int_0^\infty 2\pi r \bar{w} \left[(\bar{t} - t_a) - \frac{L_v}{c_{pa}} \bar{\sigma} \right] dr = 0, \quad (\text{A.28})$$

where t and t_a are the temperature of the plume and the ambient, measured in °C. σ is the plume specific liquid moisture (we assume that the ambient specific liquid moisture is $\sigma_a = 0$, which is valid whenever it is not raining). $L_v = L_v(\bar{t}) = 4.1868 [597.31 - 0.57 \bar{t}]$ represents the latent heat and is measured in J/g, and $c_{pa} = 1.006$ J/(g K) is the specific heat of air at constant pressure. Defining $\Theta = \int_0^\infty 2\pi r \bar{w} (\bar{t} - t_a) dr$ and $W = \int_0^\infty 2\pi r \bar{w} \sigma dr$ as the respective mean temperature deficiency flux and specific liquid moisture flux, the thermal energy conservation equation is given as

$$\frac{d}{dz} \left(\Theta - \frac{L_v}{c_{pa}} W \right) = 0. \quad (\text{A.29})$$

Similarly the moisture conservation equation is given as

$$\frac{d}{dz} \int_0^\infty 2\pi r \bar{w} [(\bar{q} - q_a) + \bar{\sigma}] = 0, \quad (\text{A.30})$$

where q and q_a are the respective specific humidities of the plume and the ambient. Defining the specific humidity deficiency flux as $H = \int_0^\infty 2\pi r \bar{w} (\bar{q} - q_a) dr$, moisture conservation is expressed as

$$\frac{d}{dz} (H + W) = 0. \quad (\text{A.31})$$

A.4 Governing equations for a uniform cooling tower plume

Sections A.1, A.2 and A.3 show that the governing equations pertain only to the mean flow quantities, thus the overbar can be dropped for simplicity. Assuming **“top-hat” profiles for plume velocity, temperature, specific humidity and liquid moisture**, the flux parameters can be simplified as $Q = \pi b^2 w$, $M = \pi b^2 w^2$, $\Theta = \pi b^2 w(t - t_a)$, $H = \pi b^2 w(q - q_a)$ and $W = \pi b^2 w \sigma$. Now the only unknown is how to relate the density of the moist plume to the temperature and moisture. For this purpose, an equation of state is necessary.

Here we introduce the virtual temperature when calculating plume densities. The virtual temperature, t_v , corresponds to the temperature of dry air having the same density as a parcel of moist air at an identical pressure (Curry & Webster, 1998). For purposes of including condensation, we adopt the virtual temperature for foggy air³ and use the following expression, presented by Emanuel (1994):

$$t_v = t(1 + 0.608q - \sigma), \quad (\text{A.32})$$

$$P = \rho R_a t_v, \quad (\text{A.33})$$

where t and t_v are measured in Kelvin, P is the total pressure inside/outside the plume and $R_a = 287.058 \text{ J/kg K}$ is the gas constant of air. Note that the above definition for t_v incorporates liquid moisture to express the change in bulk density as a result of condensed water. Therefore, the density difference in (A.20) can be expressed using the virtual temperature

$$g' = g \frac{\rho_a - \rho}{\rho_0} = g \frac{\rho_a - \rho}{\rho_a} = g \left(1 - \frac{\frac{P}{R_a t_{v,p}}}{\frac{P}{R_a t_{v,a}}} \right) = g \left(1 - \frac{t_{v,a}}{t_{v,p}} \right), \quad (\text{A.34})$$

where $t_{v,p}$ and $t_{v,a}$ are the virtual temperature of the plume and the ambient, respectively. Moreover, the density of ambient fluid is used as the reference density throughout the whole formulation. Thus the governing equations for a uniform plume in a homogeneous ambient are given as follows:

$$\frac{dQ}{dz} = 2\alpha\pi^{1/2} M^{1/2}, \quad (\text{A.35})$$

$$\frac{dM}{dz} = g' \frac{Q^2}{M}, \quad (\text{A.36})$$

³Moist air can be regarded as a limiting case of foggy air where the liquid moisture content is zero, i.e. $\sigma = 0$.

$$\frac{d}{dz} \left(\Theta - \frac{L_v}{c_{pa}} W \right) = 0, \quad (\text{A.37})$$

$$\frac{d}{dz} (H + W) = 0, \quad (\text{A.38})$$

where g' is given by (A.34). Equations (A.35) to (A.38) constitute four ordinary differential equations in the five unknown parameters i.e. Q , M , Θ , H and W . Model closure is achieved by noting that

$$\begin{aligned} \sigma &= 0, & \text{for } q < q_s \text{ (dry plume)} \\ q &= q_s(t, P), & \text{for } q \geq q_s \text{ (wet plume)} \end{aligned} \quad (\text{A.39})$$

where q_s is the saturation specific humidity and P is the total pressure. The former quantity is given by

$$q_s(t, P) = \frac{M_v P_{sv}(t)}{M_a [P - P_{sv}(t)] + M_v P_{sv}(t)}, \quad (\text{A.40})$$

where $M_v = 18.02 \times 10^{-3}$ kg/mol is the water molar mass, $M_a = 28.966 \times 10^{-3}$ kg/mol is the air molar mass, and P_{sv} is the saturated water vapor pressure. Within the temperature range of 0 to 200 °C, P_{sv} , measured in Pa, is given by (ASHRAE, 2013a)

$$P_{sv} = e^{C_1/t + C_2 + C_3 t + C_4 t^2 + C_5 t^3 + C_6 \ln t}, \quad (\text{A.41})$$

$$\begin{aligned} C_1 &= -5.8002206 \times 10^3 \text{ K}, & C_2 &= 1.3914993, \\ C_3 &= -4.8640239 \times 10^{-2} \text{ K}^{-1}, & C_4 &= 4.1764768 \times 10^{-5} \text{ K}^{-2}, \\ C_5 &= 1.4452093 \times 10^{-8} \text{ K}^{-3}, & C_6 &= 6.5459673. \end{aligned}$$

Recall, finally, that the total pressure inside the plume changes hydrostatically with elevation with respect to the ambient density (see (A.18)), i.e.

$$P = P_0 - \rho_a g z. \quad (\text{A.42})$$

Here, P_0 denotes the pressure at the top of the cooling tower and ρ_a can be calculated using (A.33).

Appendix B

Derivation of the integral form of governing equations for a coaxial plume in stationary ambient

B.1 Conservation of volume, thermal energy and moisture

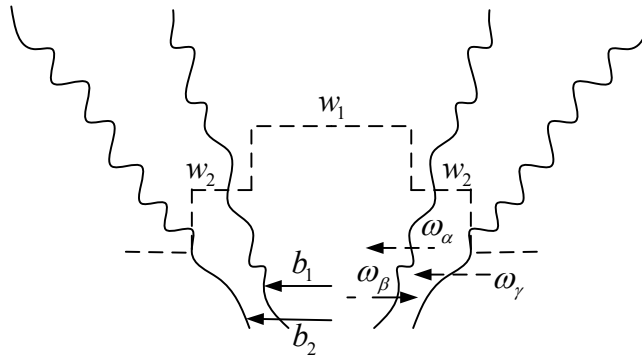


Figure B.1: Schematic of a coaxial plume in a homogeneous ambient. w_1 and w_2 are the respective vertical velocities of the inner and outer plumes, corresponding to plume radii b_1 and b_2 (denoted by solid arrows). ω_α , ω_β and ω_γ (denoted by dashed arrows) are the respective entrainment velocities from the outer to the inner plume, from the inner to the outer plume and from the ambient to the outer plume. Hereafter subscripts 1 and 2 are used to denote the inner and outer plumes, respectively.

The derivation of governing equations for a coaxial plume retains the following assumptions for a uniform plume:

- (i) Molecular diffusion is negligible compared to turbulent transport. The flow is fully turbulent thus viscous effects can be neglected.

- (ii) The vertical turbulent transport is small compared to the vertical transport by advection.
- (iii) “Top-hat” profiles are assumed for the plume vertical velocity, temperature, specific humidity and specific liquid moisture.
- (iv) The Boussinesq approximation is valid.

In the context of coaxial plumes, Morton’s entrainment assumption (Morton, 1962) for coaxial turbulent jets is adapted to relate the horizontal entrainment velocities to the plume vertical velocities, which is mathematically stated as

$$\omega_\alpha = \alpha|w_1 - w_2|, \quad \omega_\beta = \beta w_2, \quad \omega_\gamma = \gamma w_2, \quad (\text{B.1})$$

where α , β and γ are the entrainment coefficients from the outer to the inner plume, from the inner to the outer plume and from the ambient to the outer plume.

It is helpful to define an equivalent set of integral parameters as follows:

$$Q_1 = \pi b_1^2 w_1, \quad Q_2 = \pi (b_2^2 - b_1^2) w_2, \quad (\text{B.2})$$

$$M_1 = \pi b_1^2 w_1^2, \quad M_2 = \pi (b_2^2 - b_1^2) w_2^2, \quad (\text{B.3})$$

$$\Theta_1 = \pi b_1^2 w_1 (t_1 - t_a), \quad \Theta_2 = \pi (b_2^2 - b_1^2) w_2 (t_2 - t_a), \quad (\text{B.4})$$

$$H_1 = \pi b_1^2 w_1 (q_1 - q_a), \quad H_2 = \pi (b_2^2 - b_1^2) w_2 (q_2 - q_a), \quad (\text{B.5})$$

$$W_1 = \pi b_1^2 w_1 \sigma_1, \quad W_2 = \pi (b_2^2 - b_1^2) w_2 \sigma_2. \quad (\text{B.6})$$

Considering the coaxial plume as a whole, the combined volume flux, momentum flux, excess temperature flux, specific humidity flux and specific liquid moisture flux must satisfy appropriately modified forms of equations (A.7), (A.20), (A.28) and (A.30), i.e.

$$\frac{d}{dz} (Q_1 + Q_2) = 2\pi b_2 \omega_\gamma, \quad (\text{B.7})$$

$$\frac{d}{dz} (M_1 + M_2) = \pi b_1^2 g'_1 + \pi (b_2^2 - b_1^2) g'_2, \quad (\text{B.8})$$

$$\frac{d}{dz} \left[\left(\Theta_1 - \frac{L_{v,1}}{c_{pa}} W_1 \right) + \left(\Theta_2 - \frac{L_{v,2}}{c_{pa}} W_2 \right) \right] = 0, \quad (\text{B.9})$$

$$\frac{d}{dz} [(H_1 + W_1) + (H_2 + W_2)] = 0, \quad (\text{B.10})$$

where $g'_1 = g \frac{\rho_a - \rho_1}{\rho_a}$ and $g'_2 = g \frac{\rho_a - \rho_2}{\rho_a}$ are the respective reduced gravities of the inner and outer plumes. Hereafter, we seek to formulate the conservation equations for the inner plume.

Both entrainment and detrainment occur at the edge of the inner plume, thus the volume conservation reads

$$\frac{dQ_1}{dz} = -[2\pi r u]_{\text{inner plume edge}} = 2\pi b_1 (\omega_\alpha - \omega_\beta) . \quad (\text{B.11})$$

Analogously the thermal energy conservation following (A.26) reads

$$\begin{aligned} \frac{d}{dz} \left(\Theta_1 - \frac{L_{v,1}}{c_{pa}} W_1 \right) &= - \left[2\pi r u \left(t - t_a - \frac{L_v}{c_{pa}} \sigma \right) \right]_{\text{inner plume edge}} \\ &= 2\pi b_1 \left[\omega_\alpha \left(t_2 - t_a - \frac{L_{v,2}}{c_{pa}} \sigma_2 \right) - \omega_\beta \left(t_1 - t_a - \frac{L_{v,1}}{c_{pa}} \sigma_1 \right) \right] \\ &= 2\pi b_1 \left[\omega_\alpha \left(\frac{\Theta_2}{Q_2} - \frac{L_{v,2}}{c_{pa}} \frac{W_2}{Q_2} \right) - \omega_\beta \left(\frac{\Theta_1}{Q_1} - \frac{L_{v,1}}{c_{pa}} \frac{W_1}{Q_1} \right) \right] . \end{aligned} \quad (\text{B.12})$$

The moisture conservation equation is given as

$$\begin{aligned} \frac{d}{dz} (H_1 + W_1) &= - [2\pi r u (q - q_a + \sigma)]_{\text{inner plume edge}} \\ &= 2\pi b_1 [\omega_\alpha (q_2 - q_a + \sigma_2) - \omega_\beta (q_1 - q_a + \sigma_1)] \\ &= 2\pi b_1 \left(\omega_\alpha \frac{H_2 + W_2}{Q_2} - \omega_\beta \frac{H_1 + W_1}{Q_1} \right) . \end{aligned} \quad (\text{B.13})$$

Respectively subtracting equations (B.11), (B.12) and (B.13) from equations (B.7), (B.9) and (B.10) yields the conservation of volume, thermal energy and moisture for the outer plume as follows:

$$\frac{dQ_2}{dz} = 2\pi b_1 (\omega_\beta - \omega_\alpha) + 2\pi b_2 \omega_\gamma , \quad (\text{B.14})$$

$$\frac{d}{dz} \left(\Theta_2 - \frac{L_{v,2}}{c_{pa}} W_2 \right) = 2\pi b_1 \left[\omega_\beta \left(\frac{\Theta_1}{Q_1} - \frac{L_{v,1}}{c_{pa}} \frac{W_1}{Q_1} \right) - \omega_\alpha \left(\frac{\Theta_2}{Q_2} - \frac{L_{v,2}}{c_{pa}} \frac{W_2}{Q_2} \right) \right] , \quad (\text{B.15})$$

$$\frac{d}{dz} (H_2 + W_2) = 2\pi b_1 \left(\omega_\beta \frac{H_1 + W_1}{Q_1} - \omega_\alpha \frac{H_2 + W_2}{Q_2} \right) . \quad (\text{B.16})$$

Unlike the conservation of volume, thermal energy and moisture, the momentum equations become nontrivial due to different methods of evaluating the buoyant body forces acting on the inner and outer plumes. McDougall (1978, 1981) concluded that there exist two reasonable approaches to evaluate the body force. The former body force formulation (referred to as BFI by Bloomfield & Kerr, 2000) retains the assumption of a hydrostatic flow. The latter formulation (referred to as BFII by Bloomfield & Kerr, 2000) evaluates the body force of the inner plume relative to the buoyancy of the outer plume, not the ambient. In other words, the body force is determined by computing the density difference between the inner and outer plumes and by considering the acceleration of the outer plume.

B.2 Momentum conservation - BFI

BFI assumes that constant pressure surfaces are everywhere horizontal across the ambient, the outer plume, and the inner plume, i.e. $\frac{dP_a}{dz} = \frac{dP_2}{dz} = \frac{dP_1}{dz} = -g\rho_a$.

Thus the Navier-Stokes equation in the z direction for the inner plume follows (A.19)

$$u \frac{\partial w}{\partial r} + w \frac{\partial w}{\partial z} = g'_1, \quad (\text{B.17})$$

where $g'_1 = g \left(1 - \frac{t_{v,a}}{t_{v,1}}\right)$ and $t_{v,1}$ is the virtual temperature of the inner plume. Integrating (B.17) over the cross-sectional area of the inner plume yields

$$\begin{aligned} \int_0^{b_1} 2\pi r \left(u \frac{\partial w}{\partial r} + w \frac{\partial w}{\partial z} \right) dr &= \int_0^{b_1} 2\pi r g'_1 dr \\ \int_0^{b_1} 2\pi r u \frac{\partial w}{\partial r} dr &= [2\pi r u w]_0^{b_1} - \int_0^{b_1} 2\pi w \frac{\partial(ru)}{\partial r} dr \quad \leftarrow \text{integration by parts} \\ &= [2\pi r u w]_{\text{inner plume edge}} + \int_0^{b_1} 2\pi r w \frac{\partial w}{\partial z} dr \quad \leftarrow \text{using (A.4)} \\ \therefore \text{LHS} &= [2\pi r u w]_{\text{inner plume edge}} + 2 \int_0^{b_1} 2\pi r w \frac{\partial w}{\partial z} dr \\ &= [2\pi r u w]_{\text{inner plume edge}} + \frac{d}{dz} \int_0^{b_1} 2\pi r w^2 dr \\ &= 2\pi b_1 (\omega_\beta w_1 - \omega_\alpha w_2) + \frac{d}{dz} \int_0^{b_1} 2\pi r w^2 dr \\ &= \text{RHS} = \int_0^{b_1} 2\pi r g'_1 dr = \pi b_1^2 g'_1 \\ \therefore \frac{dM_1}{dz} &= \pi b_1^2 g'_1 + 2\pi b_1 (\omega_\alpha w_2 - \omega_\beta w_1), \quad (\text{BFI - inner plume}) \end{aligned} \quad (\text{B.18})$$

The momentum conservation equation for the outer plume assuming BFI is obtained by subtracting (B.18) from (B.8), from which it can be shown that

$$\frac{dM_2}{dz} = \pi (b_2^2 - b_1^2) g'_2 + 2\pi b_1 (\omega_\beta w_1 - \omega_\alpha w_2), \quad (\text{BFI - outer plume}) \quad (\text{B.19})$$

where $g'_2 = g \left(1 - \frac{t_{v,a}}{t_{v,2}}\right)$ and $t_{v,2}$ is the virtual temperature of the outer plume.

B.3 Momentum conservation - BFII

BFII regards the outer plume as the “ambient” for the inner plume. When the lines of constant pressure are not horizontal, momentum conservation must be prescribed by

referring back to the z -component of the Navier-Stokes equation¹ i.e.

$$u \frac{\partial w}{\partial r} + w \frac{\partial w}{\partial z} = -g \frac{\rho}{\rho_0} - \frac{1}{\rho_0} \frac{\partial P}{\partial z}. \quad (\text{B.20})$$

Applying this latter result to the inner plume yields

$$u_1 \frac{\partial w_1}{\partial r} + w_1 \frac{\partial w_1}{\partial z} = -g \frac{\rho_1}{\rho_0} - \frac{1}{\rho_0} \frac{\partial P_1}{\partial z}. \quad (\text{B.21})$$

Note that for a BFII formulation, the external ambient for the inner plume is the outer plume of acceleration $w_2 \frac{dw_2}{dz}$. Analogous to a uniform plume in a quiescent ambient, the pressure within the inner plume reads

$$\frac{dP_1}{dz} = -g\rho_2 - \rho_a w_2 \frac{dw_2}{dz}. \quad (\text{BFII - inner plume pressure}) \quad (\text{B.22})$$

Substituting (B.22) into (B.21) and using the Boussinesq approximation yields

$$u_1 \frac{\partial w_1}{\partial r} + w_1 \frac{\partial w_1}{\partial z} = g \frac{\rho_2 - \rho_1}{\rho_0} + w_2 \frac{dw_2}{dz} = g'_1 - g'_2 + w_2 \frac{dw_2}{dz}, \quad (\text{B.23})$$

where $w_2 \frac{dw_2}{dz}$ corresponds to the acceleration of the outer plume, which is small except near the source where w_2 changes rapidly. Replacing g'_1 in (B.18) with $g'_1 - g'_2 + w_2 \frac{dw_2}{dz}$ yields

$$\frac{dM_1}{dz} = \pi b_1^2 \left(g'_1 - g'_2 + w_2 \frac{dw_2}{dz} \right) + 2\pi b_1 (\omega_\alpha w_2 - \omega_\beta w_1). \quad (\text{BFII - inner plume}) \quad (\text{B.24})$$

The outer plume momentum flux can be inferred by subtracting (B.24) from (B.8), the latter equation describing the momentum flux of the coaxial plume as a whole. On this basis, we find that

$$\frac{dM_2}{dz} = \pi b_1^2 \left(g'_2 - w_2 \frac{dw_2}{dz} \right) + \pi (b_2^2 - b_1^2) g'_2 + 2\pi b_1 (\omega_\beta w_1 - \omega_\alpha w_2). \quad (\text{BFII - outer plume}) \quad (\text{B.25})$$

By rearrangement, (B.25) is rewritten as

$$\frac{dM_2}{dz} = \pi (b_2^2 - b_1^2) \left[g'_2 + \frac{b_1^2}{b_2^2 - b_1^2} \left(g'_2 - w_2 \frac{dw_2}{dz} \right) \right] + 2\pi b_1 (\omega_\beta w_1 - \omega_\alpha w_2), \quad (\text{B.26})$$

where the term $g'_2 + \frac{b_1^2}{b_2^2 - b_1^2} \left(g'_2 - w_2 \frac{dw_2}{dz} \right)$ is the buoyant body force of the outer plume. Thus the pressure within the outer plume, P_2 , satisfies

$$-g \frac{\rho_2}{\rho_0} - \frac{1}{\rho_0} \frac{dP_2}{dz} = g'_2 + \frac{b_1^2}{b_2^2 - b_1^2} \left(g'_2 - w_2 \frac{dw_2}{dz} \right). \quad (\text{B.27})$$

¹All equations in the formulation are within an inertial frame of reference.

After some algebra, the outer plume pressure is given by the solution of

$$\frac{dP_2}{dz} = -g\rho_a - \frac{b_1^2}{b_2^2 - b_1^2} \left[g(\rho_a - \rho_2) - \rho_a w_2 \frac{dw_2}{dz} \right]. \quad (\text{BFII - outer plume pressure}) \quad (\text{B.28})$$

When b_1 reduces to zero, i.e. the inner plume vanishes, (B.28) reverts to a hydrostatic form. In the special case where $b_2 - b_1$ is small at the source, the latter term on the RHS of (B.28) is non-negligible. Nonetheless, the theoretical results of Li *et al.* (2018) indicate that the acceleration of the outer plume is only important within a downstream distance of one or two source diameters – see their figures 3.2 c and 3.4 c. Thus the outer plume pressure can still be reasonably approximated by the hydrostatic relation, i.e. $\frac{dP_2}{dz} = -g\rho_a$. The reduced gravities for the inner and outer plume can be given as a function of pressure and virtual temperature as follows:

$$g'_1 = g \frac{\rho_a - \rho_1}{\rho_a} = g \left(1 - \frac{\frac{P_1}{Ra t_{v,1}}}{\frac{P_a}{Ra t_{v,a}}} \right) = g \left(1 - \frac{P_1}{P_a} \frac{t_{v,a}}{t_{v,1}} \right), \quad (\text{B.29})$$

$$g'_2 = g \frac{\rho_a - \rho_2}{\rho_a} = g \left(1 - \frac{\frac{P_2}{Ra t_{v,2}}}{\frac{P_a}{Ra t_{v,a}}} \right) = g \left(1 - \frac{P_2}{P_a} \frac{t_{v,a}}{t_{v,2}} \right), \quad (\text{B.30})$$

where P_1 and P_2 are calculated using (B.22) and the hydrostatic relation, respectively.

Appendix C

Derivation of the integral form of governing equations for a uniform plume in windy ambient

C.1 Control volume analysis for uniform plume in a windy ambient

Wind can influence the entrainment and trajectory of the plume simultaneously, and these effects must be quantified from a modeling point of view. Thus, in addition to the assumptions (i)-(iv) made in Appendix B, other assumptions are made as follows:

- (v) Wind can impart horizontal momentum to the plume through direct entrainment (due to the plume's self-generated turbulence) and pressure difference (the so-called drag hypothesis¹).
- (vi) The ambient flow is horizontally homogeneous and can have arbitrary vertical profile, i.e. $U_a = U_a(z)$ (see figure C.1).
- (vii) The cross section of the plume in a windy ambient is assumed to be elliptical rather than circular.

The entrainment formulation, as the closure condition for the governing equations, will be discussed later. The control volume (hereafter referred to as CV) is the shaded region in figure C.1, which is shown more clearly in figures C.2 and C.3.

¹Davidson (1989) revealed that the incorporation of entrainment alone, e.g. the model of Slawson & Csanady (1971), tends to overestimate the dilution rate and this discrepancy can be resolved by inclusion of either an added mass factor or a drag term in the momentum equation.

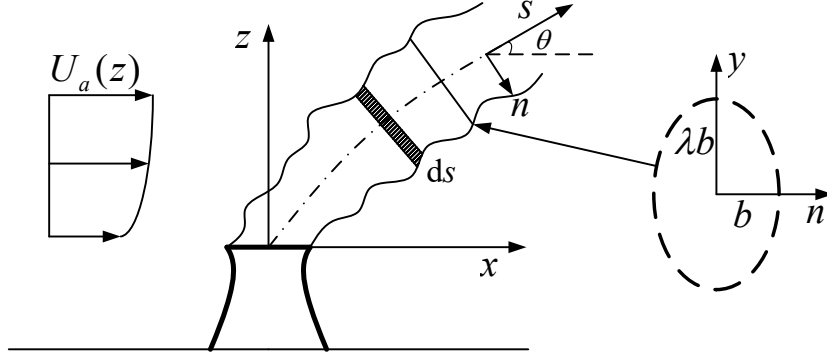


Figure C.1: Schematic of a cooling tower plume in a windy ambient. s and n are the streamwise and normal coordinates, respectively. λb ($\lambda \geq 1$) and b are the respective major and conjugate radii. x and z are the horizontal and vertical axes, and y is the axis into the page.

Defining $Q = \int_A U_p dA = \pi \lambda b^2 U_p$ as the volume flux of the plume, the volume conservation equation for the CV assuming steady, incompressible flow is

$$\sum_{\text{in}} Q = \sum_{\text{out}} Q, \quad (\text{C.1})$$

where $Q + E ds$ and $Q + dQ$ (shown in figure C.2) are the total volume fluxes into and out of the CV, respectively. E is the volume rate of entrainment of ambient fluid per unit length of plume in the streamwise direction. Thus by rearrangement (C.1) is expressed in the following differential form:

$$\frac{dQ}{ds} = E \approx 2\pi b \sqrt{\frac{\lambda^2 + 1}{2}} v_e, \quad (\text{C.2})$$

where v_e is the entrainment velocity from the ambient to the plume.

The kinematic momentum flux of the plume is defined as $M = \int_A U_p^2 dA = \pi \lambda b^2 U_p^2$. The drag force, F_D , is assumed to have the form $C_D \frac{1}{2} \rho_a (U_a \sin \theta)^2 2 \lambda b$ by regarding the CV as a rigid body, where C_D is the drag coefficient with typical values e.g. 1.5 in Wu & Koh (1978) and 2.5 in Schatzmann (1979). The steady linear momentum equation in the x direction reads

$$\sum F_x = \sum_{\text{out}} \rho M_x - \sum_{\text{in}} \rho M_x$$

The LHS is the x -component of the drag force, which is given by

$$\sum F_x = F_D \sin \theta ds$$

The former term on the RHS is given by

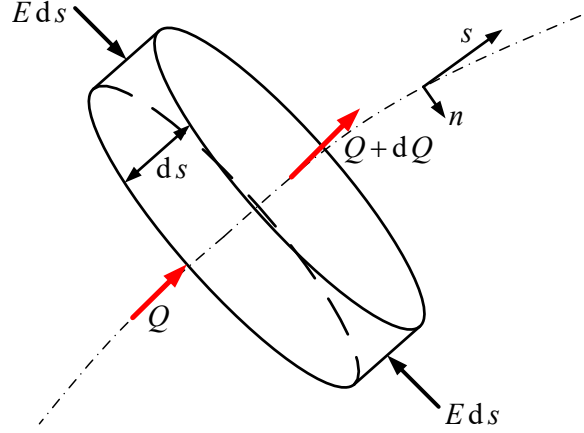


Figure C.2: Mass conservation (or volume conservation for incompressible flow) for the control volume.

$$\sum_{\text{out}} \rho M_x = \rho_p [M \cos \theta + d(M \cos \theta)]$$

The latter term on the RHS is given by

$$\sum_{\text{in}} \rho M_x = \rho_p M \cos \theta + \rho_a (E ds) U_a$$

$$\therefore \frac{d}{ds} (M \cos \theta) = E U_a + C_D \frac{1}{2} (U_a \sin \theta)^2 2 \lambda b \sin \theta. \quad (\text{C.3})$$

Analogously, the z -component momentum equation reads

$$\sum F_z = \sum_{\text{out}} \rho M_z - \sum_{\text{in}} \rho M_z$$

The drag force and buoyant force on the LHS are given by

$$\sum F_z = \mp F_D \cos \theta ds + g (\rho_a - \rho_p) \pi \lambda b^2 ds$$

where the negative (positive) sign occurs when $0 \leq \theta \leq \pi/2$ ($-\pi/2 \leq \theta \leq 0$), respectively.

The former term on the RHS is given by

$$\sum_{\text{out}} \rho M_z = \rho_p (M \sin \theta + d(M \sin \theta))$$

The latter term on the RHS is given by

$$\sum_{\text{in}} \rho M_z = \rho_p M \sin \theta$$

$$\therefore \frac{d}{ds} (M \sin \theta) = g \frac{\rho_a - \rho_p}{\rho_a} \pi \lambda b^2 \mp C_D \frac{1}{2} (U_a \sin \theta)^2 2 \lambda b \cos \theta. \quad (\text{C.4})$$

The conservation equations of thermal energy and moisture are similar to (A.29) and

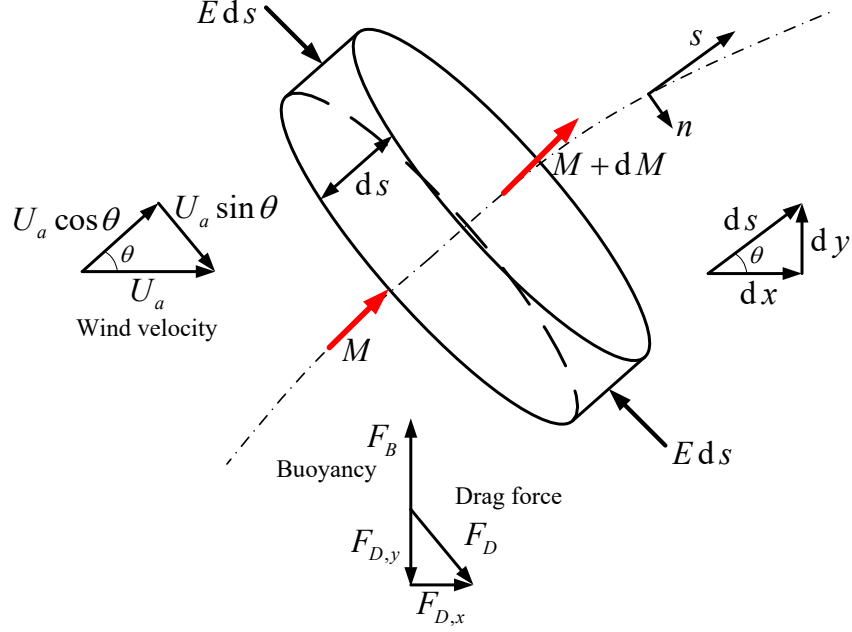


Figure C.3: Momentum conservation for the control volume.

(A.31), and are given respectively by

$$\frac{d}{ds} \left(\Theta - \frac{L_v}{c_{pa}} W \right) = - \left(\frac{dt_a}{dz} + \Gamma_a \right) Q \sin \theta, \quad (\text{C.5})$$

$$\frac{d}{ds} (H + W) = - \frac{dq_a}{dz} Q \sin \theta, \quad (\text{C.6})$$

where $\frac{dt_a}{dz}$ and $\frac{dq_a}{dz}$ are the gradients of temperature and specific humidity in the ambient and Γ_a is the atmospheric adiabatic lapse rate. Specifically, the dry adiabatic lapse rate, Γ_{ad} ($9.8^\circ\text{C}/\text{km}$), is used for the uncondensed portion of the plume; the saturated adiabatic lapse rate, Γ_{as} , is used for the condensed portion of the plume (Wigley & Slawson, 1972). Because different coordinates are used in (C.5) and (C.6), the following geometrical relations are given as

$$\frac{dx}{ds} = \cos \theta, \quad (\text{C.7})$$

$$\frac{dz}{ds} = \sin \theta. \quad (\text{C.8})$$

Thus (C.2) to (C.8) form the governing equations for a uniform moist plume in a windy ambient. The closure condition, i.e. the entrainment assumption, is discussed in section C.2.

C.2 Entrainment in a windy ambient

The near-field entrainment is dominated by the plume’s self-generated turbulence as compared to atmospheric turbulence. This latter effect is only important in the far field where the plume is largely diluted. Attempts have been made to quantify the effect of atmospheric turbulence – see Chapter 2 for details. In this section, we do not attempt to quantify the effect of atmospheric turbulence in the near field.

In a crosswind, a plume near the source is quasi-vertical before it is bent over by the wind. At this quasi-vertical stage, the entrainment can be parameterized by G.I. Taylor’s entrainment hypothesis, i.e. $v_e = \gamma_1|U_p - U_a \cos \theta|$, which quantifies the entrainment associated with the velocity difference between the plume and the ambient fluid in the streamwise direction. At the later bent-over stage, the plume quickly approaches the wind velocity and behaves like a line thermal; the associated entrainment is expressed as $v_e = \gamma_2|U_a \sin \theta|$ where $U_a \sin \theta$ is the normal component of the wind velocity as shown in figure C.3. Assuming that the two aforementioned entrainment mechanisms are linearly additive, the total entrainment is given as

$$v_e = \gamma_1|U_p - U_a \cos \theta| + \gamma_2|U_a \sin \theta|, \quad (\text{C.9})$$

which has been adapted by studies such as Hoult & Weil (1972) and Winiarski & Frick (1976). A slight modification to (C.9) is proposed to completely (or partially) eliminate the effect of entrainment due to a line thermal at the quasi-vertical stage. By this modification,

$$v_e = \gamma_1|U_p - U_a \cos \theta| + \gamma_2|U_a \sin \theta| \cos \theta, \quad (\text{C.10})$$

where a correction factor, $\cos \theta$, is added in the latter term on the RHS. Equation (C.10) has been used by studies such as Abraham (1970) and Wu & Koh (1978). Given identical values of γ_1 and γ_2 , (C.9) results in more dilution than (C.10) particularly in the quasi-vertical stage. More recently, Devenish *et al.* (2010b) proposed a more general entrainment formulation, which is given as

$$v_e = \sqrt[n]{(\gamma_1|U_p - U_a \cos \theta|)^n + (\gamma_2|U_a \sin \theta|)^n}. \quad (\text{C.11})$$

Devenish *et al.* (2010b) found that the above formulation with $n = 3/2$ produces good agreement with their numerical results and observations. The entrainment coefficients reported in related literature are summarized in table C.1.

Table C.1: “Top-hat” entrainment coefficients (γ_1 and γ_2) for plume in a crosswind.

Entrainment formulations	γ_1	γ_2
Hoult & Weil (1972)	0.11	0.6
Wu & Koh (1978)*	0.116	0.3536
Ooms & Mahieu (1981)*	0.081	0.5
Webster & Thomson (2002)*	0.11	0.5
Devenish <i>et al.</i> (2010 <i>b</i>)	0.1	0.5
Turner (1973)	–	0.6

* models with drag force hypothesis.

C.3 Dry uniform plume theory vs. experiment

Defining the flux parameters as $Q = \pi \lambda b^2 U_p$, $M = \pi \lambda b^2 U_p^2$ and $F = \pi \lambda b^2 U_p g'$ where $g' = g \frac{\rho_a - \rho_p}{\rho_a}$, the conservation equations of volume, horizontal and vertical momentum and buoyancy read as follows:

$$\frac{dQ}{ds} = I_s \sqrt{\frac{Q^2}{M}} v_e, \quad (\text{C.12})$$

$$\frac{d}{ds} (M \cos \theta) = I_s \sqrt{\frac{Q^2}{M}} v_e U_a, \quad (\text{C.13})$$

$$\frac{d}{ds} (M \sin \theta) = \frac{FQ}{M}, \quad (\text{C.14})$$

$$\frac{dF}{ds} = -QN^2 \sin \theta, \quad (\text{C.15})$$

where $N = \left(-\frac{g}{\rho_a} \frac{d\rho_a}{dz}\right)^{1/2}$ is the Brunt-Väisälä frequency and $I_s = \sqrt{\frac{2\pi(\lambda^2+1)}{\lambda}}$ is a geometrical constant associated with the presumed elliptical cross section. We only consider unstratified ambient conditions, i.e. $N = 0$, in the remainder of this section.

Another major type of theoretical model adds the contribution of plume bending due to pressure difference. To this end, the momentum equations (C.13) and (C.14) are modified as

$$\frac{d}{ds} (M \cos \theta) = I_s \sqrt{\frac{Q^2}{M}} v_e U_a + C_D \frac{1}{2} (U_a \sin \theta)^2 2\lambda \sqrt{\frac{Q^2}{\pi \lambda M}} \sin \theta, \quad (\text{C.16})$$

$$\frac{d}{ds} (M \sin \theta) = \frac{FQ}{M} - C_D \frac{1}{2} (U_a \sin \theta)^2 2\lambda \sqrt{\frac{Q^2}{\pi \lambda M}} \cos \theta, \quad (\text{C.17})$$

where $0 \leq \theta \leq \pi/2$ is assumed because the ambient is unstratified.

Analogous to the comparison in Tohidi & Kaye (2016), we compare Briggs’s “two thirds” law (Briggs, 1984), Hoult & Weil (1972), the Abraham type models (labeled with * in table

C.1) and Devenish *et al.* (2010*b*) with the experimental data of Contini & Robins (2001). The generalized Briggs's equation reads

$$z = \left[\frac{3 F_m x}{\beta_1^2 U_a^2} + \frac{3 F_b x^2}{2 \beta_2^2 U_a^3} \right]^{1/3}, \quad (\text{C.18})$$

where $\beta_1 = 0.4 + 1.2 \frac{U_a}{U_0}$ and $\beta_2 = 0.6$. The source specific buoyancy flux is $F_b = g \frac{\rho_a - \rho_0}{\rho_a} U_0 r_0^2$, in m^4/s^3 , where ρ_a is the density of ambient air, ρ_0 is the plume source density and r_0 is the plume source radius. The source specific momentum flux is $F_m = \frac{\rho_0}{\rho_a} U_0^2 r_0^2$, in m^4/s^2 .

To compare different theoretical formulations with the laboratory experiments summarized in table C.2, we choose the constant entrainment coefficients, $\gamma_1 = 0.1$ and $\gamma_2 = 0.6$. The latter is the entrainment coefficient for a cylindrical thermal (Turner, 1973). The ratio of the major to conjugate radii is assigned as $\lambda = 1.2$ according to the experimental measurements of Contini *et al.* (2011). The drag coefficient is assigned as $C_D = 1.5$, which is the default value used in Wu & Koh (1978). The comparisons between theory and experiment for cases 1 to 4, 5 to 8 and 9 to 12 are given in figures C.4, C.5 and C.6, respectively. In contrast to the overestimation of plume height in Tohidi & Kaye (2016), the Abraham formulation with the drag hypothesis results in good agreement with experimental results. Except the Abraham formulation, the Devenish formulation has better agreement in the near-field plume trajectory ($0 \leq x/D_0 \leq 20$) than do the other formulations. Excluding the drag hypothesis which is up to debate, we conclude that the Devenish formulation is probably most appropriate for modeling bent-over plumes.

Table C.2: Experimental conditions for turbulent plumes in neutral crossflows (Contini & Robins, 2001).

Experiment	D_0 (mm)	$\frac{\rho_0 - \rho_a}{\rho_a}$	Q_0 (l min ⁻¹)	U_a (cm s ⁻¹)	U_a/U_0	Fr
1	7	0.097	0.56	4.68	0.19	2.97
2				8.86	0.37	2.97
3				13.05	0.54	2.97
4				21.4	0.88	2.97
5	7	0.097	1.00	4.68	0.11	5.31
6				8.86	0.20	5.31
7				13.05	0.30	5.31
8				21.4	0.49	5.31
9	7	0.097	1.83	4.68	0.06	9.71
10				8.86	0.11	9.71
11				13.05	0.16	9.71
12				21.4	0.27	9.71

The densimetric Froude number is defined as $Fr = U_0 / \sqrt{g \frac{\rho_0 - \rho_a}{\rho_a} D_0}$.

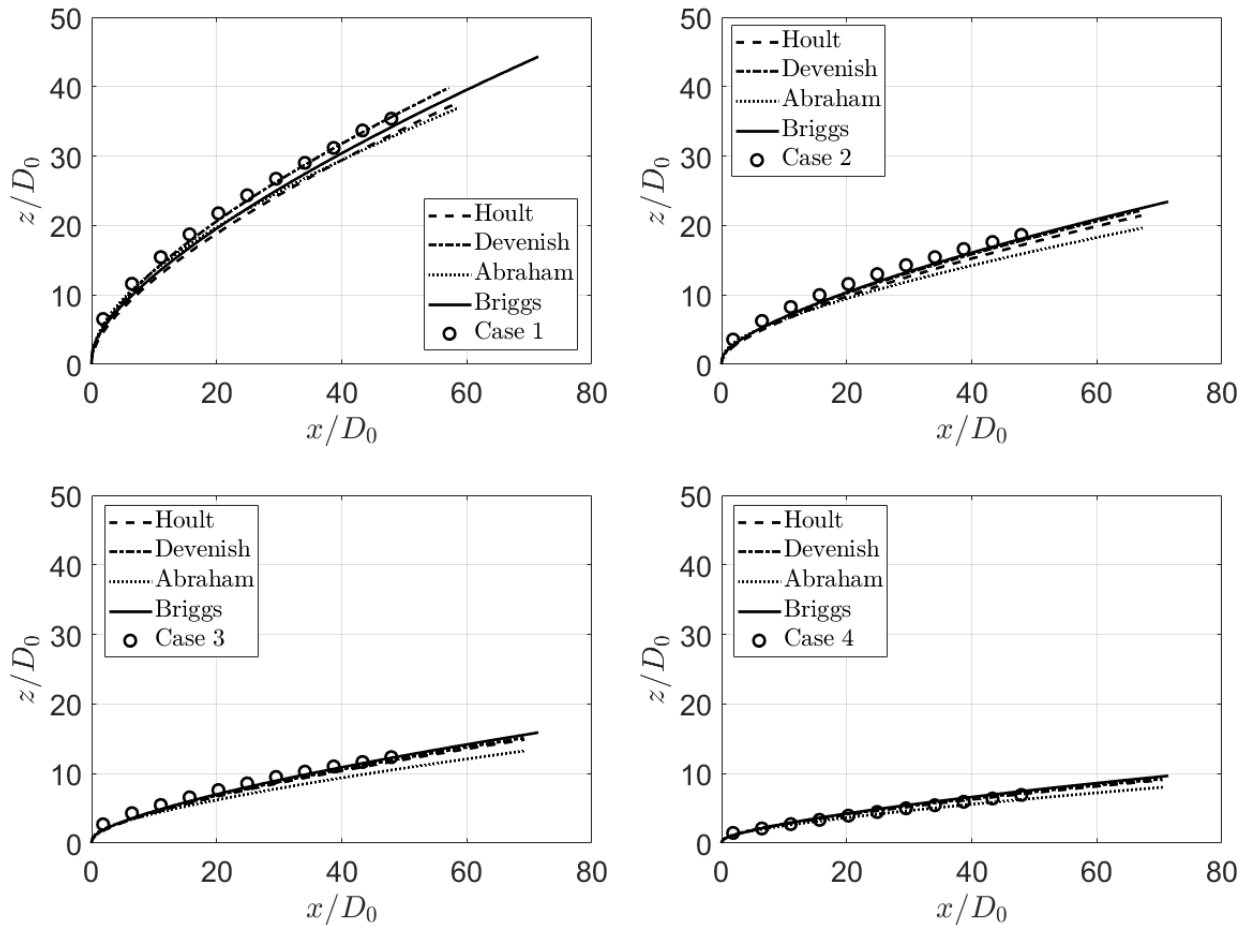


Figure C.4: Theory vs. experiment for cases 1 to 4.

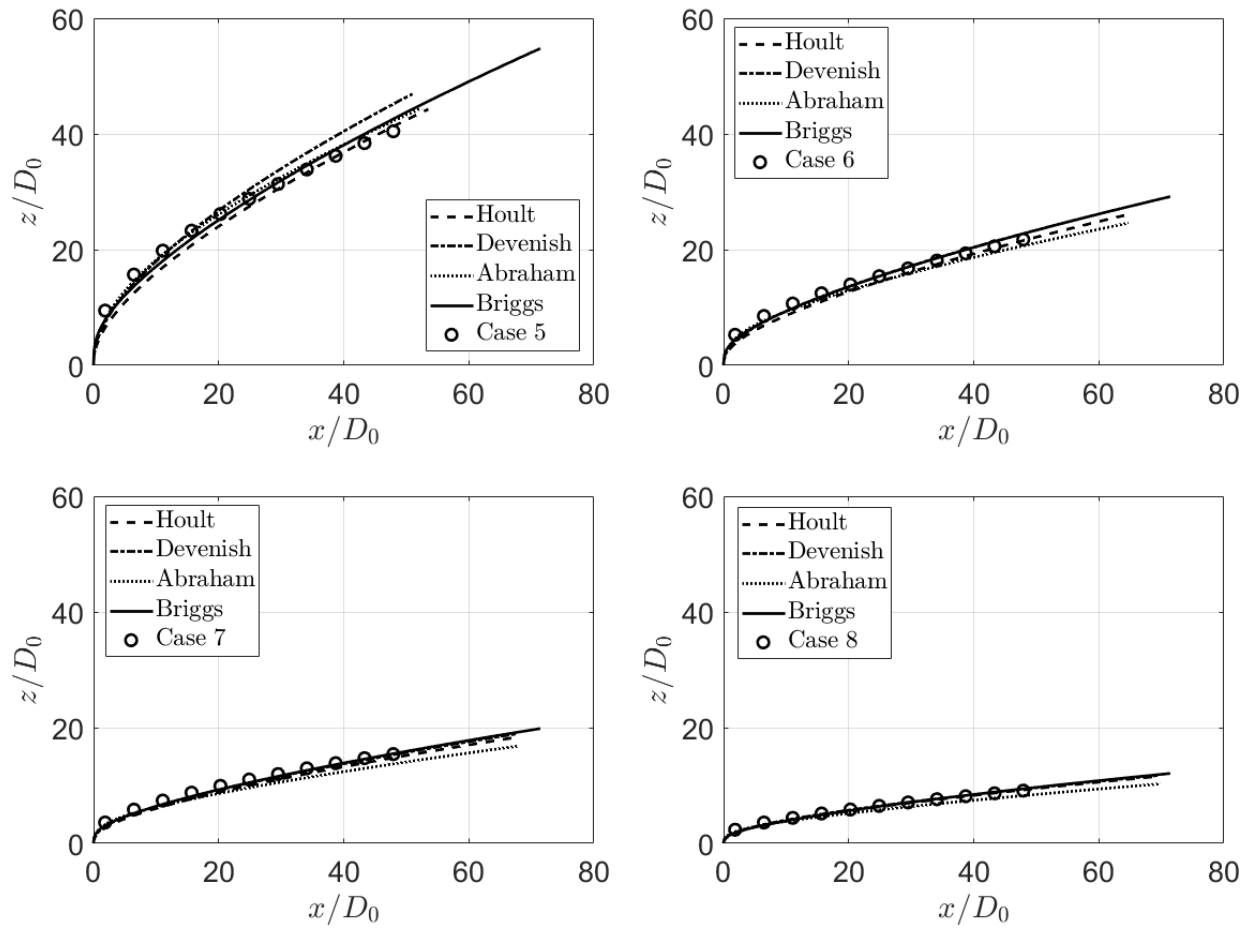


Figure C.5: Theory vs. experiment for cases 5 to 8.

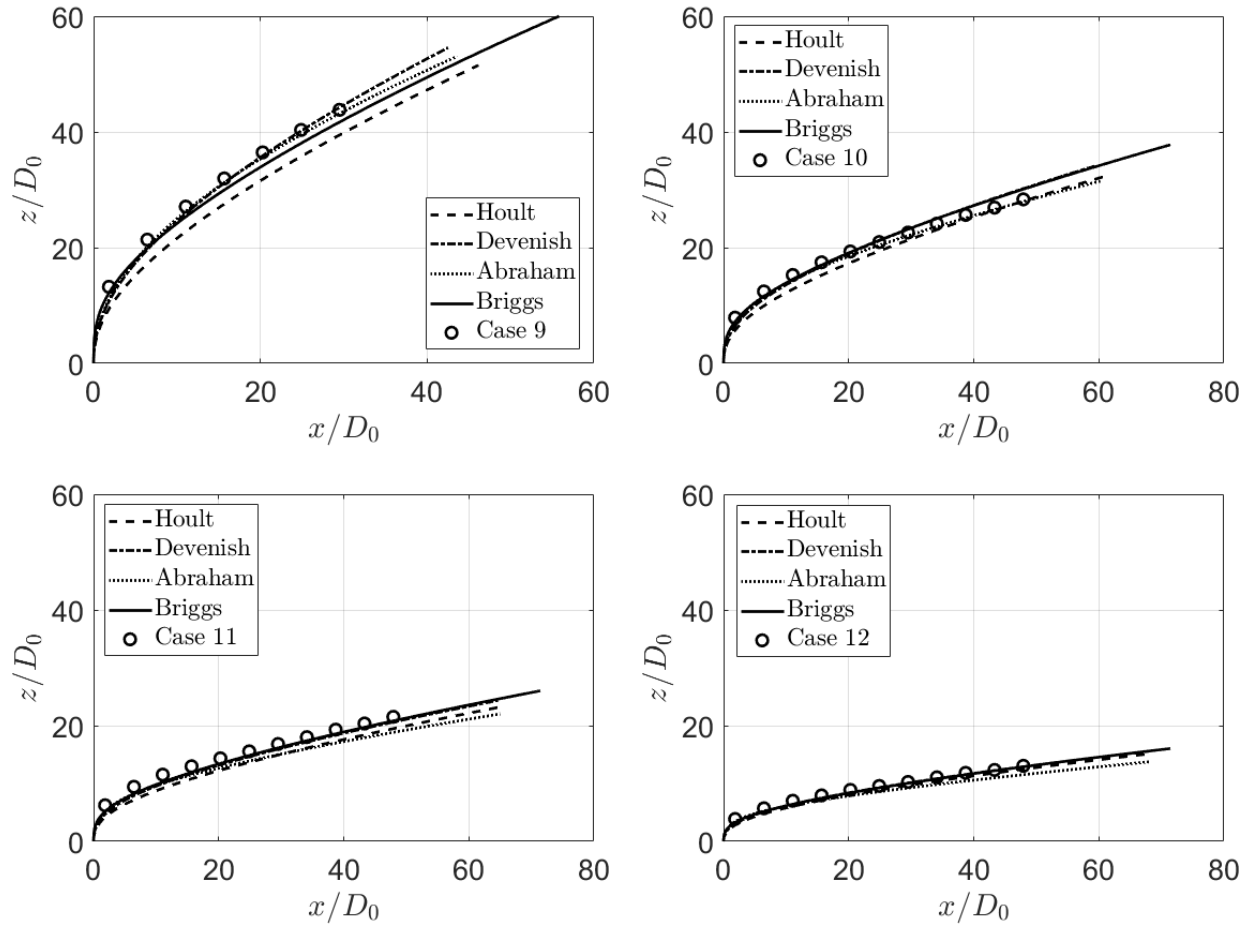


Figure C.6: Theory vs. experiment for cases 9 to 12.

Appendix D

Point source vs. line source plumes

Assuming that a line array of cooling tower plumes merge instantly upon discharge, the flow of interest is a line source plume in either a stationary or flowing ambient environment. For simplicity, we consider an idealized line source plume of length L . The analytical results of a line source plume are compared with the counterpart results of a point source plume.

D.1 Stationary ambient

Assuming top-hat profiles of velocity and buoyancy, the flux parameters are defined as follows: volume flux, $Q = 2Lbw$ where b is the half-width of the line plume, momentum flux, $M = 2Lbw^2$ and buoyancy flux, $F = 2Lbwg'$ where $g' = g \frac{\rho_a - \rho_p}{\rho_a}$. The conservation equations of volume, momentum and buoyancy are given respectively as

$$\frac{dQ}{dz} = 2L\alpha_l w, \quad (\text{D.1})$$

$$\frac{dM}{dz} = 2Lbg', \quad (\text{D.2})$$

$$\frac{dF}{dz} = -N^2 Q, \quad (\text{D.3})$$

where the buoyancy frequency is $N = 0$ for an unstratified ambient and α_l is the entrainment coefficient for a line plume. The half-width and velocity can be expressed as $b = \frac{Q^2}{2LM}$ and $w = \frac{M}{Q}$, respectively. Thus (D.1) and (D.2) can be rewritten respectively as

$$\frac{dQ}{dz} = 2L\alpha_l \frac{M}{Q}, \quad (\text{D.4})$$

$$\frac{dM}{dz} = \frac{FQ}{M}. \quad (\text{D.5})$$

The analytical solutions for Q , M , b , w and g' are respectively as follows:

$$\text{Line source plume} \left\{ \begin{array}{l} Q = (2L \alpha_l)^{2/3} F^{1/3} z \\ M = (2L \alpha_l)^{1/3} F^{2/3} z \\ b = \alpha_l z \\ w = (2L \alpha_l)^{-1/3} F^{1/3} \\ g' = (2L \alpha_l)^{-4/3} F^{4/3} z^{-1} \end{array} \right. \quad (\text{D.6})$$

The counterpart solutions for a point source plume, according to Linden (2000), are given as follows:

$$\text{Point source plume} \left\{ \begin{array}{l} Q = \frac{6}{5} \alpha \left(\frac{9}{10} \alpha \right)^{1/3} \pi^{2/3} F^{1/3} z^{5/3} \\ M = \left(\frac{9}{10} \alpha \right)^{2/3} \pi^{1/3} F^{2/3} z^{4/3} \\ b = \frac{6}{5} \alpha z \\ w = \frac{5}{6\alpha} \left(\frac{9}{10} \alpha \right)^{1/3} \pi^{-1/3} F^{1/3} z^{-1/3} \\ g' = \left(\frac{5}{6\alpha} \right) \left(\frac{9}{10} \alpha \right)^{-1/3} \pi^{-2/3} F^{2/3} z^{-5/3} \end{array} \right. \quad (\text{D.7})$$

where α is the top-hat entrainment coefficient for a point source plume. Comparing (D.6) and (D.7), the vertical velocity of a line plume remains constant whereas the vertical velocity of a point source plume decreases with elevation ($w \propto z^{-1/3}$). The reduced gravity of a line source plume decreases with elevation at a lower rate than does the reduced gravity of the point source plume.

D.2 Windy ambient

In the presence of a crosswind of speed U_a , the kinematic relation implies that

$$\frac{dz}{dx} = \frac{w}{U_a}. \quad (\text{D.8})$$

On dimensional grounds, the rise heights of point and line source plumes, z , scale respectively as

$$z \propto F^{1/3} U_a^{-1} x^{2/3}, \quad (\text{Point source plume}) \quad (\text{D.9})$$

$$z \propto \left(\frac{F}{L} \right)^{1/3} U_a^{-1} x. \quad (\text{Line source plume}) \quad (\text{D.10})$$

Using (D.8), the respective vertical velocities of point and line source plumes scale as

$$w \propto F^{1/3} x^{-1/3}, \quad (\text{Point source plume}) \quad (\text{D.11})$$

$$w \propto \left(\frac{F}{L}\right)^{1/3}. \quad (\text{Line source plume}) \quad (\text{D.12})$$

These scaling laws for bent-over plumes are in a form similar to those for vertical plumes in the case of stationary ambient.

Appendix E

Effect of condensation on plume dynamics

The following discussion uses a relatively rigorous approach to demonstrate the conclusions drawn in Appendix B.3 of Briggs (1975). Cooling tower plumes typically carry one to five times more latent heat than sensible heat. If all the water vapor within the plume were to condense completely, the buoyancy of the plume would increase severalfold resulting in a significant enhancement in plume rise. However, in practice only moderate amounts of water vapor can condense and contribute thermal energy to the surrounding air. Furthermore, since the saturation specific humidity or humidity ratio increases with temperature (see any psychrometric chart), the latent heat released paradoxically enhances the saturation capacity.

Consider the worst case scenario wherein the ambient air is fully saturated so that the cooling tower effluent becomes supersaturated upon discharge. For a graphical display of the aforementioned mixing process, it is helpful to refer to the psychrometric chart shown in figure E.1. Assume we mix m kg air at point 1 (t_1, q_1) with 1 kg air at point 2 (t_2, q_2) so that the resulting mixture at point 3' follows $t_{3'} = (mt_1 + t_2)/(m+1)$ and $q_{3'} = (mq_1 + q_2)/(m+1)$. Because air at point 3' is supersaturated, condensation occurs along a straight line 3'–3. By mass and energy conservation (i.e. $q + \sigma = \text{Const.}$ and $c_{pa} t - L_v \sigma = \text{Const.}$), the slope of line 3'–3 is $dq/dt = -c_{pa}/L_v$. Therefore, the specific liquid moisture is $\sigma = -\int_{3'}^3 dq = q_{3'} - q_3$ and the temperature of air at point 3 is $t_3 = t_{3'} + \frac{L_v \sigma}{c_{pa}}$. The specific liquid moisture as a function of the mixing ratio is shown in figure E.2.

Figure E.2 illustrates that for a fixed value of t_2 , the amount of liquid moisture reaches a maximum when m is approximately equal to unity. Thereafter, the liquid moisture is a monotone decreasing function of the mixing ratio. As expected, the amount of liquid moisture increases as t_1 decreases. For fixed t_1 meanwhile, variations in σ can be determined from the

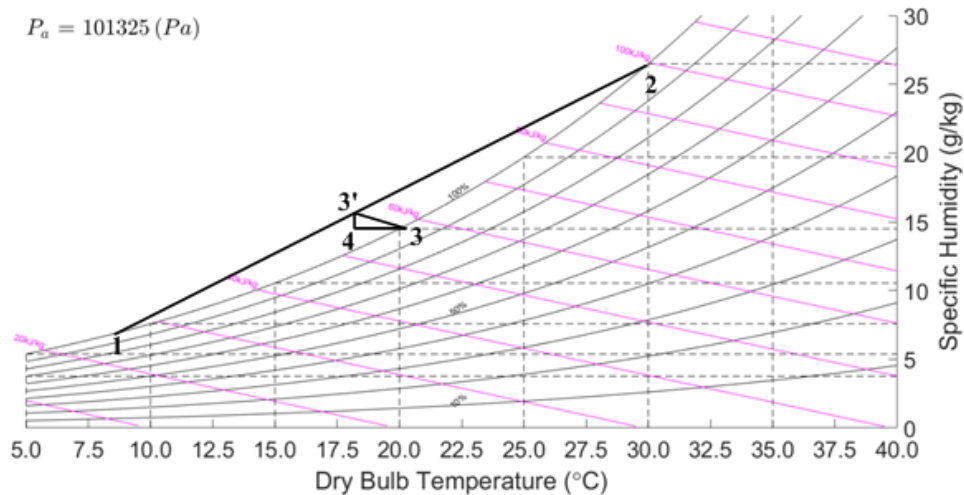


Figure E.1: Mixing process on a psychrometric chart.

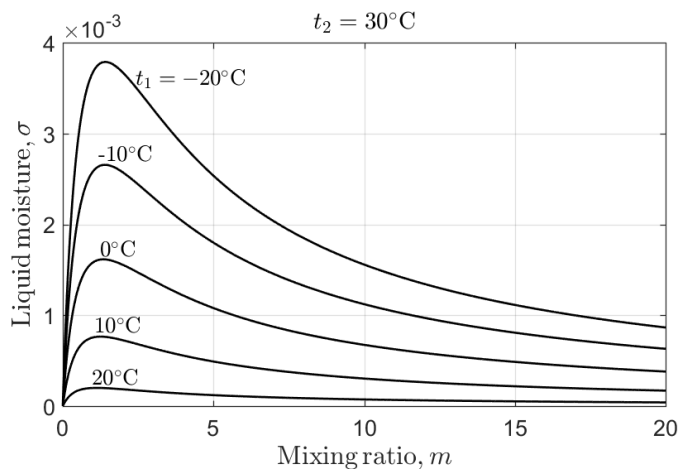


Figure E.2: Specific liquid moisture as a function of mixing ratio.

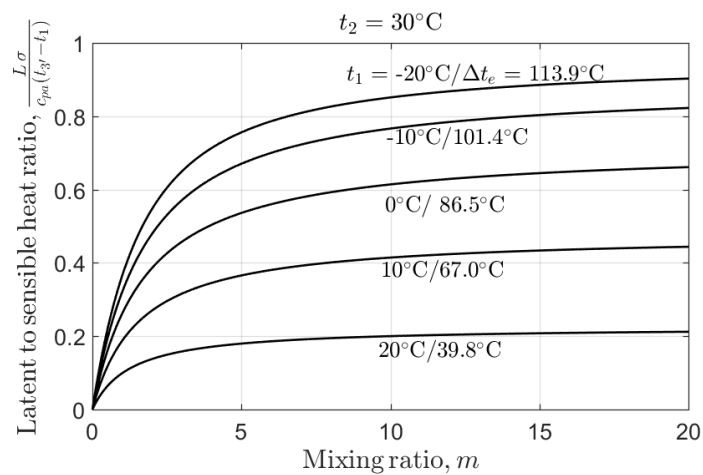


Figure E.3: Latent to sensible heat ratio as a function of mixing ratio.

length of the line segment 3'-3 from figure E.1 (Assuming a temperature-independent value for $-\frac{c_{pa}}{L_v}$, the point 3' moves along the line 2-1.) As t_1 falls, the area bounded by the straight line 1-2 and the saturation curve increases, which elongates 3'-3 thus resulting in a larger volume of liquid moisture.

As regards moist plumes emitted from evaporative cooling towers, Briggs (1975) defined the equivalent temperature excess which occurred if the entire heat load were carried in the form of sensible heat only, $\Delta t_e = \left(1 + \frac{L}{c_{pa}} \frac{q_2 - q_1}{t_2 - t_1}\right) (t_2 - t_1)$, and he stated that $\Delta t_e < 70^\circ\text{C}$ (higher values may cause plant inefficiencies). We further calculate the latent to sensible heat ratio and the so-called equivalent temperature excess shown in figure E.3. Focusing, for illustrative purposes, on the middle curve of this figure, the latent to sensible heat ratio is below 0.7 when $t_1 = 0^\circ\text{C}$, $\Delta t_e = 86.5^\circ\text{C}$ and $0 < m < 20$, which is consistent with Briggs's results. (We may, in fact, say that our results are more conservative because $\Delta t_e = 86.5^\circ\text{C} > 70^\circ\text{C}$). Furthermore, and on the basis of Briggs's "two thirds" law of plume rise, the maximum rise enhancement due to the latent heat is about $(1 + 0.7)^{1/3} - 1 \approx 20\%$.

Appendix F

Merging of two area source plumes in a linearly stratified ambient

Multiple plumes in a stratified ambient has been studied experimentally by He *et al.* (2018), numerically by Lou *et al.* (2019) and theoretically by He & Lou (2019). In the theoretical model of He & Lou (2019), the finite source effect is ignored, considering in particular those source conditions when the plume source diameter is nontrivial compared to the distance between two plume centers. In the following, we first review He and Lou's theory then incorporate the finite source effect.

F.1 Theory of He & Lou (2019)

Consistent with the procedure of Morton *et al.* (1956), the source buoyancy flux, F_0 , and the buoyancy frequency, N , are used for nondimensionalization. The dimensionless vertical velocity, volume flux, buoyancy flux and vertical distance are given respectively as follows:

$$\hat{w} = wF_0^{-1/4}N^{-1/4}, \quad \hat{Q} = QF_0^{-3/4}N^{5/4}, \quad \hat{F} = FF_0^{-1}, \quad \hat{z} = zF_0^{-1/4}N^{3/4}. \quad (\text{F.1})$$

Thus the generalized plume equations proposed by Rooney (2015) can be nondimensionalized as

$$\frac{d\hat{w}}{d\hat{z}} = \frac{\hat{F}}{\hat{w}\hat{Q}} - \frac{\hat{R}\hat{w}^2}{\hat{Q}}\alpha f_e f_m, \quad (\text{F.2})$$

$$\frac{d\hat{Q}}{d\hat{z}} = \alpha \hat{R}\hat{w} f_e f_m, \quad (\text{F.3})$$

$$\frac{d\hat{F}}{d\hat{z}} = -\hat{Q}, \quad (\text{F.4})$$

where $\hat{R} = RF_0^{-1/4}N^{3/4}$ and $f_e = \frac{\pi k}{(k+1)^{1/2}}$. The entrainment coefficient, α , is treated as a variable depending on the plume Richardson number, which is given by

$$\alpha = \alpha_j \exp \left[\ln \left(\frac{\alpha_p}{\alpha_j} \right) \left(\frac{\text{Ri}}{\text{Ri}_p} \right) \right], \quad (\text{F.5})$$

where $\alpha_j = 0.07566$ and $\alpha_p = 0.1178$ are the respective entrainment coefficients for pure jet and pure plume, and the Richardson number is defined as

$$\text{Ri} = (\text{sgn } \hat{F}) |\hat{F}|^{1/2} \hat{Q}^{-1/4} \hat{w}^{-5/4}, \quad (\text{F.6})$$

for which $\text{Ri}_p = 0.557$ for pure plume balance. Above the neutral buoyancy level, the flow behaves like a fountain and $\alpha = \alpha_j$ is assumed. Note that Ri is proportional to the flux-balance parameter, Γ . Considering plume merger, a modified Richardson number is proposed as

$$\text{Ri}_m(z) = \left[\frac{2^{1/4} - 1}{1 + \exp(-10(k-1))} + 1 \right] \text{Ri}(z), \quad (\text{F.7})$$

which allows $\text{Ri}_m \rightarrow \text{Ri}$ when $k \ll 1$ and $\text{Ri}_m \rightarrow 2^{1/4} \text{Ri}$ when $k \gg 1$. f_m is a correction factor for the entrainment assumption, which is given as

$$f_m = k^2 \exp(-k^2) + 1, \quad (\text{F.8})$$

where the maximum value occurs when $k = 1$.

The solution procedure to (F.2)-(F.4) is similar to that in Rooney (2015, 2016). The main difference is an additional initial condition, i.e. $\hat{F}(\hat{z} = 0) = 1$. Strictly speaking, Rooney's theory is only applicable to small source plumes ($\rho_0 = r_0/R$ is small) because the velocity potential contours start to distort from a circular shape as k increases. Noticeably, table I of He & Lou (2019) shows that the nonideal plumes from the experiments of He *et al.* (2018) tend to recover nonnegligible k_0 values, especially for the cases with $2R = 1.5 \times 10^{-2}$ m ($k_0 = 0.873$) and $2R = 3.0 \times 10^{-2}$ m ($k_0 = 0.461$). To this end, introducing a finite source and thereby correcting the noncircular shape at the source is expected to improve the comparison between theory and experiment.

F.2 Finite source effect

With a finite radius ρ_0 , the parameter f_e is modified as (Li & Flynn, 2020*b*)

$$f_e = \frac{\pi \left[k^2 + \rho_0^4 + 4\rho_0^2 + 2\rho_0^2 (k^2 + 4\rho_0^2)^{1/2} \right] (k^2 + 4\rho_0^2)^{1/2}}{\left[1 + \rho_0^2 + (k^2 + 4\rho_0^2)^{1/2} \right]^{1/2} \left[k^2 + 4\rho_0^2 + \rho_0^2 (k^2 + 4\rho_0^2)^{1/2} \right]}. \quad (\text{F.9})$$

Correspondingly, (F.7) is modified as

$$\text{Ri}_m(z) = \left[\frac{2^{1/4} - 1}{1 + \exp(-10(k - 1 + \rho_0^2))} + 1 \right] \text{Ri}(z), \quad (\text{F.10})$$

and (F.8) is modified as

$$f_m = \left(\frac{k}{1 - \rho_0^2} \right)^2 \exp \left[- \left(\frac{k}{1 - \rho_0^2} \right)^2 \right] + 1. \quad (\text{F.11})$$

F.3 Maximum rise height

We choose six cases in table I of He & Lou (2019) for comparison, which are listed in table F.1. The amplification coefficient ζ , defined as the ratio of the maximum rise height of two merging plumes to the counterpart rise height of an isolated plume, is shown in figure F.1. It is evident that for most cases, the present (finite source) model predicts slightly better agreement with numerical and experimental results compared to the model of He & Lou (2019). For larger separation distances (results not shown here), He & Lou (2019) found that Rooney's model results in a slight overestimation (around 3%) of ζ compared to the measured results of He *et al.* (2018). Of course, this discrepancy can be attributed to the neglect of the fountain-like flow behavior (including fountain top entrainment) and the expected impingement and merging of the laterally spreading gravity currents. However, it should be pointed out that Rooney's model, with applications to a stratified ambient, seems to allow plume merger to occur even though the plume sources are spaced sufficiently far apart. For clarity, we examine the derivative of the cross-sectional area, $\hat{A} = \hat{Q}/\hat{w} = A \left(\hat{R}/R \right)^2$, which is defined mathematically by

$$\frac{d\hat{A}}{d\hat{z}} = 2\alpha\hat{R}f_e f_m - \frac{\hat{F}}{\hat{w}^3}. \quad (\text{F.12})$$

Thus the decrease in \hat{F} serves to enhance the rate of increase in \hat{A} . Apparently, there is a sharp increase in \hat{A} when \hat{F} changes sign below and above the neutral buoyancy height. At this level, and returning to Rooney's theory whereby \hat{A} corresponds to the area of the velocity potential contours, the individual plumes are forced to merge due to the large increase in \hat{A} .

Another phenomenon worth noting is that the amplification coefficient can be below unity – see e.g. the magenta square predicted in the numerical simulation of Lou *et al.* (2019) for case 6 in table F.1. This is probably due to the merging of the downflowing outer plumes in the upper turbulent fountain flow. For simplicity, we consider the merging of two turbulent

Table F.1: Cases with nonnegligible ρ_0 in table I of He & Lou (2019). The numbers in brackets correspond to the case numbers in table I of He & Lou (2019).

Cases	ρ_0	\hat{R}	Ri_0
1 (11)	0.467	0.178	0.174
2 (6)	0.467	0.195	0.276
3 (1)	0.467	0.220	0.421
4 (12)	0.233	0.352	0.173
5 (7)	0.233	0.384	0.275
6 (2)	0.233	0.443	0.423

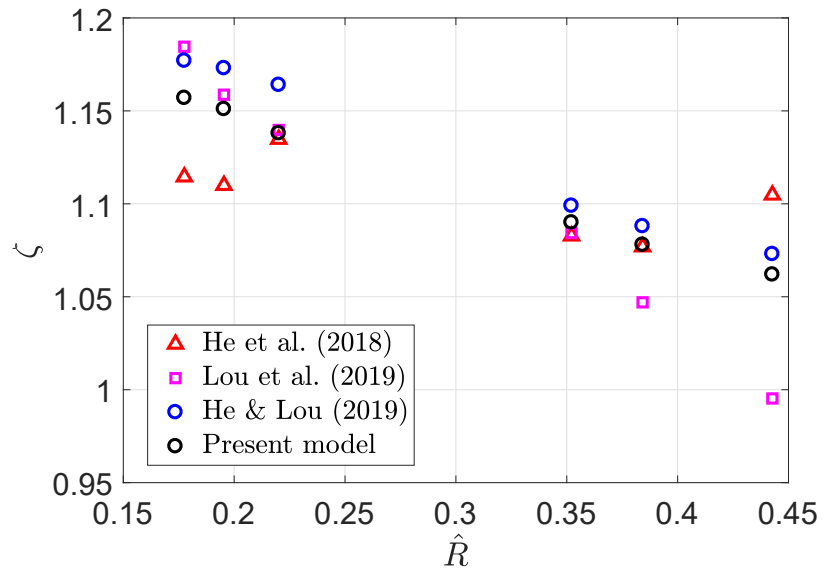


Figure F.1: [Color] Amplification coefficient, ζ , as a function of the dimensionless separation distance, \hat{R} .

fountains as shown in figure F.2. The right panel of figure F.2 shows a special case wherein the downflowing outer plumes begin to merge. It is expected that the combined outer plume post merger is denser than an isolated outer plume. This former denser outer plume fluid is subsequently entrained into the upflowing (negatively) buoyant jet, which now “carries” heavier fluid. As a result, the final fountain rise height decreases when the outer plumes merge. A future work of possible interest is to couple turbulent fountain models (Bloomfield & Kerr, 2000; Hunt & Debugne, 2016) and the plume merger model of Rooney (2015, 2016).

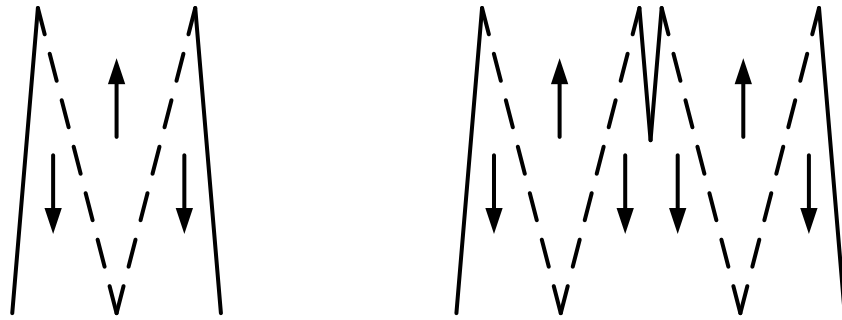


Figure F.2: Schematics of single (left) and two merging (right) turbulent fountains. Dashed and solid lines represent the boundaries of the inner (upflow) and outer (downflow) plumes, respectively. The arrows denote the flow directions.